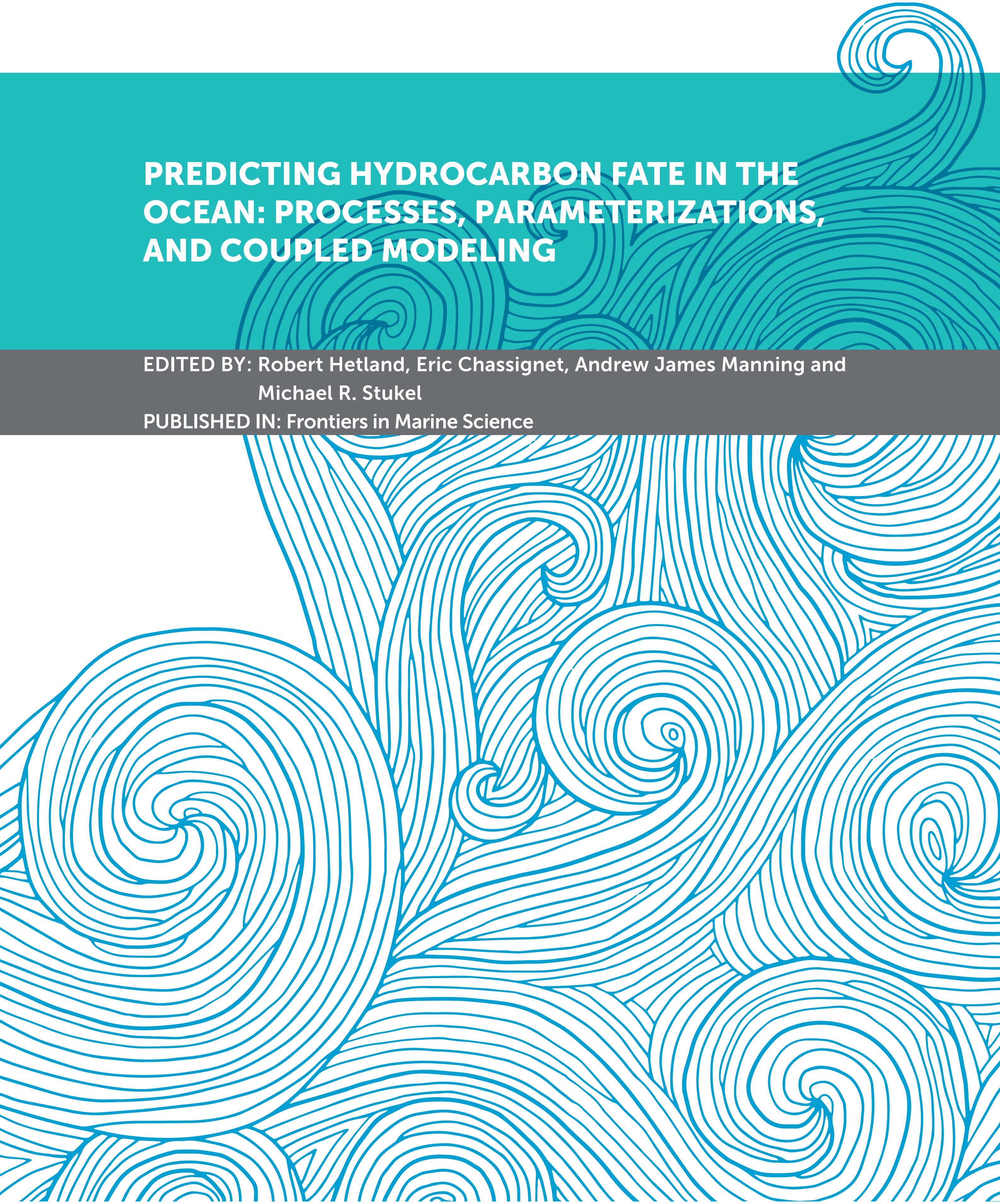

PREDICTING HYDROCARBON FATE IN THE OCEAN: PROCESSES, PARAMETERIZATIONS, AND COUPLED MODELING

EDITED BY: Robert Hetland, Eric Chassignet, Andrew James Manning and
Michael R. Stukel

PUBLISHED IN: Frontiers in Marine Science

frontiers Research Topics

ISSN 1664-8714
ISBN 978-2-88974-734-4
DOI 10.3389/978-2-88974-734-4

About Frontiers

Frontiers is more than just an open-access publisher of scholarly articles: it is a pioneering approach to the world of academia, radically improving the way scholarly research is managed. The grand vision of Frontiers is a world where all people have an equal opportunity to seek, share and generate knowledge. Frontiers provides immediate and permanent online open access to all its publications, but this alone is not enough to realize our grand goals.

Frontiers Journal Series

The Frontiers Journal Series is a multi-tier and interdisciplinary set of open-access, online journals, promising a paradigm shift from the current review, selection and dissemination processes in academic publishing. All Frontiers journals are driven by researchers for researchers; therefore, they constitute a service to the scholarly community. At the same time, the Frontiers Journal Series operates on a revolutionary invention, the tiered publishing system, initially addressing specific communities of scholars, and gradually climbing up to broader public understanding, thus serving the interests of the lay society, too.

Dedication to Quality

Each Frontiers article is a landmark of the highest quality, thanks to genuinely collaborative interactions between authors and review editors, who include some of the world's best academicians. Research must be certified by peers before entering a stream of knowledge that may eventually reach the public - and shape society; therefore, Frontiers only applies the most rigorous and unbiased reviews.
Frontiers revolutionizes research publishing by freely delivering the most outstanding research, evaluated with no bias from both the academic and social point of view. By applying the most advanced information technologies, Frontiers is catapulting scholarly publishing into a new generation.

What are Frontiers Research Topics?

Frontiers Research Topics are very popular trademarks of the Frontiers Journals Series: they are collections of at least ten articles, all centered on a particular subject. With their unique mix of varied contributions from Original Research to Review Articles, Frontiers Research Topics unify the most influential researchers, the latest key findings and historical advances in a hot research area! Find out more on how to host your own Frontiers Research Topic or contribute to one as an author by contacting the Frontiers Editorial Office: frontiersin.org/about/contact

PREDICTING HYDROCARBON FATE IN THE OCEAN: PROCESSES, PARAMETERIZATIONS, AND COUPLED MODELING

Topic Editors:
Robert Hetland, Texas A&M University, United States
Eric Chassignet, Florida State University, United States
Andrew James Manning, HR Wallingford, United Kingdom
Michael R. Stukel, Florida State University, United States

Citation: Hetland, R., Chassignet, E., Manning, A. J., Stukel, M. R., eds. (2022). Predicting Hydrocarbon Fate in the Ocean: Processes, Parameterizations, and Coupled Modeling. Lausanne: Frontiers Media SA. doi: 10.3389/978-2-88974-734-4

Table of Contents

frontiers
in Marine Science

ORIGINAL RESEARCH
published: 27 January 2021
doi: 10.3389/fmars.2020.605804

Very High Resolution Tools for the Monitoring and Assessment of Environmental Hazards in Coastal Areas

Guillermo García-Sánchez[1], **Ana M. Mancho**[1*], **Antonio G. Ramos**[2], **Josep Coca**[2], **Begoña Pérez-Gómez**[3], **Enrique Álvarez-Fanjul**[3], **Marcos G. Sotillo**[3], **Manuel García-León**[3], **Víctor J. García-Garrido**[4] and **Stephen Wiggins**[5]

[1] Instituto de Ciencias Matemáticas, CSIC, Madrid, Spain, [2] División de Robótica y Oceanografía Computacional, IUSIANI, Universidad de Las Palmas de Gran Canaria, Las Palmas de Gran Canaria, Spain, [3] Área de Conocimiento y Análisis del Medio Físico, Ente Público Puertos del Estado, Spain, [4] Departamento de Física y Matemáticas, Universidad de Alcalá, Alcalá de Henares, Spain, [5] School of Mathematics, University of Bristol, Bristol, United Kingdom

OPEN ACCESS

Edited by:
Andrew James Manning,
HR Wallingford, United Kingdom

Reviewed by:
Andrea Cucco,
National Research Council (CNR), Italy
Manu Soto,
University of the Basque Country, Spain

***Correspondence:**
Ana M. Mancho
a.m.mancho@icmat.es

Specialty section:
This article was submitted to Marine Pollution, a section of the journal Frontiers in Marine Science

Received: *13 September 2020*
Accepted: *23 December 2020*
Published: *27 January 2021*

Citation:
García-Sánchez G, Mancho AM, Ramos AG, Coca J, Pérez-Gómez B, Álvarez-Fanjul E, Sotillo MG, García-León M, García-Garrido VJ and Wiggins S (2021) Very High Resolution Tools for the Monitoring and Assessment of Environmental Hazards in Coastal Areas. Front. Mar. Sci. 7:605804. doi: 10.3389/fmars.2020.605804

Recently, new steps have been taken for the development of operational applications in coastal areas which require very high resolutions both in modeling and remote sensing products. In this context, this work describes a complete monitoring of an oil spill: we discuss the performance of high resolution hydrodynamic models in the area of Gran Canaria and their ability for describing the evolution of a real-time event of a diesel fuel spill, well-documented by port authorities and tracked with very high resolution remote sensing products. Complementary information supplied by different sources enhances the description of the event and supports their validation.

Keywords: high resolution radar, high resolution hydrodynamic model, dynamical systems, coastal monitoring and management, model assessment and verification

1. INTRODUCTION

On Friday 21st April 2017, the passenger ferry “Volcán de Tamasite” collided with the “Nelson Mandela” dike of the Port of La Luz (Las Palmas de Gran Canaria) at 7:00 p.m.. As a consequence of the impact, two of the outermost fuel supply pipes along the dike were broken and diesel fuel poured into the sea. The national pollution alert was declared at 7:30 p.m., and the company responsible for the pipelines started working on emptying the damaged pipes. These works ended on the 24th of April 2017. Around 65 m^3 of diesel fuel was estimated to be spilled along the Northeastern (NE) sector of Gran Canaria island. The rate of evaporation/dispersion ranged from 80% by day. On the 23rd of April at 7:00 a.m., satellite images reported the two major spill spots targeted near the coast. Both spots, of 0.9 and 2.4 km^2, respectively, were dispersed at ground level at the NE sector of the island, 12 km far south from the Port of La Luz, by the Maritime Security Service fleet (SASEMAR). Consistently, on this day, local newspapers reported a 13 km long fuel filament placed 1 km far away, at the east of Gran Canaria (TeldeActualidad/EFE, 2017). The national pollution alert ended on the 25th of April, although the monitoring and surveillance along the eastern sector of the island continued until the 5th of May. Along these days, some scarce and dispersed pollutant spots were reported and tracked by aerial and marine surveys some miles away from the coast until that date, when the event was officially declared as “finished” (CIAIM, 2018). **Figure 1** displays the ferry crash point (in red) together with some specific coastal areas, where the arrival of pollution could have

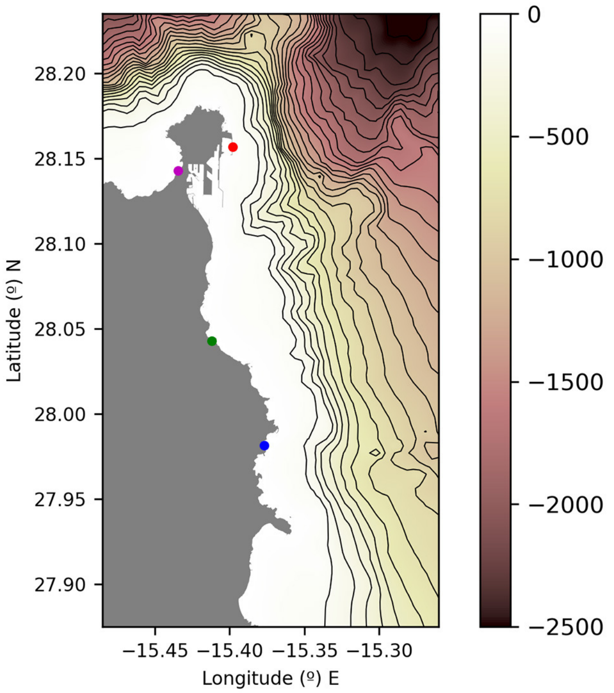

FIGURE 1 | A map of the N-NE Gran Canaria Coast, displaying the ferry crash point (red) together with some highly vulnerable regions. These areas are: Las Canteras beach in the city of Las Palmas (magenta), a desalinization/hydroelectric power plant (green), and the Port of Taliarte (fishing and aquaculture facilities) (blue). Contourlines represent the bathymetry in meters.

a very negative impact (in magenta, green and blue). These vulnerable areas are: Las Canteras, a beach in the city of Las Palmas, along with a desalinization plant, a fish farm, and a thermoelectric plant, all in the eastern coast of the island.

Pollutant transport monitoring in coastal areas is essential because of the many critical activities occurring in them. Recently, it has been reported how the analysis of ocean currents, which are operationally delivered by ocean forecasting services (De Dominicis et al., 2016), combined with the use of remote sensing techniques (Cheng et al., 2011; Marta-Almeida et al., 2013; Xu et al., 2013) and dynamical systems tools (Olascoaga and Haller, 2012; García-Garrido et al., 2016) are capable of providing important feedback to emergency services. Currently, synergies between these capabilities for coastal applications are flourishing due to the fact that remote sensing and modeling capabilities are reaching very resolved metric scales, thus providing the bedrock for future smart coasts.

Remote sensing capabilities allow for a direct observation of extended areas. The limitations of these capabilities are due to the satellite swath, revisit time, atmospheric conditions and cloud coverage for optical sensors. During the reported event, optical images from Sentinel 2 and Landsat 7 and 8 were available and analyzed. These specific image products were useful in the past for oil spill monitoring (Pisano et al., 2015; García-Garrido et al., 2016) and we explore their potential in this study. Additionally, Synthetic Aperture Radar (SAR) images have been demonstrated to be a very adequate tool for remote detection of oil spills (Cheng et al., 2011; Xu et al., 2013; Pisano et al., 2015), specially due to their high spatial resolution and all-weather and all-day capabilities. During this case study, SAR images from Sentinel 1A and 1B were available. Spatial resolution of Sentinel 1 and 2 is very high (up to 10 m), while that of Landsat 7 and 8 is lower (up to 30 m).

Ocean model products also provide direct information on extensive areas. To perform this study, we have used two modeled data sources for ocean currents in the area of interest: (1) The regional forecast product for the IBI (Iberia-Biscay-Ireland) area, operationally delivered by the CMEMS Service and (2) a very high resolution coastal model system, specifically developed by Puertos del Estado (PdE) for the Port of La Luz. The IBI product shows a kilometric resolution (derived from the 1/36° NEMO model application), too coarse for the coastal event under study. Nevertheless, we have applied the PdE ROMS model application that downscales the regional IBI solution for the Gran Canaria area by means of 2 nested grids (a coastal one, with $\sim$ 350 m horizontal resolution, which we refer to as the CST model, and a very high resolution local domain, specifically focused on the Puerto de la Luz area with $\sim$ 40 m resolution, which we refer to as the PRT model). Transport processes associated with these currents are subject to uncertainties, such as those inherent in the modeled velocity fields, as they depend on assumptions taken in the modeling processes. Each result on the velocity fields produced by different model hypotheses may characterize pollutant dispersion differently, and thus we address the issue on how to compare outputs. Our analysis goes beyond the tracking of individual pollutant trajectories by exploiting ideas from dynamical systems theory that involve the determination of geometrical structures in the ocean surface which define regions where fluid particle trajectories have qualitatively distinct dynamical behavior (Wiggins, 2005; Mancho et al., 2006; García-Garrido et al., 2015, 2016; Balibrea-Iniesta et al., 2019). These geometrical structures provide a signature for a specific velocity field, highlighting the essential transport features associated to it.

This paper is organized as follows. Section 2 describes the data sources used in this work: satellite data, ocean models and the transport problem. Section 3 presents the results, a discussion on how the dynamical systems approach supports the interpretation of transport, and a discussion on uncertainty quantification. Finally, Section 4 reports the conclusions of this work.

2. DATA AND METHODOLOGY

2.1. Satellite Imagery and Remote Sensing

The following high-resolution satellite image data sources, corresponding to the dates for which the "Volcán de Tamasite" ferry crash event took place, were downloaded (at no cost) and adequately processed:

- SAR data from Sentinel 1 (A,B), Level-1 IW GRDH (Interferometric Wide Swath Ground Range Detected) with high resolution, was obtained from the Sentinel Data Hub (https://scihub.copernicus.eu/).

- Sentinel 2A MultiSpectral Instrument (MSI) Level 1C data was also downloaded from the Sentinel Data Hub.
- Landsat 7 ETM+ (Enhanced Thematic Mapper Plus) and Landsat 8 OLI (Operational Land Imager) level 1C data was downloaded from the U.S. Geological Survey (https://earthexplorer.usgs.gov/).

The images were processed using the following tools. Sentinel 1 data was processed using SNAP (https://step.esa.int/main/toolboxes/snap/) SAR tools. Sentinel 2 MSI, Landsat 7 ETM+ and Landsat 8 OLI were processed using the Acolite toolbox (Vanhellemont, 2019). The chronological sequence of satellite images available during the event is provided in the following list:

- 04/21/2017: Sentinel 1B, 7:04 p.m., a few minutes prior to the accident.
- 04/23/2017: Sentinel S1A 07:00 a.m., *in situ* confirmed spill patterns were weakly visible.
- 04/26/2017: Landsat 8 11:30 a.m., cloudless, no spill patterns identified.
- 04/27/2017: Sentinel 1A 7:00 p.m., no spill patterns identified.
- 04/29/2017: Sentinel 1B 07:00 a.m., no spill patterns identified.
- 05/01/2017: Sentinel 2A 11:50 a.m., cloudy.
- 05/03/2017: Sentinel 1B 7:00 p.m., no spill patterns identified.
- 05/04/2017: Landsat 7 11:30 a.m., no spill patterns identified.

With the purpose of identifying water discoloration due to the spill, the inspection of optical images was performed both through RGB composites and remote sensing reflectance spectra. However, this analysis did not provide insights for the event, and we do not report further about them. SAR images were also examined. Due to the spreading tasks done by the emergency services and the characteristics of the targeted oil spill, an intense signal was not expected. However, weak patterns (lately confirmed through *in-situ* observations) were identified on one Sentinel 1A image obtained on Sunday 23rd of April 2017 at 07:00 a.m. At that time, the Spanish coastguard fleet (SASEMAR) had already begun the daily operations (06:00 a.m.). **Figure 2** displays this SAR Sentinel-1A image. **Figures 2A–C** show "low-roughness" spots around NE Gran Canarian waters, indicating potential positions for the diesel oil spill drift, after the ferry crash. The two "low-roughness" spots appearing in the image (marked with red circles in **Figures 2A–C**) were on ground confirmed spills (and dispersed) by three SASEMAR ships and one helicopter. Indeed, at the time of the Sentinel 1A passing over, two ships confirmed the spill spot at the North, in the vicinity of the Port. The spill spot located 12 km south from the Port, in the neighborhood of the Marine Eolic Platform facility (www.plocan.eu) and 1 km far away from land, drifting southwards, was confirmed by a third ship and one helicopter (CIAIM, 2018).

2.2. Ocean Models

Ocean currents in the area of interest are supplied by two sources. One is the Copernicus Marine Service model for the Iberian-Biscay-Irish region (CMEMS IBI-PHY, IBI hereafter) available from http://marine.copernicus.eu/. Currents obtained from this product in the area of the accident are displayed in **Figure 5A**), where the accident location is marked with a red dot. IBI outputs have too coarse resolutions for the scale of the event we want to describe. For this reason, we used specific high-resolution modeled currents for the Port of La Luz, downscaling the IBI regional solution through two offline nested domains, with resolutions of 350 m in the intermediate coastal domain (the CST model) and 40 m in the local domain that covers the port waters (the PRT model). Details about the model product configurations and their quality are given next:

- **CMEMS IBI-PHY:** The CMEMS IBI provides operational regional short-term (5-days) hydrodynamic forecasts of a range of physical parameters (currents, temperature, salinity, and sea level) since 2011 (Sotillo et al., 2015). IBI is based on an eddy-resolving NEMO model application (v3.6) that includes high-frequency processes required to characterize regional-scale marine processes. The model application runs at a $1/36^\circ \sim 2.5\,\mathrm{km}$ horizontal resolution and final products are routinely delivered in a service domain extending between 26°N and 56°N and 19°W and 5°E, see **Figure 3**. The NEMO model (Madec and NEMO Team, 2019) solves the three-dimensional finite-difference primitive equations in spherical coordinates discretized on an Arakawa C-grid and 50 geopotential vertical levels (z coordinate), assuming hydrostatic equilibrium and the Boussinesq approximation. Partial bottom cell representation of the bathymetry (a composite of ETOPO2 and GEBCO8) allows an accurate representation of the steep slopes characteristic of the IBI area. The IBI system is forced with up-to-date high-frequency $1/8^\circ \sim 12.5\,\mathrm{km}$ hourly meteorological forecasts provided by the ECMWF (European Centre for Medium-Range Weather Forecasts). Variables, such as 10 m wind, surface pressure, 2 m temperature, relative humidity, precipitation, shortwave and longwave radiative fluxes are used as forcing, being a CORE empirical bulk formulae (Large and Yeager, 2004) used to compute surface (latent and sensible) heat and freshwater (evaporation-precipitation) fluxes and surface stress.

  The IBI regional system is nested into the CMEMS Global solution, using as open boundary conditions daily outputs from this CMEMS global eddy resolving system. Tidal solution is also added at the boundaries (at that time, IBI system was using 11 tidal harmonics). An atmospheric pressure component is also included assuming pure isostatic response at open boundaries (inverse barometer approximation). The CMEMS IBI system uses a SAM2-based data assimilation scheme to enhance its predictive skills by constraining the model in a multivariate way with a wealth of observations: Altimeter data (i.e., along-track sea level anomalies), *in-situ* temperature and salinity vertical profiles and satellite-derived sea surface temperature are regularly assimilated to estimate periodically initial conditions. Further details on the data assimilation scheme and on the analysis generated can be seen in the CMEMS IBI Product User Manual report (Amo et al., 2020), available at CMEMS, where more details of the operational suite can be found.

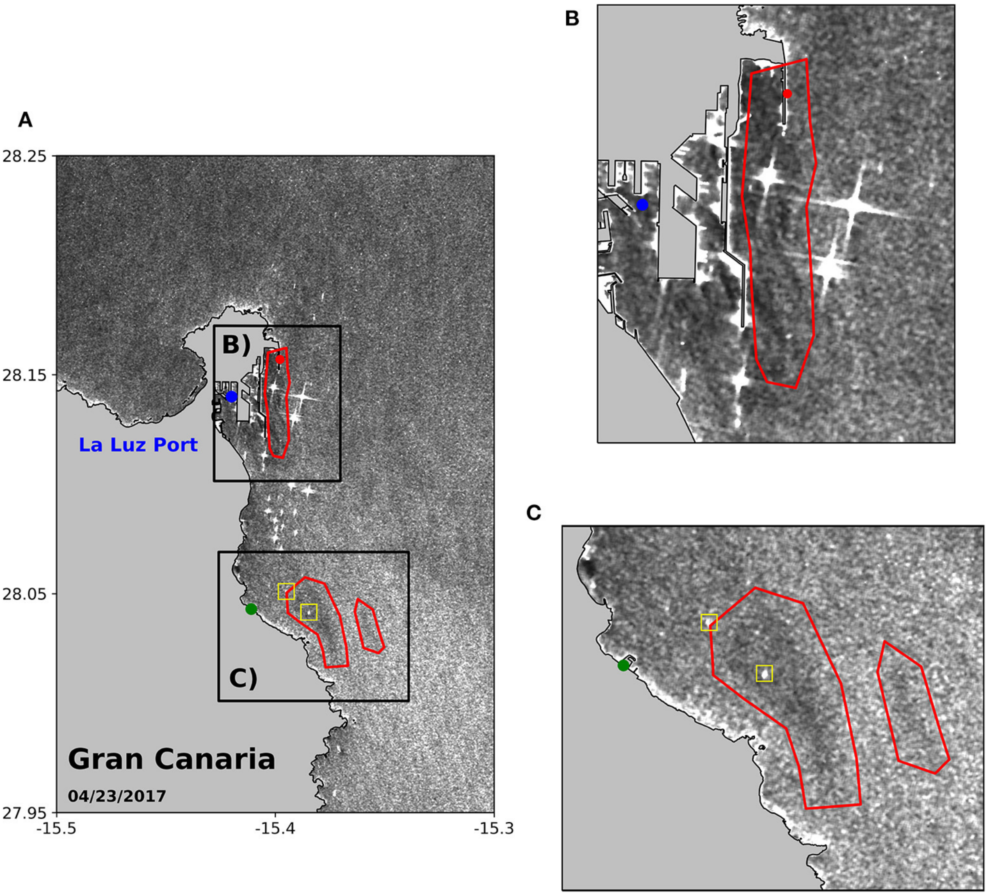

FIGURE 2 | (A) SAR Sentinel-1A image obtained on Sunday 23rd of April 2017 at 07:00 a.m.. The image shows two areas with "low-roughness" spots that were ground confirmed spills by three ships and one helicopter of the Spanish Coastguard fleet (SASEMAR), who started to work on the affected areas on that day at 06:00 a.m.; **(B)** The Northern spilling area (red area) was dispersed in the neighborhood of the Port by two ships. The broken fuel lines were finally closed at 20:30 p.m., several hours after the Sentinel-1B passing over that region (07:00 a.m.); **(C)** The Southern spilled area reported by the SAR Sentinel-1B was located 12 km south from the Port, in the Marine Eolic Facility (www.plocan.eu) waters. This spill was validated by SASEMAR and coastguard helicopter flights (also reported in the SAR image). Both spots drifted southwards 1 km away from the coast, until the pollution alert ended on the 25th of April at 8:30 a.m. SASEMAR's Airplane, however, continued surveying the whole Eastern coastline of the island until the 8th of May 2017 (CIAIM, 2018).

We have used the data set IBI_ANALYSIS_FORECAST_PHYS_005_001 with horizontal resolution of 1/36° ∼ 2.5 km on a regular latitude/longitude equirectangular projection of the Northwest African waters domain. Daily 3D fields are available over 50 geopotential vertical levels, but in this study hourly fields provided for the upper layer are used (Aznar et al., 2016). The IBI ocean model forecasts are continuously monitored, using to this aim the NARVAL multi-parameter multi-platform validation toolbox (Lorente et al., 2019). This multi-parametric ocean model skill assessment is performed by the IBI-MFC using all available operational observational sources in the IBI model domain. The list of observational data source used in the IBI validation includes remote sensed data (i.e., satellite L3 and L4 SST and sea level anomaly products, together with surface currents from coastal HF-Radars stations) and *in-situ* observations (from moorings and tide gauges and sea level essential variables such as surface temperature, salinity, currents and sea level; as well as from ARGO floats for 3D temperature and salinity). See further details in Lorente et al. (2019) for a complete list of the observational products and platforms used, as well as the regions covered, to operationally validate the IBI ocean model product. Furthermore, the CMEMS IBI-MFC forecast model products are qualified before their entry into operational service. Main results from this scientific qualification of the IBI ocean model products can be seen in the comprehensive product quality document delivered together with the IBI product (the CMEMS IBI-MFC Quality Information Document, available online Sotillo et al., 2020a). This product quality report points out the good agreement on average between the model system and the available observations. Being particularly true for sea level when compared to along-track altimetry and tide gauge stations (in these coastal stations, model tidal and residual sea level measures are also close to the tide gauge observations used). The comparison with *in-situ* temperature-salinity profiles, all of them off-the-shelf, also shows good IBI model performances, especially below the thermocline. In the Canary Island region, model differences with observations are low (root mean square errors (RMSE) and biases of 0.45 °C and 0.07 °C and 0.15 and 0.01 psu, for temperature and salinity, respectively; values obtained from the comparison of IBI with full ARGO profiles during the 2-year period 2013–2015). Concerning the Sea Surface Temperature (SST), the IBI system performs well in average, but can locally display high biases. Thus, RMSE computed over the whole IBI domain over a 6-year period is around 0.6 °C. This IBI referential product quality report shows also some IBI metrics for surface currents. However, it warns about the difficulty to assess such variable, mostly due to the very scarce availability of long time series of velocity measurements, and the very limited representativity of such measurements (there are only a few local measurements available, making it impossible to build regional metrics for surface currents, such as the ones provided for the SST and sea level fields or the 3D temperature and salinity).

- **PdE La Luz Port model:** CMEMS IBI provides a regional solution at kilometric scales. The IBI horizontal resolution in clearly not enough to characterize coastal events such as the one we discuss in this work. Therefore, a local high-resolution dataset is needed to characterize circulation patterns in the Puerto de la Luz. In the framework of the H2020 IMPRESSIVE Project, PdE has developed a new model setup for this port, covering also nearby waters along the Eastern coast of Gran Canaria island. This newly developed model setup, with a very high resolution, has been specifically designed for the Puerto de la Luz, and used by PdE to test some model updates that will be used in the future to upgrade the PdE SAMOA port forecast systems (Sotillo et al., 2020b), currently implemented and running operationally in different Spanish Port Authorities. The high-resolution hydrodynamic module is based on the ROMS (Shchepetkin and McWilliams, 2005) model (version 3.7). ROMS is a time split-explicit, free-surface, terrain-following-coordinate oceanic model that has been applied successfully for oceanographic forecasting at other Spanish harbors (Grifoll et al., 2012). The proposed nesting strategy comprises two off-line nested domains: a coastal one nested with IBI with a horizontal resolution of 350 m and ranging from shallow waters to water depths around 2000 m (hereafter coastal model); and a local one (with a horizontal resolution of 40 m), nested in the previous one (hereafter local model). We illustrate it in **Figure 3**. Due to the sudden sharp slope gradients at the continental shelf, the vertical discretization has been setup at 30 sigma levels for the coastal model. At the local model, 15 sigma levels were found to be enough for handling the bathymetry. The vertical discretization follows the S-coordinate system described in Song and Haidvogel (1994). The bathymetry for both domains was built using a combination of bathymetric data from EMODNET (with an approximate resolution of 230 m) and from specific local high-resolution sources provided by the local Port Authority. Furthermore, within a transition region (2 km) along the open boundaries of the coastal model, the bathymetry from the CMEMS-IBI system is used to accommodate the high-resolution information and keep consistent the transports associated with IBI velocities imposed as open boundary conditions. In the local model, an updated and higher resolution bathymetry is also applied, adjusting the open boundary to the coastal bathymetries. The bathymetry information interpolated over the mesh is smoothed using a Shapiro filter (Shapiro, 1970) with an r-factor criterion below 0.25. The bottom boundary layer has been parameterized with a logarithmic profile using a characteristic bottom roughness height of 0.002 m. The turbulence closure scheme for the vertical mixing is the generic length scale (GLS) tuned to behave as k-ε (Warner et al., 2005). Horizontal harmonic mixing of momentum is defined with constant values of $5\,\mathrm{m}^2/\mathrm{s}$. Moreover, the atmospheric forcings come from the HARMONIE model (Bengtsson et al., 2017) with spatial resolution of 2.5 km. The following atmospheric variables are used: wind fields, sea-level pressure, temperature at 2 m elevation, relative humidity at 2 m elevation, precipitation, long wave and solar radiation.

With respect to the quality assessment of very high resolution coastal model systems, covering a very limited spatial domain such as the one we present here for La Luz Port, it is important to remark that one of the main bottlenecks identified is the lack of an adequate near-real-time delivery of operational observations. This lack of operational observations, specially on coastal areas, restricts the systematic production and exploitation of quality assessments of operational ocean model products such as the ones used here. Indeed, in a recent review performed by EuroGOOS for European coastal operational ocean model services (Capet et al., 2020), it is pointed out that only 20% of operational models currently available for European seas provide a dynamic uncertainty together with their forecast products. Unfortunately, this is the case in terms of validation of the Port of La Luz model currents for the dates (21-23 April 2017) of the event here studied. There is no option to analyze the quality of the surface current modeled fields for such specific dates due to the lack of *in-situ* or remote sensing observations in the area. Nevertheless, there is some information on the model dynamical performance derived from other validation exercise performed on different essential ocean variables and temporal periods that can illustrate the capability of the model setup proposed to reproduce the coastal dynamics in the area.

As previously mentioned, the Coastal and Port model systems implemented in La Luz Port are an evolution of the PdE operational SAMOA model setup, used for operational forecasting in the island of Gran Canaria (Sotillo et al., 2020b). In this work, the quality of 1-year SAMOA ocean forecast products (operationally available for 9 Spanish Ports) was assessed by comparison with observations, both from *in-situ* moorings and remotely sensed products. It is important to highlight how the SAMOA model systems focused on the Canary Islands (4 out of 9 SAMOA system existing at that time) show the best agreement for SSH when compared to hourly sea level observations from tide gauges (with reported correlation coefficients around 0.98 and RMSE that ranges between 0.07 and 0.16 m). The performance of coastal SAMOA systems appears to be rather consistent in terms of SST, according to the skill metrics obtained (correlation values above 0.89 and RMSE usually in the range 0.2 − −0.4 °C, considering more than 3,200 hourly observations for each case). Indeed, the SAMOA system running in Gran Canaria shows the second best performance of a PdE SAMOA operational model when compared to hourly SST observations from a coastal buoy (in this case, moored close to the Port of La Luz).

Currently, PdE is working on a similar model setup as the one we have used for the analysis of the Tamasite event, validating their model system with several observational data sources available over that period (i.e., HF Radar and *in-situ* mooring).

2.3. The Transport Problem

The transport process of oil particles can be described by a concentration field $C(\mathbf{x}, t)$ which depends on time t and the position $\mathbf{x}$. The position $\mathbf{x}$, has three components considering that oil particles move on the ocean surface and may also sink. The evolution of the concentration $C(\mathbf{x}, t)$ is affected by the flow, represented by the velocity field $\mathbf{v}(\mathbf{x}, t)$, and molecular diffusion. It is described by the following advection-diffusion equation (De Dominicis et al., 2013):

$$\frac{\partial C}{\partial t} + \mathbf{v} \cdot \nabla C = D\nabla^2 C\,, \tag{1}$$

Here D is the is the molecular diffusion coefficient. At the ocean scale, the diffusion transport is much smaller than the convective transport (Monroy, 2019) and hence the Equation (1) reduces to:

$$\frac{dC}{dt} = 0\,, \tag{2}$$

where d/dt is the total time derivative. Equation (2) implies that the quantity C is conserved along fluid parcel trajectories and behaves as a passive tracer. Particles with a finite size and different density to that of water may not instantly follow fluid velocities. Other mechanisms besides passive advection contribute to their transport, such as gravity forces, their finite size, inertia and history dependence (Maxey and Riley, 1983; Cartwright et al., 2010). Results in Monroy et al. (2017) confirm, however, that for a wide range of particles that sediment in turbulent ocean flows, the description of passive tracers is appropriate, except for the addition of a constant vertical velocity arising from the particle weight. In particular, for the case of the diesel fuel under study, weight effects are negligible and therefore we considered that it follows fluid parcels. This approach is rather reasonable for diesel fuel since it is less dense than salty water and moves mainly horizontally, close to the surface, slightly below the waterline, and thus it is not subjected to direct wind sailing effects. Studies such as (Lekien et al., 2005; Olascoaga and Haller, 2012; García-Garrido et al., 2016) confirm that considering advection as the dominant contribution to pollutant transport provides very good results.

Fluid parcels follow trajectories $\mathbf{x}(t)$ on the ocean surface that evolve according to the dynamical system:

$$\frac{d\mathbf{x}}{dt} = \mathbf{v}(\mathbf{x},\, t)\,, \tag{3}$$

where the position is described in longitude (λ) and latitude (ϕ) coordinates, that is, $\mathbf{x} = (\lambda, \phi)$, and $\mathbf{v}$ represents the velocity field. In longitude/latitude coordinates, the dynamical system in Equation (3) can be rewritten as:

$$\begin{cases} \dfrac{d\lambda}{dt} = \dfrac{u(\lambda, \phi, t)}{R\cos\phi} \\[2ex] \dfrac{d\phi}{dt} = \dfrac{v(\lambda, \phi, t)}{R} \end{cases}, \tag{4}$$

where R is the Earth's radius. This equation assumes that the vertical velocity component in the ocean is small compared to the horizontal ones and for that reason it has been disregarded. The two velocity components are determined by the zonal (u) and meridional (v) velocities, which are obtained from the different ocean models: IBI, CST, and PRT. We have tracked fluid parcels that evolve according to velocities supplied by these three models. Due to the limitations of CST or PRT models in terms of spatial domain (the PRT domain is only focused on inner port waters and the nearby ones, and CST is focused on an area of the coast, see **Figure 3**) in order to be able to track fluid parcels outside their geographical coverage, the zonal and meridional velocity fields need to be composed with IBI fields. **Figure 4A** illustrates a sketch of two grids corresponding to the IBI and CST models. **Figure 4B** shows the structured grid resulting from the composition of grids in **Figure 4A**. The grid is made up of cells with areas of different sizes. A linear interpolation is used within each cell to approximate the velocities within them. When the PRT model is used, its grid is nested within the CST grid, which in turn is nested with the IBI grid, i.e, a hierarchy of three nested data is required. The accuracy of this approach is supported, and justified, in the next section, by the agreement between the predictions made by the simulations, the oil sightings from satellite and *in-situ* observations.

There exist diverse software packages that are able to track oil spills. Among others, oil drift models include (Cheng et al., 2011; Xu et al., 2013) EUROSPILL, OILMAP (Oil Spill Model and Response System), GNOME (General NOAA Operational Modeling Environment), MOTHY (French operational oil spill drift forecast system), OSCAR (Oil Spill Contingency and Response), ADIOS2 (Automated Data Inquiry for Oil Spills), OSIS (Oil Spill Identification System), and Medslik-II (De Dominicis et al., 2013). These models are focused on tracking individual fluid parcels, and they need to play with a sufficiently large number of initial parcels to maintain a good representation of the spill. Contrary to these oil spill approaches, in this work we track in time the whole area where the fuel is extended, and the algorithm self regulates the number of fluid parcels on the contour to ensure its accurate representation at all times. The area is tracked with contour advection algorithms developed in Dritschel (1989), including some modifications explained in

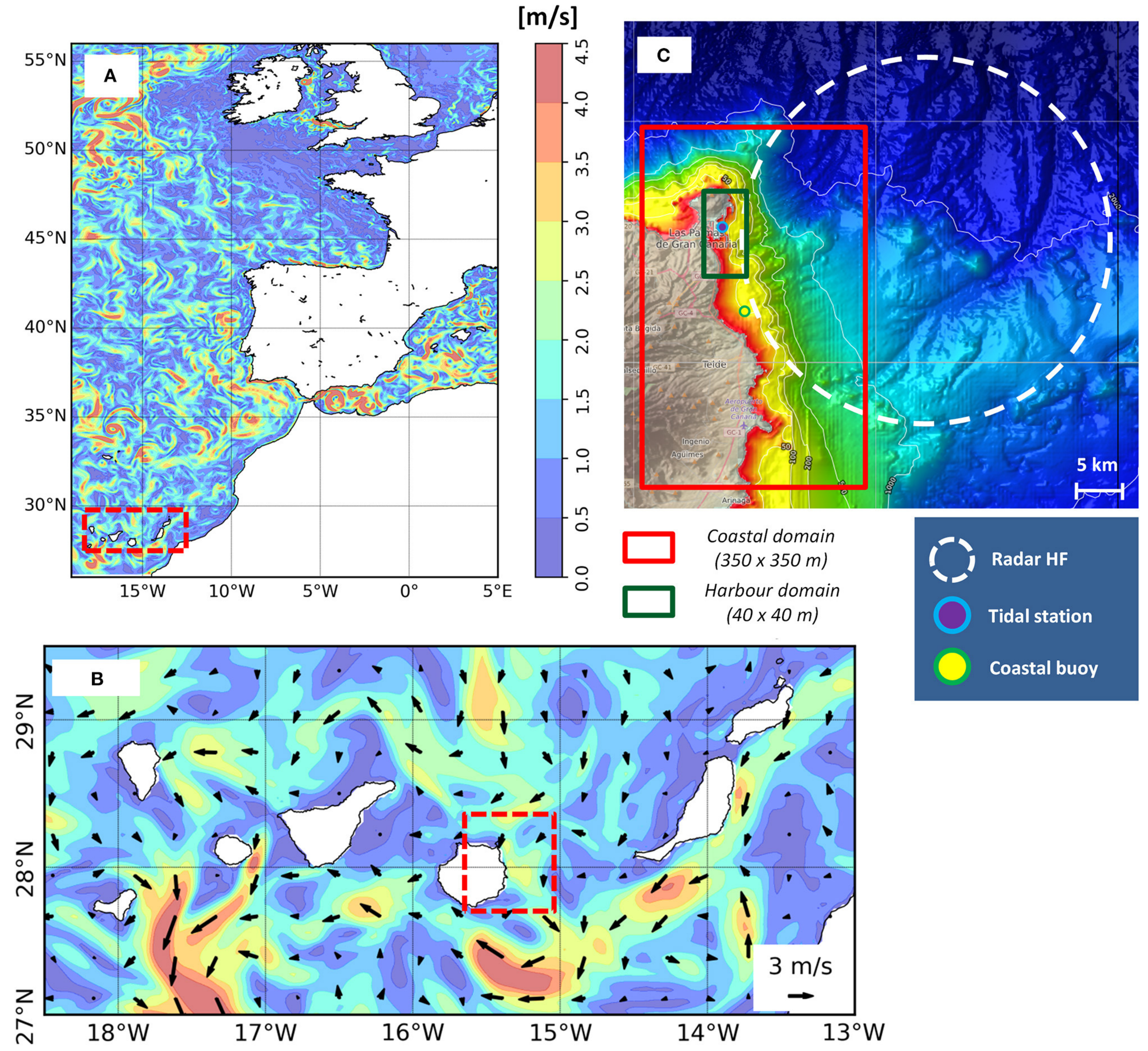

FIGURE 3 | (A) Spatial domain of the IBI-PHY model. The colored areas denote the daily-averaged surface current speed on the 21st April 2017 in units of m/s. The dotted red rectangle encloses the Canary Islands (Spain). **(B)** Zoom of the Canary Islands for the same surface currents fields depicted in **(A)**. The superposed black arrows represent the surface current field. **(C)** Nesting strategy for the Port of La Luz. The coastal domain area is enclosed in the red lined rectangle, whereas the local domain is enclosed in the green one. The colored areas show the bathymetry. The white dotted circle encloses the PLOCAN surface-current HF radar. The blue dot marks the tidal station within the harbor; whereas the yellow one marks the coastal buoy (Puertos del Estado monitoring network).

Mancho et al. (2003), Mancho et al. (2004), and Mancho et al. (2006). More specifically, the spill is modeled by an initial contour surrounding an area, A_0, with a given thickness h_0. The product $V = A_0 \cdot h_0$ is the volume of the initial spill. While the contour is advected, the initial area, whose value is typically preserved for 2D incompressible flows, is distorted.

Transformation processes like evaporation, photo oxidation, etc., act on the slick while it drifts. Evaporation is an important process for most oil spills. Oils and fuels are slowly evaporating mixtures of compounds whose long-term behavior are not always well-described by air-boundary layer interaction mechanisms, but through diffusion mechanisms (Fingas, 2014). However, the diesel under consideration has volatile components, that do evaporate via air boundary-layer-regulated mechanisms. Software packages quoted above include models to represent the weathering of the spills according to different oil properties. In our model, oil is presumed to consist of one component and its volume is assumed to decrease through evaporation

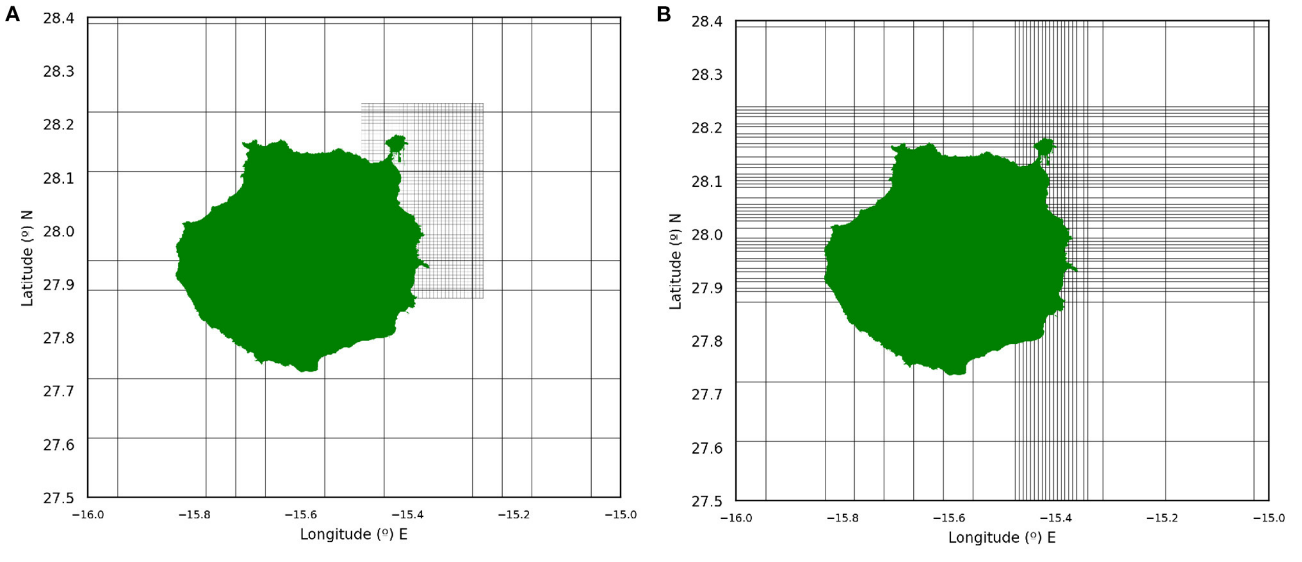

FIGURE 4 | (A) A sketch illustrating the two grids (IBI and CST) represented in the domains where the hydrodynamic models are solved; **(B)** the composition of the two grids, which results in a structured, non-uniform grid. Within each cell velocities are linearly interpolated.

by diminishing its thickness h_0. In this way spill contours are evolved uncoupled from degrading effects which are considered at representative levels as a change in the intensity color of the oil spill. The intensity will be adjusted depending on the degradation of the specific type of oil. According to McIlroy et al. (2018) and Butler (1976), the fraction of the original diesel compound remaining after evaporation can be adjusted to a kinematic law:

$$\frac{V}{V_0} = e^{-Bt}, \tag{5}$$

where V_0 is the original volume, and V is the volume at time t. According to *in-situ* reports, the spill reduced an 80% in approximately 72 h (Montero, 2017), which give us an estimation of the evaporation rate $B = 0.02235\ \text{h}^{-1}$.

3. RESULTS AND DISCUSSION

The passenger ferry crashed at the position marked by a red dot in **Figure 1**, located at 28°9.418′ N and 15°23.871′ W. **Figure 5** shows a time frame that is representative of the surface current patterns during the event. Throughout the episode, surface currents were mainly driven by large-scale circulation patterns and tides. Current fields were southward, with a modeled daily-averaged current speed of 12-16 cm/s at the eastern shelf of Gran Canaria island. IBI-PHY and the high resolution model presented similar current magnitudes. Note that only the semi-diurnal tidal current range was around 10 cm/s. Currents induced by residual tides can be considered as negligible: from the 21st to the 23rd of April, a negative surge was measured with an average value of 2 cm. At the end of the 23rd of April, though, the negative surge rose to 6 cm. Wind-induced currents had also a secondary role: measured surface wind at the tidal station was mainly from the N-NW sector, with a wind speed of 3.38 m/s (standard deviation of 0.88 m/s). There was no evidence of gustiness, either: average maximum wind speed was mild, with low variability (5.25 m/s with a std. deviation of 1.2 m/s). Finally, wave-induced currents may have had a secondary role: measured waves at the coastal buoy were moderate, with significant wave height of around 1.1 m and maximum wave heights of 1.5 m. The peak period was close to 8 s, exhibiting a young swell sea-state.

On the 23rd of April 2017 at 7:00 a.m., remote sensing images confirmed the spreading of the diesel fuel southwards, (see **Figure 2**). This is consistent with the evolution of the spill, which is modeled as a blob at the accident location, according to the three models: IBI, CST, and PRT. **Figure 6** illustrates this point. **Figure 6A** shows how it evolves according to IBI model, **Figure 6B** illustrates the evolution according to the CST model nested in IBI data, and finally (**Figure 6C**) displays the evolution according to the PRT model nested in CST and in IBI data. Arrows mark the position of the blob at successive times. The color degradation from black to white, in a gray scale represents the evaporation. All three models predict a southwards evolution, although IBI model drifts southwards faster than the others and at the observation time, i.e., 23rd of April 2017 at 7:00 a.m., the spill is outside the displayed domain. On the other hand, both CST and PRT models provide very similar outputs and predict a position for the spill at the observation time very close to the observed one. No significant differences are noticed between them, and this is somewhat expected given that the blob spends only a brief time within the very high resolution PRT domain, and it rapidly evolves toward the high resolution CST domain in the coastal area. The structure of the observed spill is not so filamentous as the simulated one, possibly because of the actions taken by

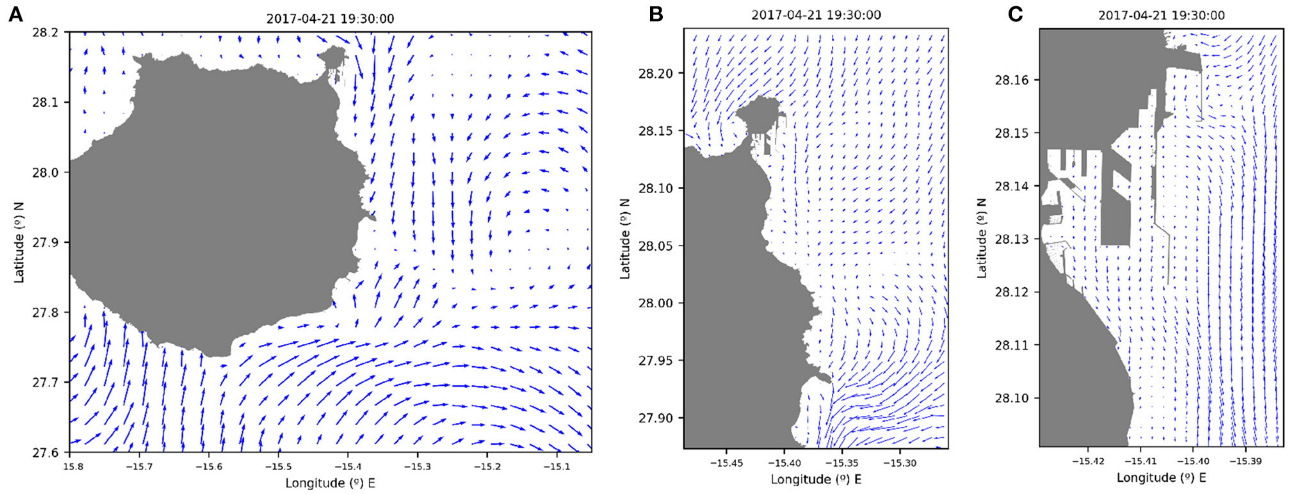

FIGURE 5 | Currents in the Gran Canaria coast at different resolutions. **(A)** Currents by the IBI model; **(B)** currents in the high resolution CST model; **(C)** currents in the very high resolution PRT model.

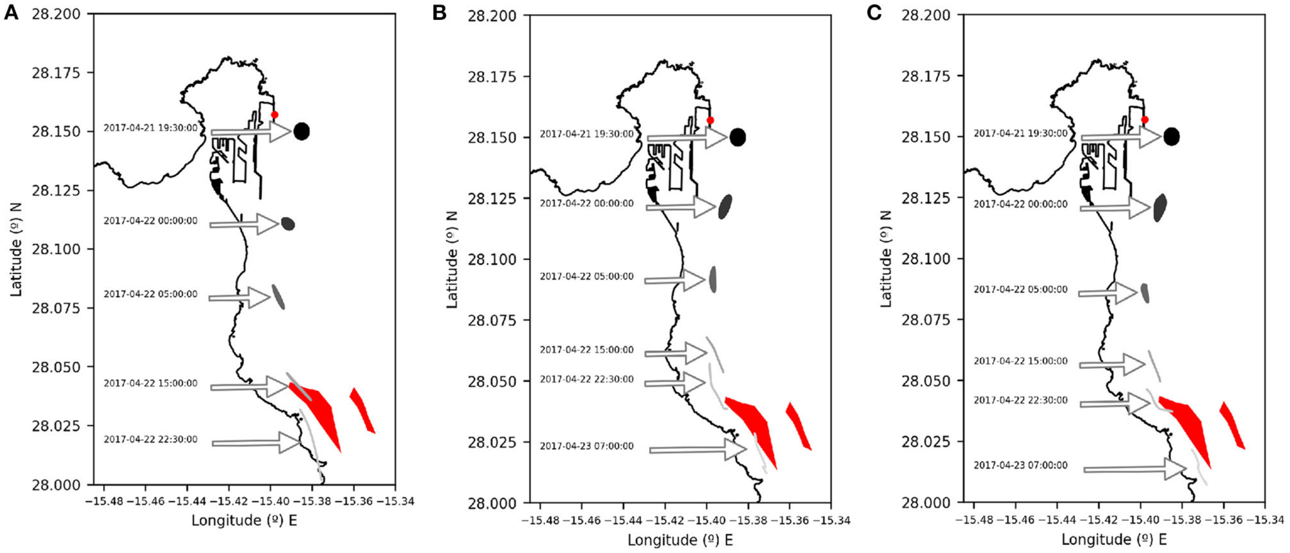

FIGURE 6 | Simulations of the evolution of the spill in the neighborhood of the accident location, according to the three models. **(A)** IBI; **(B)** CST; **(C)** PRT. Evaporation is represented by the degradation of the gray scale. The red color marks the position of accident and the observed spill on the 23rd April at 7:00 a.m.

the emergency services to dissolve it. However, it is clear that there is a significant intersection between both in space and time. The hypothesis of human interaction is consistent with the report by the "Comisión Permanente de Investigación de Accidentes e Incidentes Marítimos" (CIAMI) (CIAIM, 2018) about the presence of many boats working to repel the diesel fuel, far from the desalinization plant. Results displayed in **Figure 6**, despite similarities among models, also present differences. A natural question that arises in this context is how we can compare them. The rest of this section is focused on providing a qualitative and quantitative comparison between the transport capacity associated to each model.

3.1. The Dynamical System Perspective

A comparison of the transport processes induced by the different models requires a further step than just a contrast between individual trajectories. This can be carried out by means of applying Poincaré's idea of seeking geometrical structures in the phase space of the dynamical system described in Equation (3) that are responsible for organizing particle trajectories schematically into regions corresponding to qualitatively distinct dynamical behaviors. This approach brings an interesting new perspective into this problem. Thereby, the global behavior of particle trajectories on the ocean surface can be understood through a template (skeleton) formed by geometrical structures

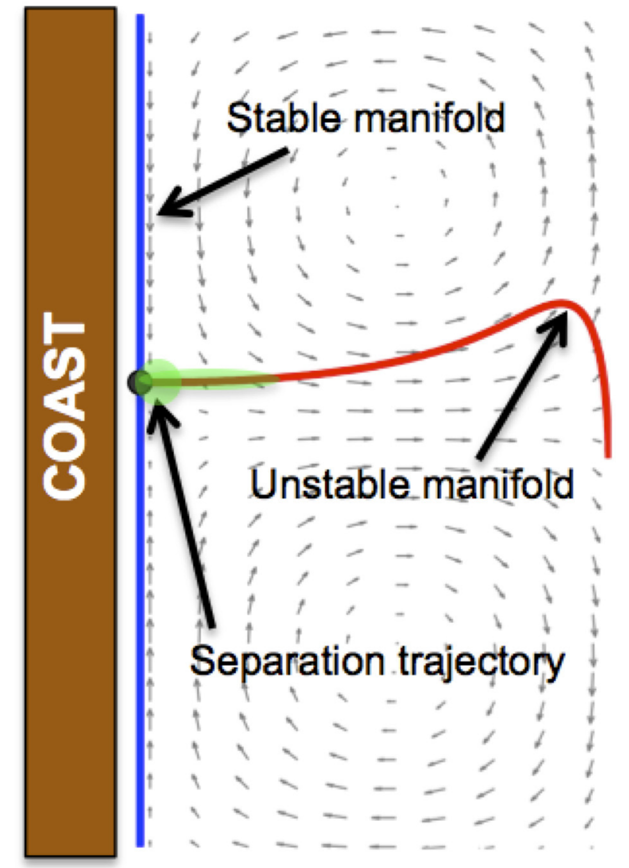

FIGURE 7 | Sketch of a hyperbolic trajectory in a detachment or separation configuration. Successive green blobs separate from the coast flowing into the ocean.

that organize flow trajectories into different ocean regions. These structures are known in the literature as Lagrangian Coherent Structures (LCS), which provide a robust way to compare transport features between velocity datasets. This is due to the fact that the geometry of LCS is preserved even for not so small velocity perturbations (Haller and Yuan, 2000). In this way, works such as (de la Cámara et al., 2010), compare transport across the stratospheric polar vortex in the atmosphere due to different models. It shows that the comparison of individual trajectories is not a robust test to quantify transport features in stratospheric datasets, while LCS are.

An essential ingredient of the geometrical structures associated with LCS are hyperbolic trajectories characterized by high contraction and expansion rates. Directions of contraction and expansion define, respectively, stable and unstable directions (García-Garrido et al., 2016; Balibrea-Iniesta et al., 2019). Of particular interest to our study are hyperbolic trajectories located on the coastline in what is known as a detachment configuration. Under this configuration, which is illustrated in **Figure 7**, material on the coast is ejected into the ocean as shown by the successive green blobs. This configuration is related to the phenomena of flow separation. The presence of these hyperbolic trajectories close to the "Nelson Mandela" dike implies a higher risk of any spill event in such a location, because diesel fuel poured into the sea close to a detachment trajectory flows away, increasing the probability of affecting critical areas as those marked in **Figure 1**.

Computing the geometrical skeleton formed by the stable and unstable manifolds of hyperbolic trajectories in the described ocean models requires additional mathematical techniques that we discuss next. To this end, we use a tool known as Lagrangian descriptors (Mendoza and Mancho, 2010; Mancho et al., 2013; Lopesino et al., 2017) that has been successfully applied in similar studies (García-Garrido et al., 2015, 2016). This tool is based on the construction of a scalar function that we call M, which is defined as follows (Madrid and Mancho, 2009):

$$M(\mathbf{x}_0, t_0, \tau) = \int_{t_0-\tau}^{t_0+\tau} \|\mathbf{v}(\mathbf{x}(t), t)\| \, dt \,, \tag{6}$$

where $\|\cdot\|$ stands for the modulus of the velocity vector. At a given time t_0, the function $M(\mathbf{x}_0, t_0, \tau)$ measures the arclength traced by the trajectory starting at $\mathbf{x}_0 = \mathbf{x}(t_0)$ as it evolves forward and backward in time for a time interval τ. Notice that we can split the computation of function M into its forward and backward contributions separately. This is important because forward integration provides information about the stable manifolds (repelling LCSs), while backward integration highlights the structure of unstable manifolds (attracting LCSs). Moreover, if we plot in the same figure the sum of both contributions, we can easily locate hyperbolic trajectories at the intersections of the stable and unstable manifolds. In fact, it can be shown that the scalar field provided by the computation of function M, when calculated over a grid of initial conditions, reveals the stable and unstable manifolds on the ocean surface at locations where the output values change abruptly, that is, at places where the gradient of the scalar field is very large. **Figure 8** displays the calculation of M in the vicinity of the crash point using the CST model in the Port of La Luz coastal area. The pattern displayed by the function M has been computed for an integration period of $\tau = 3$ days. In **Figure 8**, stable and unstable manifolds are emphasized, respectively, by the red and blue tones that enhance the "singular features" highlighted in the scalar field as a result of high gradient values. In this panel, a hyperbolic trajectory is visible as a point in a detachment configuration, similar to the one sketched in **Figure 8**. This trajectory is very close to the ferry crash point in the "Nelson Mandela" dike, which increases the riskiness of the region due to the dispersion of the spilled diesel fuel.

Figure 9 displays the M function for $\tau = 5$ days. It highlights the LCSs for the three models at the time of the accident. This allows a straightforward qualitative comparison of the transport mechanisms produced by all models. The IBI and CST models present different patterns, however both show a detachment configuration as the one displayed in **Figure 7**. This confirms that both models will predict a southwards evolution of any spill in the neighborhood of the accident point. This is so because in both cases the unstable manifold follows that orientation. As expected,

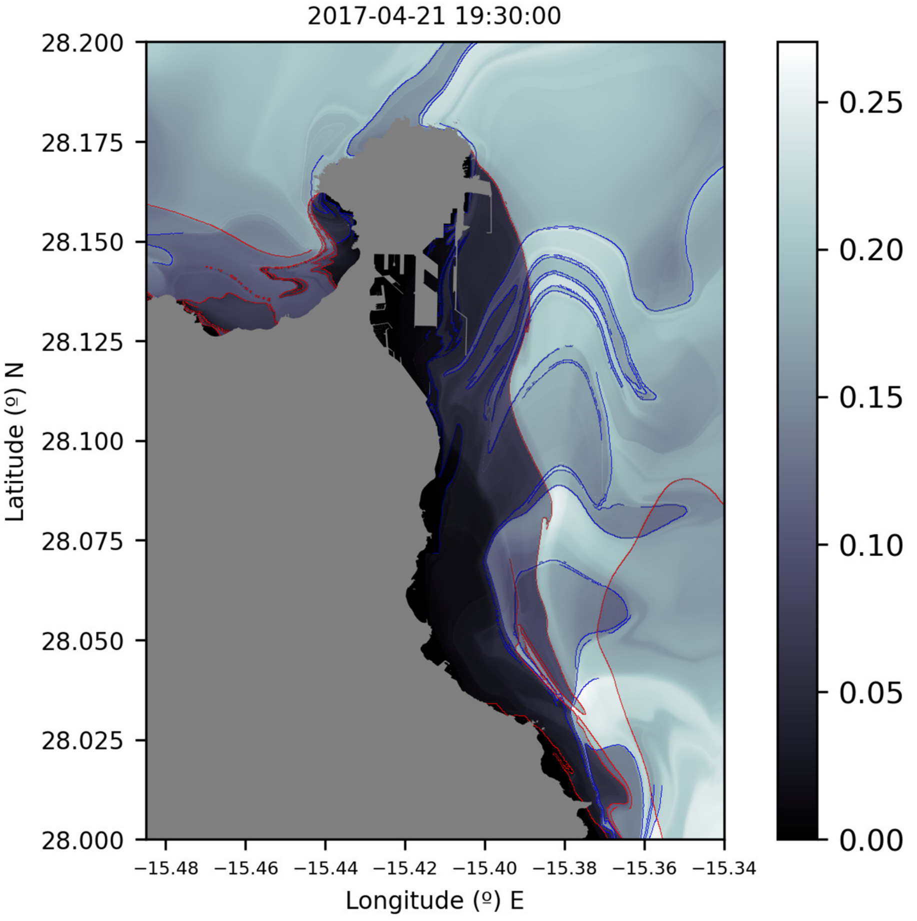

FIGURE 8 | The Lagrangian skeleton of the CST model on the 21 April 2017 at 19:30h calculated with function *M* using $\tau = 3$ days. LCSs are highlighted by the intricate curves in gray at the background, where there is a sharp change in the scalar field values of the function. Red lines are marked to emphasize the locations of the unstable manifolds (attracting LCSs), while blue lines depict the stable manifolds (repelling LCSs).

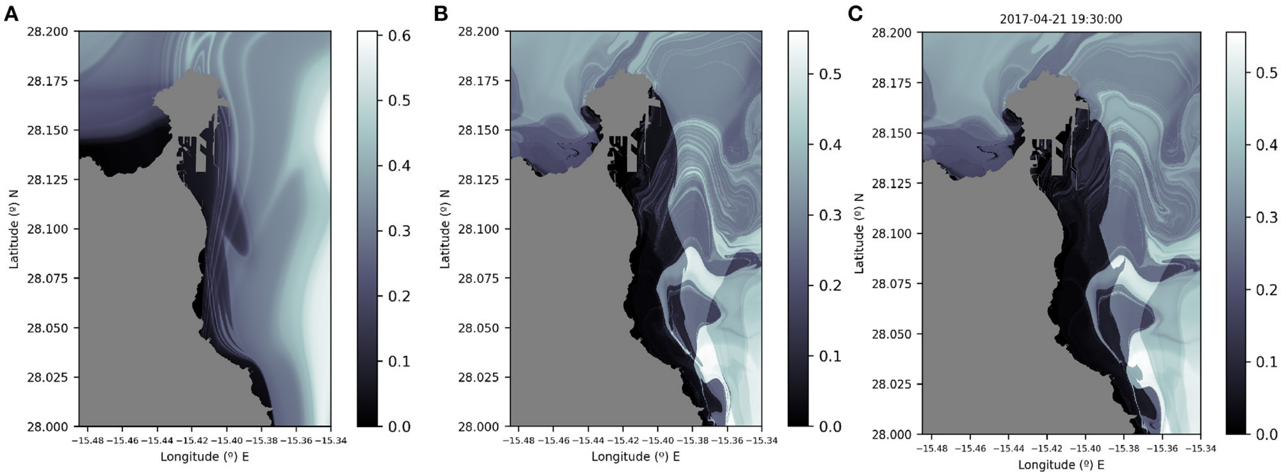

FIGURE 9 | The Lagrangian skeleton as displayed by the function *M* computed for $\tau = 5$ days on the 21 April 2017 at 19:30 h. LCSs are highlighted by the intricate curves in gray at the background, where there is a sharp change in the scalar field values of the function. **(A)** Results for the IBI model; **(B)** results for the CST model; **(C)** results for the PRT model. All three models display a detachment configuration.

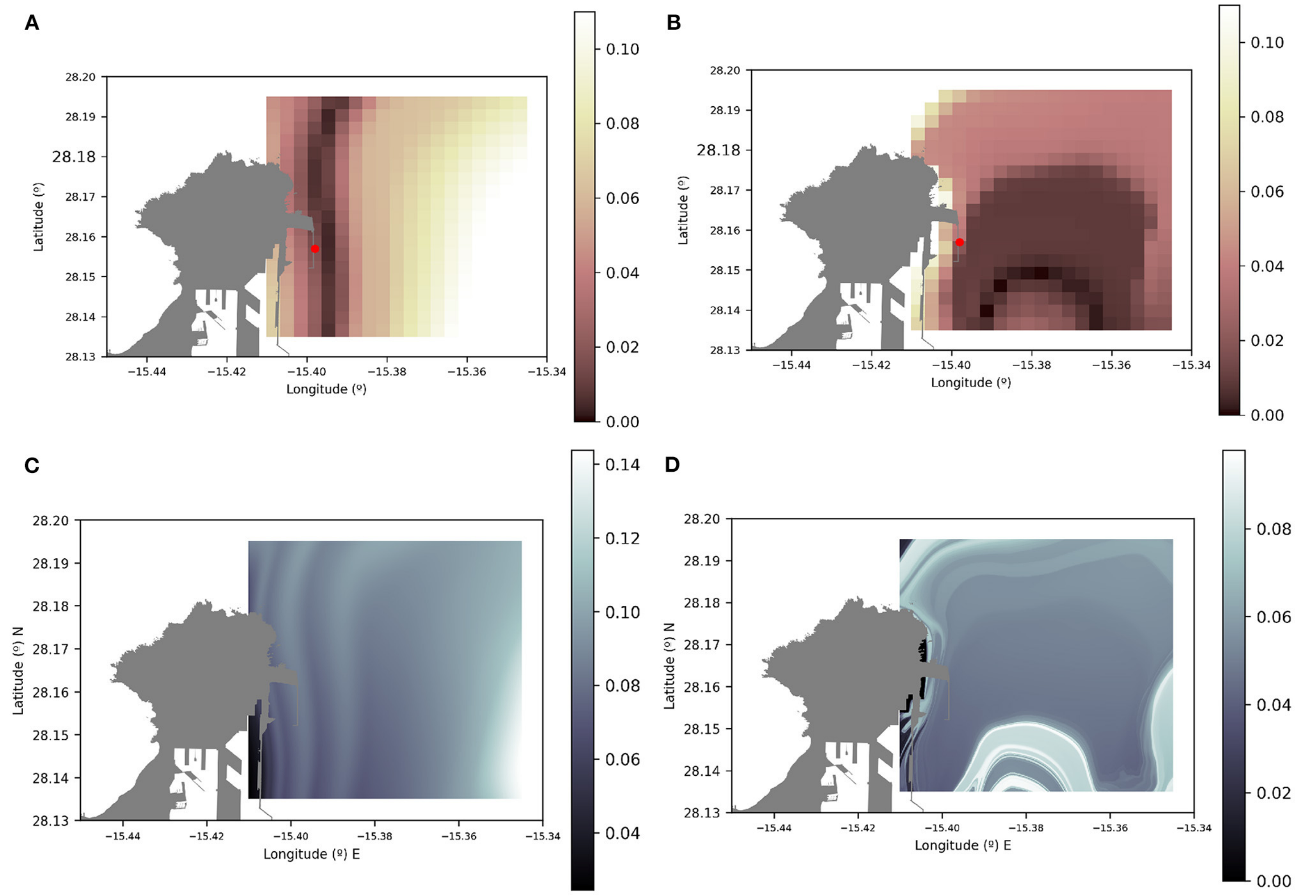

FIGURE 10 | (A,B): A quantitative measure of uncertainty based on blob initial positions and representative errors measured as distances to the target "ground truth" spill. Higher colormap values correspond to larger errors or uncertainties. The accident location is marked with a red spot. **(A)** Uncertainties associated to the IBI model; **(B)** uncertainties associated to the high resolution La Luz model. **(C,D)**: Representation of the forward integrated M function for $\tau = 3$ days highlighting the stable manifolds. **(C)** Stable manifolds associated to the IBI model; **(D)** stable manifolds associated to the CST model.

the PRT and CST models present very similar LCSs features. A comparison between **Figures 8**, **9B** show that as τ is increased in the computation of the M function, this produces a richer and more intricate LCS skeleton, since we are incorporating more information about the history of particle trajectories as they evolve in time for longer periods.

The stable and unstable manifolds highlighted in **Figure 9** are time dependent dynamical barriers that fluid parcels cannot cross. Fluid parcels tend to become aligned, for large enough transition time intervals, with unstable manifolds, which are attracting material curves that adopt convoluted shapes. This is true no matter what the initial position of the spill is. **Supplementary Videos 1**, **2** confirm this point. These movies show the evolution of several fluid blobs placed at different initial positions. At later times, all blobs are elongated and aligned with the unstable structures. This is the case, both for fluid parcels evolving according to the IBI model (**Supplementary Video 1**) and to the CST model (**Supplementary Video 2**). Similarly, but going backwards in time, blob particles align along repelling material curves, the stable manifolds, which also may be very intricate in shape. In forward time, stable manifolds represent the transition pathways toward the unstable manifolds.

3.2. Uncertainty Quantification

The Lagrangian geometrical structures computed for the PRT, CST, and IBI models allowed for a qualitative comparison among them, since they enhance similar features in what regards the presence of a separation or detachment trajectory on the coast close to the "Nelson Mandela" dike. This is a particular hyperbolic configuration that pushes material out of the coast. The flow evolution in the neighborhood of any hyperbolic trajectory is characterized by high expansion and contraction rates, which always are intrinsically related to uncertainties in the evolution. The outputs of the PRT and CST models, as already discussed, are barely distinguishable in the event scale. This is because the main differences in the circulation patterns are within the harbor. The analyzed spill was rapidly advected outside the harbor, where the solutions of both models are identical. Consequently, the very high resolution model would provide further insights only in those spills whose trajectories intersect the harbor waters.

In this section, we quantify the differences between the transport outputs by the CST and IBI models with respect to the position of the observed purple spill, which is considered a target, a "ground truth" that should be recovered by the model (see **Figure 6**). In order to achieve this, we have selected a number of positions in the neighborhood of the "Nelson Mandela" dike, which are centered within each grid element displayed in **Figures 10A,B**. The evolution of blobs of identical initial radius (0.0035°) from all those positions is different due to the chaotic nature of transport in this setting. After a time interval from the initial time, these blobs evolve and distort while they approach the target observed spill. The calculation of uncertainties associated to each grid element, is based on an error metric that considers the distance between the centroid of the simulated slick ($\mathbf{c}_m$) at a given time t^* and the centroid of the ground value slick ($\mathbf{c}_g$), i.e,

$$e(t^*) = \|\mathbf{c}_m(t^*) - \mathbf{c}_g\|\,, \tag{7}$$

where $\|\cdot\|$ is the modulus of the vector. The centroid of a finite set of N points $\{\mathbf{x}_k\}_{k\in\mathbb{N}} \in \mathbb{R}^n$ ($n = 2$ in this setting) is defined as:

$$\mathbf{c} = \frac{1}{N}\sum_{k=1}^{N}\mathbf{x}_k\,, \tag{8}$$

where $\mathbf{x}_k$ are the (lon, lat) coordinates that define the contour of the slick in an equirectangular projection. Based on this error metric, the uncertainty of the model in a given grid element is computed starting on the 21st of April 2017, at time 7:30 p.m., from a circular contour centred on the grid with a radius of 0.0035°. Then the set of errors e_i defined as in Equation (7) are considered for a sample of times t_i, where $i = 1\ldots7$, within a 3 h interval centred on the 23rd of April at 7:00 a.m., when the satellite image is taken. Finally, the minimum value of e_i in this set is taken as the representative error for each grid element. Results in a mesh next to the crash point are displayed in **Figure 10**. The error is given in degrees that can be easily transformed into kilometers. Grid elements of **Figures 10A,B** are colored in a different tone depending on this distance. The color scale is marked in the figure. It is evident that uncertainties, which are related to errors in the displacement, are greater for the IBI model than for the high resolution CST model. Using the regional solution the average error obtained is 0.07° (around 8 km), whereas using the coastal model solution the error is 0.03° (around 3 km). La Luz CST model errors are a factor 2.5 lower than the IBI model errors in good agreement with grid sizes differences.

Differences in the uncertainty distributions are visible from **Figures 10A,B**. IBI uncertainties are more significant in the right side of the mesh, while CST uncertainties are higher in the upper side. **Figures 10C,D**, show for the IBI and CST models, respectively, in the same area, the structure of the stable manifolds as highlighted by the M function. Indeed, stable manifolds are displayed by formula (6) when the integration interval is a forward time integration, i.e., $(t_0 - \tau, t_0 + \tau)$ is replaced by $(t_0, t_0 + \tau)$. Similarities between patterns in **Figures 10A,C** and those in **Figures 10B,D** are remarkable. Uncertainties seem to reach minimum values along the stable manifolds. Indeed, as explained before, and is visible from **Supplementary Videos 1**, **2**, blobs on the stable manifolds rapidly travel toward the unstable manifolds, which in turn are the attracting material curves toward which all fluid parcels evolve. In this case both IBI and CST models have their unstable manifolds aligned with the observed spill, on the 23rd of April 2017.

4. CONCLUSIONS

In this paper we have analyzed how emerging tools in coastal areas such as available very high resolution hydrodynamic models and remote sensing images from satellite, are able to provide accurate responses to the management of pollution events in port areas. In particular, the collision event of the passenger ferry "Volcán de Tamasite" in La Luz Port on April 2017 is discussed.

Very good agreement is reported between Sentinel 1 radar images and spill evolution models based on velocity fields obtained from the CMEMS IBI regional product and from the two specific model solutions: the coastal one, CST, covering waters along the eastern coast of the Gran Canaria Island and; the highest resolution one, PRT, focused exclusively in the nearby waters of Puerto de la Luz. These downstream were developed by PdE, in the framework of the IMPRESSIVE project, to downscale the CMEMS regional solution.

The evolution of the spill is implemented with contour advection algorithms that are able to track very efficiently the whole area where the fuel is extended. This is so because the algorithm is capable of self-regulating the number of fluid parcels on the contour, to ensure an accurate representation of distortions at all times. Transformation process are caused by evaporation and are expressed by means of a degradation in the gray tone representing the spill.

Transport process describing the spill evolution under the IBI, CST, and PRT models have been analyzed from the dynamical systems perspective. This perspective has allowed a qualitative comparison among them and has highlighted a similar transport scenario in the three models, in which the spreading of the fuel is controlled by the presence of a hyperbolic trajectory attached to the coast, close the "Nelson Mandela" dike, in a detachment configuration. This configuration pushes waters along the coast out into the sea. In this framework, attracting material surfaces, also called invariant unstable manifolds, are identified. Passive scalars, and fuel behaves like them, become aligned along them.

A quantitative comparison of the transport outputs by the CST and IBI models has been implemented. For blobs in a neighborhood of the accident point, an estimation of the uncertainty is provided by measuring errors or distances between simulated and observed spills. The average uncertainty is found to be lower for the CST than for the IBI model. Connections between stable manifolds and the uncertainty field have been discussed. It is observed that for both models, minimum values of the uncertainty field are aligned along stable manifolds. This is congruent with the fact that stable manifolds are optimal transport routes toward the unstable manifolds and that all models consistently present unstable manifolds aligned with the observed spill.

Summarizing, counting with a coastal downstream service focused on downscaling the regional CMEMS solution by means of a higher resolution nested model is proved to be a positive approach. In particular, high resolutions models decrease uncertainties in oil spill predictions. This confirms that high resolutions tools have the potential to be effective contributors to the decision-making processes carried out by the emergency services in the real-time management of oil spills.

DATA AVAILABILITY STATEMENT

The raw data supporting the conclusions of this article will be made available by the authors, without undue reservation.

AUTHOR CONTRIBUTIONS

GG-S did **Figures 1**, **4–6**, **8–10**. AM did **Figure 7**. GG-S and AM contributed to sections 1, 2.3, 3, 3.1, 3.2, and 4. VG-G contributed to sections 3, 3.1, and 4. SW contributed to sections 1, 3, 3.1, 3.2, and 4. AR and JC did the **Figure 2** and contributed to sections 1, 2.1, 3, and 4. BP-G, EÁ-F, MS, and MG-L did the **Figure 3** and contributed to sections 1, 2.2, 3, and 4. All authors wrote the paper.

FUNDING

The authors acknowledge support from IMPRESSIVE, a project funded by the European Union's Horizon 2020 research and innovation programme under grant agreement No 821922. The authors acknowledge support of the publication fee by the CSIC Open Access Publication Support Initiative through its Unit of Information Resources for Research (URICI). SW acknowledges the support of ONR Grant No. N00014-01-1-0769.

SUPPLEMENTARY MATERIAL

The Supplementary Material for this article can be found online at: https://www.frontiersin.org/articles/10.3389/fmars.2020.605804/full#supplementary-material

Supplementary Video 1 | The movie shows the evolution of several oil slicks overlapped with the Lagrangian Coherent Structures obtained from Copernicus IBI ocean currents (IBI model) during the Volcan de Tamasite event in April 2017 in Gran Canaria area. Oil slicks are eventually aligned with the unstable manifolds.

Supplementary Video 2 | The movie shows the evolution of several oil slicks overlapped with the Lagrangian Coherent Structures obtained from Puertos del Estado ocean currents (CST model) during the Volcan de Tamasite event in April 2017 in Gran Canaria area. Oil slicks are eventually aligned with the unstable manifolds.

REFERENCES

Amo, A., Reffray, G., Sotillo, M. G., Aznar, R., and Guihou, K. (2020). *PRODUCT USER MANUAL Atlantic -Iberian Biscay Irish- Ocean Physics Analysis and Forecast Product: IBI_ANALYSIS_FORECAST_PHYS_005_001*. Available online at: https://resources.marine.copernicus.eu/documents/PUM/CMEMS-IBI-PUM-005-001.pdf

Aznar, R., Sotillo, M., Cailleau, S., Lorente, P., Levier, B., Amo-Baladrón, A., et al. (2016). Strengths and weaknesses of the CMEMS forecasted and reanalyzed solutions for the Iberia-Biscay-Ireland (IBI) waters. *J. Mar. Syst*. 159, 1–14. doi: 10.1016/j.jmarsys.2016.02.007

Balibrea-Iniesta, F., Xie, J., García-Garrido, V. J., Bertino, L., Mancho, A. M., and Wiggins, S. (2019). Lagrangian transport across the upper Arctic waters in the Canadian Basin. *Q. J. R. Meteorol. Soc*. 145, 76–91. doi: 10.1002/qj.3404

Bengtsson, L., Andrae, U., Aspelien, T., Batrak, Y., Calvo, J., de Rooy, W., et al. (2017). The HARMONIE-AROME Model Configuration in the ALADIN-HIRLAM NWP system. *Mon. Weather Rev*. 145, 1919–1935. doi: 10.1175/MWR-D-16-0417.1

Butler, J. N. (1976). "Transfer of petroleum residues from sea to air: evaporative weathering," in *Marine Pollutant Transfer* eds H. L. Windom and R. A. Duce (Toronto, ON: Lexington Books), 201–212.

Capet, A., Fernández, V., She, J., Dabrowski, T., Umgiesser, G., Staneva, J., et al. (2020). Operational modeling capacity in European seas–An EuroGOOS perspective and recommendations for improvement. *Front. Mar. Sci*. 7:129. doi: 10.3389/fmars.2020.00129

Cartwright, J. H. E., Feudel, U., Károlyi, G., de Moura, A., Piro, O., and Tél, T. (2010). "Dynamics of finite-size particles in chaotic fluid flows," in *Non-linear Dynamics and Chaos: Advances and Perspectives* eds M. Thiel, J. Kurths, M. C. Romano, G. Károlyi, and A. Moura (Berlin; Heidelberg: Springer), 51–87. doi: 10.1007/978-3-642-04629-2_4

Cheng, Y., Li, X., Xu, Q., Garcia-Pineda, O., Andersen, O. B., and Pichel, W. G. (2011). SAR observation and model tracking of an oil spill event in coastal waters. *Mar. Pollut. Bull*. 62, 350–363. doi: 10.1016/j.marpolbul.2010.10.005

CIAIM (2018). Informe de colision del buque RO/PAX VOLCÁN DE TAMASITE contra el dique Nelson Mandela del puerto de Las Palmas de Gran Canaria, el 21 de abril de 2017. CIAIM-05/2018. Ministerio de Fomento. Gobierno de Espana. 27. Available online at: https://www.mitma.gob.es/recursos_mfom/comodin/recursos/ic_05-2018_vtamasite_web.pdf

De Dominicis, M., Bruciaferri, D., Gerin, R., Pinardi, N., Poulain, P., Garreau, P., et al. (2016). A multi-model assessment of the impact of currents, waves and wind in modelling surface drifters and oil spill. *Deep Sea Res. II Top. Stud. Oceanogr*. 133, 21–38. doi: 10.1016/j.dsr2.2016.04.002

De Dominicis, M., Pinardi, N., Zodiatis, G., and Lardner, R. (2013). MEDSLIK-II, a Lagrangian marine surface oil spill model for short-term forecasting - Part 1: theory. *Geosci. Model Dev*. 6, 1851–1869. doi: 10.5194/gmd-6-1851-2013

de la Cámara, A., Mechoso, C. R., Ide, K., Walterscheid, R., and Schubert, G. (2010). Polar night vortex breakdown and large-scale stirring in the southern stratosphere. *Clim. Dyn*. 35, 965–975. doi: 10.1007/s00382-009-0632-6

Dritschel, D. G. (1989). Contour dynamics and contour surgery: numerical algorithms for extended, high-resolution modelling of vortex dynamics in two-dimensional, inviscid, incompressible flows. *Comput. Phys. Rep*. 10, 77–146. doi: 10.1016/0167-7977(89)90004-X

Fingas, M. (2014). "Oil and petroleum evaporation," in *Handbook of Oil Spill Science and Technology* ed M. Fingas (Hoboken, NJ: John Wiley & Sons), 205–223. doi: 10.1002/9781118989982.ch7

García-Garrido, V. J., Mancho, A. M., Wiggins, S., and Mendoza, C. (2015). A dynamical systems approach to the surface search for debris associated with the disappearance of flight MH370. *Nonlin. Process. Geophys*. 22, 701–712. doi: 10.5194/npg-22-701-2015

García-Garrido, V. J., Ramos, A., Mancho, A. M., Coca, J., and Wiggins, S. (2016). A dynamical systems perspective for a real-time response to a marine oil spill. *Mar. Pollut. Bull*. 112, 201–210. doi: 10.1016/j.marpolbul.2016.08.018

Grifoll, M., Jordá, G., Sotillo, M. G., Ferrer, L., Espino, M., Sánchez-Arcilla, A., et al. (2012). Water circulation forecasting in Spanish harbours. *Sci. Mar*. 76, 45–61. doi: 10.3989/scimar.03606.18B

Haller, G., and Yuan, G. (2000). Lagrangian coherent structures and mixing in two-dimensional turbulence. *Phys. D* 147, 352–370. doi: 10.1016/S0167-2789(00)00142-1

Large, W. G., and Yeager, S. (2004). *Diurnal to Decadal Global Forcing for Ocean and Sea-Ice Models: The Data Sets and Flux Climatologies*. University Corporation for Atmospheric Research.

Lekien, F., Coulliette, C., Mariano, A., Ryan, E., Shay, L., Haller, G., et al. (2005). Pollution release tied to invariant manifolds: a case study for the coast of Florida. *Phys. D* 210, 1–20. doi: 10.1016/j.physd.2005.06.023

Lopesino, C., Balibrea-Iniesta, F., García-Garrido, V. J., Wiggins, S., and Mancho, A. M. (2017). A theoretical framework for lagrangian descriptors. *Int. J. Bifurcat. Chaos* 27:1730001. doi: 10.1142/S0218127417300014

Lorente, P., Sotillo, M. G., Amo-Baladrón, A., Aznar, R., Levier, B., Aouf, L., et al. (2019). "The NARVAL software toolbox in support of ocean models skill assessment at regional and coastal scales," in *Proceedings of the 19th International Conference on Computational Science* (Faro). doi: 10.1007/978-3-030-22747-0_25

Madec, G., and NEMO Team (2019). Nemo ocean engine. Available online at: https://www.nemo-ocean.eu/doc/

Madrid, J. A. J., and Mancho, A. M. (2009). Distinguished trajectories in time dependent vector fields. *Chaos* 19:013111. doi: 10.1063/1.3056050

Mancho, A., Small, D., and Wiggins, S. (2004). Computation of hyperbolic trajectories and their stable and unstable manifolds for oceanographic flows represented as data sets. *Nonlinear Proc. Geoph* 11, 17–33. doi: 10.5194/npg-11-17-2004

Mancho, A., Small, D., Wiggins, S., and Ide, K. (2003). Computation of stable and unstable manifolds of hyperbolic trajectories in two-dimensional, aperiodically time-dependent vectors fields. *Phys. D* 182, 188–122. doi: 10.1016/S0167-2789(03)00152-0

Mancho, A. M., Small, D., and Wiggins, S. (2006). A tutorial on dynamical systems concepts applied to Lagrangian transport in oceanic flows defined as finite time data sets: theoretical and computational issues. *Phys. Rep*. 437, 55–124. doi: 10.1016/j.physrep.2006.09.005

Mancho, A. M., Wiggins, S., Curbelo, J., and Mendoza, C. (2013). Lagrangian descriptors: a method for revealing phase space structures of general time dependent dynamical systems. *Commun. Nonlinear Sci. Num. Simul*. 18, 3530–3557. doi: 10.1016/j.cnsns.2013.05.002

Marta-Almeida, M., Ruiz-Villarreal, M., Pereira, J., Otero, P., Cirano, M., Zhang, X., et al. (2013). Efficient tools for marine operational forecast and oil spill tracking. *Mar. Pollut. Bull*. 71, 139–151. doi: 10.1016/j.marpolbul.2013.03.022

Maxey, M. R., and Riley, J. J. (1983). Equation of motion for a small rigid sphere in a nonuniform flow. *Phys. Fluids* 26:883. doi: 10.1063/1.864230

McIlroy, J. W., Smith, R. W., and McGuffin, V. L. (2018). Fixed- and variable-temperature kinetic models to predict evaporation of petroleum distillates for fire debris applications. *Separations* 5, 1–19. doi: 10.3390/separations5040047

Mendoza, C., and Mancho, A. M. (2010). The hidden geometry of ocean flows. *Phys. Rev. Lett*. 105:038501. doi: 10.1103/PhysRevLett.105.038501

Monroy, P. (2019). *Doctoral thesis: Lagrangian studies of sedimentation and transport. Impact on marine ecosystems*. Universitat de les Illes Balears. Available online at: https://ifisc.uib-csic.es/es/publications/lagrangian-studies-of-sedimentation-and-transport/

Monroy, P., Hernández-Garcia, E., Rossi, V., and López, C. (2017). Modeling the dynamical sinking of biogenic particles in oceanic flow. *Nonlin. Process. Geophys*. 24, 293–305. doi: 10.5194/npg-24-293-2017

Montero, A. R. (2017). *La reducción de la mancha de gasoil un 80% permite abrir las ocho playas*. La Provincia. Available online at: https://www.laprovincia.es/las-palmas/2017/04/25/reduccion-mancha-gasoil-80-permite-9723032.html

Olascoaga, M. J., and Haller, G. (2012). Forecasting sudden changes in environmental pollution patterns. *Proc. Natl. Acad. Sci. U.S.A*. 109, 4738–4743. doi: 10.1073/pnas.1118574109

Pisano, A., Bignami, F., and Santoleri, R. (2015). Oil spill detection in glint-contaminated near infrared modis imagery. *Remote Sens*. 7, 1112–1134. doi: 10.3390/rs70101112

Shapiro, R. (1970). Smoothing, filtering, and boundary effects. *Rev. Geophys*. 8, 359–387. doi: 10.1029/RG008i002p00359

Shchepetkin, A. F., and McWilliams, J. C. (2005). The regional oceanic modeling system (ROMS): a split-explicit, free-surface, topography-following-coordinate oceanic model. *Ocean Modell*. 9, 347–404. doi: 10.1016/j.ocemod.2004.08.002

Song, Y., and Haidvogel, D. (1994). A semi-implicit ocean circulation model using a generalized topography-following coordinate system. *J. Comput. Phys*. 115, 228–244. doi: 10.1006/jcph.1994.1189

Sotillo, M., Levier, B., Lorente, P., Guihou, K., and Aznar, R. (2020a). *CMEMS Quality Information Document for the CMEMS IBI Product: IBI_ANALYSIS_FORECAST_PHYS_005_001*. Available online at: https://resources.marine.copernicus.eu/documents/QUID/CMEMS-IBI-QUID-005-001.pdf

Sotillo, M. G., Cailleau, S., Lorente, P., Levier, B., Aznar, R., Reffray, G., et al. (2015). The MyOcean IBI Ocean Forecast and Reanalysis Systems: operational products and roadmap to the future Copernicus Service. *J. Operat. Oceanogr*. 8, 63–79. doi: 10.1080/1755876X.2015.1014663

Sotillo, M. G., Cerralbo, P., Lorente, P., Grifoll, M., Espino, M., Sanchez-Arcilla, A., et al. (2020b). Coastal ocean forecasting in Spanish ports: the SAMOA operational service. *J. Operat. Oceanogr*. 13, 37–54. doi: 10.1080/1755876X.2019.1606765

TeldeActualidad/EFE (2017). *La punta de la mancha, de 13 km. de largo, ya esta a la altura de La Garita pero a 1.000 metros de la costa*. Telde Actualidad, Available online at: https://www.teldeactualidad.com/hemeroteca/noticia/medioambiente/2017/04/23/2402.html

Vanhellemont, Q. (2019). Remote sensing of environment adaptation of the dark spectrum fi fitting atmospheric correction for aquatic applications of the Landsat and Sentinel-2 archives. *Remote Sens. Environ*. 225, 175–192. doi: 10.1016/j.rse.2019.03.010

Warner, J. C., Sherwood, C. R., Arango, H. G., and Signell, R. P. (2005). Performance of four turbulence closure models implemented using a generic length scale method. *Ocean Modell*. 8, 81–113. doi: 10.1016/j.ocemod.2003.12.003

Wiggins, S. (2005). The dynamical systems approach to Lagrangian transport in oceanic flows. *Annu. Rev. Fluid Mech*. 37, 295–328. doi: 10.1146/annurev.fluid.37.061903.175815

Xu, Q., Li, X., Wei, Y., Tang, Z., Cheng, Y., and Pichel, W. G. (2013). Satellite observations and modeling of oil spill trajectories in the Bohai Sea. *Mar. Pollut. Bull*. 71, 107–116. doi: 10.1016/j.marpolbul.2013.03.028

Conflict of Interest: The authors declare that the research was conducted in the absence of any commercial or financial relationships that could be construed as a potential conflict of interest.

frontiers
in Marine Science

ORIGINAL RESEARCH
published: 19 February 2021
doi: 10.3389/fmars.2021.576747

A Coupled Lagrangian-Earth System Model for Predicting Oil Photooxidation

Ana C. Vaz[1]*, *Robin Faillettaz*[1,2] *and Claire B. Paris*[1]*

[1] *Paris Laboratory, Department of Ocean Sciences, Rosenstiel School of Marine and Atmospheric Science, University of Miami, Miami, FL, United States,* [2] *Ifremer, STH, Lorient, France*

During the Deepwater Horizon (DWH) blowout, photooxidation of surface oil led to the formation of persistent photooxidized compounds, still found in shoreline sediments a decade later. Studies demonstrated that photooxidation modified both biodegradation rates of the surface oil and the effectiveness of aerial dispersant applications. Despite the significant consequences of this weathering pathway, the lack of measurements prevented photooxidation to be accounted for in the DWH oil budget calculations and in most predictive models. Here we develop a Lagrangian photooxidation module that estimates the dose of solar radiation individual oil droplets receive while moving in the ocean, quantifies the likelihood of photooxidative changes, and continues to track the transport of these persistent photooxidized compounds. We estimate and track the likelihood of photooxidation of Lagrangian oil droplets in the upper layers of the water column for the DWH case by coupling the net shortwave radiation from NOGAPS to the oil application of the Connectivity Modeling System (oil-CMS). The dose of solar radiation upon a droplet is computed with the intensity of the incoming irradiance at the ocean's surface, the light attenuation coefficient, and the depth of the oil droplets. Considering a range of DWH empirical irradiance thresholds, we find that photooxidation can happen at short time scales of hours to days, in agreement with the new paradigm of oil photooxidation. Furthermore, the oxidized compounds are likely to form in a 110 km radius around the response site, suggesting that the oil reaching the coastline was already photooxidized. This new dynamic coupling provides a powerful tool to test oil weathering hypotheses, refine the oil budget during the DWH, and ultimately inform rapid response in future oil spills.

Keywords: oil spill, oil photooxidation, irradiance, oil weathering, Deepwater Horizon, oil-Connectivity modeling System, oil modeling

Edited by:
Andrew James Manning,
HR Wallingford, United Kingdom

Reviewed by:
Phoebe Zito,
University of New Orleans,
United States
Michel C. Boufadel,
New Jersey Institute of Technology,
United States

***Correspondence:**
Ana C. Vaz
avaz@rsmas.miami.edu
Claire B. Paris
cparis@rsmas.miami.edu

Specialty section:
This article was submitted to
Marine Biogeochemistry,
a section of the journal
Frontiers in Marine Science

Received: *26 June 2020*
Accepted: *11 January 2021*
Published: *19 February 2021*

Citation:
Vaz AC, Faillettaz R and Paris CB (2021) A Coupled Lagrangian-Earth System Model for Predicting Oil Photooxidation.
Front. Mar. Sci. 8:576747.
doi: 10.3389/fmars.2021.576747

INTRODUCTION

The Deepwater Horizon (DWH) was an unprecedented spill: the deepest and the largest spill in history, it released over 130 million gallons of a mixture of oil and natural gas at 5000 feet under the sea surface for over 87 days (McNutt et al., 2012; Paris et al., 2018). Its unique magnitude, location, and multiphase oil composition proved a challenge for the accurate prediction of oil fate and transport at the time of the accident. In the aftermath of the DWH blowout, numerical models for the forecast of oil spills advanced significantly, and key processes driving oil fate and transport previously absent from predictive numerical tools were incorporated (Le Hénaff et al., 2012; Paris et al., 2013; Zhao et al., 2014, 2015, 2017; Lindo-Atichati et al., 2016; French-McCay et al., 2017; Gros et al., 2017; Dissanayake et al., 2018; Perlin et al., 2020; Boufadel et al., 2020; Bracco et al., 2020; Vaz et al., 2020). Yet the critical weathering pathway of near-surface photooxidation still lacks from oil spill numerical models, particularly the now well-defined effects of varying sunlight on photooxidation (Ward et al., 2018a,b; Ward and Overton, 2020). Here we fill this lacuna by translating recent laboratory and field studies into a photooxidation module for the oil fate and transport application of the Connectivity Modeling System (oil-CMS, Paris et al., 2012, 2013). The novel photooxidation Lagrangian algorithm integrates spatio-temporally explicit solar irradiance from Earth Systems models to estimate the cumulative irradiance received by each droplet as they are transported, along with estimating the likelihood of photo-induced changes on individual Lagrangian droplets.

During an oil spill, physical-chemical composition changes are set forward by a series of weathering processes including biodegradation, dissolution, evaporation, sedimentation and photooxidation once oil enters the oceanic environment (Tarr et al., 2016; Ward and Overton, 2020). It has been long known that solar radiation can change the physicochemical characteristics of oil (Payne and Phillips, 1985; Garrett et al., 1998; Lehr, 2001), and more recently two major mechanisms were described: (1) by direct photolysis of light-absorbing compounds such as PAHs (Shankar et al., 2015; Ward et al., 2020) or by (2) indirect photooxidation, which occurs when direct photolysis creates free oxygen species that can then combine with a number of hydrocarbon compounds; in this case, changes are not limited to light-absorbing ones (Shankar et al., 2015; Hall et al., 2013; Ray et al., 2014; Ray and Tarr, 2014; Ruddy et al., 2014; Ward et al., 2019). Both mechanisms thus form new products, which can be highly soluble in water and be further dispersed, or can lead to the formation of emulsifications (Payne and Phillips, 1985; Garrett et al., 1998; Lehr, 2001; Xie et al., 2007). Emulsification, on its turn, can reduce oil evaporation, change the oil spread characteristics, and enhance aggregations to organic and inorganic matter, thus increasing sedimentation (Payne and Phillips, 1985; Fingas et al., 1999; Hayworth et al., 2015; Ward and Overton, 2020). Additionally, emulsification can also affect the outcome of response alternatives since emulsions are heavier, more difficult to remove with traditional skimmers, and can turn chemical dispersants ineffective (Xie et al., 2007; Tarr et al., 2016; Ward et al., 2020). Emulsions are also the precursors of surface residual balls (SRBs), or tar balls, which can continue to reach and pollute nearshore environments years after a spill (Overton et al., 1980; Aeppli et al., 2012; Warnock et al., 2015; White et al., 2016; Aeppli et al., 2018).

At the time of the DWH spill, photooxidation was expected to occur mainly as direct photolysis, happening at temporal scales of weeks to months and affecting a small portion of the oil (Clark, 2001; National Research Council [NRC], 2003; Ward and Overton, 2020). Thus, there were not enough measurements to be considered in the DWH NOAA Oil Budget Calculator (Lehr et al., 2010) or in DWH's predictive models. The best representation of this process was limited to a parameterization of PAH photolysis using seasonal coefficients constant for the first 20 m of the water column (French-McCay, 2004; French-McCay et al., 2017). To this day, solar irradiance is still not incorporated as a spatio-temporally explicit parameter in any Lagrangian model of oil transport (Ward and Overton, 2020). However, photooxidation was a significant fate pathway of DWH oil, leading to the formation of persistent partially oxidized compounds, which are still found in shoreline sediment for nearly a decade after the oil spill (Ward et al., 2018a,b; Aeppli et al., 2018). During the DWH spill, photooxidation acted at scales of hours to days (Ward et al., 2018b), and indirect photooxidation was revealed to be a primary pathway of photooxidation (Ray et al., 2014; Ray and Tarr, 2014; Aeppli et al., 2018; Ward et al., 2018b).

Remarkably, the chemical changes induced by photooxidation on the DWH oil affected the effectiveness of surface dispersant applications, lowering its expected dispersive effect (Ward et al., 2018a). Noteworthily, solar irradiance leads to changes not only on the oil but also modified the microbial fauna facilitating biodegradation (Bacosa et al., 2015), and altered the composition of the chemical dispersants used during the response to the DWH, COREXIT 9500A and 9527 (Glover et al., 2014). Taken together, these findings reveal that photooxidation needs to be taken into account not only in predictions of oil transport, but also for the planning of response and mitigation activities (Ward and Overton, 2020). Thus, it seems fundamental for Lagrangian models of oil to consider the effect of varying solar irradiance on the outcome of a spill. Here, we further use the novel module we developed to probabilistically explore the spatial and temporal scales of photooxidized compounds (POCs) generation during the DWH, their transport and fate, and investigate the importance of considering irradiance as an explicit input on oil spill models.

METHODS

Oil-CMS Description

In this study, the far-field modeling of the blowout is done using a deep-sea oil spill application developed during and post DWH based on the Connectivity Modeling System (CMS, Paris et al., 2013), the oil-CMS (Paris et al., 2012; Perlin et al., 2020; Vaz et al., 2020). The oil-CMS is a Lagrangian model that estimates both the transport and continuous changes on the composition and fate of oil droplets. The oil-CMS uses velocity fields and observations to represent the local or regional hydrodynamic and pseudo-components, including a varying composition, to provide a detailed description of the two-phase petroleum mixture. At each time step, both transport and fate processes are calculated, and the output allows the conversion of location and droplet characteristics into four-dimensional grids of oil concentrations. The oil-CMS hindcasts the transport and fate of the surface oil, DWH plume, and deposition over a few months (Paris et al., 2012; Le Hénaff et al., 2012; Lindo-Atichati et al., 2016; Perlin et al., 2020; Berenshtein et al., 2020). It can also generate the most characteristic distributions of initial DSDs, including gaussian and log-normal (Perlin et al., 2020; Faillettaz et al., 2021).

Throughout the far-field, the advection of individual droplets is represented by a deterministic component—solved by a 4th order Runge-Kutta integration scheme of velocity fields over time and space—and an added random displacement, representing sub-grid scale turbulent diffusion (Okubo, 1971; Paris et al., 2013). To account for oil transport due to drift induced by the wind and wind-generated features, we incorporated a wind component in the surface velocities (Le Hénaff et al., 2012; Perlin et al., 2020). The vertical terminal velocities in oil-CMS are given by relationships dependent on the droplet buoyancy, density, size and shape, and the ambient fluid viscosity and density (Clift et al., 1978; Zheng et al., 2003; Paris et al., 2012). The processes affecting oil fate are calculated throughout their advection, including sedimentation, landfall, biodegradation, dissolution, and evaporation (Paris et al., 2012; Le Hénaff et al., 2012; Lindo-Atichati et al., 2016; Perlin et al., 2020).

Solar Irradiance Module Implementation in Oil-CMS

To account for the likelihood of photooxidation in oil-CMS, we calculate the incident solar irradiance, *i.e.,* the sunlight, received by each droplet and time-step, following the method described in Faillettaz et al. (unpublished). In short, at each time-step the solar shortwave irradiance from NOGAPS (Hogan et al., 1991; Rosmond et al., 2002, see section "Input Data and Modeling Scenario") is interpolated to each droplet's horizontal position. The shortwave irradiance encompasses the UV and visible irradiance (Gould et al., 2019; Clough et al., 2005) which together drive most of O_2 uptake (Ward et al., 2018a,b). The irradiance penetration in the water column is modulated by the Beer-Lambert law, $I_z = I_{0m} * exp^{-K_d*z}$, where I_{0m} is the surface irradiance, z is the droplet depth and K_d is the light attenuation coefficient, which can be defined explicitly in space and time. The oil-CMS then tracks the cumulative incident solar shortwave on each droplet over time, and these values are used to determine when photooxidation is likely to occur, based on the latest published evidence (Ward et al., 2018a,b). Thus, the cumulative irradiance is calculated over the entire dispersal of the oil droplets, which includes periods of high exposure, *e.g.,* during the day and at surface, and low to no exposure when droplets are in the subsurface and at night. Our approach is modular and can be updated to accommodate new findings of photooxidation processes and oil changes, as they become available, particularly regarding specific changes in oil composition and physicochemical characteristics with exposure to sunlight. Our approach is a significant advancement from present models, by considering the incident solar radiation on each droplet. We are also able to circumvent current empirical data limitations by using an irradiance threshold from laboratory results to calculate the likelihood of photooxidation, which can thus consider the possibility of photooxidation by both direct and indirect processes.

Input Data and Modeling Scenario

Here we focus on the DWH spill scenario. The environmental variables (zonal, meridional, and vertical velocities, temperature, and salinity) were obtained from the Gulf of Mexico HYCOM (GoM-HYCOM) hindcast (0.04° horizontal resolution, and 40 vertical layers). The GoM-HYCOM is forced by the Navy Operational Global Atmospheric Prediction System (NOGAPS) winds and surface fluxes, by large-scale model fields at the Atlantic boundary, and by data assimilation with the Navy Coupled Ocean Data Assimilation (NCODA) system. We used 3-hourly wind velocities on a 0.5° grid resolution from NOGAPS to account for surface wind drift, and the 3-hourly irradiance from the NOGAPS given on a 0.5° grid to estimate the photooxidation. Our initial droplet size distribution (DSD) is defined by a log-normal distribution with a mean of 117 μm and a standard deviation of 0.72 μm, based on published distributions of oil droplet size (Spaulding et al., 2017). Droplets are released at the trap height, which is the depth at which individual droplets and gas bubbles rise out of the initial highly buoyant and coalescent near-field plume, and its represented approximately at 300 m above Macondo wellhead (Socolofsky et al., 2011).

For the estimation of photooxidation, we used a conservative attenuation coefficient $K_d = 5\ m^{-1}$, which attenuates sunlight to 0.7% of the surface irradiance at 1 m depth. This choice of a conservative K_d is higher than typical K_d values for offshore waters in the northern GoM (mean $K_d = 0.06 \pm 0.02\ m^{-1}$, Bridges et al., 2018) to account for the oil reducing the light penetration. We have taken a probabilistic approach, whereby individual oil droplets are likely to become oxidized once solar irradiance accumulated over their trajectory (i.e., during each integration time step) reach a determined threshold. Further modeling of physicochemical changes (e.g., density, viscosity, IFT, oxidation state) of individual droplet is limited by the lack of data for specific hydrocarbon pseudo-components. Our model thus assumes that a droplet is likely to be oxidized by photooxidation once it accumulates solar irradiance up to a determined threshold. In this experiment, our thresholds were derived from the study by Ward et al. (2018a) who measured physical and chemical changes of oil under simulated sun radiation. The authors observed photooxidated oil after 24 h under a solar simulator (Suntest XLS+) generating 250 Wm^{-2} to 765 Wm^{-2} (Atlas Material Testing Solutions, 2016, Ward et al., 2018a). From the sunlight simulator's lower and higher irradiance ranges, we estimate a lower and a higher thresholds of cumulative irradiance necessary for photooxidation to occur. Here, the photooxidative thresholds are given by $T_I = Solar\_lamp\_output * time\_exposure$, which result in $1.16*10^7\ J\ m^{-2}$ for the lower limit of the sunlamp, and $6.60*10^7\ J\ m^{-2}$ for the higher limit. The spectrum of UV and visible light from the sun simulator used to estimate the doses in laboratory from Ward et al. (2018a) is comparable to the shortwave radiation provided in NOGAPS based on results from Gould et al. (2019), which revealed that the photosynthetically active radiation (PAR) estimated from

NOGAPS shortwave solar irradiance is a good representation of PAR measured in situ in the region of the Gulf adjacent to the DWH response site.

Data Analysis

Hereafter a droplet is considered 'photooxidized' once its cumulative irradiance reaches the phootoxidation thresholds defined above. To analyze the distribution and time of the likelihood of solar radiation-driven changes, for each release and photooxidized droplet we estimate: (i) the distance from the DWH response site (i.e., above the Macondo well) at which photooxidation took place, (ii) the distance traveled by a droplet from its surfacing location to where it likely photooxidized, and finally (iii) the time from surfacing to probable photooxidation (**Figure 3**). Since droplets are released in the model at the trap height (1222 m depth), it is necessary to distinguish the different temporal ranges between the time/distance from release to reaching the photooxidation threshold (i.e., the droplets' ascension and drift until photooxidation) and the time/distance traveled from droplet surfacing (i.e., when droplets reach depths of shallower than 2 m and start to accumulate incoming solar irradiance); the latter is automatically shorter than the former. We also calculated the probabilistic distribution functions (PDF) of initial distributions of POCs along the spill for both the low and high irradiance thresholds and quantified the distances from the DWH response site which encompasses 25, 50, 75, and 100% of the likelihood of photooxidized compounds formation.

Moreover, since oil-CMS simulates several processes of oil fate, we can identify the probable distributions of photooxidized droplets which were beached and/or deposited along the spill. We constructed a grid covering the northern Gulf (from 26°N to 31°N, from −98°W to −82°W), with a 0.25° resolution, using the coordinates (latitude and longitude) of each photooxidized droplet deposited on the seafloor or coastline. We then distributed the droplets along the grid, calculating the probability of landfall in each bin and plotting these as PDF maps of coastline oiling. To account for the variability of these processes, we also plotted the PDF maps at daily intervals and the overall probabilities for both scenarios (low and high irradiance thresholds).

RESULTS

The median and the median absolute deviance (mad) of the solar irradiance are shown in **Figure 1**. Solar irradiance is taken from the NOGAPS irradiance forecasts during daylight hours (*ca.* 7am to 7pm CST) over the Gulf region adjacent to the DWH response site, encompassing most of the spilled oil (from 27°N to 30°N and from 90°W to 86°W). The solar irradiance median ranges from 177 Wm^{-2} to 716 Wm^{-2} over this period, with substantial daily and weekly changes, for example between June 1st and June 4th when the median solar irradiance varies from 695.9 Wm^{-2} on June 1st to 356 Wm^{-2} on June 2nd, back to 677.7 Wm^{-2} on June 4th. The passage of Hurricane Alex through the Gulf also drives low irradiance values and high variability, with 265.1 Wm^{-2} on July 1st, 373.4 $W\ m^{-2}$ on July 3rd, and a sunnier day on July 2nd that triggered a marked increase in the median irradiance (546 Wm^{-2}). The ranges of the median absolute deviance show that the solar irradiance over this region also varies over short (hourly) time scales and spatially based on the cloud coverage (**Figure 1**).

To explore how this varying solar irradiance can affect the probability of POCs formation, we investigate the locations where photooxidation likely took place along the spill duration, considering the higher, and thus most conservative, threshold for photooxidative changes (Ward et al., 2018a). As expected from the dynamic and turbulent nature of surface currents, the oil concentrations vary along the evolution of the spill (**Figure 2**). Interestingly, the locations where most photooxidation occurs are also highly variable and not necessarily in close proximity to the response site (**Figure 2**). For example, POCs accumulate in the region around the DWH response site on June 10th (**Figure 2c**), while on other days, POCs spread around a larger region: on April 20th, POCs are formed mainly along the southern branch of the surface oil slick (**Figure 2a**), and on July 10th, our model predicts that photooxidation likely occurs to the north, east and southeast of the DWH response site along coastal regions, over the DeSoto Canyon, and towards the Gulf interior where POCs are likely distributed in a semi-circular pattern, seemly along a mesoscale eddy, which is not observed for the oil surface concentrations (**Figure 2b**).

We then examine the spatio-temporal scales of photooxidation by computing PDFs of the locations where POCs likely formed throughout the duration of the DWH oil spill (**Figures 3a,b**). These areas are widely distributed, with the higher probabilities close to the response site above the Macondo well, for both the lower (**Figure 3a**) and the higher irradiance thresholds (**Figure 3b**). Under the lower threshold scenario, probabilities of POCs formation are restricted to the open ocean, in regions closer to the DWH response site, seldom occurring in depths less than 50 m near coastal zones. Under the higher threshold of irradiance, POCs form over a broader region, reaching both areas of open ocean south of the spill location and shallower areas (< 50 m) near the coast. These differences are reflected in the distance from the response site where photooxidation is likely to occur in our model. For the lower threshold (**Figure 3a**), 25% of photooxidative changes happen in an area of 34 km around the DWH response site, 50% at 56 km, 75% at 83 km, with a maximum distance reached by a POC of 927 km. For the higher threshold, 25% of changes are likely to occur within 56 km, 50% within 78 km and 75% within 111 km, while the maximum distance traveled before reaching the oxidation threshold remained similar (928 km, **Figure 3b**). On average, the distance to photooxidation from the DWH response site varies from *ca.* 60 km for the lower threshold to 80 km for the higher threshold. When considering the sea surface area where Corexit has been applied (**Figure 4**, Office of Response and Restoration, 2020; Houma ICP Aerial Dispersant Group, 2010), 93.9% of the applications (*ca.* 973,000 Gallons) took place where 75% of the POC formation is predicted to have occurred. This value rises to 99.3% of total dispersant applications by using the lower threshold.

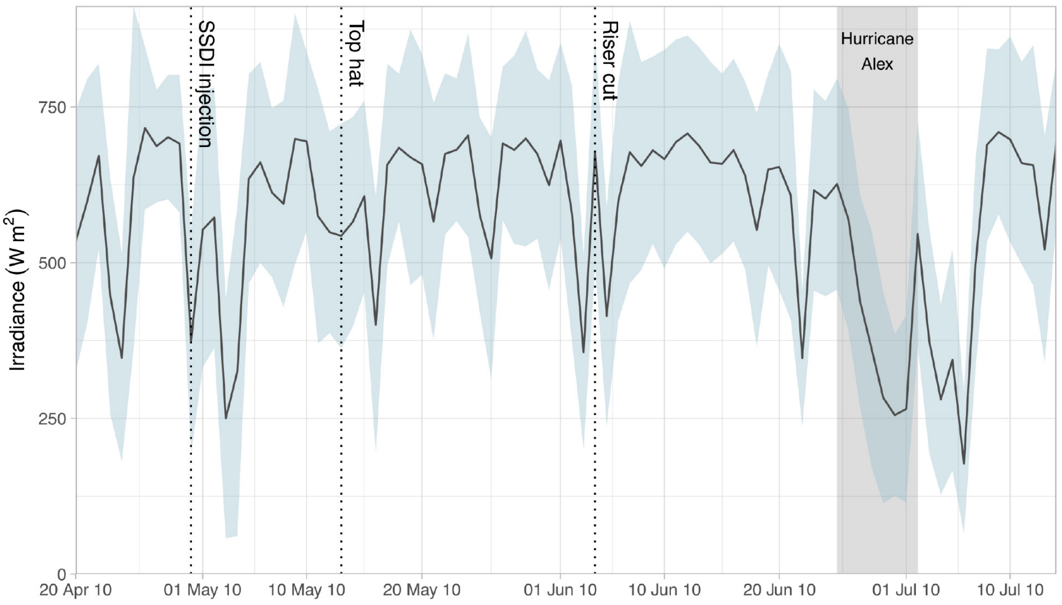

FIGURE 1 | Median (line) and median absolute deviation (mad, blue shaded area) of solar irradiance (Wm^{-2}) at the sea surface during daylight hours (7am to 7pm CST) over the area adjacent to the Macondo well and DWH response site (27°N to 30°N; 90°W to 86°W) in the Gulf of Mexico. Three-hourly shortwave solar irradiance values for the region were obtained from the 2010 NOGAPS model. Dates show significant events for response to the DWH oil spill, including the onset of SSDI (April 30th), top hat (May 13th), riser cut followed by the Lower Marine Riser Package (June 4th), and the period Hurricane Alex was present in the Gulf of Mexico (June 24th to July 2nd).

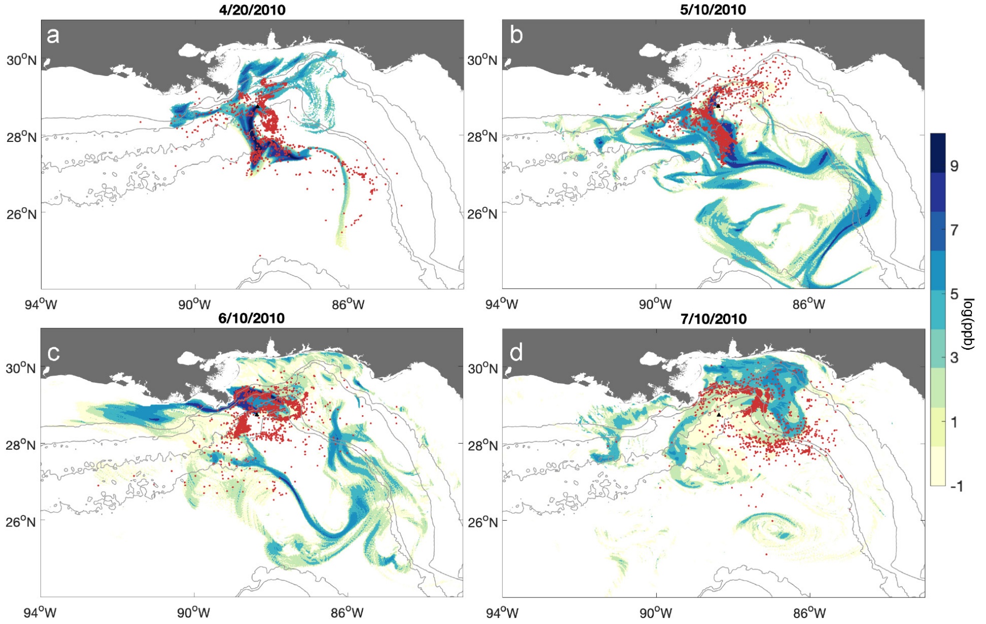

FIGURE 2 | Photooxidized components (POCs, red dots) probable formation locations, for four release days along the DWH oil spill timeline: **(a)** April 20th, 2010, **(b)** May 10th, 2010, **(c)** June 10th, 2010 and **(d)** July 10th, 2010. The background colors illustrate the oil concentration (log ppb) at the surface layer (0 to 1 m depth) 20 days after each release date. POCs are considered to form when droplets received a cumulative irradiance dose of at least 6.60*10^7 J m^{-2} (Ward et al., 2018a).

Despite the overall variability in both the locations and the transport time in which photooxidation may have taken place, we are able to delineate spatio-temporal scales to probable photooxidation (**Figures 3c,d**). The average distance traveled by droplets from their surfacing location to their photooxidation is 22.6 km for the low threshold scenario, with the 25*th* and 75*th*

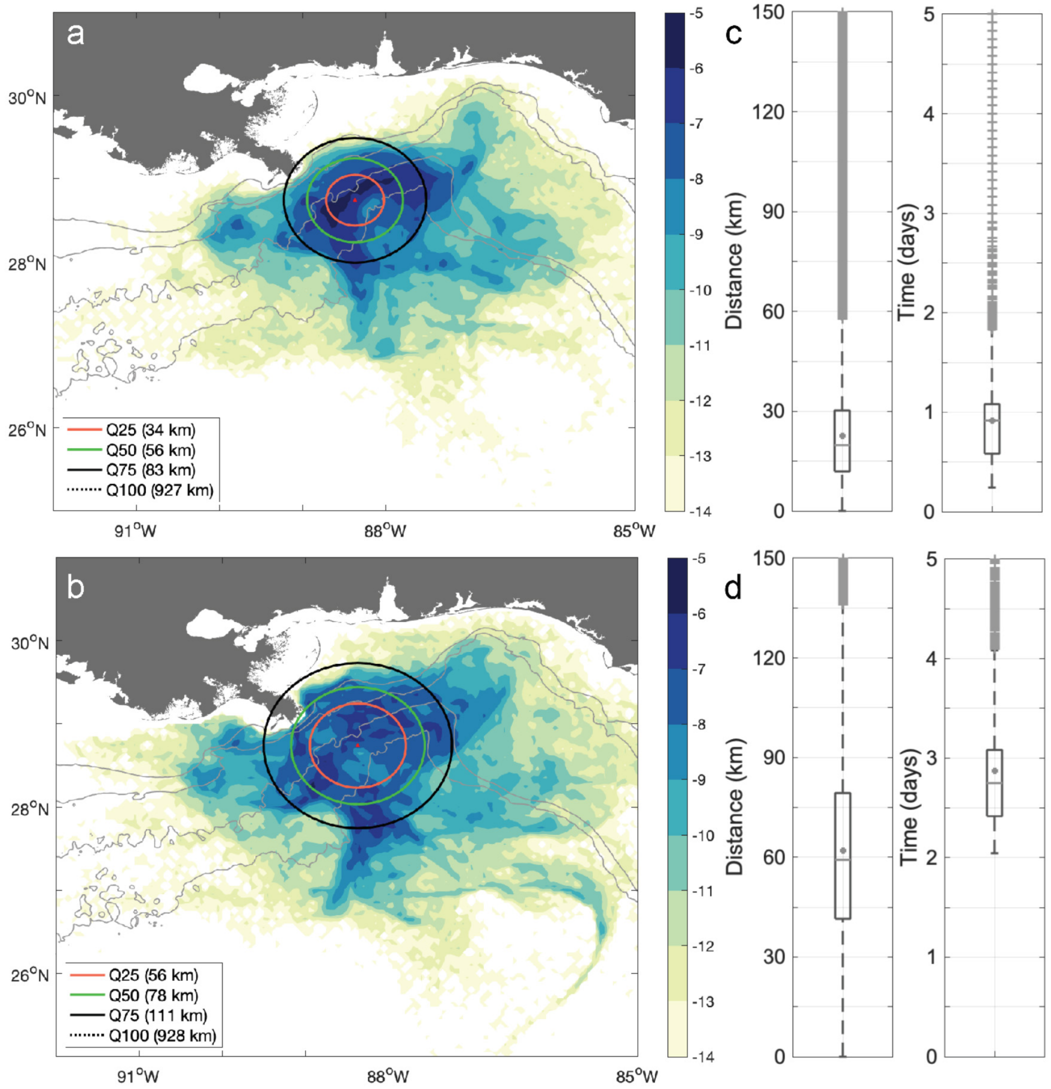

FIGURE 3 | Probability (PDF) of photooxidized components (POCs) formation during the DWH blowout **(a,b)**. Solid lines represent areas containing percentiles of POCs formation (Q25: quantile 0.25, Q50: quantile 0.5, Q75: quantile 0.75 and Q100: quantile 1), which radii are computed from the vertical axis of the Macondo well. Onset of the photooxidation process occurs as soon as the oil droplet reaches the surface, but here the likelihood of photooxidative changes is based on the observed thresholds of cumulative solar irradiance after Ward et al. (2018a). Upper panel are for the photooxidized compounds considering a lower solar irradiance threshold ($1.16*10^7$ J m^{-2}), and lower panels considering a higher solar irradiance threshold ($6.60*10^7$ J m^{-2}, Ward et al., 2018a). Boxplots (right panels, **c,d**) provide the distribution of the distance and time traveled to the likelihood of photooxidation, once the droplet reached the surface (0–1 m depth).

percentiles varying from 11.9 to 30.2 km (**Figure 3c**). For the high solar irradiance scenario, the average distance is 62 km, with the 25^{th} and 75^{th} percentiles varying from 41.4 to 79.3 km (**Figure 3d**). The average time from surfacing to photooxidation for the low threshold scenario is 0.91 days (21.9 hours), with the 25^{th} and 75^{th} percentiles ranging from 0.58 to 1 day (**Figure 3c**). For the high solar irradiance threshold case, the average time is 2.8 days (68.9 h), with the 25th and 75th percentiles varying from 2.4 to 3 days (**Figure 3d**).

The variability of incoming solar irradiance is not only reflected in the areas where photooxidation likely occur, it is also evident in the probability of POCs fate, as shown by the probability of deposition of POCs in the northern GoM (**Figure 5**). The variable nature of solar irradiance reaching the ocean surface and consequently, of light-driven processes such as photooxidation, is also evident (**Figure 5**). The oil released at the beginning of the DWH spill, on April 20th 2010, not only accumulated enough irradiance within hours of surfacing to photooxidize, as defined in our model, but it could also reach the shoreline within the first 10 days of transport (**Figure 5a**). Nonetheless, the areas most likely to receive POCs change along the duration of the spill. Oil released on April 20th and photooxidized under the higher solar irradiance threshold is most likely to reach the coast

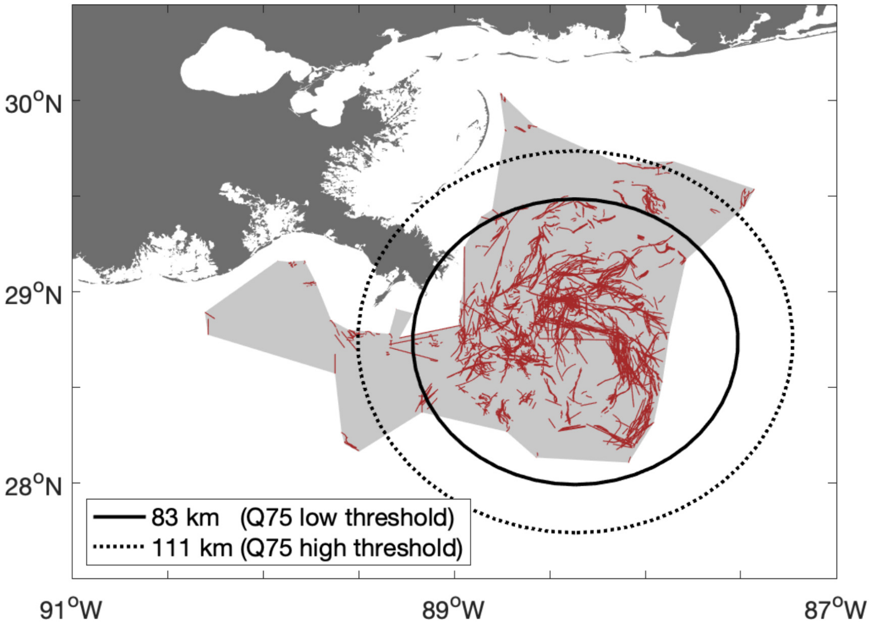

FIGURE 4 | Surface dispersant application (red tracks) and their envelope (gray polygon) during the Deepwater Horizon oil spill. Dashed and solid circles represent areas containing Q75 percentile of POCs formation, at a radial distance of 83 km and 111 km for the low and high thresholds, respectively; 93.9% and 99.3% of surface dispersant applications (total *ca.* 973,000 Gallons) occurred in the region where 75% of POC formation occurred, for the lower solar irradiance threshold (1.16*10^7 J m^{-2}) and higher irradiance threshold (6.60*10^7 J m^{-2}, Ward et al., 2018a), respectively.

of Louisiana along the Mississippi River Delta, specifically in the Lafourche Parish and Chandeleur Sound (south and east of New Orleans, respectively), and in Dauphin Islands on the Alabama coast (**Figure 5a**). Probabilities of coastline oiling are mostly distributed from Pensacola (Florida) to Marsh Island (Louisiana), yet with small probabilities of reaching as far as San Jose Islands near Corpus Christi, Texas, and Clearwater in Florida (**Figure 5a**). Conversely, the probabilities of POCs reaching the shoreline from oil spilled on May 10th are mostly distributed along the region from Marsh Island (Louisiana) to Apalachicola (Florida), with the farthest likelihoods of reaching the shore around Galveston (Texas) (**Figure 5b**). POCs from oil released on June 10th deposit in the coastline from Galveston (Texas) to Apalachicola (Florida), with higher probabilities toward the northwest of the DWH response site, around the Mississippi Delta (**Figure 5c**). For oil spewed on July 10th, shoreline POCs are mostly distributed to the Eastern Gulf, from Louisiana to Florida, with probabilities more evenly distributed along the coastline (**Figure 5**).

Despite the variable patterns of coastal oiling probabilities, we also characterize the overall probabilities along the entire duration of the oil spill, for the lower and higher solar irradiance thresholds (higher threshold results shown in **Figure 5e**). The overall probabilities of coastline deposition are similar for both scenarios, although differences are observed for the initial photooxidation locations. Low probabilities of sedimentation of POCs are spread throughout the northern Gulf, from southern Texas to Cayo Costa in southwest Florida (**Figure 5e**). The highest probabilities are confined to the northwest of the DWH response site, mostly around the banks and lobes of the Mississippi Delta. Oiling is less likely to occur around Mobile (AL) and Pensacola (FL). The time for POCs to reach the coastline is also similar for the two threshold cases, averaging 20 days and varying from 10 to 21 days (25th and 75th percentiles, respectively).

DISCUSSION

Photooxidation is, remarkably, the only major weathering process largely absent from models of oil transport (Ward and Overton, 2020), particularly due to a lack of detailed understanding of this process. The opportunity afforded by the DWH spill to contrast laboratory experiment with field measurements, has renewed the understanding of photooxidation, demonstrating that photooxidation of the DWH oil: (1) likely occurred on short timescales of hours to weeks, (2) was a relevant fate process when compared to evaporation, dissolution and biodegradation, and (3) could lower the effectiveness the application of surface dispersants (Hall et al., 2013; Ray et al., 2014; Ruddy et al., 2014; Aeppli et al., 2018; Ward et al., 2018a,b, 2019). Given this scenario, the inclusion of 4D photooxidation on oil spill models is fundamental for the accurate prediction of oil transport, fate, and the evaluation of response alternatives (Ward and Overton, 2020). The module described on this paper, developed for oil-CMS (Paris et al., 2012), is the first representation of spatio-temporally explicit photooxidation processes in a Lagrangian model of oil transport. Our framework thus fulfills the previous lacuna and contributes to advance the field of oil modeling.

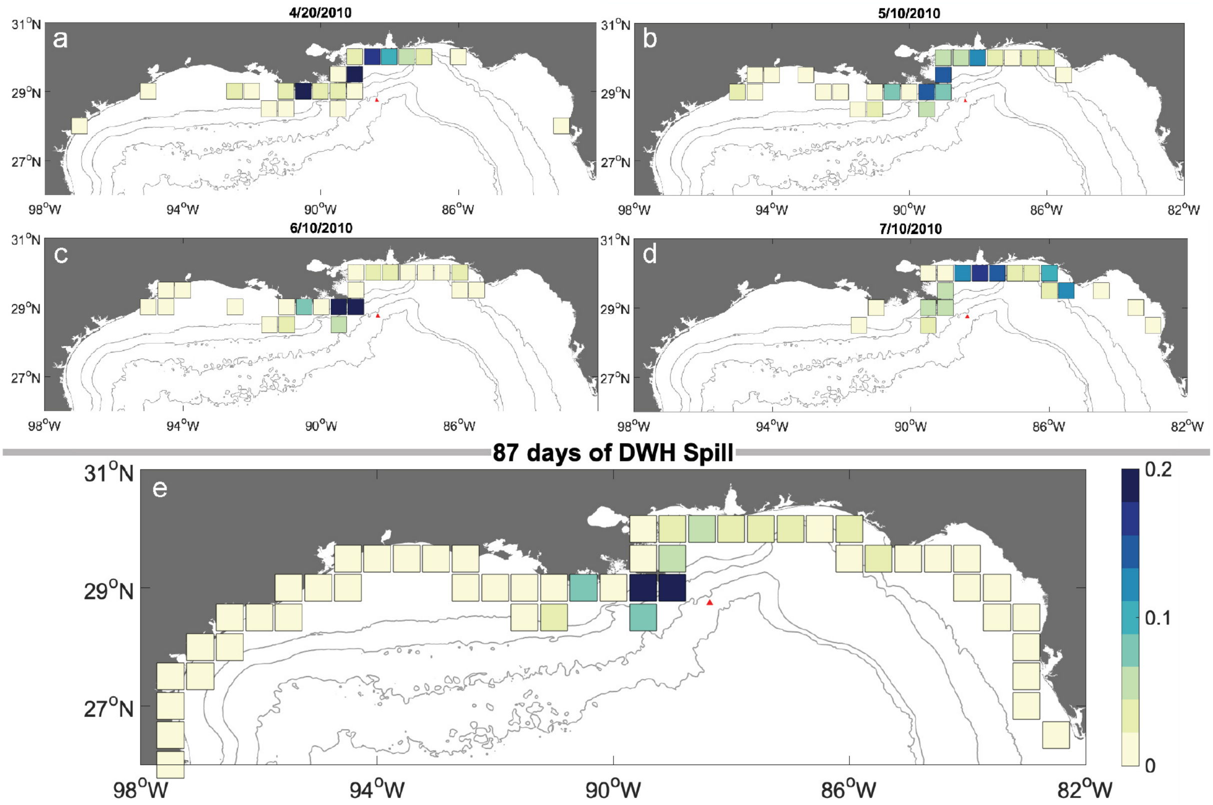

FIGURE 5 | Probability (PDFs) of sedimented photooxidized compounds from oil released on: **(a)** April 20th, 2010, **(b)** May 10th, 2010, **(c)** June 10th, 2010, **(d)** July 10th, 2010, and **(e)** during the 87 days of the DWH blowout, considering the *high solar irradiance threshold* scenario (i.e., photooxidation occurring when the droplet's cumulative irradiance reaches 6.60*10^7 Wm^{-2}, Ward et al., 2018a). Probabilities are calculated throughout the region for each 0.5° × 0.5° bins.

Our results are a strong indication that both the 4D movement of oil and spatio-temporally explicit processes driving its fate must be incorporated in oil models to fully represent this process. They further suggest that the use of constants to parameterize photooxidation cannot capture the spatio-temporal modulations of this variable process. This is exemplified in the graphs showing the locations where POCs are mostly likely formed (**Figure 3**). While the general pattern of probability of POC formation loosely follows the distribution of surface oil on this temporal snapshot, areas with higher probability of POC concentrations are not aligned with the areas with higher concentration of oil at this timeframe - 20 days after the spill - which is the average time to photooxidation from release at depth (**Figure 3**). Thus, if the likelihood of photooxidation had been estimated by a constant ratio of photooxidation based on oil concentration, it would have incorrectly captured the formation of photooxidation products. In addition, we show that solar irradiance intensity alone cannot represent the patterns of probability of photooxidation. For instance, for the period considered here, the probability of POC formation on July 10th was the one presenting the most spread throughout the surface waters of the Gulf (**Figure 5d**). Interestingly, the irradiance on July 10th is among the highest observed range over the spill region and period (*ca.* 715 Wm^{-2}; **Figure 1**) and it remains high for the next 3 days. In this example, average values of irradiance are not adequate to represent a process which is stochastic and non-linear in nature: a 4D transport (*i.e.,* in space and time) and fate model is necessary to capture the interplay between the varying solar irradiance values, the dynamic local hydrography and the droplet's evolving physicochemical properties.

Our results support that the likelihood of oil photooxidation during the DWH is spatially and temporally variable, yet mostly constrained to occur during the first 20 days after release and within a 120 km radius from the DWH response site. We show that the regions along the Northern Gulf coast to which POCs are most likely transported, accumulated and sedimented are ever changing along the spill (**Figure 5**). However, despite the variability observed over short timescales (represented by the daily PDFs of shoreline oiling), the probabilities of POCs reaching coastline are similar over entire spill for both the lower and the higher threshold to trigger photooxidation. Thus, since photooxidative processes occur on timescales of hours to days, while the oil is on the sea surface, the final distribution of POCs on the coastline is driven by circulation patterns underlying their transport and deposition. At the end of the spill, probabilities of POC distributions are spread throughout the surface waters of the Gulf of Mexico, and through the shorelines from Texas to Florida (**Figure 5**). These results indicate that not only the location where these compounds form is relevant for response and mitigation, but it is also vital to forecast where they accumulate during their transport as well as their final fate. Thus, future studies should explore not only changes in droplet's physicochemical properties, but also the influence of other physical mechanisms showed to alter oil distribution and droplet size at surface, such as waves (Zhao et al., 2014; Cui et al., 2020), and spatio-temporally explicit turbulence (Nordam et al., 2019; Boufadel et al., 2020).

Our model presents a probabilistic approach to the estimation of areas where photooxidized compounds are more likely to form, accumulate, and sediment. Comparisons of PDFs of POCs with field measurements would not yield any robust analyses given that a range of POCs cannot be captured by traditional analysis and were likely not detected during the DWH (Hall et al., 2013; Aeppli et al., 2014, 2018; Ray et al., 2014; Ruddy et al., 2014; Ward et al., 2018b). Still, our model estimates of time to initial photooxidation matched accurately the revised paradigm of photooxidation presented by Ward et al. (2018b), demonstrating its robustness. Our results show that, even for the most conservative scenario with high irradiance thresholds to photooxidation, this weathering process is likely to happen in the first 3 days after a droplet reaches the surface (**Figure 3**).

While oil deposition on beaches is well described by several studies based on the Shoreline Cleanup Assessment Technique surveys (SCAT, Michel et al., 2013; Operational Science Advisory Team III, 2013; Hayworth et al., 2015; Nixon et al., 2016), these studies assess the deposition of oil at any stage of weathering and there are no comprehensive measurements of shoreline oiling by photooxidized compounds. Oil reaching the shoreline can be further weathered by sun radiation (Hayworth et al., 2015), yet most of the photooxidation during the DWH may have occurred at surface, and the oil was transported to shore as POCs (Aeppli et al., 2018; Ward et al., 2018b). Our modeling results suggest the same: photooxidation happened in areas with depths greater than 30 m. Thus, our PDFs of POCs on shoreline can only be broadly contrasted with oil deposition from field surveys. In general, our estimates reproduce the observed extent of oiled shoreline reported by reviews of SCAT assessments (Michel et al., 2013; Operational Science Advisory Team III, 2013; Nixon et al., 2016), with probabilities of POCs reaching the coastline from Florida to Texas (**Figure 5**). The probabilities of oil reaching the farthest states (TX, FL) are small, but nonetheless there are reports of DWH tar balls reaching these areas (Operational Science Advisory Team III, 2013). Furthermore, the coastal areas most likely to receive POCs in our model are areas where SCAT reviews showed the largest accumulation of oil (Michel et al., 2013; Nixon et al., 2016), and also matched the sampling sites of oil sand patties (or SBRs) over six years following the DWH spill (Aeppli et al., 2012, 2018; White et al., 2016; Bociu et al., 2019), further supporting the representativeness of this weathering process by our model.

During the 87 days of the spill, 1.07 million gallons of Corexit 9500A and Corexit 9527A were applied at the surface by response ships and aerial applications from planes (BP Gulf Science Data, 2016). Most of the applications targeted the region in which we observed at least 75% of the formation of all POC formation in our model (**Figure 4**, Houma ICP Aerial Dispersant Group, 2010; Office of Response and Restoration, 2020). Considering a range of oil residency times at the Gulf's surface and irradiance values, Ward et al. (2018b) extrapolated their laboratory experiments and estimated regions where dispersant effectiveness was reduced; the highest distance from the DWH response site the authors estimated dispersant effectiveness would reach 45% was 124 km. In our model, this distance encompasses more than 75% of POC formation on both the higher and the lower irradiance threshold scenarios, strengthening the conclusions that applications of Corexit in this region can presented limited effectiveness to disperse this—likely photooxidized—oil.

CONCLUSION

We developed a new oil-fate module coupling the oil application of the Connectivity Modeling System (oil-CMS) with solar irradiance from Earth Systems Models (ESM) to compute spatially and temporally explicit photooxidation of petroleum fluids. The coupled oil-CMS and ESM model can successfully capture the effects of solar irradiance variability on photooxidation of the spilled hydrocarbons on a probabilistic framework. The hindcast simulations of the DWH based on observed thresholds of cumulative irradiance (Ward et al., 2018), suggest that the temporal scales to photooxidation vary from hours to days (< 3 days) from the time fresh oil reached the surface, and that photooxidation occurred mostly in a 110 km radius from the DWH response site, agreeing with the revised paradigm of photooxidation proposed by Ward et al. (2018a). By incorporating both the 4D representation of oil droplet movement and the likelihood of weathering with variable solar irradiance, our photooxidation module is a unique tool which can be used in both forecasts and hindcasts of the formation of photooxidation products during and after a marine oil spill. Our results strongly support previous conclusions that photooxidation and the fate of POCs must be taken into account during the choice of response and in the calculation of their trade-offs.

DATA AVAILABILITY STATEMENT

Data are publicly available through the Gulf of Mexico Research Initiative Information & Data Cooperative (GRIIDC) at https://data.gulfresearchinitiative.org, https://data.gulfresearchinitiative.org/data/R6.x805.000:0110, and doi: 10.7266/ADGH8VGH.

AUTHOR CONTRIBUTIONS

All authors contributed to the conception and design of the study. All authors participated in the development of the novel

CMS module, ran the simulations, and analyzed the results. AV drafted the manuscript, and all authors wrote and revised the manuscript. All authors contributed to the article and approved the submitted version.

FUNDING

This research was made possible by two grants from the Gulf of Mexico Research Initiative (GoMRI): C-IMAGE III (Center for the Integrated Modeling and Analysis of the Gulf Ecosystem) No. SA 18–16 and RECOVER 2 (Relationship of Effects of Cardiac Outcomes in fish for Validation of Ecological Risk), No. SA-1520.

ACKNOWLEDGMENTS

We thank the reviewers for their throughout and helpful comments.

REFERENCES

Aeppli, C., Carmichael, C. A., Nelson, R. K., Lemkau, K. L., Graham, W. M., Redmond, M. C., et al. (2012). Oil weathering after the Deepwater Horizon disaster led to the formation of oxygenated residues. *Environ. Sci. Technol.* 46, 8799–8807. doi: 10.1021/es3015138

Aeppli, C., Nelson, R. K., Jimenez, N., Reddy, C. M., Radovic, J. R., Bayona, J. M., et al. (2014). Assessment of photochemical processes in marine oil spill fingerprinting. *Mar. Pollut. Bull.* 79, 268–277. doi: 10.1016/j.marpolbul.2013.11.029

Aeppli, C., Swarthout, R. F., Neil, G. W. O., Katz, S. D., Nabi, D., Ward, C. P., et al. (2018). How Persistent and Bioavailable Are Oxygenated Deepwater Horizon. *Environ. Sci. Technol.* 52, 7250–7258. doi: 10.1021/acs.est.8b01001

Atlas Material Testing Solutions (2016). *Suntest XLS+*. Available online at: https://www.atlas-mts.com/products/standard-instruments/xenon-weathering/suntest/xls (accessed January 15, 2020).

Bacosa, H. P., Liu, Z., and Erdner, D. L. (2015). Natural sunlight shapes crude oil-degrading bacterial communities in northern Gulf of Mexico surface waters. *Front. Microbiol.* 6. doi: 10.3389/fmicb.2015.01325

Berenshtein, I., Perlin, N., Ainsworth, C. H., Ortega-Ortiz, J. G., Vaz, A. C., and Paris, C. B. (2020). "Comparison of the spatial extent, impacts to shorelines, and ecosystem and four-dimensional characteristics of simulated oil spills," in *Scenarios and Responses to Future Deep Oil Spills*, eds S. Murawski, et al. (Cham: Springer), doi: 10.1007/978-3-030-12963-7_20

Bociu, I., Shin, B., Wells, W. B., Kostka, J. E., Konstantinidis, K. T., and Huettel, M. (2019). Decomposition of sediment-oil-agglomerates in a Gulf of Mexico sandy beach. *Sci. Rep.* 9:10071. doi: 10.1038/s41598-019-46301-w

Boufadel, M., Liu, R., Zhao, L., Lu, Y., Özgökmen, T., Nedwed, T., et al. (2020). Transport of oil droplets in the upper ocean: impact of the eddy diffusivity. *J. Geophys. Res. Oceans* 125:e2019JC015727. doi: 10.1029/2019JC015727

BP Gulf Science Data (2016). *Application of Dispersants to Surface Oil Slicks by Aircraft and by Boat in Approved Areas of the Gulf of Mexico from April 22, 2010 to Final Application on July 19, 2010*. College Station, TX: Texas A&M University. doi: 10.7266/N70G3HK6

Bracco, A., Paris, C. B., Esbaugh, A. J., Frasier, K., Joye, S. B., Liu, G., et al. (2020). Transport, fate and impacts of the deep plume of petroleum hydrocarbons formed during the macondo blowout. *Front. Marine Sci.* 7:542147. doi: 10.3389/fmars.2020.542147

Bridges, K. N., Lay, C. R., Alloy, M. M., Gielazyn, M. L., Morris, J. M., Forth, H. P., et al. (2018). Estimating incident ultraviolet radiation exposure in the northern Gulf of Mexico during the Deepwater Horizon oil spill. *Environ. Toxicol. Chem.* 37, 1679–1687. doi: 10.1002/etc.4119

Clark, R. B. (2001). *Marine Pollution*. Oxford: Oxford University Press.

Clift, R., Grace, J., and Weber, W. E. (1978). *Bubbles, Drops, and Particles*. Mineola, N Y: Dover Publications Inc, 1978.

Clough, S. A., Shephard, M. W., Mlawer, E. J., Delamere, J. S., Iacono, M. J., Cady-Pereira, K., et al. (2005). Atmospheric radiative transfer modeling: a summary of the AER codes: Short communication. *J. Quant. Spectrosc. Radiat. Transf.* 91, 233–244. doi: 10.1016/j.jqsrt.2004.05.058

Cui, F., Daskiran, C., King, T., Robinson, B., Lee, K., Katz, J., et al. (2020). Modeling oil dispersion under breaking waves. Part I: wave hydrodynamics. *Environ. Fluid Mech.* 20, 1527–1551. doi: 10.1007/s10652-020-09753-7

Dissanayake, A. L., Gros, J., and Socolofsky, S. A. (2018). Integral models for bubble, droplet, and multiphase plume dynamics in stratification and crossflow. *Environ. Fluid Mech.* 18, 1167–1202. doi: 10.1007/s10652-018-9591-y

Faillettaz, R., Paris, C. B., Vaz, A. C., Perlin, N., Aman, Z., Schlüter, M., et al. (2021). The choice of droplet size probability distribution function for oil spill modeling is not trivial. *Mar. Pollut. Bull.* 163:11920

Fingas, M., Fieldhouse, B., and Mullin, J. (1999). Water-in-oil emulsions results of formation studies and applicability to oil spill modelling. *Spill Sci. Technol. Bull.* 5, 81–91.

French-McCay, D. P. (2004). Oil spill impact modeling: development and validation. *Environ. Toxicol. Chem.* 23, 2441–2456. doi: 10.1897/03-382

French-McCay, D., Crowley, D., and Rowe, J. (2017). Evaluation of oil fate and exposure from a deep water blowout with and without subsea dispersant injection treatment as well as traditional response activities. *Int. Oil Spill Conf. Proc.* 2017, 362–382. doi: 10.7901/2169-3358-2017.1.362

Garrett, R. M., Pickering, I. J., Haith, C. E., and Prince, R. C. (1998). Photooxidation of crude oils. *Environ. Sci. Technol.* 32, 3719–3723. doi: 10.1021/es980201r

Glover, C. M., Mezyk, S. P., Linden, K. G., and Rosario-Ortiz, F. L. (2014). Photochemical degradation of Corexit components in ocean water. *Chemosphere* 111, 596–602. doi: 10.1016/j.chemosphere.2014.05.012

Gould, R. W., Ko, D. S., Ladner, S. D., Lawson, T. A., and Macdonald, C. P. (2019). Comparison of satellite, model, and in situ values of photosynthetically available radiation (PAR). *J. Atmos. Ocean. Technol.* 36, 535–555. doi: 10.1175/JTECH-D-18-0096.1

Gros, J., Socolofsky, S. A., Dissanayake, A. L., Jun, I., Zhao, L., Boufadel, M. C., et al. (2017). Petroleum dynamics in the sea and influence of subsea dispersant injection during Deepwater Horizon. *Proc. Natl. Acad. Sci. U.S.A.* 114, 10065–10070. doi: 10.1073/pnas.1612518114

Hall, G. J., Frysinger, G. S., Aeppli, C., Carmichael, C. A., Gros, J., Lemkau, K. L., et al. (2013). Oxygenated weathering products of Deepwater Horizon oil come from surprising precursors. *Mar. Pollut. Bull.* 75, 140–149. doi: 10.1016/j.marpolbul.2013.07.048

Hayworth, J. S., Prabakhar Clement, T., John, G. F., and Yin, F. (2015). Fate of Deepwater Horizon oil in Alabama's beach system: understanding physical evolution processes based on observational data. *Mar. Pollut. Bull.* 90, 95–105. doi: 10.1016/j.marpolbul.2014.11.016

Hogan, T. F., Rosmond, T. E., and Gelaro, R. (1991). The NOGAPS forecast manual: a technical description. *NOARL Tech. Rep.* 13:220.

Houma ICP Aerial Dispersant Group (2010). *After Action Report: Deepwater Horizon MC252 Aerial dispersant Response. (TREX?013037)*. Available online at: http://www.mdl2179trialdocs.com/releases/release201501260800005/TREX-013037.pdf (May 19, 2020)

Le Hénaff, M., Kourafalou, V. H., Paris, C. B., Helgers, J., Aman, Z. M., Hogan, P. J., et al. (2012). Surface evolution of the deepwater horizon oil spill patch: combined effects of circulation and wind-induced drift. *Environ. Sci. Technol.* 46, 7267–7273. doi: 10.1021/es301570w

Lehr, W. J. (2001). "Review of the modeling procedures for oil spill weathering behavior," in *Oil Spill Modeling and Processes*, ed. C. A. Brebbia (London: WIT Press), 161.

Lehr, W. J., Bristol, S., and Possolo, A. (2010). Deepwater Horizon Oil Budget Calculator: A Report to the National Incident Command. The Federal Interagency Solutions Group, Oil Budget Calculator Science and Engineering Team. Available online at: http://www.restorethegulf.gov/sites/default/files/documents/pdf/OilBudgetCalc_Full_HQ-Print_111110.pdf (accessed March 9, 2019).

Lindo-Atichati, D., Paris, C. B., Le Hénaff, M., Schedler, M., Valladares Juárez, A. G., and Müller, A. (2016). Simulating the effects of droplet size, high-pressure biodegradation, and variable flow rate on the subsea evolution of deep plumes from the Macondo blowout. *Deep Sea Res. Part II Top. Stud. Oceanogr.* 129, 301–310. doi: 10.1016/j.dsr2.2014.01.011

McNutt, M., Camilli, R., Crone, T. J., Guthrie, G. D., Hsieh, P. A., Ryerson, T. B., et al. (2012). Review of flow rate estimates of the Deepwater Horizon oil spill. *Proc. Nat. Acad. Sci. U.S.A.* 109, 20260–20267. doi: 10.1073/pnas.1112139108

Michel, J., Owens, E. H., Zengel, S., Graham, A., Nixon, Z., Allard, T., et al. (2013). Extent and degree of shoreline oiling: deepwater horizon oil spill, Gulf of Mexico, USA. *PLoS One* 8:e65087. doi: 10.1371/journal.pone.0065087

National Research Council [NRC] (2003). *Oil in the Sea III: Inputs, Fates, and Effects*. Washington, DC: The National Academies Press. doi: 10.17226/10388

Nixon, Z., Zengel, S., Baker, M., Steinhoff, M., Fricano, G., Rouhani, S., et al. (2016). Shoreline oiling from the Deepwater Horizon oil spill. *Mar. Pollut. Bull.* 107, 170–178. doi: 10.1016/j.marpolbul.2016.04.003

Nordam, T., Kristiansen, R., Nepstad, R., and Röhrs, J. (2019). Numerical analysis of boundary conditions in a Lagrangian particle model for vertical mixing, transport and surfacing of buoyant particles in the water column. *Ocean Model.* 136, 107–119. doi: 10.1016/j.ocemod.2019.03.003

Office of Response and Restoration (2020). *Environmental Response Management Application (ERMA\$) : Gulf of Mexico*. Available online at: https://erma.noaa.gov/gulfofmexico/erma.html (accessed December 07, 2020).

Okubo, A. (1971). Oceanic diffusion diagrams. *Deep Sea Res. Oceanogr. Abstr.* 18, 789–802. doi: 10.1016/0011-7471(71)90046-5

Operational Science Advisory Team III (2013). *Investigation of Recurring Residual Oil in Discrete Shoreline Areas in the Eastern Area of Responsibility*. Available online at: https://www.restorethegulf.gov/sites/default/files/u372/OSAT%20III%20Eastern%20States.pdf (accessed September 1, 2014).

Overton, E. B., Laseter, J. L., Mascarella, S. W., Raschke, C., Nuiry, I., and Farrington, J. W. (1980). "Photochemical oxidation of IXTOC I oil," in *Proceedings of a Symposium on Preliminary Results from the September 1979 Researcher/Pierce IXTOC-I Cruise*, (Florida: Key Biscayne), 341–383.

Paris, C. B., Berenshtein, I., Trillo, M. L., Faillettaz, R., Olascoaga, M. J., Aman, Z. M., et al. (2018). BP gulf science data reveals ineffectual sub-sea dispersant injection for the macondo blowout. *Front. Mar. Sci.* 5:389. doi: 10.3389/fmars.2018.00389

Paris, C. B., Helgers, J., van Sebille, E., and Srinivasan, A. (2013). Connectivity Modeling System: a probabilistic modeling tool for the multi-scale tracking of biotic and abiotic variability in the ocean. *Environ. Model. Softw.* 42, 47–54. doi: 10.1016/j.envsoft.2012.12.006

Paris, C. B., Le Hénaff, M., Aman, Z. M., Subramaniam, A., Helgers, J., Wang, D. P., et al. (2012). Evolution of the Macondo well blowout: simulating the effects of the circulation and synthetic dispersants on the subsea oil transport. *Environ. Sci. Technol.* 46, 13293–13302. doi: 10.1021/es303197h

Payne, J. R., and Phillips, C. R. (1985). Photochemistry of Petroleum in Water. *Environ. Sci. Technol.* 19, 569–579. doi: 10.1021/es00137a602

Perlin, N., Berenshtein, I., Vaz, A. C., Faillettaz, R., Schwing, P. T., Romero, P. T., et al. (2020). "Far-field modeling of deep-sea blowout: sensitivity studies of initial conditions, biodegradation, sedimentation and SSDI on surface slicks and oil plume concentrations," in *Deep Oil Spills: Facts, Fate, Effects*, eds S. A. Murawski, C. Ainsworth, S. Gilbert, D. Hollander, C. B. Paris, M. Schlüter, et al. (Cham: Springer).

Ray, P. Z., Chen, H., Podgorski, D. C., Mckenna, A. M., and Tarr, M. A. (2014). Sunlight creates oxygenated species in water-soluble fractions of Deepwater horizon oil. *Oceanography* 280, 636–643. doi: 10.5670/oceanog.2016.77

Ray, P. Z., and Tarr, M. A. (2014). Petroleum films exposed to sunlight produce hydroxyl radical. *Chemosphere* 103, 220–227. doi: 10.1016/j.chemosphere.2013.12.005

Rosmond, T. E., Teixeira, J., Peng, M., Hogan, T. F., and Pauley, R. (2002). Navy operational global atmospheric prediction system (NOGAPS): forcing for ocean models. *Oceanography* 15, 99–108. doi: 10.5670/oceanog.2002.40

Ruddy, B. M., Huettel, M., Kostka, J. E., Lobodin, V. V., Bythell, B. J., McKenna, A. M., et al. (2014). Targeted petroleomics: analytical investigation of macondo well oil oxidation products from Pensacola Beach. *Energy Fuels* 28, 4043–4050. doi: 10.1021/ef500427n

Shankar, R., Shim, W. J., An, J. G., and Yim, U. H. (2015). A practical review on photooxidation of crude oil: laboratory lamp setup and factors affecting it. *Water Res.* 68, 304–315. doi: 10.1016/j.watres.2014.10.012

Socolofsky, S. A., Adams, E. E., and Sherwood, C. R. (2011). Formation dynamics of subsurface hydrocarbon intrusions following the Deepwater Horizon blowout. *Geophys. Res. Lett.* 38:L09602. doi: 10.1029/2011GL047174

Spaulding, M. S., Li, Z., Mendelsohn, D., Crowley, D., French-McCay, D., and Bird, A. (2017). Application of an integrated blowout model system, OILMAP DEEP, to the Deepwater Horizon (DWH) Spill. *Mar. Pollut. Bull.* 120, 37–50. doi: 10.1016/j.marpolbul.2017.04.043

Tarr, M. A., Zito, P., Overton, E. B., Olson, G. M., Adhikari, P. L., and Reddy, C. M. (2016). Weathering of oil spilled in the marine environment. *Oceanography* 29, 126–135. doi: 10.5670/oceanog.2016.77

Vaz, A. C., Paris, C. B., Dissanayake, A. L., Socolofsky, S. A., Gros, J., and Boufadel, M. C. (2020). "Dynamic coupling of near-field and far-field models," in *Deep Oil Spills: Facts, Fate, Effects*, eds S. A. Murawski, C. Ainsworth, S. Gilbert, D. Hollander, C. B. Paris, M. Schlüter, et al. (Cham: Springer).

Ward, C. P., and Overton, E. B. (2020). How the 2010 Deepwater Horizon spill reshaped our understanding of crude oil photochemical weathering at sea: a past, present, and future perspective. *Environ. Sci. Process. Impacts* 22, 1125–1138. doi: 10.1039/d0em00027b

Ward, C. P., Reddy, C. M., and Overton, E. B. (2020). *Why Sunlight Matters for Marine Oil Spills. Eos 101*. Available online at: https://doi.org/10.1029/2020EO143427 (accessed August 14, 2020).

Ward, C. P., Armstrong, C. J., Conmy, R. N., French-McCay, D. P., and Reddy, C. M. (2018a). Photochemical oxidation of oil reduced the effectiveness of aerial dispersants applied in response to the deepwater horizon spill. *Environ. Sci. Technol. Lett.* 5, 226–231. doi: 10.1021/acs.estlett.8b00084

Ward, C. P., Sharpless, C. M., Valentine, D. L., French-mccay, D. P., Aeppli, C., White, H. K., et al. (2018b). Partial photochemical oxidation was a dominant fate of deepwater horizon surface oil. *Environ. Sci. Technol.* 52, 1797–1805. doi: 10.1021/acs.est.7b05948

Ward, C. P., Sharpless, C. M., Valentine, D. L., Aeppli, C., Sutherland, K. M., Wankel, S. D., et al. (2019). Oxygen isotopes (δ18O) trace photochemical hydrocarbon oxidation at the sea surface. *Geophys. Res. Lett.* 46, 6745–6754. doi: 10.1029/2019GL082867

Warnock, A. M., Hagen, S. C., and Passeri, D. L. (2015). Marine tar residues: a review. *Water Air Soil Pollut.* 226:68.

White, H. K., Wang, C. H., Williams, P. L., Findley, D. M., Thurston, A. M., Simister, R. L., et al. (2016). Long-term weathering and continued oxidation of oil residues from the Deepwater Horizon spill. *Mar. Pollut. Bull.* 113, 380–386. doi: 10.1016/j.marpolbul.2016.10.029

Xie, H., Yapa, P. D., and Nakata, K. (2007). Modeling emulsification after an oil spill in the sea. *J. Mar. Syst.* 68, 489–506. doi: 10.1016/j.jmarsys.2007.02.016

Zhao, L., Boufadel, M. C., Adams, E., Socolofsky, S. A., King, T., Lee, K., et al. (2015). Simulation of scenarios of oil droplet formation from the Deepwater Horizon blowout. *Mar. Pollut. Bull.* 101, 304–319. doi: 10.1016/j.marpolbul.2015.10.068

Zhao, L., Boufadel, M. C., King, T., Robinson, B., Gao, F., Socolofsky, S. A., et al. (2017). Droplet and bubble formation of combined oil and gas releases in subsea blowouts. *Mar. Pollut. Bull.* 120, 203–216. doi: 10.1016/j.marpolbul.2017.05.010

Zhao, L., Torlapati, J., Boufadel, M. C., King, T., Robinson, B., and Lee, K. (2014). VDROP: a comprehensive model for droplet formation of oils and gases in liquids - Incorporation of the interfacial tension and droplet viscosity. *Chem. Eng. J.* 253, 93–106. doi: 10.1016/j.cej.2014.04.082

Zheng, L., Yapa, P. D., and Chen, F. (2003). A model for simulating deepwater oil and gas blowouts - Part I: theory and model formulation. *J. Hydraulic Res.* 41, 339–351. doi: 10.1080/00221680309499980

Conflict of Interest: The authors declare that the research was conducted in the absence of any commercial or financial relationships that could be construed as a potential conflict of interest.

frontiers in Marine Science

ORIGINAL RESEARCH
published: 23 February 2021
doi: 10.3389/fmars.2021.618463

Validation of Oil Trajectory and Fate Modeling of the Deepwater Horizon Oil Spill

Deborah P. French-McCay[1]*, Malcolm L. Spaulding[2], Deborah Crowley[1], Daniel Mendelsohn[1], Jeremy Fontenault[1] and Matthew Horn[1]

[1] RPS, Ocean Science, South Kingstown, RI, United States, [2] Department of Ocean Engineering, University of Rhode Island, Narragansett, RI, United States

Trajectory and fate modeling of the oil released during the Deepwater Horizon blowout was performed for April to September of 2010 using a variety of input data sets, including combinations of seven hydrodynamic and four wind models, to determine the inputs leading to the best agreement with observations and to evaluate their reliability for quantifying exposure of marine resources to floating and subsurface oil. Remote sensing (satellite imagery) data were used to estimate the amount and distribution of floating oil over time for comparison with the model's predictions. The model-predicted locations and amounts of shoreline oiling were compared to documentation of stranded oil by shoreline assessment teams. Surface floating oil trajectory and distribution was largely wind driven. However, trajectories varied with the hydrodynamic model used as input, and was closest to observations when using specific implementations of the HYbrid Coordinate Ocean Model modeled currents that accounted for both offshore and nearshore currents. Shoreline oiling distributions reflected the paths of the surface oil trajectories and were more accurate when westward flows near the Mississippi Delta were simulated. The modeled movements and amounts of oil floating over time were in good agreement with estimates from interpretation of remote sensing data, indicating initial oil droplet distributions and oil transport and fate processes produced oil distribution results reliable for evaluating environmental exposures in the water column and from floating oil at water surface. The model-estimated daily average water surface area affected by floating oil > 1.0 g/m^2 was 6,720 km^2, within the range of uncertainty for the 11,200 km^2 estimate based on remote sensing. Modeled shoreline oiling extended over 2,600 km from the Apalachicola Bay area of Florida to Terrebonne Bay area of Louisiana, comparing well to the estimated 2,100 km oiled based on incomplete shoreline surveys.

Keywords: Deepwater Horizon, oil spill model, oil trajectory, oil fate, model validation, deep water blowout, oil exposure, Lagrangian model

Edited by:
Robert Hetland,
Texas A&M University, United States

Reviewed by:
Thadickal V. Joydas,
King Fahd University of Petroleum and Minerals, Saudi Arabia
Edward Eric Adams,
Massachusetts Institute of Technology, United States
Matthieu Le Hénaff,
University of Miami, United States

****Correspondence:***
Deborah P. French-McCay
debbie.mccay@rpsgroup.com

Specialty section:
This article was submitted to Marine Pollution, a section of the journal Frontiers in Marine Science

Received: *17 October 2020*
Accepted: *02 February 2021*
Published: *23 February 2021*

Citation:
French-McCay DP, Spaulding ML, Crowley D, Mendelsohn D, Fontenault J and Horn M (2021) Validation of Oil Trajectory and Fate Modeling of the Deepwater Horizon Oil Spill. Front. Mar. Sci. 8:618463. doi: 10.3389/fmars.2021.618463

INTRODUCTION

Given the catastrophic nature of the Deepwater Horizon (DWH) oil spill of April–July 2010, considerable effort has been applied by many to understand the oil movements and fate, exposure of environmental resources, and potential impacts on biota and ecosystems. Under United States law, the Natural Resource Damage Assessment (NRDA) was undertaken by the Deepwater Horizon

Natural Resource Damage Assessment Trustee Council (2016) to evaluate exposures to oil and quantify injuries to biota and the Gulf of Mexico (GOM) ecosystem resulting from the spill, supported by hundreds of studies and thousands of scientists and engineers. As logistics constrained obtaining enough field data to completely characterize the contamination in space and time during and after the period of oil and gas release, as part of the NRDA effort in support of the trustees, we pursued a numerical modeling effort to quantify oil movements, concentrations, exposures of water column biota and biological effects. As a first step, oil trajectory and fate modeling was performed using the established and verified model SIMAP (Spill Impact Model Application Package; French McCay, 2003, 2004; French McCay et al., 2015a, 2018b). The results of the oil trajectory and fate modeling were then used to evaluate exposure and biological effects of fish and invertebrates in the GOM (French McCay et al., 2015a,b,c,d,e). Subsequent to the NRDA settlement in 2016, the oil trajectory and fate modeling was refined as part of model validation studies (French McCay et al., 2018a,c) and pursuant to on-going efforts to evaluate the environmental effects of the spill.

The extent of oil contamination from the DWH was visibly evident during 2010 across the northern GOM in remote sensing imagery (Garcia-Pineda et al., 2013a,b; MacDonald et al., 2015; Svejkovsky et al., 2016) and based on field observations (see review in Deepwater Horizon Natural Resource Damage Assessment Trustee Council, 2016). Oil released from the broken riser both dispersed at depth and rose through nearly a mile of water column before reaching the surface. There are substantial uncertainties in the spill trajectory and spatial-temporal distributions of oil arising from the differences and uncertainties in wind and ocean current model data used to force the oil spill model, as is evident when comparing published oil spill model trajectories (Adcroft et al., 2010; MacFadyen et al., 2011; Liu et al., 2011; Mariano et al., 2011; North et al., 2011, 2015; Dietrich et al., 2012; Paris et al., 2012; Le Heìnaff et al., 2012; Kourafalou and Androulidakis, 2013; Jolliff et al., 2014; Boufadel et al., 2014; Goni et al., 2015; Testa et al., 2016; Özgökmen et al., 2016; Weisberg et al., 2017). Hence, we examined implications of using various wind and current data sets, as well as assumptions related to wind drift of surface oil, to determine the inputs yielding the most accurate trajectory for evaluating the oil fate and environmental exposures resulting from the spill. The trajectories were compared to observational data such as floating oil distributions based on remote sensing, shoreline oil surveys, chemical analyses of field samples, and sensor data. It is important to consider the influence of uncertainties in the input data driving transport, as well as other model inputs, on exposure concentrations relevant to evaluating biological effects.

Thus, the objective of this article was to evaluate the accuracy of DWH model trajectories and oil distributions in the water column and at the surface based on various input data sets and implications to quantification of oil fate and exposure concentrations. The details of the modeled mass balance, exposure concentrations and biological effects are to be described in other publications (in preparation).

MATERIALS AND METHODS

Approach

Model simulations were performed using four available meteorological and seven hydrodynamic model products covering the northeastern GOM. In addition, measured currents were used to evaluate transport along the continental slope. Model trajectories were also performed with winds alone to evaluate the influence of the currents. Wind drift and horizontal dispersion coefficients were altered to evaluate sensitivity to those assumptions. The model trajectories and concentration distributions were compared to observations of surfacing oil, remote sensing data-based observations, shoreline oiling distributions, fluorescence and other sensor data indicating the path of the deep plume, and chemistry sample results. The focus of this article is on the influence of physical forcing data (currents and winds) on distributions of surface and shoreline oil. Subsurface oil and oil component concentrations were compared to field measurement data in French McCay et al. (2018a,c), demonstrating sensitivity to the current data used as input.

Model Description

Spill Impact Model Application Package quantifies oil movements and concentrations of pseudo-components representing groups of petroleum compounds of like properties in droplet and dissolved phases in the water column, in floating oil slicks, emulsions and residuals, and as mass stranded on shorelines, settling to sediments, volatilized to the atmosphere, degraded in/on the water, shorelines and sediments, and as removed by response activities (i.e., mechanical removal and burning). Processes modeled included spreading (gravitational and by shearing), evaporation of volatile and semi-volatile oil pseudo-components from surface oil, current transport on the surface and in the water column, randomized dispersion from small-scale motions (mixing), emulsification, entrainment of oil as droplets into the water (natural and facilitated by dispersant application), dissolution of soluble and semi-soluble pseudo-components, volatilization of dissolved compounds from the surface wave-mixed layer, adherence of oil droplets to suspended particulate matter (SPM), adsorption of semi-soluble compounds to SPM, sedimentation, stranding on shorelines, and degradation (using pseudo-component-specific first-order biodegradation and photo-oxidation rates). Sublots of the discharged oil are represented by Lagrangian Elements (LEs, called “spillets”), each characterized by location, state (floating, subsurface droplet, on sediment, and ashore), mass of the various pseudo-components, water content of the oil, thickness, diameter (i.e., a floating spill is treated as a flat cylinder with increasing area as oil spreads locally), density, viscosity, and associated SPM mass. A separate set of LEs is used to track mass, spatial distribution of the diffusing mass, and movements of the dissolved components.

The SIMAP model’s algorithms and assumptions are fully described in French McCay et al. (2018b). The surface oil entrainment algorithm is described in Li et al. (2017a,b). Brief descriptions of the SIMAP oil trajectory and fate model, along with validation studies for two major oil spills, the *North Cape* and the *Exxon Valdez* oil spills, are available in French McCay (2003, 2004). Thus, only the most pertinent algorithms to this reported effort are described here.

Transport is modeled as the sum of advective velocities by currents input to the model, wind-driven drift of floating oil, vertical movement of subsurface particles according to (droplet and SPM) buoyancy (using modified Stokes Law; White, 2005), and randomized turbulent diffusive velocities in two (floating oil) or three (subsurface oil) dimensions (French McCay, 2004; French McCay et al., 2018b). The wind-driven drift due to waves (i.e., Stokes drift) and Ekman transport at the surface was either modeled, based on the results of Stokes drift and Ekman transport modeling by Youssef (1993) and Youssef and Spaulding (1993), which indicates about 3.5% of wind speed 20 degrees to the right of downwind for a fully developed sea offshore, or assumed a constant (range 1–4%) of wind speed and either downwind or at a specified angle. Environmental data such as temperature, salinity, SPM concentrations, water depth, and habitat characteristics were input as spatial data sets, varying temporally as appropriate (e.g., temperature and salinity).

Another key input influencing oil trajectory is the droplet size distribution (DSD) of the oil released at depth. The oil and gas from the DWH were released as part of a momentum-dominated jet, which became a buoyant plume (Camilli et al., 2010; Socolofsky et al., 2011, 2015a,b; Johansen et al., 2013; Spaulding et al., 2015, 2017; Gros et al., 2017). As seawater entrained into the buoyant plume and gas dissolved or escaped, the plume became neutrally buoyant with the surrounding seawater at about 200–400 m above the release point, as was evident in observational data (Camilli et al., 2010; Diercks et al., 2010; Valentine et al., 2010; Reddy et al., 2012; Spier et al., 2013; Payne and Driskell, 2016, 2017, 2018; Driskell and Payne, 2018). Thus, oil droplets were initialized in the SIMAP model at this "trap height" in droplet sizes estimated by Spaulding et al. (2015; 2017; using the Li et al., 2017a algorithm) based on daily estimates of the oil volume released, the percentage of gas and dispersant (from subsea injection) in the oil and gas plume, the depth of the release, the orifice configurations, and the environmental conditions, all of which are important controlling variables to the DSD (National Academies of Sciences Engineering and Medicine, 2020).

Model developments reflected by the DWH analysis herein include the updated oil entrainment algorithm (Li et al., 2017a,b), increased numbers of pseudo-components tracked (from 7 to 19), refinements in biodegradation and photolysis rates, the ability to utilize 4-dimentionally varying environmental data sets provided in a variety of grid types, and increased resolution via the numbers of spillets used and the concentration outputs. The Li et al. (2017a,b) model allowed the implications of both surface and subsea dispersant applications on oil droplet size to be addressed. The later four developments were needed to address the vast extent of the GOM affected, including resolving concentrations over ∼2,000 m of water column. Instantaneous, surface spills previously addressed (e.g., French McCay, 2003, 2004) had not required as much resolution, given that most of the oil was on/in surface waters and many of the components evaporated immediately.

Model Inputs

Winds

Four wind reanalysis products covering 2010 in the northeastern GOM obtained from National Oceanic and Atmospheric Administration (NOAA) and United States Navy government websites were used as model inputs.

- The North American Mesoscale Forecast System (NAM) data set provided by NOAA National Center for Environmental Prediction (NCEP)[1] was at approximately 12 km resolution and 1-h time steps.
- The North American Regional Reanalysis (NARR) data set provided by NOAA NCEP[2] was available at 3-h time steps and approximately 0.3° (32 km) resolution.
- The Climate Forecast System Reanalysis (CFSR) data set provided by NOAA NCEP was a reanalysis of 2010 at a horizontal resolution of 0.5°[3].
- The Navy Operational Global Atmospheric Prediction System (NOGAPS) data set provided by the United States Navy had horizontal resolution of 0.5°, with a time step of 6 h[4].

Currents

Current measurements. Acoustic Doppler Current Profiler (ADCP) data meeting quality criteria (French McCay et al., 2018a,c) were available for April–September 2010 from 17 locations along the continental slope of the Northeastern GOM (**Figure 1**). Four ADCPs were deployed near the DWH wellhead site: Development Driller 3 (#42916 at 88.363°W, 28.731°N sampling 65–1,184 m), Discoverer Enterprise (#42868 at 88.356°W, 28.745°N sampling 78–1,166 m), and a pair (88.434°W, 28.742°N) sampling the upper water column (<100 m) and waters deeper than 1,000 m (1,021–1,501 m) set out by a cooperative NRDA plan on June 18, 2010 (Mulcahy, 2010). During the period from April–July 2010, the temporally averaged current velocity at station 42,916 was 2.2 cm/s (0.04 kt) to the northeast and 3.9 cm/s (0.08 kt) to the southwest at 64 and 1,087 m below the water surface, respectively. The maximum current was 51 cm/s in the surface layer.

The ADCP data meeting quality criteria were used in SIMAP model simulations for comparison with simulations run with hydrodynamic model results. The velocity at the location of each spillet used for transport calculations at each time step was interpolated from the data taken at the 17 ADCP stations using an inverse distance-weighted scheme employing all sensors. The ADCP coverage extended along the continental slope in the area of concern, but there were no data on the shelf. In addition, the interpolation provided a smoothed current field, and did not resolve smaller scale features and shear less than the scale of the distance between ADCP moorings (order of 30–100 km).

---

[1] https://www.ncdc.noaa.gov/data-access/model-data/model-datasets/north-american-mesoscale-forecast-system-nam

[2] http://www.emc.ncep.noaa.gov/mmb/rreanl/

[3] https://www.ncdc.noaa.gov/data-access/model-data/model-datasets/climate-forecast-system-version2-cfsv2

[4] https://www.ncdc.noaa.gov/data-access/model-data/model-datasets/navy-operational-global-atmospheric-prediction-system

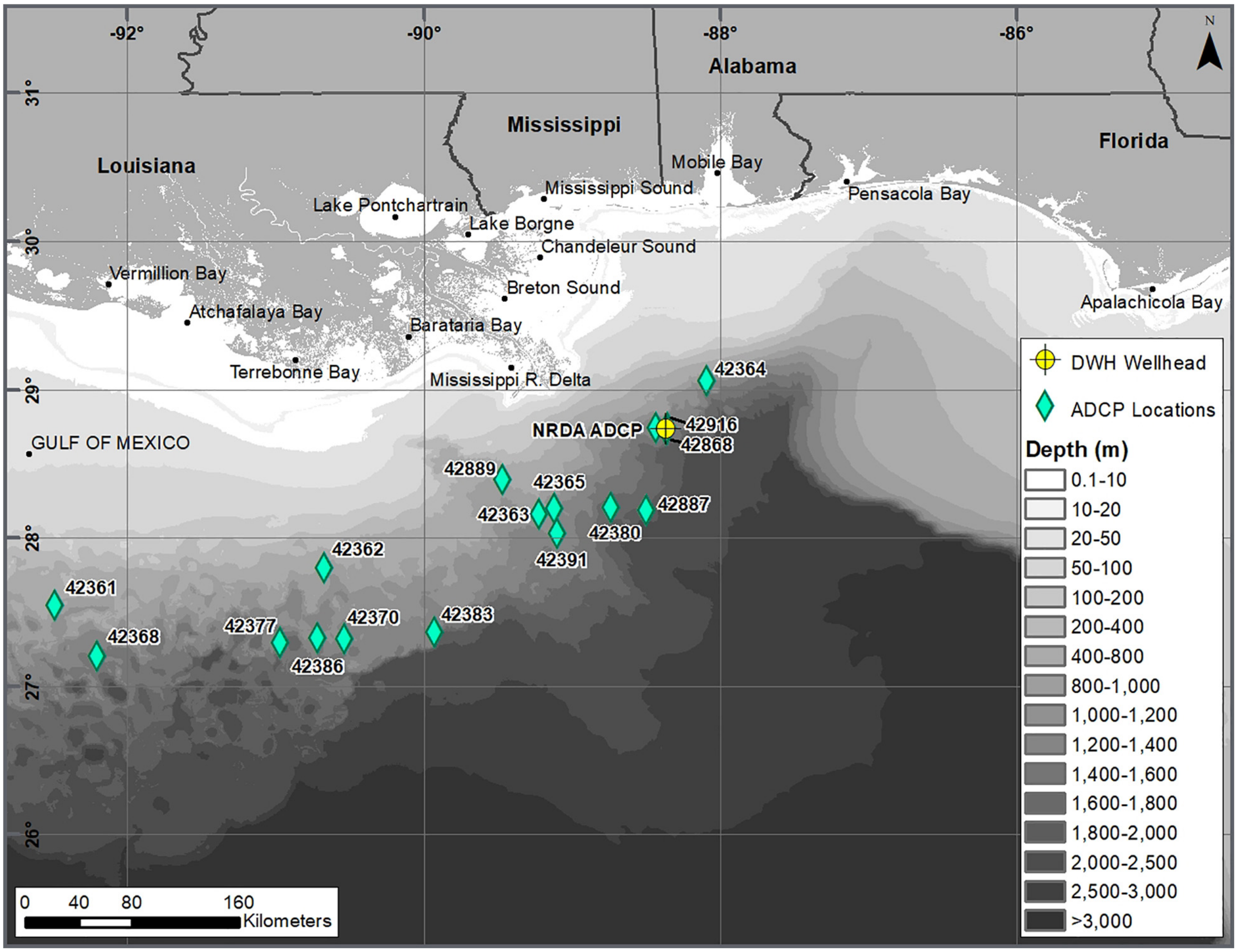

FIGURE 1 | Map of the northern Gulf of Mexico region exposed to floating and shoreline oil from the DWH spill, showing 17 ADCP locations. (The DWH wellhead is indicated by the crossed circle. Three ADCP locations are close to the wellhead).

Also, ADCPs do not provide estimates of surface currents. Thus, simulations using ADCPs were realistic only for oil transport below the 40 m mixed layer in areas where ADCP data were available, i.e., over the continental slope.

Hydrodynamic models. Seven data sets of currents predicted by hydrodynamic models were evaluated. The wind data from the model used to force the hydrodynamics, along with the current data, was used in the oil spill modeling.

- HYCOM-FSU: Florida State University (FSU) performed a HYbrid Coordinate Ocean Model (HYCOM) hindcast simulation for 2010 forced with NARR winds. Data provided had 3–4 km horizontal resolution, 20 hybrid layers in the vertical, and current predictions every 3 h (Chassignet and Srinivasan, 2015).
- HYCOM-NRL Reanalysis: The United States Naval Research Laboratory's (NRL) HYCOM + NCODA GOM 1/25° Reanalysis product GOMu0.04/expt_50.1 for 2010 forced with CFSR winds, ∼3.5 km resolution at mid-latitudes, 36 coordinate surfaces in the vertical, and current predictions every 3 h, was downloaded in March 2015[5,6].
- HYCOM-NRL Real-time: The NRL Real-time operational forecast GLOBAL HYCOM (Chassignet et al., 2009) simulations for 2010 (HYCOM + NCODA GOM 1/25° Analysis GOMl0.04/expt_31.0) were forced with NOGAPS winds. Model resolution is 1/25° (∼3.5 km) in the horizontal, with 20 vertical layers, and hourly data[7].
- SABGOM: The South Atlantic Bight and Gulf of Mexico (SABGOM) Regional Ocean Modeling System (ROMS) application was developed by North Carolina State University (NCSU) for the GOM (Hyun and He, 2010; Xue et al., 2013). The horizontal resolution is ∼5 km with 36

---

[5] http://tds.hycom.org/thredds/catalog/datasets/GOMu0.04/expt_50.1/data/netcdf/catalog.html

[6] http://hycom.org/data/gomu0pt04/expt-50pt1

[7] https://www.hycom.org/data/goml0pt04/expt-31pt0

terrain-following vertical layers. SABGOM was forced with NARR winds. Current predictions were provided every 3 h.

- IAS ROMS: The Intra-Americas Sea Regional Ocean Modeling System (IAS ROMS) was developed from SABGOM. It was applied with a grid resolution of ∼6 km in the horizontal and 30 levels in the vertical. An IAS ROMS simulation (version "4C") for 2010, that included a 2-km nested grid within the larger IAS ROMS domain, was run as part of the trustees' NRDA program and provided by Chao et al. (2014) in April 2014 (model described in Chao et al., 2009). This simulation forced with NAM winds provided hourly data.
- NCOM Real Time: The Naval Oceanographic Office (NAVOCEANO) ran the three-dimensional operational global nowcast/forecast system Global NCOM through 2013. NCOM was based on the Princeton Ocean Model (POM) with time invariant hybrid (sigma over Z) vertical coordinates with 40 levels[8]. Predictions were provided every 3 h.
- NGOM: The NOAA National Ocean Service (NOAA/NOS) Coast Survey Development Laboratory (CSDL) ran the NOS GOM Nowcast/Forecast Model (NGOM), a GOM implementation of the POM, in real time during the spill, forced by NAM winds. The resolution is 5–6 km in the northeastern and central GOM, with 37 levels in the vertical. Predictions were provided every 3 h.

Geographical data

A rectilinear grid was used to designate the location of the shoreline, the water depths (bathymetry), and the habitat or shore types. NOAA Office of Response and Restoration, Environmental Sensitivity Index data[9] were used to define shoreline habitat types, reclassifying Environmental Sensitivity Index codes to a simpler habitat classification, i.e., rocky, cobble, sand, mud, wetland, and artificial (man-made) shore types. Bathymetric data were obtained from the General Bathymetric Chart of the Oceans Digital Atlas (General Bathymetric Chart of the Oceans, 2009) one arc-minute gridded data set, which is based on quality-controlled ship depth soundings interpolated using satellite-derived gravity data as a guide.

Oil loading onto shorelines was assumed to occur up to a maximum holding capacity that was related to shore type (and so shoreline wave climate, slope, width, and grain size) and the beaching oil's viscosity. Shore holding capacities as a function of oil viscosity were developed for each shore type based on observations from the *Amoco Cadiz* spill in France and the *Exxon Valdez* spill in Alaska, as described in French et al. (1996) and French McCay et al. (2018c).

Environmental conditions

In order to utilize the same temperature and salinity distributions for all model runs, and given the uncertainties in the subsea distributions and currents predicted by the hydrodynamic models, monthly mean water temperature and salinity data from the World Ocean Atlas (Boyer et al., 2004) were input on a three-dimensional grid. The floating oil model trajectory was not sensitive to the difference in resolution between the atlas data and the hydrodynamic model data, since most of the oil surfaced within hours of release. A synoptic map of SPM concentrations was defined for use in the oil spill modeling by combining results from field and modeling studies with satellite imagery depicting SPM plumes (French McCay et al., 2018a,c).

For the base cases, the horizontal diffusion (randomized turbulent diffusion) coefficient was assumed 100 m^2/s for floating oil, 2 m^2/s in surface waters (above 40 m), and 0.1 m^2/s in waters below 40 m. The vertical diffusion coefficient was assumed 10 cm^2/s in surface and 1–0.1 cm^2/s in deep waters. The coefficients were also varied in sensitivity analyses up to one order of magnitude larger and smaller. These values are based on empirical data reviewed for the deep-water GOM (French McCay et al., 2015a; based on Okubo and Ozmidov, 1970; Okubo, 1971, Csanady, 1973; Socolofsky and Jirka, 2005, Ledwell et al., 2016).

Oil properties, composition, and degradation

The spilled oil was a light GOM crude oil. The liquid "dead" oil (i.e., oil without the C1 to C4 natural gas hydrocarbons) densities at 5, 15, and 30°C were 0.8560, 0.8483, and 0.8372 g/cm^3, respectively; dynamic viscosity was 10.93 cp at 5°C, 7.145 cp at 15°C, and 4.503 cp at 30°C; and IFT was 19.63 mN/m (Stout, 2015b). Based on its asphaltene (0.27%) and resin (10.1%) content (in un-weathered dead oil, Stout, 2015b) and behavior of similar light crude oils (Fingas and Fieldhouse, 2012), the fresh oil would form an unstable emulsion. After weathering concentrated asphaltenes and resins sufficiently, the oil was observed and assumed to form a mesostable water-in-oil emulsion (mousse) up to a maximum water content of 64% water (Belore et al., 2011).

Concentrations of volatile-insoluble and soluble to semi-soluble hydrocarbons and related compounds were calculated for 18 pseudo-components used to characterize the dead oil [including nine soluble/semi-soluble and volatile/semi-volatile components defined by octanol-water partition coefficient (K_{ow}) range, eight insoluble and volatile/semi-volatile aliphatic components defined by boiling ranges, and one residual oil component; French McCay et al., 2015a, 2018b] and input to the SIMAP oil fates model, along with fractions of the oil volatilized in boiling cut temperature ranges (Stout, 2015a; Stout et al., 2016a). Physical-chemical properties of each pseudo-component were developed by French McCay et al. (2015a).

First-order biodegradation rates in the water column used as model input were based on reviews by French McCay et al. (2015a, 2018a,b) to develop pseudo-component-specific rates. Photo-oxidation rates of polycyclic aromatic compounds by ultraviolet light were developed by French McCay et al. (2018d).

Amounts and droplet sizes of released oil

The DWH spill location (88.367°W, 28.740°N in Mississippi Canyon Block 252, MC252; **Figure 1**) was ∼80 km southeast of the mouth of the Mississippi River in ∼1,500 m of water. The amount of oil (C5+) released to the environment (totaling 4.1 million bbl, ∼554 thousand metric tons, MT; i.e., not including the amount recovered at the release site) was specified from April 22, 2010 at 10:30AM CDT (local time) for 2015 hours (i.e.,

---

[8] http://ecowatch.ncddc.noaa.gov/global-ncom/

[9] http://response.restoration.noaa.gov/esi

84 days until July 15, 2010 at 2:30PM CDT) in 15-min time-step increments using daily estimates based on information provided by the Flow Rate Technical Group (McNutt et al., 2011, 2012), as summarized by Lehr et al. (2010). The oil mass was initialized in the SIMAP model at depths and in DSDs calculated via the nearfield and droplet size models, reflecting subsea dispersant application activities (Li et al., 2017a; Spaulding et al., 2017).

From April 28 to June 3, oil and gas flowed from both the broken end of the fallen riser and holes in a kink in the riser pipe just above the blowout preventor. After June 3 (when the fallen riser pipe section was sawed off and Top Hat #4 with a recovery pipe was placed over the riser), oil was released only from the riser pipe, around the top hat immediately above the blowout preventor. The median droplet diameters of the riser flows (~2–3 mm) were significantly larger than those from the kink release (~300–500 μm), due to the much higher exit velocity from the kink relative to the larger diameter riser release. For most model simulations, the best estimate of the DSD was used, which was a bimodal distribution based on partial dispersant treatment of the oil in the blowout plume (details in Spaulding et al., 2015, 2017). Sensitivity to the bounding range DSDs resulting from assumed high (100%) and low (50%) effectiveness of the subsea dispersant injections (Spaulding et al., 2015, 2017) was examined for simulations using HYCOM-FSU.

Response activities

Modeled response activities at the water surface included removal by *in situ* burning and dispersant application to floating oil from the air and vessels. Spatially explicit quantitative measurements of oil volume mechanically removed were not available; therefore, mechanical cleanup was not included in the model simulations. Polygons were input to the model specifying amounts of oil burned or treated by dispersant, and where and when the response activities occurred. Details are provided in French McCay et al. (2018c).

Quantitative estimates of oil volume removed by *in situ* burning were obtained from the Response After-Action Report by Mabile and Allen (2010; summarized by Lehr et al., 2010; Allen et al., 2011). Time ranges for burns each day were composited into a daily burn time window. The mass rate of removal on a given date was calculated as the total burn volume times typical floating oil density in the areas of the burns, 0.97 g/cm^3, divided by the time range of burning that day. The model removed oil mass at this daily rate within each time and spatial window up to the maximum daily mass prescribed by the model input.

Surface dispersant application data were obtained from response records (NOAA, 2013). The volume of oil treated per dispersant volume applied (i.e., the dispersant-to-oil ratio) was based on assumptions in Lehr et al. (2010), who assumed that the minimum, median, and maximum ratios were 5, 10, and 20 by weight of oil, not including the water in mousse. The median value (1:10) was used as the base case. The fraction of oil dispersed into the water column (i.e., efficiency) was calculated using the entrainment algorithm (Li et al., 2017b) based on the assumed dispersant-to-oil ratio and resulting interfacial tension (based on data from Venkataraman et al., 2013).

Analysis of Results

To evaluate model agreement with observations, modeled floating oil distributions were compared to interpretations of remote sensing imagery, modeled shoreline oiling was compared to field survey data, and modeled subsea concentrations were compared to chemistry sample data and sensor-based indicators (e.g., fluorescence peaks).

Floating Oil

Remote sensing (satellite) imagery data were used to evaluate the distributions of surface oil over time. Remote sensing interpretations, developed as part of the trustees' NRDA program in support of the Deepwater PDARP/PEIS (Deepwater Horizon Natural Resource Damage Assessment Trustee Council, 2016) for April to August 2010 were downloaded from the NOAA GOM ERMA website (http://gomex.erma.noaa.gov/erma.html) on January 27, 2016 (ERMA, 2016). Data from four sensors were available: Satellite Synthetic Aperture Radar (SAR), MODIS Visible, MODIS Thermal IR Sensor data (MTIR), and Landsat Thematic Mapper (TM).

Synthetic Aperture Radar images were analyzed for presence and thickness category (thick or thin) of floating oil by Deepwater Horizon Natural Resource Damage Assessment Trustee Council (2016; based on Garcia-Pineda et al., 2009, 2010, 2013a,b; Graettinger et al., 2015). MacDonald et al. (2015) used a neural network analysis of SAR images to quantify the magnitude (averaging 70 μm for thick and 1 μm for thin) and distribution of surface oil in the GOM from persistent, natural seeps and from the DWH discharge. SAR resolutions ranged from 25 to 100 m per pixel, with a few images at 6 m per pixel (Graettinger et al., 2015; ERMA, 2016).

MODIS Visible data were available for 18 days depicting surface oil, at a pixel resolution of 250 or 500 m, depending on the spectral band. The images were classified into three oil thickness classes: thin oil class (primarily silver sheen and rainbow, using NOAA, 2016), a thick oil class (transitional dark to dark color), and a moderately thick oil class (metallic sheen) that falls between the other two classes (Graettinger et al., 2015; ERMA, 2016).

MODIS Thermal IR data at a pixel resolution of 1,000 m were available for 25 days during the spill period. The images were classified into a thin oil class [primarily silver sheen and rainbow, using NOAA (2016) nomenclature], a thick oil class (transitional dark to dark color), and a moderately thick oil class that falls between the other two classes (Graettinger et al., 2015; ERMA, 2016).

Useful Landsat TM data were available over a spatially limited area on 8 days when DWH oil was on the surface of the northern GOM. Landsat TM satellite data have a pixel resolution of about 30 m. Ocean Imaging estimated the areal coverage per pixel of three oil thickness classes: a very thick class comprising heavy emulsions, a moderately thick class of dark/opaque oil, and a thin oil category that is thicker than sheen but thinner than dark/opaque oil. The Landsat TM oil thickness analyses did not classify oil sheens (Graettinger et al., 2015; ERMA, 2016).

For comparisons with model results, floating oil distributions from 84 dates and times were used, these being times where the image was judged sufficiently synoptic of the area of the floating oil. These included 34 SAR, 18 MODIS Visible, 25 MODIS Thermal IR, and 7 Landsat TM images (**Supplementary Table 1**). The three thickness classes of the MODIS Visible, MODIS Thermal IR, and Landsat TM images were assumed 1, 10, and 50 μm thick on average, based on ranges estimated by Graettinger et al. (2015). Graettinger et al. (2015) and MacDonald et al. (2015) aggregated the pixelated data as gridded data in a 5 × 5 km^2 geographic grid and developed statistical models to interpolate between observations in space and time. However, since the interpolations may have missed weather-related and other events between actual observations, comparisons of the SIMAP model results to imagery results were made using the pixelated data based on the observational data, without use of the interpolations. These non-interpolated data were gridded in the same 5 km by 5 km grid used by the Deepwater Horizon Natural Resource Damage Assessment Trustee Council (2016; Graettinger et al., 2015; ERMA, 2016).

For both the remote sensing data and the model, at each observation time for the remote sensing, the percentage of floating oil present in each grid cell was calculated in three ways.

- The *relative area* of oil in each grid cell indicated the distribution of oil cover. For remote sensing data, the area within the cell covered by oil was divided by the total area of oil in all cells estimated from the imagery. For the model, the area covered by spillets falling in the cell was divided by the total area covered by all floating spillets at that time step (accounting for overlapping spillet areas, avoiding double-counting).
- The *estimated volume* of oil in each grid cell was calculated for remote sensing data from the area covered by each thickness category. For the model, the total mass in spillets falling in the cell was used as an index of volume.
- The *relative volume* of oil in each grid cell accounts for the relative distribution of oil, irrespective of the actual amounts, which are subject to the assigned oil thickness. For remote sensing data, the volume of oil in each cell was divided by the total volume of oil in all cells estimated from the imagery. For the model, the total mass in spillets falling in the cell was divided by the total mass of all floating spillets in all cells at that time step. The mass was not corrected for oil density to convert to volume. Thus, all spillets were assumed to be of equal density for this index.

The Root Mean Square Error (RMSE) was calculated for each date/time there was an observation available. The RMSE is a frequently used measure of the differences between values predicted by a model and the values observed, and thus is a measure of accuracy. The individual differences (residuals) are aggregated in the RMSE as a single measure of predictive power (Fitzpatrick, 2009). For each pair of grids, the RMSE was calculated by summing the squares of the differences between modeled and the observed over all cells of the grid, where ***n*** = total number of cells in each grid:

$$RMSE = \sqrt{\frac{\sum \left(observed - modeled\right)^2}{n}}$$

RMSE values were averaged over all dates, in order to judge relative fit comparing dates and/or among simulations, the minimum RMSE indicating the best fit.

Shoreline Oil Distributions

Available data for shore oiling consisted of maps of where oil was first observed on various shoreline segments and assessments by the Shoreline Cleanup and Assessment (SCAT) program during Response. A binary discriminator test (Fitzpatrick, 2009) was used to evaluate the timing of oil coming ashore in the model, as compared with observations made by the SCAT program. The presence or absence of oil according to SCAT observations and the model predictions were gridded using the 5 km by 5 km Albers grid (ERMA, 2016) employed by the Deepwater Horizon Natural Resource Damage Assessment Trustee Council (2016) in their evaluations of oil exposure after the DWH spill. A cell was considered to have oil presence if any shore segment within the cell was observed oiled by the SCAT teams.

SCAT data were downloaded from ERMA in July of 2014 as shape files[10]. The observational data were binned into 10-day intervals, from April 22 to September 30, 2010. In the analysis, only those SCAT segments where oil was observed to arrive before September 30 were considered as oiled. Segments checked during the 10-day interval, but where no oil was observed to arrive, were considered as "no oil." Segments where oil was observed to arrive after September 30, but earlier observations showed it did not arrive there before September 30, were coded as "no oil." Note that the shorelines were not searched synoptically, and areas were not visited for days or weeks; thus, the time oil was first observed could have been a considerable time after the actual initial oiling. Also, the Deepwater Horizon Natural Resource Damage Assessment Trustee Council (2016) used additional observations and SAR to identify where oil came ashore, to develop more comprehensive maps of the locations where oil came ashore during and after (including after September 30) the spill. However, we relied solely on the SCAT survey data, as the SAR-based data were localized analyses at specific instances.

Subsea Oil

Modeled subsea concentrations were compared to chemistry sample data and sensor-based indicators (e.g., fluorescence peaks) both qualitatively, to evaluate oil locations, and quantitatively, to evaluate concentrations. We used chemical measurements of samples taken May 11 (the first date available) – July 15, 2010 and processed by the trustees' quality-controlled NRDA program (Deepwater Horizon Natural Resource Damage Assessment Trustee Council, 2016; described in Horn et al., 2015; Payne and Driskell, 2015b, 2016, 2017, 2018; Driskell and Payne, 2018). The NRDA sample data set is available in ERMA (2016). Details of the model comparisons to subsea chemistry data are in French McCay et al. (2015a, 2018a). We summarize those findings below as part of the present analysis of the influence of physical forcing on the model trajectories and oil distributions.

---

[10] http://gomex.erma.noaa.gov/erma.html

RESULTS AND DISCUSSION

The model trajectory selected as the base case for waters above 200 m was that forced with the hydrodynamic and wind input combination (i.e., HYCOM-FSU currents and NARR winds) yielding the best agreement with floating oil distributions and shoreline oiling over time. In deep water, ADCP data yielded the best agreement with oil contaminant distributions >200 m and defining the deep plume. Videos of the floating oil movements color-coded by "age" (time since release) and of the oil droplet trajectory below 900 m are in **Supplementary Material**.

Floating Oil

In prior modeling examining mass balance and fate of oil released from hypothetical oil and gas blowouts in nearby locations of the GOM (French McCay et al., 2018d, 2019), the initial DSD was the most influential input controlling the amount of oil surfacing. For a spill at 1,400 m, with a trap height at 1,100 m (i.e., similar to the DWH spill), a DSD with a median droplet size <700 μm reduced the amount of surfacing oil dramatically, whereas the amount of oil surfacing was similar for all DSDs with larger median droplet sizes (French McCay et al., 2019). As the breadth of (range of droplet sizes in) the DSD has been found to be narrow (Li et al., 2017a), most of the mass in the DSD is in droplet sizes close to the median droplet diameter.

In all model simulations, oil droplets >0.7 mm diameter, weathered by dissolution such that their density when they reached the surface approached 940 kg/m^3 (in agreement with measurements of "fresh" floating oil by Stout et al., 2016a), rose to the surface in <17 h. Droplets 1 and 3 mm in diameter surfaced in 11 and 3 h, respectively. ADCP-measured currents at the wellhead averaged <5 cm/s between 40 and 1,400 m. Assuming a mean current of 5 cm/s during their rise, 0. 7-, 1-, and 3-mm droplets would travel ∼2, 3 and 0.5 km horizontally, respectively. Svejkovsky and Hess (2012); Svejkovsky et al. (2016) and Payne and Driskell (2015d, 2018) observed fresh oil surfacing <4 km from the wellhead on various dates in May and June 2010. Ryerson et al. (2012) observed fresh (as evidenced by measured volatiles in the air above) oil surfacing at 1.0 ± 0.5 km from the wellhead June 8–10, 2010, which based on ADCP measurements at that time implied a 10-h surfacing time. Ryerson et al. (2012) noted that visual observations from response vessels suggested a ∼3-h lag time between deliberate intervention at the well and the onset of changes in the freshly surfaced oil. These observations imply that much of the surfaced oil was comprised of droplets ∼1–3 mm in diameter. Droplets smaller than 0.7 mm rose over a longer period and so were carried progressively farther from the release point. Droplets less than ∼100 μm did not rise appreciably and formed the deep-water plume along with dissolved hydrocarbons. Thus, the DSD could affect the surfacing locations of the oil, and the floating oil distribution, depending on the relative amounts of mass in these size ranges. Floating oil would be more spread out from the well if most of the mass was in droplet sizes <700 μm than it would be if most of the mass were in droplets >700 μm.

Figure 2 shows the cumulative days of oil presence on the water surface based on SAR analysis (data from ERMA, 2016, produced by Graettinger et al., 2015). **Figure 3** and **Supplementary Figures 1–10** summarize the oiled footprints (north of 27°N and east of 92°W, the domain used for comparisons to focus on most of the oil and limit the number of null cells) for the model trajectories forced by various winds and currents as cumulative days of oil presence on the water surface in each grid cell over the simulation. The average RSME values over all dates of comparison for these runs, assuming the floating oil horizontal dispersion coefficient was 100 m^2/s and using the modeled wind drift, are in **Table 1**. For the base case using HYCOM-FSU and NARR winds, and all simulations using other hydrodynamics, the DSD was the best estimate, as described in Spaulding et al. (2015, 2017). High and low cases in **Table 1** represent the potential range of DSDs (Spaulding et al., 2015, 2017).

Considering the RSME means for all three metrics, the base case using HYCOM-FSU with NARR winds produced a trajectory that best fit the remote sensing data. IAS ROMS showed second best agreement to the remote sensing in terms of the relative spatial distribution of floating oil (relative area and relative volume). However, the HYCOM-NRL Reanalysis with CFSR winds showed the same degree of agreement with the remote-sensing data as the HYCOM_FSU/NARR simulation in terms of oil volume distribution (**Table 1**). SABGOM moved more oil northeast toward Florida in June than did the other hydrodynamics (**Supplementary Figure 3**). The HYCOM-NRL Real-time hydrodynamics transported more oil southeast toward southern Florida (**Supplementary Figure 2**) than was observed in the remote sensing (**Figure 2**). The RMSE values show poorer agreement of the model with the remote sensing products when no currents and only winds are used, than for when any of the hydrodynamic models are used (**Table 1**), indicating that the hydrodynamic model currents improved the trajectories over wind drift alone. Use of ADCP data for surface transport (extrapolated from below 40 m) resulted in better agreement to the observational data than without currents, suggesting that transport of droplets rising from depth, and thus the DSD, influenced the floating oil distribution. While the mapped comparison (**Supplementary Figure 7**) showed the floating oil distribution reasonably agreed with the observations, there was no ADCP data on the shelf or nearshore, such that along-shore transport was not captured and there was not enough eastward or westward spread of the oil. Thus, the simulations using hydrodynamic modeled currents produced better agreement with the observed floating oil distributions than simulations using ADCP data for currents. However, as will be discussed in section "Subsea Oil," modeled oil distributions below 40 m were in better agreement with ADCP-based observational data than simulations using any of the hydrodynamic models.

Across the range of potential subsea dispersant effectiveness assumptions (high and low cases in **Table 1**), the DSDs influenced the volume distribution of the floating oil to a similar degree as varying the hydrodynamic model input. However, the relative area and relative volume RMSE values did not change much with change in DSD within the potential range (Spaulding et al., 2015, 2017), whereas those metrics were sensitive to the hydrodynamic input. The best-estimate DSD used for the base case with

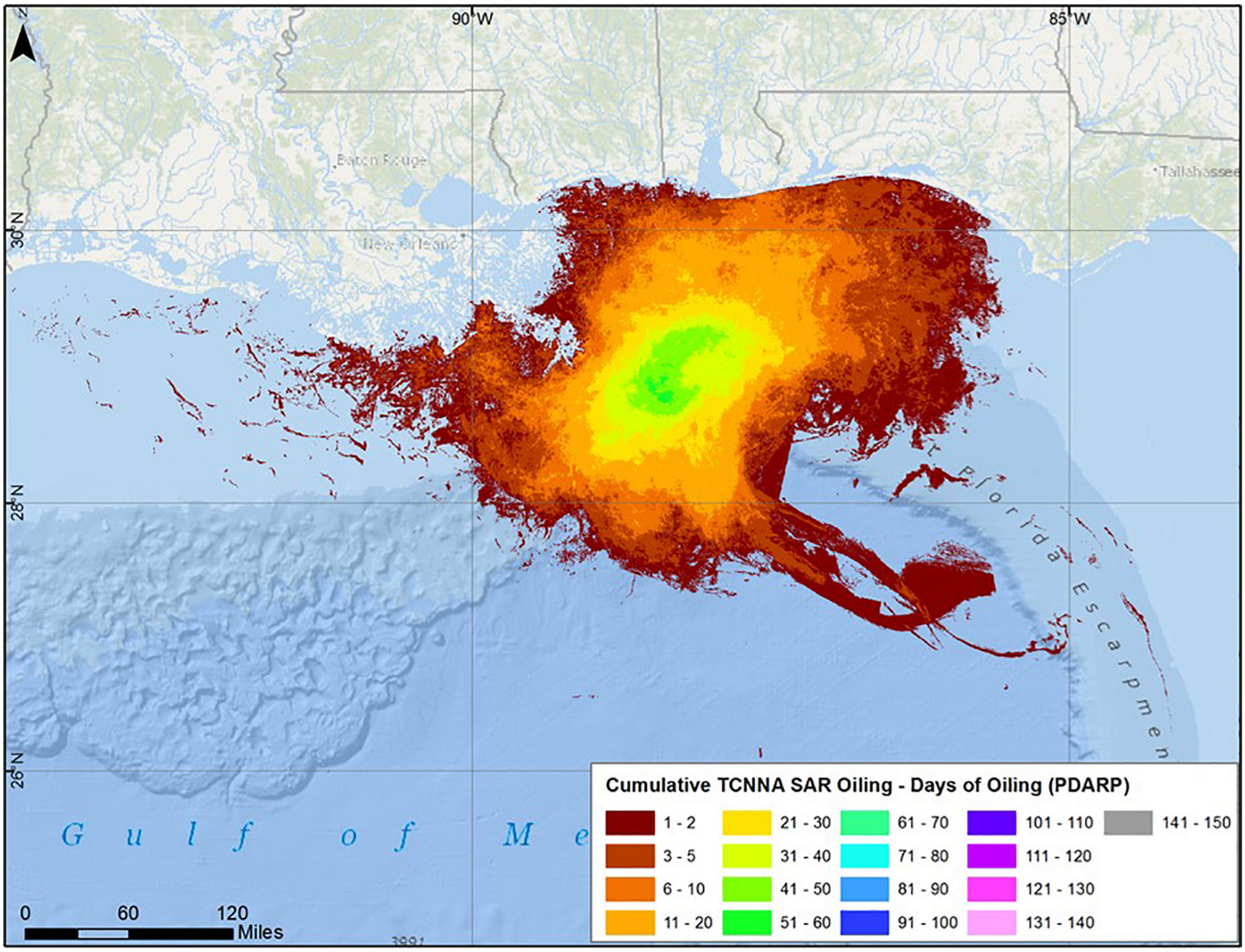

FIGURE 2 | Cumulative days of oil presence on the water surface, based on remote sensing (SAR) analysis (data from ERMA, 2016).

HYCOM-FSU yielded the lowest RMSEs overall (**Table 1**). Thus, the floating oil spatial and volume distributions were sensitive to the hydrodynamics used. The relative spatial distribution of the floating oil was not sensitive to the plausible DSD inputs because the substantial mass in large droplets (>0.7 mm) surfaced close to the well and resulted in similar trajectories, regardless of the amount in those droplet sizes. If the DSD were skewed to much smaller sizes than those examined, the relative spatial distribution would be affected, and floating oil would be more broadly distributed since smaller droplets would be carried farther from the well before surfacing. However, such DSDs are not realistic for the DWH spill where the conditions and dispersant volumes applied at depth were not conducive to creating smaller droplet sizes (Adams et al., 2013; Zhao et al., 2014, 2015; Socolofsky et al., 2015b; Spaulding et al., 2015, 2017; Nissanka and Yapa, 2016; Testa et al., 2016; Gros et al., 2017; Li et al., 2017a; Daae et al., 2018; National Academies of Sciences Engineering and Medicine, 2020). The extremely low estimates of the median (<100 μm) and maximum (<300 μm) droplet diameters (for both untreated and treated oil) of Paris et al. (2012) and Aman et al. (2015) were not representative of the DWH conditions (see Adams et al., 2013; Testa et al., 2016), nor are they consistent with the field evidence.

As SIMAP is a Lagrangian model, the diffusion coefficients moved the spillet centers randomly each time step at a scale determined by the coefficient. Those displacement distances were small relative to the ~5-km concentration grid used to compare the model to the remote sensing data. Thus, the RMSE values changed slightly (<10%) with differing floating oil horizontal dispersion coefficients from 5 to 200 m^2/s, indicating this assumption had little influence on the results at the scale of a 5 km grid. The hydrodynamic models did not resolve the surface oil drift in the upper wave-mixed layer resulting from wave motions and Ekman flow. Simulations using the Youssef and Spaulding (1993) model of these processes, as well as varying percentages-of-wind-speed drift rates (2–4%) and angles (0–20°) to the right of downwind, showed that the best fit was consistently that using the Youssef and Spaulding (1993, 1994) model, as opposed to using a constant wind drift percentage and angle for all dates, although the differences between the results were small on most days (results not shown). Moreover, there was much more variation between

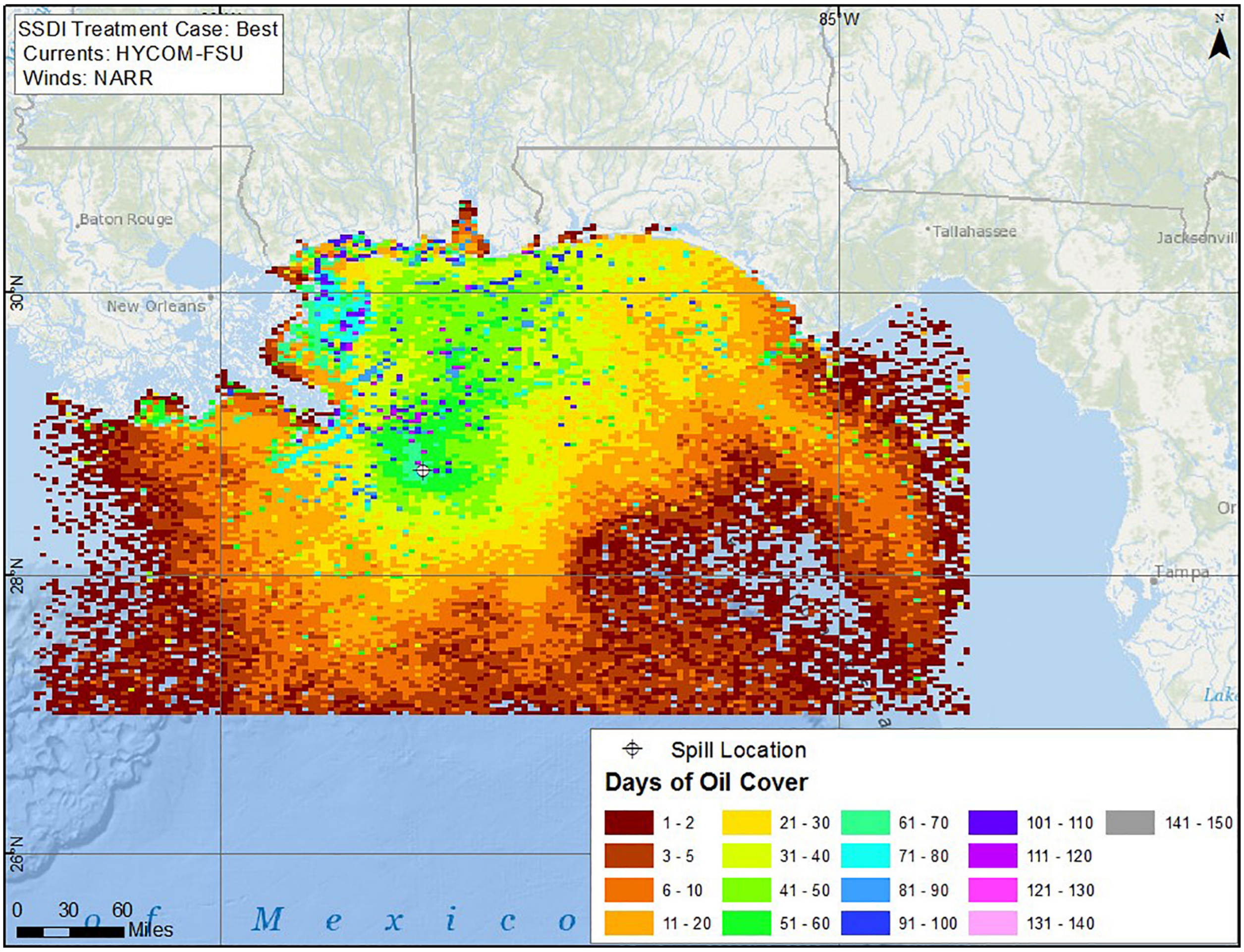

FIGURE 3 | Cumulative days of oil presence on the water surface, based on the base case model simulation using HYCOM-FSU currents and NARR winds.

runs with different currents and winds used for forcing than the differences due to variation in wind drift model or the horizontal dispersion coefficient. Thus, variations of wind drift and horizontal dispersion coefficient assumptions were not examined further. Use of 800,000 spillets instead of 100,000 spillets (as used for the simulations presented) to represent the floating oil slightly improved the model agreement with the observed for the HYCOM-FSU base case, as the additional spillets filled in some of the areas where remote sensing data indicated oil was present. However, model run time was increased considerably in the tests using more spillets.

Snapshots of surface oil distributions over time, predicted by the model using HYCOM-FSU currents and based on remote sensing data, are compared in the **Supplementary Material**. Comparative snapshots for other model simulations are available in French McCay et al. (2018c). **Figure 3** and **Supplementary Figures 1–10** summarize the trajectories and comparisons. The remote sensing data indicate the floating oil was primarily in a circular area near and just north of the DWH wellhead. The simulations using HYCOM-FSU (**Figure 3**), HYCOM-NRL Reanalysis (**Supplementary Figure 1**), and IAS ROMS (**Supplementary Figure 6**) show similar patterns. The results of the simulations with other currents show excursions too far northeast (SABGOM, **Supplementary Figure 3**; NCOM Real-time, **Supplementary Figure 4**), and too much dispersion in all directions (HYCOM-NRL Real-time, **Supplementary Figure 2**; NGOM, **Supplementary Figure 5**). The three simulations using no currents and NAM, NARR or NOGAPS winds (**Supplementary Figures 8–10**) are similar, and do not transport of the floating oil enough to the east or west. Otherwise, the no-current simulations result in realistic floating oil patterns centered just north of the wellhead. The simulation using ADCP currents and NARR winds generates results similar to no currents and NARR winds (**Supplementary Figure 7**), because the ADCP currents are relatively weak in the offshore area and do not cover the shelf or nearshore. These results indicate the importance of the wind drift in transporting the floating oil, but that the currents used can change the patterns dramatically.

The modeled number of days of oil cover for the base case using HYCOM-FSU (**Figure 3**) is of the same range as the SAR-based estimates (**Figure 2**) in the area of the wellhead and off the Mississippi River Delta. However, the duration of oil cover in the

TABLE 1 | RMSE (mean over all dates) comparing modeled to remote sensing data for floating oil distributions, varying currents and winds used as input.

Currents	Winds	RMSE: relative area	RMSE: relative volume	RMSE: volume (m^3)
HYCOM-FSU (base case)	NARR	0.00053	0.00082	17.3
HYCOM-FSU (high)	NARR	0.00052	0.00080	17.7
HYCOM-FSU (low)	NARR	0.00054	0.00083	19.6
SABGOM	NARR	0.00057	0.00090	21.2
HYCOM-NRL Reanalysis	CFSR	0.00061	0.00100	17.3
HYCOM-NRL Real-time	NARR	0.00058	0.00088	19.4
NCOM Real-time	NARR	0.00060	0.00090	21.3
NGOM-NOAA Real-time	NARR	0.00059	0.00088	19.1
IAS ROMS	NAM	0.00056	0.00087	19.7
ADCP	NARR	0.00068	0.00107	21.6
None	NAM	0.00070	0.00104	22.9
None	NARR	0.00072	0.00109	25.3
None	NOGAPS	0.00075	0.00112	25.5

For all model simulations except those noted as high or low, the best estimate of the droplet size distribution was used. High and low represent the range of potential droplet size distributions by varying subsea dispersant effectiveness from high to low (Relative area and relative volume are unitless).

area near the coast of Mississippi and Alabama is higher in the model than the SAR data indicate. Also, floating oil trapped near shore in the model remained longer than observed. Mechanical removal, on water or on shorelines, was not included in the simulations, and this could potentially account for at least some of the observed reduction in the nearshore floating oil.

The RMSE values for the base case using HYCOM-FSU currents (**Figure 4**) show the best agreement in terms of relative area or relative volume distribution in early June, whereas the model estimated volume of oil was most similar to the remote-sensing based estimates in April-early May and in July. The results for other current-wind combinations showed similar temporal patterns. The relatively high RMSE values for spatial coverage in April were because the modeled distribution remained more localized around the wellhead than the remote sensing indicated. The relatively high RMSE value for relative volume on May 17 was for the MODIS visual image of that date, when the "Tiger Tail" feature (i.e., the extension to the southeast as oil sheen was drawn into a cyclonic eddy) was seen in the imagery (Walker et al., 2011; Olascoaga and Haller, 2012) but not indicated by the model (i.e., the hydrodynamic model did not locate the eddy in the same location at that time).

The modeled maximum amount of oil in each grid cell at any time in the simulation is shown in **Figure 5**. Using gridding with a cell size of 25 km^2, MacDonald et al. (2015) estimated the footprint of aggregated floating oil and oil emulsions, where oil coverage exceeded ~ 1 g/m^2 at some time during the spill, which extended over 149,000 km^2. By comparison, the base case model prediction, using the same resolution and threshold, was 194,000 km^2. The model predictions included some low concentrations of floating oil in areas far from the well where oil was not detected by the remote sensing. These small patches of highly weathered oil residuals ($>$20 days old) in the outskirts (see the video of the floating oil movements color-coded by age in **Supplementary Material**) were likely undetected in the remote sensing analyses because of the resolution of those sensors. The modeled time-averaged mean oil cover (**Figure 6**) is similar in pattern and of the same magnitudes as the estimates made by MacDonald et al. (2015) based on SAR analysis. Their estimated daily average footprint was 11,200 km^2 (SD = 8,430 km^2). The model estimate (base case) of the daily average surface area affected by floating oil $>$1.0 g/m^2 was 6,720 km^2 (SD = 4,960 km^2), not significantly different from the remote sensing daily estimate.

Note that the gridded summaries of floating oil distributions, both for the model and for the remote sensing data, provided average amounts of oil mass over the cell area. They should not be interpreted as an actual oil thickness, as the oil is patchy and of varying thicknesses within the cells. The remote sensing data are typically expressed as volumes per cell for this reason. Furthermore, the total area of the cells where oil is present is larger than the actual oil coverage at any given time. The modeled areas covered by oil, the sum of the areas covered by spillets (representing patches) at a single time step, were an order of magnitude lower than those estimated from the gridding. The mean swept area from April 24 to August 3, 2010 (101 days) was 1,960 km^2/day for the model base case.

The modeled amount of floating oil for the base case simulation is compared to remote-sensing based estimates in **Figure 7**. The modeled floating oil volumes, and to some degree the remote-sensing-based estimates, are inversely related to wind speed, as wind events entrain oil into the water and oil accumulates on the water surface during calm periods. While there is considerable variability in the remote-sensing based estimates, in large part due to uncertainty in the oil thickness estimates (Graettinger et al., 2015) used, the model predictions over time are within the range of the remote-sensing estimates. From May 1 to July 31, 2010, the modeled floating oil volumes averaged 27,100 m^3 (26,500 MT), whereas the remote-sensing based estimates averaged 25,900 m^3. The average floating oil volumes were 27,700 m^3 (27,200 MT) and 29,400 m^3 (28,800 MT) for the high and low effectiveness cases, respectively. With no subsea dispersant use, the model predicted an average of 29,800 m^3 (29,200 MT) of floating oil in May–July 2010.

Shoreline Oil Distributions

Approximately 2,100 km of beaches and coastal wetlands were exposed to MC252 oil in 2010, according to the Deepwater Horizon Natural Resource Damage Assessment Trustee Council (2016; Nixon et al., 2016). The oil was documented by shoreline assessment teams as stranding on 1,773 km of shoreline. Deepwater Horizon Natural Resource Damage Assessment Trustee Council (2016) mapped maximum observed oiling, categorized as not surveyed, no oil seen, or various degrees of oiling. Many areas were not surveyed, including much of Mobile Bay and considerable areas of wetlands in Louisiana. Thus, the 2,100 km estimate likely underestimates the actual length of shoreline affected by oil.

Modeled shoreline oiling results are summarized in **Table 2**. For simulations run without currents, the length of shoreline

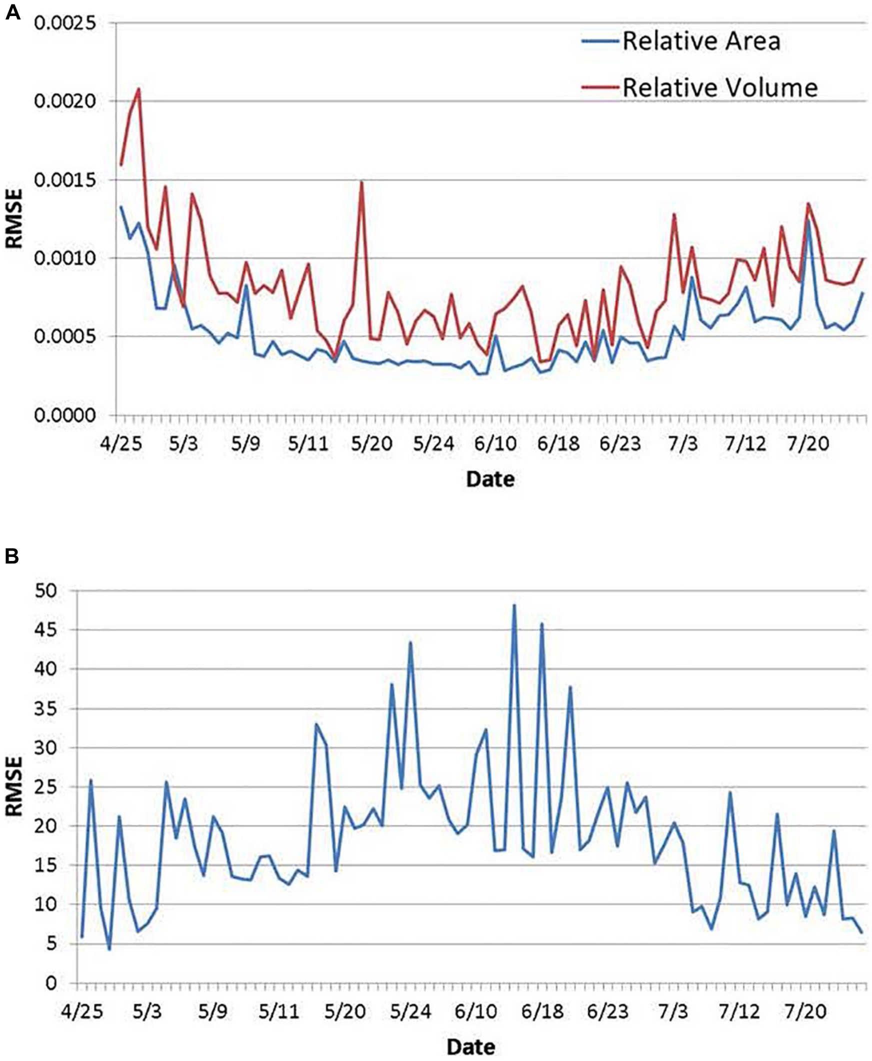

FIGURE 4 | RMSE of relative area and volume (as fractions, panel **A**) and of oil volume (m^3, panel **B**) for the base case model simulation (using HYCOM-FSU) compared to remote sensing-based data.

oiled is smaller and focused on the area between the Mississippi River Delta and Alabama. The total length of shore oiled estimated by the Deepwater Horizon Natural Resource Damage Assessment Trustee Council (2016; Nixon et al., 2016) was 2,113 km. The categories of degree of oiling used by the Trustees cannot be translated to oil loading amounts (g/m^2). The total lengths of shoreline oiling predicted by the model using most of the hydrodynamic model currents (except NGOM) are 2,000–2,700 km oiled, with the base case predicting 2,568 km oiled. These results are in good agreement with the observations, considering some areas were not surveyed.

Figure 8 and **Supplementary Figures 11–16** summarize the comparisons of the modeled shoreline oiling with SCAT-based observations, showing the variability resulting from different current and wind inputs. These maps color code where oil came ashore in the model but where the shoreline had not been surveyed ("no observed coverage, modeled oil"), as well as where both modeled and observed indicate oil ("match"), where both observed and the model indicate no oil ("no observed oil"), where there are false negatives (observed only), and where there are false positives (modeled only).

The modeled shoreline oiling for the base case compares well with the observations (**Figure 8**), the model showing oiling from the Apalachicola Bay area of Florida to Terrebonne Bay area of Louisiana. Note that the model predicted shore oiling inside Mobile Bay in areas where it was not observed. However, as most of Mobile Bay's shoreline areas were not surveyed, oiling of those areas is unknown. No oil was reported in some of the small bays along the Florida panhandle. However, booming may have prevented oil from entering those inlets, whereas booming was not included in these model simulations.

Simulations using HYCOM-NRL Reanalysis currents with CFSR winds (**Supplementary Figure 11**), HYCOM-NRL Real-time currents with NARR winds (**Supplementary Figure 12**),

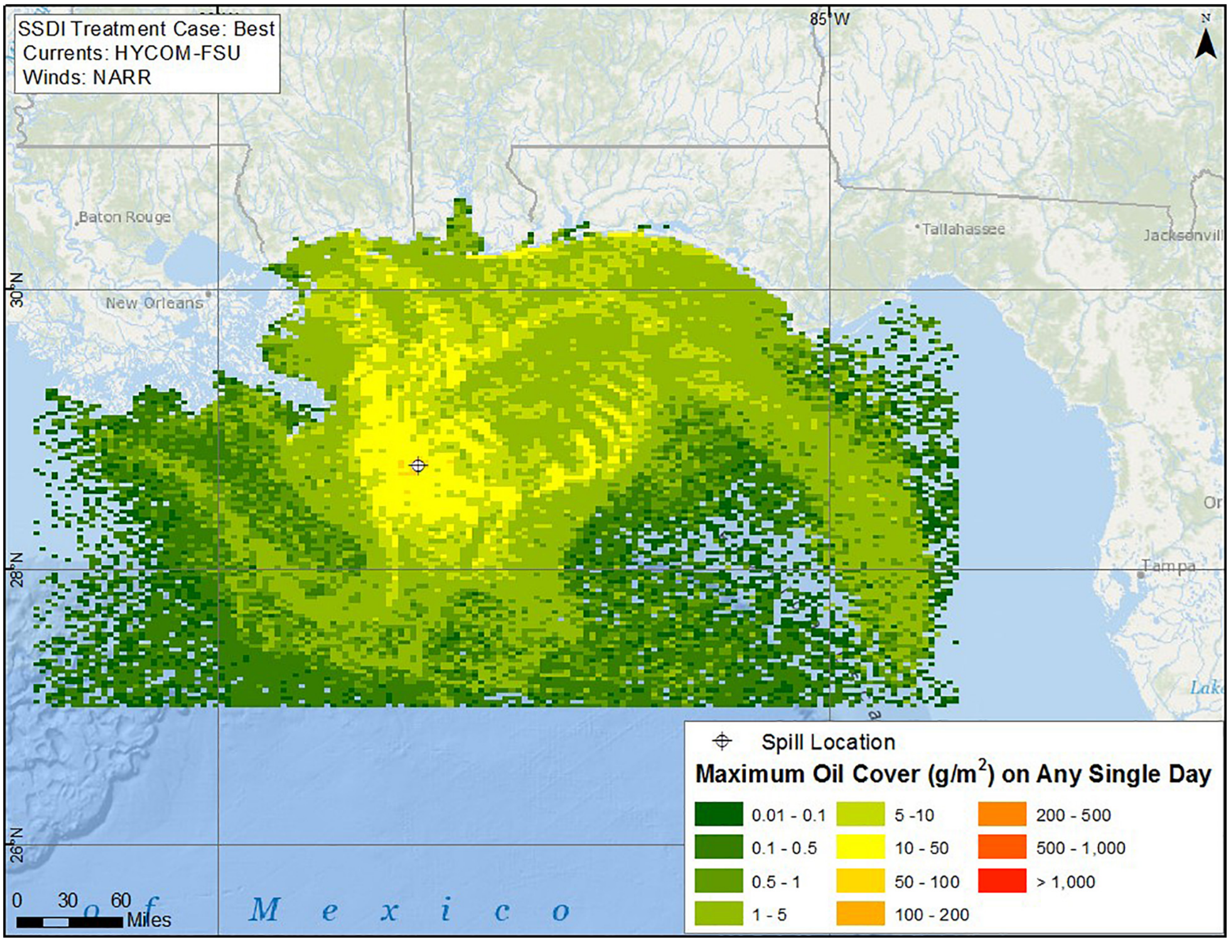

FIGURE 5 | Modeled maximum amount of oil in each grid cell at any time in the simulation (as g/m^2 averaged over the grid cell), based on the base case model simulation.

and NCOM Real-time with NARR winds (**Supplementary Figure 14**), predict similar oiling patterns to the base case using HYCOM-FSU currents and NARR winds (**Figure 8**). SABGOM spreads oil to shorelines too far to the east and into western Louisiana where no oiling was observed (**Supplementary Figure 13**). NGOM currents with NARR winds and the IAS ROMS simulations carry too much oil to western Louisiana and Texas but otherwise show good agreement with the SCAT observations (**Supplementary Figures 15, 16**). Simulations made with no currents, forced with winds only, and those forced with ADCP currents and NARR winds, do not bring as much oil ashore west of the Mississippi River Delta as was observed. Thus, coastal currents prevailing toward the west apparently transported the oil to those areas. Also, currents brought the oil east to Florida, as winds alone do not account for that shoreline oiling.

The shoreline oil distributions were more accurate when westward flows near the Mississippi Delta were simulated in the forcing hydrodynamic model. Novelli et al. (2020) identified westward flows as due to easterly winds. Kourafalou and Androulidakis (2013); Androulidakis and Kourafalou (2013), and Androulidakis et al. (2015, 2018) examined and stressed the importance of the Mississippi outflow in controlling nearshore oil movements and shoreline oiling distributions. The HYCOM models seemed to have captured these dynamics reasonably well in simulating conditions in the summer of 2010, whereas the ROMS implementations examined did not reflect those dynamics. It is possible that Mobile Bay was protected by freshwater outflows not captured in any of the hydrodynamic models. However, oiling data in Mobile Bay were insufficient to determine how much entered the bay.

Weisberg et al. (2017) concluded that the general circulation from the hydrodynamics modeling could account for transporting the Deepwater Horizon oil to near shore, but that the waves, via Stokes drift, were responsible for the actual beaching of the oil. In our analysis, we found the wind drift (i.e., including Ekman flow and Stokes drift) was the primary driver for bringing oil to shore. Le Heìnaff et al. (2012) and Boufadel et al. (2014) also concluded that wind drift was the most important factor bringing oil ashore. Using several hydrodynamic models as input, Boufadel et al. (2014)

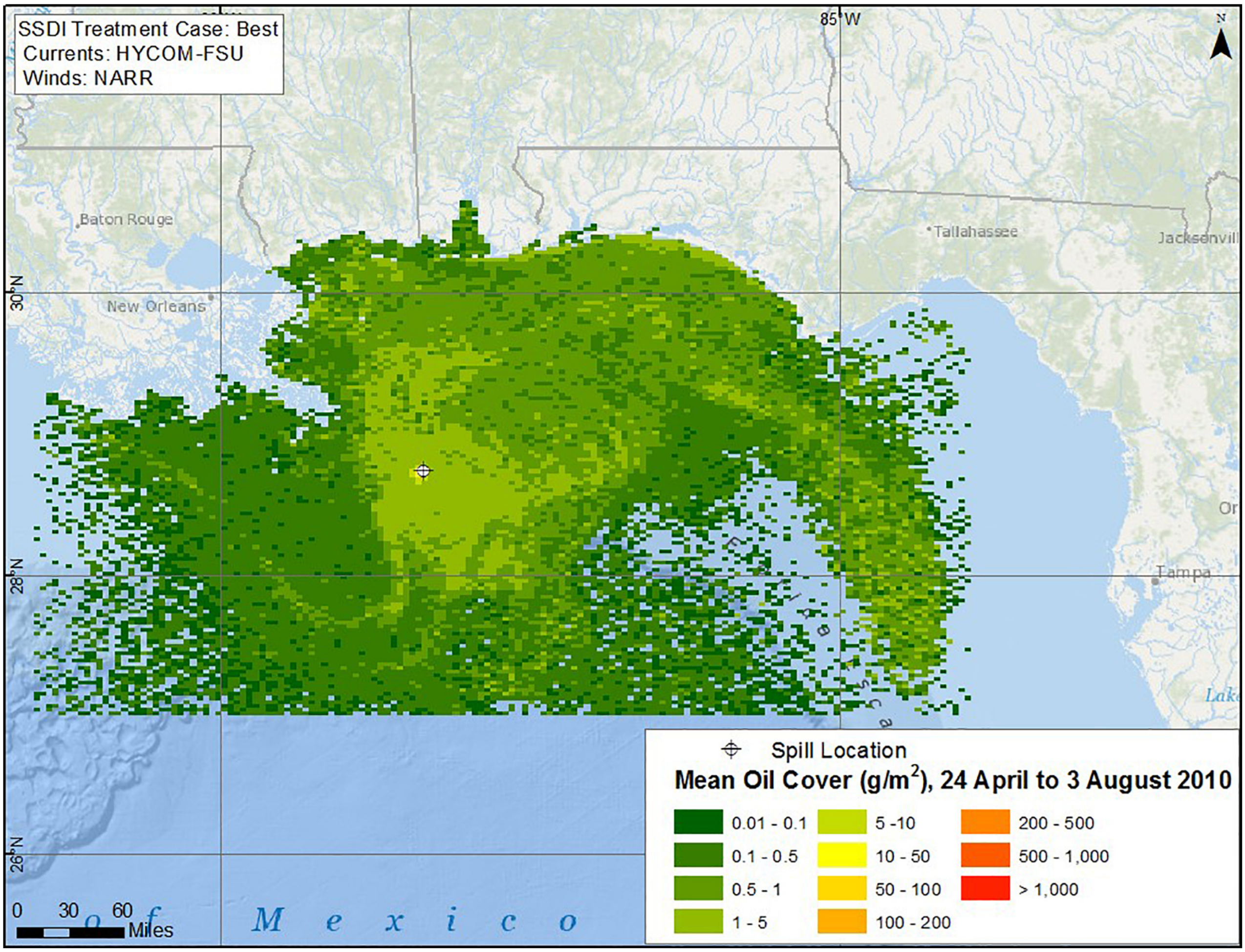

FIGURE 6 | Time-averaged mean floating oil concentration (g/m^2) in each cell for the period when oil was observed by SAR, 24 April to 3 August 2010, based on the base case model simulation.

concluded that the wind drift rate was 1–4% of wind speed. Studies by Novelli et al. (2020) found that along-shore easterly winds followed by southerly wave-induced surface drift brought drifters, and so the DWH oil, ashore. Conversely, westerly winds moved the surface water and drifters away from shore. However, to the degree that the circulation modeling includes the wind-forced circulation, the relative importance of what is considered due to hydrodynamic inputs versus "wind drift" would vary. Dietrich et al. (2012) performed a detailed analysis comparing modeled oil drift using hydrodynamic and wave models as compared to satellite imagery, finding the best agreement using their implementations of Simulating WAves Nearshore (SWAN) and ADvanced CIRCulation (ADCIRC) models as the sole forcing. The inclusion of wind drift on top of the hydrodynamic and wave models transported the oil too fast. Thus, careful consideration is needed to determine the degree to which wind drift should be applied in the oil spill model, depending on the forcing and resolution included in the hydrodynamics and wave models.

Figure 9 maps the modeled shoreline oiling for the base case using HYCOM-FSU, along with modeled concentrations of sedimented oil by August 31, 2010 (Sedimentation is discussed below). Maps of the results for the base case simulation for each of the 16 10-day intervals from April 22 to September 30 are available in French McCay et al. (2018c). No oil came ashore in the first 10-day period, April 22–May 1, in either the model or SCAT observations. The oil's arrival to shore was in good agreement with the SCAT observations for most areas and observation periods. The exception was that the (base case) model did not bring as much oil ashore west of the Mississippi River Delta during early to mid-June as was observed. Oil did come ashore in that simulation later in June and in July.

Subsea Oil

Comparisons of modeled subsea oil component concentrations to field chemistry samples are described in French McCay et al. (2018a). Here we summarize those findings and evaluate the modeled movements of the oil below 200 m using various current data as input.

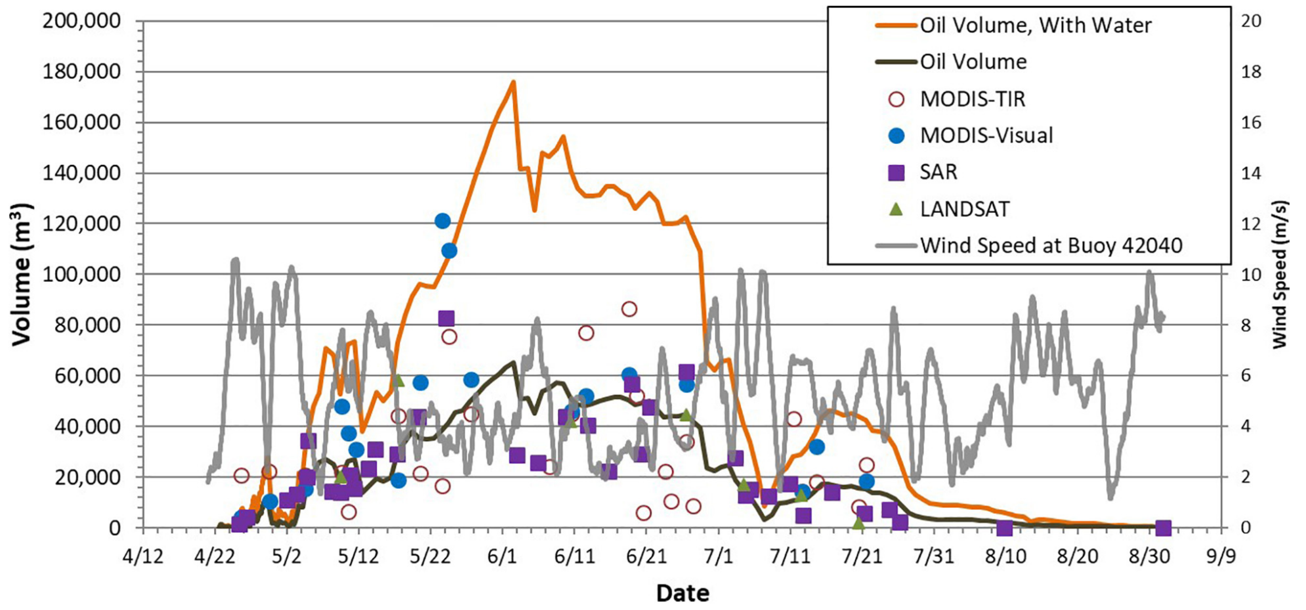

FIGURE 7 | Volume of surface floating oil, including the oil only or with the water in emulsions, for the base case model and calculated from remote sensing data; wind speeds at NOAA buoy 42040.

Camilli et al. (2010) detected the deep plume at ∼1,000–1,200 m during June 23–27, 2010. Their Sentry's methane *m/z* signal at 35 km from the source was only 53% less than that at 5.8 km, suggesting that plume extended considerably beyond the 35 km survey bound at that time. The model using ADCP data simulated the plume as extending to the southwest 60 km on June 23 and 82 km on June 27 (video of spillet movements below 900 m in **Supplementary Material**), consistent with the observations by Camilli et al. (2010).

While the oil-affected volume has been described as an inverted cone over the well with large droplets rising in the center and progressively smaller ones further from the well (e.g., Ryerson et al., 2012; Spier et al., 2013), due to ADCP-documented current shear and varying rise rates for different diameter droplets, "plumes" of rising oil droplets followed different trajectories during their ascent toward the surface, a behavior captured in our model simulations (French McCay et al., 2018a,c). In addition, while rising, the intermediate-sized droplets lost some of their relative buoyancy due to weathering (dissolution and biodegradation), as well as potentially combining with SPM in the water column. The ambient current higher in the water column is increasingly stronger than in deep water (Hyun and He, 2010), such that the intermediate sized droplets would have separated to form "multiple plumes" of slowly rising droplets in the upper layers mimicking the deep water plume. Fluorescence anomalies (peaks) and water column hydrocarbon chemistry data (Camilli et al., 2010; Valentine et al., 2010; Spier et al., 2013; as well as NRDA data, Horn et al., 2015 and Payne and Driskell, 2015a,c, 2018) showed relatively high concentrations in finite "clouds" of particulate- and dissolved-phase oil at various depths above the intrusion at ∼1,100–1,200 m. The SIMAP model simulated these behaviors and distribution. Sensitivity analyses by North et al. (2011, 2015) and Paris et al. (2012) showed similar behavior: droplets with diameters of <50 µm formed distinct subsurface plumes that were transported horizontally and remained in the subsurface for >1 month; while droplets with diameters ≥90 µm rose to the surface, more rapidly at larger diameters.

TABLE 2 | Shoreline oiling results for model cases, varying currents and winds used as input.

Currents	Winds	Length of shore oiled (km)	Mass of oil ashore (MT)
HYCOM-FSU	NARR	2,568	64,407
HYCOM-NRL Reanalysis	CFSR	1,993	25,045
HYCOM-NRL Real-time	NARR	2,698	58,164
SABGOM	NARR	2,658	91,677
NCOM Real-time	NARR	2,385	85,485
NGOM-NOAA Real-time	NARR	3,540	91,089
IAS ROMS	NAM	2,507	67,850
ADCPs	NARR	1,857	56,189
None	NAM	1,436	38,306
None	NARR	1,550	49,039
None	NOGAPS	1,013	33,483

Fluorescence peaks (relative high values) and dissolved oxygen "sags" (relatively low values) in vertical profiles associated with elevated hydrocarbon concentrations in water samples were consistently observed at depths ∼1,000–1,300 m mainly southwest of the wellhead (Joint Analysis Group, 2010; French McCay et al., 2015a, 2018a; Horn et al., 2015). In the deep plume, the ADCP-measured speeds averaged 3.9 cm/s to the southwest. Measured current speeds were consistently <10 cm/s at all depths

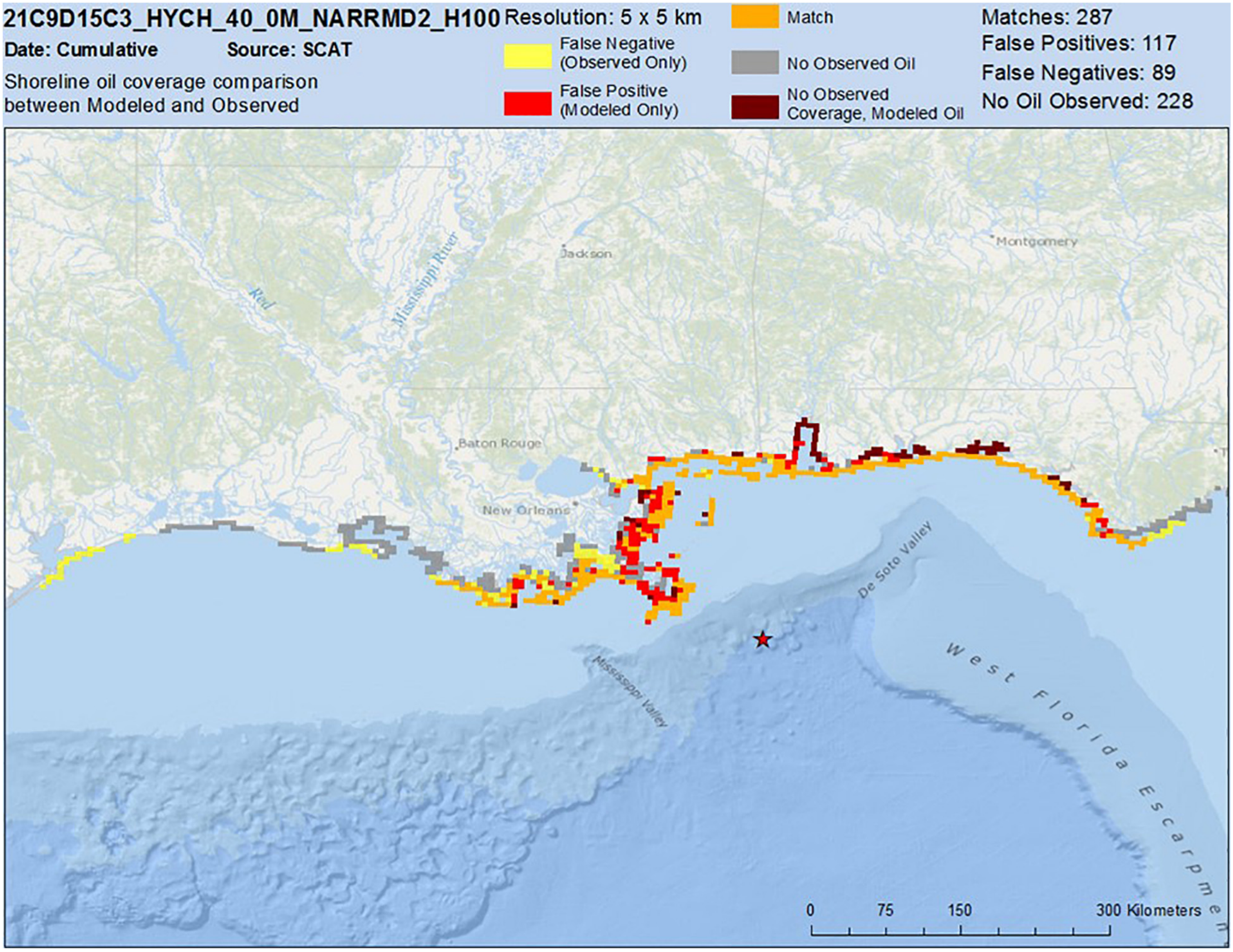

FIGURE 8 | Comparison of model predictions, for the base case simulation using HYCOM-FSU Reanalysis currents and NARR winds, to SCAT-based observations of cumulative amount of oil coming ashore by September 30, 2010.

and for most of the period of the oil release. ADCP data in ∼30–60 m vertical bins throughout the upper ∼1,000 m of the water column showed currents in adjacent depths differing by as much as 120° in direction during May–June 2010 (French McCay et al., 2015a, 2018a).

In contrast, in the area of the DWH wellhead, all of the hydrodynamic models examined (three HYCOMs: HYCOM_FSU, HYCOM-NRL Reanalysis, HYCOM-NRL Real-time; two ROMS: SABGOM, IAS ROMS; and two POMs: NCOM Real-time, NGOM) calculated much higher speeds for the currents in the deep plume and water column below 200 m than is indicated by the ADCPs. Furthermore, the movements were less consistently toward the southwest than indicated by the ADCP and field observation data. This was evident in trajectories of oil droplets below 200 m. The video of the oil droplet trajectory below 900 m using ADCP data in the **Supplementary Material** summarizes the movements of oil in the deep plume. Snapshots in the deep plume and at intermediate depths from trajectories using the hydrodynamic models are available in French McCay et al. (2018a,c).

The hydrodynamic models produced current fields below 200 m that at times agreed with the ADCP data, and in other times diverged in direction and speed. The HYCOM-FSU model produced a trajectory of small droplets in deep water (French McCay et al., 2018a,c) that was most similar to that using the ADCP data (video of the oil droplet trajectory below 900 m using ADCP data in **Supplementary Material**). The ROMs models tended to transport the small droplets along the bathymetry toward the southwest in narrow smooth flows much faster than indicated by the ADCP data. The IAS ROMS simulation (described in French McCay et al., 2015a, 2016) was very similar to the SABGOM simulation (in French McCay et al., 2018a,c). The HYCOM-NRL Real-time and HYCOM-NRL Reanalysis both predicted the deep plume moved primarily northeastward from April through July of 2010, such that the modeled deep plume did not extend southwestward in July as observed (French McCay et al., 2018c). The POM models (NGOM is shown in French McCay et al., 2018a) predicted movements at times to the northeast and other times to the southwest, but the timing of movements in these directions did not agree with

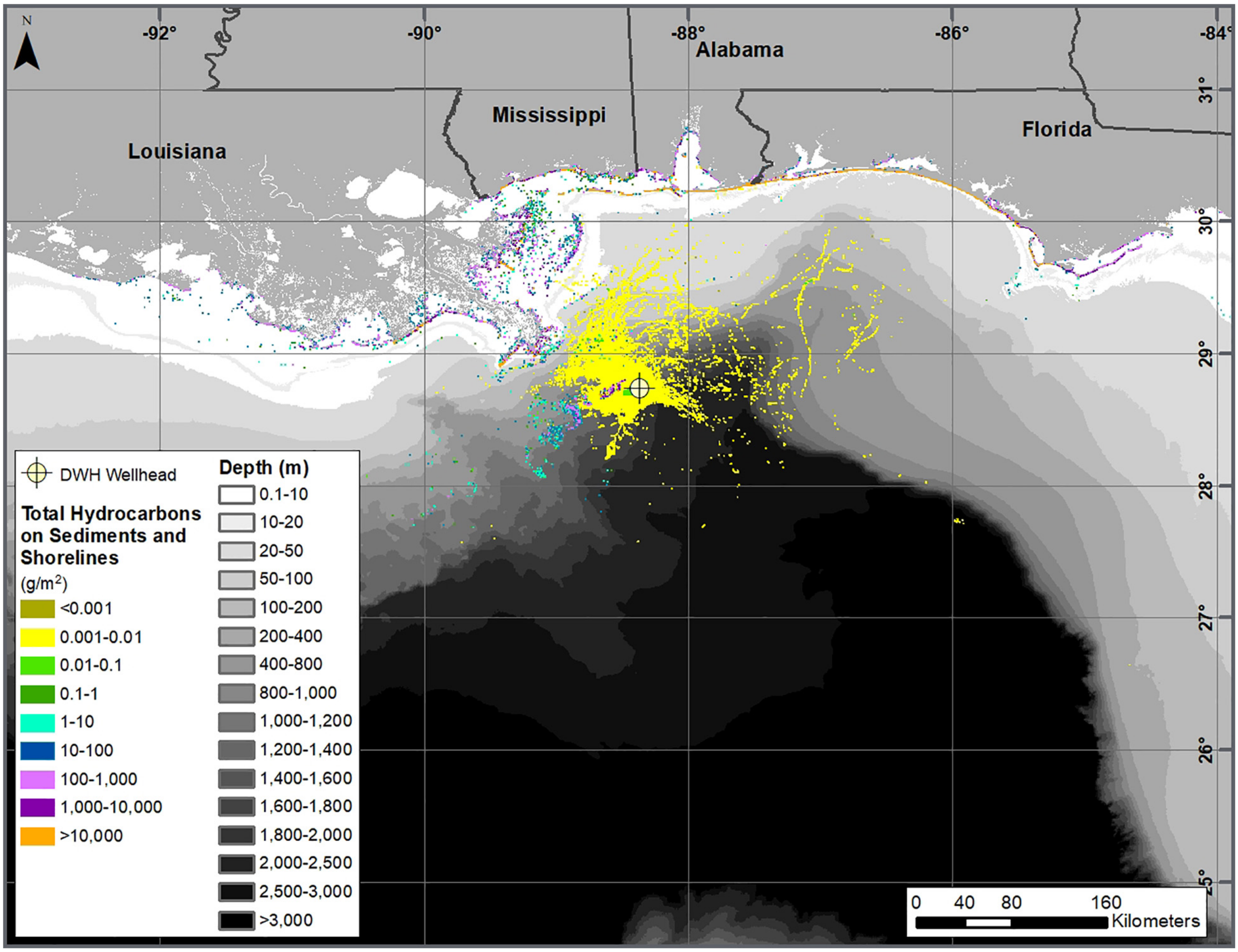

FIGURE 9 | Cumulative amount of oil coming ashore and settling to sediments (in g/m^2) by August 31, 2010 for the base case simulation using HYCOM-FSU currents and NARR winds.

the ADCP and observational data. The NRL NCOM model was superseded by NRL's HYCOM, which produced more realistic (slower) currents at depth, and so the NCOM simulations were not considered further.

Given the more narrow and accurate surfacing locations (see section "Floating Oil"), the simulation using ADCPs was the most realistic for depths below 200 m. While the interpolation of the ADCP data was not a hydrodynamic model, which conserved mass and momentum, the ADCP current data does indicate the actual flow field and which of the hydrodynamic models most closely simulated it (i.e., the HYCOM-FSU model).

In the SIMAP model simulations using the ADCP data and using HYCOM-FSU, the concentrations of droplets and dissolved constituents were highest close to the source (i.e., ∼1,200 or ∼1,300 m). Because the smaller oil droplets were spread out by spatially and time-varying currents as they rose through the water column, the modeled concentrations decreased considerably higher in the water column. Oil concentrations in the deep water were low and in a narrow cylinder stretching toward the surface in April, when the release was not treated with dispersants at the release point and the oil was mostly in the form of large droplets >0.7 mm in diameter. During May when the kink holes appeared and subsea dispersant began to be applied, such that small droplets were formed in addition to droplets >0.7 mm in diameter (Spaulding et al., 2015, 2017), the modeled subsurface concentrations were much higher, and the contamination was dispersed over a wider area. As shown by the sample data (Horn et al., 2015; Payne and Driskell, 2018), the deep plume of small droplets and dissolved components persisted from May to July. The model results show more extensive plumes in deep water in June–July when more effective subsea dispersant applications were used than prior to June 3. See French McCay et al. (2015a, 2016, 2018a,c) for further detail and maps depicting the concentration distributions in space and time.

Oil Sedimentation

Oil from the DWH spill was identified in the sediments in the offshore area surrounding and down-stream of the well site

(Joye et al., 2011; Montagna et al., 2013; Valentine et al., 2014; Romero et al., 2015; Stout and Payne, 2016a; Stout et al., 2016b). Valentine et al. (2014) noted that the pattern of contamination indicates deep-ocean intrusion layers as the source, consistent with deposition of a "bathtub ring" formed from an oil-rich layer of water impinging laterally upon the continental slope (at a depth of ∼900–1,300 m) and a higher-flux "fallout plume" where oil-SPM aggregates sank to underlying sediment (at a depth of ∼1,300–1,700 m).

Figure 9 maps the modeled sedimentation by August 31, 2010 for the base case using HYCOM-FSU for surface waters and ADCP data in deep water. The modeled sedimentation in deep water due to fallout by interactions with SPM and the bathtub ring impingement was in consistent locations to those mapped by Valentine et al. (2014), Stout et al. (2016a), and Romero et al. (2015). The model also predicted considerable sedimentation in the nearshore waters of Louisiana.

CONCLUSION

Summary of Findings

The modeled spatial distribution of surface oil was validated by comparison to remote sensing data. As the model ran continuously from April 22 through September of 2010, disagreement would be expected for older oil. However, freshly surfacing oil reset the modeled origin of the slicks on a continuous basis. The results indicate the importance of the wind drift in transporting the floating oil northward toward shore (consistent with Dietrich et al., 2012; Le Heìnaff et al., 2012; Boufadel et al., 2014; Weisberg et al., 2017), but that the currents used can change the patterns considerably. The model-predicted amount of floating oil agreed with remote-sensing based estimates, confirming the modeled DSDs and fate processes were realistic.

The modeled shoreline oiling for the base case (∼2,600 km oiled) compares well with the observations (∼2,100 km oiled; Nixon et al., 2016), with the model showing oiling from the Apalachicola Bay to Terrebonne Bay. The model predicted oiling on shore in areas that were not surveyed, so oiling of those areas based on observations is unknown. Other model simulations demonstrated the variability resulting from different current and wind inputs. Shoreline oiling events were discontinuous and occurred when winds (via wind drift) carried oil onshore.

Simulations of subsurface oil movements using current data from seven hydrodynamic models resulted in very different trajectories, and to varying degrees the hydrodynamic models generally over-estimated the speed of the currents in the area of the wellhead. Published DWH oil trajectory simulations (MacFadyen et al., 2011; Mariano et al., 2011; North et al., 2011, 2015; Dietrich et al., 2012; Le Heìnaff et al., 2012; Paris et al., 2012; Boufadel et al., 2014; Lindo-Atichati et al., 2014; Testa et al., 2016; Weisberg et al., 2017) show highly variable paths and concentrations as well. MacFadyen et al. (2011); Mariano et al. (2011), Le Heìnaff et al. (2012); Dietrich et al. (2012), Boufadel et al. (2014), and Weisberg et al. (2017) compared their predicted surface oil movements to field data, finding wind drift to be important to transport, along with the hydrodynamic model produced currents. However, they did not analyze subsea movements of the oil in comparison to observations. In our modeling studies, the base case simulation using currents generated by the HYCOM-FSU hydrodynamics model (Chassignet and Srinivasan, 2015) consistently resulted in both a subsea trajectory and concentration fields most similar to that predicted by the ADCP measurement-based current field below 200 m. The flow was generally toward the southwest, as the ADCPs indicated occurred (French McCay et al., 2018a). The HYCOM used by Paris et al. (2012), which was apparently the same HYCOM-NRL Real-time product we used, also showed similar movements of small droplets in the deep plume.

Because most of oil forming the surface slicks was from large droplets that surfaced near well, it was not very displaced by deep currents. Thus, use of the various hydrodynamic models for transport below 200 m did not greatly influence the surfacing locations to the point where it would be perceptible in the overall distribution of floating oil (i.e., as compared to synoptic remote-sensing based maps of oil distributions). Thus, the modeling problem can be treated in two domains: waters below 200 m in the offshore and surface waters above 200 m both offshore and over the shelf to nearshore.

Implications for Modeling Environmental Exposures

This modeling effort is unique and ground-breaking in several ways. The objective is to quantify by modeling oil transport, fate, exposure concentrations, and (as part of follow-on studies) biological effects (French McCay et al., 2015a,b,c,d,e being the first syntheses of these efforts). Thus, the modeling predicted oil transport, fate and exposures continuously over the entire spill period, including in deep water and surface waters. Transport modeling evaluated nine potential hydrodynamic inputs (seven models, measurement data and an assumption of no currents). The complexities of the oil composition and weathering were tracked using pseudo-components, such that exposure concentrations could be characterized by concentrations of each pseudo-component in the mixtures. Most fate processes were quantified as well, as opposed to evaluating implications of certain assumed inputs, such as droplet size or biodegradation rates. However, some fate processes could not be quantified for lack of sufficient information, such as related to marine oil snow formation and its flux to the sea floor. The exposure modeling (French McCay et al., 2015b,c) involved distribution, behavioral analysis and simulation of movements of many biological groups and life stages, recording their exposure histories to oil components, the results of which are being analyzed. We have also made a concerted effort to validate the model simulations at each stage of the overall effort. Such a comprehensive modeling and validation exercise has not been attempted previously.

The importance of data assimilation is well-established for calibrating physical models with observational information, and the tested and literature-reported hydrodynamic models do include assimilation of such information as sea surface height and temperature. However, data assimilation techniques have not been applied in oil spill models. Rather, many of the literature-reported oil trajectory model exercises (such as some of those noted above) ran short-term trajectories from known oil positions, as opposed to long simulations where displacement errors would compound. MacFadyen et al. (2011) described their approach for modeling during the response period where trajectories were reinitialized from identified remote sensing-based observations, and different hydrodynamic models were used over time, in order to obtain the more accurate trajectories.

While such a nudging-based initialization approach was considered and tested, whereby oil positions were updated with remote sensing observations, as was done for the response modeling (MacFadyen et al., 2011), this led to discontinuities in the concentrations of oil on the surface and in the water column beneath it. Thus, the exposures to biota were not reflective of reality and under-estimated when oil was repositioned. Further, weathering history of each oil spillet was needed to evaluate the composition of the exposure concentrations. Remote sensing analyses did identify thick and thin oil but did not provide enough information to track which parcel of oil moved where, such that weathered versus fresh oil could be tracked and repositioned appropriately. Thus, a more sophisticated "nudging" approach would be needed to improve the oil trajectory over what would be predicted from the hydrodynamic modeled currents and meteorological models wind products.

However, the predicted surface oil distributions were reasonable as compared to the remote sensing and shoreline oiling data. This suggests that the data assimilation techniques employed by the hydrodynamic and meteorological models were sufficient to produce reliable oil trajectories. On-going improvements in hydrodynamic modeling and data assimilation techniques should continue to improve oil spill model predictions of oil movements in the surface layer.

On the whole, the predictions of subsurface oil movement below 200 m were not nearly as reliable as for the floating oil. A major limitation is the availability of measurement data to assimilate into the hydrodynamic models. ADCP, temperature and salinity measurements throughout the water column in deep water over the full domain of interest could allow data assimilation to tune the hydrodynamics to better reflect the field conditions. Data assimilative techniques have been included in all seven of the hydrodynamic models evaluated, but likely these will need more development to handle the deep-water three-dimensional flow fields. In addition, analysis techniques are needed for evaluating model performance in simulating deep-water flows, analogous to those used for surface water dynamics (e.g., Halliwell et al., 2014).

With respect to quantifying exposures and biological effects, the results will depend on the areas and volumes affected at exposure concentrations that potentially could cause adverse effects (French McCay et al., 2004; French McCay, 2009). If biota have similar densities in areas affected by the model, as in areas oiled in the field, then the modeling results will be reliable, even if the specific path of the floating oil or subsurface plume is not precisely located. For wildlife, the modeled swept area by surface oil determines numbers of animals affected. For water column biota, the effects are related to the volume exceeding concentrations of concern. Biological densities are more uniform (on average) in offshore pelagic waters than they would be near the coast. Thus, accuracy of the trajectory and exposure concentrations are more important nearshore than in open waters offshore. The modeled movements and amounts of oil floating over time were found to be in good agreement with estimates from interpretation of remote sensing data, indicating initial oil droplet distributions and oil transport and fate processes produced oil distribution results reliable for evaluating environmental exposures in the water column and from floating oil at water surface.

Both organisms and oil components are highly patchy and variable over time. Present models cannot deterministically predict these fine scale dynamics. Further, biological distribution data are not available to precisely quantify fine scale distributions of all species and life stages. However, statistically describing the oil exposures, toxicological effects, and biological distributions should lead to reliable results. This approach also allows quantification of the uncertainties related to potential adverse effects. Model analyses have demonstrated the importance of the currents, winds and initial DSD to exposure concentrations, and have provided best estimates and uncertainty bounds for assessments. Analyses of potential exposures and biological effects based on these validated oil fate simulations using HYCOM-FSU and ADCP data are being developed, using methods and data similar to those described in French McCay et al. (2015b,c,d), such that the impacts of the DWH oil spill can be better understood.

DATA AVAILABILITY STATEMENT

Publicly available datasets were analyzed in this study. This data can be found here: The remote sensing, Shoreline Cleanup and Assessment, sensor and chemistry datasets analyzed for this study can be found in the ERMA Repository: The ERMA® Deepwater Gulf Response Web Application. https://erma.noaa.gov/gulfofmexico/erma.html#/layers=3+10717+16023+17774+32237+32238+32239+32240&x=−89.48747&y=27.92566&z=6.4&panel=layer and https://erma.noaa.gov/admin/folder/4481. Folder Name DWH Remote Sensing Products Folder Path Deepwater Horizon MC 252 Incident > Imagery & Remote Sensing Products > DWH Remote Sensing Products.

AUTHOR CONTRIBUTIONS

DF, MS, and DM designed the study. DF, MS, DC, DM, MH, and JF analyzed the data. DF wrote the manuscript. All authors listed have made a substantial, direct and intellectual contribution to the work, and approved it for publication.

FUNDING

Funding of this research was provided in part by the National Oceanic and Atmospheric Administration Damage Assessment, Remediation and Restoration Program (NOAA Contract No. AB133C-11-CQ-0050), and in part by the United States Department of the Interior, Bureau of Ocean Energy Management, Environmental Studies Program, Washington, DC (BOEM Contract Number M11PC00028). Some of the information developed was used in the development of the Draft Programmatic Damage Assessment and Restoration Plan/Draft Programmatic Environmental Impact Statement (pDARP, Deepwater Horizon Natural Resource Damage Assessment Trustee Council, 2016) for the DWH spill. The opinions expressed by the authors are their own and do not necessarily reflect the opinion or policy of the U.S. Government. Any use of trade, firm, or product names is for descriptive purposes only and does not imply endorsement by the U.S. Government.

ACKNOWLEDGMENTS

The authors acknowledge the contributions of Katherine Jayko, Cheryl Morse, and Tatsu Isaji of RPS for model code preparation, testing and debugging. Zhengkai Li and Yong Kim, formerly of RPS, contributed to data collection, quality control, and compilation efforts used to provide model inputs. Rachel Shmookler, also formerly of RPS, performed computations related to the shoreline oiling data. We thank three reviewers for their constructive comments, which improved the clarity of this manuscript.

SUPPLEMENTARY MATERIAL

The Supplementary Material for this article can be found online at: https://www.frontiersin.org/articles/10.3389/fmars.2021.618463/full#supplementary-material

REFERENCES

Adams, E. E., Socolofsky, S. A., and Boufadel, M. (2013). Comment on "Evolution of the macondo well blowout: simulating the effects of the circulation and synthetic dispersants on the subsea oil transport". *Environ. Sci. Technol.* 47, 11905–11905. doi: 10.1021/es4034099

Adcroft, A., Hallberg, R., Dunne, J. P., Samuels, B. L., Galt, J. A., Barker, C. H., et al. (2010). Simulations of underwater plumes of dissolved oil in the Gulf of Mexico. *Geophys. Res. Lett.* 37:L18605. doi: 10.1029/2010GL044689

Allen, A. A., Mabile, N. J., Jaeger, D., and Costnzo, D. (2011). The use of controlled burning during the Gulf of Mexico Deepwater Horizon MC-252 oil spill response. *Int. Oil Spill Conf. Proc.* 2011:abA194. doi: 10.7901/2169-3358-2011-1-194

Aman, Z. M., Paris, C. B., May, E. F., Johns, M. L., and Lindo-Atichati, D. (2015). High-pressure visual experimental studies of oil-in-water dispersion droplet size. *Chem. Eng. Sci.* 127, 392–400.

Androulidakis, Y., Kourafalou, V., Ozgokmen, T., Garcia-Pineda, O., Lund, B., Le Hénaff, M., et al. (2018). Influence of river-induced fronts on hydrocarbon transport: a multiplatform observational study. *J. Geophys. Res. Oceans* 123, 3259–3285. doi: 10.1029/2017JC013514

Androulidakis, Y. S., and Kourafalou, V. H. (2013). On the processes that influence the transport and fate of Mississippi waters under flooding outflow conditions. *Ocean Dyn.* 63, 143–164. doi: 10.1007/s10236-012-0587-8

Androulidakis, Y. S., Kourafalou, V. H., and Schiller, R. V. (2015). Process studies on the evolution of the Mississippi River plume: impact of topography, wind and discharge conditions. *Cont. Shelf Res.* 107, 33–49. doi: 10.1016/j.csr.2015.07.014

Belore, R. C., Trudel, B. K., and Morrison, J. (2011). Weathering, emulsification, and chemical dispersibility of Mississippi Canyon 252 crude oil: field and Laboratory studies. *Int. Oil Spill Conf. Proc.* 2011:abs247. doi: 10.7901/2169-3358-2011-1-247

Boufadel, M. C., Abdollahi-Nasab, A., Geng, X., Galt, J., and Torlapati, J. (2014). Simulation of the landfall of the deepwater horizon oil on the shorelines of the Gulf of Mexico. *Environ. Sci. Technol.* 48, 9496–9505. doi: 10.1021/es5012862

Boyer, T., Levitus, S., Garcia, H., Locarnini, R. A., Stephens, C., and Antonov, J. (2004). Objective analyses of annual, seasonal, and monthly temperature and salinity for the World Ocean on a $\frac{1}{4}$E Grid. *Int. J. Climatol.* 25, 931–945.

Camilli, R., Reddy, C. M., Yoerger, D. R., Van Mooy, B. A. S., Jakuba, M. V., Kinsey, J. C., et al. (2010). Tracking hydrocarbon plume transport and biodegradation at Deepwater Horizon. *Science* 330, 201–204. doi: 10.1126/science.1195223

Chao, Y., He, R., Farrara, J., and Zhang, C. (2014). *ROMS Hydrodynamic Modeling. Report to NOAA OR&R NRDA Program*. Saint Petersburg, FL: National Oceanic and Atmospheric Administration, 64.

Chao, Y., Li, Z., Farrara, J. D., McWilliams, J. C., Bellingham, J., Capet, X., et al. (2009). Development, implementation and evaluation of a data-assimilative ocean forecasting system off the central California coast. *Deep Sea Res. II* 56, 100–126. doi: 10.1016/j.dsr2.2008.08.011

Chassignet, E. P., Hurlburt, H. E., Metzger, E. J., Smedstad, O. M., Cummings, J. A., Halliwell, G. R., et al. (2009). US GODAE: global ocean prediction with the HYbrid Coordinate Ocean Model (HYCOM). *Oceanography* 22, 64–75. doi: 10.5670/oceanog.2009.39

Chassignet, E. P., and Srinivasan, A. (2015). *Data Assimilative Hindcast for the Gulf of Mexico. US Dept. of the Interior, Bureau of Ocean Energy Management, OCS Study BOEM 2015-035*. Sterling VA: BOEM, 40.

Csanady, G. T. (1973). *Turbulent Diffusion in the Environment*. Dordrecht: D. Reidel Publishing Company.

Daae, R. L., Skancke, J., Brandvik, P. J., and Faksness, L.-G. (2018). The sensitivity of the surface oil signature to subsurface dispersant injection and weather conditions. *Mar. Pollut. Bull.* 127, 175–181. doi: 10.1016/j.marpolbul.2017.11.067

Deepwater Horizon Natural Resource Damage Assessment Trustee Council, (2016). The Deepwater Horizon Oil Spill Final Programmatic Damage Assessment and Restoration Plan and Final Programmatic Environmental Impact Statement. National Oceanic and Atmospheric Administration, Office of Response and Restoration. Available online at: http://www.gulfspillrestoration.noaa.gov/restoration-planning/gulf-plan/ (accessed July 10, 2016).

Diercks, A. R., Highsmith, R. C., Asper, V. L., Joung, D., Zhou, Z., Guo, L., et al. (2010). Characterization of subsurface polycyclic aromatic hydrocarbons at the Deepwater Horizon site. *Geophys. Res. Lett.* 37:L20602. doi: 10.1029/2010GL045046

Dietrich, J. C., Trahana, C. J., Howard, M. T., Fleming, J. G., Weaver, R. J., Tanakae, D. S., et al. (2012). Surface trajectories of oil transport along the northern coastline of the Gulf of Mexico. *Cont. Shelf Res.* 41, 17–47. doi: 10.1016/j.csr.2012.03.015

Driskell, W. B., and Payne, J. R. (2018). Macondo oil in northern Gulf of Mexico waters – part 2: dispersant-accelerated PAH dissolution in the Deepwater Horizon plume. *Mar. Pollut. Bull.* 129, 412–419. doi: 10.1016/j.marpolbul.2018.02.057

ERMA, (2016). *The ERMA§Deepwater Gulf Response Web Application*. Tokyo: ERMA.

Fingas, M., and Fieldhouse, B. (2012). Studies on water-in-oil products from crude oils and petroleum products. *Mar. Pollut. Bull.* 64, 272–283. doi: 10.1016/j.marpolbul.2011.11.019

Fitzpatrick, J. J. (2009). Assessing skill of estuarine and coastal eutrophication models for water quality managers. *J. Mar. Syst.* 76, 195–211. doi: 10.1016/j.jmarsys.2008.05.018

French, D., Reed, M., Jayko, K., Feng, S., Rines, H., Pavignano, S., et al. (1996). *The CERCLA type A Natural Resource Damage Assessment Model for Coastal* *and Marine Environments (NRDAM/CME), Technical Documentation, Vol. I - V. Final Report, submitted to the Office of Environmental Policy and Compliance, U.S. Dept. of the Interior, Washington, DC, April, 1996*. Springfield, VA: National Technical Information Service,

French McCay, D., Horn, M., Li, Z., Crowley, D., Spaulding, M., Mendelsohn, D., et al. (2018c). *Simulation Modeling of Ocean Circulation and Oil Spills in the Gulf of Mexico, Volume III: Data Collection, Analysis and Model Validation*. New Orleans, LA: US Department of the Interior, 313.

French McCay, D., Jayko, K., Li, Z., Horn, M., Isaji, T., and Spaulding, M. (2018b). "Volume II: appendix II – oil transport and fates model technical manual," in *Simulation Modeling of Ocean Circulation and Oil Spills in the Gulf of Mexico*, eds C. W. Galagan, D. French McCay, J. Rowe, and L. McStay, (New Orleans, LA: US Department of the Interior), 422.

French McCay, D., Whittier, N., Sankaranarayanan, S., Jennings, J., and Etkin, D. S. (2004). Estimation of potential impacts and natural resource damages of oil. *J. Hazardous Mater.* 107, 11–25. doi: 10.1016/j.jhazmat.2003.11.013

French McCay, D. P. (2003). Development and application of damage assessment modeling: example assessment for the north cape oil spill. *Mar. Pollut. Bull.* 47, 341–359. doi: 10.1016/s0025-326x(03)00208-x

French McCay, D. P. (2004). Oil spill impact modeling: development and validation. *Environ. Toxicol. Chem.* 23, 2441–2456. doi: 10.1897/03-382

French McCay, D. P., Jayko, K., Li, Z., Horn, M., Kim, Y., Isaji, T., et al. (2015a). *Technical Reports for Deepwater Horizon Water Column Injury Assessment – WC_TR14: Modeling Oil Fate and Exposure Concentrations in the Deepwater Plume and Cone of Rising Oil Resulting from the Deepwater Horizon Oil Spill. DWH NRDA Water Column Technical Working Group Report. Prepared for National Oceanic and Atmospheric Administration by RPS ASA, South Kingstown, RI, USA. September 29, (2015a). Administrative Record no. DWH-AR0285776*. Washington, DC: U.S. Department of the Interior.

French McCay, D. P., Li, Z., Horn, M., Crowley, D., Spaulding, M., Mendelsohn, D., et al. (2016). "Modeling oil fate and subsurface exposure concentrations from the Deepwater Horizon oil spill," in *Proceedings of the 39th AMOP Technical Seminar on Environmental Contamination and Response*, Vol. 39, (Ottawa, ON: Environment Canada), 115–150.

French McCay, D., Crowley, D., and McStay, L. (2019). Sensitivity of modeled oil fate and exposure from a subsea blowout to oil droplet sizes, depth, dispersant use, and degradation rates. *Mar. Pollut. Bull.* 146, 779–793. doi: 10.1016/j.marpolbul.2019.07.038

French McCay, D., Crowley, D., Rowe, J., Bock, M., Robinson, H., Wenning, R., et al. (2018d). Comparative risk assessment of spill response options for a deepwater oil well blowout: Part I. Oil spill modeling. *Mar. Pollut. Bull.* 133, 1001–1015. doi: 10.1016/j.marpolbul.2018.05.042

French McCay, D., Horn, M., Li, Z., Jayko, K., Spaulding, M., Crowley, D., et al. (2018a). "Modeling distribution fate and concentrations of deepwater horizon oil in subsurface waters of the Gulf of Mexico," in *Chapter 31 in Oil Spill Environmental Forensics Case Studies*, eds S. Stout, and Z. Wang, (Amsterdam: Elsevier), 683–736. doi: 10.1016/b978-0-12-804434-6.00031-8

French McCay, D., Rowe, J., Balouskus, R., Morandi, A., and McManus, R. C. (2015e). *Technical Reports for Deepwater Horizon Water Column Injury Assessment – WC_TR.28: Injury Quantification for Planktonic Fish and Invertebrates in Estuarine, Shelf and Offshore Waters. DWH NRDA Water Column Technical Working Group Report. Prepared for National Oceanic and Atmospheric Administration by RPS ASA, South Kingstown, RI, USA. Administrative Record no. DWH-AR0172019.pdf, DWH-AR0172219.xlsx-DWH-AR0172227.xlsx*. Washington, DC: U.S. Department of the Interior.

French McCay, D. P. (2009). "State-of-the-art and research needs for oil spill impact assessment modeling," in *Proceedings of the 32nd AMOP Technical Seminar on Environmental Contamination and Response, Emergencies Science Division*, (Ottawa, ON: Environment Canada), 601–653.

French McCay, D. P., Balouskus, R., McManus, M. C., Schroeder, M., Rowe, J. J., and Bohaboy, E. (2015d). *Technical Reports for Deepwater Horizon Water Column Injury Assessment – WC_TR.12: Evaluation of Production Foregone as the Result of Direct Kill of Fish and Invertebrate Individuals. DWH NRDA Water Column Technical Working Group Report. Prepared for National Oceanic and Atmospheric Administration by RPS ASA, South Kingstown, RI, USA. Administrative Record no. DWH-AR0285169.pdf, DWH-AR0285305.xlsx-DWH-AR0285361.xlsx*. Washington, DC: U.S. Department of the Interior.

French McCay, D. P., McManus, M. C., Balouskus, R., Rowe, J. J., Schroeder, M., Morandi, A., et al. (2015c). *Technical Reports for Deepwater Horizon Water Column Injury Assessment: WC_TR.10: Evaluation of Baseline Densities for Calculating Direct Injuries of Aquatic Biota During the Deepwater Horizon Oil Spill. DWH NRDA Water Column Technical Working Group Report. Prepared for National Oceanic and Atmospheric Administration by RPS ASA, South Kingstown, RI, USA. Administrative Record no. DWH-AR0285021.pdf, DWH-AR0285141.xlsx, DWH-AR02851412.xlsx*. Washington, DC: U.S. Department of the Interior.

French McCay, D. P., Morandi, A., McManus, M. C., Schroeder Gearon, M., Jayko, K., and Rowe, J. J. (2015b). *Technical Reports for Deepwater Horizon Water Column Injury Assessment – WC_TR.09: Vertical Distribution Analysis of Plankton. DWH NRDA Water Column Technical Working Group Report. Prepared for National Oceanic and Atmospheric Administration by RPS ASA, South Kingstown, RI, USA. DWH NRDA Water Column Technical Working Group Report. Prepared for National Oceanic and Atmospheric Administration by RPS ASA, South Kingstown, RI, USA. Administrative Record no. DWH-AR0195958.pdf, DWH-AR0171921.xlsx, DWH-AR0171922.xlsx*. Washington, DC: U.S. Department of the Interior.

Garcia-Pineda, O., MacDonald, I., Hu, C., Svejkovsky, J., Hess, M., Dukhovskoy, D., et al. (2013a). Detection of floating oil anomalies from the Deepwater Horizon oil spill with synthetic aperture radar. *Oceanography* 26, 124–137. doi: 10.5670/oceanog.2013.38

Garcia-Pineda, O., MacDonald, I., Zimmer, B., Shedd, B., and Roberts, H. (2010). Remote sensing evaluation of geophysical anomaly sites in the outer continental slope, northern Gulf of Mexico. *Deep Sea Res. II Top. Stud. Oceanogr.* 57, 1859–1869. doi: 10.1016/j.dsr2.2010.05.005

Garcia-Pineda, O., MacDonald, I. R., Li, X., Jackson, C. R., and Pichel, W. G. (2013b). Oil spill mapping and measurement in the Gulf of Mexico with textural classifier neural network algorithm (TCNNA). *IEEE J. Select. Top. Appl. Earth Observ. Rem. Sens.* 6, 2517–2525. doi: 10.1109/jstars.2013.2244061

Garcia-Pineda, O., Zimmer, B., Howard, M., Pichel, W., Li, X., and MacDonald, I. R. (2009). Using SAR images to delineate ocean oil slicks with a texture classifying neural network algorithm (TCNNA). *Can. J. Rem. Sens.* 35, 411–421. doi: 10.5589/m09-035

General Bathymetric Chart of the Oceans, (2009). *Centenary Edition of the GEBCO Digital Atlas. Published on behalf of the Intergovernmental Oceanographic Commission (IOC) and the International Hydrographic Organization (IHO) as part of the General Bathymetric Chart of the Oceans*. Liverpool: British Oceanographic Data Centre.

Goni, G. J., Trinanes, J. A., MacFadyen, A., Streett, D., Olascoaga, M. J., Imhoff, M. L., et al. (2015). "Variability of the deepwater horizon surface oil spill extent and its relationship to varying ocean currents and extreme weather conditions," in *Mathematical Modelling and Numerical Simulation of Oil Pollution Problems*, ed. M. Ehrhardt, (Cham: Springer International Publishing Switzerland), 1–22. doi: 10.1007/978-3-319-16459-5_1

Graettinger, G., Holmes, J., Garcia-Pineda, O., Hess, M., Hu, C., Leifer, I., et al. (2015). *Integrating Data from Multiple Satellite Sensors to Estimate Daily Oiling in the Northern Gulf of Mexico during the Deepwater Horizon Oil Spill. DWH Natural Resource Exposure NRDA Technical Working Group Report, FE_TR.31*. Washington, DC: NOAA, 46.

Gros, J., Socolofsky, S. A., Dissanayake, A. L., Jun, I., Zhao, L., Boufadel, M. C., et al. (2017). Petroleum dynamics in the sea and influence of subsea dispersant injection during Deepwater Horizon. *Proc. Natl. Acad. Sci. U.S.A.* 114, 10065–10070. doi: 10.1073/pnas.1612518114

Halliwell, G. R. Jr., Srinivasan, A., Kourafalou, V., Yang, H., Willey, D., Le Hénaff, M., et al. (2014). Rigorous evaluation of a fraternal twin ocean OSSE system for the open Gulf of Mexico. *J. Atmos. Oceanic Technol.* 31, 105–130. doi: 10.1175/JTECH-D-13-00011

Horn, M., French McCay, D., Payne, J., Driskell, W., Li, Z., Grennan, M., et al. (2015). *Technical Reports for Deepwater Horizon Water Column Injury Assessment –Volume III. Water Column Chemical and Physical Data from the Deepwater Horizon Blowout. RPS ASA, South Kingstown, RI, USA, August (2015). DWH-AR0024617.pdf (main), DWH-AR0024364.pdf (Appendix B), DWH-AR0024462.pdf (Appendix C), DWH-AR0023990.pdf (Appendix D)*. Washington, DC: U.S. Department of the Interior.

Hyun, K. H., and He, R. (2010). Coastal upwelling in the South Atlantic Bight: a revisit of the 2003 cold event using long term observations and model hindcast solutions. *J. Mar. Syst.* 83, 1–13. doi: 10.1016/j.jmarsys.2010.05.014

Johansen, O., Brandvik, P., and Farook, U. (2013). Droplet breakup in subsea oil releases – Part 2: predictions of droplet size distributions with and without injection of chemical dispersants. *Mar. Pollut. Bull.* 73, 327–335. doi: 10.1016/j.marpolbul.2013.04.012

Joint Analysis Group, (2010). *Joint Analysis Group (JAG) Review of R/V Brooks McCall Data to Examine Subsurface Oil*. Available online at: http://www.ncddc.noaa.gov/activities/healthy-oceans/jag/reports/ (accessed November 1, 2011).

Jolliff, J. K., Smith, T. A., Ladner, S., and Arnone, R. A. (2014). Simulating surface oil transport during the Deepwater Horizon oil spill: experiments with the BioCast system. *Ocean Modell.* 75, 84–99. doi: 10.1016/j.ocemode.2014.01.004

Joye, S. I, MacDonald, R., Leifer, I., and Asper, V. (2011). Magnitude and oxidation potential of hydrocarbon gases released from the bp oil well blowout. *Nat. Geosci.* 4, 160–164. doi: 10.1038/ngeo1067

Kourafalou, V. H., and Androulidakis, Y. S. (2013). Influence of Mississippi River induced circulation on the Deepwater Horizon oil spill transport. *J. Geophys. Res.* 118, 3823–3842. doi: 10.1002/jgrc.20272

Le Heìnaff, M., Kourafalou, V. H., Paris, C. B., Helgers, J., Aman, Z. M., Hogan, P. J., et al. (2012). Surface evolution of the Deepwater Horizon oil spill patch: combined effects of circulation and wind-induced drift. *Environ. Sci. Technol.* 46, 7267–7273. doi: 10.1021/es301570w

Ledwell, J. R., He, R., Xue, Z., DiMarco, S. F., Spencer, L. J., and Chapman, P. (2016). Dispersion of a tracer in the deep Gulf of Mexico. *J. Geophys. Res. Oceans* 121, 1110–1132. doi: 10.1002/2015jc011405

Lehr, W., Bristol, S., and Possolo, A., (2010). *Oil Budget Calculator, Deepwater Horizon, Technical Documentation. A Report to the National Incident Command. The Federal Interagency Solutions Group, Oil Budget Calculator Science and Engineering Team*. Available online at: http://www.restorethegulf.gov/sites/default/files/documents/pdf/OilBudgetCalc_Full_HQ-Print_111110.pdf (accessed on April 1, 2012)

Li, Z., Spaulding, M., and French McCay, D. (2017b). An algorithm for modeling entrainment and naturally and chemically dispersed oil droplet size distribution under surface breaking wave conditions. *Mar. Pollut. Bull.* 119, 145–152. doi: 10.1016/j.marpolbul.2017.03.048

Li, Z., Spaulding, M. L., French McCay, D., Crowley, D., and Payne, J. R. (2017a). Development of a unified oil droplet size distribution model with application to surface breaking waves and subsea blowout releases considering dispersant effects. *Mar. Pollut. Bull.* 114, 247–257. doi: 10.1016/j.marpolbul.2016.09.008

Lindo-Atichati, D., Paris, C. B., Le Hénaff, M., Schedler, M., Valladares Juárez, A. G., and Müller, R. (2014). Simulating the effects of droplet size, high-pressure biodegradation, and variable flow rate on the subsea evolution of deep plumes from the Macondo blowout. *Deep Sea Res. II Top. Stud. Oceanogr.* 129, 301–310. doi: 10.1016/j.dsr2.2014.01.011

Liu, Y., Weisberg, R. H., Hu, C., and Zheng, L. (2011). Tracking the Deepwater Horizon Oil spill: a modeling perspective. *Eos Trans. Am. Geophys. Union* 92, 45–46. doi: 10.1029/2011eo060001

Mabile, N., and Allen, A. (2010). *Controlled Burns After Action Report, Burns on May 28th - August 3, 2010, Contolled Burn Group, Report prepared by Nere' Mabile & Al Allen, August 8, 2010*. 28. Available online at: https://www.erma.noaa.gov/dwh/erma.html (accessed August 16, 2017).

MacDonald, I. R., Garcia-Pineda, O., Beet, A., Daneshgar Asl, S., Feng, L., Graettinger, G., et al. (2015). Natural and unnatural oil slicks in the Gulf of Mexico. *J. Geophys. Res. Oceans* 120, 364–368. doi: 10.1002/2015JC011062

MacFadyen, A., Watabayashi, G. Y., Barker, C. H., and Beegle-Krause, C. J. (2011). "Tactical modeling of surface oil transport during the Deepwater Horizon spill response," in *Monitoring and Modeling the Deepwater Horizon Oil Spill: A Record-Breaking Enterprise*, eds Y. Liu, A. MacFadyen, Z.-G. Ji, and R. H. Weisberg, (Washington, DC: American Geophysical Union), 167–178. doi: 10.1029/2011GM001128

Mariano, A., Kourafalou, V., Srinivasan, A., Kang, H., Halliwell, G., Ryan, E., et al. (2011). On the modeling of the 2010 Gulf of Mexico oil spill. *Dyn. Atmos. Oceans* 52, 322–340. doi: 10.1016/j.dynatmoce.2011.06.001

McNutt, M., Camilli, R., Guthrie, G., Hsieh, P., Labson, V., Lehr, B., et al. (2011). *Assessment of Flow Rate Estimates for the Deepwater Horizon / Macondo Well Oil Spill. Flow Rate Technical Group report to the National Incident Command, Interagency Solutions Group, March 10, 2011*. Washington, DC: U.S. Department of the Interior.

McNutt, M. K., Camilli, R., Crone, T. J., Guthrie, G. D., Hsieh, P. A., Ryerson, T. B., et al. (2012). Review of flow rate estimates of the Deepwater Horizon oil spill, science applications in the Deepwater horizon oil spill special feature. *Proc. Natl. Acad. Sci. U.S.A.* 109, 20260–20267. doi: 10.1073/pnas.1112139108

Montagna, P. A., Baguley, J. G., Cooksey, C., Hartwell, I., Hyde, L. J., Hyland, J. L., et al. (2013). Deep-sea benthic footprint of the deepwater horizon blowout. *PLoS One* 8:e70540. doi: 10.1371/journal.pone.0070540

Mulcahy, R. (2010). *Water Column Injury Ephemeral Data Collection: ADCP Monitoring Plan (M/V Bunny Bordelon) (May 26, 2010). Originated as a Requirement by D. French McCay, Y. Kim, and Laurie Sullivan, (2010). Deepwater Horizon NRDA > Administrative Record > Pre-assessment – Water Column*. Available online at: http://www.doi.gov/deepwaterhorizon/adminrecord/Pre-assessment-Water-Column.cfm (accessed October 21, 2015).

National Academies of Sciences, Engineering, and Medicine, (2020). *The Use of Dispersants in Marine Oil Spill Response*. Washington, DC: The National Academies Press, 340. doi: 10.17226/25161

Nissanka, I. D., and Yapa, P. D. (2016). Calculation of oil droplet size distribution in an underwater oil well blowout. *J. Hydraulic Res.* 54, 307–320. doi: 10.1080/00221686.2016.1144656

Nixon, Z., Zengel, S. A., Baker, M., Steinhoff, M., Fricano, G., Rouhani, S., et al. (2016). Shoreline oiling from the Deepwater Horizon oil spill. *Mar. Pollut. Bull.* 107, 170–178. doi: 10.1016/j.marpolbul.2016.04.003

NOAA, (2013). *Deepwater Horizon MC 252 Incident/Response Operations/Dispersant Operations/Aerial Dispersant Applications*. Washington, DC: NOAA.

NOAA, (2016). *Open Water Oil Identification Job Aid for Aerial Observation*. Washington, DC: U.S. Department of Commerce.

North, E. W., Adams, E. E., Schlag, Z., Sherwood, C. R., He, R., Hyun, K. H., et al. (2011). "Simulating oil droplet dispersal from the Deepwater horizon spill with a Lagrangian approach," in *Monitoring and Modeling the Deepwater Horizon Oil Spill: A Record-Breaking Enterprise*, eds Y. Liu, A. MacFadyen, Z.-G. Ji, and R. H. Weisberg, (Washington, DC: American Geophysical Union), 217–226. doi: 10.1029/2011gm001102

North, E. W., Adams, E. E., Thessen, A., Schlag, E. Z., He, R., Socolofsky, S., et al. (2015). Assessing the influence of droplet size and biodegradation on the transport of subsurface oil droplets during the Deepwater Horizon spill: a model sensitivity study. *Environ. Res. Lett.* 10:024016. doi: 10.1088/1748-9326/10/2/024016

Novelli, G., Guigand, C. M., Boufadel, M. C., and Özgökmen, T. M. (2020). On the transport and landfall of marine oil spills, laboratory and ?eld observations. *Mar. Pollut. Bull.* 150:110805. doi: 10.1016/j.marpolbul.2019.110805

Okubo, A. (1971). Oceanic diffusion diagrams. *Deep Sea Res.* 8, 789–802. doi: 10.1016/0011-7471(71)90046-5

Okubo, A., and Ozmidov, R. V. (1970). Empirical dependence of the coefficient of horizontal turbulent diffusion in the ocean on the scale of the phenomenon in question. *Atmos. Ocean Phys.* 6, 534–536.

Olascoaga, M., and Haller, G. (2012). Forecasting sudden changes in environmental pollution patterns. *Proc. Natl. Acad. Sci. U.S.A.* 109, 2738–2743.

Özgökmen, T. M., Chassignet, E. P., Dawson, C. N., Dukhovskoy, D., Jacobs, G., Ledwell, J., et al. (2016). Over what area did the oil and gas spread during the 2010 Deepwater Horizon oil spill? *Oceanography* 29, 96–107. doi: 10.5670/oceanog.2016.74

Paris, C. B., Hénaff, M. L., Aman, Z. M., Subramaniam, A., Helgers, J., Wang, D.-P., et al. (2012). Evolution of the Macondo well blowout: simulating the effects of the circulation and synthetic dispersants on the subsea oil transport. *Environ. Sci. Technol.* 46, 13293–13302. doi: 10.1021/es303197h

Payne, J. R., and Driskell, W. B. (2015a). "2010 DWH offshore water column samples—forensic assessments and oil exposures," in *PECI Technical Report to the Trustees in Support of the PDARP*, Available online at: www.doi.gov/deepwaterhorizon/admin/record (accessed October 21, 2015).

Payne, J. R., and Driskell, W. B. (2015b). "Deepwater Horizon oil spill NRDA offshore adaptive sampling strategies and field observations," in *PECI Technical Report to the Trustees in support of the PDARP*, Available online at: www.doi.gov/deepwaterhorizon/admin/record (accessed October 21, 2015).

Payne, J. R., and Driskell, W. B. (2015c). "Forensic fingerprinting methods and classification of DWH offshore water samples," in *PECI Technical Report to the Trustees in Support of the PDARP*, Available online at: www.doi.gov/deepwaterhorizon/admin/record (accessed October 21, 2015).

Payne, J. R., and Driskell, W. B. (2015d). "Dispersant effects on waterborne oil profiles and behavior during the Deepwater Horizon Oil Spill," in *DWH NRDA Chemistry Technical Working Group Report, August 30, 2015*, (Washington, DC: U.S. Department of the Interior), 22. (accessed October 21, 2015).

Payne, J. R., and Driskell, W. B. (2016). "Water column sampling for forensics," in *Standard Handbook Oil Spill Environmental Forensics – Fingerprinting and Source Identification*, 2 Edn, eds S. Stout, and Z. Wang, (Amsterdam: Elsevier), 983–1014.

Payne, J. R., and Driskell, W. B. (2017). Water-column measurements and observations from the Deepwater Horizon oil spill natural resource damage assessment. *Int. Oil Spill Conf. Proc.* 2017, 3071–3090. doi: 10.7901/2169-3358-2017.1.3071

Payne, J. R., and Driskell, W. B. (2018). Macondo oil in northern Gulf of Mexico waters – part 1: assessments and forensic methods for Deepwater Horizon offshore water samples. *Mar. Pollut. Bull* 129, 399–411. doi: 10.1016/j.marpolbul.2018.02.055

Reddy, C. M., Arey, J. S., Seewald, J. S., Sylva, S. P., Lemkau, K. L., Nelson, R. K., et al. (2012). Composition and fate of gas and oil released to the water column during the Deepwater Horizon oil spill. *Proc. Natl. Acad. Sci. U.S.A.* 109, 20229–20234.

Romero, I. C., Schwing, P. T., Brooks, G. R., Larson, R. A., Hastings, D. W., Flower, B. P., et al. (2015). Hydrocarbons in Deep-sea sediments following the 2010 Deepwater Horizon blowout in the Northeast Gulf of Mexico 1-23. *PLoS One* 10:e0128371. doi: 10.1371/journal.pone.0128371

Ryerson, T. B., Camilli, R., Kessler, J. D., Kujawinski, E. B., Reddy, C. M., Valentine, D. L., et al. (2012). Chemical data quantify Deepwater Horizon hydrocarbon flow rate and environmental distribution. *Proc. Natl. Acad. Sci. U.S.A.* 109, 20246–20253.

Socolofsky, S. A., Adams, E. E., Boufadel, M. C., Aman, Z. M., Johansen, Ø, Konkel, W. J., et al. (2015b). Intercomparison of oil spill prediction models for accidental blowout scenarios with and without subsea chemical dispersant injection. *Mar. Pollut. Bull.* 96, 110–126.

Socolofsky, S. A., Adams, E. E., and Sherwood, C. R. (2011). Formation dynamics of subsurface hydrocarbon intrusions following the Deepwater Horizon blowout. *Geophys. Res. Lett.* 38:L09602.

Socolofsky, S. A., Dissanayake, A. L., Jun, I., Gros, J., Arey, J. S., and Reddy, C. M. (2015a). "Texas A&M Oilspill Calculator (TAMOC) modeling suite for subsea spills." in *Proceedings of the Thirty-Eighth AMOP Technical Seminar*. (Ottawa, ON: Environment Canada), 153–168.

Socolofsky, S. A., and Jirka, G. H. (2005). *Environmental Fluid Mechanics. Part I: Mass Transfer and Diffusion. Engineering – Lectures*. College Station, TX: Texas A&M University, 184.

Spaulding, M., Li, Z., Mendelsohn, D., Crowley, D., French McCay, D., and Bird, A. (2017). Application of an integrated blowout model system, OILMAP DEEP, to the Deepwater Horizon (DWH) spill. *Mar. Pollut. Bull.* 120, 37–50.

Spaulding, M. L. (1988). A state-of-the-art review of oil spill trajectory and fate modeling. *Oil Chem. Pollut.* 4, 39–55.

Spaulding, M. L., Mendelsohn, D., Crowley, D., Li, Z., and Bird, A. (2015). *Draft Technical Reports for Deepwater Horizon Water Column Injury Assessment: WC_TR.13: Application of OILMAP DEEP to the Deepwater Horizon Blowout. DWH NRDA Water Column Technical Working Group Report. Prepared for National Oceanic and Atmospheric Administration by RPS ASA, South Kingstown, RI 02879. Administrative Record no. DWH-AR0285366.pdf*. Washington, DC: U.S. Department of the Interior.

Spier, C., Stringfellow, W. T., Hazen, T. C., and Conrad, M. (2013). Distribution of hydrocarbons released during the 2010 MC252 oil spill in deep offshore waters. *Environ. Pollut.* 173, 224–230.

Stout, S. A. (2015a). *Physical and Chemical Properties of the Fresh MC252 Macondo-1 well crude oil. NewFields Technical Report to the Trustees in support of the pDARP*. Washington, DC: U.S. Department of the Interior, 21.

Stout, S. A. (2015b). *Bulk Chemical and Physical Properties of Fresh and Weathered Macondo Crude Oil*. Washington, DC: U.S. Department of the Interior, 18.

Stout, S. A., and Payne, J. R. (2016a). Macondo oil in deep-sea sediments: Part 1 – sub-sea weathering of oil deposited on the seafloor. *Mar. Pollut. Bull.* 111, 365–380.

Stout, S. A., and Payne, J. R. (2016b). Chemical composition of floating and sunken in-situ burn residues from the Deepwater horizon oil spill. *Mar. Pollut. Bull.* 108, 186–202. doi: 10.1016/j.marpolbul.2016.04.031

Stout, S. A., and Payne, J. R. (2017). Footprint, weathering, and persistence of synthetic-base drilling mud olefins in deep-sea sediments following the Deepwater Horizon disaster. *Mar. Pollut. Bull.* 118, 328–340.

Stout, S. A., Payne, J. R., Emsbo-Mattingly, S. D., and Baker, G. (2016a). Weathering of field-collected floating and stranded Macondo oils during and shortly after the Deepwater Horizon oil spill. *Mar. Pollut. Bull.* 105, 7–22. doi: 10.1016/j.marpolbul.2016.02.044

Stout, S. A., Payne, J. R., Ricker, R. W., Baker, G., and Lewis, C. (2016b). Macondo oil in deep-sea sediments: Part 2 – distribution and distinction from background and natural oil seeps. *Mar. Pollut. Bull.* 111, 381–401. doi: 10.1016/j.marpolbul.2016.07.041

Stout, S. A., Rouhani, S., Liu, B., Oehrig, J., Ricker, R. W., Baker, G., et al. (2017). Assessing the footprint and volume of oil deposited in deep-sea sediments following the Deepwater Horizon oil spill. *Mar. Pollut. Bull.* 114, 327–342.

Svejkovsky, J., and Hess, M. (2012). Expanding the utility of remote sensing data for oil spill response. *Photogram. Eng. Rem. Sens.* 78, 1011–1014.

Svejkovsky, J., Hess, M., Muskat, J., Nedwed, T. J., McCall, J., and Garcia, O. (2016). Characterization of surface oil thickness distribution patterns observed during the Deepwater Horizon (MC-252) oil spill with aerial and satellite remote sensing. *Mar. Pollut. Bull.* 110, 162–176.

Testa, J. M., Eric Adams, E., North, E. W., and He, R. (2016). Modeling the in?uence of deep water application of dispersants on the surface expression of oil: a sensitivity study. *J. Geophys. Res. Oceans* 121, 5995–6008. doi: 10.1002/2015JC011571

Valentine, D. L., Fisher, G. B., Bagby, S. C., Nelson, R. K., Reddy, C. M., Sylva, S. P., et al. (2014). Fallout plume of submerged oil from Deepwater Horizon. *Proc. Natl. Acad. Sci. U.S.A.* 111, 15906–15911. doi: 10.1073/pnas.1414873111

Valentine, D. L. K., Kessler, J. D., Redmond, M. C., Mendes, S. D., Heintz, M. B., Farwell, C., et al. (2010). Propane respiration jump-starts microbial response to a deep oil spill. *Science* 330, 208–211.

Venkataraman, P., Tang, J., Frenkel, E., Mcpherson, G. L., He, J., Raghavan, S. R., et al. (2013). Attachment of a hydrophobically modified biopolymer at the oil-water interface in the treatment of oil spills. *Appl. Mater. Interf.* 5, 3572–3580.

Walker, N., Pilley, C., D'Sa, E., Leben, R., Coholan, P., Brickley, P., et al. (2011). Impacts of loop current frontal cyclonic eddies and wind forcing on the 2010 Gulf of Mexico oil spill. *Geophys. Monogr. Ser.* 195, 103–116.

Weisberg, R. H., Zheng, L., and Liu, Y. (2017). On the movement of Deepwater Horizon Oil to northern Gulf beaches. *Ocean Model.* 111, 81–97. doi: 10.1016/j.ocemod.2017.02.002

White, F. M. (2005). *Viscous Fluid Flow*, 3rd Edn. New York, NY: McGraw-Hill.

Xue, Z., He, R., Fennel, K., Wei, C., Lorentz, S., and Hopskinson, C. (2013). Modeling ocean circulation and biogeochemical variability in the Gulf of Mexico. *Biogeosciences* 10, 7219–7234.

Youssef, M. (1993). *The Behavior of the Near Ocean Surface Under the Combined Action of Waves and Currents in Shallow Water*. 212. Ph. D. Thesis, University of Rhode Island, Kingston RI.

Youssef, M., and Spaulding, M. L. (1993). "Drift current under the action of wind waves," in *Proceedings of the 16th Arctic and Marine Oil Spill Program Technical Seminar, Calgary, Alberta, Canada, Emergencies Science Division*, (Ottawa, ON: Environment Canada), 587–615.

Youssef, M., and Spaulding, M. L. (1994). "Drift current under the combined action of wind and waves in shallow water," in *Proceedings of the Seventeenth Arctic and Marine Oilspill Program (AMOP) Technical Seminar*, (Ottawa, ON: Environment Canada), 767–784.

Zhao, L., Boufadel, M. C., Adams, E., Socolofsky, S. A., King, T., Lee, K., et al. (2015). Simulation of scenarios of oil droplet formation from the Deepwater Horizon blowout. *Mar. Pollut. Bull.* 101, 304–319.

Zhao, L., Boufadel, M. C., Socolofsky, S. A., Adams, E., King, T., and Lee, K. (2014). Evolution of droplets in subsea oil and gas blowouts: development and validation of the numerical model VDROP-J. *Mar. Pollut. Bull.* 83, 58–69.

Conflict of Interest: DF, DC, DM, JF, and MH were employed by RPS Group while performing this research.

The remaining authors declare that the research was conducted in the absence of any commercial or financial relationships that could be construed as a potential conflict of interest.

frontiers in Marine Science

ORIGINAL RESEARCH
published: 09 March 2021
doi: 10.3389/fmars.2021.628827

The Role of Biophysical Stickiness on Oil-Mineral Flocculation and Settling in Seawater

Leiping Ye[1,2]*, *Andrew J. Manning*[2,3,4], *James Holyoke*[2,5], *Jorge A. Penaloza-Giraldo*[2] *and Tian-Jian Hsu*[2]

[1] *School of Marine Sciences, Sun Yat-sen University, and Southern Marine Science and Engineering Guangdong Laboratory (Zhuhai), Zhuhai, China,* [2] *Department of Civil and Environmental Engineering, Center for Applied Coastal Research, University of Delaware, Newark, DE, United States,* [3] *HR Wallingford Ltd., Coasts and Oceans Group, Wallingford, United Kingdom,* [4] *School of Biological and Marine Sciences, University of Plymouth, Plymouth, United Kingdom,* [5] *Department of Civil, Architectural and Environmental Engineering, University of Texas at Austin, Austin, TX, United States*

Biophysical cohesive particles in aquatic systems, such as extracellular polymeric substances (EPS) and clay minerals, play an important role in determining the transport of spilled oil contamination and its eventual fate, particularly given that suspended sediment and microbial activities are often prevalent and diverse in natural environments. A series of stirring jar tests have been conducted to understand the multiple structures characteristics of the oil-mineral aggregates (OMAs) and EPS-oil-mineral aggregates (EPS-OMAs). OMAs and EPS-OMAs have been successfully generated in the laboratory within artificial seawater using: Texas crude oil (Dynamic viscosity: 7.27×10^{-3} Pa·s at 20°C), two natural clay minerals (Bentonite and Kaolin clay), and Xanthan gum powder (a proxy of natural EPS). A magnetic stirrer produced a homogeneous turbulent flow with a high turbulence level similar to that under natural breaking waves. High-resolution microscopy results show that EPS, kaolinite, and bentonite lead to distinguished oil floc structures because of the different stickiness character of EPS and mineral clay particles. With relatively low stickiness, kaolinite particles tend to attach to an oil droplets surface (droplet OMAs) and become dominant in small-sized flocs in the mixture sample. In contrast, the more cohesive bentonite particles stickiness could adsorb with oil droplets and are thus dominated by larger sized flocs. Biological EPS, with the highest stickiness, demonstrated that it could bond multiple small oil droplets and form a web structure trapping oil and minerals. Generally, adding EPS leads to flake/solid OMAs formation, and individual oil droplets are rarely observed. The inclusion of ESP within the matrix, also reduced the dependence of settling velocity on floc size and mineral type.

Keywords: biophysical stickiness, extracellular polymeric substance (EPS), oil-mineral aggregates (OMAs), flocculation, settling velocity

Edited by:
Xiaoshan Zhu,
Tsinghua University, China

Reviewed by:
Jia-Jang Hung,
National Sun Yat-sen University, Taiwan
Xuxu Wu,
University of Hull, United Kingdom

***Correspondence:**
Leiping Ye
yeleiping@mail.sysu.edu.cn

Specialty section:
This article was submitted to Marine Pollution, a section of the journal Frontiers in Marine Science

Received: *13 November 2020*
Accepted: *17 February 2021*
Published: *09 March 2021*

Citation:
Ye L, Manning AJ, Holyoke J, Penaloza-Giraldo JA and Hsu T-J (2021) The Role of Biophysical Stickiness on Oil-Mineral Flocculation and Settling in Seawater. Front. Mar. Sci. 8:628827. doi: 10.3389/fmars.2021.628827

INTRODUCTION

With increasing human activities and industrial development within the marine environment, water resource quality, and subsequent recovery, from contamination by industrial dumping and oil spillages have been a major challenge (Doshi et al., 2018); especially in estuarine and coastal regions where they have high sensitivity to the ecosystem and public health (Barbier et al., 2011).

In recent decades, oil spill contamination has tended to occur more commonly in coastal water systems (Peterson et al., 2003; Radoviæ et al., 2012). In particular, the largest oil spill event in human history (at the time of publication) occurred in 2010, and was the Deepwater Horizon (DWH) oil spill. DWH released approximately 4.9 million barrels (or 779 million L) of crude oil into the Gulf of Mexico (Crone and Tolstoy, 2010; Atlas and Hazen, 2011). It was estimated that almost 1,773 km of the shoreline habitat was directly affected by the DWH spill (Michel et al., 2013). Besides the huge negative ecological impact in the nearby regions of the spill site and the shoreline, there was an unexpected sedimentation of oil-associated marine snow throughout the water column and down to the seafloor; this was an additional long-term impact on the benthic zones (Daly et al., 2016; Passow and Ziervogel, 2016; Romero et al., 2017).

Due to their lower relative density, most of the leaked oil contaminants were expected to float on seawater as the weathering processes proceeded. However, it was found that a considerable amount of oil droplets aggregated with the various suspended materials (Passow et al., 2012; Passow and Ziervogel, 2016), including: sediments, detritus, phytoplankton, and fecal pellets, and significantly facilitated by biologically secreted substances (Passow and Alldredge, 1995; Malpezzi et al., 2013), namely the Transparent Exopolymer Particles (TEP) or more generally the Extracellular Polymeric Substance (EPS). These oil-containing aggregates, called Marine Oil Snows (MOS) would finally settle to the seafloor as they were transported in the seawater (Daly et al., 2016; Passow et al., 2019).

After oil spills occur, chemical dispersants are often initially used to treat the visible surface contaminants (Kujawinski et al., 2011; Lubchenco et al., 2012; McNutt et al., 2012). However, after the oil slick is dispersed into smaller oil droplets, there could be a higher probability that the oil droplets aggregate with other cohesive suspended materials in the water column to enhance MOS flocculation and settling (Fu et al., 2014; Kleindienst et al., 2015). Since cohesive sediment flocculation is extremely common in estuarine and coastal water systems with energetic flows (Manning and Dyer, 2007; Manning and Schoellhamer, 2013), oil droplets can readily flocculate with clay minerals, and also EPS from phytoplankton exudation, thus forming oil-particle aggregates (OPAs) (e.g., Zhao et al., 2014). These OPAs may significantly influence the entire subaquatic ecosystem (Teal and Howarth, 1984; Kingston, 2002; Fisher et al., 2016). Therefore, interactions between oil, cohesive minerals, and EPS play a notable role in the fate of oil spills in a natural ecosystem, and it becomes highly desirable to understand the formation, properties, and settling velocity of OPAs.

Various approaches have been reported to clean up oil-contaminated waters and these can be classified as: physical, chemical, and biological methods (Hoang et al., 2018). Physical methods are mainly using floating devices (e.g., booms) to gather an oil slick together to facilitate more effective removal or burning of a large amount of oil collected on the water surface. To accelerate the natural weathering processes, chemical dispersants are widely used to disperse the oil slick down to smaller oil droplets. These two types of methods may not be always effective and may even lead to secondary contamination. Therefore biological methods, such as adding microbes to enhance the oil bio-degradation, could be the most environmental-friendly approach. However, bio-degradation by the microbes and their bacteria function, can be time-consuming and their overall effectiveness may be highly dependent upon other environmental factors such as: nutrient levels, salinity, temperature, and the types of bacteria present (Atlas and Bartha, 1992, Atlas, 1995); hence more fundamental research is needed.

In recent years, many biologically related oil aggregates studies have been predominantly focused on MOS though both field observations (e.g., Passow et al., 2012; Daly et al., 2016) and laboratory experiments (e.g., Passow et al., 2017). These investigations provide clear evidence that high concentration oil-associated marine oil snows (MOS) exist in the vicinity of surface oil and the sub-surface oil plumes. Moreover, riverine suspended mineral particles and soot (a by-product of burned oil) are also very likely to interact with oil to form sinking oil-mineral aggregations (OMAs) in addition to MOS (Daly et al., 2016). With the combination of OMAs and EPS (or more generally called OPAs), flocculation and settling processes become ever more complex.

Clay mineral particles, such as kaolinite and bentonite, have been proven to aggregate with oil, and form OMAs (Khelifa et al., 2002; Muschenheim and Lee, 2002; Stoffyn-Egli and Lee, 2002). The settling velocity of these OMAs can be up to several mm/s, and their characteristics are highly dependent upon the base mineral stickiness (Ye et al., 2020). As aggregation is a complex process involving encounter, contact, and sticking (Hill and Nowell, 1990) controlled by flow turbulence, by directly controlling turbulence level, the biological EPS functions on OMAs flocculation may be better understood in the controlled laboratory experiments. Parsons et al. (2016) has demonstrated that only a very small amount of EPS ($<0.1\%$) can dramatically stabilize sedimentary beds, because EPS has an extremely high stickiness/stickiness. Therefore, the appreciable role of EPS in controlling the flocculation process requires improved quantification.

Many field studies measuring TEP concentration in the coastal/estuarine zone show TEP concentration as Xanthan gum equivalent concentration (e.g., Passow, 2012; Malpezzi et al., 2013). Although the Xanthan gum equivalent concentration is based on colorimetric determination, and hence it does not directly provide quantitative information on stickiness. A limited number of studies, such as Engel (2000), exhibit a positive correlation between TEP concentration and stickiness. In many laboratory sediment transport studies, pure Xanthan gum has been used extensively to model the benthic biota secreted EPS (e.g., Malarkey et al., 2015; Parsons et al., 2016), which is an important factor influencing the cohesive sediment dynamics (Tolhurst et al., 2002). Therefore, Xanthan gum has been used to simulate biological EPS in the present study.

EPS has the potential to become a practical and viable substance for stabilizing oil droplets in the aquatic environment, when accompanied by natural clay minerals. Scientifically, as natural EPS and sediments are ubiquitous in the marine environment, understanding the role of EPS in controlling the flocculation of sediment and stabilize oil droplets is a critical element to the understanding of the fate of spilled oil.

The primary goal of this study is to deduce the influence EPS has on oil-mineral flocculation. As a first step, the experiments are designed without considering the chemical dispersant, in order to better quantify the effect of EPS on oil-mineral flocs by making a direct comparison with earlier work on oil-mineral flocs without EPS (Ye et al., 2020). Relatively higher concentrations (~500 mg/l) of suspended minerals and EPS are applied artificially in controlled laboratory experiments in order to obtain discernable differences for inter-comparison. Data obtained from controlled laboratory experiments of six cases are analyzed with three main objectives: (1) To understand the EPS-OMAs structures formed with two different types of common clay minerals, using high-resolution digital microscopy; (2) to measure physical characteristics of EPS-OMAs, such as their sizes and settling velocities using a high magnification floc video camera; and most importantly, (3) synthesize measured and statistically analyzed data to gain insights into how EPS participation influences oil containment within flocs, floc structure, and settling dynamics. The EPS-OMA parameters derived from this laboratory research can be applied to the predictive modeling framework for oil spills; a preliminary endeavors can be found in Cui et al. (2021) in this issue.

MATERIALS AND METHODS

Laboratory jar test experiments were undertaken at the Center for Applied Coastal Research, University of Delaware utilizing a magnetic stirring system, with a self-designed turbulence monitoring frame attached (see Ye et al., 2020). The resultant OMAs were measured with a LabSFLOC-2 (the 2nd version of Laboratory Spectral Flocculation Characteristics instrument, Manning et al., 2010) aside of the jar test apparatus. Each experimental run adopted a uniform stirring speed of 490 rpm (equivalent to turbulence dissipation rate at $\varepsilon = 0.02\ m^2/s^3$, and shear rate parameter $G = \sqrt{\varepsilon/\nu}\ \ 140\ s^{-1}$, Ye et al., 2020). As discussed in Ye et al. (2020), this was a relatively high shear rate parameter and similar to the highly turbulence conditions experienced under breaking waves. To prepare each sample, 1 Liter of artificial seawater was used for each run and the salinity was set (using laboratory grade sodium chloride) nominally to 35 ppt. White Kaolin clay (92.3 ± 2.5% Kaolinite), Wyoming sodium Bentonite clay (85.2 ± 2.3% Montmorillonite), Xanthan gum, and raw Texas crude oil (Dynamic viscosity: 7.27×10^{-3} Pa·s at 20°C) were each added to the artificial seawater solution using a mini pipette.

To generate the flocs, the oil-to-sediment (or EPS) ratio was 2:1, and a sediment (or EPS) concentration of 500 mg/l was used. This oil-to-sediment ratio was utilized, in order to maximize the oil trapping efficiency in the mineral particles/flocs present. Pe-test assessments were initially conducted to deduce the optimal duration required for flocs to reach the equilibrium phase in the stirring jar tests (>2 hrs). Six OMA samples were selected and studied here (see **Table 1**, C01–06). Cases C04, C05, C06 are the primary focus of this study, which is to investigate the effect of EPS on OMAs. Cases C01, C02, and C03 are the corresponding baseline OMA samples, and part of these OMA results (already reported in Ye et al., 2020) are also presented in order to demonstrate the contrasting effects of EPS.

Each experimental jar test run had a nominal 2 h duration before they were collected for analysis using the LabSFLOC-2 system (Manning et al., 2007, 2017). As demonstrated by Ye et al. (2020), for the given turbulence level, the flocculation process reaches equilibrium within the 2 hrs experimental run time. The total floc population characteristics were observed using the LabSFLOCS-2 system which comprised a high-resolution (one pixel~5 μm) video camera that observes and records individual flocs whilst settling in a dedicated settling column. The analyzed digital floc data provided by LabSFLOCS-2 includes complete population mass-balanced: floc numbers, floc size, floc effective density (floc bulk density minus the fluid density), settling velocity, and fractal dimensions. Each floc data size spectrum was segregated into 12 size bands (SB) from <20 microns in SB1 to >640 microns in SB12.

In order to also examine the detailed structures of the OMAs and EPS-OMAs and the capability of these flocs to contain oil droplets, representative equilibrium floc samples were collected at the completion of each run and subsequently analyzed using a digital microscope (AmScope Inc.). Analysis of the microscopy images from the equilibrium stage (C01-06, **Table 1**), enabled the number of free oil droplets, total flocs, and OMAs to be measured and statistically assessed. These values were counted from a snapshot digital image obtained from the microscope for a given sample. For each sample, nominally 30 images were analyzed and various statistics, including mean ($\overline{N}$) and median values of all identical flocs, and the lower and higher 25% values from the mean were all obtained. See Ye et al. (2018, 2020) for further information on the control experiments for OMA cases without EPS.

RESULTS

Aggregates Structures

Multiple types of equilibrium EPS-OMAs structures were examined using high-resolution microscopy, and compared with the well-known droplet OMAs and flake/solid OMAs (Stoffyn-Egli and Lee, 2002) formed by oil droplets and mineral. A key finding reported by Ye et al. (2020) regarding the existence of droplet OMA and flake/solid OMA, is their dependence on the mineral stickiness. Under the applied high turbulence level, the averaged droplet size was calculated to be about 57 μm (see **Figure 1A**). The less sticky individual kaolinite particles and micro-flocs, were seen to directly attach to the oil droplets forming droplet OMAs (see **Figure 1B**). In contrast, oil tended to be directly adsorbed into the high stickiness bentonite aggregate structures forming flake/solid OMAs (see **Figure 1C**), and the individual droplets were no longer observed. In the equally mixed kaolinite-bentonite sample, both types of OMAs were observed (see **Figure 1D**), but the overall settling velocity statistics are closer to the sticker bentonite-oil characteristics.

TABLE 1 | A summary on proportions of mineral clay, Xanthan gum and oil in each experimental run.

Case	Kaolinite clay (mg)	Bentonite clay (mg)	Xanthan gum (mg)	Texas crude oil (mg)	Saline water (ml)
C01	500	/	/	1,000	1,000
C02	/	500	/	1,000	1,000
C03	250	250	/	1,000	1,000
C04	500	/	500	1,000	1,000
C05	/	500	500	1,000	1,000
C06	250	250	500	1,000	1,000

/: none mineral or EPS added.

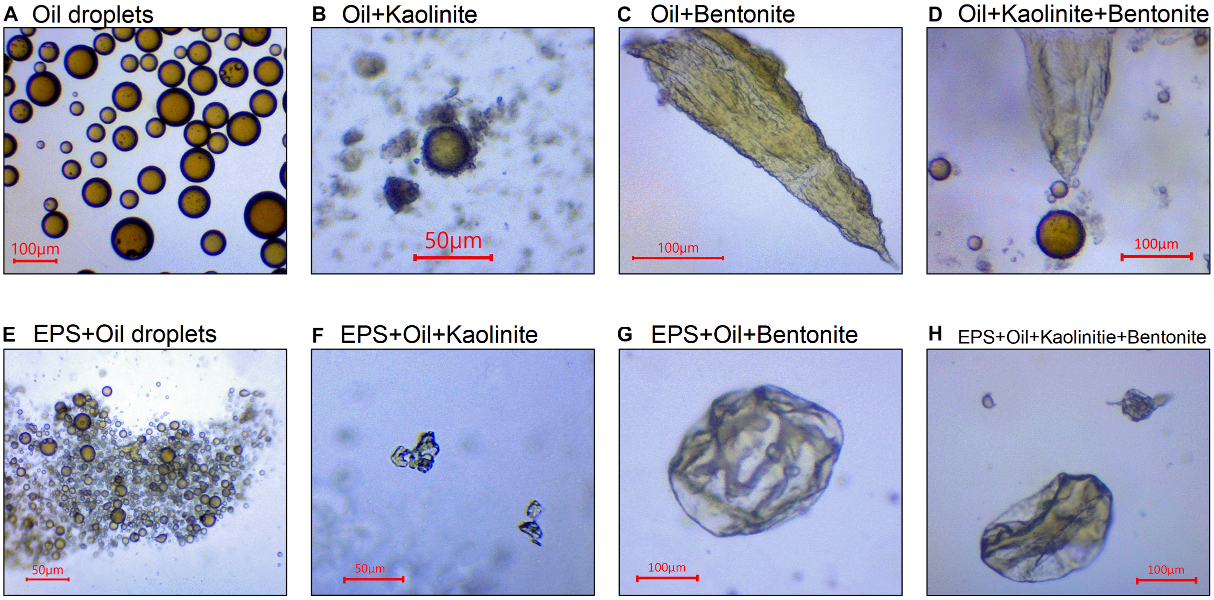

FIGURE 1 | Microscopy images for pure oil droplets **(A)**, oil-Kaolinite floc/droplet OMA **(B)**, oil-Bentonite floc/flake OMA **(C)**, mixed oil-Kaolinite-Bentonite floc **(D)**, structure of EPS bonding large number of small oil droplets **(E)**, EPS-oil-Kaolinite floc **(F)**, EPS-oil-Bentonite floc **(G)**, and mixed EPS-oil-Kaolinite-Bentonite floc **(H)**. (**A–C** and **D** are adopted from Ye et al., 2020).

For the EPS and oil mixture (**Figure 1E**), a large number of oil droplets flocculated to form large-sized (several hundred micrometers) structures. Interestingly, those droplets absorbed into the EPS structure did not exceed 10∼20 μm in size, which is 3–4 times smaller than the size of pure oil droplets (**Figure 1A**) generated under the same turbulent dissipation rate. This reduced oil droplet size with EPS is comparable to the size-scale of the smallest microflocs (i.e., smallest disaggregated floc size fractions typically observed in a very high turbulent flow; Keyvani and Strom, 2014). In other words, the structure of oil droplets in EPS, even though they can still be discerned, have reduced nearly two orders of magnitudes in volume.

Through the scrutiny of a plethora of microscopy images from the EPS-oil-Kaolinite floc sample (e.g., **Figure 1F**), the flocs show the presence of oil, EPS and minerals all closely aggregated together forming a structure similar to solid/flake OMAs, and no individual droplet OMA were observed. This highlights the key difference in the flocs resulting from the addition of the extremely sticky EPS to the suspension matrix. The results suggest that EPS significantly reduces the droplet size (see **Figure 1E**) down to a size-scale similar to those of diminutive microflocs, and hence prevents the prospect of mineral floc bonding. Moreover, we can speculate that the high stickiness of EPS, may encourage the oil to be absorbed into the aggregate structure in a similar way to the effect of high stickiness depicted by bentonite. Following this concept, it is unsurprising and logical to observe numerous sizeable EPS-oil-Bentonite flocs formed in **Figure 1G**; these are similar to the compact dense oil-Bentonite OMA (**Figure 1C**), but encompassing supplemental EPS. The EPS-oil-kaolinite-bentonite flocs (see **Figure 1H**) also shows a consistent solid/flake structure in which no droplet OMA were observed, in contrast to their no-EPS counterpart (**Figure 1D**).

Oil Droplet Numbers

Motivated by the distinctive floc structures exhibited in **Figure 1** (due to different mineral clays and the addition of EPS), it is anticipated that these flocs may also contain a dissimilar amount of oil droplets. The oil trapping efficiency for different samples is quantified by counting the number of oil droplets present in each sample (Khelifa et al., 2002) on attaining quasi-equilibrium

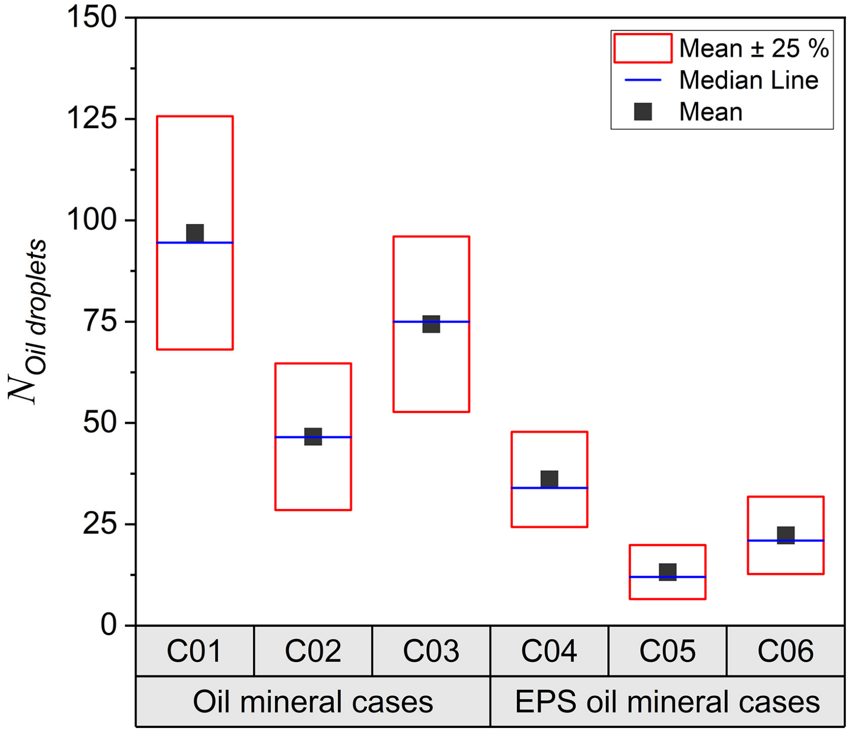

FIGURE 2 | Box charts of oil droplets numbers, analyzed by microscopy images collected from the bulk sediment mixture samples at the equilibrium. Each dot represents number obtain from an image and each sample was analyzed by 30 images randomly taken under microscope covering thousands of individual flocs statistically.

(see **Figure 2**). The case of oil and kaolinite (C01) has the highest number of free oil droplets remaining after 2 h of agitation (mean value $\overline{N} = 95$), whilst the bentonite case (C02) shows almost half the number of oil droplets ($\overline{N} = 47$). This result indicates that bentonite is approximately twice as effective in containing oil droplets in OMAs.

With the addition of EPS to the kaolinite and bentonite samples (C04 and C05), both cases show significant (nearly a factor 3–5) reductions in the number of free oil droplets ($\overline{N} = 32$ and $\overline{N} = 10$ for C04 and C05, respectively) compared to those without EPS (C01 and C02). In particular, the EPS-oil-bentonite sample (C05 in **Figure 2**) has the highest capability to contain oil droplets, with the fewest free oil droplet still present in the sample on completing a 2 h flocculation jar-test. Both of the samples with kaolinite-bentonite mixtures, revealed the remnant number of oil droplets ($\overline{N} = 72$ for C03 and $\overline{N} = 20$ for C06) were lower than kaolinite related samples (C01 and C04, respectively), but greater than bentonite related samples (C02 and C05, respectively); while adding EPS reduced the free oil droplets almost by a factor of 3 (i.e., comparing C03 and C06). More analyses confirming these finding will be discussed in the section "How the Aggregate Structures Determine the Oil Trapping Efficiency?"

Total Floc Characteristics

Key floc population characteristics (including floc size, settling rate, and density) were provided by the LabsFLOCS-2 system. To illustrate the effects of EPS on the resultant flocculation, the samples have been grouped into three for inter-comparison: Group #1) oil-Kaolinite floc (C01, OMA_K) and EPS-oil-Kaolinite (C04, EPS-OMA_K) samples; Group #2) oil-Bentonite (C02, OMA_B) and EPS-oil-Bentonite (C05, EPS-OMA_B) samples; and Group #3) oil-Kaolinite-Bentonite (C03, OMA_{K-B}) and EPS-oil-Kaolinite-Bentonite (C06, EPS-OMA_{K-B}) samples.

OMA_K and EPS-OMA_K (Group #1)

The oil-Kaolinite flocs (OMA_K) have a size range from 20 to 350 microns (more than 85% were smaller than 160 micron—the nominal microfloc:macrofloc size division boundary) and settling velocity range from 0.04 to 4 mm/s (**Figure 4A** floc data measured using the LabSFLOC-2 instrumentation). Adding EPS (EPS-OMA_K) expands the floc size range from 18 to 500 microns in size (with more than 80% smaller than 160 microns) and 0.02 to 8 mm/s in settling velocity (**Figure 4B**). Generally, adding EPS widen the range of observed floc sizes and settling velocities.

The distribution of the number of floc in the kaolinite cases reveal that the OMA_K and EPS-OMA_K have the most flocs present in SBs2–3 (~990 flocs). In fact, the most notable effect of adding EPS is the new existence of the largest flocs in SB8 (~40 flocs) and SB9 (~6 flocs), indicating observed floc sizes in the range of 320 microns to 480 microns. The effective density trend generally decreases from small-sized flocs down to larger-sized flocs for both oil-kaolinite and EPS-oil-kaolinite cases. Moreover, adding EPS increased the effective density of small flocs (see EPS-OMA_K in SB2–4), but the effective density of the macroflocs in

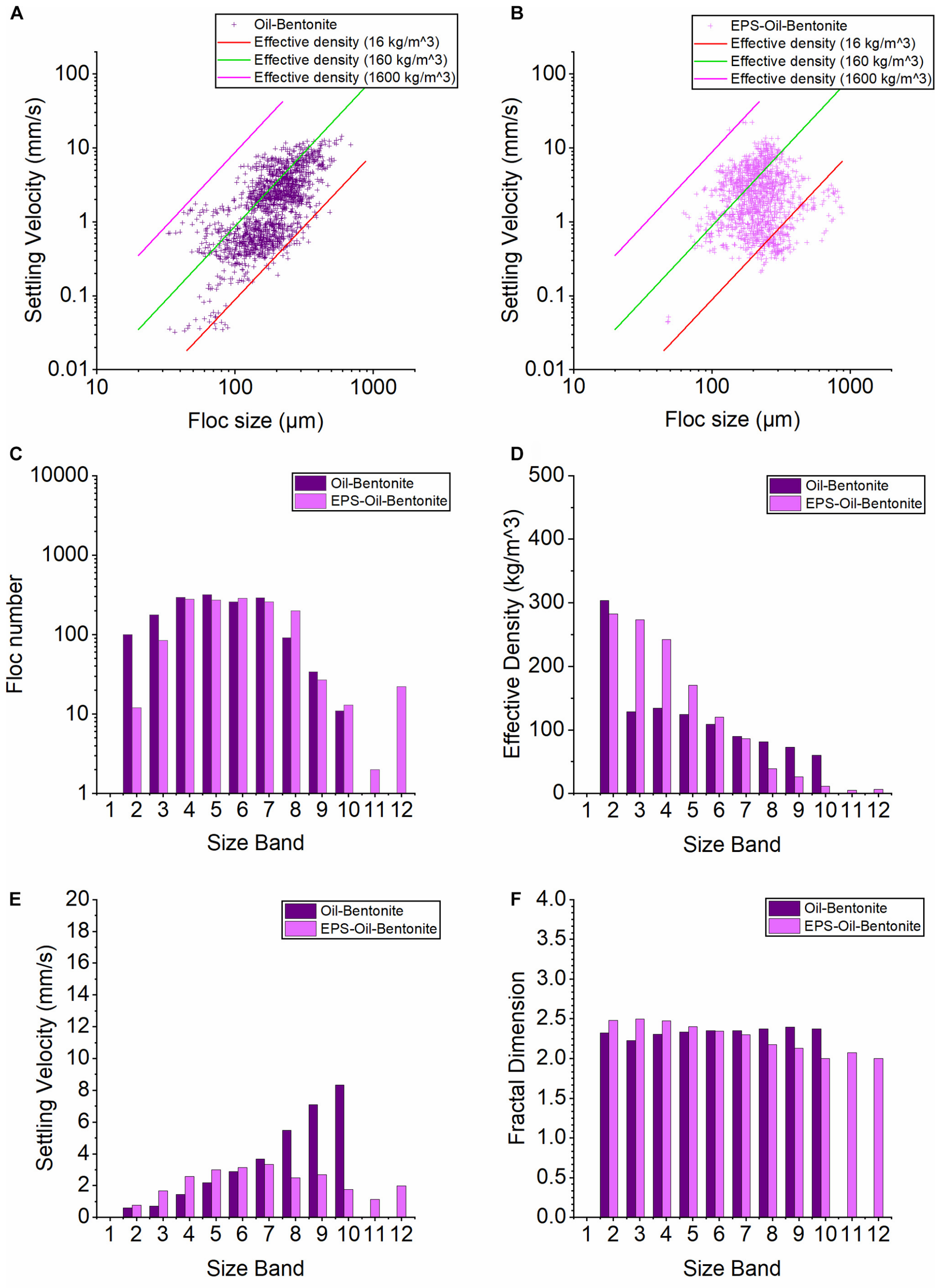

Size Band	1	2	3	4	5	6	7	8	9	10	11	12
Size Range (µm)	20-40	40-80	80-120	120-160	160-200	200-240	240-320	320-400	400-480	480-560	560-640	>640

FIGURE 3 | Floc characteristics from the LabSFLOC-2 analysis of Bentonite cases. **(A,B)** show the plots of floc sizes vs. settling velocities of oil-Bentonite and EPS-oil-Bentonite, respectively. The three diagonal lines each represent contours of a constant effective density (calculated using Stokes Law) 1,600 kg/m^3 (pink line, equivalent to a quartz particle), 160 kg/m^3 (green) and 16 kg/m^3 (red line). **(C–F)** show the 12 Size Bands (SB) trends of floc number, settling velocity, floc density and fractal dimensions for oil-Bentonite (dark purple) and EPS-oil-Bentonite (light purple) samples.

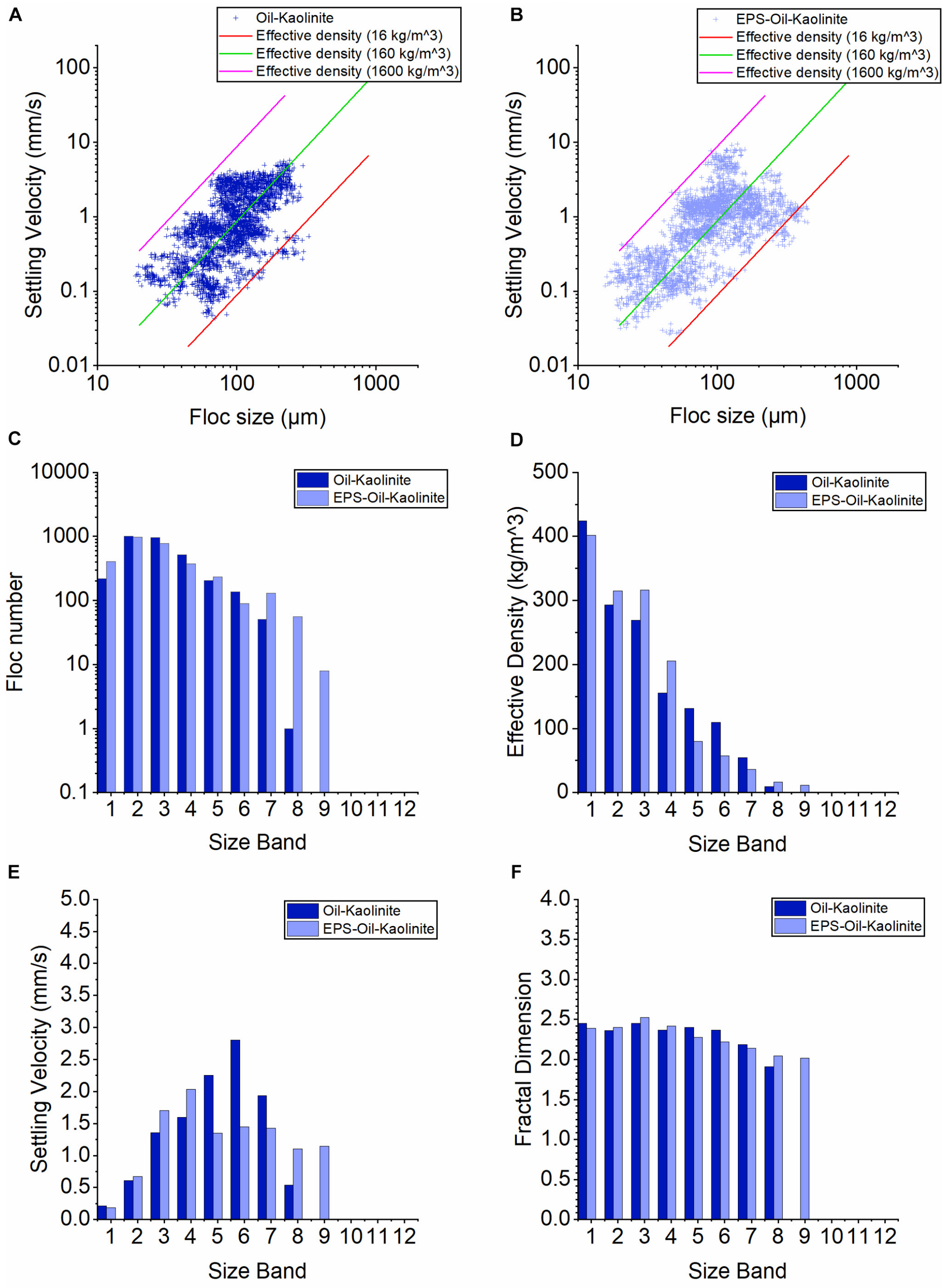

Size Band	1	2	3	4	5	6	7	8	9	10	11	12
Size Range (μm)	20-40	40-80	80-120	120-160	160-200	200-240	240-320	320-400	400-480	480-560	560-640	>640

FIGURE 4 | Floc characteristics from the LabSFLOC-2 analysis of Kaolinite cases. **(A,B)** show the plots of floc sizes vs. settling velocities of oil-Kaolinite and EPS-oil-Kaolinite, respectively. The three diagonal lines each represent contours of a constant effective density (calculated using Stokes Law) 1,600 kg/m^3 (pink line, equivalent to a quartz particle), 160 kg/m^3 (green) and 16 kg/m^3 (red line). **(C–F)** show the 12 Size Bands (SB) trends of floc number, settling velocity, floc density and fractal dimensions for oil-Kaolinite (blue), EPS-oil-Kaolinite (light blue) samples.

SB5–7 (160–320 μm) still predominantly reduced (**Figure 4D**). The newly formed large macroflocs in SB8–9 (320–480 μm) by adding EPS exhibited very low effective densities ranging between 10 and 20 kg/m^3; this indicates that these macroflocs are both fragile and highly porous.

Both cases show similar increase in trends of settling velocities from SB1 to SB4. The OMA$_K$ case has a peak settling velocity in SB6 of 2.7 mm/s, then slows down through SB7–SB8 to a velocity of under 0.5 mm/s. While the EPS-OMA$_K$ case shows a more stable settling velocity in SB5–7 at 1.2–1.3 mm/s, then slightly reduces in SB8–9 to around 1 mm/s (**Figure 4E**). By adding EPS, the newly formed large macroflocs in SB8–9 reveals the settling velocity of just 1 mm/s is primarily a product of their low floc effective density. Consistent with the feature observed in effective density, adding EPS slightly increase settling velocity of smaller flocs in SB2–4. Overall, adding EPS reduces the variability of settling velocity as a function of floc size, which is a trend that will be examined more later. The fractal dimensions of both OMA$_K$ and EPS-OMA$_K$ cases show a slight peak in SB3 at 2.4 and 2.5, respectively, then due to low-density flocs in the large size bands, the fractal dimension gradually decreases to about 2.0 for SBs 4–9.

OMA$_B$ and EPS-OMA$_B$ (Group #2)

The sizes of oil-Bentonite OMA$_B$ range from 32 to 600 μm and their settling velocities range from 0.03 to 10 mm/s (**Figure 3A**) while the EPS-OMA$_B$ sample shows OMA sizes range from 50 to 900 microns and the settling velocity is between 0.04 and 20 mm/s (**Figure 3B**). Clearly, both floc size and settling velocity shift toward respective larger values on adding EPS.

The floc numbers for OMA$_B$ and EPS-OMA$_B$ are similar in SB4–7 (250∼300 in each SB). However, adding EPS clearly reduces the floc numbers in the two smallest size bands (SB2 and SB3), whilst generating even larger marcoflocs (now exceeding 560 microns) that extend into SBs11–12. The effective density generally decreases as floc size increases for both OMA$_B$ and EPS-OMA$_B$ cases (**Figure 3D**). Noticeably, the effective density of OMA$_B$ rapidly decreases by more than 50% as the floc population transits from SB2 to SB3, and then continues to gradually decrease through SB4 to SB10 (**Figure 3D**). For the small to medium-sized flocs in SB3–6, adding EPS notably increases the effective density, but in the larger-sized macrofloc of SBs8–10, the effective densities are significantly reduced compared with those of OMA$_B$ (**Figure 3D**). The introduction of EPS was intrinsic in the formation of the very large macroflocs present in SBs11–12 and thus the EPS also contributed to their very low floc effective densities; this will be examined further in the Discussion.

The settling velocity of OMA$_B$ shows a monotonically increasing trend from small to larger-sized SBs (**Figure 3E**), especially in SB8–10 where the settling velocities reach 5∼9 mm/s. This is because the decrease in effective density of OMA$_B$ is very mild in SB3–10, and hence these floc settling velocities were primarily controlled by floc size. However, due to the effect of EPS, the effective density of EPS-OMA$_B$ shows a more abrupt decrease with respect to increasing floc size. As a result, the settling velocities of the large macroflocs (SB7–11) of EPS-OMA$_B$ display a reduction in fall rate, and also indicate a relatively weak dependence on floc size (**Figure 3E**).

Generally, adding EPS tends to increase the settling velocity of smaller microflocs, and the variability of settling velocity as a function of floc size is much smaller in EPS-OMA$_B$; these features are consistent with those observed in the kaolinite cases (C01 and C03). The fractal dimension of OMA$_B$ is around 2.2–2.3 (**Figure 3F**). In contrast, adding EPS increased the fractal dimension up to 2.5 in small-sized microflocs in SB1–2, but the value dropped to just below 2.0 in larger macroflocs in SB8–12. This trend is slightly more pronounced, but generally consistent with the kaolinite cases shown in **Figure 4**.

OMA$_{K-B}$ and EPS-OMA$_{K-B}$ Flocs (Group #3)

The floc sizes and settling velocities of the mixed oil-Kaolinite-Bentonite sample (OMA$_{K-B,}$ C03) ranges from 15 to 400 microns and 0.03 to 15 mm/s, respectively (**Figure 5A**). The stickier EPS-OMA$_{K-B}$ saw flocs sizes of 16–800 microns (C06) and settling velocities between 0.08 and 12 mm/s (**Figure 5B**). For Group #3 flocs, adding EPS slightly narrows the settling velocity range, presumably because EPS has the effect of rescinding the existence of droplet OMAs.

The floc numbers in both samples show peaks in SB2 (650 and 850 flocs, respectively) and then they both decrease with growing floc size (**Figure 5C**). However, it is evident that adding EPS to the suspension matrix produces more large-sized EPS-OMA$_{K-B}$ macroflocs in SB7∼9 (240–480 μm). The newly observed macroflocs in the upper size bands (SB10–12, > 480 μm), were consistent with the EPS-OMA$_K$ and EPS-OMA$_B$ reported earlier for Groups #1 and #2. The OMA$_{K-B}$ and EPS-OMA$_{K-B}$ samples both exhibit very high effective densities within SB1, when compared with the remainder of the SBs (**Figure 5D**). However, this particular feature was already present in the kaolinite-bentonite sample (without oil and EPS) reported by Ye et al. (2020), and it is ostensively an idiosyncratic feature associated with clay mineral mixtures. Consistent with other EPS cases (C04, C05), the addition of EPS to the suspension matrix appears to affect the interparticle bonding at that SB1size-scale and promote an increase in the floc effective density.

Although both cases show a gradual decrease in floc effective density as the population progresses from SB1 to SB12, the OMA$_{K-B}$ sample demonstrates an effective density 2–3 times higher than that present in the EPS-OMA$_{K-B}$ sample (**Figure 5D**). In particular, the flocs in SBs10–12 from the EPS-OMA$_{K-B}$ sample had extremely low effective densities of 4.6, 1.9, 1.6 kg/m^3, respectively. Compared to OMA$_{K-B}$ sample, EPS-OMA$_{K-B}$ shows a much more gradual increase in settling velocities as the population grows from SB1 to SB8. Therefore, the OMA$_{K-B}$ shows a 3-fold faster settling velocity than the EPS- OMA$_{K-B}$ sample (**Figure 5E**). The overall range of EPS-OMA$_{K-B}$ settling velocity was predominantly between 1 and 2 mm/s. Again, by adding EPS to the suspension, this had the resultant effect of significantly reducing the variability of the settling velocity.

A peak fractal dimension of 2.75 was observed in SB1 for both cases. This is presumably due to the presence of numerous high effective density small flocs formed with the bentonite-kaolinite clay mixture. Beyond SB1, the OMA$_{K-B}$ sample depicts a relatively uniform fractal dimension around 2.5; while the

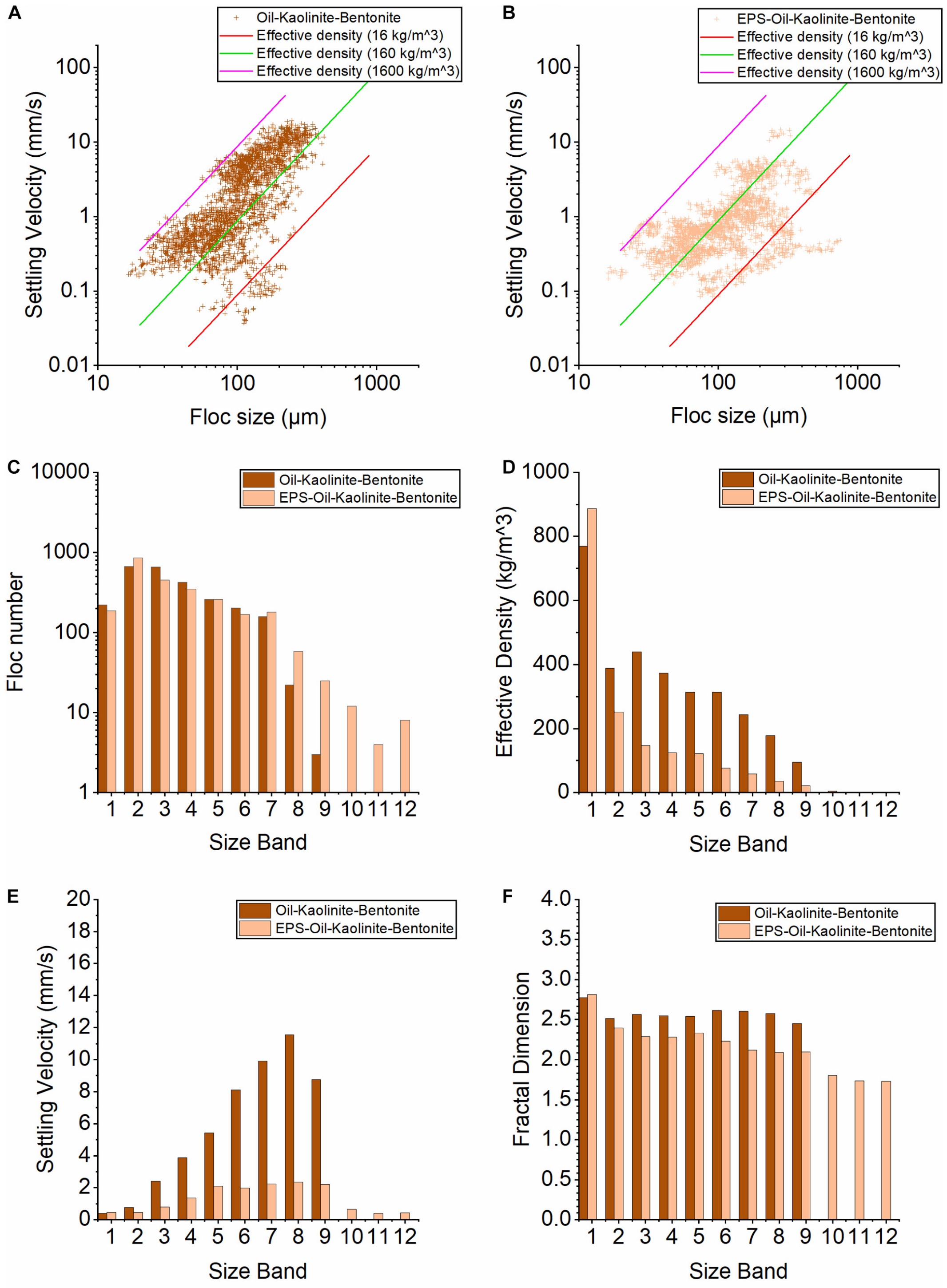

Size Band	1	2	3	4	5	6	7	8	9	10	11	12
Size Range (μm)	20-40	40-80	80-120	120-160	160-200	200-240	240-320	320-400	400-480	480-560	560-640	>640

FIGURE 5 | Floc characteristics from the LabSFLOC-2 analysis of mixed Kaolinite and Bentonite cases. **(A,B)** show the plots of floc sizes vs. settling velocities of oil-Kaolinite-Bentonite and EPS-oil-Kaolinite-Bentonite, respectively. The three diagonal lines each represent contours of a constant effective density (calculated using Stokes Law) of 1,600 kg/m^3 (pink line, equivalent to a quartz particle), 160 kg/m^3 (green), and 16 kg/m^3 (red line). **(C–F)** show the 12 Size Bands (SB) trends of floc number, settling velocity, floc density, and fractal dimensions for oil-Kaolinite-Bentonite (dark orange) and EPS-oil-Kaolinite-Bentonite (orange) samples.

EPS- OMA_{K-B} sample shows a notably lower fractal dimension, which gradually reduces from 2.4 in SB2 to below 1.8 in SB12 (**Figure 5F**). Adding EPS produces many large but very low effective density macroflocs with fractal dimensions < 2.

DISCUSSION

Floc Structures Determine Oil-Trapping Efficiency

The results presented suggest that the capability of flocs to contain oil droplets strongly depends on the stickiness of the constituents forming the floc. As shown in Ye et al. (2020), bentonite clay is more cohesive than kaolinite clay. This explains why bentonite flocs of sample C02, have two-times less free oil droplets remaining compared to kaolinite-based flocs. However, the high stickiness of EPS seems to play an even more significant role in increasing the potential for flocs to contain oil droplets, as adding EPS (see C04, C05, C06) reduced the number of free oil droplets by about a factor 2–3, when compared to a non-EPS counterpart (C01, C02, C03).

In addition to oil droplet numbers shown in **Figure 2**, microscopy image analysis also provides statistical trend information for both the OMAs and pure mineral flocs, and thus the total number of flocs can be obtained (**Figures 6A–C**) for each of the six samples. Clearly, droplets OMA can readily identified from the characteristic shape of oil droplets attached in OMAs. The solid and flake OMAs can be identified by their oily color (brown) in the OMA with dense structures that are different from those of pure mineral floc (**Figure 1**). Interestingly, all the samples show similar numbers of OMAs with variability within 15%, except for the EPS-oil-kaolinite sample (C04), which has about 50% higher number of OMAs than other samples (**Figure 6A**).

It is important to point out that for kaolinite sample C01, there is a significant number of mineral flocs, which is about 3 times more than that in the bentonite sample (C02, **Figure 6B**). As already discussed in Ye et al. (2020), a much smaller number of flocs present in the bentonite sample is due to bentonite clay's high stickiness encouraging potential flocculation. Similarly, adding EPS to the suspension matrix in samples C04, C05 and C06 also crucially reduces the number of mineral flocs by a factor 4 for kaolinite (comparing C01 and C04), a factor 2 for Bentonite (comparing C02 and C05), and a 3-fold reduction for mixed kaolinite-bentonite samples (comparing C03 and C06). This also suggests that EPS encourages flocculation by notably increasing the stickiness of the floc structure, and thus the increase is particularly pronounced for the less cohesive kaolinite clay samples.

By summing the OMAs and pure mineral flocs present in each respective population (**Figures 6A,B**), we can calculate the total number flocs for each of the six cases (see **Figure 6C**). To evaluate the oil trapping efficiency, the ratio of OMAs numbers to total floc numbers for each of the six cases are shown in **Figure 6D**. All the EPS-oil-mineral samples (C04–06) have a much higher ratio of OMA (around 0.5–0.6) than those of oil-mineral samples (C01–03) without the EPS addition (around 0.1∼0.2); this advocates the superior capability of EPS in trapping oil droplets. Amongst all the six samples, the OMA_K sample (C01) shows that OMAs only consist of less than 10% of the flocs present. This rises by 15% with OMAs accounting for one quarter of OMA_B sample (C02). The inclusion of EPS (EPS-OMA_B sample) further stimulated the development of OMAs to nominally 60% of the total flocs (see **Figure 6D**).

Since it is known that bentonite is more cohesive than kaolinite, while adding EPS also increases the floc stickiness considerably, it becomes evident that the stickiness of flocs and the number of OMAs are positively correlated. By adopting the assumption that we can utilse the ratio of OMA number to total floc number to quantitatively represent oil trapping efficiency. By adding sticky EPS to the oil-kaolinite sample (C04) significantly increase the number of OMAs to contribute about 45% of the total flocs, which is 5-fold increase in oil trapping efficiency. The addition of EPS to the oil-bentonite sample (C05), the OMA accounts for half of the total flocs, and when compared to that of C02, the oil trapping efficiency is only increased by a factor 2. A 4-fold oil trapping efficiency from adding EPS to a mixed kaolinite-bentonite matrix was observed when comparing samples C03 and C06.

Overall, the capability of flocs to contain oil droplets is highly dependent on stickiness. Bentonite clay is appreciably more cohesive than kaolinite clay minerals, and by adding EPS to the suspension matrix, it further magnifies flocculation potential and stickiness. It is also important to note that whilst pure kaolinite clay exhibits low stickiness, the addition of EPS can significantly enhance the stickiness. In summary, EPS plays a key role in increasing the stickiness of flocs, and its effect appears to overcome the natural stickiness of clay minerals. The importance of biological flocculation in OMAs has been recognized by an earlier review paper of Muschenheim and Lee (2002), and the results now presented provide quantitative evidence that EPS increases oil trapping efficiency.

Floc Characteristics Determined by Stickiness

Oil has been observed to exist in turbulent waters in the form of oil droplets, OMAs, and EPS-OMAs in our laboratory experiments (**Figure 1**). The results presented herein show the dramatic effects that biological cohesive EPS and physical mineral cohesive particles have on the flocculation with oil droplets in the seawater. The two types of natural common clay minerals, kaolinite and bentonite, each with different characteristic levels of particle stickiness (controls flocculation rate, Ye et al., 2020) have been seen to flocculate with oil droplets and thus easily form OMA with unique structures and characteristics.

The addition of EPS in oil-minerals mixture leads to the formation of very large-sized macroflocs which were absent in the samples lacking EPS. In addition, EPS also increases the effective density and settling velocity in small-sized microflocs, but demonstrated the opposite effect in larger-sized macroflocs (**Figures 4D,E**, **3D,E**). The combination of oil and EPS increasing aggregate density when compared to oil-free samples, has also recently been reported by Passow et al. (2019). In the mixed

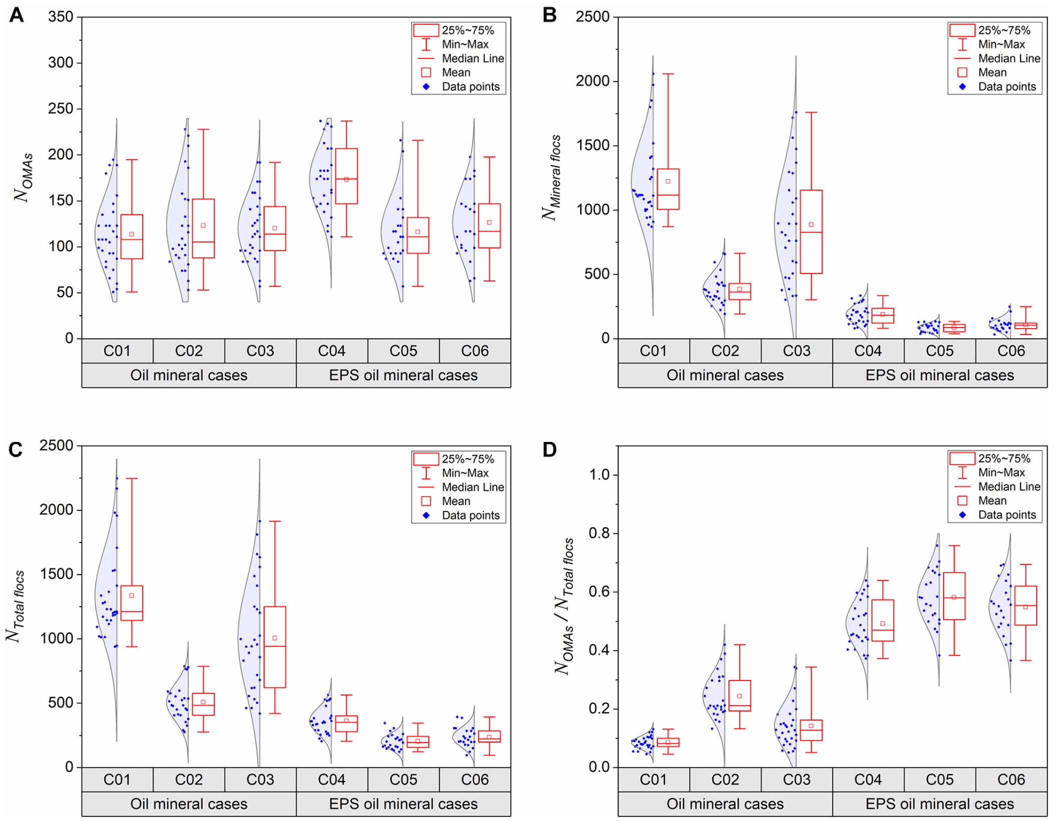

FIGURE 6 | Box charts of oil-mineral aggregate numbers **(A)**, pure mineral floc numbers **(B)**, Total floc numbers **(C)**, and ratios OMA to total floc numbers **(D)** in each experimental sample (C01–06, **Table 1**), analyzed by microscopy images collected from the bulk sediment mixture samples at the equilibrium. Each dot represents number obtain from an image and each sample was analyzed by 30 images randomly taken under microscope covering thousands of individual flocs statistically.

kaolinite and bentonite cases, a reduction of both effective density and settling velocity is observed for almost all the size bands when adding EPS into the oil-mineral suspension mixture (**Figures 5D,E**). While the stickiness of mineral particles in isolation has significant effects on determining the unique structure and settling velocity of OMAs, the inclusion of EPS within the flocculation matrix not only further enhances the stickiness character of suspended materials, but also directly determines the final form of an aggregate. The unique role of biological stickiness in dominating the flocculation of suspended minerals and oil droplets in seawater requires further quantitative investigations. These important floc characteristics are directly related to the OMA structures, and this finding is discussed in more detail next.

When comparing kaolinite and bentonite clays, notably more oil participates in bentonite OMA flocculation (i.e., much less free oil droplets left, see **Figure 2**), and the number of OMA occupies a larger percentage of the total flocs observed in bentonite samples (**Figure 6D**). With the greater stickiness and flocculation potential of bentonite mineral particles (Ye et al., 2020), pure bentonite flocs generally have much larger sizes and higher porosities than their kaolinite floc equivalents. With adequate stirring time in seawater, the more porous bentonite flocs can absorb more oil within the aggregate structure; meanwhile the original fluffy mineral flocs, after absorbing oil, become more compact and form the flake/solid OMAs (Ye et al., 2020, see also **Figure 1C**). Compared with kaolinite particles, which simply attach to the oil droplets surface to form droplet OMAs (see **Figure 1B**), the same amount of bentonite shows a much higher capability to absorb oil into OMA than kaolinite. This explains why more oil droplets are contained in OMAs, and thus less free oil droplets remain in the bentonite sample cases (**Figure 2**). With the same turbulent flow energy, more oil droplets are potentially more likely to collide and be captured by larger bentonite macroflocs, than those smaller flocs in kaolinite cases.

In the previous study of Ye et al. (2020), the significant differences in floc density and settling velocity between kaolinite OMAs and bentonite OMAs were attributed to clay stickiness and floc structure. Particularly, the less naturally cohesive kaolinite and oil tend to form droplet OMAs which produce many low-density flocs in the larger size bands, whilst the more cohesive bentonite produces relatively dense (relative to pure bentonite flocs) flake/solid OMAs. Here, we observed that EPS also has a substantial effect in controlling the floc structure. Particularly, the droplet OMAs are no longer observed in kaolinite flocs when EPS is added. Therefore, the main difference due to clay-type observed in Ye et al. (2020) is not obvious once EPS is participating in the flocculation process. The overall floc characteristics seem to be dictated by EPS, and the settling velocity is in the vicinity of 1 mm/s for EPS-OMA$_K$ and 2 mm/s for EPS-OMA$_B$ (**Figures 4**, **3**).

The function of biological EPS in flocculation is unique and different from that of mineral particles. Unlike the London-van der Waals forces and inter-particle electrostatic bonding between pure mineral particle flocculation, or the surface attaching and the porous absorbing between mineral flocs and oil droplets, the fixative form of EPS in an aquatic suspension can effectively trap oil droplets, OMAs, and mineral particles/flocs all into mixed EPS-OMA. It is expected that the collisional efficiency and flocculation potential improve with increased EPS during high turbulent flow episodes. This is confirmed by the observation of a dramatic reduction of the oil droplets numbers and the amount remaining in the samples of EPS-OMAs (such as C04–06) after the turbulent stirring duration (**Figure 2**). Although EPS-OMA could be broken-up at some point with the high flow turbulence, their secondary flocculating capability through further collisions during agitation can be much higher than those samples void of EPS, because of the highly sticky EPS still present in each fractured floc unit.

Implication and Application

The capability of mineral particles or EPS in aggregating oil into flocs, and the quantification of their effective density and settling velocity, are all vitally important when predicting the fate of spilled oil (e.g., Daly et al., 2016; Dukhovskoy et al., this issue). From the microscopy observations, EPS tends to bind around oil or mineral units via a sticky web-like structure which largely enhances the total stickiness between the particles or floc units. As long as the EPS attaches within OMAs, the flocs can be hard to break up and became more stable when compare with non-EPS flocs. Therefore the involvement of EPS, means fewer oil droplets can be left isolated and larger OMAs are obtained than those for equivalent non-EPS cases (**Figure 5A**). Interestingly, although more oil droplets may participate in EPS-OMA flocculation, the numbers of OMAs may not increase (**Figure 5B**) because the higher stickiness level significantly enhance the size of EPS-OMA (∼800 microns) rather than the EPS-OMA numbers. This feature is particularly pronounced in bentonite cases, as they already demonstrate a naturally high mineral stickiness. Ye et al. (2020) quantified several key differences in the OMAs formed by pure bentonite clay and pure kaolinite clay due to mineral stickiness. A key finding from the present study further suggests that the sticky web structure provided by EPS dominates the stickiness already provided by the clay mineral, and hence when EPS is present, the variability of OMA physical properties may be less pronounced. A direct result of the EPS domination in the flocculation processes relevant to the sinking of oil, as reveal by the present study (see **Figures 4E**, **3E**, **5E**), is that it tends to produce a more homogeneous floc settling velocity variability across the entire floc size spectrum.

With the addition of EPS to the suspension matrix, the oil droplets may be dispersed (i.e., the droplet size becomes smaller; compare **Figures 1A,E**) and persist within EPS structures as stabilized droplets. This is consistent with the recent findings that EPS may reduce surface tension, and hence function in a similar way as chemical dispersants (e.g., Schwehr et al., 2018; Xu et al., 2019). We like to point out that the artificial EPS and oil droplets investigated here are both carbon rich and nutrient depleted, and adding further nutrients may be effective in enhancing microbial degradation on oil following EPS-OMAs flocculation (Quigg et al., 2016). With its low cost and non-toxic characteristics, EPS may become a more efficient alternative way of dealing with the oil spills, and with none of the detrimental secondary environmental contamination of current chemical approaches to oil spills. It is also important to incorporate the effect of EPS in the understanding of the fate of spilt oil and spill management.

CONCLUSION

In this study, we utilized a high-resolution microscope and a LabSFLOC-2 system to investigate the structures and characteristics of EPS-OMA, and the unique effect of biological stickiness on the OMA formation. This study quantitatively reveals that the inclusion of EPS in the suspension matrix (not generally considered in previous OMA studies), leads to flake/solid OMAs formation and this has a dramatic effect on both the trapping and stabilization of oil droplets in OMAs. Both EPS-oil-kaolinite aggregates and EPS- oil-bentonite aggregates show a similar mixed flaky structure in lieu of droplets OMAs. However, the bentonite cases show larger sized EPS-OMAs (∼900 microns) than those of equivalent kaolinite cases (∼400 microns). The EPS-OMA density and settling velocity, show an increase in smaller sized microflocs and a corresponding reduction in larger sized flocs for all the pure mineral samples.

Overall, the addition of EPS reduces the variability of settling velocity as a function of floc size and clay mineral type. Since EPS is ubiquitous in natural marine environments, and it is one of the most important biologically cohesive materials in the aquatic system, it's role in adsorbing oil, attaching minerals, forming EPS-OMAs and influencing the fate of oil, all needs to be incorporated in future spill modeling approaches. To expand the study for oil spill mitigation, the effect of chemical dispersants would require further investigated. More scenarios representative of combinations of lower levels of cohesive sediment concentrations, less EPS, and lower turbulent energy, should all be also studied in order to improve oil spill modeling predictions within those natural aquatic zones.

DATA AVAILABILITY STATEMENT

The datasets presented in this study can be found in online repositories. The names of the repository/repositories and accession number(s) can be found below: https://data.gulfresearchinitiative.org (doi: 10.7266/n7-0nav-gs95).

AUTHOR CONTRIBUTIONS

T-JH, AM, and LY organized the research and experiments. JH, JP-G, and LY conducted the laboratory work. AM helped the LabSFLOC-2 data analysis. LY wrote up and revised the manuscript draft. T-JH and AM helped to comment and revise the manuscript. All authors contributed to the article and approved the submitted version.

FUNDING

This research was made possible by a grant from the Gulf of Mexico Research Initiative to support CSOMIO (Consortium for Simulation of Oil-Microbial Interactions in the Ocean) (Grant no. SA18–10), and in part by the National Science Foundation OCE-1924532. AM's contribution toward this research was also partly supported by the National Science Foundation grant OCE-1736668, and HR Wallingford company research FineScale project (Grant no. ACK3013_62). HR Wallingford. HR Wallingford was not involved in the study design, collection, analysis, interpretation of data, the writing of this article or the decision to submit it for publication. LY's contribution was also partly supported by Southern Marine Science and Engineering Guangdong Laboratory (Zhuhai) (No. 311020003).

REFERENCES

Atlas, R. M. (1995). Petroleum biodegradation and oil spill bioremediation. *Mar. Pollut. Bull.* 31, 178–182. doi: 10.1016/0025-326x(95)00113-2

Atlas, R. M., and Bartha, R. (1992). "Hydrocarbon biodegradation and oil spill bioremediation," in *Advances in Microbial Ecology*, ed. K. C. Marshall (Boston, MA: Springer), 287–338. doi: 10.1007/978-1-4684-7609-5_6

Atlas, R. M., and Hazen, T. C. (2011). Oil biodegradation and bioremediation: a tale of the two worst spills in us history. *Environ. Sci. Technol.* 45, 6709–6715. doi: 10.1021/es2013227

Barbier, E. B., Hacker, S. D., Kennedy, C., Koch, E. W., Stier, A. C., and Silliman, B. R. (2011). The value of estuarine and coastal ecosystem services. *Ecol. Monogr.* 81, 169–193.

Crone, T. J., and Tolstoy, M. (2010). Magnitude of the 2010 gulf of Mexico oil leak. *Science* 330, 634–634. doi: 10.1126/science.1195840

Cui, L., Harris C. K., and Tarpley, D. R. N. (2021). Formation of Oil – Particle-Aggregates (OPAs): Numerical Model Formulation and Calibration. *Frontiers in Marine Science*. In revision.

Daly, K. L., Passow, U., Chanton, J., and Hollander, D. (2016). Assessing the impacts of oil associated marine snow formation and sedimentation during and after the deep water horizon oil spill. *Anthropocene* 13, 18–33. doi: 10.1016/j.ancene.2016.01.006

Doshi, B., Sillanpää, M., and Kalliola, S. (2018). A review of bio-based materials for oil spill treatment. *Water Res.* 135, 262–277. doi: 10.1016/j.watres.2018.02.034

Engel, A. (2000). The role of transparent exopolymer particles (TEP) in the increase in apparent particle stickiness (α) during the decline of a diatom bloom. *J. Plankton Res.* 22, 485–497. doi: 10.1093/plankt/22.3.485

Fisher, C. R., Montagna, P. A., and Sutton, T. T. (2016). How did the Deepwater Horizon oil spill impact deep-sea ecosystems? *Oceanography* 29, 182–195. doi: 10.5670/oceanog.2016.82

Fu, J., Gong, Y., Zhao, X., O'reilly, S. E., and Zhao, D. (2014). Effects of oil and dispersant on formation of marine oil snow and transport of oil hydrocarbons. *Environ. Sci. Technol.* 48, 14392–14399. doi: 10.1021/es5042157

Hill, P. S., and Nowell, A. R. M. (1990). The potential role of large, fast-sinking particles in clearing nepheloid layers. *Philos. Trans. R. Soc. Lond. Ser. A Math. Phys. Sci.* 331, 103–117. doi: 10.1098/rsta.1990.0059

Hoang, A. T., Pham, V. V., and Nguyen, D. N. (2018). A report of oil spill recovery technologies. *Int. J. Appl. Eng. Res.* 13, 4915–4928.

Keyvani, A., and Strom, K. (2014). Influence of cycles of high and low turbulent shear on the growth rate and equilibrium size of mud flocs. *Mar. Geol.* 354, 1–14. doi: 10.1016/j.margeo.2014.04.010

Khelifa, A., Stoffyn-Egli, P., Hill, P. S., and Lee, K. (2002). Characteristics of oil droplets stabilized by mineral particles: effects of oil type and temperature. *Spill Sci. Technol. Bull.* 8, 19–30. doi: 10.1016/s1353-2561(02)00117-2

Kingston, P. F. (2002). Long-term environmental impact of oil spills. *Spill Sci. Technol. Bull.* 7, 53–61. doi: 10.1016/s1353-2561(02)00051-8

Kleindienst, S., Paul, J. H., and Joye, S. B. (2015). Using dispersants after oil spills: impacts on the composition and activity of microbial communities. *Nat. Rev. Microbiol.* 13, 388–396. doi: 10.1038/nrmicro3452

Kujawinski, E. B., Kido Soule, M. C., Valentine, D. L., Boysen, A. K., Longnecker, K., and Redmond, M. C. (2011). Fate of dispersants associated with the Deepwater Horizon oil spill. *Environ. Sci. Technol.* 45, 1298–1306.

Lubchenco, J., McNutt, M. K., Dreyfus, G., Murawski, S. A., Kennedy, D. M., Anastas, P. T., et al. (2012). Science in support of the Deepwater Horizon response. *Proc. Natl. Acad. Sci. U.S.A.* 109, 20212–20221.

Malarkey, J., Baas, J. H., Hope, J. A., Aspden, R. J., Parsons, D. R., Peakall, J., et al. (2015). The pervasive role of biological cohesion in bedform development. *Nat. Commun.* 6, 1–6.

Malpezzi, M. A., Sanford, L. P., and Crump, B. C. (2013). Abundance and distribution of transparent exopolymer particles in the estuarine turbidity maximum of Chesapeake Bay. *Mar. Ecol. Prog. Ser.* 486, 23–35. doi: 10.3354/meps10362

Manning, A., and Schoellhamer, D. (2013). Factors controlling floc settling velocity along a longitudinal estuarine transect. *Mar. Geol.* 345, 266–280. doi: 10.1016/j.margeo.2013.06.018

Manning, A. J., and Dyer, K. R. (2007). Mass settling flux of fine sediments in Northern European estuaries: measurements and predictions. *Mar. Geol.* 245, 107–122. doi: 10.1016/j.margeo.2007.07.005

Manning, A. J., Friend, P. L., Prowse, N., and Amos, C. L. (2007). Preliminary findings from a study of Medway Estuary (UK) natural mud floc properties using a laboratory mini-flume and the LabSFLOC system. *Continent. Shelf Res.* 27, 1080–1095. doi: 10.1016/j.csr.2006.04.011

Manning, A. J., Langston, W. J., and Jonas, P. J. C. (2010). A review of sediment dynamics in the Severn Estuary: influence of flocculation. *Mar. Pollut. Bull.* 61, 37–51. doi: 10.1016/j.marpolbul.2009.12.012

Manning, A. J., Whitehouse, R. J. S., and Uncles, R. J. (2017). "Suspended particulate matter: the measurements of flocs," in *ECSA Practical Handbooks on Survey and Analysis Methods: Estuarine and Coastal Hydrography and Sedimentology, Chapter 8*, eds R. J. Uncles and S. Mitchell (Cambridge: Cambridge University Press), 211–260. doi: 10.1017/9781139644426

McNutt, M. K., Camilli, R., Crone, T. J., Guthrie, G. D., Hsieh, P. A., Ryerson, T. B., et al. (2012). Review of flow rate estimates of the Deepwater Horizon oil spill. *Proc. Natl. Acad. Sci. U.S.A.* 109, 20260–20267.

Michel, J., Owens, E. H., Zengel, S., Graham, A., Nixon, Z., Allard, T., et al. (2013). Extent and degree of shoreline oiling: Deepwater Horizon oil spill, Gulf of Mexico, USA. *PLoS One* 8:e65087. doi: 10.1371/journal.pone.0065087

Muschenheim, D. K., and Lee, K. (2002). Removal of oil from the sea surface through particulate interactions: review and prospectus. *Spill Sci. Technol. Bull.* 8, 9–18. doi: 10.1016/s1353-2561(02)00129-9

Parsons, D. R., Schindler, R. J., Hope, J. A., Malarkey, J., Baas, J. H., Peakall, J., et al. (2016). The role of biophysical cohesion on subaqueous bed form size. *Geophys. Res. Lett.* 43, 1566–1573. doi: 10.1002/2016gl067667

Passow, U. (2012). The abiotic formation of TEP under different ocean acidification scenarios. *Mar. Chem.* 128, 72–80. doi: 10.1016/j.marchem.2011.10.004

Passow, U., and Alldredge, A. L. (1995). A dye—binding assay for the spectrophotometric measurement of transparent exopolymer particles (TEP). *Limnol. Oceanogr.* 40, 1326–1335. doi: 10.4319/lo.1995.40.7.1326

Passow, U., Sweet, J., Francis, S., Xu, C., Dissanayake, A. L., Lin, Y.-Y., et al. (2019). Incorporation of oil into diatom aggregates. *Mar. Ecol. Prog. Ser.* 612, 65–86. doi: 10.3354/meps12881

Passow, U., Sweet, J., and Quigg, A. (2017). How the dispersant Corexit impacts the formation of sinking marine oil snow. *Mar. Pollut. Bull.* 125, 139–145. doi: 10.1016/j.marpolbul.2017.08.015

Passow, U., and Ziervogel, K. (2016). Marine snow sedimented oil released during the Deepwater Horizon spill. *Oceanography* 29, 118–125. doi: 10.5670/oceanog.2016.76

Passow, U., Ziervogel, K., Asper, V., and Diercks, A. (2012). Marine snow formation in the aftermath of the Deepwater Horizon oil spill in the Gulf of Mexico. *Environ. Res. Lett.* 7:035301. doi: 10.1088/1748-9326/7/3/035301

Peterson, C. H., Rice, S. D., Short, J. W., Esler, D., Bodkin, J. L., Ballachey, B. E., et al. (2003). Long-term ecosystem response to the exxon valdez oil spill. *Science* 302, 2082–2086. doi: 10.1126/science.1084282

Quigg, A., Passow, U., Chin, W. C., Xu, C., Doyle, S., Bretherton, L., et al. (2016). The role of microbial exopolymers in determining the fate of oil and chemical dispersants in the ocean. *Limnol. Oceanogr. Lett.* 1, 3–26. doi: 10.1002/lol2.10030

Radoviæ, J. R., Domínguez, C., Laffont, K., Díez, S., Readman, J. W., Albaigés, J., et al. (2012). Compositional properties characterizing commonly transported oils and controlling their fate in the marine environment. *J. Environ. Monit.* 14, 3220–3229. doi: 10.1039/c2em30385j

Romero, I. C., Toro-Farmer, G., Diercks, A.-R., Schwing, P., Muller-Karger, F., Murawski, S., et al. (2017). Large-scale deposition of weathered oil in the gulf of Mexico following a deep-water oil spill. *Environ. Pollut.* 228, 179–189. doi: 10.1016/j.envpol.2017.05.019

Schwehr, K. A., Xu, C., Chiu, M.-H., Zhang, S., Sun, L., Lin, P., et al. (2018). Protein/polysaccharide ratio in exopolymeric substances controlling the surface tension of seawater in the presence or absence of surrogate Macondo Oil with and without Corexit. *Mar. Chem.* 206, 84–92. doi: 10.1016/j.marchem.2018.09.003

Stoffyn-Egli, P., and Lee, K. (2002). Formation and characterization of oil mineral aggregates. *Spill Sci. Technol. Bull.* 8, 31–44. doi: 10.1016/s1353-2561(02)00128-7

Teal, J. M., and Howarth, R. W. (1984). Oil spill studies: a review of ecological effects. *Environ. Manag.* 8, 27–43. doi: 10.1007/bf01867871

Tolhurst, T. J., Gust, G., and Paterson, D. M. (2002). The influence of an extracellular polymeric substance (EPS) on cohesive sediment stability. *Proc. Mar. Sci.* 5, 409–425. doi: 10.1016/s1568-2692(02)80030-4

Xu, C., Chin, W. C., Lin, P., Chen, H. M., Lin, P., Chiu, M. C., et al. (2019). Marine Gels, Extracellular Polymeric Substances (EPS) and Transparent Exopolymeric Particles (TEP) in natural seawater and seawater contaminated with a water accommodated fraction of Macondo oil surrogate. *Mar. Chem.* 215, 1010–1016.

Ye, L., Manning, A. J., and Hsu, T. J. (2020). Oil-mineral flocculation and settling velocity in saline water. *Water Res.* 173, 115569. doi: 10.1016/j.watres.2020.115569

Ye, L., Manning, A. J., Hsu, T.-J., Morey, S., Chassignet, E. P., and Ippolito, T. A. (2018). Novel application of laboratory instrumentation characterizes mass settling dynamics of oil-mineral aggregates (OMAs) and oil-mineral-microbial interactions. *Mar. Technol. Soc. J.* 52, 87–90. doi: 10.4031/MTSJ.52.6.14

Zhao, L., Torlapati, J., Boufadel, M. C., King, T., Robinson, B., and Lee, K. (2014). V-drop: a comprehensive model for droplet formation of oils and gases in liquids incorporation of the interfacial tension and droplet viscosity. *Chem. Eng. J.* 253, 93–106. doi: 10.1016/j.cej.2014.04.082

Conflict of Interest: AM was employed by HR Wallingford Ltd., United Kingdom.

The remaining authors declare that the research was conducted in the absence of any commercial or financial relationships that could be construed as a potential conflict of interest.

frontiers
in Marine Science

TECHNOLOGY AND CODE
published: 10 March 2021
doi: 10.3389/fmars.2021.629299

Development of the CSOMIO Coupled Ocean-Oil-Sediment-Biology Model

Dmitry S. Dukhovskoy[1]*, Steven L. Morey[2], Eric P. Chassignet[1], Xu Chen[1], Victoria J. Coles[3], Linlin Cui[4], Courtney K. Harris[4], Robert Hetland[5], Tian-Jian Hsu[6], Andrew J. Manning[6,7,8], Michael Stukel[9], Kristen Thyng[5] and Jiaze Wang[3]

[1] Center for Ocean-Atmospheric Prediction Studies, Florida State University, Tallahassee, FL, United States, [2] School of the Environment, Florida A&M University, Tallahassee, FL, United States, [3] Horn Point Laboratory, University of Maryland Center for Environmental Science, Cambridge, MD, United States, [4] Department of Physical Sciences, Virginia Institute of Marine Science, William and Mary, Gloucester Point, VA, United States, [5] Department of Oceanography, Texas A&M University, College Station, TX, United States, [6] Center for Applied Coastal Research, University of Delaware, Civil and Environmental Engineering, Newark, DE, United States, [7] HR Wallingford Ltd., Coasts and Oceans Group, Wallingford, United Kingdom, [8] Energy and Environment Institute, University of Hull, Hull, United Kingdom, [9] Department of Earth, Ocean, and Atmospheric Science, Florida State University, Tallahassee, FL, United States

OPEN ACCESS

Edited by:
Patrick Reis-Santos,
University of Adelaide, Australia

Reviewed by:
Jesus Dubert,
University of Aveiro, Portugal
George Zodiatis,
University of Cyprus, Cyprus

***Correspondence:**
Dmitry S. Dukhovskoy
ddukhovskoy@fsu.edu

Specialty section:
This article was submitted to Marine Pollution, a section of the journal Frontiers in Marine Science

Received: *14 November 2020*
Accepted: *15 February 2021*
Published: *10 March 2021*

Citation:
Dukhovskoy DS, Morey SL, Chassignet EP, Chen X, Coles VJ, Cui L, Harris CK, Hetland R, Hsu T-J, Manning AJ, Stukel M, Thyng K and Wang J (2021) Development of the CSOMIO Coupled Ocean-Oil-Sediment- Biology Model. Front. Mar. Sci. 8:629299. doi: 10.3389/fmars.2021.629299

The fate and dispersal of oil in the ocean is dependent upon ocean dynamics, as well as transformations resulting from the interaction with the microbial community and suspended particles. These interaction processes are parameterized in many models limiting their ability to accurately simulate the fate and dispersal of oil for subsurface oil spill events. This paper presents a coupled ocean-oil-biology-sediment modeling system developed by the Consortium for Simulation of Oil-Microbial Interactions in the Ocean (CSOMIO) project. A key objective of the CSOMIO project was to develop and evaluate a modeling framework for simulating oil in the marine environment, including its interaction with microbial food webs and sediments. The modeling system developed is based on the Coupled Ocean-Atmosphere-Wave-Sediment Transport model (COAWST). Central to CSOMIO's coupled modeling system is an oil plume model coupled to the hydrodynamic model (Regional Ocean Modeling System, ROMS). The oil plume model is based on a Lagrangian approach that describes the oil plume dynamics including advection and diffusion of individual Lagrangian elements, each representing a cluster of oil droplets. The chemical composition of oil is described in terms of three classes of compounds: saturates, aromatics, and heavy oil (resins and asphaltenes). The oil plume model simulates the rise of oil droplets based on ambient ocean flow and density fields, as well as the density and size of the oil droplets. The oil model also includes surface evaporation and surface wind drift. A novel component of the CSOMIO model is two-way Lagrangian-Eulerian mapping of the oil characteristics. This mapping is necessary for implementing interactions between the ocean-oil module and the Eulerian sediment and biogeochemical modules. The sediment module is a modification of the Community Sediment Transport Modeling System. The module simulates formation of oil-particle aggregates in the water column. The biogeochemical module simulates microbial communities adapted to the local environment and to elevated concentrations of oil components in the water column. The sediment and biogeochemical modules both reduce water column oil components. This paper provides an overview of the CSOMIO coupled modeling system components and demonstrates the capabilities of the modeling system in the test experiments.

Keywords: oil plume modeling, oil spill, oil biodegradation, Deepwater Horizon, Gulf of Mexico modeling, oil-particle aggregates, oil weathering process, oil transport and fate

INTRODUCTION

The Deepwater Horizon (DWH) blowout at the Mississippi Canyon (MC252) Macondo well in the northern Gulf of Mexico released 4.9 million barrels (780,000 m^3) of crude oil (Lubchenco et al., 2010). The oil spill occurred at the seabed about 1,500 m below the surface making this one of the deepest spill events in the history of the oil industry. Though the surface oil slick was expansive with a footprint of over 11,800 km^2 (Özgökmen et al., 2016), a substantial amount of oil remained in the deep ocean layers (Lubchenco et al., 2012). Observations during the DWH blowout identified a "subsurface plume"—a 100–150 m thick layer of hydrocarbons at 1,300–1,100 m depth trapped between the cold abyssal water and the permanent thermocline traveling southwest (Melvin et al., 2016). The pathways and fate of this subsurface oil from the DWH remain largely unknown because observations, tracking, and simulation of the oil in the subsurface layers are challenging (Camilli et al., 2010; French-McCay et al., 2016). At the same time, a better understanding of the processes governing the eventual fate of oil released in the deep ocean and accurate prediction of oil movement, degradation, interaction with suspended material, as well as its impact on the marine ecosystem in the deep ocean is essential for risk assessment and mitigation of potential future spills.

The DWH blowout revealed a lack of modeling capacity to simulate and predict the pathways of fate of subsurface oil (Bracco et al., 2020). Most available models at that time simulated surface oil drift and weathering (Reed et al., 1999; Lehr et al., 2002) and oil plume dynamics in the near-field (several meters to about 100 m) above the wellhead orifice, e.g., Chen and Yapa, 2003). The DWH spill event stimulated unprecedented efforts to advance oil transport and fate modeling resulting in notable improvements in the simulations of the near-field plume dynamics (Yapa et al., 2012; Spaulding et al., 2017), oil transport in the ocean (so-called far-field models, e.g., Paris et al., 2012; Lindo-Atichati et al., 2016; Zodiatis et al., 2017), and coupling of near-field and far-field dynamics (Vaz et al., 2019). However, in many oil spill models, processes for removing oil from the system, such as sedimentation, biodegradation, and atmospheric weathering, are modeled with simple parameterizations. Such models are limited in their ability to fully simulate pathways for hydrocarbons moving through seawater into sediments and the marine ecosystem, because they do not include important feedback mechanisms between oil and biological and geochemical interaction processes.

The Consortium for Simulation of Oil-Microbial Interactions in the Ocean (CSOMIO), funded by the Gulf of Mexico Research Initiative, has developed a modeling system (**Figure 1**) that dynamically couples components for simulating ocean hydrodynamics, oil transport, dispersion and weathering, oil-particle aggregate (OPA) formation and settling, and the lower trophic level marine ecosystem. This CSOMIO Coupled Model is an adaptation and extension of the Coupled Ocean-Atmosphere-Wave-Sediment Transport (COAWST, Warner et al., 2010) modeling system. A biogeochemical modeling component incorporating microbial activities is implemented in the system and adapted for the presence of hydrocarbons. The sediment transport component of COAWST (the Community Sediment Transport Modeling System, CSTMS) is modified to include computationally efficient flocculation parameterizations for OPAs developed from laboratory experiments. The hydrodynamic modeling component of COAWST (the Regional Ocean Modeling System, ROMS) is modified to simulate three-dimensional oil transport and compositional changes (weathering). A two-way Lagrangian-Eulerian mapping technique is developed to link together modeling components allowing for interaction between the sub-models and tracking of hydrocarbons from a source blowout to deposition in sediment, microbial degradation, and evaporation while being transported through the ocean. The CSOMIO modeling system can be integrated in online and offline configurations.

This paper presents the first three-dimensional model that couples hydrodynamics, oil weather and transport, microbial feedbacks, and sedimentation for a realistic application of an oil spill scenario. In the following sections, description of the CSOMIO modeling components and the two-way Lagrangian-Eulerian mapping is provided. The paper also presents results of test experiments with the new modeling system. Test simulations are conducted with the model configured for the northern Gulf of Mexico region near the location of the DWH oil spill. Details of the model parameters and forcing fields are listed in **Table 1**. Test simulations have been performed with online and

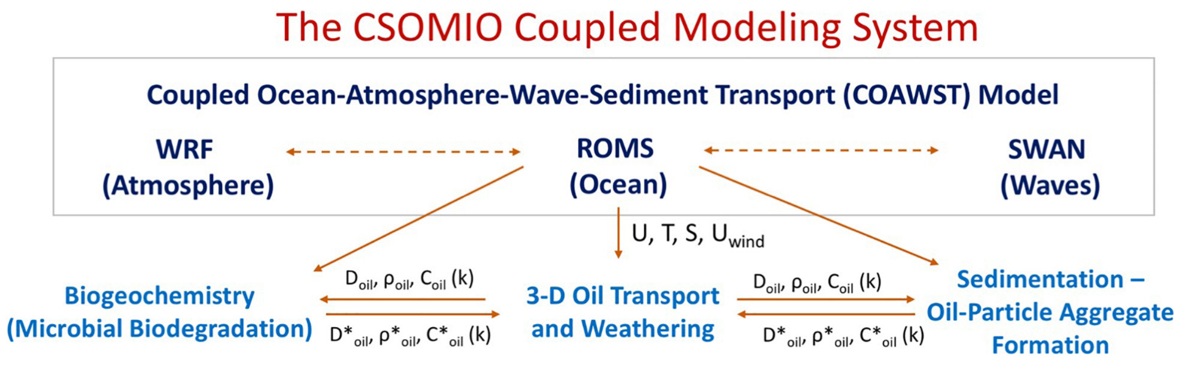

FIGURE 1 | Chart diagram presenting the CSOMIO modeling system and interaction among the components.

TABLE 1 | Model parameters for test simulations.

Parameter		Value/name	Units/notes
Domain, min/max longitude, latitude		94W/84W, 25N/31N	Degrees
Horizontal grid spacing (Δη, Δξ)		0.04, 0.04	Degrees
Vertical grid		50	Terrain-following layers with enhanced resolutions in the near-surface and near-bottom layers
River runoff		32 river sources, daily average discharges	Calculated from US Geological Survey data as described in Hiester et al. (2016)
Atmospheric fields		Climate Forecast Reanalysis System	CFSR (Saha et al., 2010)
Lateral boundary conditions		0.08° Global HYCOM reanalysis	https://www.hycom.org/dataserver/gofs-3pt1/reanalysis
Oil flow rate		3,000	m^3 day^{-1}
$\overline{D}_{oil}$		0.35×10^{-3}	m
C_W		0.01	
ρ_{SW}, water density near the DWH at several depth levels in ROMS	−0.5 m	1024.83	kg m^{-3}
	−8.5 m	1024.84	kg m^{-3}
	−25 m	1024.84	kg m^{-3}
	−50 m	1025.41	kg m^{-3}
	−105 m	1026.33	kg m^{-3}
	−145 m	1026.67	kg m^{-3}
	−190 m	1026.89	kg m^{-3}
	−275 m	1027.04	kg m^{-3}
	−500 m	1027.31	kg m^{-3}
	−1,000 m	1027.63	kg m^{-3}
	−1,300 m	1027.70	kg m^{-3}
ρ_S		800	kg m^{-3}
ρ_A		850	kg m^{-3}
ρ_{RA}		1,030	kg m^{-3}

offline configurations of the CSOMIO model. Specific details of the model configuration for particular tests are provided in the text. A list of variables used in the test is given in **Table 2**.

CSOMIO COUPLED OCEAN-OIL-SEDIMENT-BIOLOGY MODEL

Oil Transport and Weather Model (OTWM)

The Oil Transport and Weather Model (OTWM) is a particle trajectory simulation system coupled to the hydrodynamic model ROMS. The OTWM is a far-field model simulating three-dimensional movement of oil. In general, oil released from a wellhead contains high concentration of gasses and leaves the wellhead at high speed. Due to different temporal and spatial scales, a special class of models (so-called near-field models) is employed to simulate processes of a fast rising of mixture of oil, gas, and seawater and formation of oil droplets occurring within several to ∼100 m (trap height) above the wellhead (Socolofsky et al., 2011, 2016; Paris et al., 2012). After gas-saturated components leave the plume, the dynamics of the plume, represented as a mixture of oil droplets, are then controlled by the buoyant velocity and ocean currents and can be simulated by far-field models (Yapa and Zheng, 1997; Lardner and Zodiatis, 2017; Bracco et al., 2020; Perlin et al., 2020).

The OTWM simulates movement of oil using a Lagrangian approach that describes the oil dynamics through advection and diffusion of individual elements (hereinafter referred to as "floats" following terminology used in ROMS), each representing a cluster of oil droplets (section "Representation of Oil in the OTWM"). The code employs a Lagrangian float module in ROMS with added vertical velocity of oil particles in the water column calculated from oil characteristics (section "Buoyant Velocity of Oil Droplets") and wind-driven surface drift (section "Wind Drift of Surfaced Oil"). The chemical composition of oil is described in terms of three classes of compounds: saturates, aromatics, and heavy oil (resins and asphaltenes). For each Lagrangian element, the OTWM simulates time-evolving changes of the following oil characteristics: location (depth and horizontal coordinates), density (changing chemical compounds), and mean size of oil droplets. The OTWM also incorporates the impact of surface wind drift and weathering (evaporation) effects.

TABLE 2 | List of variables, their notations and units.

Variable	Notation	Units
Mean oil droplet size of a cluster of particles represented by a Lagrangian float	D_{oil}	m, μm
Mean oil droplet density of a cluster of particles represented by a Lagrangian float	ρ_{oil}	kg m^{-3}
Mean oil droplet volume of a cluster of particles represented by a Lagrangian float	v_{oil}	m^3
Mean oil droplet size over all oil droplets (parameter of the Gamma distribution) (input)	$\overline{D}_{oil}$	M
Density of saturates (input)	ρ_S	kg m^{-3}
Density of aromatics (input)	ρ_A	kg m^{-3}
Density of resins and asphaltenes (input)	ρ_{RA}	kg m^{-3}
Density of the i^{th} oil compound	$\tilde{\rho}_{oil}(i)$	kg m^{-3}
Wind drag coefficient (input)	C_w	
Oil viscosity of the i^{th} compound	$\tilde{\mu}_{oil}(i)$	cP = 10^{-3} Pa s
Number of oil particles in a Lagrangian float	N_{poil}	
Weight fraction of the i^{th} oil compound	$\tilde{\omega}_{oil}(i)$	
Number of oil compounds in the model	N_{comp}	
Total number of Lagrangian floats	N_{flt}	
Number of Lagrangian floats in a grid cell (**j**)	$n^*_{flt}(\mathbf{j})$	
Oil droplet mass	m_{oil}	kg
Mass of the i^{th} oil compound in Lagrangian float	$\tilde{m}_{oil}$	kg
Mass of the i^{th} compound in a grid cell	$\tilde{M}^*_{oil}$	kg
Mas of the oil in Lagrangian float	M_{oil}	
Mass of the oil in a grid cell	M^*_{oil}	kg
Oil temperature	t_K	°K
Oil temperature	t_{oil}	°C
Oil surface time	T	min
Volume of the oil in Lagrangian float	ϑ_{oil}	m^3
Concentration of the i^{th} oil compound in a grid cell	$\tilde{C}^*_{oil}(i)$	kg m^{-3}
Oil concentration in a grid cell	C^*_{oil}	kg m^{-3}

Representation of Oil in the OTWM

The volume of oil released during an oil spill event is discretized by Lagrangian floats. The number of floats (N_{flt}), their release locations, duration, and discharge frequency are specified by the user. Each float represents a finite number (a cluster) of individual oil particles characterized by mean oil droplet size (D_{oil}) and density (ρ_{oil}).

Oil Droplet Size

During subsurface oil spills, oil forms droplets of varying sizes. Oil droplet size is an important characteristic of oil that controls the buoyancy and ascent rate of the droplet (section "Buoyant Velocity of Oil Droplets"). Oil droplets have a wide range of sizes observed in the marine environment and laboratory experiments (e.g., Li et al., 2008). The distribution of oil droplet sizes during the DWH spill event is uncertain due to several oil releases through kink holes of different sizes during the pre-riser cut vs. a single release during the post-riser cut, spill exit velocity, and unknown effects of dispersant applied directly during the spill. The study by Spaulding et al. (2017) suggests that before the pre-riser cut time (June 3, 2010) small droplets formed due to mechanical dispersion driven by high exit velocities at the kink holes, and dispersant application had a smaller effect. During the post-cut period, oil dispersion was mainly caused by the application of dispersants, which were more effectively applied. Spaulding et al. (2017) indicates that treated oil would have droplet sizes ranging from 20 to 500 μm, whereas untreated oil would have oil droplet sizes from 1,000 to 10,000 μm. Analysis of samples collected in the water column in the vicinity of the wellhead in June 2010 from the R/V Jack Fritz 3 cruises (Davis and Loomis, 2014) showed that oil droplets that remained in the water column by the time the sampling occurred were $\leq$ 300 μm (Spaulding et al., 2017).

In the OTWM, the oil droplet sizes (D_{oil}) are randomly generated for individual Lagrangian floats using a Gamma distribution (Vilcáez et al., 2013)

$$f\left(D_{oil};\ \alpha, \lambda\right) = \frac{\lambda^{\alpha}\left(D_{oil}\right)^{\alpha-1}e^{-\lambda D_{oil}}}{\Gamma(\alpha)}, \tag{1}$$

where α is a free parameter that controls the spread of the Gamma probability density function. In the experiments described in this paper, $\alpha = 4.94$ corresponding to the coefficient of variation 0.4 in Vilcáez et al. (2013); λ is another parameter of the Gamma distribution determined as $\lambda = \alpha/\overline{D}_{oil}$, where $\overline{D}_{oil}$ is specified by the user in the input file. In the test experiments presented in this paper, $\overline{D}_{oil}$ = 350 μm unless mentioned otherwise. The specified parameters are used to randomly generate $D_{oil}(i)$ for the Lagrangian floats $i = 1, \ldots, N_{flt}$ (**Figure 2A**). In this particular set of $D_{oil}(i)$, the maximum oil droplet size is 1,429 μm and the minimum size is 9 μm. Note that the model assumes a minimum droplet size of 0.19 μm, which is a size at which droplets are generally dissolved (North et al., 2015).

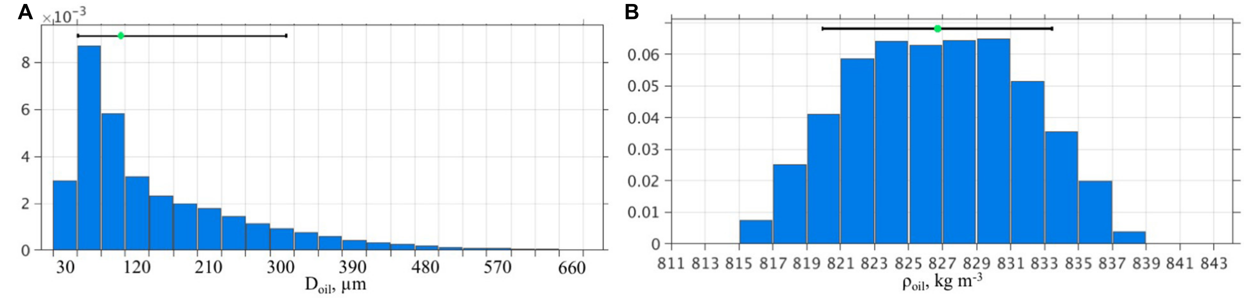

FIGURE 2 | Histograms showing the distributions of initial oil particle sizes **(A)** and densities **(B)** for the Lagrangian floats in CSOMIO experiments. The black horizontal lines show the interdecile range and the green bullet is the median.

Oil Droplet Density

Crude oil is a mixture of thousands of hydrocarbons ranging from smaller, volatile compounds to large, non-volatile compounds (Speight, 2007). Properties of oil, such as viscosity, density, specific gravity, solubility, and flash point, are determined by the oil chemical structure (Fingas, 2015a). A common classification of oil chemical structure is given in terms of four compounds: saturates, aromatics, resins, and asphaltenes (SARA) (e.g., Klein et al., 2006).

The OTWM is developed for a multi-compound representation of oil chemical structure. The number of compounds and their characteristics (densities, weight fraction) are specified by the user. In the presented experiments, the OTWM was set for three oil compounds representing saturated, aromatic, and heavy polar compounds, including resins and asphaltenes (SAR+A). Compositional information for Macondo oil was deduced from water column samples collected at the Macondo well in June 2010 (Reddy et al., 2012, 74% saturated, 16% aromatics, and 10% polar hydrocarbons). These values are used as the mean fractions of the compounds in generating densities of the oil particles densities (ρ_{oil}), as follows.

The compositional structure of the oil is prescribed to each Lagrangian float by randomly assigning the weight fractions of aromatics ($\widetilde{\omega}_A$) and heavy polar hydrocarbons ($\widetilde{\omega}_{RA}$). The fractions are derived from uniform distributions as $\widetilde{\omega}_A \sim U(0.085,\ 0.235)$ and $\widetilde{\omega}_{RA} \sim U(0.06,\ 0.14)$ yielding the fraction of saturates as $\widetilde{\omega}_S = 1 - (\widetilde{\omega}_A + \widetilde{\omega}_{RA})$. Note that by doing so, the mean fraction of each compound matches the estimates of the compositional structure of Macondo oil reported in Reddy et al. (2012).

The oil droplet density is estimated using the mixing rule for a regular solution (Yarranton et al., 2015) as

$$\frac{1}{\rho_{oil}} = \frac{\widetilde{\omega}_S}{\widetilde{\rho}_S} + \frac{\widetilde{\omega}_A}{\widetilde{\rho}_A} + \frac{\widetilde{\omega}_{RA}}{\widetilde{\rho}_{RA}} = \sum_{i=1}^{N_{comp}} \frac{\widetilde{\omega}_i}{\widetilde{\rho}_i}, \tag{2}$$

where i is float index (i = 1, ..., N_{flt}), $\widetilde{\rho}_S$, $\widetilde{\rho}_A$, and $\widetilde{\rho}_{RA}$ are densities of the individual compounds specified in the input file, N_{comp} is the number of oil compounds in the model (3 in this model configuration). In the numerical experiments presented here, the following values were used ρ_S = 800 kg m^{-3}, ρ_A = 850 kg m^{-3}, and ρ_{RA} = 1,030 kg m^{-3}. The densities are normally distributed across the floats (**Figure 2B**), with the mean value (826.2 kg m^{-3}) close to the mean oil droplet density of 820 kg m^{-3} reported by Reddy et al. (2012). Note that the compound densities do not change during the simulation. Instead, weight fractions are changed during the weathering, biodegradation and sedimentation processes resulting in changing (increasing) densities of the oil particles (sections "Surface Evaporation of Oil," Sediment Model," and "Biogeochemical Model").

Buoyant Velocity of Oil Droplets

In the subsurface layers, vertical velocity of oil (w_{oil}) in the OTWM is a combination of hydrodynamic vertical velocity, random component (approximating diffusion) and buoyant velocity (w_b) driven by the buoyancy force in the water column. Two approaches (the two-equation algorithm and integrated algorithm) for calculating the buoyant velocity of oil droplets are implemented in the OTWM based on Zhang and Yapa (2000). The choice of the algorithm is specified by the user.

The Two-Equation Algorithm

The two-equation algorithm for the oil droplet buoyant velocity is based on the Stokes law that is valid for a small Reynolds number

$$Re = \frac{\rho_{sw} D_{oil} w_b}{\mu_{sw}}, \tag{3}$$

where ρ_{sw} is ambient sea water density (**Table 1**) and μ_{sw} is dynamic viscosity of ambient sea water. Two equations for oil droplet buoyant velocities are used for different Re. The choice of the equations is based on a critical diameter d_c

$$d_c = \frac{9.52\mu_{sw}^{2/3}}{\left(g\rho_{sw}\triangle\rho\right)^{1/3}}, \tag{4}$$

where g is the gravitational acceleration and $\triangle\rho = \rho_{sw} - \rho_{oil}$.

The buoyant velocity is calculated as

$$w_b = \begin{cases} \frac{gD_o^2 il\Delta\rho}{18\mu_s w}, & D_{oil}<d_c \\ \left(\frac{8gD_{oil}\Delta\rho}{3\rho_{sw}}\right)^{1/2}, & D_{oil}\geq d_c \end{cases} \tag{5}$$

The Integrated Algorithm

For the integrated approach, the buoyant velocity is a function of the particle shape that is related to the particle size (equivalent particle diameter Doil) grouped in to three categories.

(1) For a spherical shape ($D_{oil} \leq 1$ mm), the buoyant velocity is calculated as

$$w_b = \frac{Re\mu_{sw}}{\rho_{sw} D_{oil}} \tag{6}$$

(2) Ellipsoid shape ($1 \text{ mm} < D_{oil} \leq 15$ mm).

The criteria for this regime are $M < 10 - 3$ and $E0 < 40$. The coefficients M and E0 are defined as

$$M = \frac{g\mu_s^4 w \Delta\rho}{\rho_{sw}^2 \sigma_{ow}^3} \tag{7}$$

$$E_0 = \frac{g \triangle \rho D_{oil}^2}{\sigma_{ow}} \tag{8}$$

where σ_{ow} is oil - water interfacial tension determined as a function of water temperature (t°C) by Peters and Arabali (2013)

$$\sigma_{ow} = (0.1222t + 32.82) \cdot 10^{-3} \tag{9}$$

The buoyant velocity is determined as

$$w_b = \frac{\mu_{sw}}{\rho_{sw} D_{oil}} M^{-0.149} (J - 0.857) \tag{10}$$

where

$$J = \begin{cases} 0.94H^{0.757}, & 2 < H \leq 59.3 \\ 3.42H^{0.441}, & H > 59.3 \end{cases} \tag{11}$$

$$H = \frac{4}{3} E_0 M^{-0.149} \left(\frac{\mu_w}{\mu_{sw}}\right)^{-0.14}, \tag{12}$$

where μ_{sw} is dynamic viscosity of sea water $[\text{kg}\cdot(\text{m}\cdot\text{s})^{-1}]$ determined by Sharqay et al. (2010)

$$\mu_{sw} = \mu_w (1 + A \cdot S + B \cdot S^2) \tag{13}$$

$$A = 1.541 + 1.998 \cdot 10^{-2} t - 9.52 \cdot 10^{-5} t^2 \tag{14}$$

$$B = 7.974 - 7.561 \cdot 10^{-2} t + 4.724 \cdot 10^{-4} t^2 \tag{15}$$

where S is salinity ($\text{g}\cdot\text{kg}^{-1}$), and μ_w is dynamic viscosity of pure water given as

$$\mu_w = 4.2844 \cdot 10^{-5} + \left[0.157(t + 64.993)^2 - 91.296\right]^{-1} \tag{16}$$

(3) For a spherical cap (large size droplets, $E_0 > 40$), the buoyant velocity is

$$w_b = 0.711 \sqrt{\frac{g D_{oil} \triangle \rho}{\rho_{sw}}} \tag{17}$$

Note that for the presented OTWM simulations the spherical cap regime is not used due to smaller oil droplet sizes (**Figure 2A**).

Sensitivity Experiments With Buoyant Velocity Algorithms

The buoyant velocity of an oil particle is important because it determines the ascent rate of the particles and thus, the surface time and the duration of time during which the particle is subject to subsurface biodegradation processes and interaction with suspended sediments.

Sensitivity simulations employing the two algorithms for the oil droplet buoyant velocity are performed in order to test the sensitivity of the simulated oil vertical velocity to the choice of the algorithm (**Figure 3**). The simulations are conducted with OTWM coupled to ROMS and neither biogeochemical nor sediment-OPA modules being activated. Except for the buoyant velocity algorithms, the experiments are identical. To account for near-field dynamics of the turbulent plume and multiple release locations during the pre-cutting of the broken riser, Lagrangian floats are released at several locations within a few hundred meters around the wellhead (88.36°W and 27.738°N) at ∼1,400 m. The simulations last 7 days with Lagrangian floats released every 1.29 min at each location. A total of 40,000 floats are released during this simulation.

The vertical velocities of oil (w_{oil}) from the two simulations are similar for the oil droplets smaller than ∼300 μm but are different for the larger oil particles (**Figure 3A**). The two-equation algorithm produces notably faster ascent velocities than the integrated algorithm for the larger oil droplets with $D_{oil} > 300$ μm. In the presented simulations, the median D_{oil} is ∼100 μm and the 90th percentile is ∼310 μm (**Figure 2A**). Thus, simulated vertical speed is similar in the experiments employing different algorithms for ∼90% of the oil particles (**Figures 3C,D**).

The difference in w_{oil} for oil particles affects the time required for Lagrangian floats to reach the surface (**Figure 3B**). For the range of oil particles' sizes considered in the test simulation, the difference in an oil surfacing time from the two simulations is small (the medians are 125 and 121 h for the integrated and two-equation algorithm, respectively). The simulation with the two-equation algorithm predicts the fastest oil surfacing time ∼6–12 h earlier than in the experiment using the integrated formula. In the two-equation simulation, the first group of oil floats reaches the surface in the first 6–12 h, whereas this is 12–24 h in the simulation with the integrated algorithm. Nevertheless, qualitatively the difference between the experiments is barely noticeable in the three-dimensional distribution of the oil particles (**Figures 3E,F**).

The surfacing time of the first oil during the DWH is uncertain. Available reports on the timeline of the oil spill indicate that no leaking oil was observed on the surface until the morning of April 23, 2010, i.e., roughly 24 h after the oil rig sank (U.S. Senate Committee on Environment and Public Works, 2010). Hence, the surfacing time of oil estimated from both test simulations look reasonable.

Wind Drift of Surfaced Oil

As oil surfaces, it becomes subject to direct atmospheric forcing. This is expressed as wind drift, or the advective velocity of oil particles due to wind. This correction of the surface oil velocity is commonly used in surface oil drift models to

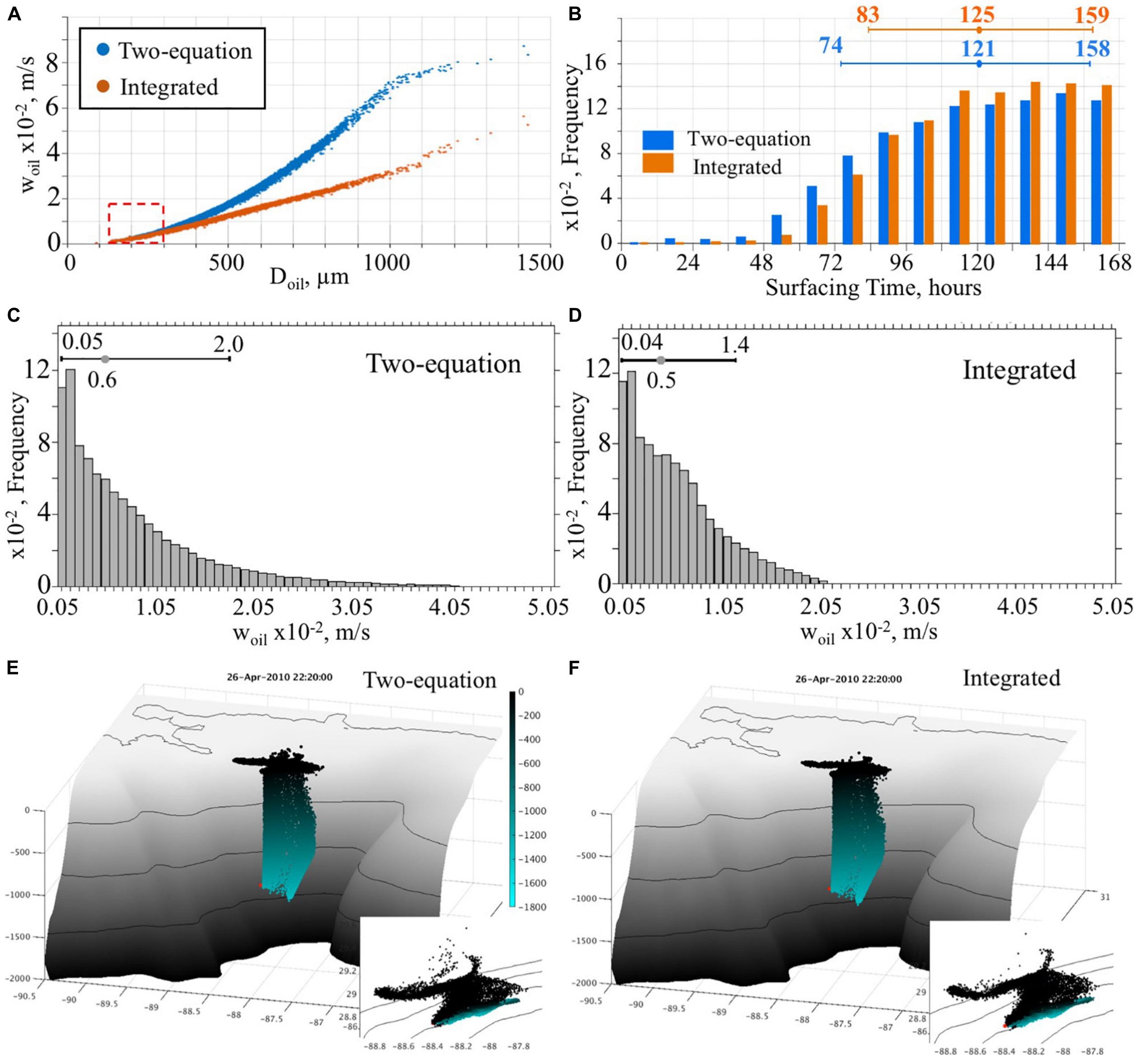

FIGURE 3 | (A) oil droplet vertical velocity vs. oil droplet size from OTWM simulations using two-equation and integrated algorithms of buoyant velocity. The red dashed box indicates the interdecile region for D_{oil} from **Figure 2A**. **(B)** The surfacing time (hours after release) of oil droplets estimated from the 7 day test simulations with two algorithms for buoyant velocity. At the top, the median, 10th and 90th percentiles are presented. **(C,D)** Histograms showing w_{oil} distribution in the OTWM simulations using two-equation (left) and integrated (right) algorithms of buoyant velocity. **(E,F)** 3-dimensional distribution of the Lagrangian floats in the water column in the OTWM simulations using different formulations of buoyant velocities after 7 days of the simulation. The insets show the float positions projected onto the sea surface plane. Colors designate particles' depth in the water column.

compensate for coarse vertical representation of surface velocity in hydrodynamic models (Abascal et al., 2009). Following MacDonald et al. (2016), the oil particles trajectories at the surface are computed as a superposition of advective velocity and turbulent diffusion

$$\frac{d\mathbf{x}}{dt} = \mathbf{u}_a(\mathbf{x}, t) + \mathbf{u}_d(\mathbf{x}, t), \tag{18}$$

where $\mathbf{u}_a$ is the advective (oil drift) velocity and $\mathbf{u}_d$ is the diffusive velocity. The advective velocity is calculated as a linear combination of the surface ocean currents, 10 m wind vector and waves

$$\mathbf{u}_a = \mathbf{u}_c + C_w |\mathbf{u}_{10}| \Theta + C_s \mathbf{u}_s, \tag{19}$$

where $\mathbf{u}_c$ is the ocean surface current velocity of seawater estimated from the topmost grid layer of an ocean model, C_w is the wind drag coefficient, $\mathbf{u}_{10}$ is the wind velocity 10 m above the sea surface, Θ is a unit vector directed at an angle θ relative to the wind (wind deflection angle), Cs is the wave coefficient and $\mathbf{u}_s$ is the wave-induced Stokes drift. Typically, the wind drag coefficient varies from 0.025 to 0.044 (American Society of Civil Engineers Committee on Modeling Oil Spills, 1996). The wind deflection angle is typically 20 degrees clockwise from the wind direction (in the Northern Hemisphere). The OTWM uses wind-dependent formulation for the wind deflection angle (Samuels et al., 1982)

$$\theta = -25^o exp\left(-10^{-8}|\mathbf{u}_{10}|/\nu_k g\right), \tag{20}$$

where ν_k is the kinematic viscosity of the sea water.

In many applications, wind and wave effects are combined and both represented by the wind drag coefficient. For example, under light wind conditions without breaking waves Reed et al. (1994) found that $C_w = 0.035$ provided realistic simulation of oil slick drift in offshore areas. In the presented numerical experiments, wave effects are not explicitly added to $\mathbf{u}_a$. It should be noted, however, that the value of C_w needs to be adjusted based on the accuracy of representation of true ("skin") surface currents (a current within a thin surface layer whose thickness is on the order of oil thickness) by $\mathbf{u}_c$. In many applications, $\mathbf{u}_c$ is the near-surface velocity from a hydrodynamic model and, as such, represents velocity averaged over the top model layer, whose thickness exceeds the thickness of the surface current. Thus, $\mathbf{u}_c$ may substantially differ from the true "skin" surface velocity. This is demonstrated by the study of Morey et al. (2018) who analyzed trajectories of satellite-tracked surface drifters in the northern Gulf of Mexico and found a notable velocity shear within the upper meter of the ocean. Therefore, $\mathbf{u}_c$ needs correction. However, the correction strongly depends on the vertical resolution of the near-surface layers in the model. Models with finer vertical surface layers need weaker adjustments, and C_w and the turning angle should be smaller (van der Mheen et al., 2020). In the OTWM, C_w is specified by the user and provided in the float input file. The wind effect can be eliminated by setting Cw to 0 in the float input file. Another option is to undefine the wind drift in the preprocessing definitions. The second option is required if a simulation is performed without wind (or atmospheric) forcing. In the presented experiments for the given ROMS configuration, $C_w = 0.01$. For future development of the CSOMIO model, C_w could be parameterized as a function of the thickness of the uppermost model grid layer, which is represented by $\mathbf{u}_c$.

Turbulent diffusive velocities $\mathbf{u}_d$ are approximated as random fluctuations defined based on "random walk" (Garcia-Martinez and Flores-Tovar, 1999; Lonin, 1999; Isobe et al., 2009)

$$\mathbf{u}_d = U_d \varsigma exp\left(i2\pi\varsigma\right), \tag{21}$$

where ς is a random variable from the standard Gaussian distribution and

$$U_d = \sqrt{\frac{c_0 K_h}{\triangle t}}, \tag{22}$$

where c_0 is a constant, K_h is the horizontal diffusion.

Surface Evaporation of Oil

Evaporation dominates the early stage of oil weathering at the ocean surface. Historical estimates of oil evaporation from the ocean surface range from 20 to 80% of their volume during the first few days. The National Incident Command estimated that 25% of the total oil released evaporated during the DWH spill (Lubchenco et al., 2010). Evaporation processes are faster than dissolution and degradation processes (i.e., oxidation and biodegradation).

Physical and chemical processes that control oil evaporation cannot be described as a single relationship due to the complexity of oil's chemical structure and numerous factors affecting physics and the chemistry of oil compounds (Fingas, 1995, 1996). In practice, evaporation curves are empirically derived for particular types of oil from field observations and laboratory tests. Oil evaporation rates vary greatly with time, and individual compounds can have drastically different evaporation rates. The most intense evaporation typically occurs during the first 24 h as lighter compounds evaporate, after which the overall evaporation rate decreases. During this process, light oils change their chemical and physical properties becoming more viscous. Heavy oils become solid-like and may form tar balls and tar mats (Fingas, 2012; Zodiatis et al., 2017).

Several algorithms are available for modeling oil evaporation. French-McCay and Payne (2001) presented a pseudo-component approach to simulate oil weathering. Using this approach, the oil is treated as seven pseudo-components defined by distillate cut and compound classification (three aromatic fractions, three aliphatic fractions, and one non-volatile fractions). Stiver and Mackay (1984) presented a method known as the "evaporative exposure approach." Based on laboratory experiments and analytical considerations, Fingas (2012, 2015b) suggested a different approach for oil evaporation modeling. In contrast to the previous two approaches, he argued that oil evaporation is diffusion limited by the oil itself and hence it is not air-boundary-layer regulated. Experiments demonstrated that evaporation rates for oils, and even a light product gasoline, were not significantly increased with increasing wind speed. Also, the experiments showed no correlation between oil area and evaporation rate (in contrast to air-boundary-layer regulated liquids, such as water). The experiment showed that oil temperature was the main factor determining the evaporation rate.

In the OTWM, a multi-component approach based on Fingas (2012) is implemented to simulate evaporation of the oil at the ocean surface. This approach is necessary for tracking changes in oil composition, density, and oil particle sizes. The evaporation algorithm is activated when a Lagrangian float is at the surface. The percentage of evaporated oil is calculated for each compound (i) separately

$$E_{oil(i)} = \left[E + 0.675 + 0.045\left(t_{oil} - 15\right)\right]\ln(T), \tag{23}$$

where t_{oil} is oil temperature (taken as ambient ocean temperature), T is the cumulative time of the oil at the surface in minutes (where $T > 1.0$ to avoid negative evaporation), and E is the evaporation equation parameter given by

$$E = 15.4 - 14.5\rho_i + 2.58(\widetilde{\mu}_{oil}(i))^{-1}, \tag{24}$$

where ρ_i is density of the i^{th} oil compound (kg m^{-3}) and $\widetilde{\mu}_{oil}(i)$ is dynamic viscosity (cP) of the i^{th} oil compound. The oil dynamic viscosity (in cP) is calculated as Sanchez-Minero et al. (2014)

$$\mu_{oil(i)} = a \cdot exp\left(bt_K^{-3}\right), \tag{25}$$

where t_K is oil temperature (in °K) and coefficients a and b are correlating parameters in the viscosity correlation

$$\begin{aligned} a = {} & 3.9 \times 10^{-5} API^3 - 4.0 \times 10^{-5} \\ & API^2 + 0.1226 API - 0.7626, \end{aligned} \tag{26}$$

$$b = 9.1638 \times 10^9 API^{-1.3257}. \tag{27}$$

In the above formulas, API is the American Petroleum Institute gravity calculated for the oil compounds as

$$API = \frac{141.5}{SG} - 131.5, \tag{28}$$

where SG is specific gravity of the oil.

For heavy oil compounds (API < 10.0), the oil viscosity is estimated using one of the methods discussed in Bahadori et al. (2015)

$$\mu_{oil(i)} = 10^a t_K^b, \tag{29}$$

where the coefficients are

$$a = -71523 API + 22.13766, \tag{30}$$

$$b = 0.269024 API - 8.26. \tag{31}$$

An example of evaporation curves for the three compounds used in the presented OTWM (saturates, aromatics and resins-asphaltenes) calculated using Eqs. (23)–(31) is shown in **Figure 4A**.

After each time step, changes driven by evaporation in the characteristics of oil droplets are updated as follows. The new weight fraction of the i^{th} oil compound is

$$\tilde{\omega}_{oil}^{(k+1)}(i) = \frac{\tilde{m}_{oil}^{(k+1)}(i)}{m_{oil}^{(k+1)}}, \tag{32}$$

where $m_{oil}^{(k+1)}$ is the updated mass of the oil particle (next time step k+1) and $\tilde{m}_{oil}^{(k+1)}(i)$ is new mass of the oil i^{th} compound in the oil particle given as

$$\tilde{m}_{oil}^{(k+1)}(i) = (1 - E_{oil}(i))\, \tilde{m}_{oil}^{(k)}(i). \tag{33}$$

Here, $\tilde{m}_{oil}^{(k)}(i)$ is mass of the oil i^{th} compound at the time step k and the mass of the oil droplet is

$$m_{oil}^{(k)} = \sum_{i=1}^{N_{comp}} \tilde{m}_{oil}^{(k)}(i). \tag{34}$$

The updated weight fraction (Eq. 32) for the individual compounds is used to update oil droplet densities ($\rho_{oil}^{(k+1)}$) using Eq. 2. Next, new values of the oil droplet mass and density are used to update oil droplet size (D_{oil}) by updating volume of the oil droplet first

$$v_{oil}^{(k+1)} = \frac{m_{oil}^{(k+1)}}{\rho_{oil}^{(k+1)}}, \tag{35}$$

where $m_{oil}^{(k+1)}$ has been updated using new $\tilde{m}_{oil}^{(k+1)}(i)$ in Eq. 34. The new oil droplet size ($D_{oil}^{(k+1)}$) is derived from Eq. 35 assuming a spherical shape of the particle

$$D_{oil}^{(k+1)} = 2\left(\frac{3}{4\pi} v_{oil}^{(k+1)}\right)^{1/3}. \tag{36}$$

Examples of updated oil droplet density and size derived from the evaporation rate are shown in **Figures 4B,C**.

The impact of oil evaporation is demonstrated by looking at the distributions of oil droplet densities and sizes at the beginning and at the end of a test ROMS-OTWM simulation lasting 7 days (**Figure 5**). The analysis only includes the oil droplets that were on the surface for at least 4 days. The histograms demonstrate that after being subject to surface weathering (evaporation) oil particles become denser and smaller, as expected.

Sediment Model

To account for interactions between oil, and suspended sediment, the CSOMIO model built on the Community Sediment Transport Modeling System (CSTMS), which has previously been coupled with the ROMS hydrodynamic model (Warner et al., 2008), and has been used for simulations of sediment transport in the northern Gulf of Mexico (e.g., Xu et al., 2011; Zang et al., 2018; Harris et al., 2020). The sediment model represents a user-specified number of sediment classes. Properties for each class, which include diameter, density, settling velocity, and erosion rate parameter, are specified as input parameters and held constant throughout the simulation. Most applications of CSTMS have assumed non-cohesive sediment behavior (Warner et al., 2008). However, a more recent development added flocculation processes (Winterwerp et al., 2006; Manning et al., 2017) to the model (Sherwood et al., 2018) using a population balance model based on FLOCMOD (Verney et al., 2011), which uses a finite number of floc classes, and accounts for aggregation and disaggregation of flocs (Soulsby et al., 2013; Mehta et al., 2014) by moving sediment mass between the floc classes within each model grid cell. Implementation of the flocculation model requires additional model parameters including the fractal dimension (e.g., Kranenburg, 1994; Dyer and Manning, 1999), collision efficiency (e.g., Molski, 1989; Parsons et al., 2016; Hope et al., 2020), and fragmentation rate (see Sherwood et al., 2018).

The CSOMIO-sediment model extends the existing CSTMS to account for formation of OPA (Cui et al., 2020). Specifically, we adapted and modified FLOCMOD to incorporate an Oil-Particle-Aggregate Module (OPAMOD) within the CSTMS and added a new type of tracer to represent OPAs. OPAMOD uses the oil characteristics (droplet size, density, and concentration) and the suspended sediment characteristics (diameter, density, and concentration) to calculate the formation or growth of OPAs in the water column. At the end of flocculation process, concentrations of suspended sediment, oil, and OPAs are updated. OPAMOD included interactions between oil droplets and sediment flocs, oil droplets and OPAs, and sediment flocs and OPAs. The model was validated with a zero-dimensional simulation (Cui et al., 2020), which performed well when compared to laboratory data reported by Ye et al. (2020).

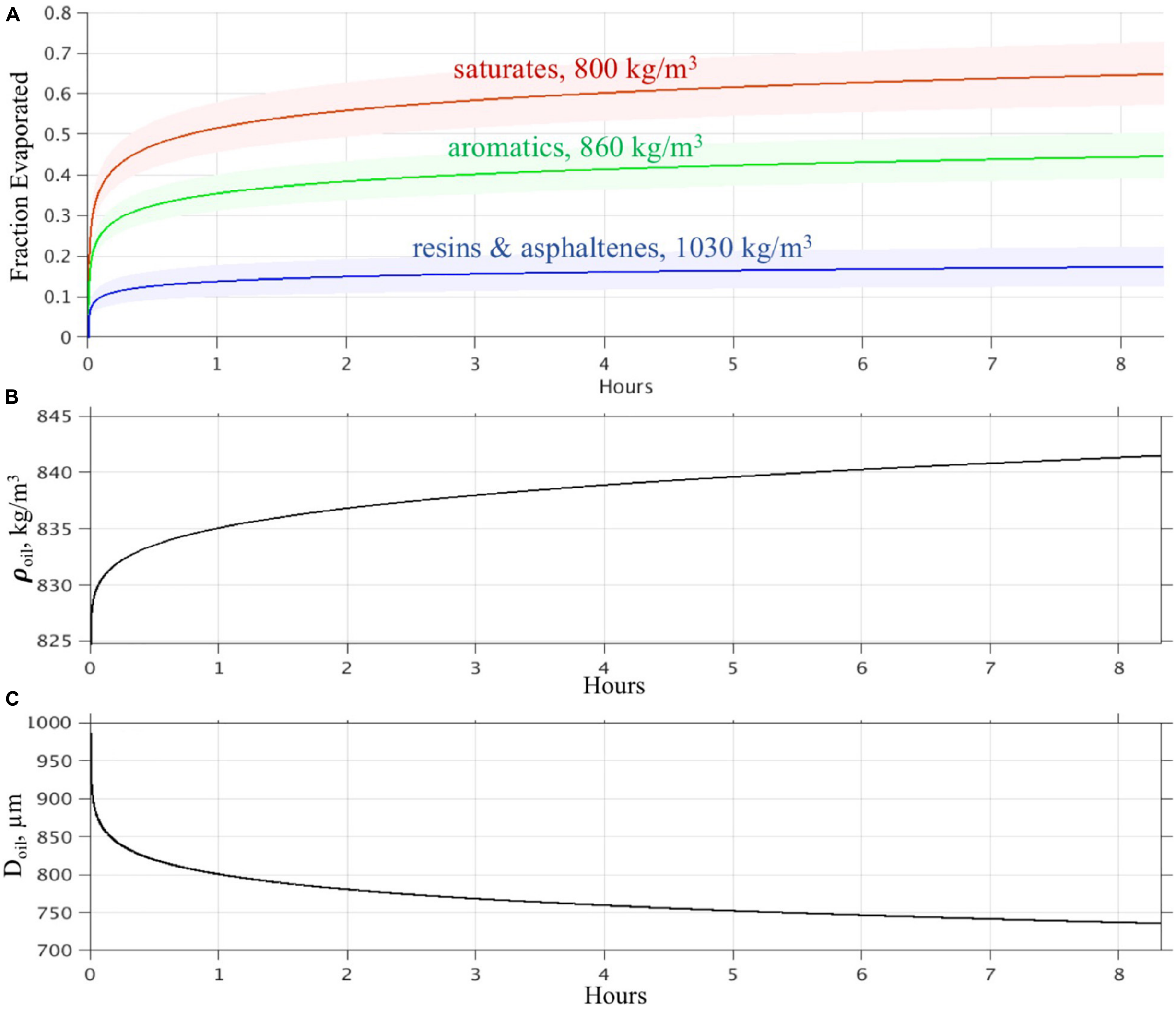

FIGURE 4 | (A) Evaporation curves for saturates, aromatics, and heavy oil compounds calculated using the approach discussed in section "Surface Evaporation of Oil." The densities of the compounds are listed in the figure. The solid lines are the evaporation curves for 25°C. The shades highlight the range of the evaporation curves calculated for temperatures from 15 to 35°C for each compound. The horizontal axis is hours. **(B)** Change of the oil droplet density due to evaporation. **(C)** Change of the oil droplet size due to evaporation.

For the fully coupled, three-dimensional simulation, the sediment model used three cohesive sediment classes (one representing seabed material, two representing sediment delivered by the Mississippi River); and four OPA classes. The properties are shown in **Table 3**. The suspended sediment concentration for seabed mud class was initialized with 0.01 kg m^{-3} within the bottom grid cells. The sediment concentrations from river input were extracted from a realistic simulation, which used riverine discharge from USGS gauge data (Harris et al., 2020). In OPAMOD, the fractal dimension was assumed to be 2.39. The fractal dimension of 2.39 was obtained using model calibration simulations to match laboratory results that studied the formation of OPA (Cui et al., 2020; Ye et al., 2020). The collision efficiency was set to 0.55 for the interaction between oil and sediment particles, and 0.35 for the interaction between sediment and OPAs, following Bandara et al. (2011). For the configuration presented in this paper, resuspension was neglected by defining a high critical shear stress for sediment. Resuspension was neglected in this study for multiple reasons. First, the main purpose of the sediment module in this coupled model is to capture the sedimentation of oil via the formation of OPAs. This sedimentation acts to enhance the delivery of oil to the seafloor, which is the effect we intended to represent. To consider the ultimate fate of the oil that is within OPA, over longer timescales, would require that we also account for resuspension of the OPA. Simulation of resuspension requires parameters for the critical shear stress for erosion. However, the critical shear stress of OPA is unknown, which makes the simulation of resuspension challenging.

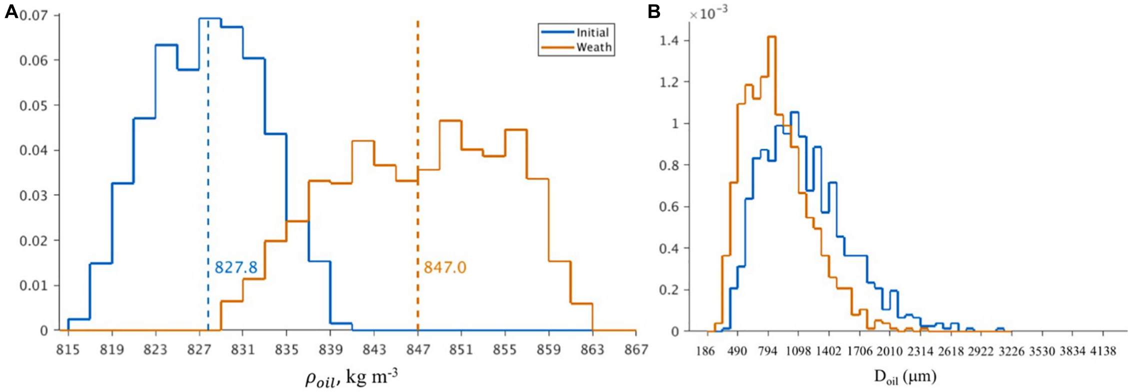

FIGURE 5 | (A) Histograms of the oil droplet densities (ρ_{oil}) at the beginning (blue) and end (orange) of a 7 day ROMS-OTWM simulation that includes oil evaporation as the only loss term. Only particles that remained at the surface at least 4 days are considered. The vertical dashed lines indicate the mean. **(B)** Similar to **(A)** but for the oil droplet sizes (D_{oil}).

TABLE 3 | Properties of sediment and OPAs.

Particle type	D_50 10^{-3} (m)	Settling velocity 10^{-3} (m s^{-1})
Mud 1 (seabed)	0.125	1.0
Mud 2 (Small Riverine)	0.063	0.09
Mud 3 (Large Riverine)	0.5	1.67
OPA 1	0.256	2.61
OPA 2	0.63	7.63
OPA 3	1.0	10.0
OPA 4	1.8	10.0

Biogeochemical Model

The CSOMIO biological sub-model (BIO) is based on the ROMS Fennel et al. (2006) subroutine, which has been used extensively in the Gulf of Mexico and which provides a simple but complete biogeochemical model for the upper ocean. Although a number of improvements have been made to that model to better simulate the low oxygen zone extending beneath the Mississippi River plume (e.g., Laurent et al., 2012), the main CSOMIO goal was to incorporate the representation of the hydrocarbon-degrading microbes in open ocean regions. This has been achieved by incorporating elements of the Coles et al. (2017) gene-based model to integrate hydrocarbon-degrading bacteria. Three additional organisms are added to represent hydrocarbon-degrading bacteria. These are not randomly selected, but rather optimized as small cells of order 1 micron in diameter that degrade hydrocarbons while using nitrate or ammonium as a nitrogen source. Some additional model changes are also required. First, energy acquisition and nutrient acquisition are separated to allow for the use of pure carbon-based substrates as energy sources. To determine the yield on these hydrocarbons, theoretical approaches are used based on the Gibbs free energy of the reaction, following Reed et al. (2014), which was based on the work of Roden and Jin (2011). Conceptually, the yield is the ratio of the biomass increase to the hydrocarbon substrate uptake. Because the yield estimates are based on nutrient and substrate replete conditions, the maximum uptake rate of substrate is assumed to equal the maximum organismal growth rate divided by yield.

The three hydrocarbon groups in the CSOMIO model are intended to span a broad range of similar hydrocarbons with similar lability, and thus representative formula are computed for each group from the observed dissolved concentrations (Diercks et al., 2010; Mason et al., 2012; Reddy et al., 2012). The computational yield is then determined based on the redox reaction of each representative chemical compound (Saturates $C_{10}H_{22}$, yield = 5.7322 moles C biomass / mole of electron donors, Aromatics C_7H_8, yield = 3.3792 moles C biomass / mole of electron donors, heavy oil $C_{30}H_{52}$, yield = 15.6952 moles C biomass / mole of electron donors). Hydrocarbon uptake is not necessarily limited by nutrient availability. Organisms are able to use hydrocarbons for energy without adding biomass when nutrients are unavailable, however, mortality continues to reduce organismal biomass in the absence of active growth. Since these organisms are designed to be specialized as hydrocarbon degraders, there are no additional metabolic strategies available to the organisms for growth. In prior modeling efforts (Valentine et al., 2012), secondary substrates in the degradation of a hydrocarbon and the organisms that utilize them were added to a model, however, here the focus is solely on a single degradation step consistent with the available data for validation.

The equations modulating bacterial growth are

$$G_k = \mu_{max}(1.066)^T \tag{37}$$

$$\mu_k = G_k \frac{S_k k_{sk}}{1 + S_k k_{sk}} \left[\left(\frac{NH_4 k_{NH4}}{1 + NH_4 k_{NH4}} \right)^{-1} \frac{NO_3 k_{NO3}}{1 + NO_3 k_{NO3}} + \frac{NH_4 k_{NH4}}{1 + NH_4 k_{NH4}} \right], \tag{38}$$

$$\frac{dB_k}{dt} = \mu_k B_k - m B_k \tag{39}$$

$$\frac{dS_k}{dt} = -\frac{G_k}{Y_k}\frac{S_k k_{sk}}{1+S_k k_{sk}}B_k \tag{40}$$

where μ_{max} is the maximum growth constant for each bacteria taxon. G_k is the organismal maximum growth rate given the ambient temperature conditions (T) following the same formulations used in the Fennel et al. (2006) model. μ_k then represents the actual growth rate of the organism once limited by both energy substrate S_k and the half saturation coefficient, k_s for that substrate, and by nitrogen availability as expressed through the combination of NO_3 and NH_4 concentration and their half saturation coefficients k_{no3} and k_{nh4}. B_k is the organismal biomass, and m is the linear mortality coefficient. Absent grazing information on these bacteria we select a simple mortality function. Y_k is the yield determined by

$$Y_k = \frac{2.08 - 0.0211\Delta G_{e^{-1}}}{24.6}. \tag{41}$$

The energy yield G_{e-} is computed from the Gibbs free energy and the stoichiometry of the electron donor in the redox reaction, and the molecular weight of the microbial biomass is 24.6 $g\left(C - molbiomass\right)^{-1}$, which is derived from the generic microbial biomass formula of $CH_{1.8}O_{0.5}N_{0.2}$ (Roels, 1981). The values of each coefficient are described in **Table 4**.

Trace amounts of dissolved hydrocarbons in each group are maintained as Eulerian tracers in the model to allow for the maintenance of the hydrocarbon-degrading microorganisms. When Lagrangian oil is converted to the Eulerian framework, these two components are additive and the ratio is stored at each grid point. The bacteria convert hydrocarbons to biomass and carbon dioxide, and then the ratio is used to deconvolve the oil concentration back to the Lagrangian framework.

TABLE 4 | Coefficients for the biochemical model.

Parameter		Modeled value, units
μ_{max}	Saturated degrader	$0.5062 day^{-1}$
	Aromatic degrader	$0.2219 day^{-1}$
	Resins degrader	$0.1777 day^{-1}$
k_s	Saturates $C_{10}H_{22}$	1 μM
	Aromatics C_7H_8	1 μM
	Resins $C_{30}H_{52}$	1 μM
k	Nitrate NO3	0.5 μM
	Ammonium NH4	0.5 μM
m	Saturated degrader	2×10^{-6} day^{-1}
	Aromatic degrader	2×10^{-6} day^{-1}
	Resins degrader	2×10^{-6} day^{-1}
Y_k	Saturates $C_{10}H_{22}$	5.7322 C-mol biomass/ ED-mol
	Aromatics C_7H_8	3.3792 C-mol biomass/ ED-mol
	Resins $C_{30}H_{52}$	15.6952 C-mol biomass/ ED-mol
ΔG_{e-}	Saturates $C_{10}H_{22}$	−6,584.5 kJ/ ED-mol
(T = 278.15 K;	Aromatics C_7H_8	−3,841.1 kJ/ED-mol
P = 12 Mpa)	Resins $C_{30}H_{52}$	−18,200.0 kJ/ED-mol

Online and Offline Configurations

The CSOMIO modeling system can be integrated in online and offline configurations. The advantage of the offline version is reduced computational time. To run offline, the physics base of the model should be integrated using ROMS and saved at an adequate frequency. Then, the tracer and oil can be run with the offline version of ROMS using these saved physics fields (u, v, ubar, vbar, zeta, and optionally the vertical salinity diffusion coefficient) to transport the tracer and oil instead of integrating all of the computations simultaneously, saving computational time. The offline ROMS version is modified so that when the appropriate flags are chosen, the physics base numerics are not run and instead the simulation reads in the saved velocity fields, then uses those values to run only the tracer and oil transport routines in ROMS. The physics fields are read in as climatology and forced fully for every grid node; they are linearly interpolated in time between available time steps just as climatology can be. Details of the computational savings and setup approach as well as details in the ROMS code modifications are available in Thyng et al. (2021).

TWO-WAY EULERIAN-LAGRANGIAN MAPPING

The components of the CSOMIO model are linked together using a two-way Lagrangian-Eulerian mapping technique. The technique maps oil characteristics from a Lagrangian to Eulerian framework (Lagrangian-Eulerian mapping, LEM) in order to simulate oil biodegradation and sedimentation processes. After modification by the sedimentation and biogeochemical submodels, oil fields are mapped back to the Lagrangian framework (Eulerian-Lagrangian mapping, ELM) for the oil model. Implementation of the algorithm in the ROMS-OTWM code includes test subroutines verifying that the overall mass of oil is conserved during LEM and ELM. In order to distinguish variables in the Eulerian framework from the same variables in Lagrangian space, the Eulerian variables are denoted with an asterisk.

Lagrangian-Eulerian Mapping

Description of the Methodology

LEM consists of several steps. First, the Lagrangian floats whose position is given by a vector $\mathbf{x}_l$ ($l = 1, \ldots, N_{flt}$) are clustered into groups bounded by grid cell faces, i.e., for every grid cell $\mathbf{j} = \{j_1, j_2, j_3\}$ a set of Lagrangian floats is defined as

$$S_{\mathbf{j}} = \left\{\mathbf{x}_l \in \mathbb{R}^3 : ||\mathbf{x}_l - \mathbf{x}_{\mathbf{j}}^{(0)}||_2 < ||\mathbf{x}_l - \mathbf{x}_{\mathbf{k}}^{(0)}||_2,\ for\ \forall\, \mathbf{k} \neq \mathbf{j}\right\} \tag{42}$$

where $\mathbf{x}_{\mathbf{j}}^{(0)}$ is a center point of the grid cell $\mathbf{j}$ and l is the float index.

Both the biogeochemical and sediment-OPA (OPAMOD) modules require information about the concentration of oil compounds. Hence, each compound is next mapped onto Eulerian space. The mass of oil compounds (index i) is integrated over the grid cells ($\mathbf{j}$) where $S\mathbf{j}$ is not empty,

$$\tilde{M}^{*}_{oil}\left(\mathbf{j};\, i\right) \;=\; \sum_{l\in S(\mathbf{j})\neq\emptyset} \vartheta_{oil}(l)\rho_{oil}(l)\widetilde{\omega}_{oil}(i,\, l), \tag{43}$$

where l is the float index and $\vartheta_{oil}(l)$ is the volume of oil represented by the l^{th} Lagrangian float. In general, ϑ_{oil} can vary across the floats if the oil discharge rate varies in time. In the presented experiments, the discharge rate is constant (3000 m^3/day) and thus, initially ϑ_{oil} is the same across the floats being determined as

$$\vartheta_{oil} \;=\; \frac{\mathfrak{D}_{oil}}{\mathfrak{D}_{flt}}, \tag{44}$$

where $\mathfrak{D}_{oil}$ is the discharge of oil (specified by the user in the input file) and $\mathfrak{D}_{flt}$ is the release frequency of the Lagrangian floats (specified in the input file). Concentrations of the oil compounds ($\tilde{C}^{*}_{oil}$) in the grid cell ($\mathbf{j}$) are

$$\tilde{C}^{*}_{oil}\left(\mathbf{j};\, i\right) \;=\; \frac{\tilde{M}^{*}_{oil}\left(\mathbf{j};\, i\right)}{V_{grid}(\mathbf{j})}, \tag{45}$$

where V_{grid} is the volume of the grid cell. Mean oil droplet size in a grid cell required for the sediment-OPA model is obtained as

$$D^{*}_{oil}(\mathbf{j}) \;=\; \frac{1}{n^{*}_{flt}(\mathbf{j})} \sum_{l\in S(j)} D_{oil}(l). \tag{46}$$

where $n^{*}_{flt}(\mathbf{j})$ is the number of Lagrangian floats in the grid cell ($\mathbf{j}$).

Test Simulations With LEM

A test simulation with the ROMS-OTWM and engaged LEM algorithm was performed. In the simulation, neither the biogeochemical nor sediment-OPA modules are activated, so that no changes in oil characteristics on the Eulerian framework are anticipated to occur. In this case, identical fields should be observed in Lagrangian and Eularian spaces. Results of the test simulation demonstrate accurate mapping of the oil characteristics from Lagrangian to Eulerian framework in horizontal and vertical dimensions. As an example, locations of Lagrangian floats and mean oil droplet size (D_{oil}) in the model surface layer are shown for some time instance (**Figure 6A**). The mapping onto the Eulerian model grid frame preserves the spatial pattern of the oil distribution (**Figure 6B**). Peak values of the mean oil droplet size of individual floats are smoothed by cell-averaging (Eq. 46). Note that reverse mapping (Eulerian-Lagrangian) restores the maxima for the individual floats, therefore the impact of the mapping on D_{oil} is assumed to be minimal. The number of floats used for the derivation of the grid cell mean characteristics (n^{*}_{flt}) per grid cell is shown in **Figure 6C**. The mapping preserves the ratio between the oil compounds. The concentration of saturates (**Figure 6D**) is notably higher than the concentration of aromatics (**Figure 6E**) and asphaltenes (**Figure 6F**), as expected. In the vertical dimension, oil concentration in grid cells mapped from Lagrangian framework (**Figure 7A**) captures the plume structure in the water column in agreement with the original Lagrangian fields (**Figure 7C**). In agreement with expectation, the concentration generally follows the number of Lagrangian floats in the grid cells (**Figure 7B**).

Eulerian-Lagrangian Mapping

Description of the Methodology

After the oil has been subject to biodegradation and sedimentation processes simulated in the biogeochemical and sediment-OPA modules, the modified oil fields (denoted in this section with index k+1) need to be mapped back to the Lagrangian framework and then updated by the OTWM. In the model, both the biogeochemical and sedimentation processes modify concentrations of the oil compounds but do not explicitly modify the size of oil particles. Therefore, the reverse mapping from the Eulerian to Lagrangian framework interprets changes in $\tilde{C}^{*}_{oil}$ in terms of oil droplet characteristics for each Lagrangian float. The assumption is that floats clustered in one grid cell undergo similar changes during biodegradation and sedimentation, and that changes of oil droplets are proportional to their size.

First, the new mass fraction of the oil compounds is updated at every grid cell ($\mathbf{j}$) by calculating the reduction of concentration for the oil compounds (i)

$$r^{*}\left(\mathbf{j};\, i\right) \;=\; \frac{\tilde{C}^{*(k+1)}_{oil}\left(\mathbf{j};\, i\right)}{\tilde{C}^{(k+1)}_{oil}\left(\mathbf{j};\, i\right)}. \tag{47}$$

Assuming similar reduction of the oil compounds across all particles in a given grid cell ($\mathbf{j}$), the new mass fraction of the oil compounds in the Lagrangian elements within the grid cell is

$$\widetilde{\omega}^{(k+1)}_{oil}\left(\mathbf{j};\, i\right) \;=\; \frac{r^{*}\left(\mathbf{j};\, i\right)\widetilde{\omega}^{(k)}_{oil}(\mathbf{j};\, i)}{\sum_{i}^{N_{comp}} r^{*}\left(\mathbf{j};\, i\right)\widetilde{\omega}^{(k)}_{oil}(\mathbf{j};\, i)}. \tag{48}$$

Next, oil particle densities in the Lagrangian elements within the grid cell are updated

$$\rho^{(k+1)}_{oil}(l \in S(\mathbf{j})) \;=\; \left[\sum_{i\,=\,1}^{N_{comp}} \frac{\widetilde{\omega}^{(k+1)}_{oil}\left(\mathbf{j};\, i\right)}{\widetilde{\rho}_{oil}(i)}\right]^{-1}. \tag{49}$$

In order to update oil droplet size using Eq. 36, a new volume of oil particles ($v^{(k+1)}_{oil}$) is needed. This information is neither explicitly provided by the sediment nor by the biogeochemical modules. The following approach has been employed to derive $v^{(k+1)}_{oil}$. Let

$$v^{(k+1)}_{oil} \;=\; \alpha v^{(k)}_{oil}, \tag{50}$$

where α is an unknown coefficient. Using the fact that mass of the oil is conserved in the Lagrangian and Eulerian spaces, the following is true

$$M^{*(k+1)}_{oil}\left(\mathbf{j}\right) \;=\; V_{grid}\left(\mathbf{j}\right) \sum_{i\,=\,1}^{N_{comp}} C^{*(k+1)}_{oil}\left(\mathbf{j};\, i\right) \;=$$

$$\sum_{l\in S(\mathbf{j})} N^{(k+1)}_{poil}(l)\cdot \rho^{(k+1)}_{oil}(l)\cdot v^{(k+1)}_{oil}(l), \tag{51}$$

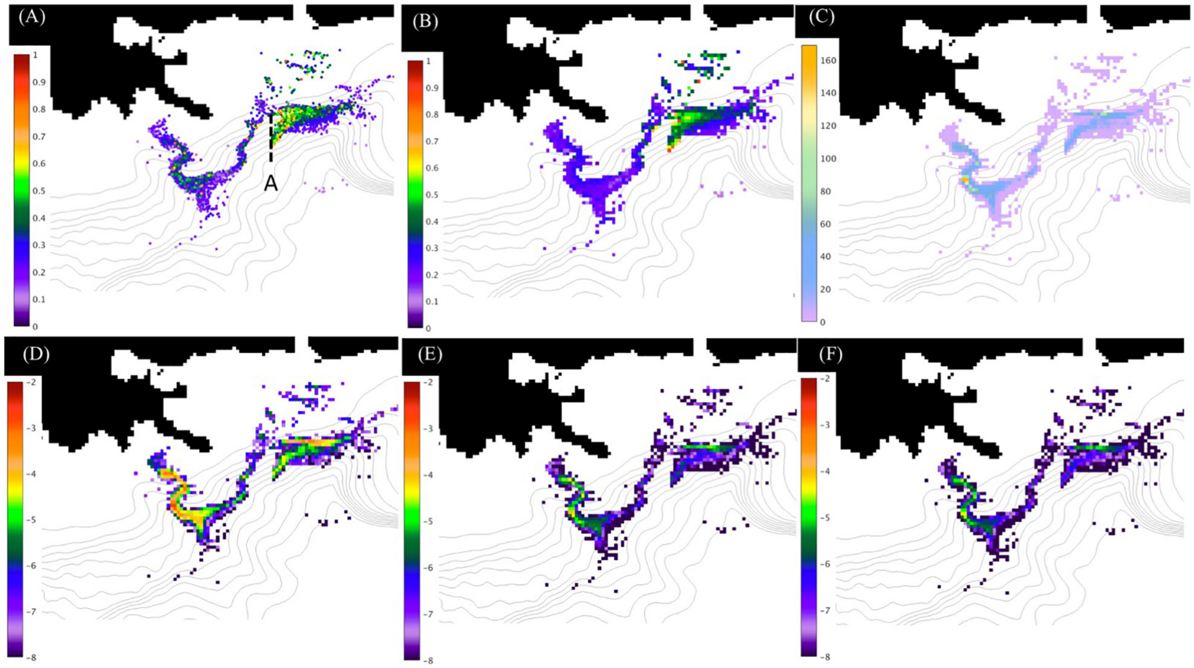

FIGURE 6 | Demonstration of the LEM in a ROMS-OTWM test simulation in the model surface layer. **(A)** The dots indicate locations of individual Lagrangian floats. Colors show mean oil droplet size D_{oil} (μm). The dashed line A is the transect shown in **Figure 7**. **(B–F)** oil characteristics mapped onto an Eulerian model grid frame. **(B)** Mean oil droplet size in the grid cells D^*_{oil} (μm). **(C)** Number of floats per grid cell. **(D)** Concentration of oil compound #1 (saturates), $\tilde{C}^*_{oil}(1)$ (natural log scale, kg m^{-3}). **(E)** Concentration of oil compound #2 (aromatics), $\tilde{C}^*_{oil}(2)$. **(F)** Concentration of oil compound #3 (resins and asphaltenes), $\tilde{C}^*_{oil}(3)$.

where $N^{(k+1)}_{poil}$ is the number of oil particles in Lagrangian float l. In order to close the problem, it is assumed that the number of particles does not change during the biodegradation or formation of OPAs (only depletion of compounds occurs). Then, N_{poil} for a given Lagrangian float can be estimated from the initial fields as

$$N_{poil} = \frac{M_{oil}}{\rho_{oil} v_{oil}} = \frac{\vartheta_{oil}}{v_{oil}}, \tag{52}$$

where M_{oil} is the mass of the oil in a Lagrangian float. Then, using Eqs 35 and 51, α can be found as (note $v^{(k)}_{oil}$ at time k in the equation)

$$\alpha = \frac{M^{*(k+1)}_{oil}(\mathbf{j})}{\sum_{l \in S(\mathbf{j})} N_{poil}(l) \cdot \rho^{(k+1)}_{oil}(l) \cdot v^{(k)}_{oil}(l)}. \tag{53}$$

Test Simulations With ELM

For testing the ELM, a more elaborate set of numerical experiments is prepared. One experiment is integrated with both the LEM and ELM implemented, but neither biogeochemical degradation nor sediment-OPA formation is activated. In the second experiment, the biogeochemical model is implemented and coupled with the ROMS-OTWM via LEM-ELM. In the first experiment, no changes in oil characteristics are expected to occur before the floats reach the surface. The purpose of these experiments is to validate that LEM-ELM does not change oil mass and oil characteristics in the first experiment and accurately maps changes in oil characteristics onto Lagrangian space in the second experiment.

Both experiments are integrated for 7 days. The changes in oil characteristics are analyzed over the ascent time of the floats, from the release of the floats near the bottom until they reach the surface where the oil is subject to surface evaporation. In the experiments, the median of the ascent time is 2.4 days and the 90th percentile is 4.9 days.

In agreement with expectations, changes are not observed in the first experiment without subsurface oil degradation (the dashed lines in **Figure 8**). Thus, the LEM and ELM do not excite spurious changes in the oil characteristics. In the second experiment, subsurface biodegradation results in changes across the oil parameters that is also in agreement with expectations. For all floats, oil droplet density increases with time (**Figure 8A**), whereas both mass and size decrease as a result of oil consumption by microbes simulated in the biochemical model. In agreement with previous studies, lighter compounds of oil undergo biodegradation at a faster rate than the heavier oil. In the test simulation, both aromatics and saturates are consumed at a high rate, whereas the mass of the asphaltenes and resins barely changes (**Figure 8E**).

FULLY COUPLED TEST SIMULATION

To demonstrate the performance of the fully coupled CSOMIO model, a test simulation has been conducted. In this test

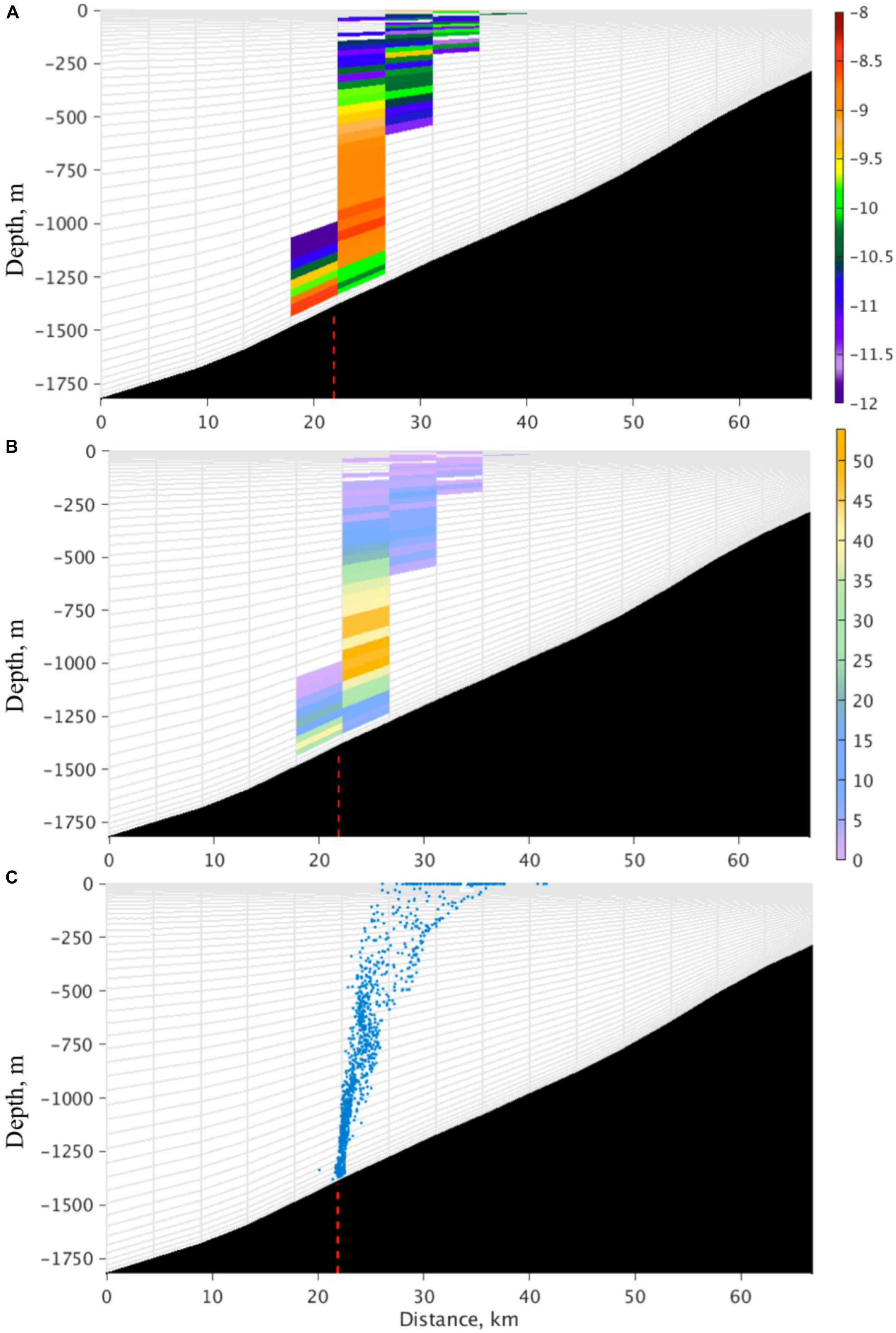

FIGURE 7 | LEM of oil characteristics in the vertical. **(A)** Vertical distribution of oil concentration (C^*_{oil}, kg m^{-3}) on natural logarithmic scale along section A, shown in **Figure 6A**. The grid cells are indicated with gray lines. **(B)** Vertical distribution of Lagrangian float counts in the grid cells. The fields shown in **(A,B)** are obtained by LEM. **(C)** Lagrangian float positions. The red dashed line indicates location of the DWH and the approximate release location of the floats.

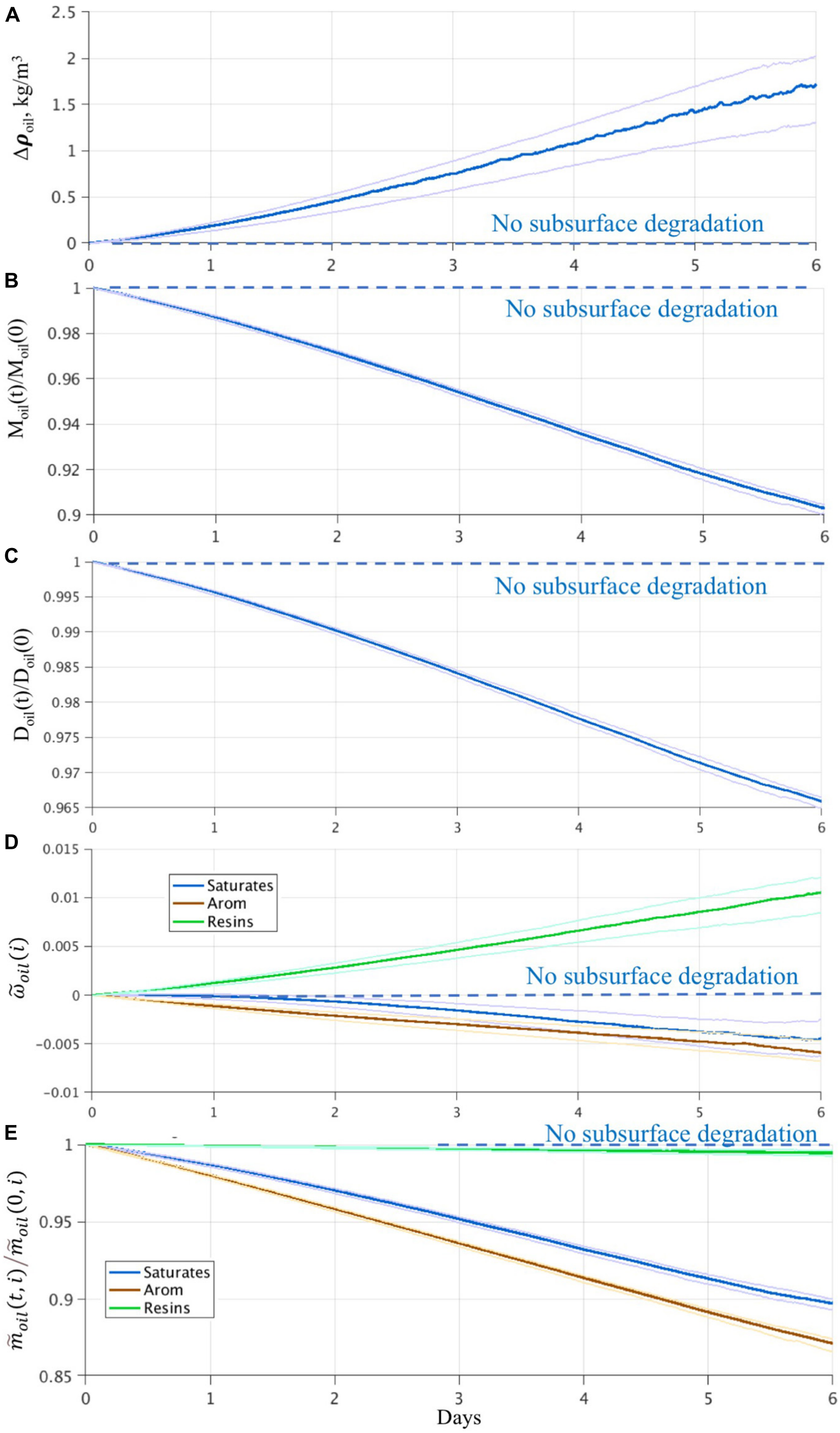

FIGURE 8 | Statistics of changes in oil characteristics in the experiments using LEM and ELM with and without subsurface biodegradation from a coupled ROMS-OTWM-Biogeochemical model. **(A)** Change of oil droplet density (kg m^{-3}). **(B)** Reduction of the oil droplet mass relative to the original mass. **(D)** Reduction of the oil droplet size relative to the initial size. **(C)** Weight fraction of oil compounds. **(E)** Reduction of mass of oil compounds. The estimates are obtained from all floats over the first 6 days after the floats are released at the bottom and until they reach the surface. The solid line is the median, the lighter lines are the inter-quartile range. The horizontal dashed line indicates no change in oil characteristics in the experiment without subsurface degradation. The change in oil characteristics due to biodegradation demonstrates the impact of biogeochemical model coupling using LEM and ELM. The horizontal axis is subsurface time (days) of oil particles from the release until particles reach the surface.

simulation, oil floats are released near the bottom (∼1,400 m) at five locations around the Macondo wellhead (the locations are within ∼100 m) at a frequency of one float every 2.7 min. A constant oil flow rate of 3,000 m^3 day^{-1} is prescribed, thus one float represents 1.1 m^3 of oil. The total number of floats is 80,000. All other forcing fields and characteristics are identical to the test simulations presented earlier in the paper. The model is integrated for 30 days with the fully coupled ROMS-OTWM-OPAMOD-biogeochemical. It should be mentioned that the test simulation was not designed to hindcast the DWH event. Such an effort would require additional tuning of free parameters in the model (Morey et al., 2018.). The purpose of this test simulation was merely to demonstrate the performance of the CSOMIO modeling system with all components coupled.

In the upper ocean, we see the oil has spread approximately 400 km around the release location during the simulation (**Figure 9**) and most of the oil has drifted toward the coast. There is a substantial amount of oil in the subsurface layers, as well (**Figure 9A**). Mass density of the oil compounds differ because of different biodegradation and weathering rates, as well as different initial distributions of the oil compounds (**Figure 5A**). At the surface, saturates has the fastest depletion rate due to evaporation, whereas resins and asphaltenes have the slowest evaporation. Therefore, mass density of the heavy oil compounds (**Figure 9D**) is comparable to mass density of the other two compounds (**Figures 9B,C**) and it is even higher in the western part of the simulated spill where the oil has been subject to evaporation over a longer period of time.

During the oil spill, the most rapid increase is simulated for bacteria 2 (**Figures 10A,B**) feeding on saturates. It takes time for a bacterial community to respond, thus higher concentrations of bacteria 2 and bacteria 3 are observed farther away from the spill location in the oil that remains the longest in the subsurface layers (**Figures 10A,C**). Bacteria 4, feeding on the heavy oil compounds, has the slowest increase rate (**Figures 10E,F**). Its concentration has barely increased over the simulation time and is similar to the background concentration. In the vertical sections, elevated concentrations of the oil-degrading bacteria highlight the track of the oil plume in the subsurface layers (**Figures 10B,D,F**).

Formation of the sediment OPAs is mainly limited to the deep region within 100–150 km of the release location (**Figure 11**) because of the high concentration of oil droplets in the near-bottom layer over this area. Spatial distribution of the OPAs is inhomogeneous and extends in the eastern direction due to the mean near-bottom flow over the simulated time period. Sediment OPA1 has higher concentration and is more widely spread compared to the other OPA classes.

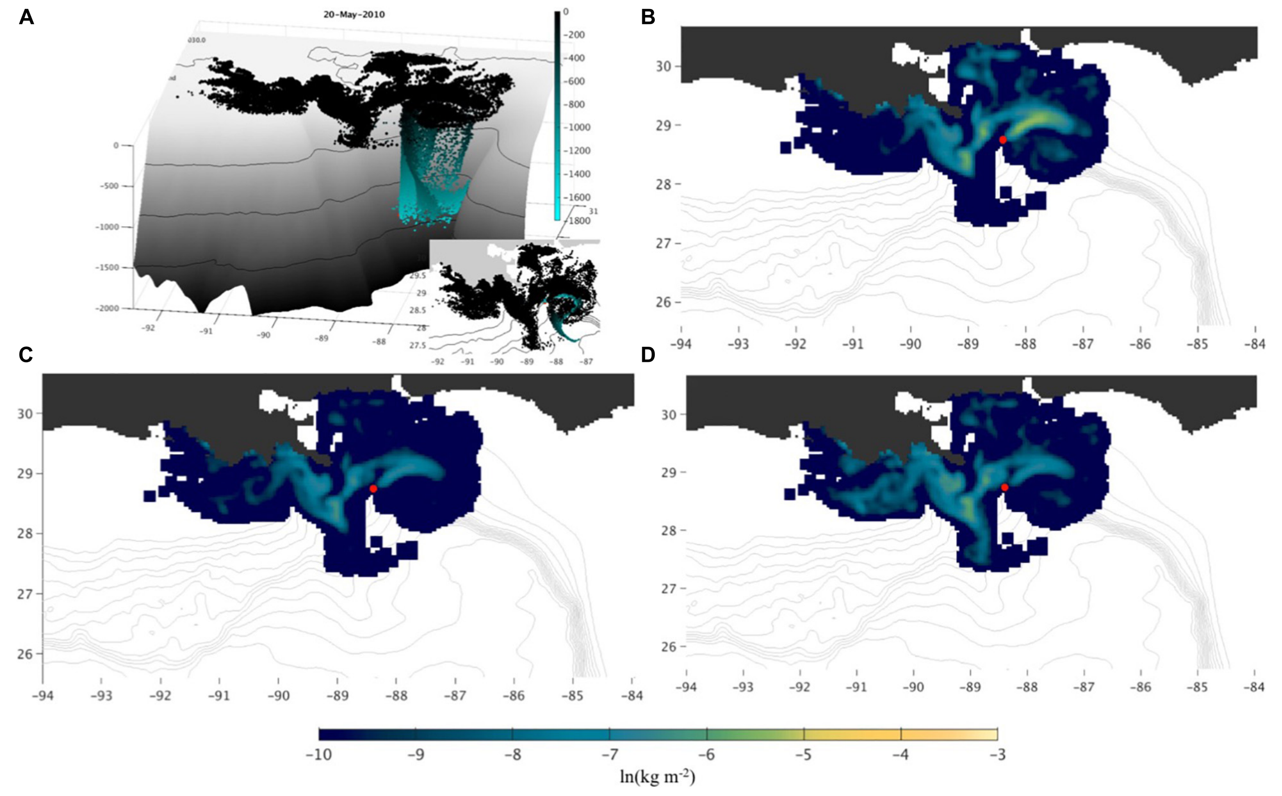

FIGURE 9 | Simulated oil from the test experiment with the fully coupled ROMS-OTWM-OPAMOD-Biogeochemical model after 30 days of simulation. **(A)** Three-dimensional distribution of Lagrangian floats representing clusters of oil particles. The red dot indicates release location at the bottom. Colors designate particles' depth in the water column. **(B–D)** Mass density (kg m^{-2}) of the oil compounds (saturates, aromatics, resins and asphaltenes, respectively) in the upper 50 m. Mass density is on the natural logarithmic scale.

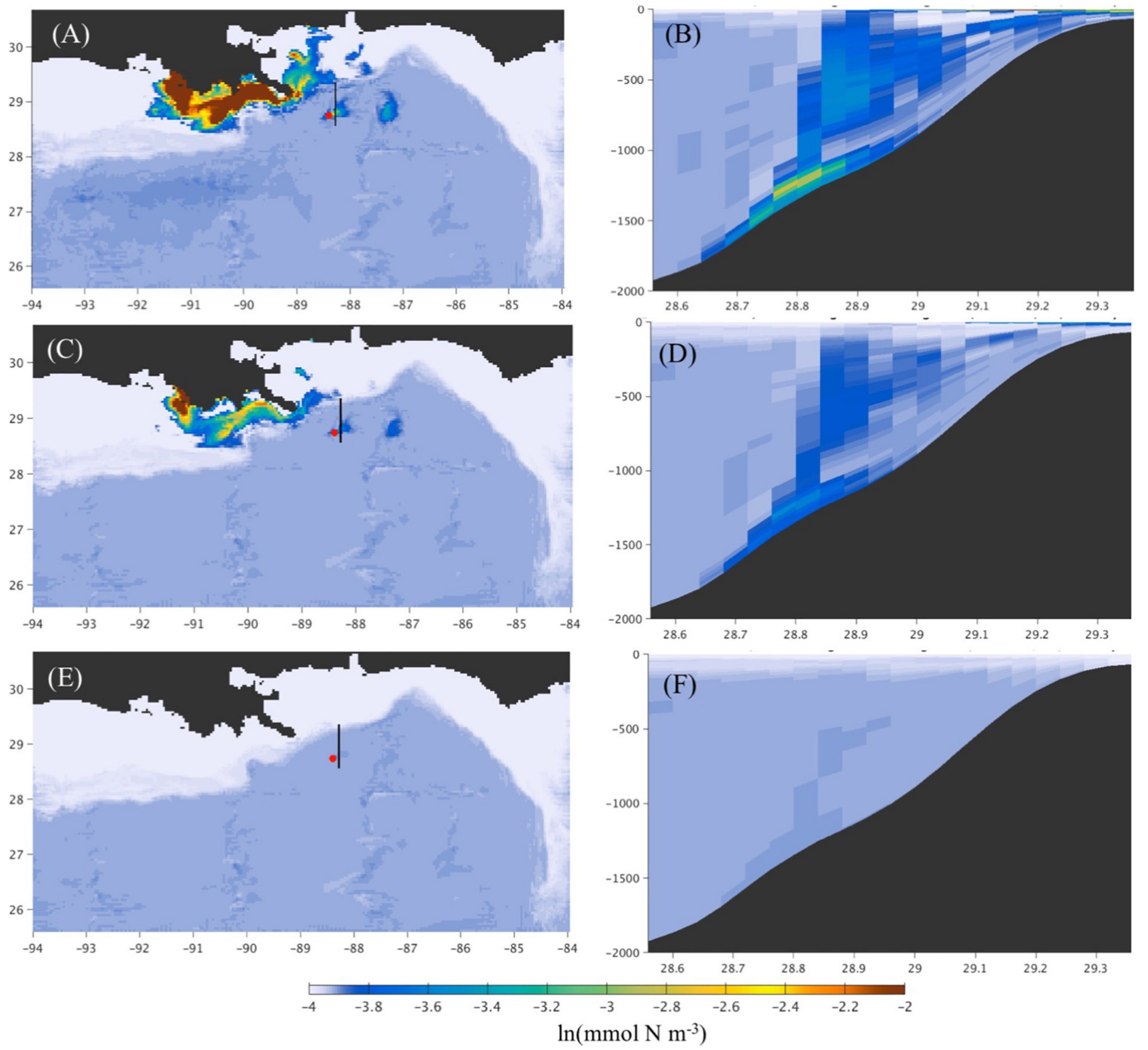

FIGURE 10 | Dissolved bacteria concentration (mmol N m^{-3}) from the test experiment with the fully coupled ROMS-OTWM-OPAMOD-Bgeochemical model after 30 days of simulation. **(A,C,E)** Spatial distribution of bacteria 2 (saturates), 3 (aromatics), and 4 (heavy oil), respectively, in the near-bottom layer (5th layer from the bottom). The red dot is the release location of the Lagrangian floats. **(B,D,F)** are the vertical distribution of bacteria 2, 3, 4 concentration along the section indicated with the black line in the left figures. Plots are in the natural logarithmic scale.

This is consistent with results from sensitivity tests in a one-dimensional (vertical) model (Cui et al., 2020), that is, with intermediate fractal dimensions (2.39 in this study), the diameter of the dominant OPA classes fall in the range of 180–360 μm (the diameter of OPA1 here is 256 μm). Because the settling velocity of OPA types 2–4 are greater than that of the OPA1 (see **Table 3**), they deposit and settle into slower moving water more quickly than OPA1. This results in OPA1 being more widely dispersed than the more slowly settling classes of OPA.

The results of this test simulation demonstrate the capabilities of the CSOMIO modeling system in a coupled configuration. Model components of oil, sediment, and biology interact and show the generally expected responses.

SUMMARY AND CLOSING REMARKS

The newly developed CSOMIO coupled modeling system presented here is designed to simulate three-dimensional movement of oil in the ocean and compositional changes of oil (weathering) in the water column and at the surface, with explicitly modeled interactions with evolving sediment and biological components as opposed to prescribed

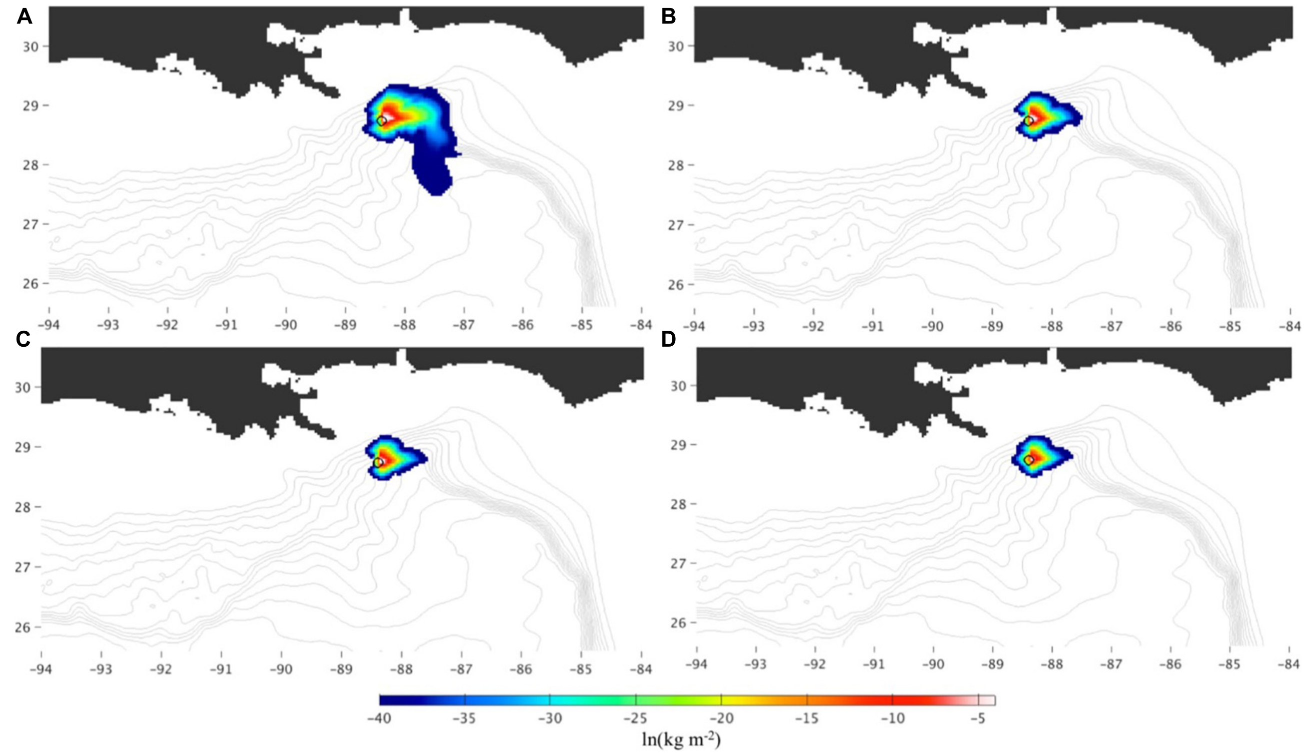

FIGURE 11 | Sediment OPAs (kg m^{-2}) from the test experiment with the fully coupled ROMS-OTWM-OPAMOD-Biogeochemical model after 30 days of simulation. The OPAs are depth-integrated. Sediment OPAs 1–4 are shown in **(A–D)**, respectively.

parameterizations. The system is based on COAWST (Warner et al., 2010) and includes oil transport and weathering (OTWM), OPAMOD, and biogeochemical modules that can be integrated in a coupled or uncoupled configuration. For coupling OTWM with OPAMOD and biogeochemical modules, a two-way Lagrangian-Eulerian mapping has been developed and implemented for mass-conservative two-way exchange of the information between the Lagrangian and Eulerian frameworks. The system can be integrated in online or offline configuration. The latter drastically reduces computational time and is particularly useful for performing multiple simulations with a fully coupled CSOMIO model.

In the simulations described in this paper, the chemical composition of oil is described in terms of three chemical compounds (saturates, aromatics, resins and asphaltenes or SAR+A). This allows for tracking changes of individual oil compounds. This is important for realistic representation of oil weathering because different oil compounds have dramatically different degradation rates. Moreover, simulations of biogeochemical processes and OPA formation rely on information about individual oil compounds in the ocean.

Numerous test runs have been conducted to assess performance of the individual components of the modeling system, as well as the whole system both in online and offline configurations. Results of these simulations (some of which have been presented here) demonstrate realistic movement of oil in the water column and at the surface, as well as its interaction with the sedimentation and biochemical constituents. The modeling code can be configured for simulation of particular spill events (see Morey et al., 2018). The following parameters need to be validated and adjusted for an individual oil spill event.

(1) Oil density parameters. Oil chemical composition differs depending on its origin. The difference is due to varying proportions of the compounds in different type of oils. Hence, densities of the oil compounds need to be adjusted for any particular oil. Weight fractions of the oil compounds are specified in the code (hard coded) and can be easily changed. The code can also be modified to include more than three (currently) oil compounds.
(2) Parameters controlling the ascent rate of oil particles in the float input file ($\overline{D}_{oil}$ and algorithm for computing oil particle vertical velocity).
(3) Surface oil drift parameters (C_w). Wind drag coefficient should be tuned for ocean surface currents depending on how accurately these currents represent wind-driven surface flow.
(4) Characteristics and representation of the oil spill (flow rate, release locations and frequency of Lagrangian floats).

The existing CSOMIO code is a ready-to-use tool, however, the model would benefit from future applications to realistic simulations during which the code could undergo further testing and improvements. The code is publicly available through the Gulf of Mexico Research Initiative Information and Data Cooperative (GRIIDC) (Dukhovskoy et al., 2020). The version of the code available through the GRIIDC does not currently have the offline capability.

Several additions to the model could be made to improve the performance of the CSOMIO model:

1. Optimization of the Lagrangian float code to better perform on parallel multiprocessor systems. The performance of the this module degrades as the number of floats increases;
2. Implementation of variable number of oil compounds (which is currently set to three);
3. Addition of a near-field module to simulate initial size of droplets distribution near the oil release;
4. Representation of other weathering processes (photo oxidation, emulsification, wave mixing);
5. Addition of wave effect to the surface oil drift;
6. Addition of droplet size dependent hydrocarbon uptake, because the surface area is thought to determine uptake rather than concentrations.
7. Addition of biological aggregates comprising oil and sediment particles (Alldredge and Silver, 1988; Passow et al., 2012; Daly et al., 2016).
8. Development of a rapid deployment tool suite that allows for model reconfiguration for other regions without extensive and time-consuming preparation of forcing fields and initial conditions.

DATA AVAILABILITY STATEMENT

The datasets presented in this study can be found in online repositories. The names of the repository/repositories and accession number(s) can be found below: https://data.gulfresearchinitiative.org. The dataset page is https://data.gulfresearchinitiative.org/data/R6.x803.000:0017. The dataset doi: 10.7266/JYQJVN6N.

AUTHOR CONTRIBUTIONS

DD developed OWTM, ELM, LEM codes and wrote the first draft of the manuscript. CH, LC, AM, and T-JH developed and tested OPAMOD. VC, JW, MS, and XC developed and tested the biochemical model. DD, KT, XC, and SM implemented and tested the offline algorithm in CSOMIO. CH, LC, VC, and JW wrote sections of the manuscript. All authors contributed to conception and design of the study. All authors contributed to writing, read, and approved the submitted version.

FUNDING

This research was made possible by the grant from the Gulf of Mexico Research Initiative. This manuscript is Contribution No. 3992 of the Virginia Institute of Marine Science, William and Mary.

ACKNOWLEDGMENTS

We thank Tracy Ippolito (FSU) for proofreading the manuscript and for the administrative support during the CSOMIO project.

REFERENCES

Abascal, A. J., Castanedo, S., Mendez, F. J., Medina, R., and Losada, I. J. (2009). Calibration of a Lagrangian transport model using drifting buoys deployed during the Prestige oil spill. *J. Coastal Res.* 25, 80–90. doi: 10.2112/07-0849.1

Alldredge, A. L., and Silver, M. W. (1988). Characteristics, dynamics and significance of marine snow. *Prog. Oceanogr.* 20, 41–82. doi: 10.1016/0079-6611(88)90053-5

American Society of Civil Engineers Committee on Modeling Oil Spills (1996). State-of-the-art review of modeling transport and fate of oil spills. *J. Hydraul. Eng.* 122, 594–609.

Bahadori, A., Mahmoudi, M., and Nouri, A. (2015). Prediction of heavy-oil viscosities with a simple correlation approach. *Oil Gas Facil.* 4, 66–72. doi: 10.2118/157360-PA

Bandara, U. C., Yapa, P. D., and Xie, H. (2011). Fate and transport of oil in sediment laden marine waters. *J. Hydro Environ. Res.* 5, 145–156. doi: 10.1016/j.jher.2011.03.002

Bracco, A., Paris, C. B., Esbaugh, A. J., Frasier, K., Joye, S. B., Liu, G., et al. (2020). Transport, fate and impacts of the deep plume of petroleum hydrocarbons formed during the Macondo blowout. *Front. Mar. Sci.* 7:764. doi: 10.3389/fmars.2020.542147

Camilli, R., Reddy, C. M., Yoerger, D. R., Van Mooy, B. A. S., Jakuba, M. V., Kinsey, J. C., et al. (2010). Tracking hydrocarbon plume transport and biodegradation at Deepwater Horizon. *Science* 330, 201–204. doi: 10.1126/science.1195223

Chen, F., and Yapa, P. D. (2003). A model for simulating deep water oil and gas blowouts – Part II: comparison of numerical simulations with Deepspill field experiments. *J. Hydr. Res.* 41, 353–365. doi: 10.1080/00221680309499981

Coles, V. J., Stukel, M. R., Brooks, M. T., Burd, A., Crump, B. C., Moran, M. A., et al. (2017). Ocean biogeochemistry modeled with emergent trait-based genomics. *Science* 358, 1149–1154. doi: 10.1126/science.aan5712

Cui, L., Harris, C. K., and Tarpley, D. R. N. (2020). Formation of oil-particle-aggregates (OPAs): numerical model formulation and calibration. *Front. Mar. Sci.*

Daly, K. L., Passow, U., Chanton, J., and Hollander, D. (2016). Assessing the impacts of oil-associated marine snow formation and sedimentation during and after the Deepwater Horizon oil spill. *Anthropocene* 13, 18–33. doi: 10.1016/j.ancene.2016.01.006

Davis, C. S., and Loomis, N. C. (2014). *Deepwater Horizon Oil Spill (DWHOS) Water Column Technical Working Group, Image Data Processing Plan: Holocam Description of Data Processing Methods Used to Determine Oil Droplet Size Distributions from in situ Holographic Imaging During June 2010 on Cruise M/V Jack Fitz 3*. Woods Hole, MA: Woods Hole Oceanographic Institution and MIT.

Diercks, A. R., Highsmith, R. C., Asper, V. L., Joung, D., Zhou, Z., Guo, L., et al. (2010). Characterization of subsurface polycyclic aromatic hydrocarbons at the deepwater horizon site. *Geophys. Res. Lett.* 37, 1–6. doi: 10.1029/2010GL045046

Dukhovskoy, D., Harris, C., Cui, L., Coles, V., Wang, J., Chen, X., et al. (2020). *CSOMIO Open Source Model System*. Tallahassee, FL: GRIDC Gulf of Mexico Research Initiative.

Dyer, K. R., and Manning, A. J. (1999). Observation of the size, settling velocity and effective density of flocs, and their fractal dimensions. *J. Sea Res.* 41, 87–95. doi: 10.1016/s1385-1101(98)00036-7

Fennel, K., Wilkin, J., Levin, J., Moisan, J., O'Reilly, J., and Haidvogel, D. (2006). Nitrogen cycling in the middle atlantic bight: results from a three-dimensional model and implications for the North Atlantic nitrogen budget. *Glob. Biogeochem. Cycles* 20, 1–14. doi: 10.1029/2005GB002456

Fingas, M. (1995). A literature review of the physics and predictive modelling of oil spill evaporation. *J. Hazard. Mater.* 42, 157–175. doi: 10.1016/0304-3894(95)00013-k

Fingas, M. (1996). The evaporation of oil spills: prediction of equations using distillation data. *Spill Sci. Technol. Bull.* 3, 191–192. doi: 10.1016/s1353-2561(97)00009-1

Fingas, M. (2012). Studies on the evaporation regulation mechanisms of crude oil and petroleum products. *Adv. Chem. Eng. Sci.* 2, 246–256. doi: 10.4236/aces.2012.22029

Fingas, M. (2015b). "Evaporation modeling," in *Handbook of Oil Spill Science and Technology*, ed. M. Fingas (Hoboken, NJ: John Wiley & Sons), 201–242.

Fingas, M. (2015a). "Introduction to oil chemistry and properties," in *Handbook of Oil Spill Science and Technology*, ed. M. Fingas (Hoboken, NJ: John Wiley & Sons), 51–77.

French-McCay, D., Li, Z., Horn, M., Crowley, D., Spaulding, M. L., Mendelson, D., et al. (2016). "Modeling oil fate and subsurface exposure concentrations from the deepwater horizon oil spill," in *Proceedings of the Thrity-ninth AMOP Technical Seminar*, (Ottawa, ON: Environment and Climate Change Canada), 115–150.

French-McCay, D., and Payne, J. R. (2001). "Model of oil fate and water concentrations with and without application of dispersants," in *Proceedings of the 24th Arctic and Marine Oilspill (AMOP) Technical Seminar, Edmonton, Alberta, Canada, June 12-14, 2001*, (Vancouver, BC: Environment Canada), 611–645.

Garcia-Martinez, R., and Flores-Tovar, H. (1999). Computer modeling of oil spill trajectories with a high accuracy method. *Spill Sci. Technol. B.* 5, 323–333. doi: 10.1016/s1353-2561(99)00077-8

Harris, C. K., Syvitski, J., Arango, H. G., Meiburg, E. H., Cohen, S., Jenkins, C. J., et al. (2020). Data-driven, multi-model workflow suggests strong influence from hurricanes on the generation of turbidity currents in the Gulf of Mexico. *J. Mar. Sci. Eng.* 8:28. doi: 10.3390/jmse8080586

Hiester, H.R., Morey, S. L., Dukhovskoy, D., Chassignet, E. P., Kourafalou, V. H., and Hu, C. (2016). A topological approach for quantitative comparisons of ocean model fields to satellite ocean color data. *Methods Oceanogr.*. 17, 232–250.

Hope, J. A., Malarkey, J., Baas, J. H., Peakall, J., Parsons, D. R., Manning, A. J., et al. (2020). Interactions between sediment microbial ecology and physical dynamics drive heterogeneity in contextually similar depositional systems. *Limnol. Oceanogr.* 65, 2403–2419. doi: 10.1002/lno.11461

Isobe, A., Kako, S., Chang, P., and Matsuno, T. (2009). Two-way particle-tracking model for specifying sources of drifting objects: application to the East China sea shelf. *J. Atmos. Oceanic Technol.* 26, 1672–1682. doi: 10.1175/2009JTECHO643.1

Klein, G. C., Angstrom, A., Rodgers, R. P., and Marshall, A. G. (2006). Use of Saturates/ Aromatics/ Resins/ Asphaltenes (SARA) fractionation to determine matrix effects in crude oil analysis by electrospray ionization fourier transform ion cyclotron resonance mass spectrometry. *Energy Fuels* 20, 668–672. doi: 10.1021/ef050353p

Kranenburg, C. (1994). The fractal structure of cohesive sediment aggregates. *Estuar. Coast. Shelf Sci.* 39, 451–460. doi: 10.1006/ecss.1994.1075

Lardner, R., and Zodiatis, G. (2017). Modelling oil plumes from subsurface spills. *Mar. Pollut. Bull. Bull.* 124, 94–101. doi: 10.1016/j.marpolbul.2017.07.018

Laurent, A., Fennel, K., Hu, J., and Hetland, R. (2012). Simulating the effects of phosphorus limitation in the Mississippi and atchafalaya river plumes. *Biogeosciences* 9, 4707–4723. doi: 10.5194/bg-9-4707-2012

Lehr, W., Jones, R., Evans, M., Simecek-Beatty, D., and Overstreet, R. (2002). Revisions of the ADIOS oil spill model. *Environ. Modell. Softw.* 17, 191–199.

Li, Z., Lee, K., King, T., Boufadel, M. C., and Venosa, A. D. (2008). Assessment of chemical dispersant effectiveness in a wave tank under regular non-braking and wave breaking wave conditions. *Mar. Pollut. Bull.* 56, 903–912. doi: 10.1016/j.marpolbul.2008.01.031

Lindo-Atichati, D., Paris, C. B., Le Hénaff, M., Schedler, M., Valladares Juárez, A. G., and Müller, A. (2016). Simulating the effects of droplet size, high-pressure biodegradation, and variable flow rate on the subsea evolution of deep plumes from the Macondo blowout. *Deep Sea Res. II Top. Stud. Oceanogr.* 129, 301–310. doi: 10.1016/j.dsr2.2014.01.011

Lonin, S. A. (1999). Lagrangian model for oil spill diffusion at sea. *Spill Sci. Technol. B* 5, 331–336. doi: 10.1016/s1353-2561(99)00078-x

Lubchenco, J., McNutt, M., Lehr, B., Sogg, M., Miller, M., Hammond, S., et al. (2010). *Deepwater Horizon/BP Oil Budget: What Happened to the Oil? National Oceanic and Atmospheric Administration Report*. Silver Spring, MD: National Oceanic and Atmospheric Administration.

Lubchenco, J., McNutt, M. K., Dreyfus, G., Murawski, S. A., Kennedy, D. M., Anastas, P. T., et al. (2012). Science in support of the Deepwater Horizon response. *Proc. Nat. Acad. Sci. U.S.A.* 109, 20212–20221. doi: 10.1073/pnas.1204729109

MacDonald, I. R., Dukhovskoy, D., Bourassa, M., Morey, S., Garcia-Pindea, O., Daneshgar, A., et al. (2016). *Remote Sensing Assessment of Surface Oil Transport and Fate during Spills in the Gulf of Mexico*. New Orleans, LA: U.S. Department of the Interior, 115.

Manning, A. J., Whitehouse, R. J. S., and Uncles, R. J. (2017). "Suspended particulate matter: the measurements of flocs," in *ECSA Practical Handbooks on Survey and Analysis Methods: Estuarine and Coastal Hydrography and Sedimentology, Chapter 8*, eds R. J. Uncles and S. Mitchell (Cambridge: Cambridge University Press), 211–260. doi: 10.1017/9781139644426

Mason, O. U., Hazen, T. C., Borglin, S., Chain, P. S. G., Dubinsky, E. A., Fortney, J. L., et al. (2012). Metagenome, metatranscriptome and single-cell sequencing reveal microbial response to Deepwater Horizon oil spill. *ISME J.* 6, 1715–1727. doi: 10.1038/ismej.2012.59

Mehta, A. J., Manning, A. J., and Khare, Y. P. (2014). A Note on the Krone deposition equation and significance of floc aggregation. *Mar. Geol.* 354, 34–39. doi: 10.1016/j.margeo.2014.04.002

Melvin, A. T., Thibodeaux, L. J., Parsons, A. R., Overton, E., Valsaraj, K. T., and Nandakumar, K. (2016). Oil-material fractionation in Gulf deep water horizontal intrusion layer: Field data analysis with chemodynamic fate model for Macondo 252 oil spill. *Mar. Pollut. Bull.* 105, 110–119. doi: 10.1016/j.marpolbul.2016.02.043

Molski, A. (1989). On the collision efficiency approach to flocculation. *Coll. Polym. Sci.* 267, 371–375. doi: 10.1007/BF01413632

Morey, S., Wienders, N., Dukhovskoy, D. S., and Bourassa, M. A. (2018). Measurement characteristics of near-surface currents from ultra-thin drifters, drogued drifters, and HF radar. *Rem. Sens.* 10:1633. doi: 10.3390/rs10101633

North, E. W., Adams, E. E., Thessen, A. W., Schalg, Z., He, R., Socolofsky, S. A., et al. (2015). The influence of droplet size and biodegradation on the transport of subsurface oil droplets during theDeepwater Horizon spill: a model sensitivity study. *Environ. Res. Lett.* 10:024016. doi: 10.1088/1748-9326/10/2/024016

Özgökmen, T. M., Chassignet, E. P., Dawson, C. N., Dukhovskoy, D., Jacobs, G., Ledwell, J., et al. (2016). Over what area did the oil and gas spread during the 2010 Deepwater Horizon oil spill? *Oceanography* 29, 96–107.

Paris, C. B., Le Hénaff, M., Aman, Z. M., Subramaniam, A., Helgers, J., Wang, D. P., et al. (2012). Evolution of the Macondo well blowout: simulating the effects of the circulation and synthetic dispersants on the subsea oil transport. *Environ. Sci. Technol.* 46, 13293–13302. doi: 10.1021/es303197h

Parsons, D. R., Schindler, R. J., Hope, J. A., Malarkey, J., Baas, J. H., Peakall, J., et al. (2016). The role of biophysical cohesion on subaqueous bed form size. *Geophys. Res. Lett.* 43, 1566–1573. doi: 10.1002/2016GL067667

Passow, U., Ziervogel, K., Asper, V., and Diercks, A. (2012). Marine snow formation in the aftermath of the Deepwater Horizon oil spill in the Gulf of Mexico. *Environ. Res. Lett.* 7:035301.

Perlin, N., Berenshtein, I., Vaz, A. C., Faillettaz, R., Schwing, P. T., Romero, P. T., et al. (2020). "Far-field modeling of deep-sea blowout: sensitivity studies of initial conditions, biodegradation, sedimentation and SSDI on surface slicks and oil plume concentrations," in *Deep Oil Spills: Facts, Fate, Effects*, eds S. A. Murawski, C. Ainsworth, S. Gilbert, D. Hollander, C. B. Paris, M. Schlüter, et al. (Cham: Springer).

Peters, F., and Arabali, D. (2013). Interfacial tension between oil and water measured with a modified contour method. *Coll. Surf. A Physiochem. Eng. Aspects* 426, 1–5.

Reddy, C. M., Arey, J. S., Seewald, J. S., Sylva, S. P., Lemkau, K. L., Nelson, R. K., et al. (2012). Composition and fate of gas and oil released to the water column during the Deepwater Horizon oil spill. *Proc. Natl. Acad. Sci. U.S.A.* 109, 20229–20234. doi: 10.1073/pnas.1101242108

Reed, D. C., Algar, C. K., Huber, J. A., and Dick, G. J. (2014). Gene-centric approach to integrating environmental genomics and biogeochemical models. *Proc. Natl. Acad. Sci. U.S.A.* 111, 1879–1884. doi: 10.1073/pnas.1313713111

Reed, M., Johansen, O., Brandvik, P. J., Daling, P., Lewis, A., Fiocco, R., et al. (1999). Oil spill modeling towards the close of the 20th century: overview of the state of the art. *Spill Sci. Technol. Bull.* 5, 3–16. doi: 10.1016/s1353-2561(98)00029-2

Reed, M., Turner, C., and Odulo, A. (1994). The role of wind and emulsification in modelling oil spill and surface drifter trajectories. *Spill SciTechnol. B.* 1, 143–157.

Roden, E. E., and Jin, Q. (2011). Thermodynamics of microbial growth coupled to metabolism of glucose, ethanol, short-chain organic acids, and hydrogen. *Appl. Environ. Microbiol.* 77, 1907–1909. doi: 10.1128/AEM.02425-10

Roels, J. A. (1981). The application of macroscopic principles to microbial metabolism. *Ann. N. Y. Acad. Sci.* 369, 113–134. doi: 10.1111/j.1749-6632.1981.tb14182.x

Sanchez-Minero, F., Sanchez-Reyna, G., Ancheyta, J., and Marroquin, G. (2014). Comparison of correlations based on API gravity for predicting viscosity of crude oils. *Fuel* 138, 193–199. doi: 10.1016/j.fuel.2014.08.022

Saha, S., Moorthi, S., H?L Pan, X. W., Wang, J., Nadiga, S., Tripp, P., et al. (2010). The NCEP climate forecast system reanalysis. *Bull. Am. Meteorol. Soc.* 91, 1015–1058. doi: 10.1175/2010BAMS3001.1

Samuels, W. B., Huang, N. E., and Amstutz, D. E. (1982). An oilspill trajectory analysis model with a variable wind deflection angle. *Ocean Eng.* 9, 347–360.

Sharqay, M. H., Lienhard, J. H., and Zubair, S. M. (2010). Thermophysical properties of seawater: a review of existing correlations and data. *Desal. Water Treat.* 16, 354–380. doi: 10.5004/dwt.2010.1079

Sherwood, C. R., Aretxabaleta, A. L., Harris, C. K., Rinehimer, J. P., Verney, R., and Ferré, B. (2018). Cohesive and mixed sediment in the Regional Ocean Modeling System (ROMS v3.6) implemented in the Coupled Ocean–Atmosphere–Wave–sediment transport modeling system (COAWST r1234). *Geosci. Model Dev.* 11, 1849–1871. doi: 10.5194/gmd-11-1849-2018

Socolofsky, S. A., Adams, E. E., Paris, C. B., and Yang, D. (2016). How do oil, gas, and water interact near a subsea blowout? *Oceanography* 29, 64–75. doi: 10.5670/oceanog.2016.63

Socolofsky, S. A., Adams, E. E., and Sherwood, C. R. (2011). Formation dynamics of subsurface hydrocarbon intrusions following the Deepwater Horizon blowout. *Geophys. Res. Lett.* 38:L09602. doi: 10.1029/2011GL047174

Soulsby, R. L., Manning, A. J., Spearman, J., and Whitehouse, R. J. S. (2013). Settling velocity and mass settling flux of flocculated estuarine sediments. *Mar. Geol.* 339, 1–12. doi: 10.1016/j.margeo.2013.04.006

Spaulding, M. S., Li, Z., Mendelsohn, D., Crowley, D., French-McCay, D., and Bird, A. (2017). Application of an integrated blowout model system, OILMAP DEEP, to the deepwater horizon (DWH) spill. *Mar. Pollut. Bull.* 120, 37–50. doi: 10.1016/j.marpolbul.2017.04.043

Speight, J. G. (2007). *The Chemistry and Technology of Petroleum*, 4th Edn.Boca Raton, FL: CRC Press, 980.

Stiver, W., and Mackay, D. (1984). Evaporation rate of spills of hydrocarbons and petroleum mixtures. *Environ. Sci. Technol.* 11, 834–840. doi: 10.1021/es00129a006

Thyng, K. M., Kobashi, D., Ruiz-Xomchuk, V., Qu, L., Chen, X., and Hetland, R. D. (2021). Performance of offline passive tracer advection in the Regional Ocean Modeling System (ROMS; v3.6, revision 904). *Geosci. Model Dev.* 14, 391–407. doi: 10.5194/gmd-14-391-2021

U.S. Senate Committee on Environment and Public Works (2010). *Timeline of the Gulf Coast Oil Spill and Emergencey Response*. Available online at: https://www.epw.senate.gov/public/index.cfm/2010/5/post-8408bd41-802a-23ad-4464-ad127e495a41 (accessed May 7, 2010).

Valentine, D. L., Mezić, I., Maćešić, S., Črnjarić-Žic, N., Ivić, S., Hogan, P. J., et al. (2012). Dynamic autoinoculation and the microbial ecology of a deep water hydrocarbon irruption. *Proc. Natl. Acad. Sci. U.S.A.* 109, 20286–20291. doi: 10.1073/pnas.1108820109

van der Mheen, M., Charitha, P., Simone, C., and Moritz, W. (2020). Depth-dependent correction for wind-driven drift current in particle tracking applications. *Front. Mar. Sci.* 7:305. doi: 10.3389/fmars.2020.00305

Vaz, A. C., Paris, C. B., Dissanayake, A. L., Socolofsky, S. A., Gros, J., and Boufadel, M. C. (2019). "Dynamic coupling of near-field and far-field models," in *Deep Oil Spills: Facts, Fate, Effects*, eds S. A. Murawski, C. Ainsworth, S. Gilbert, D. Hollander, C. B. Paris, M. Schlüter, et al. (Cham: Springer), doi: 10.1007/978-3-030-11605-7_9

Verney, R., Lafite, R., Brun-Cottan, J. C., and Le Hir, P. (2011). Behaviour of a floc population during a tidal cycle: laboratory experiments and numerical modelling. *Continent. Shelf Res.* 31, S64–S83. doi: 10.1016/j.csr.2010.02.005

Vilcáez, J., Liu, L., and Hubbard, S. S. (2013). A new model for the biodegradation kinetics of oil droplets: application to the Deepwater Horizon oil spill in the Gulf of Mexico. *Geochem. Trans.* 14:4.

Warner, J. C., Armstrong, B., He, R., and Zambon, J. B. (2010). Development of a coupled ocean-atmosphere-wave-sediment transport (COAWST) modeling system. *Ocean Model.* 35, 230–244. doi: 10.1016/j.ocemod.2010.07.010

Warner, J. C., Sherwood, C. R., Signell, R. P., Harris, C. K., and Arango, H. G. (2008). Development of a three-dimensional, regional, coupled wave, current, and sediment-transport model. *Comput. Geosci.* 34, 1284–1306. doi: 10.1016/j.cageo.2008.02.012

Winterwerp, J. C., Manning, A. J., Martens, C., de Mulder, T., and Vanlede, J. (2006). A heuristic formula for turbulence-induced flocculation of cohesive sediment. *Estuar. Coast. Shelf Sci.* 68, 195–207. doi: 10.1016/j.ecss.2006.02.003

Xu, K., Harris, C. K., Hetland, R. D., and Kaihatu, J. M. (2011). Dispersal of Mississippi and Atchafalaya sediment on the Texas–Louisiana shelf: Model estimates for the year 1993. *Continent. Shelf Res.* 31, 1558–1575. doi: 10.1016/j.csr.2011.05.008

Yapa, P. D., Wimalaratne, M. R., Dissanayake, A. L., and DeGraff, J. A. Jr. (2012). How does oil and gas behave when released in deepwater? *J. Hydro Environ. Res.* 6, 275–285. doi: 10.1016/j.jher.2012.05.002

Yapa, P. D., and Zheng, L. (1997). Simulation of oil spills from underwater accidents I: model development. *J. Hydraul. Res.* 35, 673–687. doi: 10.1080/00221689709498401

Yarranton, H. W., Okafor, J. C., Ortiz, D. P., and van den Berg, G. A. (2015). Density and refractive index of petroleum, cuts, and mixtures. *Energy Fuels* 29, 5723–5736. doi: 10.1021/acs.energyfuels.5b01376

Ye, L., Manning, A. J., and Hsu, T.-J. (2020). Oil-mineral flocculation and settling velocity in saline water. *Water Res.* 173:115569. doi: 10.1016/j.watres.2020.115569

Zang, Z., Xue, Z. G., Bao, S., Chen, Q., Walker, N. D., Haag, A. S., et al. (2018). Numerical study of sediment dynamics during hurricane Gustav. *Ocean Model.* 126, 29–42. doi: 10.1016/j.ocemod.2018.04.002

Zhang, L., and Yapa, P. D. (2000). Buoyant velocity of spherical and nonspherical bubbles/ droplets. *J. Hydraul. Eng.* 126, 852–854. doi: 10.1061/(asce)0733-9429(2000)126:11(852)

Zodiatis, G., Lardner, R., Alves, T. A., Krestenitis, Y., Perivoliotis, L., Sofianos, S., et al. (2017). Oil spill forecasting (prediction) in: THE SEA: the science of Ocean Prediction. *J. Mar. Res.* 75, 923–953.

Conflict of Interest: AM was employed by company HR Wallingford Ltd., United Kingdom.

The remaining authors declare that the research was conducted in the absence of any commercial or financial relationships that could be construed as a potential conflict of interest.

frontiers in Marine Science

ORIGINAL RESEARCH
published: 13 May 2021
doi: 10.3389/fmars.2021.629476

Formation of Oil-Particle-Aggregates: Numerical Model Formulation and Calibration

Linlin Cui[1]*, Courtney K. Harris[1]* and Danielle R. N. Tarpley[1,2]

[1] Virginia Institute of Marine Science, William & Mary, Gloucester Point, VA, United States, [2] Coastal and Hydraulics Laboratory, United States Army Corps of Engineers, Vicksburg, MS, United States

Edited by:
Andrew James Manning,
HR Wallingford, United Kingdom

Reviewed by:
Byung Joon Lee,
Kyungpook National University,
South Korea
Junhong Liang,
Louisiana State University,
United States

***Correspondence:**
Linlin Cui
lcui@vims.edu
Courtney K. Harris
ckharris@vims.edu

Specialty section:
This article was submitted to
Marine Pollution,
a section of the journal
Frontiers in Marine Science

Received: *14 November 2020*
Accepted: *14 April 2021*
Published: *13 May 2021*

Citation:
Cui L, Harris CK and Tarpley DRN (2021) Formation of Oil-Particle-Aggregates: Numerical Model Formulation and Calibration. Front. Mar. Sci. 8:629476. doi: 10.3389/fmars.2021.629476

When oil spills occur in turbid waters, the oil droplets and mineral grains can combine to form oil-particle aggregates (OPAs). The formation of OPAs impacts the vertical transport of both the oil and the mineral grains; especially increasing deposition of oil to the seabed. Though the coastal oceans can be very turbid, to date, few numerical ocean models have accounted for aggregation processes that form OPAs. However, interactions between oil and mineral aggregates may be represented using techniques developed to account for sediment aggregation. As part of Consortium for Simulation of Oil Microbial Interactions in the Ocean (CSOMIO), we modified an existing, population dynamics-based sediment flocculation model to develop OPAMOD, a module that accounts for the formation of OPAs. A zero-dimensional model using OPAMOD is shown to be capable of reproducing the size distribution of aggregates from existing laboratory experimental results. Also using the zero-dimensional model, sensitivity tests were performed on two model parameters, the fractal dimension and collision efficiency. Results showed that fractal dimension played a role in the OPA size distribution by influencing the effective particle density, which modified the number concentration of flocs for a given mass concentration. However, the modeled particle characteristics and oil sequestration were relatively insensitive to collision efficiency. To explore OPA formation for an outer continental shelf site, two simulations were conducted using a one-dimensional (vertical) implementation of the model. One scenario had high sediment concentration near the seabed to mimic storm-induced resuspension. The other scenario represented river plume sediment delivery by having high sediment concentration in surface waters. Results showed that OPA formation was sensitive to the vertical distribution of suspended sediment, with the river plume scenario creating more OPA, and sequestering more oil within OPA than the storm resuspension scenario. OPAMOD was developed within the Coupled Ocean-Atmosphere-Wave-and-Sediment Transport (COAWST) modeling system, therefore the methods and parameterizations from this study are transferrable to a three-dimensional coupled oil-sediment-microbial model developed by CSOMIO within the COAWST framework.

Keywords: oil-particle aggregates, flocculation, fractal dimension, numerical modeling, oil spill

INTRODUCTION

Oil spills have detrimental impacts on coastal ecosystems and marine life (Nixon et al., 2016; Bam et al., 2018; Robinson and Rabalais, 2019; Martin et al., 2020). As a result, oil models have been developed to predict the transport and fate of oil, often by employing Lagrangian particle tracking (Zhu et al., 2018). However, predicting the fate of oil is difficult as it is influenced by a variety of processes, such as spreading, evaporation, and degradation for surface slicks; and emulsification, degradation, and dissolution for oil droplets in the subsurface. In addition, aggregation of oil and suspended particulate material has been considered an important process to remove free oil (Lee, 2002; Payne et al., 2003). It was reported that significant oil sedimentation can occur when suspended particulate concentrations reach 0.01 kg m^{-3}, and large deposition events were associated with sediment concentrations of at least 0.1 kg m^{-3} (Boehm, 1987). The Mississippi River mouth delivers significant quantities of both freshwater and sediment into the northern Gulf of Mexico. Suspended sediment concentrations vary seasonally. The Mississippi River discharge peak occurs during the spring, when it is about twice as high as the low flow in the fall (Thorne et al., 2008). A previous study showed that the formation of OPAs in the Mississippi River varied depending on the time of year with a higher probability during winter and spring when suspended sediment concentrations were high, $\sim$0.35 kg m^{-3} (Danchuk and Willson, 2011). With an aggregation kinetic model, Sterling et al. (2004) found that the timescale for aggregation of oils and clays was within an order of magnitude for the timescale of clay settling, thus, aggregation provided a mechanism for oil sedimentation. Nevertheless, numerical models for oil-sediment interactions are limited, especially in three-dimensional oil models for the coastal ocean.

When oil interacts with organic matter, such as bacteria, phytoplankton, or detritus; they can form a type of aggregate called Marine Oil Snow (MOS). Marine Oil Snow Sedimentation and Flocculent Accumulation (MOSSFA) is a significant pathway for the fate of oil. Studies showed that $\sim$4–31% of the Deepwater Horizon oil settled on the seafloor *via* MOSSFA (Valentine et al., 2014). These aggregates are more common in areas where primary productivity is high and suspended sediment concentrations are relatively low (<0.01 kg m^{-3}), such as the open ocean (Daly et al., 2016). Compared to OPA, the MOS tend to reach larger diameters (Stoffyn-Egli and Lee, 2002). Simulation of MOS has obtained substantial interest since the Deepwater Horizon oil spill. For example, Dissanayake et al. (2018) developed a one-dimensional model to simulate MOS formation and settling in the ocean. This provided valuable insight into the vertical processes that govern MOSSFA formation and transport, but to date these processes have not been included in a three-dimensional model capable of estimating dispersal.

Different terminologies have been used to describe aggregates that incorporate oil along with sediment, such as oil-mineral aggregate (OMA) (Lee and Stoffyn-Egli, 2001; Ye et al., 2020), oil-sediment aggregate (OSA) (Bandara et al., 2011), and oil-particle aggregate (OPA) (Fitzpatrick et al., 2015; Zhao et al., 2016). We use the term OPA in this study, because this has been preferred to describe microscopic aggregates. In terms of structure, three types of OPAs were identified from microscopy imageries: droplet OPAs, solid OPAs, and flake OPAs (Stoffyn-Egli and Lee, 2002). Droplet OPAs are single or multiple oil droplets coated by sediment particles; solid OPAs are a mixture of oil and sediment particles where clear oil droplets cannot be seen; flaked OPAs have a membrane-like shape, are fragile and break apart in high shear conditions, thus they are rarely observed in nature (Stoffyn-Egli and Lee, 2002). When oil is delivered to areas of high turbidity, such as surf zones and river plumes, OPAs provide a means of delivering oil to the seafloor (Daly et al., 2016). In general, OPAs observed *in situ* are small (<50 micron–1 mm) (Stoffyn-Egli and Lee, 2002). Sediment mineralogy can affect the formation and shape of OPAs. A recent laboratory study investigated the formation of OPAs with crude oil and two types of cohesive minerals: kaolinite and bentonite clay (Ye et al., 2020). They showed that bentonite clay had a higher stickiness than kaolinite, and tended to produce solid, higher-settling velocity OPAs. Based on these results, along with the fact that bentonite is more like the clay observed near Mississippi River Delta than kaolinite (Jaisi et al., 2008), solid OPAs formed from oil and bentonite clay were considered in this study.

Numerical flocculation models that represent particle aggregation and breakup have a long history within sediment-transport (Lick et al., 1992; Winterwerp, 1998), and can provide a method to represent OPA formation. There are two main approaches to representing particle sizes in these sediment flocculation models. The first type are distribution-based models, in which floc size distribution is fixed but the modeled sizes change in response to turbulence, concentration, etc. (Khelifa and Hill, 2006; Winterwerp et al., 2006). The other method uses size-class-based models that calculate the particle population by distributing mass among a discrete number of fixed size classes (Verney et al., 2011). Unlike distribution-based models, size-class-based models can provide detailed information about floc populations. Recently, a size-class-based flocculation model (FLOCMOD) (Verney et al., 2011) has been implemented within the COAWST (Coupled-Ocean-Atmosphere-Wave-Sediment Transport) model (Sherwood et al., 2018) and tested in an idealized, partially mixed estuary to investigate cohesive sediment distribution over a tidal cycle (Tarpley et al., 2019). To date, however, these types of flocculation models have solely been used to characterize the fate and aggregation of sediment. We expand upon these by using the FLOCMOD numerical framework to account for the formation of OPA that incorporate oil, sediment, and water within aggregates.

An important parameter in representing the formation and evolution of aggregates of particles is the fractal dimension, which generally represents the shape and packing of an aggregate (Wiesner, 1992; Kranenburg, 1994). Fractal dimension has been used to represent sediment flocs, marine snow, and oil-mineral aggregates, among other aggregate types. Fractal dimensions can range from 1 to 3, with a value of three representing a solid particle, such as sand grains. Natural sediment flocs typically have a fractal dimension close to 2.1 (Tambo and Hozumi, 1979; Kranenburg, 1994), with broadly reported fractal dimensions with the range of 1.7 $\sim$ 2.85 (Wiesner, 1992).

However, for sediment flocs, some studies have reported higher fractal dimensions, between 2.6 and 3.0 (Lee et al., 2002). Fractal dimensions have also been reported for marine snow, falling in the range of 1.3 ∼ 2.3 (Burd and Jackson, 2009). The main factors that can affect the fractal dimension include turbulence (Logan and Kilps, 1995; Dyer and Manning, 1999), the shape (e.g., ellipsoidal and spherical) of the primary particles (Perry et al., 2012), and the makeup of the components (e.g., mineral types, organic matters, and oil) (Lee et al., 2002; Jarvis et al., 2005; Ye et al., 2020). In the laboratory, fractal dimensions can be indirectly estimated from properties related to aggregate size, such as settling velocity. Based on this method, Ye et al. (2020) reported that fractal dimension of kaolinite-oil aggregates varied from 2.4 to 2.6, while fractal dimension of bentonite-oil aggregates was in the range of 2.2–2.4. Flocculation and aggregation models often assume a single average fractal dimension throughout all size ranges. For instance, Dissanayake et al. (2018) chose a fractal dimension of 2.2 to represent the MOS aggregates in their one-dimensional model. FLOCMOD also assumes a constant fractal dimension (Verney et al., 2011; Sherwood et al., 2018). For example, Tarpley et al. (2019) used a fractal dimension of 2.4 for FLOCMOD in a two-dimensional sediment transport model.

An objective of our study was to develop a module capable of simulating oil-particle aggregation that could be coupled to other components of the COAWST modeling system. To accomplish this, we developed OPAMOD, a population-balance module based on FLOCMOD, but modified to account for the formation of OPAs. Further motivation was to facilitate the use of OPAMOD within a three-dimensional implementation of COAWST that coupled hydrodynamic, sediment, microbial, and oil components (Dukhovskoy et al., 2021). This coupled model included hydrodynamics, sediment transport, and biogeochemical modules available from ROMS (Shchepetkin and McWilliams, 2005; Fennel et al., 2006; Haidvogel et al., 2008; Warner et al., 2008). To these modules, Dukhovskoy et al. (2021) added OPAMOD, OWTM (the Oil Weathering and Transport Module), and a module to account for biological weathering of oil (Coles et al., 2020). They then used the fully coupled model to estimate oil dispersal for situation similar to the Deepwater Horizon event for a timescale of several days. To be useful within the fully coupled model required that OPAMOD carry a moderate computational expense. Additionally, the application focused on transport of oil droplets over the continental slope and outer continental shelf, where sediment concentrations and turbulence levels are relatively low. This meant that our formulation could focus on the aggregate formation process to account for settling of oil *via* OPA, and neglect potential breakup of OPA once formed as has been done by similar models (Bandara et al., 2011; Zhao et al., 2016).

The rest of this paper describes the development of OPAMOD and two stand-alone applications. Specifically, Section "Materials and Methods" describes model development. A zero-dimensional model implementation was then used to validate model performance based on available laboratory data, and test its sensitivity to parameters (Section "Zero-Dimensional Model Implementation and Results"). Next, a one-dimensional model was used to represent an oil spill on a continental slope setting to evaluate the relative importance of OPA formation under storm, and freshwater plume scenarios (Section "Scenarios: Implementation of One-Dimensional Model"). Conclusions and discussion are given in Section "Conclusion and Discussion."

MATERIALS AND METHODS

This section describes the modeling framework and assumptions used to represent the formation of OPAs. The new module, OPAMOD, was implemented within the hydrodynamic model, ROMS, which is the ocean model component of COAWST.

Existing COAWST System Including FLOCMOD

The COAWST modeling system was developed to couple the ROMS hydrodynamic model with Weather Research and Forecasting Model (WRF) and Simulating Waves Nearshore (SWAN) to provide two-way links between the hydrodynamic (ROMS), atmospheric (WRF), and wave (SWAN) models (Warner et al., 2010). ROMS is capable of solving for the transport of tracer fields, including salinity, temperature, sediment, etc. (Haidvogel et al., 2008). The Community Sediment Transport Modeling System (CSTMS) was implemented in ROMS for sediment transport and evolution of bottom morphology (Warner et al., 2008). Further model development added processes of sediment flocculation (FLOCMOD) including aggregation and disaggregation (Sherwood et al., 2018). FLOCMOD is a population-balance module using a finite number of floc size classes based on Verney et al. (2011). Each floc class is assumed to have the same fractal dimension, but assigned a different floc diameter, floc density, and setting velocity. FLOCMOD has been tested in one-dimensional simulations to reproduce a tidal cycle variation of sediment flocs from a laboratory experiment (Sherwood et al., 2018), and two-dimensional simulation for an idealized, muddy estuary (Tarpley et al., 2019). Within this paper we implemented COAWST to use ROMS, CSTMS, and the newly developed OPAMOD in zero-dimensional and one-dimensional configurations, as described below.

OPA Module Development

To account for OPA, the tracer fields in ROMS were expanded to include sediment flocs, oil droplets, and OPAs. These tracers for flocs, oil droplets, and OPAs were represented using a finite number of classes; each with a prescribed diameter, settling velocity, and density.

Assumptions

Our approach used a population-balance model for OPA formation and growth, specifically representing interactions between three types of tracers: oil droplets, sediment flocs, and OPAs (**Figure 1**). In nature, the formation, aggregation, and disaggregation of an OPA is complicated. Interactions include

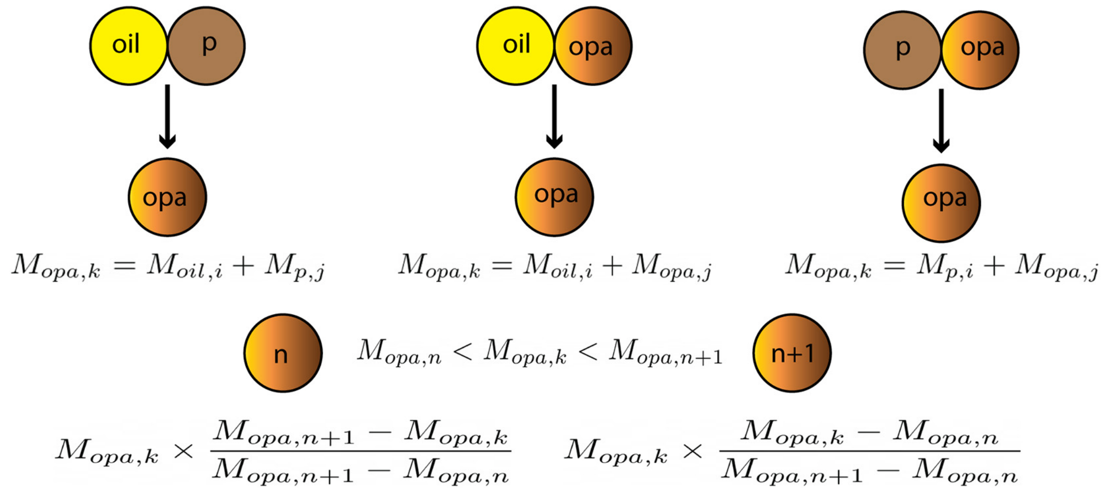

FIGURE 1 | Schematic of modeled formation processes for OPA. $M_{opa,k}$ is the mass of newly formed OPA of class *k*, which is the mass addition of two collision components (e.g., collision between the *ith* – class oil $M_{oil,i}$ and the *jth* – class sediment $M_{p,j}$). Assuming that $M_{opa,k}$ falls between two OPA classes, then this mass is mass-linearly distributed into the two neighboring classes [i.e. the *nth* and *(n+1)th* OPA classes].

collisions between particles and droplets that can form larger particles or droplets; or can result in the breakup into smaller particles and droplets (Lee et al., 1997). An oil droplet can coalesce with other oil droplets to form a larger oil droplet; or with sediment flocs to create OPAs; also, an oil droplet can interact with OPAs. Likewise, a sediment floc can combine with other sediment flocs to form larger flocs; or with oil droplets to form OPAs; or interact with existing OPAs. Finally, OPAs can interact with other OPAs. The simulation was conducted with concentration thresholds for both sediment and oil; i.e., the OPA aggregation process was not invoked when concentrations were below 0.001 kg m^{-3}. To reduce model complexity while addressing the primary goal of providing estimates of OPA formation and sinking for use on continental shelves, the following assumptions were made:

(1) Including all potential aggregation and disaggregation processes in the model would require a large number of parameters and high degree of complexity. As noted above, a variety of aggregation processes can occur in coastal systems that include sediment and oil droplets. To reduce the complexity and increase computational efficiency, the implementation of this model only considered interactions between oil droplets and sediment flocs, oil droplets and OPAs, and sediment flocs and OPAs (**Figure 1**), following Zhao et al. (2016).
(2) Collision between two entities can result from turbulent motions, differential settling, and Brownian motion. Collisions due to Brownian motion are unimportant in ocean systems and shear-induced collisions are dominant in turbulent environments (Sherwood et al., 2018), therefore, we only implemented collisions due to fluid shear in the model.
(3) Sediment flocs, oil droplets, and OPAs were assumed to be spherical.
(4) The fractal behavior of OPAs was assumed to be the same as that of sediment flocs, which is consistent with laboratory observations of Ye et al. (2020). Therefore, the effective density was related to the primary particle diameter and density through fractal dimension in the following relationship (Kranenburg, 1994):

$$\rho_e = (\rho_s - \rho_w)(\frac{D}{D_p})^{n_f - 3} \tag{1}$$

where ρ_e is the effective density of the floc or OPA, ρ_s is the density of the particle, and ρ_w is the density of water. D is the diameter; and D_p is the diameter of the primary particle, i.e. the smallest floc particle. The fractal dimension is n_f.
(5) Each sediment class and OPA class was assigned a diameter, density, and settling velocity as model input parameters.
(6) Formed OPAs are considered to be stable, i.e., the model neglected OPA breakup processes. This assumption is consistent with previous models (Bandara et al., 2011; Zhao et al., 2016), and seemed reasonable for meeting the primary objective of accounting for OPA formation, settling and subsequent removal of oil from the water column. It effectively considers the OPA to be resilient to breakup and avoids an added complexity in the model of specifying the particle makeup that would be produced *via* breakup.

Governing Equations of OPA Formation Process

At model implementation, the input files specify the number of tracer classes to be included; specifically, the value of *nsed* represents the number of sediment floc classes, *noil* represents the number of oil droplet classes, and *nopa* represents the number of OPA classes. Changes to the number concentration (i.e. $N_{OIL,i}$, $N_{P,j}$, and $N_{OPA,i}$) due to mass exchanges among classes were simulated to represent aggregation between two different class types. The model tracks the time variation of the number concentration of OPA in the m^{th} class ($N_{OPA,m}$) as the sum of gain and loss terms:

$$\begin{aligned}\frac{dN_{OPA,m}}{dt} &= \underbrace{\sum_{i=1}^{noil}\sum_{j=1}^{nsed}\alpha A\left(i,j\right) N_{OIL,i}N_{P,j}}_{oil-sediment\ gain} + \underbrace{\sum_{i=1}^{nopa}\sum_{j=1}^{nsed}\alpha A\left(i,j\right) N_{OPA,i}N_{P,j}}_{opa-sediment\ gain} \\ &+ \underbrace{\sum_{i=1}^{noil}\sum_{j=1}^{nopa}\alpha A\left(i,j\right) N_{OIL,i}N_{OPA,j}}_{oil-opa\ gain} - \underbrace{N_{OPA,m}\sum_{j=1}^{nsed}\alpha A\left(m,j\right) N_{P,j}}_{opa-sediment\ loss} \\ &- \underbrace{N_{OPA,m}\sum_{j=1}^{noil}\alpha A\left(i,j\right) N_{OIL,j}}_{oil-opa\ loss} \end{aligned} \qquad (2)$$

where α represents collision efficiency. Note that this formulation used a single value for α regardless of the types of particles involved in a collision. Zhao et al. (2016) developed an estimate for coagulation efficiency applied on the conceptual basis of sediment particles coating an oil droplet. Dissanayake et al. (2018) cited values of alpha that ranged from 0.08 to 0.8, depending on the makeup of the particle (i.e., organic material, mineral content, oil content). However, these were not directly applicable to the solid OPAs conceptualized for this study, nor could they be directly implemented within the full coupled model. Additionally, our sensitivity study below indicated that the model was not particularly sensitive to α. For these reasons we used a constant value for α, though it would be relatively straightforward to use particle-type dependent values provided guidance for its parameterization. Finally, the collision probability, $A\left(i,j\right)$ is given by:

$$A\left(i,j\right) = \frac{1}{6}G(D_i + D_j)^3 \qquad (3)$$

where D_i and D_j are diameters of two colliding entities; G is the shear rate, which can be expressed by energy dissipation rate ε and kinematic viscosity ν, as $G = \sqrt{\varepsilon/\nu}$.

The time variation of the number concentration of sediment particles in the i^{th} class ($N_{P,i}$) is calculated as:

$$\frac{dN_{P,i}}{dt} = \underbrace{-N_{P,i}\sum_{j=1}^{noil}\alpha A\left(i,j\right) N_{OIL,j}}_{oil-sediment\ loss} - \underbrace{N_{P,i}\sum_{j=1}^{nopa}\alpha A\left(i,j\right) N_{OPA,j}}_{opa-sediment\ loss} \qquad (4)$$

Finally, the time variation of the number concentrations of oil droplets in the i^{th} class ($N_{OIL,i}$) is calculated as:

$$\frac{dN_{OIL,i}}{dt} = \underbrace{-N_{OIL,i}\sum_{j=1}^{nsed}\alpha A\left(i,j\right) N_{P,j}}_{oil-sediment\ loss} \underbrace{-N_{OIL,i}\sum_{j=1}^{nopa}\alpha A\left(i,j\right) N_{OPA,j}}_{oil-opa\ loss} \qquad (5)$$

OPAMOD classifies OPAs by density ($\rho_{i,opa}$), vertical terminal velocity ($w_{i,opa}$), and median diameter ($D_{i,opa}$), for OPA sizes i=1, … *nopa*. Since OPAMOD tracks a finite number of OPA classes, the mass of each newly formed OPA is mass-linearly distributed into two neighboring classes (Bandara et al., 2011; Verney et al., 2011) rather than assigning the total mass to one class (**Figure 1**).

ZERO-DIMENSIONAL MODEL IMPLEMENTATION AND RESULTS

OPAMOD was implemented within a quasi-zero-dimensional framework, as described below. This was first used to demonstrate that the model results compared favorably to laboratory observations of OPA properties, and to aid with selection of model parameters (Section "Model Comparison With Laboratory Experimental Data"). Next, the zero-dimensional implementation was used to evaluate the sensitivity of OPA properties to the choice of the collision efficiency and fractal dimension (Section "Sensitivity Tests").

Model Comparison With Laboratory Experimental Data

The first set of model results were compared with experimental data from Ye et al. (2020) who conducted six laboratory experiments to investigate characteristics (e.g., settling velocity, effective density, and fractional dimension) of OPAs formed from kaolinite or bentonite clays mixed with crude oil. Previous studies have shown that when the ratio of oil to sediment is close to two, it can reach a maximum OPA formation efficiency (Guyomarch et al., 2002; Khelifa et al., 2008). Ye et al. (2020) therefore generated OPAs by adding 0.5 g of clay and 1.0 g of Texas crude oil into a jar containing 1.0 L of artificial seawater. The mixture was stirred at 490 rpm, which gave an estimated turbulence dissipation rate ε about 0.02 m^2s^{-3}. The turbulence was maintained for up to 2 h, and then flocs and OPAs were collected and analyzed from materials after they settled overnight. Statistical analysis of these experimental samples showed that the floc and OPA sizes varied from 20 to 700 μm. Bentonite clays tended to generate compact, negatively buoyant OPAs (Ye et al., 2020).

To compare with these laboratory measurements, we configured a quasi-zero-dimensional model in ROMS to simulate the scenario where OPAs formed from oil and bentonite clay. The shear rate G was specified as 20 s^{-1} over the simulation time of 2 h, replicating the laboratory experiment. In actuality, the ROMS implementation was a small three-dimensional grid, but the model was effectively zero-dimensional because conditions were uniform, the horizontal boundary conditions were periodic, and settling velocities were set to zero to maintain a vertically uniform suspension. The quasi-zero-dimensional simulation therefore operated as uniform in all three directions, so that the only mechanism for changes to the distributions of sediment, oil droplets, and OPA were *via* the OPAMOD terms. The model used five sediment classes, twelve OPA classes, and six oil classes (**Table 1**). The initial concentrations of sediment and oil, shown in **Figure 2**, were 0.5 and 1.0 kg m^{-3}, respectively, to match laboratory conditions (Ye et al., 2020). The sediment mass concentration was evenly distributed among the five sediment classes (**Figure 2A**), and the initial oil distribution was as shown (**Figure 2B**). In this simulation, the collision efficiency was 0.35, and fractal dimension was 2.3, which were obtained using model calibration simulations to match the laboratory results. The primary particle diameter was 4 μm, which matched the value used by Ye et al. (2020).

Within the model, the mixtures of sediment and oil quickly combined to form OPAs, and the OPA concentrations and size distributions reached a steady state within the first few minutes of the simulation. **Figure 3** compares the number fraction of modeled and experimental OPAs. The size distribution produced by the model had good agreement with experimental data. The modeled OPA size peaked in class 6 ($D = 220$ μm), which accounted for about 18% of the total number of OPA, while the experimental OPA size peaked in class 5 ($D = 180$ μm) with a number fraction of ∼20% (**Figure 3A**). Both the modeled and experimental OPAs were mainly composed of small and medium aggregates (>95% of the population, **Figure 3B**). However, the number fraction of modeled small OPAs (class 2 and 3, $D = 60$ and 100 μm) slightly exceeded that of experimental ones (**Figure 3B**).

Sensitivity Tests

Next, sensitivity tests were run to evaluate the impact of uncertainties in model parameters on the resulting size distributions of OPAs. The primary model parameters, fractal dimension and collision efficiency (n_f in Equation 1; and α in Equations 2, 4, 5), were each varied for a series of model runs, and the resultant effect on the size distribution of OPAs was assessed. The final size distribution of OPAs was seen to be quite sensitive to the fractal dimension, and insensitive to collision efficiency.

Collision efficiency (α) represents the probability with which colliding constituents (sediment, oil droplets, or OPA) combine to form larger OPA. Values reported in the literature include 0.4 for heterogeneous collision efficiency (e.g., oil-clay), and 0.7 for homogeneous collision efficiency (e.g., sediment-sediment), respectively (Sterling et al., 2004; Bandara et al., 2011). Six numerical experiments were run to test how variations in collision efficiency influenced modeled OPA

TABLE 1 | Diameters (*D*, μm) for sediment (MUD, five size classes), OPA (twelve size classes), and oil droplets (six size classes).

	1	**2**	**3**	**4**	**5**	**6**	**7**	**8**	**9**	**10**	**11**	**12**
MUD	30	60	100	140	180							
OPA	30	60	100	140	180	220	280	360	440	520	600	680
Oil	40	60	80	100	120	140						

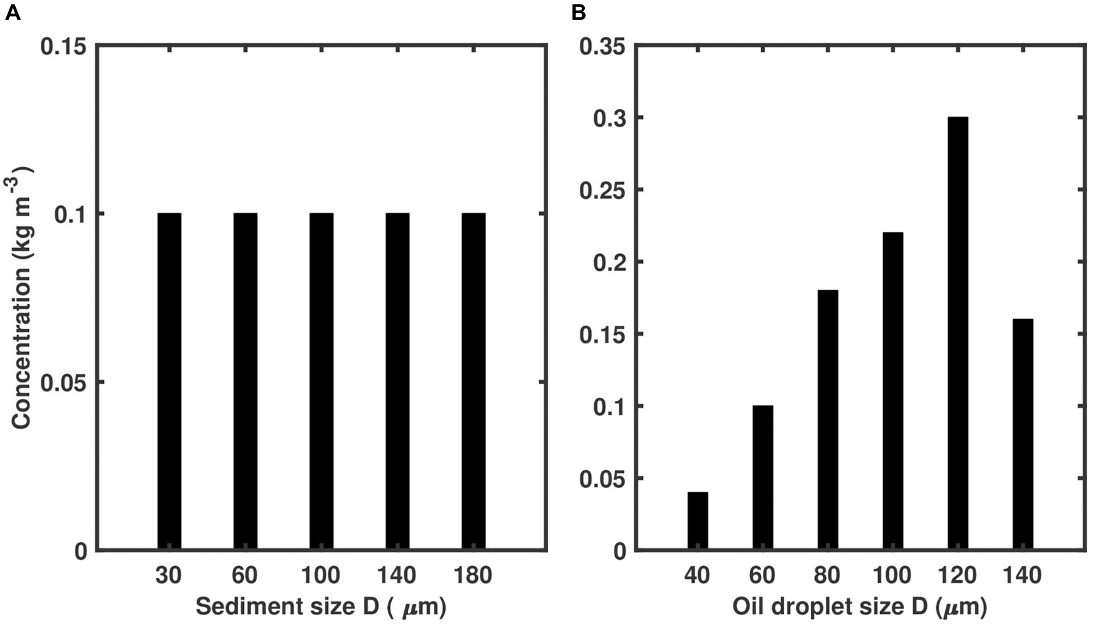

FIGURE 2 | Initial size mass concentration distributions for OPAMOD simulation of **(A)** sediment particles, and **(B)** oil droplets.

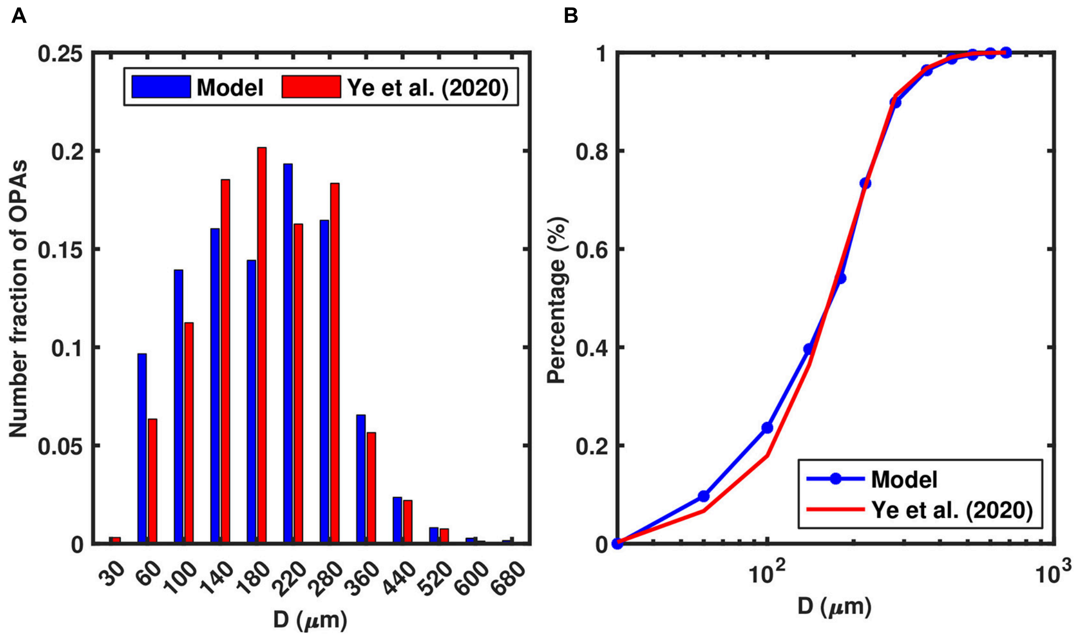

FIGURE 3 | Comparison of the number fraction of oil-bentonite aggregates between the lab experiments (Ye et al., 2020) and 0-D model that included OPAMOD after a simulation time of 2 h. **(A)** Histogram of OPA sizes, **(B)** Cumulative number percentage of OPAs.

formation, with collision efficiencies that ranged from 0.2 to 0.7. For these simulations, the fractal dimension (n_f) was held constant at 2.3. The final OPA size distributions for these simulations are shown in **Figure 4**. The case that had a higher collision efficiency had slightly higher OPA concentrations in the middle-sized classes (180 μm $< D <$ 360 μm), and concentrations were slightly shifted to the larger OPA classes for the case having lower collision efficiency. The modeled OPA size distributions were fairly insensitive to collision efficiency.

Next, to estimate the relative influence of fractal dimension on the size distribution of OPAs, six numerical experiments were run where fractal dimension was varied from 2.0 to 2.5. For these simulations, collision efficiency was held at 0.3. Note that because fractal dimension represents the shape and packing of aggregates, particles with higher fractal dimensions are denser than particles of the same diameter with lower fractal dimension (Equation 1). Each of these sensitivity tests had the same initial sediment concentration by mass (0.1 kg m^{-3}, matching Ye et al., 2020). Because they had different fractal dimensions, however they were each initialized with different number concentrations ($N_{P,i}$). As the fractal dimension for the test increased, the initial number of sediment particles decreased. Because the population balance equations are based on number concentrations, this had an impact on the frequency of collisions and thus likelihood of formation of OPAs. The results of the fractal dimension sensitivity tests are illustrated as the final OPA size distributions by number of particles (**Figure 5A**), and the final size distribution by mass concentration (**Figure 5B**). As the assumed fractal dimension increased, the OPA size distribution shifted from coarse toward fine aggregates. For the sensitivity test that used a fractal dimension of 2.5, the finer classes ($D \leq$ 140 μm) accounted for almost 65% of the number concentration (**Figure 5A**). For the simulation that used a fractal dimension of 2.0, finer classes made up less than 10% of the total (**Figure 5A**). For simulations with intermediate fractal dimensions (2.2 and 2.3), the intermediate classes (D from 180 to 360 μm) contained greater than 60% of the number concentrations. In terms of mass concentrations, as the fractal

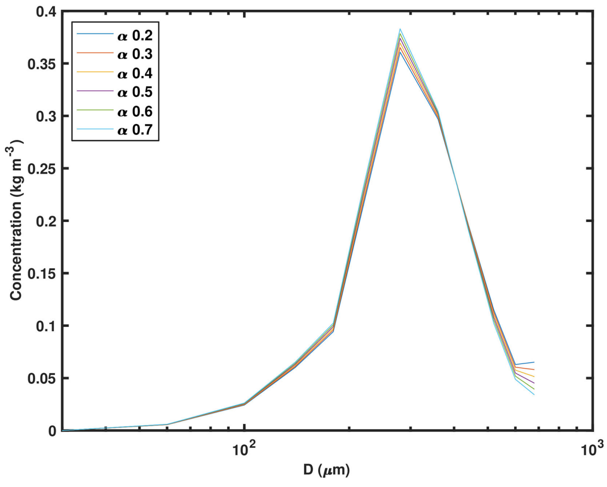

FIGURE 4 | Size distribution by mass concentration of OPA at the end of 2 h simulation calculated using different collision efficiencies (see legend). A fractal dimension of n_f = 2.3 was used for these simulations.

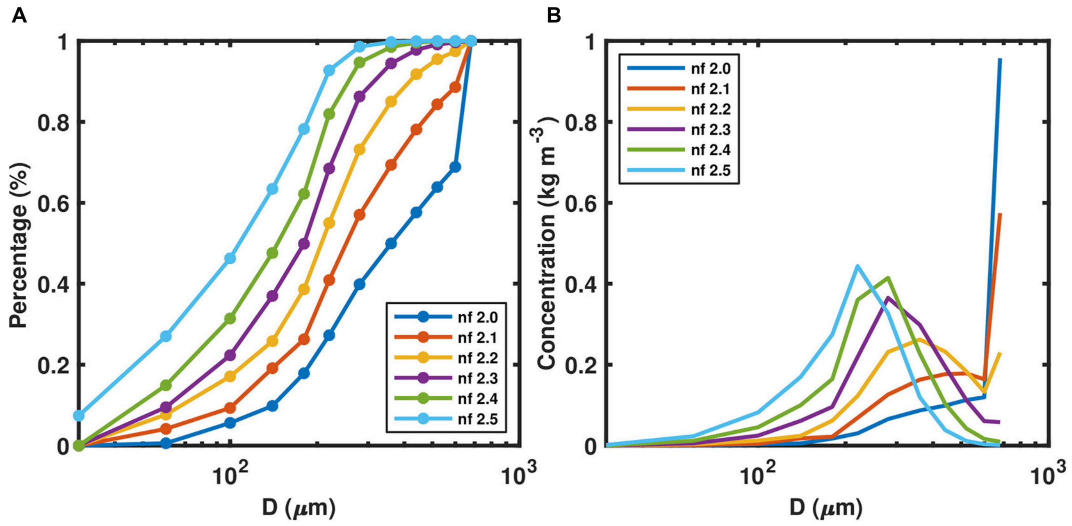

FIGURE 5 | Size distributions of OPA calculated at the end of 2 h simulation using different fractal dimensions (see legend). A collision efficiency of 0.3 was used for these simulations. **(A)** The cumulative distribution by % of the number of particles. **(B)** Size distribution by mass concentration.

dimension decreased, the OPA shifted toward the larger diameter particles (**Figure 5B**).

SCENARIOS: IMPLEMENTATION OF ONE-DIMENSIONAL MODEL

Next, the formation of OPA was examined in the context of an oceanographic water column, using a quasi-one-dimensional approach. These scenarios were motivated by consideration of a contamination event at the Taylor Energy Company's Mississippi Canyon Block 20 platform (MC20), and used oceanographic fields (SSC, velocity) from a three-dimensional numerical model as described below.

Background of MC20 Site

In September of 2004, Hurricane Ivan passed through the northern Gulf of Mexico as a category 3 storm generating 22 m waves, and destroying seven drilling platforms (Mason, 2019). The Taylor Energy Mississippi Canyon 20 (MC20) oil and gas drilling platform, which is located about 16 km southeast of the mouth of the South Pass of the Mississippi River, was toppled by storm-triggered submarine mudslides. On 17 September 2004, 1 day after the passage of Ivan, surface oil slicks were found around the MC20 site. About 10 days later, satellite images showed oil floating over the sediment-laden coastal waters offshore of the Mississippi delta (Mason, 2019). Since then, oil plumes and surface oil slicks have been observed at the MC20 site from ships and satellite remote sensing (Mason, 2019). Estimates of the oil flux rate span from roughly 9–108 barrels of oil per day, based on acoustic surveys and bubblometer surveys (MacDonald et al., 2019). The MC20 site is located at a water depth of approximately 140 m, where the fine sediment (silt and clay) percentage exceeds 90% (Mason, 2019).

Sediment from the Mississippi River is widely dispersed within 20–40 km from the bird-foot delta (Xu et al., 2011). Located within 16 km of the South Pass of the Mississippi River, the MC20 site is therefore often influenced by the Mississippi River freshwater and sediment plume. Additionally, during large storms, this location may be impacted a bottom nepheloid layer sourced from sediment resuspended from the adjacent continental shelf by energetic waves. However, it is difficult to quantify potential interactions between oil released at this site, and sediments in either the surface freshwater plume, or in a bottom nepheloid layer. Therefore, the MC20 scenario provides a good example to implement one-dimensional (vertical) model to explore the potential for sediment / oil interactions to impact the dispersal of oil in similar settings.

Configuration of One-Dimensional Model

The quasi-one-dimensional model was configured to generally represent steady conditions for the MC20 site. The one-dimensional model was actually a small three-dimensional implementation, with 5×6 horizontal grid cells, and 50 vertical grid cells. Lateral periodic boundary conditions were applied meaning that anything exiting the domain horizontally reentered on the upstream side, creating a uniform flow field in the horizontal. The oil concentration was initialized to be vertically uniform and set to 0.2 kg m^{-3}, based on estimates from the BP/Deepwater Horizon Oil Spill (Sammarco et al., 2013). The size distribution of oil was assumed to be the same mass percentage as in the 0D simulation (**Figure 2B**). Hydrodynamic and suspended sediment conditions were obtained from a 1-year long ROMS simulation (1 October, 2007 through 30 September, 2008) of the northern Gulf of Mexico that included times of large river discharge, and two hurricanes (Harris et al., 2020). The one-dimensional model started from rest and was nudged to a steady flow condition; matching values of velocity, temperature, salinity, and suspended sediment concentrations extracted from a larger-scale ROMS simulation (Harris et al., 2020). After a 2 h spin-up time to allow for the flow to accelerate and reach steady state, OPAMOD was activated. The fractal dimension and collision efficiency were set to 2.3 and 0.35, respectively. As done for the zero-dimensional model (Section "Zero-Dimensional Model Implementation and Results"), the one-dimensional sediment-OPAMOD model used five cohesive sediment classes, twelve OPA classes, and six oil droplet classes (**Table 1**). The effective density (Equation 1) and settling velocity for sediment flocs and OPAs are shown in **Tables 2**, **3**, respectively. Here settling velocity are obtained from laboratory experiment (Ye et al., 2020). To avoid complexity in the suspended concentrations, and because little is known about either the erosion thresholds for OPA or the characteristics of eroded OPA; the critical shear stress was defined a high value (10 Pa) to prevent erosion from occurring. Rather, the initial suspended sediment concentrations were derived from the larger scale ROMS model of Harris et al. (2020), which did include both river plume sedimentation and seabed resuspension.

TABLE 2 | Effective density (ρ_e, kg m^{-3}) and settling velocity (w_s, mm s^{-1}) for sediment size classes.

	1	2	3	4	5
ρ_e	396.56	244.11	170.72	134.90	113.14
w_s	0.135	0.480	1.105	1.480	1.886

The fractal dimension was 2.3 in the calculation.

TABLE 3 | Effective density (ρ_e, kg m^{-3}) and settling velocity (w_s, mm s^{-1}) for OPA size classes.

	1	2	3	4	5	6
ρ_e	396.56	244.11	170.72	134.90	113.14	98.31
w_s	0.433	0.597	0.725	1.459	2.186	2.873
	7	**8**	**9**	**10**	**11**	**12**
ρ_e	83.04	69.64	60.51	53.84	48.71	44.62
w_s	3.673	5.497	7.087	8.348	13.696	11.003

The fractal dimension was 2.3 in the calculation.

Hurricane Scenario

First, the one-dimensional model was implemented to study oil-sediment interaction under energetic waves to explore interactions between oil contamination and a bottom nepheloid layer created by resuspended sediment during a tropical storm. The model results from Harris et al. (2020) estimated that about 30% of the suspended sediment delivered to the continental slope of the northern Gulf of Mexico for the 1-year simulation

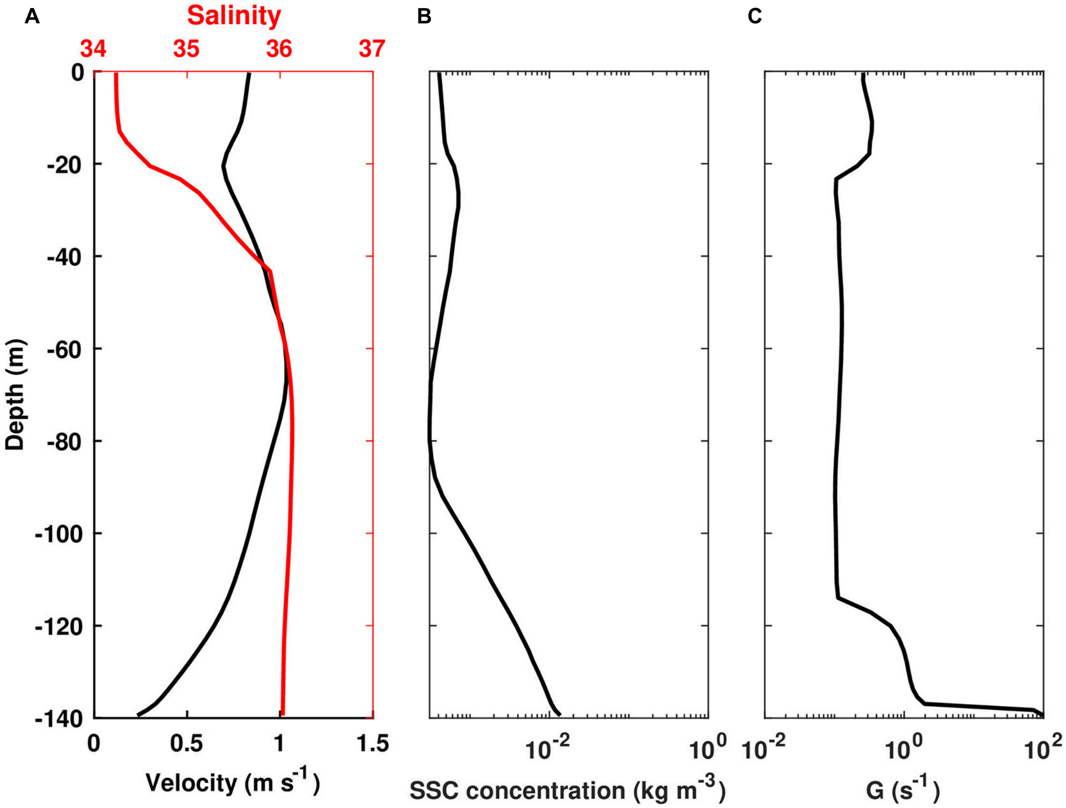

FIGURE 6 | Profiles of **(A)** velocity and salinity, **(B)** initial suspended sediment mass concentration, and **(C)** shear rate for the hurricane scenario (**A,B** are based on model output from Harris et al., 2020. **C** is from 1D model output).

period occurred during hurricanes Gustav and Ike. For this scenario we therefore used Hurricane Gustav, the second most catastrophic hurricane of the year 2008 (Brown et al., 2010). Gustav made landfall in southeast Louisiana on 1 September 2008 as category 2 hurricane. Model results indicated that wave-induced bottom orbital velocities exceeded 4 m s^{-1} in coastal areas and wave-induced resuspensions occurred offshore to water depth of 189 m (Harris et al., 2020). **Figure 6A** shows the vertical profiles of velocity and salinity used as forcing, which were extracted from the three-dimensional model output from Harris et al. (2020). The velocity exceeded 1.0 m s^{-1} at mid-depth. The salinity profile showed an upper mixed layer extending to about 15 m depth. Fresher water in the mixed layer indicated the influence of the Mississippi River plume. The vertical profile of initial sediment concentration included a ∼40 m thick bottom nepheloid layer where concentrations increased to about 0.01 kg m^{-3} near the seafloor (**Figure 6B**). The sediment concentration was assumed to be evenly distributed among five sediment classes at each vertical level. The simulation period was 12 h, which allowed OPAMOD to operate for 10 h.

Figures 7A,B show the depth-integrated OPA and suspended sediment concentrations, respectively. After the initial 2-h hydrodynamic spin-up time, OPAMOD was activated in the model and the mixture of oil and sediment began to form OPA. The depth-integrated OPA mass concentration peaked around

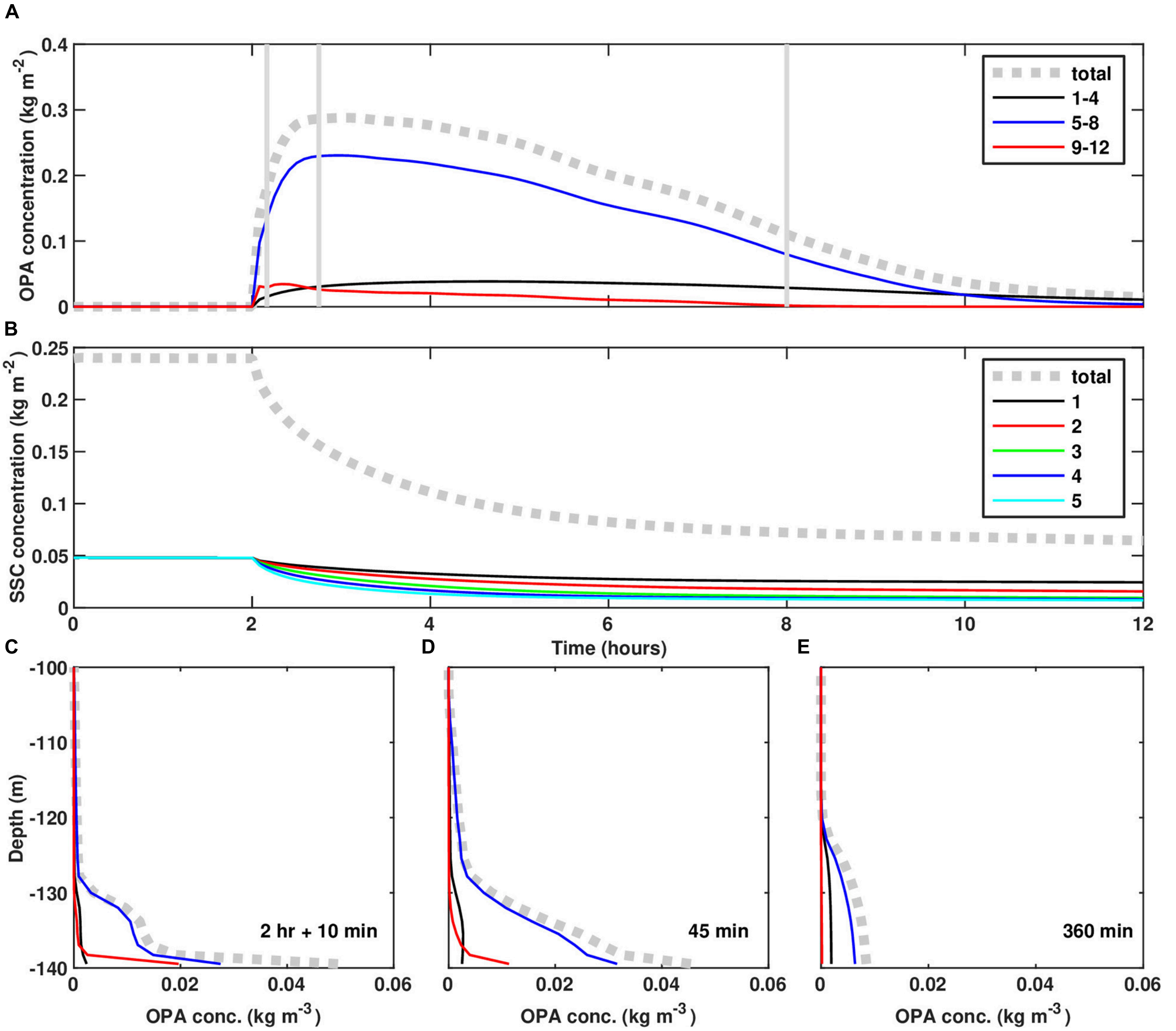

FIGURE 7 | Time-series for the hurricane scenario of depth-integrated **(A)** OPA mass concentration and **(B)** SSC mass concentration. Profiles of OPA mass concentration at **(C)** 10 min, **(D)** 25 min, and **(E)** 360 min after activating OPAMOD, respectively. Lines in panels **(C–E)** share the same legend shown in panel **(A)**, with dotted gray line representing the total OPA size classes, black line representing the OPA size classes from 1 to 4, blue line representing the OPA size classes from 5 to 8, and red line representing the OPA size classes from 9 to 12, respectively.

45 min after the aggregation process commenced, and increased to about 0.3 kg m^{-2}. During this time, depth-integrated sediment concentrations saw a rapid decrease (from 0.25 to < 0.1 kg m^{-2}), as suspended sediment was converted to OPA. After the peak, OPA concentrations decreased over the next 8 h as the OPAs settled to the seafloor (**Figure 7A**). The size distribution of OPAs mainly fell in the medium size range (classes 5–8, having $D = 180 - 360\ \mu m$), whose concentration was about 10 times greater than that of small and large size ranges.

Vertical profiles of the OPA concentrations show that the aggregation process was evident in the bottom 40 m of water (**Figures 7C–E**). Directly after OPAMOD was initiated, OPA concentrations were especially high in the bottom few meters of the water column (**Figure 7C**) where sediment concentration was high (e.g., see **Figure 6B**) and turbulence was energetic (**Figure 6C**). The smaller classes of OPA ($D < 180\ \mu m$) were fairly well-mixed throughout the bottom boundary layer (black lines in **Figures 7A,C–E**), but did not reach high mass concentrations. The medium size classes of OPA ($D = 180 - 360\ \mu m$) dominated the presence of OPA, and were distributed through the bottom boundary layer (depths of ~130–140 m in **Figures 7C–E**). The larger OPA (red lines in **Figures 7A,C–E**, $D > 360\ \mu m$) settled to the seafloor quickly.

River Plume Scenario

Next, the one-dimensional model was applied to examine how sediment from river discharge can affect OPA formation. The velocity and salinity forcing came from the same model simulation as in hurricane scenario (i.e., Harris et al., 2020), but conditions including velocities, salinity, and suspended sediment concentrations were extracted for a period in March of 2008 that had elevated river discharge. The maximum velocity was ~ 0.8 m s^{-1} in the surface layer (**Figure 8A**). The vertical salinity profile reflected the influence of the Mississippi River plume in this locality, with a salinity difference greater than 10 PSU in the upper 20 m (**Figure 8A**). The suspended sediment concentration peaked near 30 m water depth, reaching ~ 0.017 kg m^{-3} (**Figure 8B**). The initial oil concentration was the same as used in the hurricane scenario, again initialized to be vertically uniform at 0.2 kg m^{-3}, based on Sammarco et al. (2013). The simulation period was 48 h, with the OPAMOD being activated after the first 2 h to allow for spin up of the hydrodynamic model.

Figures 9A,B show the depth-integrated OPA and suspended sediment mass concentrations, respectively. It took about 4 h for the mass concentration of suspended OPA to reach a maximum (**Figure 9A**, the first and second vertical gray lines). Suspended sediment mass concentrations began decreasing when OPAMOD was initiated (time = 2 h, **Figure 9B**), as sediment became

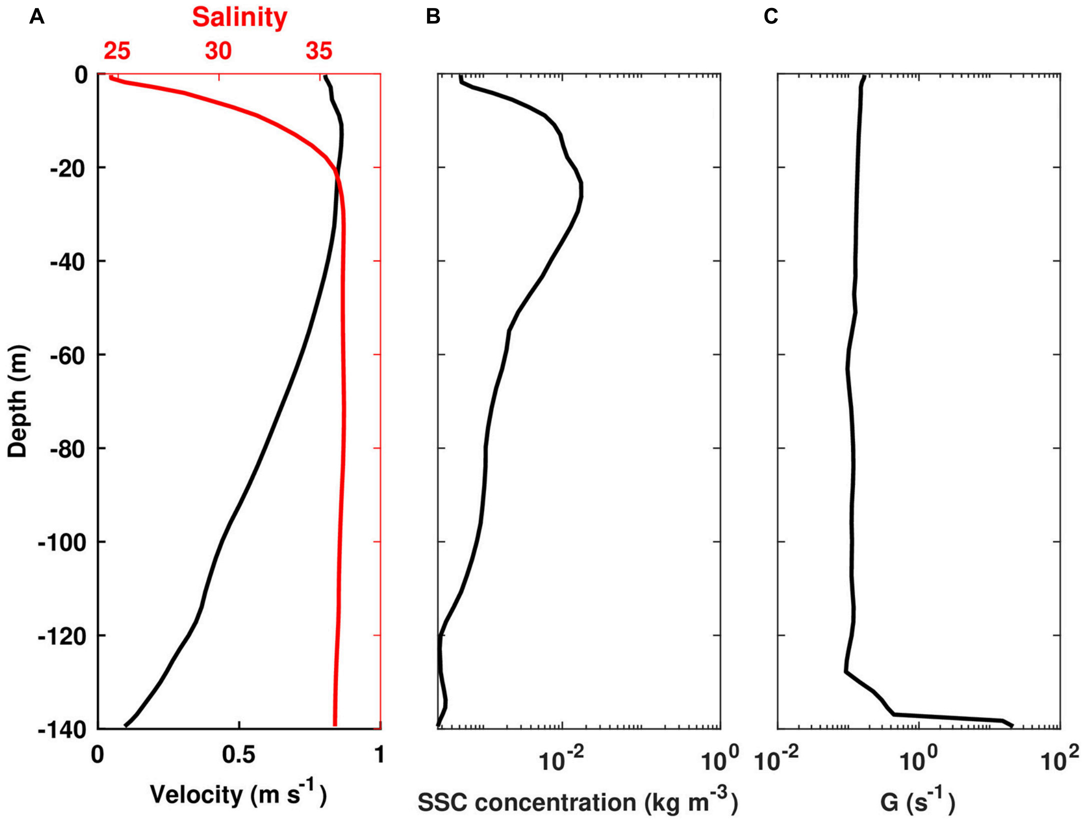

FIGURE 8 | Profiles of **(A)** velocity and salinity, **(B)** initial suspended sediment mass concentration, and **(C)** shear rate for the river plume scenario (**A,B** are based on model output from Harris et al., 2020. **C** is from 1D model output).

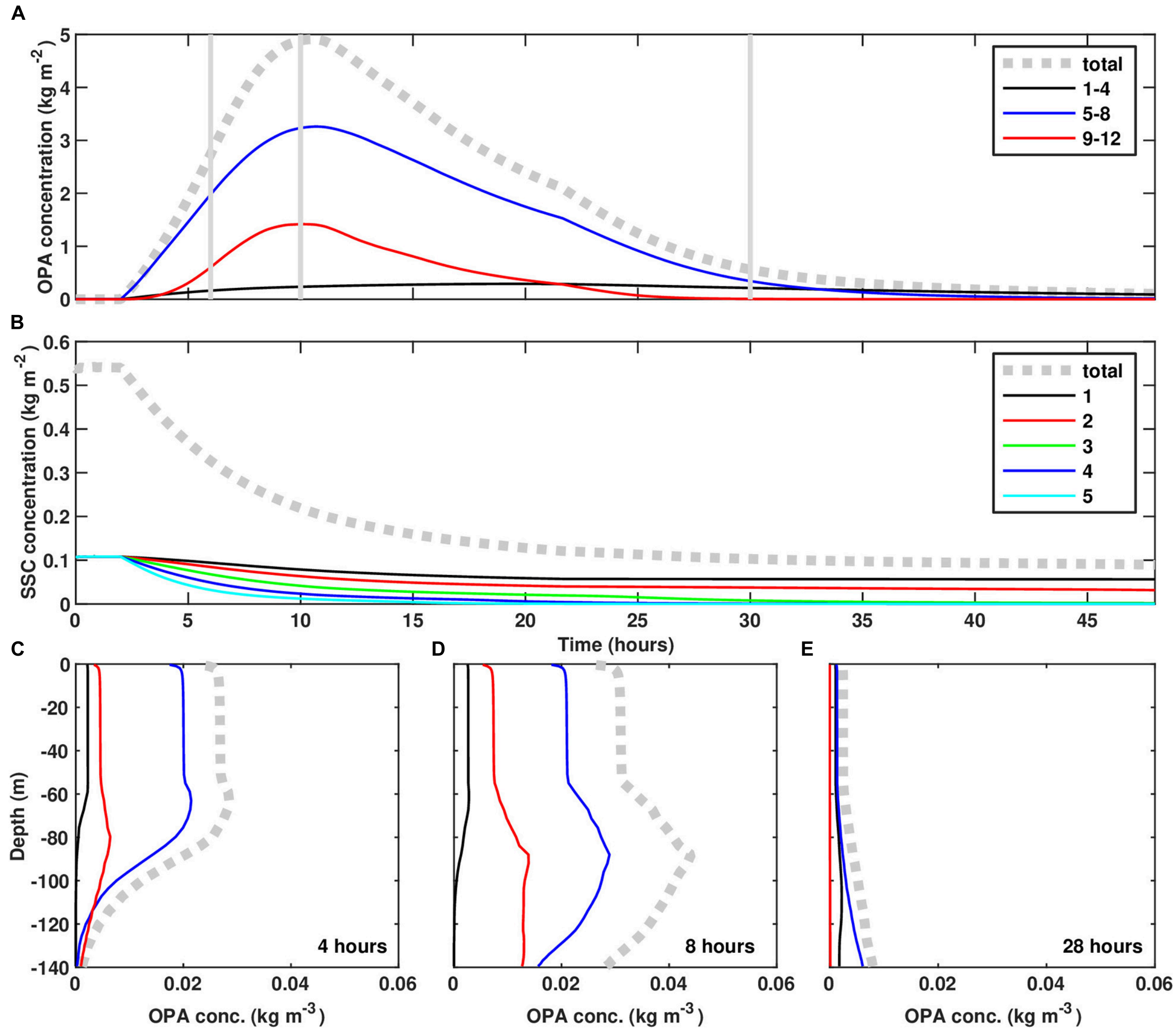

FIGURE 9 | Time-series for the river plume scenario of depth-integrated **(A)** OPA mass concentration and **(B)** SSC mass concentration. Profiles of OPA concentration at **(C)** hour 4, **(D)** hour 8, and **(E)** hour 28 after activating OPAMOD, respectively. Lines in panels **(C–E)** share the same legend shown in panel **(A)**, with dotted gray line representing the total OPA size classes, black line representing the OPA size classes from 1 to 4, blue line representing the OPA size classes from 5 to 8, and red line representing the OPA size classes from 9 to 12, respectively.

incorporated into OPA. Then, for the next ~30 h, the suspended sediment and OPA mass concentrations both decreased as sediment continued to be incorporated into OPA, and both OPA and sediment settled to the seafloor (**Figure 9A**). For the river plume case, the OPA mass concentrations were mainly distributed within the medium ($D = 180 - 360$ μm), and larger ($D > 360$ μm) sizes (red and blue lines in **Figure 9A**), though the medium sizes had a longer residence time in the water column.

The vertical concentration profiles show that OPA were present throughout the water column (**Figures 9C–E**). Initially, elevated suspended OPA concentrations were formed in the upper water column, where suspended sediment was available, so that OPA appeared in the top 80 m of the water column (**Figure 9C**). The higher settling velocities of the OPA, relative to the suspended sediment, caused the OPA to sink out of surface waters, but they continued to grow by scavenging the residual oil in the water column. While the smaller OPA sizes ($D < 180$ μm) were present in the freshwater plume, they did not reach large concentrations (**Figures 9C–E**), but instead served mainly to "seed" the growth of the larger sized OPAs. The medium and larger sizes reached notably high concentrations in the water column, and because they have relatively high settling velocities, provided a downward flux that resulted in elevated suspended OPA concentrations in the mid-water column (**Figure 9D**). After approximately 28 h, OPAs completely settled to the seafloor (**Figure 9E**).

CONCLUSION AND DISCUSSION

An oil-particle-aggregate module was developed and implemented in ROMS within the COAWST framework. Implementation of a quasi-zero-dimensional simulation demonstrated the ability to predict OPA formation and reproduce the particle size distribution observed in a laboratory study. Both the modeled and laboratory results showed that OPAs were dominated by small and medium sized aggregates ($D \leq 360$ μm). Comparison with laboratory results showed that our implementation of OPAMOD in ROMS behaved reasonably, indicating that the model can be a useful tool in representing the removal of oil *via* OPA formation. Sensitivity tests were conducted to examine how the model responded to two parameters: fractal dimension and collision efficiency. Results showed that the modeled size distributions were much more sensitive to fractal dimension than collision efficiency. According to Equation 1, floc density varies with fractal dimension; when a smaller fractal dimension was assumed, the initial number concentrations of sediment increased, which encouraged the formation of more and larger OPA.

Simulations of OPA formation impacted by a surface river plume and a hurricane event were conducted by configuring a quasi-one-dimensional model using conditions based on a 140-m deep site near Mississippi River Delta. These two scenarios allowed us to compare the relative importance of surface suspended sediments associated with a freshwater plume to bottom nepheloid layer suspended sediments associated with a resuspension event. Model results showed that the plume conditions were more effective at forming OPAs and creating a deposition event of OPAs. The main difference between these two scenarios was the vertical distributions of suspended sediment. In the hurricane scenario, high sediment concentrations were located in a bottom nepheloid layer. Thus, newly formed OPAs quickly settled out of the water column. In comparison, suspended sediment concentration was high in the surface layer for the river plume scenario. OPAs formed in surface waters, which gave OPAs longer residence times in the water column. During settling, OPAs scavenged more residual oil and sediment in the water column. For comparison, the depth-integrated suspended sediment mass concentration ($\sim$0.5 kg m^{-2}, **Figure 9B**) in the river plume scenario was about double that of the hurricane scenario (**Figure 9A**), but the maximum depth-integrated OPA mass concentration ($\sim$5 kg m^{-2}, **Figure 9B**) in the river plume scenario was about 15 times greater than that in the hurricane scenario (**Figure 7A**). Additionally, in the river plume scenario, the OPA remained in the water column for a longer time period, because the settling distance was so much greater. This implies that OPA formation *via* river plume sediment would lead to a more widely dispersed depositional footprint, compared to OPA formation *via* storm resuspension. Additionally, because river plume generated OPAs had longer residence times in the water column compared to resuspension generated OPAs, they would have more opportunity for degradation *via* water column weathering and consumption prior to deposition.

The current study is the first attempt of integrating an OPA module within a coupled hydrodynamic and sediment transport model. The one-dimensional model was run for scenarios representative of conditions that could lead to OPA formation over the Gulf of Mexico continental slope. In order to fully represent the formation and dispersal of OPA, however, OPAMOD can be implemented within a model that also accounts for horizontal transport. This has been done within a three-dimensional, fully coupled model which included OPAMOD, developed by the Consortium for Simulation of Oil-Microbial Interactions in the Ocean (CSOMIO) (Dukhovskoy et al., 2021). Implemented to represent the transport and fate of oil sourced from an oil spill in the northern Gulf of Mexico, this three-dimensional model represented oil transformations and transport, biological processes and feedbacks with oil (Coles et al., 2020) and formation of OPA through OPAMOD. The full three-dimensional coupled model therefore accounts for water column transport of hydrocarbons, as well as biodegradation, and delivery to the seabed *via* OPAs (Dukhovskoy et al., 2021). For the case modeled, the source of oil was in very deep waters and the results showed that the feedbacks between microbial processes and oil were more significant than OPA formation (Dukhovskoy et al., 2021). We postulate that the OPA formation would be significant for cases where the source of oil was near a turbid river plume, as shown for our one-dimensional river plume scenario; or in shallower water where resuspension creates higher turbidity.

However, application of OPAMOD to scenarios that have the potential for resuspension would require further model development to account for the resuspension of OPA and potential breakup of OPA under energetic conditions. For the current implementations, we set the erosion parameters for OPA to be very large so that resuspension would not occur. However, previously deposited OPA might be resuspended later, under more energetic conditions, thus providing a source of contamination some time after the initial contamination event. The model is equipped to account for resuspension, but would require proper parameterization of critical shear stress and the erosion rate parameter (Warner et al., 2008; Sherwood et al., 2018), from field or laboratory studies. Including OPA breakup would be more difficult, because the mass balance equations would need to specify the products formed by the disaggregation of large OPA. Within FLOCMOD, the fragmentation distribution function (FDBS) specifies how sediment mass from a larger floc is distributed into smaller flocs upon breakup (Verney et al., 2011; Sherwood et al., 2018). Similarly, inclusion of OPA breakup would require specification of how to partition the oil and sediment mass into smaller OPA, and / or sediment or oil classes.

The current formulation of OPAMOD also does not account for interactions between the biogenic detritus, oil, and sediment, which have been shown to form MOSSFA (Vonk et al., 2015; Quigg et al., 2020). Additionally, recent laboratory studies have shown that the collision efficiency for OPA formation may be sensitive to organic content of the particles (Ye et al., 2021). Adding coupling between the sediment, OPA, and biological modules within the CSOMIO model (Dukhovskoy et al., 2021) would be relatively straightforward because all of these components have been coded within the ROMS and COAWST frameworks. This model could become an important tool in determining the fate of oil and prediction of the impact of future oil spills.

DATA AVAILABILITY STATEMENT

The datasets presented in this study can be found on an online repository. The name of the repository/repositories and accession numbers can be found below: https://data.gulfresearchinitiative.org/. The dataset page is https://data.gulfresearchinitiative.org/data/R6.x803.000:0009.

AUTHOR CONTRIBUTIONS

LC, CH, and DT: conceptualization and writing-review and editing. LC and CH: methodology. LC: model development, implementation, analysis, and writing-original draft preparation. CH: supervision and funding acquisition. All authors have read and agreed to the published version of the manuscript.

FUNDING

This research was made possible by a grant from the Gulf of Mexico Research Initiative to support CSOMIO (Consortium for Simulation of Oil-Microbial Interactions in the Ocean) (GoMRI Award R01983).

ACKNOWLEDGMENTS

Leiping Ye (Sun Yat-sen University) provided laboratory data from his publications. The authors appreciate input from the CSOMIO group during model development, including Eric Chassignet, Dmitry Dukhovskoy, Tian-Jian Hsu, Andrew Manning, and Steve Morey. We appreciate input from the two reviewers, which greatly helped us to improve the manuscript. The authors acknowledge William and Mary Research Computing (https://www.wm.edu/it/rc) for providing computational resources that have contributed to the results reported within this paper. This paper is Contribution No. 4007 of the Virginia Institute of Marine Science, William & Mary.

REFERENCES

Bam, W., Hooper-Bui, L. M., Strecker, R. M., Adhikari, P. L., and Overton, E. B. (2018). Coupled effects of oil spill and hurricane on saltmarsh terrestrial arthropods. *PLos One* 13:e0194941. doi: 10.1371/journal.pone.0194941

Bandara, U. C., Yapa, P. D., and Xie, H. (2011). Fate and transport of oil in sediment laden marine waters. *J. Hydro Environ. Res.* 5, 145–156. doi: 10.1016/j.jher.2011.03.002

Boehm, P. D. (1987). "Transport and transformation processes regarding hydrocarbon and metal pollutants in offshore sedimentary environments," in *Long-Term Environmental Effects of Offshore Oil and Gas Development*, eds D. F. Boesch and N. N. Rabalais (London: Elsevier Appled Science), 233–287.

Brown, D. P., Beven, J. L., Franklin, J. L., and Blake, E. S. (2010). Atlantic hurricane season of 2008*. *Mon. Weather Rev.* 138, 1975–2001. doi: 10.1175/2009mwr3174.1

Burd, A. B., and Jackson, G. A. (2009). Particle Aggregation. *Ann. Rev. Mar. Sci.* 1, 65–90. doi: 10.1146/annurev.marine.010908.163904

Coles, V. J., Wang, J., Mason, O., and Stukel, M. R. (2020). Understanding how emergent community trait-based modeling (genome-based emergent ocean microbial ecosystem model) influences biogeochemical, ecological, and microbial system responses. *Paper Presented at the 2020 Ocean Science Meeting*, San Diego, CA.

Daly, K. L., Passow, U., Chanton, J., and Hollander, D. (2016). Assessing the impacts of oil-associated marine snow formation and sedimentation during and after the deepwater Horizon oil spill. *Anthropocene* 13, 18–33. doi: 10.1016/j.ancene.2016.01.006

Danchuk, S., and Willson, C. S. (2011). Influence of seasonal variability of lower Mississippi River discharge, temperature, suspended sediments, and salinity on oil-mineral aggregate formation. *Water Environ. Res.* 83, 579–587. doi: 10.2175/106143010x12780288628453

Dissanayake, A. L., Burd, A. B., Daly, K. L., Francis, S., and Passow, U. (2018). Numerical modeling of the interactions of oil, marine snow, and riverine sediments in the ocean. *J. Geophys. Res. Oceans* 123, 5388–5405. doi: 10.1029/2018JC013790

Dukhovskoy, D. S., Morey, S. L., Chassignet, E. P., Chen, X., Coles, V. J., Cui, L., et al. (2021). Development of the CSOMIO coupled ocean-oil-sediment-biology model. *Front. Mar. Sci.* 8:629299. doi: 10.3389/fmars.2021.629299

Dyer, K. R., and Manning, A. J. (1999). Observation of the size, settling velocity and effective density of flocs, and their fractal dimensions. *J. Sea Res.* 41, 87–95. doi: 10.1016/S1385-1101(98)00036-7

Fennel, K., Wilkin, J., Levin, J., Moisan, J., O'Reilly, J., and Haidvogel, D. (2006). Nitrogen cycling in the Middle Atlantic Bight: results from a three-dimensional model and implications for the North Atlantic nitrogen budget. *Glob. Biogeochem. Cycles* 20: GB3007. doi: 10.1029/2005GB002456

Fitzpatrick, F. A., Boufadel, M. C., Johnson, R., Lee, K. W., Graan, T. P., Bejarano, A. C., et al. (2015). *Oil-Particle Interactions and Submergence From Crude Oil Spills in Marine and Freshwater Environments: Review of the Science and Future Research Needs: Open-File Report*. Reston, VA: USGS.

Guyomarch, J., Le Floch, S., and Merlin, F.-X. (2002). Effect of suspended mineral load, water salinity and oil type on the size of oil–mineral aggregates in the presence of chemical dispersant. *Spill Sci. Technol. Bull.* 8, 95–100. doi: 10.1016/S1353-2561(02)00118-4

Haidvogel, D. B., Arango, H., Budgell, W. P., Cornuelle, B. D., Curchitser, E., Di Lorenzo, E., et al. (2008). Ocean forecasting in terrain-following coordinates: formulation and skill assessment of the regional ocean modeling system. *J. Comput. Phys.* 227, 3595–3624. doi: 10.1016/j.jcp.2007.06.016

Harris, C. K., Syvitski, J., Arango, H. G., Meiburg, E. H., Cohen, S., Jenkins, C. J., et al. (2020). Data-driven, multi-model workflow suggests strong influence from hurricanes on the generation of turbidity currents in the Gulf of Mexico. *J. Mar. Sci. Eng.* 8:28. doi: 10.3390/jmse8080586

Jaisi, D. P., Ji, S., Dong, H., Blake, R. E., Eberl, D. D., and Kim, J. (2008). Role of microbial Fe(III) reduction and solution chemistry in aggregation and settling of suspended particles in the Mississippi river delta plain, Louisiana, USA. *Clays Clay Miner.* 56, 416–428. doi: 10.1346/CCMN.2008.0560403

Jarvis, P., Jefferson, B., and Parsons, S. A. (2005). How the natural organic matter to coagulant ratio impacts on floc structural properties. *Environ. Sci. Technol.* 39, 8919–8924. doi: 10.1021/es0510616

Khelifa, A., Fingas, M., and Brown, C. A. (2008). *Effects of Dispersants On Oil-SPM Aggregation and Fate in US Coastal Waters.* Final Report Grant Number. NA04NOS4190063. Ottawa, ON: The Coastal Response Research Center.

Khelifa, A., and Hill, P. S. (2006). Models for effective density and settling velocity of flocs. *J. Hydraul. Res.* 44, 390–401. doi: 10.1080/00221686.2006.9521690

Kranenburg, C. (1994). The fractal structure of cohesive sediment aggregates. *Estuar. Coast. Shelf Sci.* 39, 451–460. doi: 10.1006/ecss.1994.1075

Lee, D. G., Bonner, J. S., Garton, L. S., Ernest, A. N. S., and Autenrieth, R. L. (2002). Modeling coagulation kinetics incorporating fractal theories: comparison with observed data. *Water Res.* 36, 1056–1066. doi: 10.1016/S0043-1354(01)00281-0

Lee, K. (2002). Oil–particle interactions in aquatic environments: influence on the transport, fate, effect and remediation of oil spills. *Spill Sci. Technol. Bull.* 8, 3–8. doi: 10.1016/S1353-2561(03)00006-9

Lee, K., Lunel, T., Wood, P., Swannell, R., and Stoffyn-Egli, P. (1997). Shoreline cleanup by acceleration of clay-oil flocculation processes. *Int. Oil Spill Conf. Proc.* 1997, 235–240. doi: 10.7901/2169-3358-1997-1-235

Lee, K., and Stoffyn-Egli, P. (2001). Characterization of oil-mineral aggregates. *Int. Oil Spill Conf. Proc.* 2001, 991–996. doi: 10.7901/2169-3358-2001-2-991

Lick, W., Lick, J., and Ziegler, C. K. (1992). Flocculation and its effect on the vertical transport of fine-grained sediments. *Hydrobiologia* 235, 1–16. doi: 10.1007/BF00026196

Logan, B. E., and Kilps, J. R. (1995). Fractal dimensions of aggregates formed in different fluid mechanical environments. *Water Res.* 29, 443–453. doi: 10.1016/0043-1354(94)00186-B

MacDonald, I. R., Taylor, J. C., Roa, C., and O'Reilly, C. (2019). "Chapter 8. Estimates of oil flux to the ocean at MC20 using optical and acoustical methods," in *An Integrated Assessment of Oil and Gas Release into the Marine Environment at the Former Taylor Energy MC20 Site. NOAA National Ocean Service, National Centers for Coastal Ocean Science. NOAA Technical Memorandum 260*, eds A. L. Mason, J. C. Taylor, and I. R. MacDonald (Silver Spring, MD: NCCOS), 107–118.

Martin, C. W., Lewis, K. A., McDonald, A. M., Spearman, T. P., Alford, S. B., Christian, R. C., et al. (2020). Disturbance-driven changes to northern Gulf of Mexico nekton communities following the deepwater horizon oil spill. *Mar. Pollut. Bull.* 155:111098. doi: 10.1016/j.marpolbul.2020.111098

Mason, A. L. (2019). *An Integrated Assessment of Oil and Gas Release into the Marine Environment at the Former Taylor Energy MC20 Site.* NOAA Technical Memorandum NOS NCCOS 260. Silver Spring, MD: NCCOS, 147. doi: 10.25923/kykm-sn39

Nixon, Z., Zengel, S., Baker, M., Steinhoff, M., Fricano, G., Rouhani, S., et al. (2016). Shoreline oiling from the deepwater horizon oil spill. *Mar. Pollut. Bull.* 107, 170–178. doi: 10.1016/j.marpolbul.2016.04.003

Payne, J. R., Clayton, J. R., and Kirstein, B. E. (2003). Oil/suspended particulate material interactions and sedimentation. *Spill Sci. Technol. Bull.* 8, 201–221. doi: 10.1016/S1353-2561(03)00048-3

Perry, J. D., Gostomski, E., Matthews, L. S., and Hyde, T. W. (2012). The influence of monomer shape on aggregate morphologies. *Astron. Astrophys.* 539:7. doi: 10.1051/0004-6361/201117940

Quigg, A., Passow, U., Daly, K. L., Burd, A., Hollander, D. J., Schwing, P. T., et al. (2020). "Marine oil snow sedimentation and flocculent accumulation (MOSSFA) events: learning from the past to predict the future," in *Deep Oil Spills: Facts, Fate, and Effects*, eds S. A. Murawski, C. H. Ainsworth, S. Gilbert, D. J. Hollander, C. B. Paris, M. Schlüter, et al. (Cham: Springer International Publishing), 196–220.

Robinson, E. M., and Rabalais, N. N. (2019). The effects of oil on blue crab and periwinkle snail interactions: a mesocosm study. *J. Exp. Mar. Biol. Ecol.* 517, 34–39. doi: 10.1016/j.jembe.2019.05.012

Sammarco, P. W., Kolian, S. R., Warby, R. A. F., Bouldin, J. L., Subra, W. A., and Porter, S. A. (2013). Distribution and concentrations of petroleum hydrocarbons associated with the BP/deepwater horizon oil spill. Gulf Mexico. *Mar. Pollut. Bull.* 73, 129–143. doi: 10.1016/j.marpolbul.2013.05.029

Shchepetkin, A. F., and McWilliams, J. C. (2005). The regional oceanic modeling system (ROMS): a split-explicit, free-surface, topography-following-coordinate oceanic model. *Ocean Modell.* 9, 347–404. doi: 10.1016/j.ocemod.2004.08.002

Sherwood, C. R., Aretxabaleta, A. L., Harris, C. K., Rinehimer, J. P., Verney, R., and Ferré, B. (2018). Cohesive and mixed sediment in the regional ocean modeling system (ROMS v3.6) implemented in the coupled ocean–atmosphere–wave–sediment transport modeling system (COAWST r1234). *Geosci. Model Dev.* 11, 1849–1871. doi: 10.5194/gmd-11-1849-2018

Sterling, M. C., Bonner, J. S., Page, C. A., Fuller, C. B., Ernest, A. N. S., and Autenrieth, R. L. (2004). Modeling crude oil droplet-sediment aggregation in nearshore waters. *Environ. Sci. Technol.* 38, 4627–4634. doi: 10.1021/es035467z

Stoffyn-Egli, P., and Lee, K. (2002). Formation and characterization of oil–mineral aggregates. *Spill Sci. Technol. Bull.* 8, 31–44. doi: 10.1016/S1353-2561(02)00128-7

Tambo, N., and Hozumi, H. (1979). Physical characteristics of flocs—II. *Strength floc Water Res.* 13, 421–427. doi: 10.1016/0043-1354(79)90034-4

Tarpley, D. R. N., Harris, C. K., Friedrichs, C. T., and Sherwood, C. R. (2019). Tidal variation in cohesive sediment distribution and sensitivity to flocculation and bed consolidation in an idealized, partially mixed estuary. *J. Mar. Sci. Eng.* 7:334. doi: 10.3390/jmse7100334

Thorne, C., Harmar, O., Watson, C., Clifford, N., Biedenham, D., and Measures, R. (2008). *Current and Historical Sediment Loads in the Lower Mississippi River. (University of Nottingham School of Geography, Final Report to US Army European Research Office, London, Under Contract 1106- EN-01)* Nottingham: University of Nottingham School of Geography.

Valentine, D. L., Fisher, G. B., Bagby, S. C., Nelson, R. K., Reddy, C. M., Sylva, S. P., et al. (2014). Fallout plume of submerged oil from deepwater horizon. *Proc. Natl. Acad. Sci.* 111:15906. doi: 10.1073/pnas.1414873111

Verney, R., Lafite, R., Brun-Cottan, J. C., and Le Hir, P. (2011). Behaviour of a floc population during a tidal cycle: laboratory experiments and numerical modelling. *Cont. Shelf Res.* 31, S64–S83. doi: 10.1016/j.csr.2010.02.005

Vonk, S. M., Hollander, D. J., and Murk, A. J. (2015). Was the extreme and wide-spread marine oil-snow sedimentation and flocculent accumulation (MOSSFA) event during the deepwater horizon blow-out unique? *Mar. Pollut. Bull.* 100, 5–12. doi: 10.1016/j.marpolbul.2015.08.023

Warner, J. C., Armstrong, B., He, R., and Zambon, J. B. (2010). Development of a coupled ocean–atmosphere–wave–sediment transport (COAWST) modeling system. *Ocean Modell.* 35, 230–244. doi: 10.1016/j.ocemod.2010.07.010

Warner, J. C., Sherwood, C. R., Signell, R. P., Harris, C. K., and Arango, H. G. (2008). Development of a three-dimensional, regional, coupled wave, current, and sediment-transport model. *Comput. Geosci.* 34, 1284–1306. 10.1016/j.cageo.2008.02.012

Wiesner, M. R. (1992). Kinetics of aggregate formation in rapid mix. *Water Res.* 26, 379–387. doi: 10.1016/0043-1354(92)90035-3

Winterwerp, J. C. (1998). A simple model for turbulence induced flocculation of cohesive sediment. *J. Hydraul. Res.* 36, 309–326. doi: 10.1080/00221689809498621

Winterwerp, J. C., Manning, A. J., Martens, C., de Mulder, T., and Vanlede, J. (2006). A heuristic formula for turbulence-induced flocculation of cohesive sediment. *Estuar. Coast. Shelf Sci.* 68, 195–207. doi: 10.1016/j.ecss.2006.02.003

Xu, K., Harris, C. K., Hetland, R. D., and Kaihatu, J. M. (2011). Dispersal of Mississippi and Atchafalaya sediment on the Texas–Louisiana shelf: model estimates for the year 1993. *Cont. Shelf Res.* 31, 1558–1575. doi: 10.1016/j.csr.2011.05.008

Ye, L., Manning, A. J., Holyoke, J., Penaloza-Giraldo, J. A., and Hsu, T.-J. (2021). The role of biophysical stickiness on oil-mineral flocculation and settling in seawater. *Front. Mar. Sci.* 8:628827. doi: 10.3389/fmars.2021.628827

Ye, L., Manning, A. J., and Hsu, T.-J. (2020). Oil-mineral flocculation and settling velocity in saline water. *Water Res.* 173:115569. doi: 10.1016/j.watres.2020.115569

Zhao, L., Boufadel, M. C., Geng, X., Lee, K., King, T., Robinson, B. H., et al. (2016). A-DROP: a predictive model for the formation of oil particle aggregates (OPAs). *Mar. Pollut. Bull.* 106, 245–259. doi: 10.1016/j.marpolbul.2016.02.057

Zhu, Z., Waterman, D. M., and Garcia, M. H. (2018). Modeling the transport of oil–particle aggregates resulting from an oil spill in a freshwater environment. *Environ. Fluid Mech.* 18, 967–984. doi: 10.1007/s10652-018-9581-0

Conflict of Interest: The authors declare that the research was conducted in the absence of any commercial or financial relationships that could be construed as a potential conflict of interest.

frontiers in Marine Science

ORIGINAL RESEARCH
published: 01 July 2021
doi: 10.3389/fmars.2021.630183

Resuspension, Redistribution, and Deposition of Oil-Residues to Offshore Depocenters After the Deepwater Horizon Oil Spill

Arne R. Diercks[1], Isabel C. Romero[2]*, Rebekka A. Larson[3], Patrick Schwing[2,3], Austin Harris[1], Samantha Bosman[4], Jeffrey P. Chanton[4] and Gregg Brooks[3]*

[1] Division of Marine Science, School of Ocean Science and Engineering, The University of Southern Mississippi, Hattiesburg, MS, United States, [2] College of Marine Science, University of South Florida, St. Petersburg, FL, United States, [3] Department of Marine Science, Eckerd College, St. Petersburg, FL, United States, [4] Department of Earth Ocean and Atmospheric Science, Florida State University, Tallahassee, FL, United States

OPEN ACCESS

Edited by:
Robert Hetland,
Texas A&M University, United States

Reviewed by:
J. German Rodriguez,
Technological Center Expert in Marine and Food Innovation (AZTI), Spain
Edward B. Overton,
Louisiana State University, United States

****Correspondence:***
Arne R. Diercks
arne.diercks@usm.edu
Isabel C. Romero
isabelromero@usf.edu

Specialty section:
This article was submitted to Marine Pollution, a section of the journal Frontiers in Marine Science

Received: *16 November 2020*
Accepted: *25 May 2021*
Published: *01 July 2021*

Citation:
Diercks AR, Romero IC, Larson RA, Schwing P, Harris A, Bosman S, Chanton JP and Brooks G (2021) Resuspension, Redistribution, and Deposition of Oil-Residues to Offshore Depocenters After the Deepwater Horizon Oil Spill. Front. Mar. Sci. 8:630183. doi: 10.3389/fmars.2021.630183

The focus of this study was to determine the long-term fate of oil-residues from the 2010 Deepwater Horizon (DwH) oil spill due to remobilization, transport, and re-distribution of oil residue contaminated sediments to down-slope depocenters following initial deposition on the seafloor. We characterized hydrocarbon residues, bulk sediment organic matter, ease of resuspension, sedimentology, and accumulation rates to define distribution patterns in a 14,300 km^2 area southeast of the DwH wellhead (1,500 to 2,600 m water depth). Oil-residues from the DwH were detected at low concentrations in 62% of the studied sites at specific sediment layers, denoting episodic deposition of oil-residues during 2010–2014 and 2015–2018 periods. DwH oil residues exhibited a spatial distribution pattern that did not correspond with the distribution of the surface oil slick, subsurface plume or original seafloor spatial expression. Three different regions were apparent in the overall study area and distinguished by the episodic nature of sediment accumulation, the ease of sediment resuspension, the timing of oil-residue deposition, carbon content and isotopic composition and foram fracturing extent. These data indicate that resuspension and down-slope redistribution of oil-residues occurred in the years following the DwH event and must be considered in determining the fate of the spilled oil deposited on the seafloor.

Keywords: resuspension, hydrocarbons, accumulation rates, radiogeochemistry, geochronology, Lead-210, radiocarbon, deep sea Gulf of Mexico

INTRODUCTION

A large percentage of the oil released during the 2010 Deepwater Horizon (DwH) spill in the northern Gulf of Mexico (GoM) was either chemically or naturally dispersed (Lehr et al., 2010; Lubchenco et al., 2012) and/or settled to the seafloor associated with the Marine Oil Snow Sedimentation and Flocculent Accumulation event (MOSSFA) (Passow et al., 2013; Daly et al., 2016). MOSSFA consisted of oil residues mixed with organic and inorganic particles, including bacteria, phytoplankton, microzooplankton, zooplankton fecal pellets, detritus, and terrestrially derived lithogenic particles (Daly et al., 2020). The observed MOSSFA event transported a significant portion of the released oil to the seafloor in a short time (Passow et al., 2012; Joye et al., 2013; Ziervogel et al., 2016; Romero et al., 2017). Increased short-term (months) sedimentation rates reflected the rapid transport of sediments to the seafloor associated with the MOSSFA event (Brooks et al., 2015; Romero et al., 2015, 2017; Yan et al., 2016; Larson et al., 2018). Layers of detectable oil-contaminated sediment were deposited on the seafloor directly below the extent of the surface slick or under the southwest deep sea plume (Valentine et al., 2014; Brooks et al., 2015; Chanton et al., 2015; Romero et al., 2015, 2017; Larson et al., 2018). However, a sampling bias toward seafloor locations under the surface slicks and the deep plumes (Camilli et al., 2010; Diercks et al., 2010) exists, and sediments were sampled at only few of the locations outside these areas (Schwing et al., 2017).

Lehr et al. (2010) estimated that 11–30% of the released oil was unaccounted for or listed as "other" (i.e., difficult to measure/quantify including oil on beaches, in tar balls, in shallow subsurface mats, and deep-sea sediments). While the sedimentation of oil is often discussed, for example, Jernelöv and Lindén (1981) speculated that 25% of the 475,000 metric tons of oil released from the 1979 Ixtoc spill went to the seafloor, its role has never properly been assessed. Valentine et al. (2014) estimated that 1.8 to 14.4% of the DwH oil remained in subsurface plumes and was deposited on the seafloor around the wellhead, while Chanton et al. (2015) indicated that between 0.5 and 9.1% of the total oil released by the DwH spill reached the seafloor in continental shelf to deep-sea areas. Covering a larger area from the coast to deep-sea, Romero et al. (2017) using 158 hydrocarbon compounds calculated that 21 ± 10% of the total oil released and not recovered by the DwH spill was deposited on ~110,000 km^2 of the seafloor, in which 32,648 km^2 corresponded to offshore deep-sea areas. Similarly, Schwing et al. (2017) indicated that increased sediment deposition occurred throughout an area of 12,805–35,425 km^2 in deep-sea sediments. In contrast, the surface oil slick covered a more extensive area, from 141,581 km^2 for 1 day, to 42,023 km^2 for 10 days and 14,357 km^2 for 30 days (Crowsey, 2013). All together, these studies define the spatial footprint of the MOSSFA event, including areas that lacked detectable oil. However, up to date, no study has addressed the potential role of post-depositional processes in changing the initial distribution of MOSSFA in sediments.

Natural heterogeneity of bottom topography and circulation processes are key drivers in redistributing materials to deeper areas in the GoM by erosion, transport and deposition of contaminated sediments beyond the surface extent of the once existing oil surface slick or the subsurface plumes(s). The northern GoM deep seafloor depositional environment is of high diversity resulting in non-homogeneous distribution and burial of material arriving from the overlying water column. Seafloor sedimentation is affected by currents, bottom morphology, and physical forcing events of different temporal and spatial scales that rework deposited material within the Bottom Nepheloid Layer (BNL) (Lampitt, 1985; Turnewitsch et al., 2004, 2013, 2017).

Large-scale gravity flow events (e.g., turbidity currents) can move large quantities of sediment downslope, regardless of overlying currents, following gravitational pull and the path of least resistance on the seafloor. Mobilized sediments flow along pathways based on the highly variable seafloor morphology, with its hills, slopes and channels, allowing for erosion and deposition beyond the spatial extent of the once existing oil slick or subsurface plumes(s). These processes can lead to a redistribution of sediments and potential sediment focusing in deep-sea depocenters that were targeted in this study. Previous studies in the deep eastern Gulf of Mexico show redistribution of sediments by gravity flow processes to be common, specifically on the Mississippi Fan, adjacent to our study area (Coleman et al., 1986; Cremer and Stow, 1986; Normark et al., 1986; Stow et al., 1986; Thayer et al., 1986). Based primarily on sedimentary structures, dominant processes are interpreted to be low-density with fine-grained turbidity currents deposited very rapidly in channel and overbank settings, as well as slides and slumps. Turbidity currents likely occur up to 5–6 times per year, possibly in pulses, and accumulation lasts hours to days before overlying sediments are deposited, all of which may explain the lack of extensive bioturbation, exceptionally high rates of accumulation, and excellent preservation (Coleman et al., 1986).

We tested the hypothesis that DwH impacted sediments that were initially deposited on the seafloor beneath the surface oil slicks and plumes, were subsequently remobilized and transported down-slope in the years following the DwH spill. Sediment accumulation on the seafloor is not a simple one-time process during which material settles to the seafloor, and not all the material accumulates (i.e., is buried) at the location of the initial deposition. Sediment cores were collected to determine if the sediments at the coring sites were impacted by the DwH spill. The distribution of contaminated sediments mapped in the years following the spill is likely an underestimation (e.g., Valentine et al., 2014; Chanton et al., 2015; Romero et al., 2017) due to resuspension and redistribution processes (e.g., Diercks et al., 2018) following their initial deposition on the seafloor. Characterization of the spatial distribution of oil-contaminated sediments along the continental slope at depths >1,500 m is critical for understanding the long-term fate of the spilled oil from the DwH in deep-sea areas.

MATERIALS AND METHODS

Watershed Modeling and Site Selection

Based on the recently published high resolution bathymetry by Kramer and Shedd (2017), a high resolution watershed drainage model was created, restricted to vertical bin resolution of 5 m to guide the site selection for *in situ* sediment coring. Stream lengths of <1 km were excluded in the graphic representation of the model data (**Figure 1**) to allow for better visibility in the larger scale maps of the study area. Sampling sites were determined based on the geomorphology of the seafloor, slope angle and the flow direction from the watershed drainage model. Selection of sampling sites was based primarily on areas on the seafloor where we expected sediments to be remobilized from and where they eventually would be deposited to (i.e., depocenters). We classified these areas into channels, lee

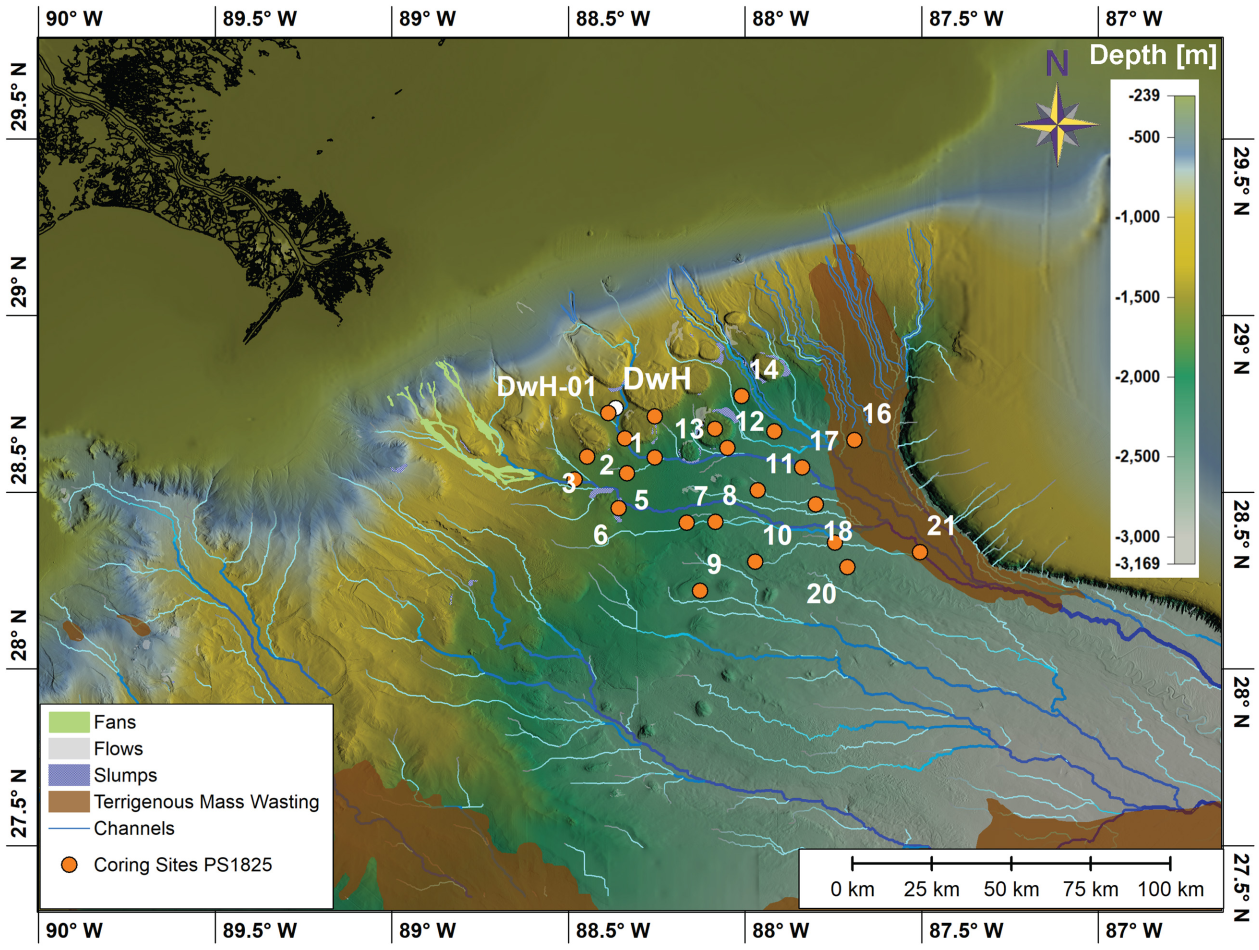

FIGURE 1 | Location of coring sites with watershed model results (blue shaded lines). Included are geomorphological and sedimentological data from the Bureau of Ocean Energy and Management (BOEM). These data include locations of flows, fans, and terrigenous mass wasting areas, slumps, and channels.

depocenters, and bathymetric depressions (**Table 1**). Channels can be erosional and/or depositional in nature. Channels act as conduits for the downslope mass movement of sediments, and although commonly erosional when active, are most often depositional over the long term. Lee depocenters are located in the lee or "down-slope shadow" of morphologic highs. They become centers of deposition as the energy level of the transport mechanism decreases in the lee of the morphological high (Turnewitsch et al., 2013). Similar depositional conditions are expected over large flat areas which are characterized as low energy environments. Isolated valleys or bathymetric depressions, valleys surrounded by morphological highs isolating them from any horizontal gravitational outflow, are similar in that the energy level tends to decrease in these features, which promotes deposition

Collection of Sediment Cores

Sediment samples were collected during the RV *Point Sur* cruise 18–25 in May of 2018, using a MC-800 multi corer (10 cm diameter × 70 cm long tubes) at the studied sites (**Figure 1** and **Table 1**). The Ocean Instruments MC-800 multi corer collected eight cores simultaneously and each core was used for a separate analysis (e.g., one core for bulk isotope analyses, one for short-lived radioisotope geochronology and sedimentology, one for XRF scanning, two for flume studies, one for hydrocarbon biomarkers, one for foraminiferal analyses, and one archived).

Sediment Resuspension Flume

To analyze resuspension behavior of the core samples, a linear closed loop flume was constructed. The resuspension flume (**Supplementary Figure 1**) was designed based on the Sedflume published by Borrowman et al. (2006). A 95 cm long 15 cm wide and 5 cm high closed channel was connected to a reservoir, through 5 cm diameter PVC pipes. In the upstream section of the flume, a DIGITEN model FL-1608 Hall Sensor flowmeter was installed in line before the flow diverter that converted the 5 cm PVC pipe into the rectangular test section of the flume. This flow diverter together with 147 cm of rectangular channel before the core insertion point allowed for full development of turbulent

TABLE 1 | Table of morphological classification and flume experiment data with surface sediment properties.

Site	Latitude (N)	Longitude (W)	Depth (m)	Depocenter type	Sediment structure type	Intervals with structures (cm)	Region	Flow speed at initial erosion (cm s^{-1})	Total volume eroded (cm^3)	Average particle size (mm^2)	Flow speed of first peak in sediment volume (cm s^{-1})	Volume eroded before first peak (cm^3)
1	28.7143	−88.2552	1,703	Channel	A		1	ND	ND	ND	ND	ND
2	28.6526	−88.3393	1,750	Lee	A		1	ND	ND	ND	ND	ND
3	28.6007	−88.4467	1,725	Lee	A		1	ND	ND	ND	ND	ND
4	28.5365	−88.4817	1,743	Lee	A		1	4.57	26.52	0.45	13.72	10.82
5	28.5473	−88.336	1,890	Lee	A		2	1.14	20.41	0.63	8	0.03
6	28.4558	−88.3568	1,910	Lee	A and B		2	4.57	56.34	0.51	16	43.66
7	28.4143	−88.1656	2,064	Depression	A and B		3	1.14	34.37	0.45	11.43	16.67
8	28.4205	−88.0844	2,170	Channel	A	0–23	3	3.43	11.93	0.45	14.86	0.26
9	28.221	−88.1269	2,272	Depression	A	0–25	3	3.43	5.63	0.39	5.72	0.02
10	28.3023	−87.9702	2,290	Channel	A and B	0–5	3	2.29	21.01	0.39	6.86	0.05
					A	15–20	3					
11	28.5048	−87.964	2,282	Depression	A and B	0–10	3	2.29	535.51	0.49	6.86	9.66
					A	18–20	3					
12	28.6253	−88.0489	2,179	Lee	A	0–6	2	3.43	44.6	0.46	8	0.34
13	28.6796	−88.0848	1,763	Depression	A and C		2	2.29	24.69	0.5	13.72	12.32
14	28.7718	−88.0096	1,946	Channel	A and C		2	1.14	190.52	0.47	6.86	3.81
15	28.6728	−87.916	2,410	Channel levee	A	0–5	3	2.29	72.44	0.44	12.57	12.84
16	28.6473	−87.6902	2,381	Channel (confluence)	A	0–7	3	2.29	48.25	0.46	10.29	1.84
17	28.57	−87.8378	2,344	Channel	A	0–7	3	2.29	23.32	0.46	11.43	9.31
18	28.4662	−87.7996	2,393	Channel	A	0–7	3	2.29	4.41	0.43	9.14	0
19	28.3574	−87.7451	2,459	Channel	A	0–20	3	1.14	37.77	0.4	10.29	2.37
20	28.2046	−87.7103	2,448	Depression/plain			3	1.14	65.5	0.44	6.86	1.12
21	28.3306	−87.5042	2,584	Channel (confluence)	C	Oct-20	3	4.57	18.95	0.42	16	6.53
30	28.5959	−88.2514	1,986	Depression/channel (?)	A	0–25	2	3.43	71.92	0.46	12.57	22.31
DwH01	28.7241	−88.3872	1,570	DwH wellhead	A	02-May	1	1.14	20.24	0.42	12.57	8.32

ND indicates no data if core tops were too disturbed or not enough multicores collected on that site to allow flume analysis.
*Labels: A, sub-parallel laminae/wavy bedding; B, color banded units; C, inclined beds (**Figure 2**).*

flow within the rectangular channel. At 147 cm beyond the flow diverter, a 10 cm diameter core opening was located at the base of the flume, allowing for insertion of the core into the flume. At the end of the rectangular section, another diverter reduced the diameter back to a 5 cm pipe through which the water was directed into a filtration system and the filtered, clean water was returned by the pump into the flume channel, thus creating the closed loop system.

A core extruding mechanism secured the core tube in the bottom of the flume during the test and permitted smooth controlled and undisturbed insertion of the core sediment into the flume. Cores had been collected and stored with a large amount of original seawater in the core tube overlying the sediment water interface. The flume was filled with filtered artificial salt water (salinity $\sim$ 35) prior to each test, and drained and cleaned after each experiment. The closed loop system provided an instantaneous movement of water within the entire flume when the pump was turned on.

During each test, a Sony 4k camcorder, mounted 20-cm beyond the core, with its focal point set at the center of the channel, recorded video data of calibrated particle size distribution of the material being eroded from the core top and transported down-channel. Time synchronized video footage was post processed using the GNU software FFMPEG into individual tagged image format files (TIF). For every 30 frames (video recorded at 30 frames per second), four images were extracted evenly spaced for every second of video time. Given the dimensions of the camera to the flume setup, this allowed for particles to be imaged in at least three consecutive images at the highest flow speed. Once all TIF images were extracted, they were analyzed using the Image Pro Plus® software. All images were normalized into 8-bit gray scale images. A standard area of interest (AOI) with calibrated known dimensions was extracted from the image. The AOI was saved as separate file. The next image in time was loaded normalized, had the AOI applied and saved. During the following step, the first AOI was subtracted from the second AOI, leaving in the resulting image only particles that had shifted (moved within the channel) in position. Every stationary object was removed in the image subtraction process. All visible particles in the resulting image were counted and grouped into 10 size bins ranging from 0.2 mm^2 to >1.8 mm^2 in 0.2 mm^2 steps.

Core Splitting and Extrusion

With the exception of the flume cores, sediment cores were either split longitudinally or extruded upward from the core base for sampling. Sediment cores were extruded at 2 mm intervals for surficial sediment (2–10 mm) to ensure the highest possible resolution of recently deposited sediments, and subsequently at 5 mm intervals to the base of the core. Cores were volumetrically extruded according to the method described in Schwing et al. (2016). One core from each deployment was split longitudinally, photographed and described visually. This included assessment of stratigraphic integrity and a variety of sedimentary structures that are indicators of down-slope transport mechanisms.

Short-Lived Radioisotopes

Short-lived radioisotope analyses were performed to provide age control and accumulation rates over the past ∼100 years. Samples were analyzed for short-lived radioisotopes by gamma spectrometry on Series HPGe (High-Purity Germanium) Coaxial Planar Photon Detectors for activities of total Lead-210 ($^{210}Pb_{Tot}$) at 46.5 kiloelectron volts (keV), Lead-214 (^{214}Pb) at 295 keV and 351 keV, Bismuth-214 (^{214}Bi) at 609 keV, and total Thorium-234 ($^{234}Th_{Tot}$) at 63 keV. Samples were also analyzed for Cesium-137 (^{137}Cs) at 661 keV, and Berilium-7 (^{7}Be) at 477 keV, but these radioisotopes were below detection in all samples and therefore will not be discussed. Data were corrected for emission probability at the measured energy, counting time, sample mass, and converted to activity (disintegrations per minute per gram, dpm/g), using the International Atomic Energy Association (IAEA) organic standard IAEA-447 for calibration (Kitto, 1991; Larson et al., 2018).

The activities of the ^{214}Pb (295 keV), ^{214}Pb (351 keV), and ^{214}Bi (609 keV) were averaged as a proxy for the Radium-226 (^{226}Ra) activity of the sample or the "supported" Lead-210 ($^{210}Pb_{Sup}$) that is produced *in situ* (Smith et al., 2002; Baskaran et al., 2014; Swarzenski, 2014). The $^{210}Pb_{Sup}$ activity was subtracted from the $^{210}Pb_{Tot}$ activity to calculate the "unsupported" or "excess" Lead-210 ($^{210}Pb_{xs}$), which is used for dating within the last ∼100 years.

The Constant Rate of Supply (CRS) algorithm was employed to assign specific ages to sedimentary intervals within the $^{210}Pb_{xs}$ profile. The CRS algorithm is appropriate under conditions of varying accumulation rates (Appleby and Oldfield, 1983; Binford, 1990). Mass accumulation rates (MAR) were calculated for each data point (i.e., "date"), based upon the CRS model results. The use of MAR corrects for differential sediment compaction down core, thereby enabling a direct comparison of $^{210}Pb_{xs}$ accumulation rates throughout a core (i.e., over the last ∼120 years). MAR were calculated as follows:

$$MAR\ (g/cm^2/year) = dry\ bulk\ density \times LAR \tag{1}$$

Where:

$$Dry\ bulk\ density\ (g/cm^3) = sample\ dry\ mass\ (g) \div sample\ volume\ (cm^3) \tag{2}$$

$$LAR = linear\ accumulation\ rate\ (cm/year) \tag{3}$$

$^{210}Pb_{xs}$ profiles were evaluated for the number of plateaus, the accumulation (mm) that was associated with plateaus e.g., accumulated as a pulse events, and the % of the total accumulation (mm) that occurred as a pulse. To quantify the accumulation for each core from episodic sedimentation a "Pulse Index" (P.I.) was calculated with the number of plateaus contributing 15% toward the index, the % of total accumulation that occurred with pulses (plateaus) contributing 50% toward the index, and the average MAR (1950–2018) contributing 35% toward the index (**Supplementary Table 1** and **Supplementary Figure 2**).

Sedimentology

Sediment texture and composition analyses were conducted on extruded samples and included bulk density, grain size, and composition. One core per site was used to calculate pore water content and bulk density. Sample volume was calculated using the inner diameter of the core barrel and sampling interval (i.e., height). Samples were weighed immediately after extrusion to provide the wet mass required for determining pore water content. Each sample was then freeze-dried and weighed for dry mass to calculate dry bulk density (Binford, 1990; Appleby, 2001).

Grain size was determined by wet sieving the sample through a 63 μm screen. The fine-size (<63 μm) fraction was analyzed by pipette (Folk, 1965) to measure the relative percentage of silt (%silt) and clay (%clay). The sand-size (>63 μm) fraction was volumetrically too small to analyze further and is reported here as %sand. %Gravel and %sand were determined by dry sieving the >63 micron fraction. Carbonate content (%carbonate) was determined by the acid leaching method according to Milliman (1974). Total organic matter (%TOM) was determined by loss on ignition (LOI) at 550°C for at least 2.5 h (Dean, 1974). The non-carbonate and non-organic fraction is reported here as %terrigenous. Although, technically this fraction may include non-terrigenous components such as biogenic silica, glauconite and volcanic ash, they are only found in trace amounts in this general area (Stow et al., 1986), as Mississippi River input is such a dominant sediment source.

Carbon Isotopes

Samples for bulk isotopic analyses were treated with 10% HCl to remove carbonates, rinsed with DI water, freeze dried, and then ground with mortar and pestle prior to isotope analyses. Stable carbon ($\delta^{13}C$, %C) was measured using a Carlo-Erba elemental analyzer coupled to an isotope ratio mass spectrometer at the University of Maryland Center for Environmental Science Chesapeake Biological Laboratory. Samples were prepared for measurement of natural abundance of radiocarbon at the

National High Magnetic Field laboratory. Acid treated sediment was combusted in quartz tubes at 850°C for 4 h and then the pure CO_2 was collected on a vacuum line using a series of cold traps to remove water vapor and non-condensable gases following the methods of Choi and Wang (2004). The purified CO_2 was flame sealed in a 6 mm ampoule and sent to Woods Hole National Ocean Sciences Accelerator Mass Spectrometry where the samples were prepared as graphic targets and analyzed by accelerator mass spectrometry (Vogel et al., 1984). The radiocarbon signatures are reported in $\Delta^{14}C$ notation as described by Stuiver and Polach (1977). The ^{14}C blanks were generally between 1.2 and 5 μg of carbon, producing a negligible effect on samples, which were over 1200 μg of carbon. The analysis of 22 replicate sediment samples yielded an average analytical reproducibility of $\pm 6.8‰$ for $\Delta^{14}C$ and 0.2‰ for $\delta^{13}C$. Forty coal samples, representing fossil ^{14}C dead carbon, were analyzed to access our procedural blank of combustion, graphitization, and target preparation, over the course of this study. The average $\Delta^{14}C$ value was $-995 \pm 7‰$. We also ran 25-azalea leaf standards collected in Tallahassee, Florida in 2013; the average $\Delta^{14}C$ value was $31 \pm 8‰$.

Benthic Foraminifera

Following extrusion (methods provided above), five sub-samples from the surface of the sediment cores (0–2, 2–4, 4–6, 6–8, and 8–10 mm) and one sub-sample from down-core (20–22 mm) were used for benthic foraminifera analysis following methods similar to Schwing et al. (2018). Briefly, sub-samples were weighed and washed with a sodium hexametaphosphate solution through a 63-μm sieve to disaggregate detrital particles from foraminiferal tests (Osterman, 2003). The fraction remaining on the sieve (>63-μm) was dried in an oven at 32°C for 12 h, weighed again, and stored at room temperature (Osterman, 2003). Between 200 and 400 individuals from each subsample were identified to the species-level and counted. The fraction of the sample that was identified was then weighed. It was necessary to count between 200 and 400 individuals per sample to distinguish 2% significant variability in density and relative abundance between sample intervals (Patterson and Fishbein, 1989). Multiple taxonomic references were used (d'Orbigny, 1826, 1839; Williamson, 1858; Jones and Parker, 1860; Parker and Jones, 1865; Brady, 1878, 1879, 1884; Cushman, 1922, 1923, 1927; Stewart and Stewart, 1930; Phleger and Parker, 1951; Parker et al., 1953; Parker, 1954). The number of specimens with visibly fractured tests was counted and reported as the fracture percentage versus the total number of specimens identified as a taphonomical indicator of turbulent flow redistribution (Ash-Mor et al., 2017).

Hydrocarbon Analyses

Samples were kept frozen until freeze-dried at the Marine Environmental Chemistry Laboratory (MECL, College of Marine Science, University of South Florida). Approximately 1.0 g of freeze-dried and homogenized sediment was extracted using an Accelerated Solvent Extraction system (ASE® 200, Dionex) under high temperature (100°C) and pressure (1500 psi) with hexane:dichloromethane (9:1 v:v). Deuterated standards were added to samples prior to extraction to monitor matrix effects and correct for losses during extraction (d10-acenaphthene, d10-phenanthrene, d10-fluoranthene, d12-benz(a)anthracene, d12-benzo(a)pyrene, d14-dibenz(ah)anthracene, d_{50}-tetracosane, d_{15}–pentadecane, d_{32}–dotriacontane, d_4-cholastane). For extraction in the ASE, we applied a one-step extraction and clean up procedure using a predetermined packing of the extraction cells (Kim et al., 2003; Choi et al., 2014; Romero et al., 2018) using a 11 ml extraction cell with glass fiber filter (pre-combusted at 450°C for 4 h), 5 g silica gel (high purity grade, 100–200 mesh, pore size 30A, Sigma Aldrich, United States; pre-combusted at 450°C for 4 h, and deactivated 2%), and sand (pre-combusted at 450°C for 4 h). Sediment extracts were concentrated to ~2 ml in a RapidVap (LABONCO RapidVap® Vertex™ 73200 series) and further concentrated to about 100–300 μl by gently blowing with a nitrogen stream. An internal standard was added (d14-terphenyl; Ultra Scientific ATS-160-1) to all samples prior to GC/MS analysis. All solvents used were at the highest purity available. Two extraction control blanks were included with each set of samples (18 samples).

We followed modified EPA methods and QA/QC protocols (8270D, 8015C). Targeted compounds included aliphatics (C12–C37 *n*-alkanes, isoprenoids), PAHs (2–6 ring polycyclic aromatic hydrocarbons including alkylated homologs), and biomarkers [C27–C35 hopanoids, C27–C29 steranes, C20–C28 triaromatic steroids (TAS)]. Hydrocarbon compounds were quantified using GC/MS/MS (Agilent 7680B gas chromatograph coupled with an Agilent 7010 triple quadrupole mass spectrometer) in multiple reaction monitoring mode (MRM) to target multiple chemical fractions in one-run-step. Molecular ion masses for hydrocarbon compounds were selected from previous studies (Romero et al., 2015, 2018; Sørensen et al., 2016; Adhikari et al., 2017) (**Supplementary Tables 2a,b**). All samples were analyzed in splitless injections, inlet temperature of 295°C, constant flow rate of 1 ml/min, and a MS detector temperature of 250°C using a RXi-5sil chromatographic column. The GC oven temperature program was 60°C for 2 min, 60°C to 200°C at a rate of 8°C/min, 200°C to 300°C at a rate of 4°C/min and held for 4 min, and 300°C to 325°C at a rate of 10°C/min and held for 5 min. Source electron energy was operated at 70 eV, and argon was used as the collision gas at 1 mTorr pressure.

For accuracy and precision of analyses we included laboratory blanks for every 12–14 samples, spiked controls for every 14–18 samples, tuned MS/MS to PFTBA (perfluorotributylamine) daily, checked samples with a standard reference material (NIST 2779) daily, and reanalyzed sample batches when replicated standards exceeded ±20% of relative standard deviation (RSD), and/or when recoveries were low. Recovery ranged within QA/QC criteria of 50–120%. PAH concentrations are reported as recovery corrected. Each analyte was identified using certified standards (Chiron S-4083-K-T, Chiron S-4406-200-T, NIST 2779) and performance was checked using a 5-point calibration curve (0.04, 0.08, 0.31, 1.0 ppm). Quantitative determination of compounds was conducted using response factors (RFs) calculated from the certified standard NIST2779.

Hydrocarbon compounds are expressed as sediment dry weight concentrations.

Hydrocarbon Source Identification

We used a tiered analytical approach for the identification of hydrocarbon sources in the sediment samples collected. First, we determined the concentration of hydrocarbon groups in the sediment samples (aliphatics, PAHs, and biomarkers (hopanoids, steranes, and TAS) to establish temporal (as profiles) and spatial (surface maps) changes of hydrocarbon concentrations and composition. Second, we determined and compared diagnostic oil ratios between potential sources and the samples (for details see below). Third, we compared the distribution pattern of *n*-alkanes and PAHs among samples.

Diagnostic oil ratios were calculated for all crude oil standards (NIST Macondo oil: MC252; Southern Louisiana Sweet crude oil: LC; southern GoM Akal Bravo oil: AB) and samples to discriminate hydrocarbon sources. Careful should be taken when applying diagnostic ratios to deep-sea sediments because of multiple weathering processes affecting the composition of hydrocarbons during sinking through the water column and after reaching the seafloor. For example, low molecular weight PAHs (LMW, containing 2–3 ring PAHs) are abundant in petrogenic sources while high molecular weight PAHs (HMW, containing 4–6 ring PAHs) are abundant in pyrogenic sources. However, HMW PAH can become more abundant due to the loss of LMW PAHs during weathering processes (e.g., dissolution, biodegradation). Alkane ratios were used to identify natural vs. oil sources (carbon preference index: CPI (C25–C33) = Σodd Cn/Σeven Cn) if samples were weathered (low molecular weight alkanes: % *n*-alkanes = ΣC14–C24/sum (C12–C37)*100). Samples with CPI < 2.0 and % *n*-alkanes < 25% indicate a weathered petrogenic source (Xing et al., 2011; Romero et al., 2015, 2021; Herrera-Herrera et al., 2020).

Other compounds, more resistant to weathering, can be used to identify specific oil sources (hopanes, steranes, triaromatic steroids). However, diagnostic oil biomarker ratios (using hopane, sterane, and triaromatic steroid compounds) known to fingerprint DwH oil or other crude oils have mostly been tested in samples collected from coastal environments (Wang and Fingas, 2003, Wang et al., 2006; Mulabagal et al., 2013; Aeppli et al., 2014) and a few in deep-sea sediments (Romero et al., 2015, 2017; Stout et al., 2016). In addition, some of these biomarker compound groups (e.g., steranes) have been shown to degrade in the marine environment years after an oil spill (Wang et al., 2001; Prince et al., 2002; Gros et al., 2014). Therefore, we tested if biomarker ratios used in previous studies (Wang and Fingas, 2003, Wang et al., 2006; Mulabagal et al., 2013; Aeppli et al., 2014; Romero et al., 2015, 2017) can be used to fingerprint deep-sea sediments, where organic matter and oil residues are naturally exposed to long-term weathering processes. Specifically, we compared the MC252 oil standard (NIST 2779) with samples collected at the DwH site (DwH-01), an area known to contain weathered oil residues from the DwH spill (Chanton et al., 2015; Romero et al., 2015; Stout et al., 2016). Also, samples from the DwH-01 site, the closest site to the DwH wellhead, sampled from 2011 to 2013, showed the presence and preservation of oil residues in the sediments from the DwH spill (Romero et al., 2017).

Only diagnostic ratios with a difference within ±20% between samples from site DWH-01 and the average of MC252 oil standard ($N = 60$) were used. In previous fingerprinting studies, this criteria for the difference between samples and an oil standard has been established based on the relative standard deviation value (RSD: 14–20%) of a standard analyzed over a period of time (analytical uncertainty) (Aeppli et al., 2014; Meyer et al., 2017). Our analysis of biomarkers using GC/MS/MS-MRM had an RSD of 4.8% over a time period of 6 months using the MC252 oil standard. The application of GC/MS/MS-MRM increases selectivity, improved baseline and signal-to-noise ratio, and successfully separates target compounds from interferences compared to the conventional GC/MS-SIM method (Adhikari et al., 2017). Altogether, the GC/MS/MS-MRM method improves the analytical uncertainty in the analysis of biomarker compounds. However, environmental sample replicates collected in deep-sea areas of the GoM have shown that RSD varies between 4% to 22% for biomarker compounds, indicating natural variability in the area (Romero et al., 2015). Therefore, diagnostic biomarker ratios of DwH oil residues at depth were selected using the RSD value of 20%, to account for the natural variability in deep sea environments. Ratios with a difference within ±20% between samples from site DWH-01 and the average of MC252 oil standard seem resistant to weathering and other natural processes at depth in the GoM, and are suitable for fingerprinting. The matching ratios were then calculated for all sites studied and analyzed using a Principal Component Analysis (PCA; JMP® Pro 14.0). Also, cross plots of alkane diagnostic ratios were done to identify oil vs. natural sources in the region. In addition, the relative abundance (%) of hydrocarbon groups was plotted for each site studied to identify areas with high content of LMW PAHs (2–3 rings) due to inputs from natural seeps.

Only samples indicating oil content (using alkane ratios), no natural seep inputs (with low %LMW PAHs), a distinct distribution pattern of *n*-alkanes and PAHs indicating weathered oil residues, and a match with the MC252 oil standard (using biomarker ratios) were identified to contain DwH oil residues as the most probable oil source.

RESULTS

All sites yielded sediment cores with active deposition over the past ∼100 years. Core analyses revealed a range of sediment textures, composition and accumulation rates indicating that sedimentation processes varied throughout the study area. Downcore data were utilized for some analyses to provide a longer time-scale context (**Figure 2**) and to assess the historical prevalence of down-slope sediment transport as indicated by various sedimentary structures present throughout the study area. All other analyses focused on the surficial sediments (0–20 mm) to identify recent patterns that may be associated with deposition and redistribution of DwH contaminated sediments. We have provided maps in figures and supplementary figures as a mechanism to visualize the data and to communicate

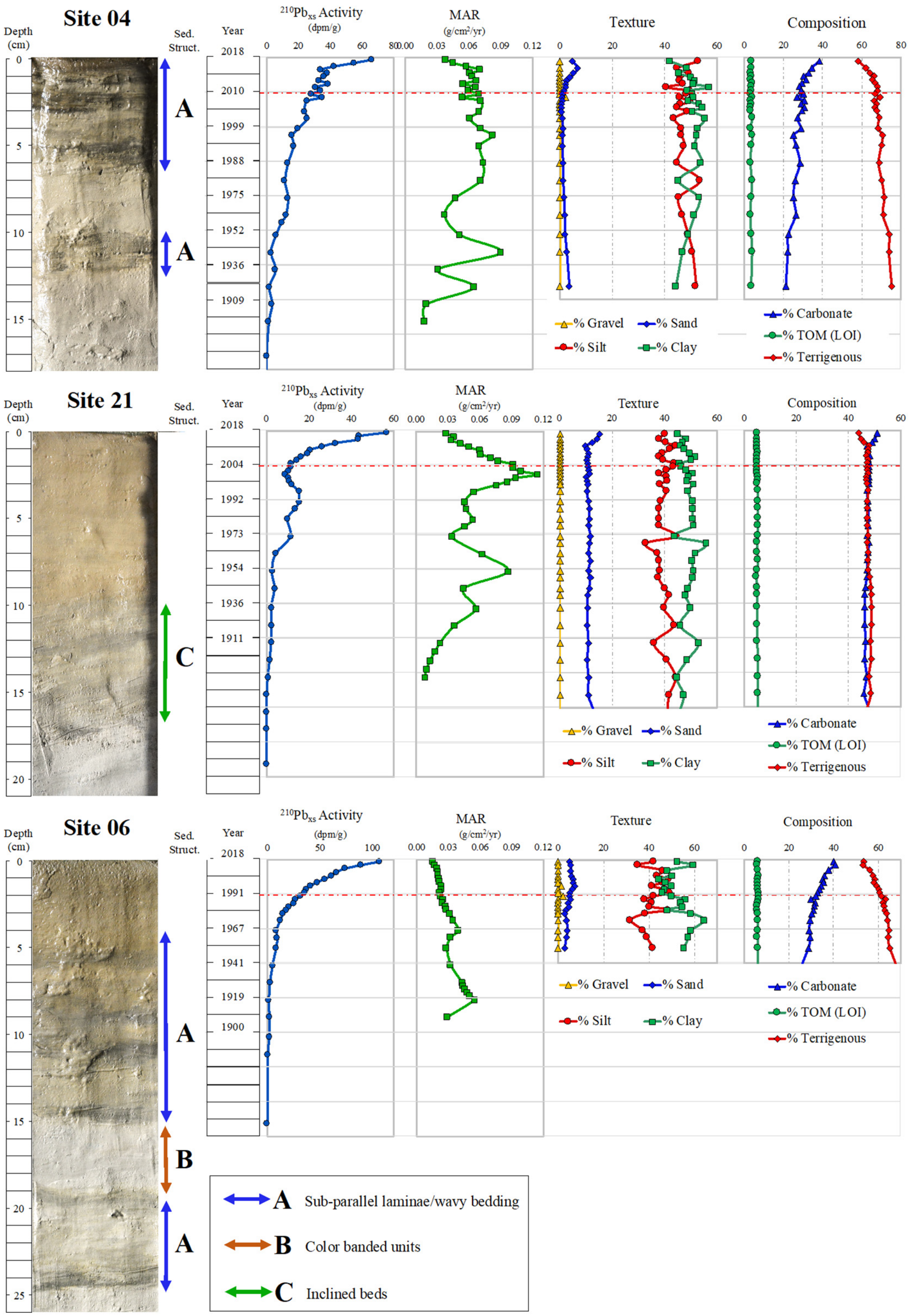

FIGURE 2 | Core logs for Site 4 (Region 1), Site 6 (Region 2), and Site 21(Region 3) showing sedimentary structures indicative of sediment re-deposition by gravity flow processes, $^{210}Pb_{xs}$ profiles and MARs, and sediment texture and composition to assess historical prevalence of downslope sediment transport and accumulation. (Labels: A, sub-parallel laminae/wavy bedding; B, color banded units; C, inclined beds).

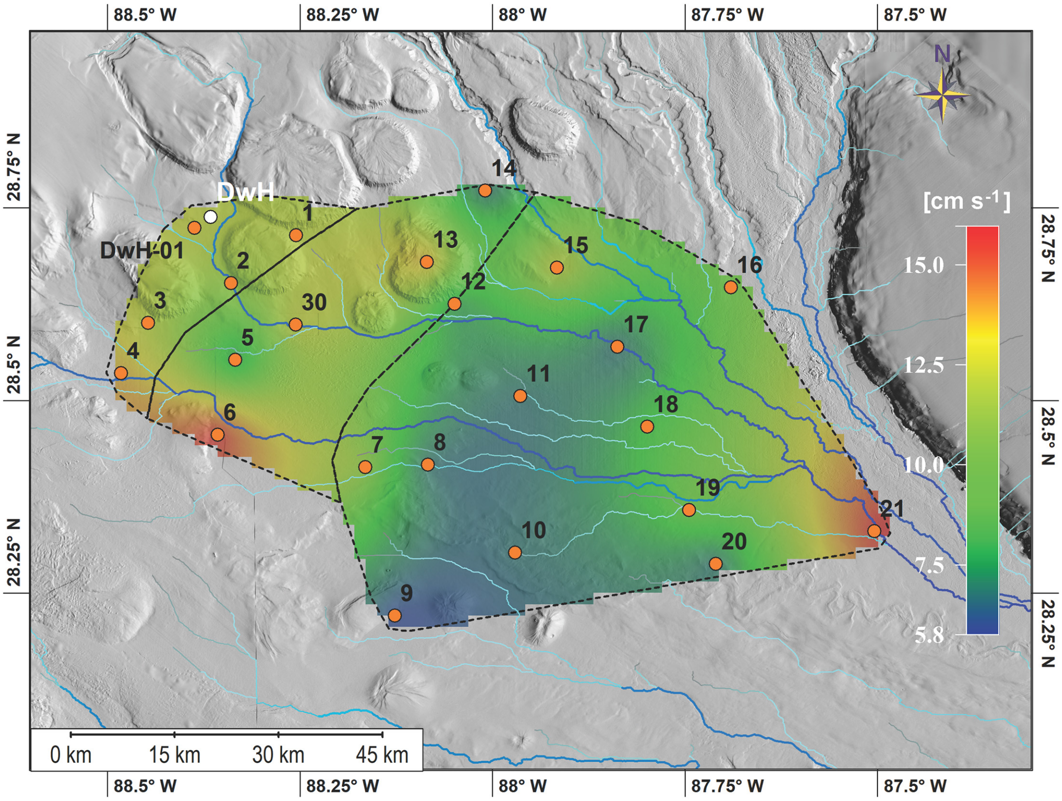

FIGURE 3 | Heat map of flow speed of first peak in particle resuspension. Regions discussed are outlined by the dashed black lines. Region 1 is in the NW and Region 3 in the SE. Blue lines indicate channels as modeled by watershed analysis.

the observed variations in the data. Interpolations of data in the areas between the individual coring locations were dependent on parameters set in the contouring program (Golden Software Surfer 9.0) and were thus not discussed in this manuscript.

Flume

Flume experiments showed that sediment particle erosion behavior was not uniform across the various sedimentary environments on the seafloor (**Table 1**). The uppermost layer of sediment (top 2 mm) from each core eroded at different flow speeds, producing maximum peaks in total number of particle counts at flow speeds from 5.72 cm s^{-1} to 16 cm s^{-1} (**Table 1** and **Figure 3**). Several sediment cores exhibited a second peak at higher flow speeds (sites 10, 11, 14, 17, and 20). In all cores (sites 8, 9, 10, 17, 19, and 20) that had a first peak in particle resuspension at low flow speeds, a decrease in resuspended particle concentration was observed following the initial peak resuspension of particles. A second larger peak, produced by a complete collapse of the surface sediment layer, occurred in all cores at flow speeds exceeding 13.7 cm s^{-1}. Sediments from cores that did not have the initial peak in resuspended particles (sites 4, 5, 6, 12, 13, 15, 16, 21, 30, and DwH-01) had low numbers of particles resuspended until a rapid disintegration of the surface sediment layer occurred >13.7 cm s^{-1}.

Distinct peaks in total volume with increased flow speed were recorded for each core analyzed. Average area of individually eroded particles varied only slightly between 0.39 and 0.63 mm^2 in all cores, however, total eroded volume of particles varied from 4.4 to 535 cm^3 (**Table 1**).

Short-Lived Radioisotopes

Short-lived radioisotope analyses yielded $^{210}Pb_{xs}$ activity profiles utilized to provide age control and sedimentation rates at multicore sites over the past ~120 years. $^{210}Pb_{xs}$ profile shape and MAR, averaged over various time periods, were used to characterize the spatial patterns of sediment distribution and accumulation.

$^{210}Pb_{xs}$ activity profile shapes varied with some sites exhibiting exponential profiles and others non-exponential profiles (**Figure 2** and **Supplementary Figures 3a–c**). Non-exponential profiles ranged from small mm-scale plateaus in activity to profiles with large cm-scale plateaus. Some profiles contained few plateaus, and some contained multiple plateaus. These profiles were utilized to assess the relative magnitude and frequency of episodic or pulsed accumulation (plateaus in activity in profiles) vs. areas with stable consistent accumulation (exponential profiles).

The spatial pattern of the pulse index reveals variability in the prevalence of sediment accumulation from episodic events

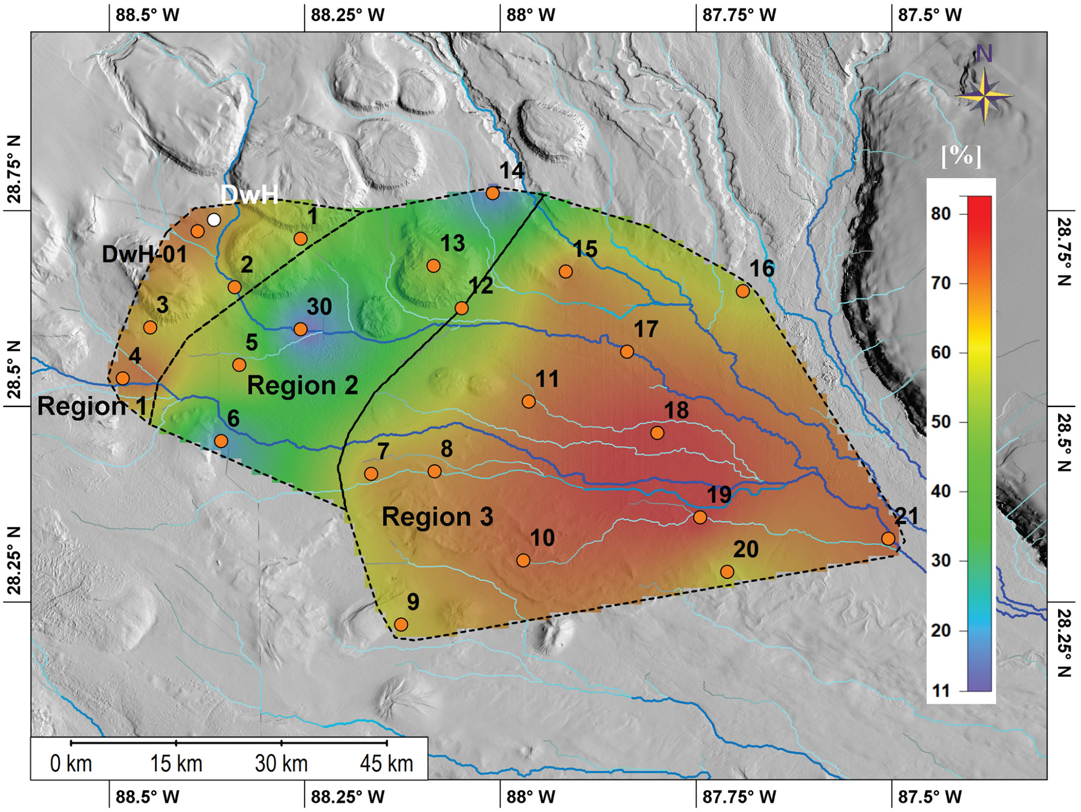

FIGURE 4 | Heat map of weighted pulsed input in study area. The three regions identified in this study are marked by black lines and are labeled Region 1, 2, and 3 form the NW to the SE. Scale describes the percentage of pulsed inputs in the study area.

over the past ~120 years (**Figure 4**). In the northwestern portion of the study area (sites 1, 2, 3, 4, and DwH-01) a high index, reflecting frequent episodic sedimentation events, was observed. The central portion of the study area consists of low index values (sites 5, 6, 12, 13, 14, and 30) reflecting a more stable, consistent sediment accumulation history. The southeastern portion of the study area shows high index values (sites 7, 8, 9, 10, 11, 15, 16, 17, 18, 19, 20, and 21) but with the highest episodic sedimentation events observed in the study area, in terms of magnitude and frequency.

Sediment MAR's were determined using $^{210}Pb_{xs}$ age dating. Differing time periods were evaluated to characterize accumulation rates from a long (1950–2018) to short periods for characterizing events pre-spill (2006–2009; **Figure 5A**), during and after the spill related to the MOSSFA event (2010–2013; **Figure 5B**), and post-spill associated to redistribution of sediments (2014–2018; **Figure 5C**). Spatial patterns of MAR's from 1950 to 2018 are consistent with the areas of episodic sedimentation identified by the $^{210}Pb_{xs}$ pulse index, further corroborating the spatial variability in the influence of episodic sedimentation events (**Figure 4**). For the three recent time periods compared in this study, there are potential shifts in "hot spots" of higher accumulation with site 18 consistently being a "hot spot" for accumulation in all three periods. Site 9 shows increased MAR's in the 2010–2013 time period. In the 2014–2018 period, there are higher MAR's at site 16 near the base of the DeSoto Canyon as compared to the 2006–2009 and 2010–2013 time periods (**Figures 5A–C**).

Sedimentology

All cores exhibited intact detailed stratigraphy, contained numerous, well-preserved primary sedimentary structures, and very few secondary sedimentary structures (e.g., bioturbation). The most common structures were thin, mm-scale, sub-parallel laminae and wavy bedded units with no clearly defined lower boundaries (**Figure 2**). These structures were found throughout the entire study area in all depocenter types (**Table 1**). Inclined and color banded beds (**Figure 2**) were less common, and sparsely dispersed throughout all but the northeastern-most portion of the study area (**Table 1**). Generally, sedimentary structures were better defined in the upper few 10's of cm of cores (**Table 1**).

Sediment grain size and composition was averaged over the surficial 0–4 mm and 10 mm intervals and varies throughout the study area. Grain size is reported as %gravel, %sand, %silt, %clay, and %mud (%silt + %clay), and composition is reported as %carbonate, %TOM (total organic matter by LOI), and %terrigenous (**Table 2** and **Supplementary Figures 4–8**). %Carbonate ranged from 45% to 60% with lowest concentrations in the NW portion of the study area and increasing to the SE. %TOM ranged from 4.4% to 7.1% with highest values in the

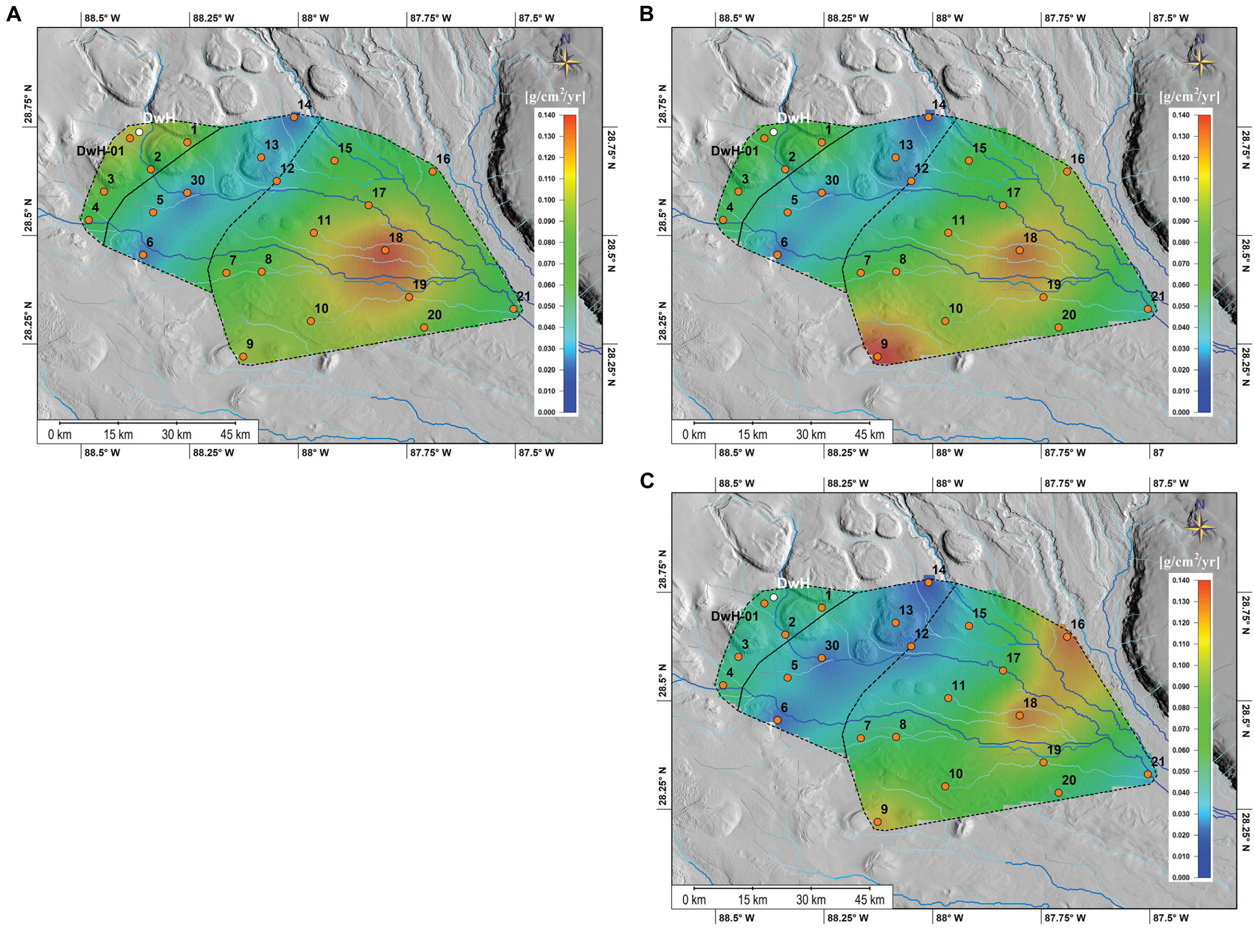

FIGURE 5 | Heat maps of average sediment accumulation rates determined from $^{210}Pb_{xs}$. **(A)** Pre-Spill (2006–2009), **(B)** 2010–2013, and **(C)** 2014–2018. Regions discussed are outlined by the dashed black lines. Region 1 is in the NW and Region 3 in the SE. Blue lines indicate channels as modeled by watershed analysis.

NW and decreasing to the SE. Sediment grain size showed more spatial variability than composition. %Gravel was zero in all sites except site 03, which contained large pteropod fragments. %Sand ranged from 0.3% to 12.9% with highest values in the SE, lowest values in the N, and moderate values in the W portion of the study area. %Silt ranged from 35.3% to 58.5% with highest values in the NW, lowest values in the NE and SE, and modest in the SW portion of the study area. %Clay ranged from 39.9% to 63.3% with highest values in the NE, modest through the central to S, and lowest in the NW and SE areas. Highest %carbonate values were consistently associated with the highest %sand, which consisted of sand size biogenic carbonate particles (**Supplementary Figures 4–8**).

Carbon Isotopes

The sedimentary organic carbon content in percent carbon by weight, %C, the stable carbon isotopic composition, $\delta^{13}C$ ‰, and the radiocarbon content, $\Delta^{14}C$ ‰, of the surface 0–2 mm layer and the 0–10 mm layer are reported in **Supplementary Table 3**. Values for the 0–10 mm depth interval were calculated as the average of the five 2 mm slices subsampled within that interval. The %organic carbon of the uppermost interval (0–2 mm) varied from 1.3 to 2.9% and generally decreased from the northwest to the southeast as the water deepened (**Figure 6**). The $\delta^{13}C$ of surface (0–2 mm) organic matter varied from −20.7 to −22.5‰ and was more depleted to the northwest and exhibited a minimum in the center of the study area (**Figure 7**). There was a significant correlation of increasing $\delta^{13}C$ with decreasing %organic carbon ($p = 0.01$, $r = 0.512$, $n = 24$). Radiocarbon content in the surficial layer (0–2 mm) varied from −167 to −319‰ across the study area (**Figure 8**). The most depleted values were observed at about 2,300 m depth on the north east and western sides of the study area. The central portion of the study area exhibited ^{14}C enriched surface sediments downslope of the DwH site, in water depths ranging from 1,700 to 2,100 m, grading to more depleted values to the southeast. None of these parameters correlated with depth.

Benthic Foraminifera

Benthic foraminifera density and fracture percentage are presented in **Supplementary Table 4**. Benthic foraminifera density ranged from 15 to 74 individuals/cm^3 and generally

TABLE 2 | Sedimentological data.

Site	%Gravel		%Sand		%Silt		%Clay		%Mud (silt + clay)		%Carbonate		%TOM (LOI)		%Terrigenous	
Interval	**0–0.4 cm**	**0–1 cm**	**0–0.4 cm**	**0–1 cm**	**0–0.4 cm**	**0–1 cm**	**0–0.4 cm**	**0–1 cm**	**0–0.4 cm**	**0–1 cm**	**0–0.4 cm**	**0–1 cm**	**0–0.4 cm**	**0–1 cm**	**0–0.4 cm**	**0–1 cm**
1	0	0	1.5	1.6	60.4	58.5	38.1	39.9	98.5	98.4	35.6	34.3	8.8	7.1	55.5	58.6
2	0	0	5.2	5	42.6	41.8	52.2	53.1	94.8	95	35.3	33.9	7	7	57.7	59.1
3	0.6	0.2	5.5	5	48.3	45.7	45.6	49.1	93.9	94.8	37.6	36.4	6.4	6.5	56	57.1
4	0	0	4.9	5.7	53	49	42.1	45.3	95.1	94.3	38.3	35.1	3.6	3.4	58.1	61.4
5	0	0	5.8	6.2	47	43.6	47.2	50.3	94.2	93.8	37	36.5	7.2	6.8	55.8	56.8
6	0	0	5.3	5.6	38.7	41.8	56	52.6	94.7	94.4	40.3	38.5	6.2	6.3	53.5	55.2
7	0	0	8.5	5.8	43.7	41.6	47.8	52.6	91.5	94.2	37.4	34.9	6.5	6.5	56.1	58.6
8	0	0	5.2	4.7	39.6	39	55.3	56.3	94.9	95.3	42.6	41	6	5.9	51.5	53.1
9	0	0	1.8	2.4	48	43.9	50.2	53.7	98.2	97.6	41.8	41.6	7.1	6.8	51.2	51.6
10	0	0	8.4	8.6	49.4	44.1	42.2	47.3	91.6	91.4	43.7	43.9	6.2	5.6	50.1	50.5
11	0	0	5.7	4.5	35.5	41	58.9	54.4	94.3	95.5	42.9	41.4	6.3	5.9	50.8	52.7
12	0	0	6.9	7.1	47.4	44.7	45.7	48.2	93.1	92.9	37.2	39.5	7.4	6.6	55.4	53.9
13*	0	0	6.7	5.3	38.3	42.3	55	52.4	93.3	94.7	39.4	38	6.4	6.1	54.2	55.9
14	0	0.1	6.6	5.9	46.5	46.1	46.9	48	93.4	94	44.8	40.8	5.6	6.1	49.5	52.5
15	0	0	4.8	3.7	36.7	35.3	58.5	61	95.2	96.3	37.5	35.6	7.2	7.1	55.3	57.3
16	0	0	0.2	0.3	33.4	36.5	66.4	63.2	99.8	99.7	41.1	40.2	7	6.8	51.9	53
17	0	0	5.1	4.6	42.6	43.3	52.3	52.1	94.9	95.4	43.6	43.3	5.5	5.6	50.9	51.1
18	0	0	7.8	7.5	46.8	45.4	45.4	47.1	92.2	92.5	44.7	44.4	5.9	5.8	49.4	49.7
19	0	0	12	10.9	39.4	38.7	48.6	50.4	88	89.1	51.8	48.7	3.8	4.4	44.4	46.9
20	0	0	10.3	9.8	37.1	35.9	52.5	54.3	89.7	90.2	45.7	45.4	5.4	5.2	49	49.3
21	0	0	15.1	12.8	40	40.7	44.9	46.4	84.9	87.2	51.1	49.3	5.1	5.1	43.8	45.6
30	0	0	4.5	5.8	41.3	42.5	54.2	51.6	95.5	94.2	38.5	36.9	6.6	6.5	54.9	56.6
DWH01	0	0	2.9	2.7	44	45.6	53.1	51.7	97.1	97.3	34.4	32.6	7.4	7.1	58.2	60.3
Max	0.6	0.2	15.1	12.9	60.4	58.5	66.4	63.2	99.8	99.7	51.8	49.3	8.8	7.1	58.2	61.4
Min	0	0	0.2	0.3	33.4	35.3	38.1	39.9	84.9	87.2	34.4	32.6	3.6	3.4	43.8	45.6
Average	0	0	6.1	5.7	43.5	42.9	50.4	51.4	93.9	94.3	41	39.7	6.3	6.1	52.7	54.2

Core intervals 0–4 mm and 0–10 mm.
**Interval is 0–2 mm not 0–4 mm.*

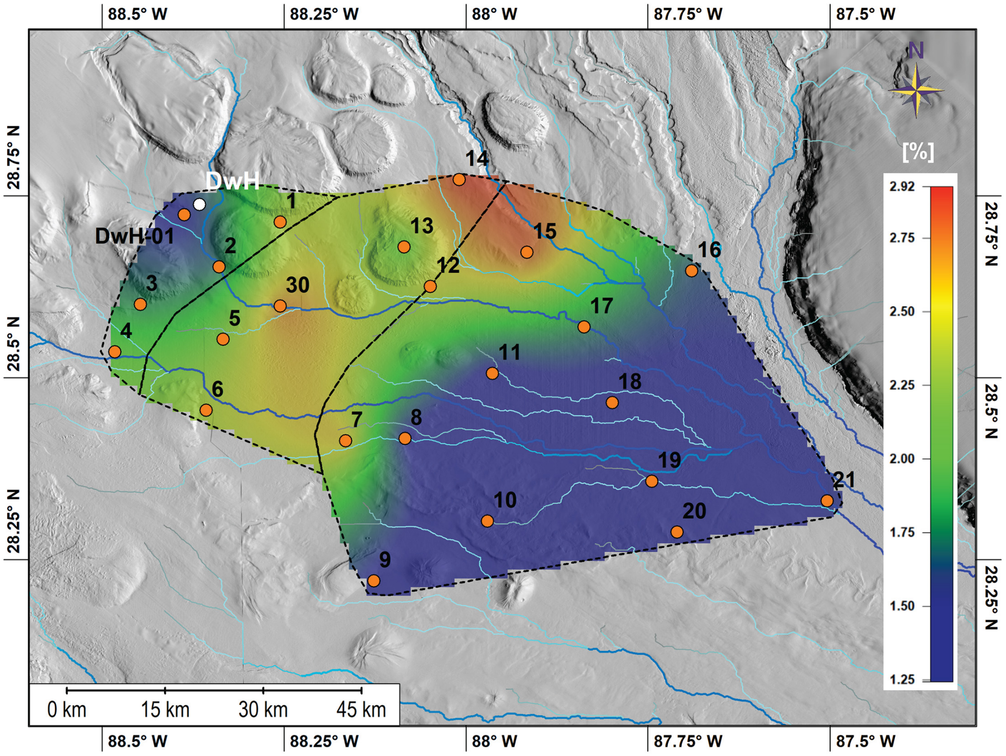

FIGURE 6 | Heat map of %carbon content of the upper 2 mm of the cores. Regions discussed are outlined by the dashed black lines. Region 1 is in the NW and Region 3 in the SE. Blue lines indicate channels as modeled by watershed analysis.

increased from the northwestern (e.g., site 1 mean density: 19 individuals/cm^3) to the southeastern (e.g., site 24 mean density: 38 individuals/cm^3) portion of the study area. Benthic foraminifera fracture percentage ranged from 7.5 to 25.1% with the highest mean fracture percentage in the north-central portion of the study area (e.g., site 12 mean: 20.6%, site 14 mean: 16.0%). Maxima in fracture percentage were typically found at 6–10 mm depth (sites 1, 9, 12, and 16). These maxima were often coincident with variability in other parameters consistent with resuspension (**Figure 9**).

Hydrocarbon Analyses

We identified 10 biomarker ratios that can be used as diagnostic biomarker ratios of DwH oil residues at depth (**Figure 10**). These biomarker ratios determined for samples from DWH-01 site lie within ±20% of the MC252 standard ratios. The fewer biomarker ratios that matched with the MC252 standard compared to coastal studies may indicate that more compounds are susceptible to multiple weathering processes at depth (e.g., dissolution, degradation, dispersion). Source apportionment of hydrocarbons in the study area after the spill was determined using principal component analysis (PCA) of the biomarker ratios identified in **Figure 10**. The PCA results in **Figure 11** show that 46% of the sites in 2010–2013 and 58% of the sites in 2014–2018 contain oil-residues similar to the MC252 oil standard (all located in the same PCA space) and distinct from other reference oil samples from the GoM. PCA results are supported by cross plots of alkane diagnostic ratios (**Figure 12**) and %abundance plots of hydrocarbon compounds groups (**Supplementary Figures 9a,b**). Caution should be taken when interpreting deep-sea data, because oil-residues deposited at depth, regardless of the source, are highly weathered. For example, **Figure 12** shows that several sites in both time periods (2010–2013: sites 1, 14, 8; 2014–2018: sites DwH-01, 1, 2, 12, 14, 16) contain oil-residues (CPI < 2.0 indicates oil-residues; %C14–C24 $< 25\%$ indicates heavily weathered samples) but with a dominant hydrocarbon source different than DwH oil, as shown by the PCA results (**Figure 11**). Also, some sites that were designated by the PCA to potentially contain mostly DwH oil-residues (shown in orange color sites 7 and 18 for 2010–2013, and sites 9 and 10 for 2014–2018) are shown in **Figure 12** to be mixed with other sources different than oil-residues (e.g., terrestrial), therefore we have classified these sites to contain mixed sources of hydrocarbons (shown in orange color in **Figures 11–13** and **Supplementary Figures 10a,b**). In addition, the results from the PCA analysis and cross plots were supported by distinct distribution patterns of *n*-alkanes and PAHs (**Supplementary Figures 11, 12**). The samples identified to contain DwH oil-residues as the potential major source for hydrocarbons in **Figures 11, 12**, have a distinct *n*-alkane composition with short-chain compounds (C12–C23) less than 2% abundance, while long-chain compounds (>C30) are more than 10% abundance (**Supplementary Figure 11** and in agreement with Stout et al., 2016). This pattern is

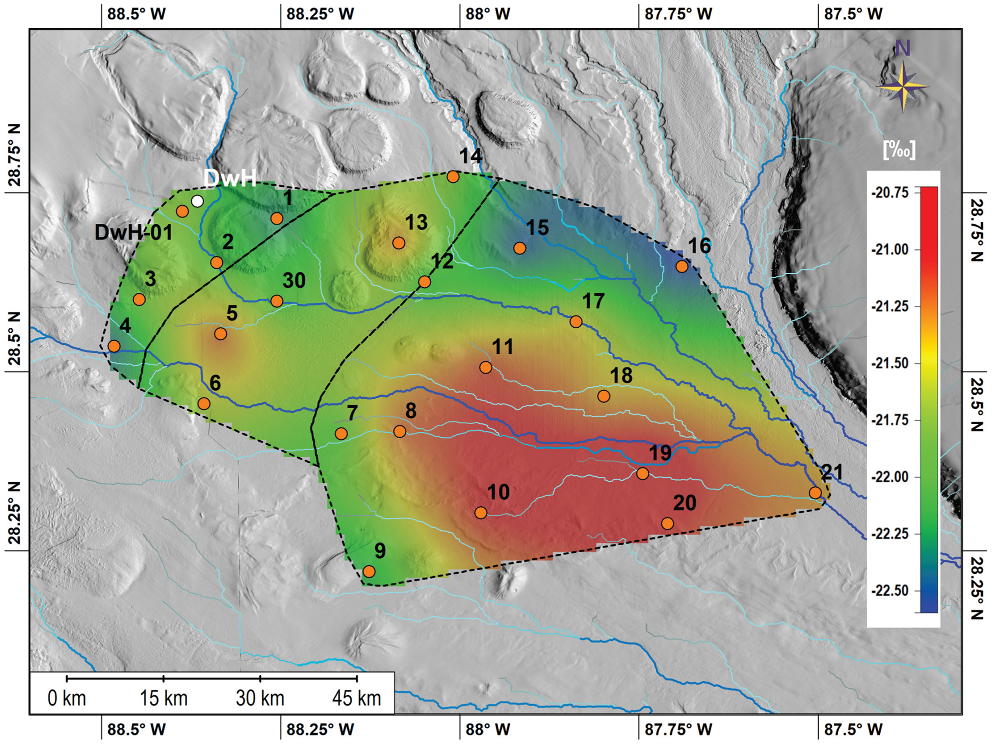

FIGURE 7 | Heat map of δ^{13}C surface isotopic composition (0–2 mm). Regions discussed are outlined by the dashed black lines. Region 1 is in the NW and Region 3 in the SE. Blue lines indicate channels as modeled by watershed analysis.

expected from severely weathered oil residues, in which long-chain *n*-alkanes are preserved due their lower susceptibility to dissolution and biodegradation. In contrast, other sources (as mixed or unknown in **Supplementary Figure 11**) show a strong odd-to-even carbon preference for long-chain *n*-alkanes, with C27, C29 and C31 as the most abundant. The observed odd-to-even carbon preference for long-chain *n*-alkanes is typical of terrestrial plants. For PAHs, the difference in distribution pattern among sources is as well observed (**Supplementary Figure 12**). The samples identified to contain DwH oil-residues as the potential major source for hydrocarbons in **Figures 11**, **12** have less %abundance of molecular markers of incomplete combustion such as Re and BeP (Ramdahl, 1983; Wang et al., 1999; Tobiszewski and Namieśnik, 2012), while 4–6 ring PAHs were more abundant due to their higher resistant to weathering processes such as dissolution and biodegradation. This pattern is more notorious by comparing the abundance of PAH compounds grouped by ring number (**Supplementary Figure 13**) showing a distribution difference among sources within each year. Also, larger changes between time periods is observed indicating potential additional weathering processing affecting mostly 5–6 ring PAHs (e.g., transformation processes, White et al., 2016). Overall, we found that 15 sites of the 24 studied sites contain DwH oil-residues as the potential major source for hydrocarbons (**Figure 13**). The results generated using multiple oil diagnostic ratios indicate the significance of using ratios from multiple compound groups (e.g., hopanes, steranes, alkanes, PAHs) for source apportionment of hydrocarbons in deep-sea areas, like in the northern GoM.

Hydrocarbon concentrations, the sum of all compounds analyzed [*n*-alkanes, isoprenoids, polycyclic aromatic hydrocarbons (PAHs), hopanes, steranes, and triaromatic steroids (TAS)] ranged from 0.2 μg/g to 11.4 μg/g, with decreasing concentrations toward southeast of the study area, with some exceptions observed at specific depth layers in the sediments (e.g., site 21) (**Figure 13**). Specifically, hydrocarbon averages >2.0 μg/g were observed in the northeast of the study area (sites DwH, 1–6, 12, 13, and 30), concentrations in the range of 0.9–2.0 μg/g were detected at the center of the study area (sites 7, 8, 11, 14, 15, 16, and 17), and concentrations <0.9 μg/g were observed in the southeast area (sites 9, 10, 19, 20, 21). This general trend in hydrocarbon concentration followed sediment grain size distribution, with higher concentrations where sediments have low carbonate content. In addition, downcore profiles show a large variability in hydrocarbon concentrations in the study area, with enhanced concentrations at specific sediment intervals (**Figure 12**). Also, specific hydrocarbon compound groups did not show a clear trend with depth (e.g., decrease with sediment depth); therefore, compound relative abundances mostly represent changes in hydrocarbon sources rather than solely biodegradation of hydrocarbons after buried (**Supplementary Figures 9a,b**). Most abundant compound groups were *n*-alkanes and high molecular weight PAHs (HMW, 4–6 rings). Profiles of HMW PAHs and LMW PAHs (low molecular weight, 2–3 rings)

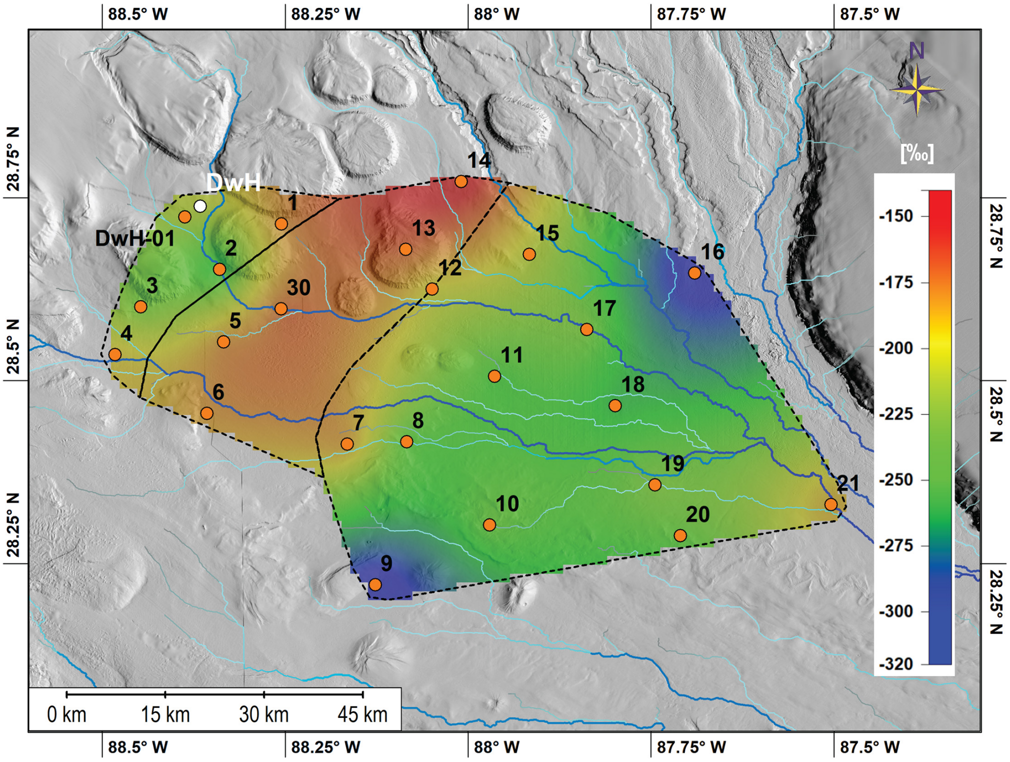

FIGURE 8 | Heat map of $\Delta^{14}C$ surface activity of the upper 2 mm of the cores. Regions discussed are outlined by the dashed black lines. Region 1 is in the NW and Region 3 in the SE. Blue lines indicate channels as modeled by watershed analysis.

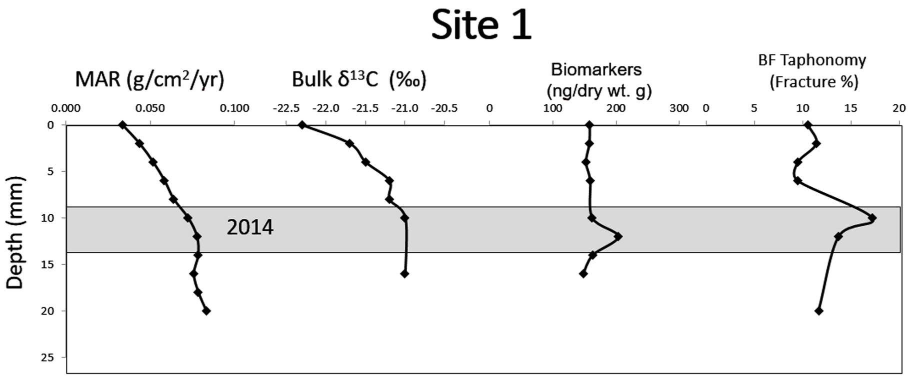

FIGURE 9 | An example of the multi-proxy assessment from station MC01, where an event was identified between 10 and 12 mm depth (year 2014) by relatively high mass accumulation rates, homogenous bulk organic stable carbon isotopes, an maxima in organic biomarkers and benthic foraminifera fracture percentage.

showed large variability in some sites in all sediment depth layers (i.e., site 10) or at specific sediment layers (i.e., sites 1, 11, 17, and 19), but in all cases HMW PAHs were more abundant.

DISCUSSION

Spatial Distribution

All sites were depositional over the past ~100 years and to various degrees contained sedimentary structures, but there were distinctive variations in accumulation patterns and sediment characteristics throughout the study area. These variations define three distinctive geographic regions with implications for the degree of influence of down-slope sediment transport on sediment accumulation patterns (**Figure 4**). Bathymetric characteristics, geographic location, and water depth also play a role in the characteristics of each region. Defining characteristics of the regions include episodic vs. stable sediment accumulation patterns as well as surficial sediment characteristics (upper 0–10 mm of cores). Using $^{210}Pb_{xs}$ age dating, cores were assessed

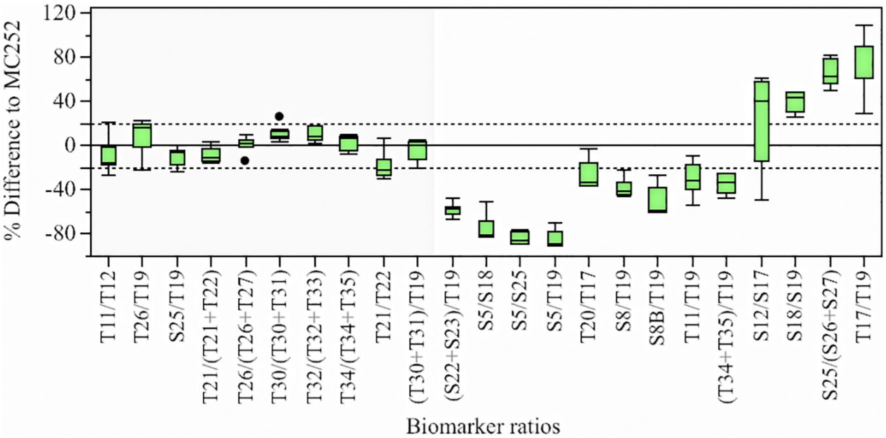

FIGURE 10 | Relative difference of biomarker ratios from DW site to the crude oil standard MC252. Graph shows green boxes as the interquartile ranges, with horizontal lines indicating median values and whiskers representing the 10th and 90th percentiles. Black circles denote outlier values, and dotted horizontal lines indicate ratios within ±20% of the MC252 standard. Information of compounds can be found in **Supplementary Tables 2a,b**.

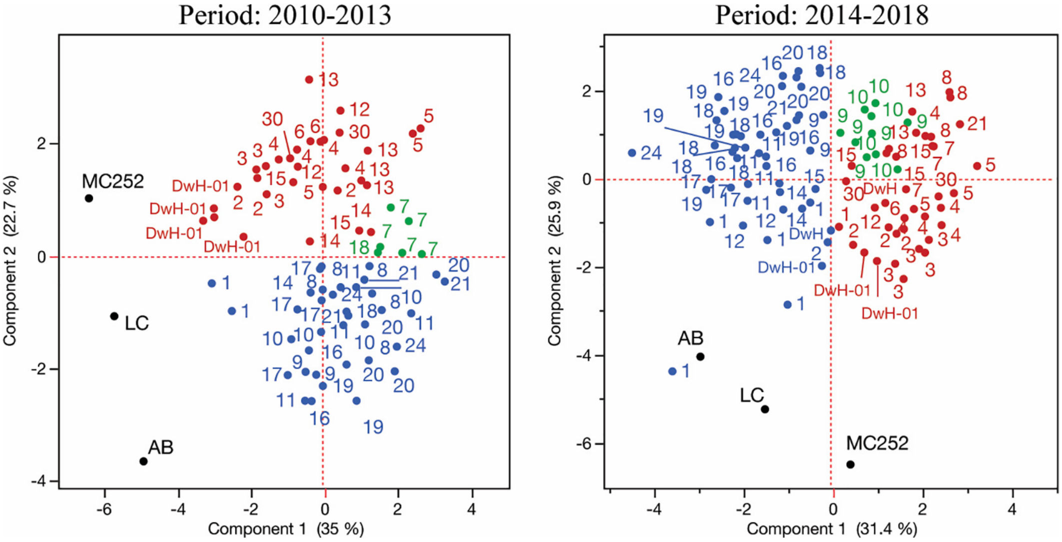

FIGURE 11 | Discrimination of diagnostic ratios in the studied area by principal component analysis (PCA) for the 2010–2013 and 2014–2018 time periods. Black circles show oil reference oils from the GoM (MC252: DWH oil; AB: southern GoM Akal Bravo oil; LC: Southern Louisiana Sweet oil), numbers indicate sites, red circles denote sites with DWH oil-residues as the potential major source, green circles indicate sites with mixed hydrocarbons sources including DWH oil-residues, and blue circles indicate other unknown sources. The diagnostic ratios used are described in the method section.

for accumulation patterns from 1950 to 2018 for longer term reference and in greater detail for three time periods, 2006–2009 (pre-spill), 2010–2013 (DwH spill/post-spill), and 2014–2018 (post-spill) to investigate the DwH spill and potential down-slope redistribution in subsequent years.

(a) Region 1 is in the NW portion of the study area directly surrounding the DwH spill site and includes our station DwH-01, and sites 1, 2, 3, and 4 (**Figure 4**).
(b) Region 2, includes sites, 5, 6, 12, 13, 14, 30, to the SE of Region 1, consisting of a "belt" running from the NE to SW (**Figure 4**).
(c) Region 3, SE of Region 2, includes sites 7, 8, 9, 10, 11, 15, 16, 17, 18, 19, 20, 21 (**Figure 4**).

Region 1, in the NW portion of the study area, received the highest inputs of contaminated sediments during and shortly after the spill as previously documented (Chanton et al., 2012, 2015; Passow et al., 2012; Joye et al., 2013; Brooks et al., 2015; Yan et al., 2016; Ziervogel et al., 2016; Romero et al., 2017) (**Figure 4**). Varying seafloor morphology with steep slopes and valleys was prevalent in this area (**Figure 1**), providing grounds for seafloor instability and higher potential for down-slope sediment transport. $^{210}Pb_{xs}$ data and sedimentary structures indicate pulsed downslope transport accompanied

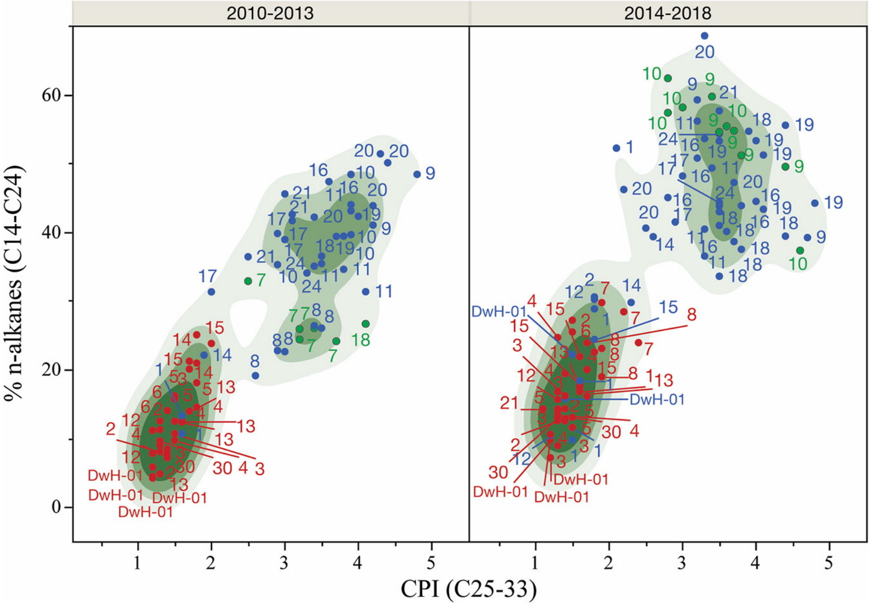

FIGURE 12 | Cross plots of diagnostic ratios for the deep-sea sites studied in the northern GoM. Numbers indicate sites, red circles denote sites with DwH oil-residues as the potential major source, green circles indicate sites with mixed hydrocarbons sources including DwH oil-residues, and blue circles indicate other unknown sources.

by episodic accumulation of sediments as being the main mechanism in sediment accumulation in this Region (**Figure 2**). Sedimentology reflects a dominance of fine-grained terrigenous source sediments with the highest %silt in the study area. The source of pulsed sediments accumulating in Region 1 likely lay upslope to the N and NW. The first peak in particle resuspension over time with increasing flow speed occurred above 10 cm s^{-1} in this Region followed by a total collapse of the sediment structure and complete erosion occurred above 13 cm s^{-1}. These high initial flow speeds needed to erode the surface indicate that this material was relatively new material that had arrived from the sea surface.

Region 2 is a transition zone from steep slopes (>10°) on the salt domes with deep incised smooth valleys between these domes (**Figure 1**) spreading out into an open plain on the seafloor with a decrease in slopes to near 0° in the more distal, SE portions. Region 1 and Region 2 had similar surface sediment characteristics. The water depth in this Region ranges from 1,250 to 1,900 m. ^{210}Pb$_{xs}$ data indicate more consistent stable accumulation with lower MAR's indicating that down-slope sediment transport is not dominantly accumulating and is likely bypassing this Region (**Figures 5A–C**). Evidence for sediment resuspension in this area by near inertial currents as well as tropical storm induced events has been reported in independent studies at these water depths (Gardner and Sullivan, 1981; Isley et al., 1990; Diercks et al., 2018), which may also limit deposition of sediments associated with down-slope transport. Sedimentology shows a decrease in %terrigenous sediments as compared to Region 1, which is expected with increased distance from the Mississippi River. In this Region, peaks in volume of particles resuspended occurred at flow speeds above 13 cm s^{-1} indicating that the cores were missing the surface layer of loose material. These sites had the highest %carbon and the most enriched Δ^{14}C values indicating deposition of younger material originating from the sea surface and not from resuspension.

The NW boundary of Region 3 can be visualized by a line drawn just north of sites 7, 12 and 15, with sites 12 and 15 being on the boundary between the two Regions (**Figure 4**). Region 3 encompasses the largest part of the study area on the seafloor with depths greater than 1,900 m. Most of the sites in Region 3 do not contain DwH oil-residues as the potential major source for hydrocarbons (eight out of eleven studied sites in this region). The majority of sites in Region 3 have higher relative abundance of C12–C25 *n*-alkanes in most sediment layers (**Supplementary Figures 9a,b**), indicating a potential larger presence of bacterial alkanes. Seafloor slope angles in this area are in general $<2^0$, sloping from the NW to the SE. Region 3 has the highest MAR's (**Figures 5A–C** and **Supplementary Figure 3**) and sediment records indicate a strong prevalence of episodic (pulses) sediment accumulation (**Figure 4**), likely associated with the down-slope transport events. The NE portion of Region 3 has the highest %clay, which may indicate accumulation of resuspended fine-grained sediments from upslope. The highest %sand values were found in the SE portion of Region 3 associated with more sand sized biogenic grains as shown by the concurrent increase in %carbonate. This was likely due to a decrease in fine-grained terrigenous sediment with further distance from the Mississippi River source. The uppermost 2 mm of sediments from cores collected in this area were easily resuspended at current speeds of 5–8 cm s^{-1}. **Figure 3** indicating that these sediments consisted of unconsolidated material. %Carbon content (**Figure 6**) for these samples were low (1.25 to 1.75%),

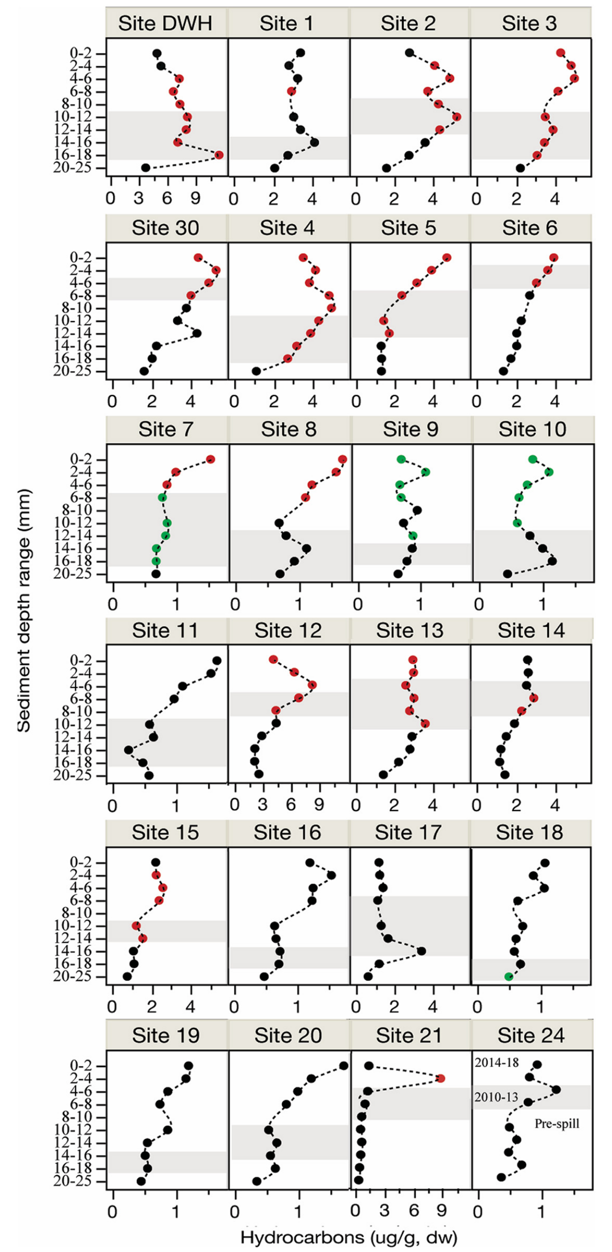

FIGURE 13 | Profiles of hydrocarbon concentrations in the study sites located in the northern GoM. Hydrocarbons refer to the sum of aliphatics, PAHs, hopanes, steranes, and TAS. Graph shows shaded areas corresponding to the time period 2010–2013, areas above and below the gray area corresponds to 2014–2018 and pre-spill periods, respectively. Red circles denote samples with DwH oil-residues as the potential major source, green circles indicate samples with mixed hydrocarbons sources including DwH oil-residues, and black circles indicate other unknown sources.

indicating older (**Figure 8**) reworked material being deposited, as discussed elsewhere (e.g., Diercks et al., 2018). We argue that these sediments either have been exposed to prolonged bacterial decomposition and remineralization after deposition on the seafloor or were transported from higher up on the slope as a result of resuspension and lateral transport. This lateral transport and redeposition of material would result in a loosely consolidated sediment layer, easier to be resuspended at lower flow speeds, and presenting the characteristics of an old sediment. This transport and redeposition of older material matches the results from the watershed model of the study area, which presented a general E to SE flow direction with a confluence of gravitational flow channels in the SE part of the Region (**Figure 1**). The model used the high-resolution seafloor morphology to determine gravity driven downslope flow and overlying water column currents were not considered.

Sedimentary structures indicative of sediment re-deposition by gravity flow processes were detected in almost all cores throughout the study area (**Figure 2** and **Table 1**). Thin, mm-scale, sub-parallel laminae and wavy-bedded units, by far the most common, were found in Regions 1, 2, and 3. The less common inclined beds and color banded units were confined to Regions 2 and 3 (**Figure 4**). All of these structures are common in adjacent Mississippi Fan deposits, and have been attributed to low density, fine-grained turbidity currents, slides and/or slumps (Coleman et al., 1986; Cremer and Stow, 1986; Normark et al., 1986; Stow et al., 1986; Thayer et al., 1986). Locations classified as depocenters exhibited two peaks in particle counts with increased flow speeds, one at low flow speeds and a second peak at higher flow speeds. This second peak coincided with the peaks from locations (erosional sites) that were missing the low flow speed peaks, indicating that the surface sediments in the depocenters were comprised of two distinctly different materials, loosely compacted material at the surface and a more consolidated layer of material below the surface. Once flow speeds in the flume reached 13 cm s^{-1} the exposed sediment in all cores eroded and disintegrated rapidly. Our results fall well within the range of prior data published in the literature. Lampitt (1985) reported that 6–8 cm s^{-1} can move low-density aggregates of phytodetritus (mm to cm in size) in the field and similar values have been reported for flume studies. Beaulieu (2003) compiled a list of theoretical, flume, and field measurements for critical erosion velocities of bioturbated silty sediments, which (Gardner et al., 2017) further summarized and concluded that resuspension of the fine silt fraction would occur as low as 11–12 cm s^{-1} and sand size fraction being resuspended at 25–30 cm s^{-1}.

Relative to levels of concern of toxic compounds analyzed in this study, we found that even though PAHs were abundant at the studied sites, most of their concentrations were lower than levels of concern for marine biota (Long et al., 1995; Bejarano and Michel, 2010) (**Supplementary Figures 10a,b**). Exceptions were found for LMW PAHs at site 1 (sediment interval 0–2 mm with concentration 0.6 μg/g), and for HMW PAHs at site DwH (sediment interval 16–25 mm with concentrations about 2.6 μg/g) and site 17 (sediment interval 16–18 mm with 2.6 μg/g concentration).

Time Periods

To better understand the role of major natural (e.g., downslope movement of particles) and anthropogenic (i.e., MOSSFA) depositional processes on the fate of DwH-derived hydrocarbons

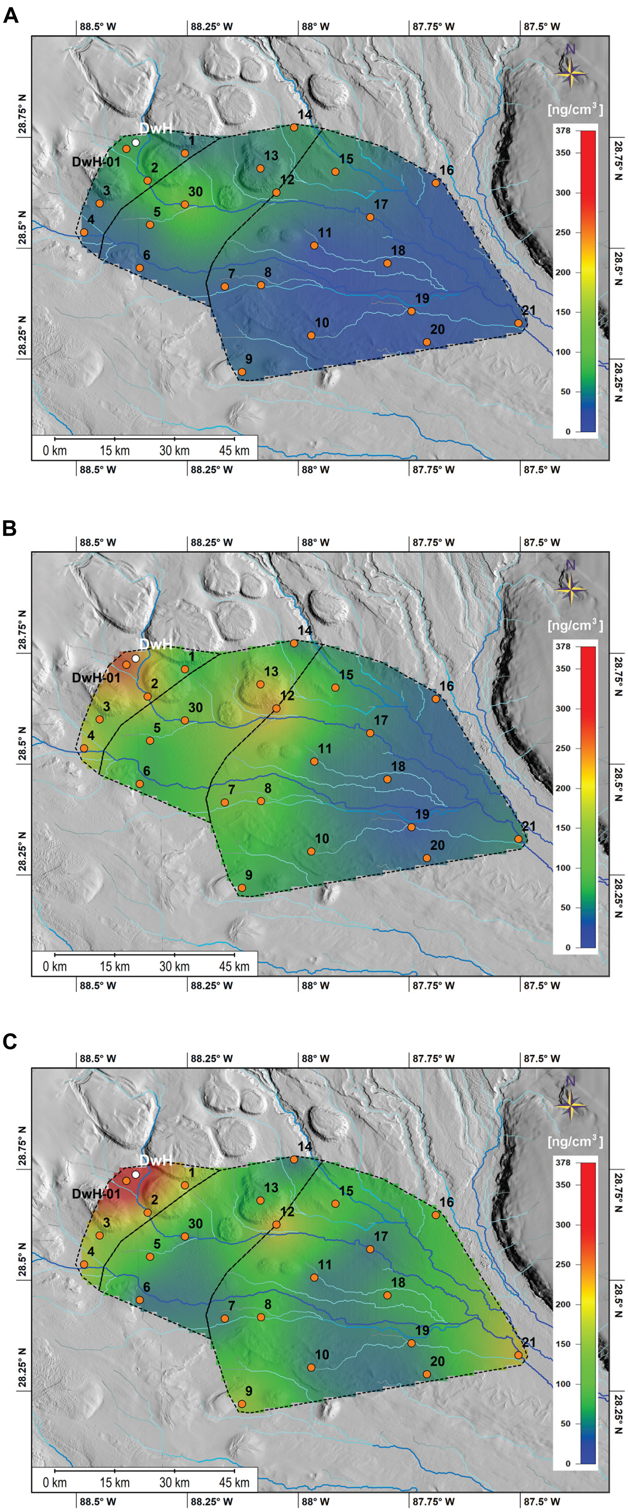

FIGURE 14 | Sediment depth-integrated biomarker concentrations in deep-sea sediments by time periods: **(A)** prespill (<2010), **(B)** spill/post-spill (2010–2013), **(C)** post-spill (2014–2018). Biomarker concentrations include the sum of hopanes (C23–C35), steranes (C27–C29), triaromatic steroids (C20–C21, C26–C28). Time periods were determined based on the established chronology.

in deep-sea environments of the GoM, data were assessed for three time-periods (pre-spill 2006–2009, spill/post-spill 2010–2013, and post-spill 2014–2018). The pre-spill (2006–2009) time interval represents sediment data from before the DwH spill and MOSSFA event and is characterized by having lower concentrations of hydrocarbons compared to the other time periods (**Figure 13**). The 2010–2013 time interval, includes the time immediately after the oil spill as well as the MOSSFA event as defined by areas sampled during and immediately after the spill (Passow et al., 2012; Brooks et al., 2015; Daly et al., 2016; Larson et al., 2018). In this time period, eleven sites of the 24 studied sites likely contain DwH oil-residues as the potential major source for hydrocarbons (**Figure 13**). Most of the eleven sites containing DwH oil-residues are in the Region 1 and 2, and only one site in Region 3 (site 15). The 2014–2018 interval represents the time post MOSSFA event, in which we identified lateral and downslope movement of material into the deeper sections of the GoM. These time periods provided the basis to test our hypothesis of a general down-slope, SE transport of material that was initially deposited during the DwH oil spill. DwH oil-residues that were deposited under the surface expression of the oil spill and the submerged oil plumes, may have been moved downslope through common processes like resuspension and gravity flows (Diercks et al., 2018).

In the time period between 2014 and 2018, MARs had returned to pre-spill levels (Larson et al., 2018), however, there was large variability between the three time periods observed in total concentration of hydrocarbons (**Figure 13**), as well as for specific hydrocarbon compounds (**Supplementary Figures 9a,b**). This variability is highlighted by the relative composition among time-periods, which indicate a highly dynamic sedimentation regime in the study area (**Supplementary Figures 5a,b**). In this time period, 14 sites of the 24 studied sites contain DwH oil-residues as the potential major source for hydrocarbons (**Figure 13**). The 14 sites containing DwH oil-residues are located in all regions and only four sites (#1, 7, 8, 21) contain DwH oil-residues in the period 2014–2018 (**Figure 13**). Mapping the most recalcitrant compounds, such as biomarkers for each time period, presents the general spatial patterns of hydrocarbon concentrations decreasing toward the southeast of the study area (**Figures 14A–C**). Most elevated concentrations were observed only post-spill (2010–2013 and 2014–2018), mostly at sites located closer to the DwH site (**Figures 14A–C**). Millimeter-scale events were identified within the upper two centimeters (**Figure 13**). These events were typically dated between 2014 and 2016 (post-DwH), are consistent with redeposition of resuspended material and were characterized by relatively high MAR, homogenous bulk organic δ^{13}C, and maxima in both organic biomarkers and benthic foraminifera fracture percentage. The uppermost 2 mm of the cores were dominated by benthic foraminifera (e.g., predominantly *Bolivina lowmani, Eponides turgidus, Trochammina inflata, Uvigerina peregrina*), planktic foraminifera (e.g., *Globigerinoides ruber, Globorotalia menardii, Orbulina universa*) and some deep-sea sediments and date to the 2016–2018 depositional period, providing an average sedimentation rate of 0.10 to 0.14 g cm^3 $year^{-1}$ as determined by MARs from $^{210}Pb_{xs}$ measurements.

CONCLUSION

Overall, our results indicate an increased spatial footprint of deposition of DwH-derived hydrocarbons for which we offer two explanations. The deposition of contaminated sediments was not previously identified due to a lack of sampling in our study area and down-slope redistribution of sediments over the 8 years following the DwH oil spill and initial MOSSFA deposition to the seafloor. We based our conclusions on the characteristics of three regions as defined by their morphological and sedimentological features as well as the likelihood of sediments accumulating in these regions through episodic down-slope transport mechanisms. The nature of the organic compounds found in some of the cores, as well as sediment composition from these regions allowed us to trace them back to the DwH oil spill (in 15 out of 24 studied sites). Region 1 showed the presence of episodic sediment accumulation and had a potential for longer term accumulation and sequestration of redistributed sediments from up-slope areas. Region 2 was defined by stable and consistent sediment accumulation with low magnitude events in down-slope sediment accumulation being very subtle in the sedimentary record. We determined that this area is less likely to accumulate and sequester redistributed sediments. Region 3 had an increased presence of episodic sediment accumulation through larger magnitude pulse events. These events lead to a higher potential for accumulation and sequestration of redistributed sediments from up-slope areas.

Our findings presented in this paper, provide evidence that the footprint of the residues from the oil spill on the seafloor changed over the time span from 2010 to 2018 expanding to the SE beyond the previous areal extent reported. In the sedimentary record, DwH oil-residues were found in sites during the post-spill periods studied (2010–2013: during the MOSSFA event; 2014–2018: post MOSSFA event; sites: DwH-01, 2, 3, 4, 5, 6, 12, 13, 15, 30) as well as in sites only during the 2014–2018 period (sites: 1, 8, 21). Specifically, sites located approximately 45 km (site 8; 28.4166° N, 88.0838° W) and 96 km (site 21; 28.3306°N, 87.5042°W) to the SE of the wellhead, indicate a larger area affected by DwH oil residues due only to down slope redistribution of organic matter by natural process at depth in the GoM. Our data thus suggest that a much larger area on the seafloor contained residues of DWH oil than previously then previously recognized and published in the literature (Lehr et al., 2010; Chanton et al., 2012; Lubchenco et al., 2012; Romero et al., 2017).

DATA AVAILABILITY STATEMENT

The datasets presented in this study can be found in online repositories. The names of the repository/repositories and accession number(s) can be found below: Data are publicly available through the Gulf of Mexico Research Initiative Information & Data Cooperative (GRIIDC) at https://data.gulfresearchinitiative.org: doi: 10.7266/n7-5xgs-mg78; doi: 10.7266/n7-ry85-yq61; 10.7266/n7-gzhr-0s83; doi: 10.7266/n7-zwvz-6a72; doi: 10.7266/n7-h6gj-1m18; doi: 10.7266/n7-391g-9t63; doi: 10.7266/N7445K2V; doi: 10.7266/n7-6bfd-g305; and doi: 10.7266/HCKBSN5J.

AUTHOR CONTRIBUTIONS

All authors listed have made a substantial, direct and intellectual contribution to the work, and approved it for publication.

FUNDING

The REDIRECT (Resuspension, Redistribution and Deposition of Deepwater Horizon recalcitrant hydrocarbons to offshore depocenter) research was made possible by a grant from The Gulf of Mexico Research Initiative (GOMRI). Also, research was supported by an Early-Career Research Fellowship from the Gulf Research Program of the National Academies of Sciences, Engineering, and Medicine to IC Romero (Grant #2000010685). The content in this publication is solely the responsibility of the authors and does not necessarily represent the official views of the Gulf Research Program of the National Academies of Sciences, Engineering, and Medicine.

ACKNOWLEDGMENTS

The authors would like to thank the crew of the R/V Point Sur for their help during the field program and the technicians Hannah Hamontree, and Olivia Traenkle for laboratory support during chemical analyses of hydrocarbons.

SUPPLEMENTARY MATERIAL

The Supplementary Material for this article can be found online at: https://www.frontiersin.org/articles/10.3389/fmars.2021.630183/full#supplementary-material

REFERENCES

Adhikari, P., Wong, R., and Overton, E. (2017). Application of enhanced gas chromatography/triple quadrupole mass spectrometry for monitoring petroleum weathering and forensic source fingerprinting in samples impacted by the deepwater horizon oil spill. *Chemosphere* 184, 939–950. doi: 10.1016/j.chemosphere.2017.06.077

Aeppli, C., Nelson, R. K., Radović, J. R., Carmichael, C. A., Valentine, D. L., and Reddy, C. M. (2014). Recalcitrance and degradation of petroleum biomarkers upon abiotic and biotic natural weathering of Deepwater Horizon oil. *Environ. Sci. Technol.* 48, 6726–6734. doi: 10.1021/es500825q

Appleby, P. G. (2001). "Chronostratigraphic techniques in recent sediments," in *Tracking Environmental Change Using Lake Sediments: Basin Analysis, Coring, and Chronological Techniques Developments in Paleoenvironmental Research*, eds W. M. Last and J. P. Smol (Dordrecht: Springer Netherlands), 171–203. doi: 10.1007/0-306-47669-x_9

Appleby, P. G., and Oldfield, F. (1983). The assessment of 210Pb data from sites with varying sediment accumulation rates. *Hydrobiologia* 103, 29–35. doi: 10.1007/BF00028424

Ash-Mor, A., Bookman, R., Kanari, M., Ben-Avraham, Z., and Almogi-Labin, A. (2017). Micropaleontological and taphonomic characteristics of mass transport deposits in the northern Gulf of Eilat/Aqaba, Red Sea. *Mar. Geol.* 391, 36–47. doi: 10.1016/j.margeo.2017.07.009

Baskaran, M., Nix, J., Kuyper, C., and Karunakara, N. (2014). Problems with the dating of sediment core using excess (210)Pb in a freshwater system impacted by large scale watershed changes. *J. Environ. Radioact.* 138, 355–363. doi: 10.1016/j.jenvrad.2014.07.006

Beaulieu, S. E. (2003). Resuspension of phytodetritus from the sea floor: a laboratory flume study. *Limnol. Oceanogr.* 48, 1235–1244. doi: 10.4319/lo.2003.48.3.1235

Bejarano, A. C., and Michel, J. (2010). Large-scale risk assessment of polycyclic aromatic hydrocarbons in shoreline sediments from Saudi Arabia: environmental legacy after twelve years of the Gulf war oil spill. *Environ. Pollut.* 158, 1561–1569. doi: 10.1016/j.envpol.2009.12.019

Binford, M. W. (1990). Calculation and uncertainty analysis of 210Pb dates for PIRLA project lake sediment cores. *J. Paleolimnol.* 3, 253–267. doi: 10.1007/BF00219461

Borrowman, T. D., Smith, E. R., Gailani, J. A., and Caviness, L. (2006). *Erodibility Study of Passaic River Sediments Using USACE Sedflume*. Fort Belvoir, VA: Defense Technical Information Center.

Brady, H. B. (1878). On the reticularian and radiolarian rhizopoda (Foraminifera and Polycystina) of the North Polar Expedition of 1875-76. *Ann. Mag. Nat. Hist.* 5, 425–440. doi: 10.1080/00222937808682361

Brady, H. B. (1879). Notes on some of the reticularian Rhizopoda of the challenger expedition, part i. on new or little known arenaceous types. *Q. J. Microsc. Sci.* 19, 20–63. doi: 10.1242/jcs.s2-19.73.20

Brady, H. B. (1884). Report on the foraminifera dredged by H.M.S. Challenger during the years 1873-1876. *Zoology* 9, 1–814.

Brooks, G. R., Larson, R. A., Schwing, P. T., Romero, I., Moore, C., Reichart, G.-J., et al. (2015). Sedimentation pulse in the NE gulf of mexico following the 2010 DWH Blowout. *PLoS One* 10:e0132341. doi: 10.1371/journal.pone.0132341

Camilli, R., Reddy, C. M., Yoerger, D. R., Van Mooy, B. A. S., Jakuba, M. V., Kinsey, J. C., et al. (2010). Tracking hydrocarbon plume transport and biodegradation at deepwater horizon. *Science* 330, 201–204. doi: 10.1126/science.1195223

Chanton, J. P., Cherrier, J., Wilson, R. M., Sarkodee-Adoo, J., Bosman, S., Mickle, A., et al. (2012). Radiocarbon evidence that carbon from the Deepwater Horizon spill entered the planktonic food web of the Gulf of Mexico. *Environ. Res. Lett.* 7:045303. doi: 10.1088/1748-9326/7/4/045303

Chanton, J., Zhao, T., Rosenheim, B. E., Joye, S., Bosman, S., Brunner, C., et al. (2015). Using natural abundance radiocarbon to trace the flux of petrocarbon to the seafloor following the deepwater horizon oil spill. *Environ. Sci. Technol.* 49, 847–854. doi: 10.1021/es5046524

Choi, M., Kim, Y.-J., Lee, I.-S., and Choi, H.-G. (2014). Development of a one-step integrated pressurized liquid extraction and cleanup method for determining polycyclic aromatic hydrocarbons in marine sediments. *J. Chromatogr. A* 1340, 8–14. doi: 10.1016/j.chroma.2014.03.015

Choi, Y., and Wang, Y. (2004). Dynamics of carbon sequestration in a coastal wetland using radiocarbon measurements. *Glob. Biogeochem. Cycles* 18:GB4016. doi: 10.1029/2004GB002261

Coleman, J. M., Bouma, A. H., Roberts, H. H., and Thayer, P. A. (1986). "Stratification in mississippi fan cores revealed by X-Ray radiography," in *Initial Reports of the Deep Sea Drilling Project*, Vol. 96, eds A. H. Bouma, J. M. Coleman, and A. W. Meyer (Washington, D.C: U.S. Government Printing Office), 505–518.

Cremer, M., and Stow, D. A. V. (1986). Sedimentary structures of fine-grained sediments from the Mississippi Fan: Thin Section Analysis. *Initial Reports of the Deep Sea Drilling Project. XCVI.*, 96, 519–532. http://deepseadrilling.org/96/volume/dsdp96_24.pdf

Crowsey, R. C. (2013). Persistence of gulf of mexico surface oil from the 2010 deepwater horizon spill. *Southeast. Geogr.* 53, 359–361. doi: 10.1353/sgo.2013.0034

Cushman, J. A. (1922). Shallow-Water Foraminifera of the Tortugas Region. *Carnegie Inst. Wash.* 17, 1–85.

Cushman, J. A. (1923). The foraminifera of the Atlantic Ocean. Part 4. Lagenidae. *Bull. U.S. Natl. Mus.* 104, 1–228. doi: 10.2113/49.suppl_2.1

Cushman, J. A. (1927). New and interesting foraminifera from Mexico and Texas. *Contributions Cushman Lab. Foraminifer. Res.* 3, 111–117.

d'Orbigny, A. D. (1826). Tableau méthodique de la classe des Céphalopodes. *Ann. Sci. Nat.* 7, 245–314.

d'Orbigny, A. D. (1839). *Voyage dans l'Amerique Meridionale*. Paris and Strasbourg: Bertrand, 1–86.

Daly, K. L., Passow, U., Chanton, J., and Hollander, D. (2016). Assessing the impacts of oil-associated marine snow formation and sedimentation during and after the Deepwater Horizon oil spill. *Anthropocene* 13, 18–33. doi: 10.1016/j.ancene.2016.01.006

Daly, K. L., Vaz, A. C., and Paris, C. B. B. (2020). The Sedimentation and Lateral Transport of Oil-Associated Marine Snow During and After the Deepwater Horizon Oil Spill. in (AGU). doi: 10.1007/978-3-030-12963-7_18

Dean, W. E. (1974). Determination of carbonate and organic matter in calcareous sediments and sedimentary rocks by loss on ignition; comparison with other methods. *J. Sediment. Res.* 44, 242–248. doi: 10.1306/74D729D2-2B21-11D7-8648000102C1865D

Diercks, A.-R., Dike, C., Asper, V. L., DiMarco, S. F., Chanton, J. P., and Passow, U. (2018). Scales of seafloor sediment resuspension in the northern Gulf of Mexico. *Elem. Sci. Anth.* 6:32. doi: 10.1525/elementa.285

Diercks, A.-R., Highsmith, R. C., Asper, V. L., Joung, D., Zhou, Z., Guo, L., et al. (2010). Characterization of subsurface polycyclic aromatic hydrocarbons at the Deepwater Horizon site. *Geophys. Res. Lett.* 37:L20602. doi: 10.1029/2010GL045046

Folk, R. L. (1965). *Petrology of Sedimentary Rocks*. Austin, TX: Hemphill.

Gardner, W. D., and Sullivan, L. G. (1981). Benthic storms: temporal variability in a deep-ocean nepheloid layer. *Science* 213, 329–331. doi: 10.1126/science.213.4505.329

Gardner, W. D., Tucholke, B. E., Richardson, M. J., and Biscaye, P. E. (2017). Benthic storms, nepheloid layers, and linkage with upper ocean dynamics in the western North Atlantic. *Mar. Geol.* 385, 304–327. doi: 10.1016/j.margeo.2016.12.012

Gros, J., Reddy, C. M., Aeppli, C., Nelson, R. K., Carmichael, C. A., and Arey, J. S. (2014). Resolving biodegradation patterns of persistent saturated hydrocarbons in weathered oil samples from the Deepwater Horizon disaster. *Environ. Sci. Technol.* 48, 1628–1637. doi: 10.1021/es4042836

Herrera-Herrera, A. V., Leierer, L., Jambrina-enríquez, M., Connolly, R., and Mallol, C. (2020). Evaluating different methods for calculating the Carbon Preference Index (CPI): implications for palaeoecological and archaeological research. *Org. Geochem.* 146:104056. doi: 10.1016/j.orggeochem.2020.104056

Isley, A. E., Dale Pillsbury, R., and Laine, E. P. (1990). The genesis and character of benthic turbid events, Northern Hatteras Abyssal plain. *Deep Sea Res. A Oceanogr. Res. Pap.* 37, 1099–1119. doi: 10.1016/0198-0149(90)90053-X

Jernelöv, A., and Lindén, O. (1981). Ixtoc I: a case study of the world's largest oil spill. *Ambio* 10:299.

Jones, J. P., and Parker, W. K. (1860). On the rhizopodal fauna of the mediterranean compared with that of the Italian and some other tertiary deposits. *Q. J. Geol. Soc. Lond.* 16, 292–307. doi: 10.1144/gsl.jgs.1860.016.01-02.41

Joye, S. B., Crespo-Medina, M., Hunter, K., Asper, V., Diercks, A., Passow, U., et al. (2013). Increased sedimentation and altered nutrient cycling in the aftermath of the Macondo oil well blowout. *Abstr. Pap. Am. Chem. Soc.* 245.

Kim, J. H., Moon, J. K., Li, Q. X., and Cho, J. Y. (2003). One-step pressurized liquid extraction method for the analysis of polycyclic aromatic hydrocarbons. *Anal. Chim. Acta* 498, 55–60. doi: 10.1016/j.aca.2003.08.049

Kitto, M. E. (1991). Determination of photon self-absorption corrections for soil samples. *Int. J. Radiat. Appl. Instrum. A* 42, 835–839. doi: 10.1016/0883-2889(91)90221-L

Kramer, K. V., and Shedd, B. (2017). *A 1.4-Billion-Pixel Map of the Gulf of Mexico Seafloor. Eos*. Available online at: https://eos.org/project-updates/a-1-4-billion-pixel-map-of-the-gulf-of-mexico-seafloor (Accessed January 11, 2018).

Lampitt, R. S. (1985). Evidence for the seasonal deposition of detritus to the deep-sea floor and its subsequent resuspension. *Deep Sea Res. A Oceanogr. Res. Pap.* 32, 885–897. doi: 10.1016/0198-0149(85)90034-2

Larson, R. A., Brooks, G. R., Schwing, P. T., Holmes, C. W., Carter, S. R., and Hollander, D. J. (2018). High-resolution investigation of event driven sedimentation: Northeastern Gulf of Mexico. *Anthropocene* 24, 40–50. doi: 10.1016/j.ancene.2018.11.002

Lehr, B., Bristol, S., and Possolo, A. (2010). *Oil Budget Calculator - Deepwater Horizon, A Report to the National Incident Command*. https://www.restorethegulf.gov/sites/default/files/documents/pdf/OilBudgetCalc_Full_HQ-Print_111110.pdf

Long, E. R., Macdonald, D. D., Smith, S. L., and Calder, F. D. (1995). Incidence of adverse biological effects within ranges of chemical concentrations in marine and estuarine sediments. *Environ. Manag.* 19, 81–97. doi: 10.1007/BF02472006

Lubchenco, J., McNutt, M. K., Dreyfus, G., Murawski, S. A., Kennedy, D. M., Anastas, P. T., et al. (2012). Science in support of the Deepwater Horizon response. *Proc. Natl. Acad. Sci. U.S.A.* 109, 20212–20221. doi: 10.1073/pnas.1204729109

Meyer, B. M., Adhikari, P. L., Olson, G. M., Overton, E. B., and Miles, M. S. (2017). *Louisiana Coastal Marsh Environments and MC252 Oil Biomarker Chemistry*. Amsterdam: Elsevier Inc.

Milliman, J. D. (1974). Marine carbonates. recent sedimentary carbonates part 1. Springer-Verlag, New York, Heidelberg, & Berlin, xv + 375 p. $25.50. *Limno. Oceanogr.* 19:876. doi: 10.4319/lo.1974.19.5.0876b

Mulabagal, V., Yin, F., John, G. F., Hayworth, J. S., and Clement, T. P. (2013). Chemical fingerprinting of petroleum biomarkers in Deepwater Horizon oil spill samples collected from Alabama shoreline. *Mar Pollut Bull* 70, 147–154. doi: 10.1016/j.marpolbul.2013.02.026

Normark, W. R., Meyer, A. W., Cremer, M., Droz, L., O'Connell, S., Pickering, K. T., et al. (1986). "Summary of drilling results for the Mississippi Fan and considerations for applications to other turbidite systems," in *Initial Reports of the Deep Sea Drilling Project*, eds A. H. Bouma, J. M. Coleman, and A. W. Meyer (Washington, DC: U.S. Government Printing Office), 425–436.

Osterman, L. E. (2003). Benthic foraminifers from the continental shelf and slope of the Gulf of Mexico: an indicator of shelf hypoxia. *Estuar. Coast. Shelf Sci.* 58, 17–35. doi: 10.1016/S0272-7714(02)00352-9

Parker, F. L. (1954). Distribution of foraminifera in the Northeastern Gulf of Mexico. *Bull. Mus. Comp. Zool.* 111, 453–588.

Parker, F. L., Phleger, F. B., and Pierson, J. F. (1953). North Atlantic foraminifera. *Rep. Swedish Deep Sea Expedition, 1947-1948* 7, 3–122.

Parker, W. K., and Jones, T. R. (1865). On some foraminifera from the coast of Norway. *Ann. Mag. Nat. Hist.* 155, 325–441.

Passow, U., Chanton, J. P., Hollander, D., and Dahly, K. (2013). *MOSSFA (Marine Oil Snow Sedimentation and Flocculent Accumulation) Working Group*. Tallahassee, FL: Florida State University.

Passow, U., Ziervogel, K., Asper, V., and Diercks, A. (2012). Marine snow formation in the aftermath of the deepwater horizon oil spill in the Gulf of Mexico. *Environ. Res. Lett.* 7:035301. doi: 10.1088/1748-9326/7/3/035301

Patterson, R. T., and Fishbein, E. (1989). Re-examination of the statistical methods used to determine the number of point counts needed for micropaleontological quantitative research. *J. Paleontol.* 63, 245–248. doi: 10.1017/S0022336000019272

Phleger, F. B., and Parker, F. L. (1951). Gulf of mexico foraminifera, Part 1 and 2. *Geol. Soc. Am. Mem.* 46.

Prince, R. C., Owens, E. H., and Sergy, G. A. (2002). Weathering of an Arctic oil spill over 20 years: the BIOS experiment revisited. *Mar. Pollut. Bull.* 44, 1236–1242. doi: 10.1016/s0025-326x(02)00214-x

Ramdahl, T. (1983). Retene–a molecular marker of wood combustion in ambient air. *Nature* 306, 580–582. https://doi.org/10.1038/306580a0

Romero, I. C., Chanton, J. P., Brooks, J. R., Bosman, S., Larson, R. A., Harris, A., et al. (2021). Molecular markers of biogenic and oil-derived hydrocarbons in deep-sea sediments following the Deepwater Horizon spill. *Front. Mar. Sci.* (in press). doi: 10.3389/fmars.2021.637970

Romero, I. C., Schwing, P. T., Brooks, G. R., Larson, R. A., Hastings, D. W., Ellis, G., et al. (2015). Hydrocarbons in deep-sea sediments following the 2010 deepwater horizon blowout in the Northeast Gulf of Mexico. *PLoS One* 10:e0128371. doi: 10.1371/journal.pone.0128371

Romero, I. C., Sutton, T., Carr, B., Quintana-Rizzo, E., Ross, S. W., Hollander, D. J., et al. (2018). Decadal Assessment of polycyclic aromatic hydrocarbons in mesopelagic fishes from the gulf of mexico reveals exposure to oil-derived sources. *Environ. Sci. Technol.* 52, 10985–10996. doi: 10.1021/acs.est.8b02243

Romero, I. C., Toro-Farmer, G., Diercks, A.-R., Schwing, P., Muller-Karger, F., Murawski, S., et al. (2017). Large-scale deposition of weathered oil in the Gulf of Mexico following a deep-water oil spill. *Environ. Pollut.* 228, 179–189. doi: 10.1016/j.envpol.2017.05.019

Schwing, P. T., Brooks, G. R., Larson, R. A., Holmes, C. W., O'Malley, B. J., and Hollander, D. J. (2017). Constraining the spatial extent of marine oil snow sedimentation and flocculent accumulation following the deepwater horizon event using an excess 210 Pb flux approach. *Environ. Sci. Technol.* 51, 5962–5968. doi: 10.1021/acs.est.7b00450

Schwing, P. T., O'Malley, B. J., and Hollander, D. J. (2018). Resilience of benthic foraminifera in the Northern Gulf of Mexico following the Deepwater Horizon event (2011–2015). *Ecol. Indic.* 84, 753–764. doi: 10.1016/j.ecolind.2017.09.044

Schwing, P. T., Romero, I. C., Larson, R. A., O'Malley, B. J., Fridrik, E. E., Goddard, E. A., et al. (2016). Sediment core extrusion method at millimeter resolution using a calibrated, threaded-rod. *J. Vis. Exp.* 114, 54363. doi: 10.3791/54363

Smith, L. M., Alexander, C., and Jennings, A. E. (2002). Accumulation in east greenland fjords and on the continental shelves adjacent to the denmark strait over the last century based on 210Pb geochronology. *ARCTIC* 55, 109–122. doi: 10.14430/arctic695

Sørensen, L., Meier, S., and Mjøs, S. A. (2016). Application of gas chromatography/tandem mass spectrometry to determine a wide range of petrogenic alkylated polycyclic aromatic hydrocarbons in biotic samples. *Rapid Commun. Mass Spectrom.* 30, 2052–2058. doi: 10.1002/rcm.7688

Stewart, R. E., and Stewart, K. C. (1930). Post-miocene foraminifera from the ventura quadrangle, ventura county, California. *J. Paleontol.* 4, 60–72.

Stout, S. A., Payne, J. R., Ricker, R. W., Baker, G., and Lewis, C. (2016). Macondo oil in deep-sea sediments: part 2 — distribution and distinction from background and natural oil seeps. *Mar. Pollut. Bull.* 111, 381–401. doi: 10.1016/j.marpolbul.2016.07.041

Stow, D. A. V., Cremer, M., Droz, L., Meyer, A. W., Normark, W. R., O'Connell, S., et al. (1986). "Facies, composition, and texture of Mississippi Fan sediments, Deep Sea Drilling Project Leg 96, Gulf of Mexico," in *Initial Reports of the Deep Sea Drilling Project*, eds A. H. Bouma, J. M. Coleman, and A. W. Meyer (Washington, DC: U.S. Government Printing Office), 475–488.

Stuiver, M., and Polach, H. A. (1977). Discussion reporting of 14 C Data. *Radiocarbon* 19, 355–363. doi: 10.1017/S0033822200003672

Swarzenski, P. W. (2014). "210Pb dating," in *Encyclopedia of scientific dating methods*, eds W. J. Rink and J. Thompson (Dordrecht: Springer Netherlands), 1–11. doi: 10.1007/978-94-007-6326-5_236-1

Thayer, P., Roberts, H. H., Bouma, A. H., and Coleman, J. M. (1986). "Sedimentology and petrology of mississippi fan depositional environments, deep sea drilling project leg 96," in *Initial Reports of the Deep Sea Drilling Project*, eds A. H. Bouma, J. M. Coleman, and A. W. Meyer (Washington, D.C: U.S. Government Printing Office), 489–504.

Tobiszewski, M., and Namieśnik, J. (2012). PAH diagnostic ratios for the identification of pollution emission sources. *Environ. Pollut.* 162, 110–119. doi: 10.1016/j.envpol.2011.10.02

Turnewitsch, R., Dale, A., Lahajnar, N., Lampitt, R. S., and Sakamoto, K. (2017). Can neap-spring tidal cycles modulate biogeochemical fluxes in the abyssal near-seafloor water column? *Prog. Oceanogr.* 154, 1–24. doi: 10.1016/j.pocean.2017.04.006

Turnewitsch, R., Falahat, S., Nycander, J., Dale, A., Scott, R. B., and Furnival, D. (2013). Deep-sea fluid and sediment dynamics—influence of hill- to seamount-scale seafloor topography. *Earth Sci. Rev.* 127, 203–241. doi: 10.1016/j.earscirev.2013.10.005

Turnewitsch, R., Reyss, J.-L., Chapman, D. C., Thomson, J., and Lampitt, R. S. (2004). Evidence for a sedimentary fingerprint of an asymmetric flow field surrounding a short seamount. *Earth Planet. Sci. Lett.* 222, 1023–1036. doi: 10.1016/j.epsl.2004.03.042

Valentine, D. L., Fisher, G. B., Bagby, S. C., Nelson, R. K., Reddy, C. M., Sylva, S. P., et al. (2014). Fallout plume of submerged oil from Deepwater Horizon.

Proc. Natl. Acad. Sci. U.S.A. 111, 15906–15911. doi: 10.1073/pnas.1414873111

Vogel, J. S., Southon, J. R., Nelson, D. E., and Brown, T. A. (1984). Performance of catalytically condensed carbon for use in accelerator mass spectrometry. *Nuclear Instruments and Methods in Physics Research Section B: Beam Interactions with Materials and Atoms*, 5, 289–293. https://doi.org/10.1016/0168-583X(84)90529-9

Wang, Z., and Fingas M. F. (2003). Development of oil hydrocarbon fingerprinting and identification techniques. *Mar Pollut Bull* 47, 423–452. doi: 10.1016/S0025-326X(03)00215-7

Wang, Z., Fingas, M., Shu, Y. Y., Sigouin, L., Landriault, M., Lambert, P., et al. (1999). Quantitative Characterization of PAHs in Burn Residue and Soot Samples and Differentiation of Pyrogenic PAHs from Petrogenic PAHs-The 1994 Mobile Burn Study. *Environ. Sci. Technol.* 33, 3100–3109. doi: 10.1021/es990031y

Wang, Z., Stout, S. A., and Fingas, M. (2006). Forensic Fingerprinting of Biomarkers for Oil Spill Characterization and Source Identification. *Environ. Forensics* 7, 105–146. doi: 10.1080/15275920600667104

Wang, Z. D., Fingas, M., Owens, E. H., Sigouin, L., and Brown, C. E. (2001). Long-term fate and persistence of the spilled Metula oil in a marine salt marsh environment - degradation of petroleum biomarkers. *J. Chromatogr. A* 926, 275–290. doi: 10.1016/s0021-9673(01)01051-2

White, H. K., Wang, C. H., Williams, P. L., Findley, D. M., Thurston, A. M., Simister, R. L., et al. (2016). Long-term weathering and continued oxidation of oil residues from the Deepwater Horizon spill. *Mar. Pollut. Bull.* 113, 380–386. doi: 10.1016/j.marpolbul.2016.10.02

Williamson, W. C. (1858). On the Recent Foraminifera of Great Britain. *Ray Society*, 1–107. https://doi.org/10.5962/bhl.title.139719

Xing, L., Zhang, H., Yuan, Z., Sun, Y., and Zhao, M. (2011). Terrestrial and marine biomarker estimates of organic matter sources and distributions in surface sediments from the East China Sea shelf. *Cont. Shelf Res.* 31, 1106–1115. doi: 10.1016/j.csr.2011.04.003

Yan, B., Passow, U., Chanton, J. P., Nöthig, E.-M., Asper, V., Sweet, J., et al. (2016). Sustained deposition of contaminants from the Deepwater Horizon spill. *Proc. Natl. Acad. Sci. U.S.A.* 113, E3332–E3340. doi: 10.1073/pnas.1513156113

Ziervogel, K., Dike, C., Asper, V., Montoya, J., Battles, J., D×souza, N., et al. (2016). Enhanced particle fluxes and heterotrophic bacterial activities in Gulf of Mexico bottom waters following storm-induced sediment resuspension. *Deep Sea Res. II Top. Stud. Oceanogr.* 129, 77–88. doi: 10.1016/j.dsr2.2015.06.017

Conflict of Interest: The authors declare that the research was conducted in the absence of any commercial or financial relationships that could be construed as a potential conflict of interest.

frontiers
in Marine Science

ORIGINAL RESEARCH
published: 06 July 2021
doi: 10.3389/fmars.2021.637970

Molecular Markers of Biogenic and Oil-Derived Hydrocarbons in Deep-Sea Sediments Following the Deepwater Horizon Spill

Isabel C. Romero[1], Jeffrey P. Chanton[2], Gregg R. Brooks[3], Samantha Bosman[2], Rebekka A. Larson[3], Austin Harris[4], Patrick Schwing[1,3] and Arne Diercks[4]*

[1] College of Marine Science, University of South Florida, Saint Petersburg, FL, United States, [2] Department of Earth, Ocean and Atmospheric Sciences, Florida State University, Tallahassee, FL, United States, [3] Marine Science Program, Eckerd College, Saint Petersburg, FL, United States, [4] Division of Marine Science, School of Ocean Science and Engineering, The University of Southern Mississippi, Hattiesburg, MS, United States

Edited by:
Robert Hetland,
Texas A&M University, United States

Reviewed by:
Shawn Doyle,
Texas A&M University, United States
Hernando Bacosa,
Mindanao State University-Iligan Institute of Technology (MSU-IIT), Philippines

***Correspondence:**
Isabel C. Romero
isabelromero@usf.edu

Specialty section:
This article was submitted to Marine Biogeochemistry, a section of the journal Frontiers in Marine Science

Received: *04 December 2020*
Accepted: *28 April 2021*
Published: *06 July 2021*

Citation:
Romero IC, Chanton JP, Brooks GR, Bosman S, Larson RA, Harris A, Schwing P and Diercks A (2021) Molecular Markers of Biogenic and Oil-Derived Hydrocarbons in Deep-Sea Sediments Following the Deepwater Horizon Spill. Front. Mar. Sci. 8:637970. doi: 10.3389/fmars.2021.637970

Following the Deepwater Horizon oil spill (DWHOS), the formation of an unexpected and extended sedimentation event of oil-associated marine snow (MOSSFA: Marine Oil Snow Sedimentation and Flocculent Accumulation) demonstrated the importance of biology on the fate of contaminants in the oceans. We used a wide range of compound-specific data (aliphatics, hopanes, steranes, triaromatic steroids, polycyclic aromatics) to chemically characterize the MOSSFA event containing abundant and multiple hydrocarbon sources (e.g., oil residues and phytoplankton). Sediment samples were collected in 2010–2011 (ERMA-NRDA programs: Environmental Response Management Application – Natural Resource Damage Assessment) and 2018 (REDIRECT project: Resuspension, Redistribution and Deposition of Deepwater Horizon recalcitrant hydrocarbons to offshore depocenter) in the northern Gulf of Mexico to assess the role of biogenic and chemical processes on the fate of oil residues in sediments. The chemical data revealed the deposition of the different hydrocarbon mixtures observed in the water column during the DWHOS (e.g., oil slicks, submerged-plumes), defining the chemical signature of MOSSFA relative to where it originated in the water column and its fate in deep-sea sediments. MOSSFA from surface waters covered 90% of the deep-sea area studied and deposited 32% of the total oil residues observed in deep-sea areas after the DWHOS while MOSSFA originated at depth from the submerged plumes covered only 9% of the deep-sea area studied and was responsible for 15% of the total deposition of oil residues. In contrast, MOSSFA originated at depth from the water column covered only 1% of the deep-sea area studied (mostly in close proximity of the DWH wellhead) but was responsible for 53% of the total deposition of oil residues observed after the spill in this area. This study describes, for the first time, a multi-chemical method for the identification of biogenic and oil-derived inputs to deep-sea sediments, critical for improving our understanding of carbon inputs and storage at depth in open ocean systems.

Keywords: hydrocarbons, deep-sea sediment, oil spill accidents, MOSSFA, marine oil snow (MOS)

INTRODUCTION

In marine systems, hydrocarbons are composed of a complex mixture of compounds that originated biologically from autochthonous (e.g., phytoplankton, microbes, seeps) and allochthonous (e.g., terrestrial, anthropogenic) sources. Organic particles that reach the seafloor undergo weathering; still, the chemical signatures related to their source and transformation processes are preserved and can be used to assess the contribution from different sources to the global carbon budget for modern sediments as well as for historical palaeoceanographic reconstructions (Zonneveld et al., 2009; Canuel and Hardison, 2016; Bianchi et al., 2018; Larowe et al., 2020). Recently, efforts have focused on identifying the chemical signature of multiple sources in sinking organic particles in the water column or on the seafloor to better understand biogenic-petrogenic interactions that influenced carbon preservation and ecosystem health in areas with abundant natural seeps and oil exploration (Adhikari et al., 2015, 2016; Romero et al., 2017; Chanton et al., 2018; White et al., 2019; Bosman et al., 2020). Despite multiple studies looking at the fate of organic matter in the environment, the identification of robust chemical markers for source apportionment and transport processes of oil residues from surface waters to deep-sea sediments is still not available.

Differentiating hydrocarbon sources is important because it provides crucial information about sea surface to seafloor connectivity (e.g., organic matter transport processes and carbon sequestration). For example, hydrocarbons are significant components in the upper ocean carbon cycle due to the pervasive natural contribution from phytoplankton (Middleditch et al., 1979; Kameyama et al., 2009; Lea-smith et al., 2015) as well as in specific regions by large extensions of oil residues released from natural seeps (MacDonald et al., 2015) or as a result of oil spills (e.g., Deepwater Horizon oil spill – DWHOS: surface slicks covered 11200 km^2, MacDonald et al., 2015; submerged plumes covered ~73200 km^2, Du and Kessler, 2012). Also, it has been observed that multiple hydrocarbon sources can interact and form biogenic-petrogenic aggregates in association with natural oil seeps, important for understanding hydrocarbon degradation and fate in the water column (D'souza et al., 2016). Furthermore, high-resolution analysis of deep-sea sediments collected in the aftermath of the DWHOS in the northern Gulf of Mexico (nGoM), revealed a large deposition of aggregates composed of inorganic and biogenic material mixed with oil residues containing varied chemical signatures (Brooks et al., 2015; Romero et al., 2015). These findings were supported by multiple observations of co-occurring phytoplankton blooms and surface oil-slicks during the DWHOS (Hu et al., 2011; Ziervogel et al., 2012; Passow et al., 2012; Vonk et al., 2015; Daly et al., 2016; Yan et al., 2016; Quigg et al., 2020). This enhanced sedimentation event was known as MOSSFA (Marine Oil Snow Sedimentation and Flocculent Accumulation) and consisted of oil residues mixed with organic and inorganic particles, including bacteria, phytoplankton, microzooplankton, zooplankton fecal pellets, detritus, and terrestrially derived lithogenic particles (Daly et al., 2020). Moreover, the deposition of oil residues as marine oil snow (MOS) and/or oil-mineral aggregates (OMAS) is not specific to the DWHOS (e.g., Niu et al., 2010; Vonk et al., 2015; Romero et al., 2016). Therefore, a better understanding of the conditions that favor MOSSFA events and its role in the fate of oil residues at depth is warranted for improving response efforts in the event of future oil spill accidents.

Offshore in the nGoM, MOSSFA was responsible for the deposition of ~4–9% of the total oil discharged and not recovered from the DWHOS (Chanton et al., 2015; Romero et al., 2017). As a result, approximately a fourfold increase in sedimentary mass accumulation rates (Brooks et al., 2015) and 2–6 fold increase in hydrocarbon concentrations were observed in deep-sea sediments (Romero et al., 2015, 2017). Based on initial estimates of combined sedimentology, geochemical, and biological approaches, MOSSFA occurred over a 4–5-month period after the DWHOS (Brooks et al., 2015; Yan et al., 2016). However, Larson et al. (2018) found that stabilization of sedimentation in the nGoM did not occur until 2013. This is supported by numerous studies showing that oil residues from the DWHOS were still in the water column in the years following the spill (Adhikari et al., 2015, 2016; Walker et al., 2017; Romero et al., 2018). MOSSFA ultimately resulted in a widespread of faunal exposures to oil residues from the water column (Murawski et al., 2014; Quintana-Rizzo et al., 2015; Ainsworth et al., 2018; Romero et al., 2018, 2020; Pulster et al., 2020; Sutton et al., 2020) to benthic environments (Montagna et al., 2013; Baguley et al., 2015; Schwing et al., 2015, 2017, 2018; Rohal et al., 2020).

Furthermore, because hydrocarbons from the DWHOS were released at 1,500 m depth, multiple chemical mixtures within the water column were formed during transport of the spilled oil to the surface, including partitioning into dissolved and undissolved hydrocarbon mixtures (Socolofsky et al., 2011; Ryerson et al., 2012; Lindo-Atichati et al., 2014). The partitioning of hydrocarbons into chemical mixtures is not unique to the DWHOS, as it has been observed previously from natural releases (Harvey et al., 1979), shallower marine oil spills (Boehm and Flest, 1982; Elordui-zapatarietxe et al., 2010), and experimental discharges (Johansen et al., 2003). Specific to the DWHOS, based on the composition and concentration of hydrocarbons in each chemical mixture, it was calculated that of the total leaked mass ~10% formed surface slicks composed of insoluble and non-volatile compounds ([≥]C12), and ~36% formed deep submerged plumes of dissolved and dispersed compounds (<C12) (Ryerson et al., 2012). Although increased concentrations outside of the submerged plumes in the water column were observed (e.g., Valentine et al., 2010; Joye et al., 2011; Romero et al., 2018), these residues were not accounted for in models or oil fate assessment studies. Also, high concentrations of MOS were observed in the vicinity of the surface oil slicks and the submerged oil plumes (e.g., Passow et al., 2012; Daly et al., 2016), but the role of MOSSFA from these different chemical oil mixtures have not been elucidated to date. This is important for further understating the efficacy of natural and chemical dispersed processes to retain oil residues at depth. Altogether, to date, the role of MOSSFA on the deposition of biogenic-petrogenic aggregates from different water masses containing

distinct chemical mixtures (e.g., surface: oil slicks, ∼900–1300 m depth: submerged plumes) is not known.

In this study, we use a wide range of data collected after the DWHOS (*n*-alkanes, isoprenoids, PAHs: polycyclic aromatic hydrocarbons including alkylated homologs, hopanes, steranes, and TAS: triaromatic steroids) to chemically characterize the MOSSFA event, which contained abundant and multiple hydrocarbon sources (e.g., oil residues and phytoplankton). The primary goal of this study was to identify molecular markers of biogenic and oil-derived hydrocarbons in deep-sea sediments collected in the aftermath of the DWHOS (2010–2011; ERMA and Gulf Science publicly available data) and years after the spill (2018; REDIRECT project). The chemical data from samples collected in 2010–2011 were used to determine where the hydrocarbons originated in the water column (surface vs. depth). This distinction was possible to observe because the surface slicks had a different chemical composition of oil-derived hydrocarbons than the submerged plumes at depth (insoluble and non-volatile compounds vs dissolved and dispersed compounds, respectively; Ryerson et al., 2012). The chemical data from samples collected in 2018 were used to improve our understanding of the changes in hydrocarbon composition after burial in deep-sea sediments and the efficacy of molecular markers to differentiate biogenic and oil-derived hydrocarbons after years of weathering. The results generated, define the chemical signature of MOSSFA relative to where it originated in the water column and its fate in deep-sea sediments, fundamental for better understanding hydrocarbon cycling in the oceans.

MATERIALS AND METHODS

Samples Collected in 2010–2011 (Publicly Available Data)

The chemical data used in this study, was collected from July 2010 to September 2011 offshore in the nGoM (deep-sea sediments, $N = 239$ sites, **Figure 1**). This dataset was obtained from publicly available databases such as ERMA Deepwater Gulf Response[1] (downloaded on June 2013) and Gulf Science[2] (downloaded on March 2013). This dataset can now be found at the DIVER database[3]. The different databases used similar chemical protocols for the analysis of hydrocarbons in sediment samples (GCMS-SIM analysis; protocols: 8270D and 8015C). Compounds include aliphatics (C12–C37 *n*-alkanes, isoprenoids), PAHs (2–6 ring polycyclic aromatic hydrocarbons including alkylated homologs), biogenic PAHs (retene, perylene), and biomarkers like hopanes (C27–C35), steranes (C27–C29), and triaromatic steroids (C26–C28) (**Supplementary Table 1**). To assure reliable results, a strict chain of custody, calibration check samples, method blanks, and matrix spike samples were conducted. A more detailed explanation of QA/QC protocol and sample collection can be found in the Analytical Quality Assurance Plan report for Mississippi Canyon 252 (NOAA, 2011) and Stout and Payne (2016a). Only sediment cores with a full analysis of >C9 hydrocarbons and containing oil residues from the DWHOS were used in this study.

The chemical data from samples collected in 2010–2011 were used to identify molecular markers of biogenic and oil-derived hydrocarbons from the chemical mixtures that formed during transport of the spilled oil to the surface (Socolofsky et al., 2011; Ryerson et al., 2012; Lindo-Atichati et al., 2014). In order to establish the connectivity between water column and sedimentary organic matter during 2010–2011, we assumed that the molecular signature of the chemical mixtures (e.g., surface slicks, submerged plumes) was not affected significantly (1) during the MOSSFA event (transport of oil residues to the seafloor), and (2) after deposition as observed in Romero et al. (2015). Here, we used chemical ratios to identify molecular signatures of MOSSFA rather than hydrocarbon concentrations, which were shown to be affected mostly during transport in the water column and by slow *in situ* biodegradation on the seafloor (Romero et al., 2017). We used the same dataset analyzed in Romero et al. (2017). Only the sites located at depths > 200 m (deep-sea area) that were contaminated with oil residues from the DWHOS (see details in Romero et al., 2017) are included here in this study (**Figure 1**). Data from each site, correspond to sediment cores divided into the surface sediment layer (top 1 cm) and downcore layer (1–3 cm). The surface sediment layer represents recently deposited organic matter on the seafloor due to the increased sedimentation event that occurred during the DWHOS (Brooks et al., 2015; Chanton et al., 2015; Romero et al., 2015; Stout and Payne, 2016a). The layer 1–3 cm in each core studied corresponds to sediments deposited before the DWHOS (Brooks et al., 2015; Romero et al., 2015, 2017).

Samples Collected in 2018 (REDIRECT Project)

We collected and analyzed deep-sea sediment cores that were sampled during the REDIRECT project (Resuspension, Redistribution, and Deposition of the Deepwater Horizon Recalcitrant Hydrocarbons to offshore Depocenters) on the R/V *Point Sur* cruise (18–25 in May of 2018) using a multi corer (MC-800) in the nGoM ($N = 11$ sites, **Figure 1**). Sediment cores were extruded at 2 mm intervals for surficial sediment (0–10 cm), and at 5 mm intervals to the base of the core using Schwing et al. (2016) method.

Samples were chemically analyzed at the Marine Environmental Chemistry Laboratory (MECL, College of Marine Science, University of South Florida) for hydrocarbons following modified EPA methods and QA/QC protocols (GCMSMS-MRM analysis; protocols: 8270D and 8015C). Targeted compounds (**Supplementary Table 1**) include aliphatics (C12–C37 *n*-alkanes, isoprenoids), PAHs (2-6 ring polycyclic aromatic hydrocarbons including alkylated homologs), biogenic PAHs (retene, perylene), and biomarkers like hopanes (C27–C35), steranes (C27–C29), and triaromatic steroids (TAS; C20–C28). Freeze-dried samples were extracted using an Accelerated Solvent Extraction system (ASE 200®, Dionex) following a one-step extraction and clean up

---

[1] https://gomex.erma.noaa.gov/

[2] http://gulfsciencedata.bp.com/

[3] https://www.diver.orr.noaa.gov/

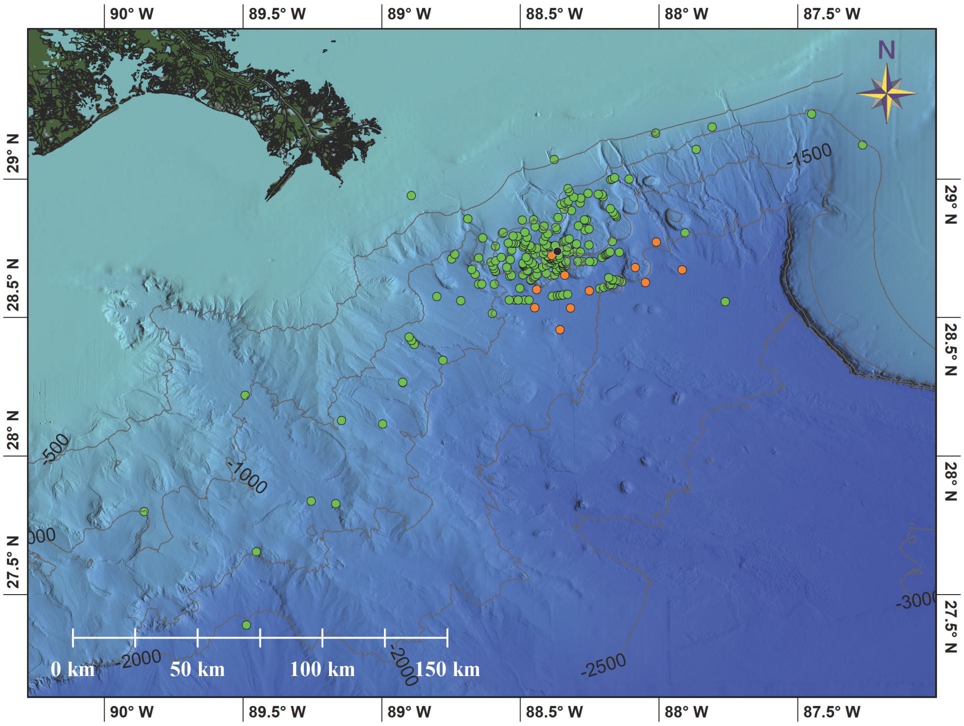

FIGURE 1 | Location of studied sites in the nGoM where sediment cores were collected between 2010 and 2011 (green circles; ERMA and Gulf Science publicly available data) and 2018 (orange circles; REDIRECT project). The Deepwater Horizon wellhead is shown as a black circle.

procedure using a predetermined packing of the extraction cells (Romero et al., 2018). Hydrocarbon compounds were quantified using GC/MS/MS (Agilent 7680B gas chromatograph coupled with an Agilent 7010 triple quadrupole mass spectrometer) in selected reaction monitoring mode (SRM) to target multiple chemical fractions in one-run-step. Molecular ion masses for hydrocarbon compounds were selected from previous studies (Romero et al., 2015, 2017; Sørensen et al., 2016; Adhikari et al., 2017) and can be found in the **Supplementary Table 2**. For accuracy and precision of analyses, we included laboratory blanks, spiked controls samples, tuned MS/MS to PFTBA (perfluorotributylamine) daily, used standard reference material (NIST 2779) daily, and reanalyzed sample batches when replicated standards exceeded ± 20% of relative standard deviation (RSD), and/or if recoveries were low. Quantitative determination of compounds was conducted using response factors (RFs) calculated from the certified standard NIST 2779.

The samples collected in 2018 were used to study how weathering processes (e.g., biodegradation) affected the chemical composition of hydrocarbons after years of being buried in deep-sea sediments. Similar to the chemical data from 2010 to 2011, we included only the sites that contained oil residues from the DWHOS (N = 11 sites, **Figure 1**), as determined previously using established hopane and sterane ratios (Diercks et al., 2021). Also, for the sediment cores collected in 2018, we used only samples that were deposited between 2010 and 2013 (N = 72 samples), the period in which enhanced sedimentation was observed due to the MOSSFA event (Larson et al., 2018). Sediment cores were analyzed for short-lived radioisotopes and $^{210}\text{Pb}_{xs}$ geochronologies were utilized to identify the sediment layer that was deposited during the period of 2010–2013. Briefly, the activities of the ^{214}Pb (295 keV), ^{214}Pb (351 keV), and ^{214}Bi (609 keV) were averaged as a proxy for the Radium-226 (^{226}Ra) activity of the sample or the "supported" Lead-210 ($^{210}\text{Pb}_{Sup}$) that is produced *in situ* (Baskaran et al., 2014; Swarzenski, 2014). The $^{210}\text{Pb}_{Sup}$ activity was subtracted from the $^{210}\text{Pb}_{Tot}$ activity to calculate the "unsupported" or "excess" Lead-210 ($^{210}\text{Pb}_{xs}$), which is used for dating within the last ~100 years. The Constant Rate of Supply (CRS) model was used to assign specific ages to sedimentary intervals within $^{210}\text{Pb}_{xs}$ profiles (Appleby and Oldfield, 1983; Binford, 1990). Short-lived radioisotope results and geochronologies for the sites studied are found in the **Supplementary Tables 3–13**.

Calculation and Statistical Analysis

Reported hydrocarbon concentrations are expressed as sediment dry weight concentrations. Low molecular weight (LMW) PAHs were calculated as the sum of all 2–3 ring PAHs, while high molecular weight (HMW) PAHs were calculated as the sum of 4–6 ring PAHs (all including alkylated homologs). LMW alkanes include the sum of C12–C23 *n*-alkanes, while HMW alkanes include the sum of C24–C37 *n*-alkanes. Hopanes, steranes and triaromatic hydrocarbons (TAS) were calculated as the sum of C23–C25, C27–C29, and C20–C28 compounds, respectively.

Multiple diagnostic ratios were calculated (**Table 1**) to characterize the chemical signature of the MOSSFA event

TABLE 1 | List of diagnostic ratios for PAHs, alkanes, and hopanes.

Ratios	Interpretation	References
%Re[1]	Product of early diagenesis or combustion of terrestrial organic matter	a
PI[2]	Pyrogenic index: distinguish pyrogenic from petrogenic PAH sources	b
Parent/alkyl[3]	Distinguish pyrogenic from petrogenic PAH sources	b
(N0–N1)/T19	Detects dissolved sources of PAHs at depth	c
De/T19[4]	Identify oil residues not affected by evaporation and dissoultion at depth	c
LMW/HMW PAHs[5]	Comparable abundance of more degradable PAHs	d
%5–6 ring PAHs[6]	Relative abundance of HMW PAHs	c
%Chrysene	Abundance of chrysene relative to the sum of all PAH compounds	e
(C15,17)/(C14,16,18)[7]	Detects biogenic alkanes in the presence of oil	f
CPI (C15–C19)[8]	Carbon preference index to distinguish phytoplankton sources from microbial and oil	g
CPI (C14–C23)[9]	Carbon preference index to distinguish natural sources from oil	h
CPI (C25–C33)[10]	Carbon preference index to distinguish natural sources from oil	h
LMW/HMW alkanes[11]	Comparable abundance of more degradable alkanes	c
%C12–C13	Relative abundance of the most degradable alkanes	c
%Terp[12]	Detects interfering compounds that coelute with T20, T26, T30, and T35	i
TS/TM	Recalcitrant biomarkers use to identify oil sources	j
T21/(T21 + T22)	Recalcitrant biomarkers use to identify oil sources	j
T26/(T26 + T27)	Recalcitrant biomarkers use to identify oil sources	j
T30/(T30 + T31)	Recalcitrant biomarkers use to identify oil sources	j
(T30 + T31)/T19	Comparable abundance of more degradable hopanes	k
(T32-T35)/T19[13]	Comparable abundance of more degradable hopanes	k
(T32 + T33)/T19	Comparable abundance of more degradable hopanes	k

See text for previous studies that have applied these ratios in marine environments (Materials and Methods section: Data Analysis).

[1] retene/ΣPAHs × 100; [2] Σ(other 3–6 ring EPA priority pollutant PAHs)/Σ(5 alkylated PAHs); [3] Σparent PAHs/Σalkyl PAHs; [4] Σ(De0–De4)/T19; [5] Σ2–3 ring/Σ4–6 ring PAHs; [6] Σ5–6 ring PAHS/ΣPAHs × 100; 7Σ(C15,C17)/Σ(C14,C16,C18) n-alkanes; 81/2(Σodd C15–C19/Σeven C15–C19); 7Σ(C15,C17)/Σ(C14,C16,C18) n-alkanes; 81/2(Σodd C15–C19/Σeven C15-C19); [9] 1/2(Σodd C14-C23/Σeven C14-C23); [10] 1/2(Σodd C25-C33/Σeven C25-C33); [11] Σ(nC12-C23)/Σ(nC24-C37); [12] Σ(T20, T26, T30,T35)/Σbiomarkers × 100; [13] Σ(T32,T33,T34,T35)/T19.

a: Abrajano and Yan, 2003; b: Wang et al., 1999a; Romero et al., 2015, 2017; c: this study; d: Romero et al., 2015, 2017; e: Wang and Fingas, 2003; Liu et al., 2012; f: White et al., 2019; g: Xing et al., 2011; h: Bray and Evans, 1961; Xing et al., 2011; Romero et al., 2015; Herrera-Herrera et al., 2020; i: Simoneit et al., 1985, 2020; Hood et al., 2002; Dembicki, 2010; Stout and German, 2018; j: Mulabagal et al., 2013; Aeppli et al., 2014; Romero et al., 2015, 2017; Wang et al., 2016; k: Aeppli et al., 2014; Romero et al., 2017.

relative to where it originated in the water column and its fate in sediments. PAH compounds were used to identify natural sources (%Re; Abrajano and Yan, 2003), discriminate petrogenic from pyrogenic sources (low vs. high values of the PI and Parent/alkyl ratios; Wang et al., 1999a; Romero et al., 2015, 2017), detect sources of dissolved oil-derived PAHs (N0-N1/T19), identify undissolved PAHs in the water column not exposed to the atmosphere (De/T19), and distinguish weathered samples (LMW/HMW PAHs, %5–6 ring PAHs, %Chrysene; Wang and Fingas, 2003; Liu et al., 2012; Romero et al., 2015, 2017; **Table 1**). Naphthalene compounds (e.g., N0, N1) were found to be abundant in the submerged plumes formed during the DWHOS (29.4–189.0 ppb; Diercks et al., 2010) due to the partitioning of more soluble PAHs during transport to surface waters (Ryerson et al., 2012) as observed as well in other marine oil spills (Gonzalez et al., 2006); therefore, they can be used as indicators of PAH inputs from near sources at depth (e.g., seeps, DWHOS wellhead). Other compounds, such as decalins (ratio: De/T19) can be used to identify the origin of oil residues in the water column due to their high evaporative (boiling point: 190°C) and low solubility (log Kow: 4.20) properties, relative to other compounds such as naphthalene (boiling point: 218°C, log Kow: 3.30). Consequently, high values of De/T19 can only be found in sediments if oil residues came from a MOSSFA event which originated at depth (didn't reach the surface and were not entrained in the submerged plumes).

Alkane compounds were used to separate biogenic inputs in the presence of oil (ratio (C15,17)/(C14,16,18; White et al., 2019), discern phytoplankton sources from microbial and oil (CPI$_{C15-C19}$; Xing et al., 2011), differentiate natural sources from oil (CPI$_{C14-C23}$, CPI$_{C25-C33}$; Bray and Evans, 1961; Xing et al., 2011; Romero et al., 2015; Herrera-Herrera et al., 2020), and distinguish weathered samples [LMW/HMW alkanes, (C12–C13)/T19] (**Table 1**).

We used hopane compounds to identify oil residues from the DWHOS using diagnostic ratios for oil identification that have been reported previously (Mulabagal et al., 2013; Aeppli et al., 2014; Romero et al., 2015, 2017; Wang et al., 2016; Diercks et al., 2021; **Table 1**). Also, we used ratios that compare hopane compounds that are more susceptible to weathering to recalcitrant hopanes (T30–T31/T19, T22–T33/T19, T32–T35/T19; **Table 1**; Aeppli et al., 2014; Romero et al., 2017). In addition, high values of %Terp typically denote potential interferences to hopanes like T20, T26, T30, and T35 (**Table 1**) due to relatively large inputs of modern biomarkers from bacterial or plant biomass (Simoneit et al., 1985, 2020; Hood et al., 2002; Dembicki, 2010; Stout and German, 2018).

For statistical analysis, all data were log-transformed or square-root transformed (if data include zeroes) to approach normal distribution. Differences in mean concentrations and ratios with respect to periods and categories were tested by one-way analysis of variance (ANOVA) followed by Tukey's HSD test. Significance was set at $P < 0.05$. Figures and statistical analyses were completed using JMP Pro 14 for Mac (JMP®, Version Pro 14. SAS Institute Inc., Cary, NC, United States, 1989–2019). Average values are shown as arithmetic mean ± 95% confidence interval.

RESULTS

Sediment Cores Collected in 2010–2011

Sediment cores collected in 2010–2011 showed significantly higher hydrocarbon concentrations (sum of PAHs, *n*-alkanes, hopanes, steranes, TAS) in the layer deposited post-spill (0–1 cm surface sediments; 99905 ± 44270 ng/g) compared to the sediments deposited pre-spill (1–3 cm layer; 16454 ± 8594 ng/g) ($p < 0.001$). This was also observed for specific hydrocarbon compound groups, including for low and high molecular weight (LMW and HMW, respectively) PAHs and *n*-alkanes ($p < 0.001$; **Figure 2**). Overall, the mean concentrations of hydrocarbon compound groups were from 5 to 7 times higher post-spill (**Figure 2**). Interestingly, the calculated 95% confidence intervals in **Figure 2** are very high in the post-spill sediment layer, explained by a large range in the concentration of hydrocarbons (sum of all compounds: 324 – 5533998 ng/g) and compound groups (**Supplementary Table 14**).

To better understand the large variation in hydrocarbons observed in the post-spill sediment layer, we plotted the most abundant compounds in the MC252 crude oil (LMW PAHs and LMW alkanes) by the hydrocarbon ranges observed in the studied area (**Supplementary Figure 1**). The distribution observed indicates a trend, described by low, medium, and high content of LMW PAHs (20.1 ± 1.4%, 35.6 ± 5.0%, and 68.0 ± 3.6%, respectively) and LMW alkanes (10.9 ± 1.1%, 22.2 ± 6.0%, and 63.9 ± 7.0%, respectively) (**Supplementary Figure 1**). By comparison, the category with low content of LMW compounds comprised 81% of the sites sampled. The medium and high categories only contained 12 and 7% of the sites sampled, respectively. No spatial trend was observed among the LMW categories within the studied area, which covers up to 180 km from the DWH rig from 200 to 2400 m depth (**Supplementary Figure 2**).

Using biomarker diagnostic ratios for oil source identification, we found that the three categories identified (low, medium, and high content of LMW compounds) lie within the values of the MC252 oil standard, indicating a match with the spilled oil from the DHWOS (**Supplementary Figure 3**). The category with low content of LMW compounds was the only category with significantly lower values for the ratios (T30 + T31)/T19 and (T32 + T33)/T19 ($P < 0.01$; **Supplementary Figure 3**). This preferential degradation of hopanoids > C31 (T30 – T33) over C30 hopane (T19) indicates significant weathering effects only in the low content category (from for example, biodegradation, dissolution), probably due to the large dispersion observed in this category (samples found up to 175 km from the DWH wellhead) (**Figure 1**; **Supplementary Figure 2**).

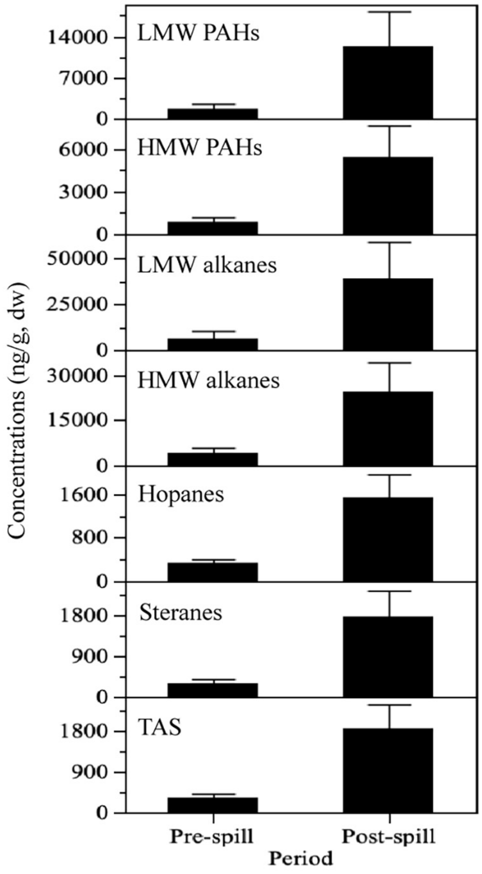

FIGURE 2 | Hydrocarbon concentrations (ng/g, dw) by periods from sediment samples collected in 2010–2011 in the nGoM. Post-pill denotes concentrations in surface sediments (top 1 cm layer in the sediment cores), and pre-spill indicate concentrations in downcore layers (1–3 cm layer). LMW PAHs: 2–3 rings, HMW PAHs: 4–6 rings, LMW alkanes: C12–C23 *n*-alkanes, HMW alkanes: C24–C37 *n*-alkanes, hopanes: C23–C35, steranes: C27–C29, and TAS: C26–C28. Data shown as mean ± 95% confidence interval.

The composition of PAHs and alkanes also indicates weathered petrogenic samples relative to DWH oil (**Figure 3**). PAHs in the DWH oil are dominated by LMW compounds (94%), with a significant lower relative abundance in the high (68%), medium (36%), and low (21%) categories (**Figure 3**). A similar trend was also observed for the relative abundance of LMW alkanes (DWH oil: 84%; high category: 64%; medium category: 22%; low category: 11%), indicating significant weathering effects in the sediment samples (**Figure 3**). In addition, each category has a distinct composition of PAHs and alkanes (**Figure 3**). For example, the PAH distribution in the category with a high content of LMW compounds is dominated by alkyl homologs of LMW and HMW PAHs, while in the medium category

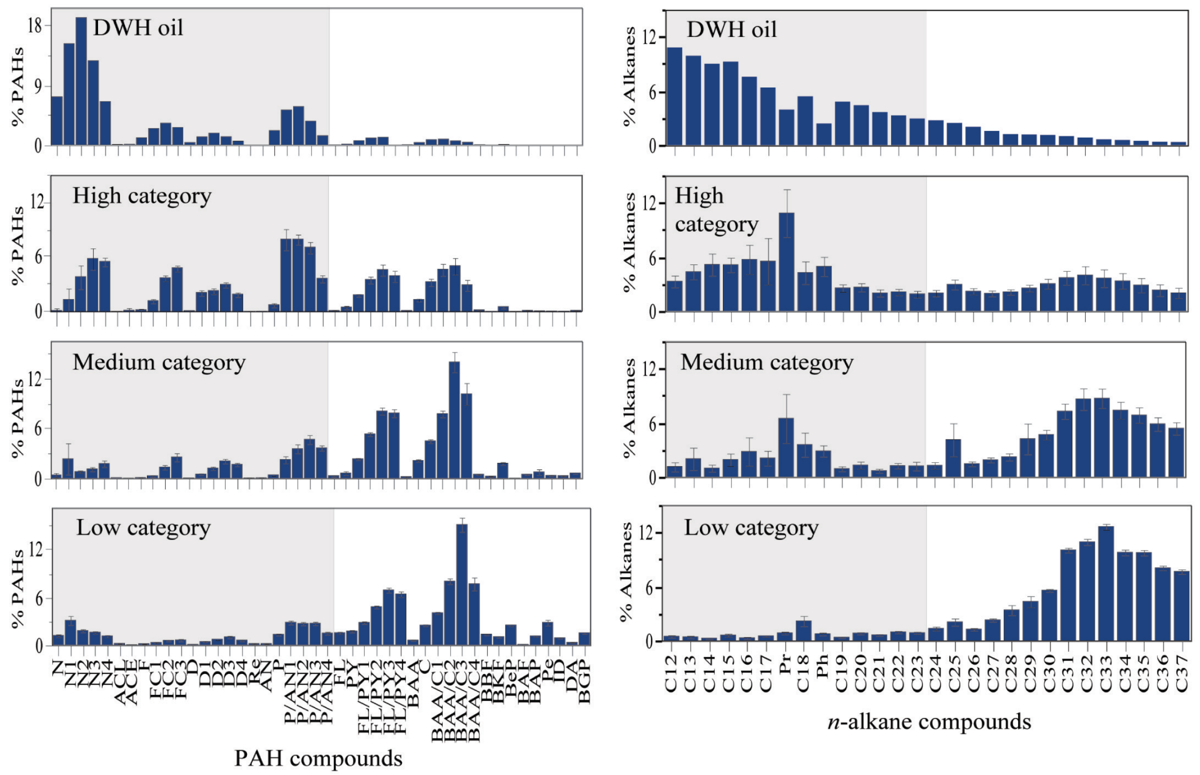

FIGURE 3 | Relative abundance of PAHs and *n*-alkanes by categories of %LMW compounds: high (PAHs: 68.0 ± 3.6%; alkanes: 63.9 ± 7.0%), medium (PAHs: 35.6 ± 5.0%; alkanes: 22.2 ± 6.0%), and low (PAHs: 20.1 ± 1.4%; alkanes: 10.9 ± 1.1%). Also, crude oil is shown as non-weathered DWH oil standard (NIST 2779). Contaminated sediments were collected in 2010–2011 in the nGoM (surface sediment layer). Data shown as mean ± 95% confidence interval.

phenanthrenes and 4-ring PAHs predominate (**Figure 3**). The category containing low content of LMW PAHs show an increase in parent compounds (e.g., FL, PY, BAA, BBF, BAP), and perylene (Pe) and naphthalene (N0, N1–N4) compounds as a consequence of weathering processes (e.g., dispersion, degradation) and mixing with other sources in the environment (e.g., seeps). For alkanes, weathering is evident with pristine (Pr) higher than C17 *n*-alkane in all categories (**Figure 3**).

Additionally, diagnostic ratios such as %retene and %terpenoids (T20, T26, T30, T35) were significantly higher in the category with low content of LMW compounds relative to the other categories and the DWH oil (∼3 and ∼2 times, respectively; $P < 0.001$; **Figure 4**). These ratios indicate the presence of other sources different than oil like organic matter from terrestrial biomass for %retene, and modern triterpenes for samples with high %terpenoids (T20, T26, T30, T35) (**Table 1**). Similarly, the ratios PI and parent/alkyl were also significantly higher in the category with low content of LMW compounds (∼4 and ∼2 times, respectively; $P < 0.001$; **Figure 4**), indicating pyrogenic sources or weathered oil. Because these samples matched with the DWH oil (**Supplementary Figure 3**), the high values in the PI and parent/alkyl ratios indicate the presence of burned oil residues rather than an increase in HMW PAHs due to loss of LMW PAHs during natural weathering processes (e.g., dissolution). The slightly higher values of the *n*-alkane biogenic ratio ([C15,17]/[C14,16,18]) in **Figure 4** indicate the presence of phytoplankton, providing further evidence that oil residues (e.g., surface slicks) mixed with biogenic organic matter were transported from the surface to deeper water depths and deposited on deep-sea sediments.

In contrast, the naphthalene ratio ([N0 + N1]/T19) was significantly higher in the sediments containing medium content of LMW compounds relative to the other categories (∼2 times; $P < 0.0001$; **Table 1** and **Figure 4**). In addition, CPI ratio < 1 was found as well in the medium category (**Table 1** and **Figure 4**). Both ratios match the chemical signature of the subsurface plumes formed during the DWHOS, in which highly soluble and volatile molecules were abundant (e.g., log K_{ow}: 3.37 for naphthalene, 3.87 for 1-methylnaphthalene), as well as short-chain *n*-alkanes without odd-to-even carbon preference (found in microorganisms and oil).

Furthermore, elevated LMW/HMW PAH and alkane ratios were observed in the category with a high content of LMW compounds relative to the other categories (∼2 and ∼4 times higher, respectively; $P < 0.001$; **Figure 4**). Similarly, ratios specific for labile *n*-alkane and hopanoids compounds (C12–C13/T19 and T32–T35/T19) were observed significantly higher in the category with a high content of LMW compounds ($P < 0.001$; **Figure 4**), indicating samples were exposed to minimum vertical transport in the water column before being deposited on the

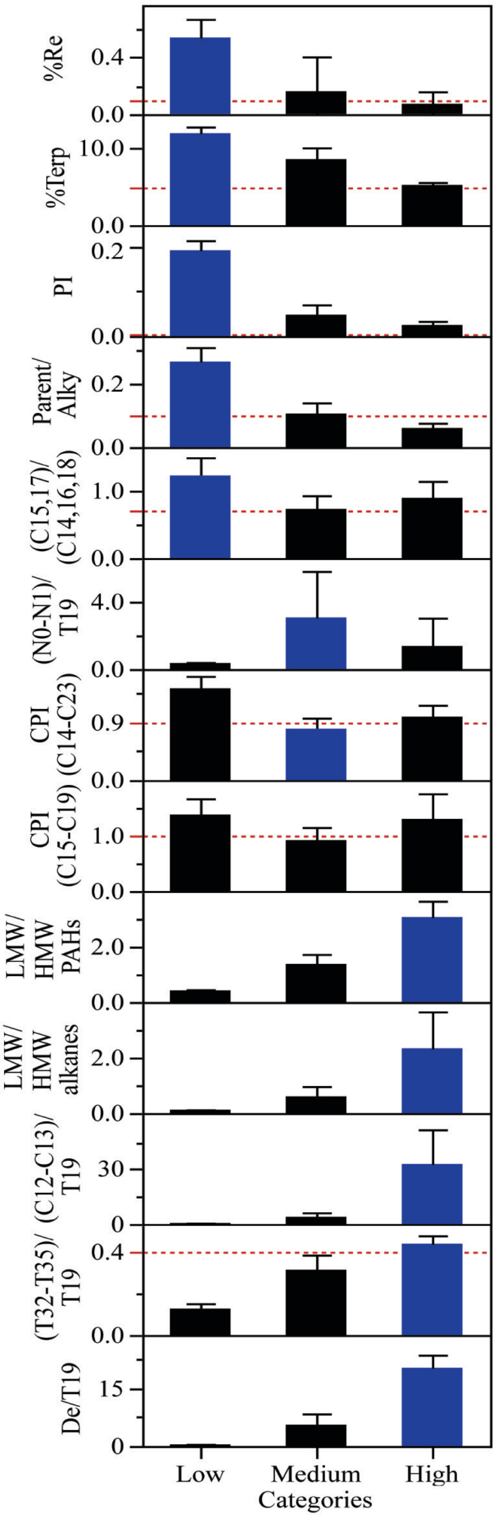

FIGURE 4 | Diagnostic ratios by categories of %LMW compounds (low, medium, and high) in contaminated sediments collected in 2010–2011 in the nGoM (surface sediment layer). DWH oil standard (NIST 2779) is shown as a dash line if values are within the range observed for the samples. Blue bars indicate values statistically different at $P < 0.001$. Data shown as mean ± 95% confidence interval.

seafloor with low weathering effects. This is supported by a similar trend in the %decalins ratio, with decreasing values from the high to the low category ($P < 0.001$; **Figure 4**). Decalin is a bicyclic-saturated hydrocarbon analog to naphthalene with similar evaporative properties but insoluble in water (**Table 1**); therefore, a higher %decalins value indicates oil residues were not evaporated (did not reach surface waters) or dissolved in the submerged plumes but remain in suspension in the water column at depth before deposition on the seafloor.

Sediment Cores Collected in 2018

The buried sediment layer deposited post-spill (2010–2013) in the cores collected in 2018 showed significantly higher hydrocarbon concentrations (3.4 ± 0.7 μg/g) compared to the sediment layer deposited pre-spill (2.2 ± 0.6 μg/g) ($p < 0.001$). This was also observed for specific hydrocarbon compound groups ($p < 0.001$; **Figure 5**). As expected, the concentrations observed in the 2010–2013 buried sediment layer was at least an order of magnitude lower than the surface sediments collected in 2010–2011 (**Figures 2**, **5**).

Different from the surface layer collected in 2010–2011, distinct LMW alkanes categories were not observed, containing similar composition (7.9 ± 3.9%, 12.6 ± 2.2%, and 10.4%, respectively) and no odd-to-even carbon preference indicating oil (short- and long-chain alkanes) and microbial (short-chain alkanes) sources (**Figure 6**). Additionally, all categories showed that alkane and biomarker diagnostic ratios matched with oil from the DWHOS (**Supplementary Figure 4**). Moreover, biodegradation seems to affect only hopane compounds > C34 strongly, as shown by the ratio T32–T33/T19 with low values in the medium and high categories relative to the MC252 oil standard (**Supplementary Figure 4**). The ratio T30–T31/T19 in the low category of the buried layer is similar to the MC252 oil standard (**Supplementary Figure 4**) but higher than the 2010–2011 surface sediments (**Supplementary Figure 3**), indicating bacterial biomass inputs during weathering (**Table 1**). This is also observed for the %Terp ratio (**Supplementary Figure 5**). In addition, diagnostic alkane ratios for phytoplankton inputs were not significantly different among categories, and oil residues were highly weathered (**Supplementary Figure 5**).

In contrast, we found that the data from the buried layer can be divided by categories of low, medium, and high content of LMW PAHs (7.8 ± 4.4%, 32.9 ± 3.1%, and 62.3%, respectively) (**Figure 6**), with similar relative amounts per category to the surface sediment layer collected in 2010–2011 (**Figure 3**). However, only 22% of the buried samples have low content of LMW PAH compounds, while 75% have medium, and only 3% (with only one sample) have a high content of LMW PAH. The composition of PAHs is very different among categories (**Figure 6**) and to the surface layer collected in 2011 (**Figure 3**). All categories in the 2010–2013 buried layer collected in 2018 have a higher content of parent compounds than observed in the surface sediments from 2011 (**Figures 3**, **6**). The effects of weathering (e.g., degradation, transformation) years after burial can also be noted in the calculated PAH ratios (**Supplementary Figure 5**), with a different trend among categories in the buried layer (**Supplementary Figure 5**) compared to the surface

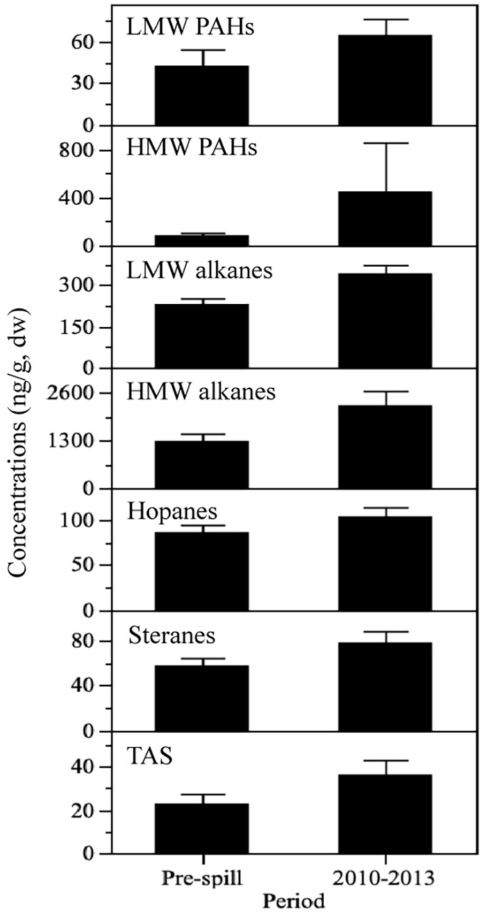

FIGURE 5 | Hydrocarbon concentrations (ng/g, dw) by periods from contaminated sediment samples collected in 2018 in the nGoM. Post-pill denotes the buried sediment layer deposited in 2010–2013, and pre-spill indicate concentrations in downcore layers deposited before 2010. LMW PAHs: 2–3 rings, HMW PAHs: 4–6 rings, LMW alkanes: C12–C23 *n*-alkanes, HMW alkanes: C24–C37 *n*-alkanes, hopanes: C23–C35, steranes: C27–C29, and TAS: C20–C28. Data shown as mean ± 95% confidence interval.

sediments from 2011 (**Figure 4**). However, specifically for the category with low content of LMW compounds, PAH ratios were similar between the two datasets (buried layer collected in 2018 vs. surface sediments from 2010 to 2011).

DISCUSSION

The present work chemically characterized the MOSSFA event and, for the first time, identifies the water masses where the hydrocarbons originated (surface vs. depth) after partitioning into chemical mixtures during transport of the spilled oil from 1500 m depth to the surface of the water column. A combination of multiple molecular markers (i.e., PAHs, alkanes, hopanes) was used to calculate diagnostic ratios and identify biogenic, and oil-derived hydrocarbon sources deposited in deep-sea sediments from the MOSSFA event (**Figure 4**).

Our results support previous studies showing biogenic and oil-derived hydrocarbon inputs from surface waters during the DWHOS (Diercks et al., 2010; Passow et al., 2012; Brooks et al., 2015; Daly et al., 2016; Yan et al., 2016; Romero et al., 2017; White et al., 2019). Exopolymeric substances (EPS) are produced by phytoplankton and bacteria exposed to oil forming aggregates that sink rapidly (Passow et al., 2012; van Eenennaam et al., 2016) while preserving the chemical signature of the oil residues distinct from background signatures (Romero et al., 2015, 2017; Stout et al., 2016; Yan et al., 2016; van Eenennaam et al., 2018). Both sources from surface waters (biogenic and oil residues from the DWHOS) were noted on the sediment samples collected in 2010–2011 with low %LMW compounds, and elevated %Terp and alkanes ratios (**Figure 4** and **Supplementary Figure 3**). Similarly, in previous studies, modern triterpenes and biogenic alkanes mixed with oil residues were observed in oil-contaminated surface waters (Stout and German, 2018; White et al., 2019) and deep-sea sediments (Romero et al., 2015; Stout et al., 2016). Also, hydrocarbons from terrestrial sources were present in the surface waters during the DWHOS (Murawski et al., 2016) that were deposited on benthic environments during the MOSSFA event as dominant siliciclastics sediment inputs (Brooks et al., 2015), supporting our observations of elevated %Re in the surface sediment layer from 2010 to 2011 (**Figure 4**).

Our results also support previous studies showing burned-oil residue inputs from surface waters during the DWHOS (low category of %LMW; ratios: PI, parent/alkyl; **Figure 4**) using similar PAH ratios (Romero et al., 2015; Shigenaka et al., 2015) or estimating relative amounts of HMW PAHs (Stout and Payne, 2016b; Fingas, 2017). As a response effort during the DWHOS, about 220,000–310,000 barrels of floating oil were burned (Mabile and Allen, 2010), producing residues that were not mechanically recovered and believed to have sunk. Burn residues in deep-sea benthic environments have been mostly detected by an increase in HMW PAHs; however, HMW PAHs can also become abundant in oil residues due to loss of LMW PAHs during natural weathering processes. Therefore, we propose using biplots of ratios like PI and %5–6 ring PAHs (**Figure 7**) to distinguish burned-oil residues from weathered-oil residues. These ratios showed no correlation with indicator ratios of natural weathering processes for PAHs (e.g., dissolution, evaporation; **Supplementary Figure 6**). The PI ratio (e.g., Wang et al., 1999b, Wang et al., 2008; Romero et al., 2015; Shigenaka et al., 2015) as well as %5–6 ring PAHs (Shigenaka et al., 2015; Romero et al., 2016; Stout et al., 2016; Fingas, 2017) have been used to differentiate petrogenic and pyrogenic sources in surface and deep-sea samples. Using available data from previous studies and our study, **Figure 7** shows the significant correlation between PI and %5–6 ring ratios ($R = 0.68$, $P < 0.001$, $N = 416$). The limits set for burned- and weathered-oil residues were based on previous studies (Wang et al., 2008; Romero et al., 2015). In **Figure 7**, the samples containing low %LMW compounds from 2010 to 2011 (indicative of MOSSFA derived from surface waters) have burned (17%), weathered (68%), and mixed (15%) oil residues. In contrast, the few samples containing low %LMW compounds in the buried sediments collected in 2018 (layer deposited in

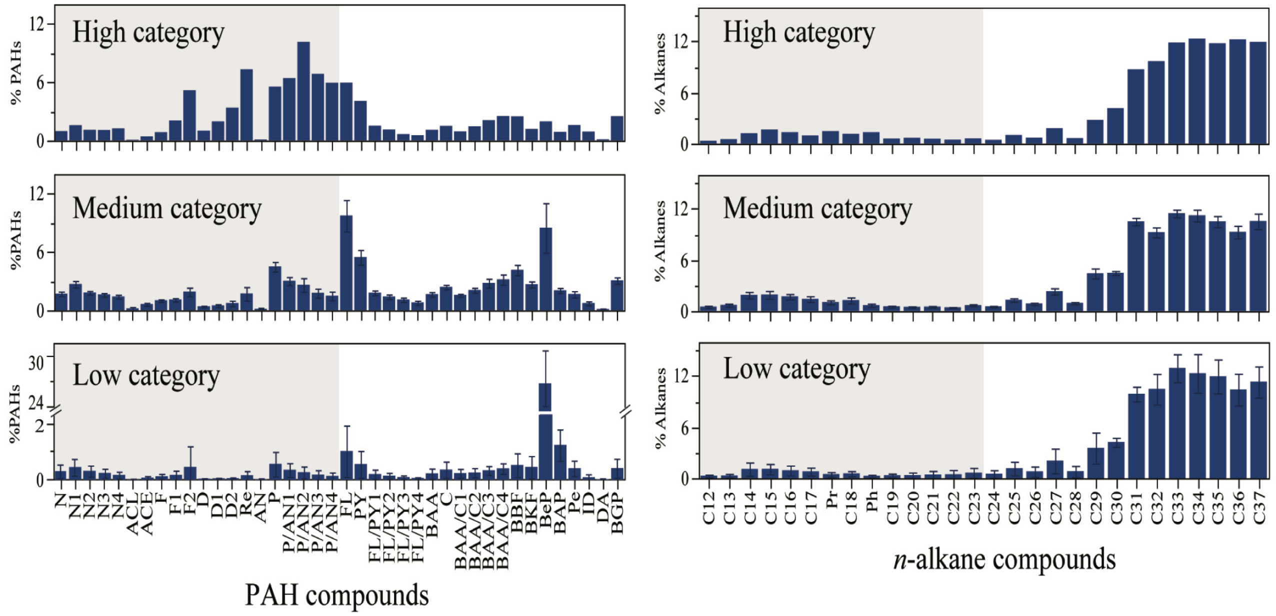

FIGURE 6 | Relative abundance of PAHs and *n*-alkanes by categories of %LMW compounds: high (PAHs: 62.3%; alkanes: 10.4%), medium (PAHs: 32.9 ± 3.1%; alkanes: 12.6 ± 2.2%), and low (PAHs: 7.8 ± 4.4%; alkanes: 7.9 ± 3.9%). Contaminated sediment samples were collected in 2018 in the nGoM (buried sediment layer deposited in 2010–2013). Data shown as mean ± 95% confidence interval.

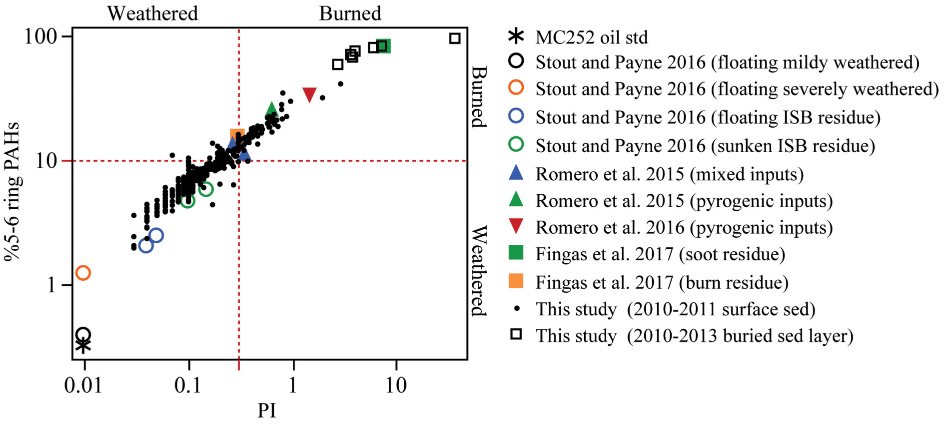

FIGURE 7 | Correlation between PAH ratios for samples analyzed in this study (low %LMW content in contaminated sediments collected in 2010–2011 and 2018) and from previous studies in the nGoM (*R* = 0.68, *P* < 0.001, *N* = 416). Both *x*-axis and *y*-axis shown in logarithmic scale (log base 10).

2010–2013) have only burned-oil residues. Overall, the trend observed in **Figure 7**, supports well previous observations of deposited burned and mixed oil residues in the DeSoto Canyon after the DWHOS (Romero et al., 2015), burn residues after the explosion of the Hercules 265 gas rig (Romero et al., 2016), and oil residues after experimental burning of crude oil (Fingas, 2017). Interestingly, floating and sunken burned oil residue samples from Stout and Payne (2016b) have relatively low %5–6 ring PAHs and PI ratio (**Figure 7**). A potential explanation is that samples in Stout and Payne (2016b) were partially burned (∼89% burn efficiency), as shown by the presence of relatively high amounts of volatile compounds such as naphthalenes and other LMW PAHs. Also, the trend between burn efficiency and the PI ratio among studies supports the trend observed in **Figure 7** (Shigenaka et al., 2015: ∼50% efficiency and PI = ∼0.1; Stout and Payne, 2016b: ∼89 efficiency and PI = 0.2; and Fingas, 2017: 99% efficiency and PI = 0.3–7.2). Moreover, Stout and Payne (2016b) found that burned oil residues can be detected by looking at the composition of aliphatics, in which *n*-alkanes > C20 are severely depleted, a pattern not explained by natural weathering processes (e.g., evaporation, biodegradation). In **Figure 7**, samples from our study located in the lower-left panel (weathered oil residues) did not have depleted *n*-alkanes > C20, indicating these samples were not burned but

TABLE 2 | Area coverage and total deposition of oil residues calculated in Romero et al. (2017) for each %LMW category and hydrocarbon range.

%LMW content category	Hydrocarbon ranges (ug/g, dw)	Area[a] (km^2)	Total deposition (tons)[ab] Average (range)
Low	<2.5	17,623	69 (61–115)
	2.5–5	6,228	85 (81–133)
	5–7.5	475	11 (11–17)
	7.5–10	418	14 (13–21)
	10–20	4,642	372 (566–630)
Low (Total)	0.1–20	29,385	551 (369–654)
Medium	20–100	3,044	258 (832–978)
High	>100	219	898 (519–1,916)

Categories for %LMW compounds are: low (PAHs: 20.1 ± 1.4%; alkanes: 10.9 ± 1.1%), medium (PAHs: 35.6 ± 5.0%; alkanes: 22.2 ± 6.0%), and high (PAHs: 68.0 ± 3.6%; alkanes: 63.9 ± 7.0%).

[a] *From Romero et al. (2017).*

[b] *Total hydrocarbon input to surface sediments in 2010–2011 (background substracted).*

can be distinguished from samples that were partially burned, such as the samples in Stout and Payne (2016b).

The trend observed in the data from the surface sediments collected in 2010–2011 also supports previous studies indicating MOSSFA was originated at depth during the DWHOS (e.g., Passow et al., 2012; Daly et al., 2016). Abundant deposition of LMW PAHs with low sedimentation at a depth of 1043 m was observed in the DeSoto Canyon after the DWHOS, attributed to the direct contact of the deep submerged plume with the continental slope surface sediments (Romero et al., 2015). In our study, the category with medium content of %LMW compounds has a chemical signature characteristic of the submerged plumes with elevated relative amounts of naphthalene compounds (**Figure 4**). In this category, 15% of the samples ($N = 5$) were not highly weathered (%Chrysene < 1.5), containing the highest relative amounts of naphthalene and LMW *n*-alkane compounds (**Supplementary Figure 7**). These samples were all located at depths higher than 1500 m (except for one sample at 1071 m; **Supplementary Figure 7**), out of the range for a direct contact of the deep plumes with the continental slope, which were observed between 900 and 1300 m (Ryerson et al., 2012). Therefore, these samples containing medium content of %LMW are evidence for MOSSFA originated at depth from the deep submerged plumes.

In contrast, the category with a high content of %LMW compounds indicates MOSSFA originated at depth in the water column, not from the submerged plumes but from contaminated sinking particles. The chemical signature of the samples with a high content of %LMW compounds (**Figure 4**) indicate MOSSFA was formed in the water column as predominant OMAS as observed previously in the water column (Joung and Shiller, 2013; Yan et al., 2016) and deep-sea sediments (Brooks et al., 2015; Romero et al., 2015; Stout and Payne, 2016a).

Altogether, using the spatial coverage of oil residues deposited after the DWHOS in deep-sea sediments by Romero et al. (2017), we found that MOSSFA from surface waters covered 90% of the deep-sea area studied and was responsible for 32% of the total deposition of oil residues observed offshore in deep-sea areas after the DWHOS (low category content of %LMW compounds; **Table 2**). In contrast, MOSSFA originated at depth from the submerged plumes covered only 9% of the deep-sea area studied and was responsible for 15% of the total deposition of oil residues observed after the DWHOS on deep-sea sediments (medium category content of %LMW compounds; **Table 2**). Furthermore, MOSSFA originated at depth but from the water column covered only 1% of the deep-sea area studied (mostly in close proximity of the DWH wellhead; **Supplementary Figure 2**) but was responsible for 53% of the total deposition of oil residues observed after the spill in this area (high category content of %LMW compounds; **Table 2**). This extensive deposition of oil-residues in the vicinity of the DWH wellhead may have been produced by the presence of larger amounts of sediment particles enhanced from the application of drilling mud to help control and stop the DWHOS (Graham et al., 2011) that mixed with the spilled oil and sank (Yan et al., 2016).

The buried samples collected 8 years after the DWHOS showed weathering after burial has affected most compounds (**Supplementary Figure 5**); therefore, the molecular markers used to identify where MOSSFA was originated in the water (ratios in **Figure 4**) cannot be applied in these sediment samples. In contrast, specific hopane and PAH ratios (**Figure 7** and **Supplementary Figure 4**) still indicate the presence of oil residues from the DWHOS and whether samples were affected or not by *in situ* burning of surface slicks. Also, biodegradation seems not to be the only weathering process affecting the buried oil residues, because Pr/C17 and Ph/C18 ratios were <1 (**Figure 6**). Transformation processes (e.g., oxidation) of oil-residues have been observed in samples collected from surface slicks or on beaches (Hall et al., 2013; White et al., 2016; Aeppli et al., 2018) and potentially also can be an important process at depth.

Overall, our analyses of multiple hydrocarbon compounds chemically characterized for the first time the MOSSFA event that formed during the DWHOS. We identified molecular markers of hydrocarbon sources (biogenic, DWHOS residues), natural and human-induced weathering processes (biodegradation, *in situ* oil burning), and hydrocarbon mixtures formed by the partitioning of oil residues in the water column. Altogether, our results provide the basis for identifying where MOSSFA originated in the water column and its fate in deep-sea benthic environments, important for response efforts in future deep oil spills.

Significant findings include (1) natural weathering processes were dominant during the DWHOS, as evidenced by the chemical signature of MOSSFA at depth, which was similar to the chemical mixtures formed during the transport of oil residues to surface waters in the water column. (2) Biodegradation of buried oil residues in deep-sea sediments is slow; therefore, a longer impact to this environment is expected, as observed from deep-sea studies looking at hydrocarbons in sediments and benthic ecological recovery (Romero et al., 2017; Rohal et al., 2020). (3) Other weathering processes different from biodegradation might occur (e.g., oxidation) in buried oil residues in deep-sea environments that still need to be studied to predict the long-term fate of oil residues from deep spills.

DATA AVAILABILITY STATEMENT

The datasets presented in this study can be found in online repositories. The names of the repository/repositories and accession number(s) can be found below: Data are publicly available through the Gulf of Mexico Research Initiative & Data Cooperative (GRIIDC) at https://data.gulfresearchinitiative.org (doi: 10.7266/N7ZG6Q71, doi: 10.7266/N7N29V16, doi: 10.7266/n7-6bfd-g305, doi: 10.7266/n7-h6gj-1m18). Publicly data from ERMA-NRDA program are available at the DIVER database (https://www.diver.orr.noaa.gov/).

AUTHOR CONTRIBUTIONS

IR carried out the laboratory and data analyses and wrote the manuscript including figures and tables. GB, RL, and PS established the chronology of cores collected in 2018. JC and AD selected sampled sites and help in the collection. SB and AH helped in collection and discussions. All co-authors contributed to the manuscript by revising, editing, and adding references and comments. All authors contributed to the article and approved the submitted version.

FUNDING

This research was made possible by a grant from The Gulf of Mexico Research Initiative (GOMRI): REDIRECT (Resuspension, Redistribution and Deposition of Deepwater Horizon recalcitrant hydrocarbons to offshore depocenter). Also, research reported in this publication was supported by an Early-Career Research Fellowship from the Gulf Research Program of the National Academies of Sciences, Engineering, and Medicine to IC Romero (Grant #2000010685). The content in this publication is solely the responsibility of the authors and does not necessarily represent the official views of the Gulf Research Program of the National Academies of Sciences, Engineering, and Medicine.

ACKNOWLEDGMENTS

The authors would like to thank the crew of the R/V *Point Sur* and R/V Weatherbird II for their help during the field program, and the technicians Hannah Hamontree, and Olivia Traenkle for laboratory support.

SUPPLEMENTARY MATERIAL

The Supplementary Material for this article can be found online at: https://www.frontiersin.org/articles/10.3389/fmars.2021.637970/full#supplementary-material

REFERENCES

Abrajano, T. A., and Yan, B. (2003). "High molecular weight petrogenic and pyrogenic hydrocarbons in aquatic environments," in *Treatise on Geochemistry Vol. Environmental Geochemistry*, ed. B. S. Lollar (Pergamon: Elsevier), 475–510.

Adhikari, P. L., Maiti, K., Bosu, S., and Jones, P. R. (2016). 234Th as a tracer of vertical transport of polycyclic aromatic hydrocarbons in the northern Gulf of Mexico. *Mar. Pollut. Bull.* 107, 1–9. doi: 10.1016/j.marpolbul.2016.04.002

Adhikari, P. L., Maiti, K., and Overton, E. B. (2015). Vertical fluxes of polycyclic aromatic hydrocarbons in the northern Gulf of Mexico. *Mar. Chem.* 168, 60–68. doi: 10.1016/j.marchem.2014.11.001

Adhikari, P. L., Wong, R. L., and Overton, E. B. (2017). Application of enhanced gas chromatography/triple quadrupole mass spectrometry for monitoring petroleum weathering and forensic source fingerprinting in samples impacted by the Deepwater Horizon oil spill. *Chemosphere* 184, 939–950. doi: 10.1016/j.chemosphere.2017.06.077

Aeppli, C., Nelson, R. K., Radović, J. R., Carmichael, C. A., Valentine, D. L., and Reddy, C. M. (2014). Recalcitrance and degradation of petroleum biomarkers upon abiotic and biotic natural weathering of Deepwater Horizon oil. *Environ. Sci. Technol.* 48, 6726–6734. doi: 10.1021/es500825q

Aeppli, C., Swarthout, R. F., O'Neil, G. W., Katz, S. D., Nabi, D., Ward, C. P., et al. (2018). How Persistent and bioavailable are oxygenated deepwater horizon oil transformation products? *Environ. Sci. Technol.* 52, 7250–7258. doi: 10.1021/acs.est.8b01001

Ainsworth, C. H., Paris, C. B., Perlin, N., Dornberger, L. N., Patterson, W. F., Chancellor, E., et al. (2018). Impacts of the Deepwater Horizon oil spill evaluated using an end-to-end ecosystem model. *PLoS One* 13:e190840. doi: 10.1371/journal.pone.0190840

Appleby, P. G., and Oldfield, F. (1983). The assessment of 210 Pb data from sites with varying sediment accumulation rates. *Hydrobiologia* 103, 29–35.

Baguley, J. G., Montagna, P. A., Cooksey, C., Hyland, J. L., Bang, H. W., Morrison, C., et al. (2015). Community response of deep-sea soft-sediment metazoan meiofauna to the Deepwater Horizon blowout and oil spill. *Mar. Ecol. Prog. Ser.* 528, 127–140. doi: 10.3354/meps11290

Baskaran, M., Nix, J., Kuyper, C., and Karunakara, N. (2014). Problems with the dating of sediment core using excess 210 Pb in a freshwater system impacted by large scale watershed changes. *J. Environ. Radioact.* 138, 355–363. doi: 10.1016/j.jenvrad.2014.07.006

Bianchi, T. S., Cui, X., Blair, N. E., Burdige, D. J., and Eglinton, T. I. (2018). Organic Geochemistry Centers of organic carbon burial and oxidation at the land-ocean interface. *Org. Geochem.* 115, 138–155. doi: 10.1016/j.orggeochem.2017.09.008

Binford, M. W. (1990). Calculation and uncertainty analysis of 210Pb dates for PIRLA project lake sediment cores. *J. Paleolimnol.* 3, 253–267.

Boehm, P. D., and Flest, D. L. (1982). Subsurface distributions of petroleum from an offshore well blowout. The Ixtoc I Blowout, Bay of Campeche. *Environ. Sci. Technol.* 16, 67–74. doi: 10.1021/es00096a003

Bosman, S. H., Schwing, P. T., Larson, R. A., Wildermann, E., Brooks, G. R., Romero, I. C., et al. (2020). The southern Gulf of Mexico: a baseline radiocarbon isoscape of surface sediments and isotopic excursions at depth. *PLoS One* 15:e0231678. doi: 10.1371/journal.pone.0231678

Bray, E. E., and Evans, E. D. (1961). Distribution of n-paraffins as a clue to recognition of source beds. *Geochemica Cosmochim.* 22, 2–15.

Brooks, G. R., Larson, R. A., Schwing, P. T., Romero, I., Moore, C., Reichart, G.-J., et al. (2015). Sedimentation pulse in the NE Gulf of Mexico following the 2010 DWH blowout. *PLoS One* 10:e0132341. doi: 10.1371/journal.pone.0132341

Canuel, E. A., and Hardison, A. K. (2016). Sources, ages, and alteration of organic matter in estuaries. *Ann. Rev. Mar. Sci.* 8, 409–434. doi: 10.1146/annurev-marine-122414-034058

Chanton, J., Zhao, T., Rosenheim, B. E., Joye, S., Bosman, S., Brunner, C., et al. (2015). Using natural abundance radiocarbon to trace the flux of petrocarbon to the seafloor following the Deepwater Horizon oil spill. *Environ. Sci. Technol.* 49, 847–854. doi: 10.1021/es5046524

Chanton, J. P., Giering, S. L. C., Bosman, S. H., Rogers, K. L., Sweet, J., Asper, V. L., et al. (2018). Isotopic composition of sinking particles: oil effects, recovery and baselines in the Gulf of Mexico, 2010-2015. *Elem. Sci. Anthr.* 6, 2010–2015. doi: 10.1525/elementa.298

Daly, K., Gilbert, S., Hollander, D. J., Paris, C. B., and Schlüter, M. (2020). "Physical processes influencing the sedimentation and lateral transport of MOSSFA in the NE Gulf of Mexico," in *Scenarios and Responses to Future Deep Oil Spills Fighting the Next War*, eds S. Murawski, C. H. Ainsworth, S. Gilbert, D. J. Hollander, C. B. Paris, M. Schluter, et al. (Cham: Springer), 300–314. doi: 10.1007/978-3-030-12963-7_18

Daly, K. L., Passow, U., Chanton, J., and Hollander, D. (2016). Assessing the impacts of oil-associated marine snow formation and sedimentation during and after the Deepwater Horizon oil spill. *Biochem. Pharmacol.* 13, 18–33. doi: 10.1016/j.ancene.2016.01.006

Dembicki, H. (2010). Recognizing and compensating for interference from the sediment ' s background organic matter and biodegradation during interpretation of biomarker data from sea floor hydrocarbon seeps: an example from the Marco Polo area seeps. *Gulf Mar. Pet. Geol.* 27, 1936–1951. doi: 10.1016/j.marpetgeo.2010.06.009

Diercks, A.-R., Highsmith, R. C., Asper, V. L., Joung, D., Zhou, Z., Guo, L., et al. (2010). Characterization of subsurface polycyclic aromatic hydrocarbons at the Deepwater Horizon site. *Geophys. Res. Lett.* 37, 1–6. doi: 10.1029/2010GL045046

Diercks, A., Romero, I. R., Schwing, P., Larson, R. A., Harris, A., Bosman, S., et al. (2021). Resuspension, Redistribution and Deposition of DwH oil-residues to offshore Depocenters. *Front. Mar. Sci.* doi: 10.3389/fmars.2021.630183

D'souza, N. A., Subramaniam, A., Juhl, A. R., Hafez, M., Chekalyuk, A., Phan, S., et al. (2016). Elevated surface chlorophyll associated with natural oil seeps in the Gulf of Mexico. *Nat. Geosci.* 9, 215–218. doi: 10.1038/NGEO2631

Du, M., and Kessler, J. D. (2012). Assessment of the spatial and temporal variability of bulk hydrocarbon respiration following the Deepwater Horizon oil spill. *Environ. Sci. Technol.* 46, 10499–10507. doi: 10.1021/es301363k

Elordui-zapatarietxe, S., Rosell-melé, A., Moraleda, N., Tolosa, I., and Albaigés, J. (2010). Phase distribution of hydrocarbons in the water column after a pelagic deep ocean oil spill. *Mar. Pollut. Bull.* 60, 1667–1673. doi: 10.1016/j.marpolbul.2010.07.001

Fingas, M. (2017). The fate of PAHs resulting from in-situ oil burns. *Intern. Oil Spill Conf. Proc.* 2017, 1041–1056.

Gonzalez, J. J., Vinas, L., Franco, M. A., Fumega, J., Soriano, J. A., Grueiro, G., et al. (2006). Spatial and temporal distribution of dissolved / dispersed aromatic hydrocarbons in seawater in the area affected by the Prestige oil spill. *Mar. Pollut. Bull.* 53, 250–259. doi: 10.1016/j.marpolbul.2005.09.039

Graham, B., Keilly, W. K., Beinecke, F., Boesch, D., Garcia, T. D., Murray, C. A., et al. (2011). *Deep water: The Gulf Oil Disaster and the Future of Offshore Drilling; Report to the President*. Washington, DC: National Commission on the BP Deepwater Horizon Oil Spill Offshore Drilling.

Hall, G. J., Frysinger, G. S., Aeppli, C., Carmichael, C. A., Gros, J., Lemkau, K. L., et al. (2013). Oxygenated weathering products of Deepwater Horizon oil come from surprising precursors. *Mar. Pollut. Bull.* 75, 140–149. doi: 10.1016/j.marpolbul.2013.07.048

Harvey, G. R., Requejo, A. G., McGillivary, P. A., and Tokar, J. M. (1979). Observation of a subsurface oil-rich layer in the open ocean. *Science* 205, 999–1001.

Herrera-Herrera, A. V., Leierer, L., Jambrina-enríquez, M., Connolly, R., and Mallol, C. (2020). Organic geochemistry evaluating different methods for calculating the Carbon Preference Index (CPI): implications for palaeoecological and archaeological research. *Org. Geochem.* 146:104056. doi: 10.1016/j.orggeochem.2020.104056

Hood, K. C., Wenger, L. M., Gross, O. P., and Harrison, S. C. (2002). Hydrocarbon systems analysis of the northern Gulf of Mexico: delineation of hydrocarbon migration pathways using seeps and seismic imaging. *Surf. Explor. Case Hist. Appl. Geochem.* 48, 25–40.

Hu, C., Weisberg, R. H., Liu, Y., Zheng, L., Daly, K. L., English, D. C., et al. (2011). Did the northeastern Gulf of Mexico become greener after the Deepwater Horizon oil spill? *Geophys. Res. Lett.* 38, 1–5. doi: 10.1029/2011GL047184

Johansen, Ø, Rye, H., and Cooper, C. (2003). DeepSpill – field study of a simulated oil and gas blowout in deep water. *Spill Sci. Technol. Bull.* 8, 433–443. doi: 10.1016/S1353-2561(02)00123-8

Joung, D., and Shiller, A. M. (2013). Trace element distributions in the water column near the Deepwater Horizon well blowout. *Environ. Sci. Technol.* 47, 2161–2168. doi: 10.1021/es303167p

Joye, S. B., Macdonald, I. R., Leifer, I., and Asper, V. (2011). Magnitude and oxidation potential of hydrocarbon gases released from the BP oil well blowout. *Nat. Geosci.* 4, 2–6. doi: 10.1038/ngeo1067

Kameyama, S., Tsunogai, U., Nakagawa, F., Sasakawa, M., Komatsu, D. D., Ijiri, A., et al. (2009). Enrichment of alkanes within a phytoplankton bloom during an in situ iron enrichment experiment in the western subarctic Pacific. *Mar. Chem.* 115, 92–101. doi: 10.1016/j.marchem.2009.06.009

Larowe, D. E., Arndt, S., Bradley, J. A., Burwicz, E., Dale, A. W., and Amend, J. P. (2020). ScienceDirect Organic carbon and microbial activity in marine sediments on a global scale throughout the Quaternary. *Geochim. Cosmochim. Acta* 286, 227–247. doi: 10.1016/j.gca.2020.07.017

Larson, R. A., Brooks, G. R., Schwing, P. T., Holmes, C. W., Carter, S. R., and Hollander, D. J. (2018). Anthropocene High-resolution investigation of event driven sedimentation: Northeastern Gulf of Mexico. *Biochem. Pharmacol.* 24, 40–50. doi: 10.1016/j.ancene.2018.11.002

Lea-smith, D. J., Biller, S. J., Davey, M. P., Cotton, C. A. R., Perez, B. M., Turchyn, A. V., et al. (2015). Contribution of cyanobacterial alkane production to the ocean hydrocarbon cycle. *Proc. Natl. Acad. Sci. U.S.A.* 112, 13591–13596. doi: 10.1073/pnas.1507274112

Lindo-Atichati, D., Paris, C. B., Le Hénaff, M., Schedler, M., Valladares Juárez, A. G., and Müller, R. (2014). Simulating the effects of droplet size, high-pressure biodegradation, and variable flow rate on the subsea evolution of deep plumes from the Macondo blowout. *Deep Sea Res. Part II Top. Stud. Oceanogr.* 129, 301–310. doi: 10.1016/j.dsr2.2014.01.011

Liu, Z., Liu, J., Zhu, Q., and Wu, W. (2012). The weathering of oil after the Deepwater Horizon oil spill: insights from the chemical composition of the oil from the sea surface, salt marshes and sediments. *Environ. Res. Lett.* 7:035302. doi: 10.1088/1748-9326/7/3/035302

Mabile, N., and Allen, A. (2010). *Controlled Burns after Action Report Burns on May 28th - August 3 2010*. Houma: Controlled Burn Group, Houma Incident Command Post.

MacDonald, I. R., Garcia-Pineda, O., Beet, A., Daneshgar, A., Feng, L., Graettinger, G., et al. (2015). Natural and unnatural oil slicks in the Gulf of Mexico. *J. Geophys. Res. Ocean.* 120, 8364–8380.

Middleditch, B. S., Chang, E. S., and Basile, B. (1979). Alkanes in plankton from the buccaneer oilfield. *Bull. Environ. Contam. Toxicol.* 427, 421–427.

Montagna, P. A., Baguley, J. G., Cooksey, C., Hartwell, I., Hyde, L. J., Hyland, J. L., et al. (2013). Deep-sea benthic footprint of the deepwater horizon blowout. *PLoS One* 8:e70540. doi: 10.1371/journal.pone.0070540

Mulabagal, V., Yin, F., John, G. F., Hayworth, J. S., and Clement, T. P. (2013). Chemical fingerprinting of petroleum biomarkers in Deepwater Horizon oil spill samples collected from Alabama shoreline. *Mar. Pollut. Bull.* 70, 147–154. doi: 10.1016/j.marpolbul.2013.02.026

Murawski, S. A., Fleeger, J. W., Patterson, W. F., Hu, C., Daly, K., Romero, I., et al. (2016). How did the Deepwater Horizon oil spill affect coastal and continental shelf ecosystems of the Gulf of Mexico? *Oceanography* 29, 160–173. doi: 10.5670/oceanog.2016.80

Murawski, S. A., Hogarth, W. T., Peebles, E. B., and Barbeiri, L. (2014). Prevalence of external skin lesions and polycyclic aromatic hydrocarbon concentrations in Gulf of Mexico fishes, post-Deepwater Horizon. *Trans. Am. Fish. Soc.* 143, 37–41. doi: 10.1080/00028487.2014.911205

Niu, H., Li, Z., Lee, K., Kepkay, P., and Mullin, J. V. (2010). Modelling the transport of oil-mineral-aggregates (OMAs) in the marine environment and assessment of their potential risks. *Environ. Model. Assess.* 16, 61–75. doi: 10.1007/s10666-010-9228-0

NOAA (2011). Analytical quality assurance plan, Mississippi Canyon 252 (Deepwater Horizon) natural resource damage assessment, Version 4.0. May 30, 2014.

Passow, U., Ziervogel, K., Asper, V., and Diercks, A. (2012). Marine snow formation in the aftermath of the Deepwater Horizon oil spill in the Gulf of Mexico. *Environ. Res. Lett.* 7:035301. doi: 10.1088/1748-9326/7/3/035301

Pulster, E. L., Gracia, A., Armenteros, M., Carr, B. E., Mrowicki, J., and Murawski, S. A. (2020). Chronic PAH exposures and associated declines in fish health indices observed for ten grouper species in the Gulf of Mexico. *Sci. Total Environ.* 703:135551. doi: 10.1016/j.scitotenv.2019.135551

Quigg, A., Passow, U., Daly, K. L., Burd, A., Hollander, D. J., Schwing, P. T., et al. (2020). "Marine oil snow sedimentation and flocculent accumulation (MOSSFA) events: learning from the past to predict the future," in *Deep Oil Spills: Facts, Fate, and Effects*, eds S. A. Murawski, C. H. Ainsworth, S. Gilbert, D. J. Hollander, C. B. Paris, M. Schlüter, et al. (Cham: Springer International Publishing), 196–220. doi: 10.1007/978-3-030-11605-7_12

Quintana-Rizzo, E., Torres, J. J., Ross, S. W., Romero, I., Watson, K., Goddard, E., et al. (2015). δ13C and δ15N in deep-living fishes and shrimps after the Deepwater Horizon oil spill. *Gulf Mexico Mar. Pollut. Bull.* 94, 241–250. doi: 10.1016/j.marpolbul.2015.02.002

Rohal, M., Barrera, N., Escobar-briones, E., Brooks, G., Hollander, D., Larson, R., et al. (2020). How quickly will the o ff shore ecosystem recover from the 2010 Deepwater Horizon oil spill? Lessons learned from the 1979 Ixtoc-1 oil well blowout. *Ecol. Indic.* 117:106593. doi: 10.1016/j.ecolind.2020.106593

Romero, I. C., Judkins, H., and Vecchione, M. (2020). Temporal variability of polycyclic aromatic hydrocarbons in deep-sea cephalopods of the Northern Gulf of Mexico. *Front. Mar. Sci.* 7:54. doi: 10.3389/fmars.2020.00054

Romero, I. C., Özgökmen, T., Snyder, S., Schwing, P., O'Malley, B. J., Beron-Vera, F. J., et al. (2016). Tracking the Hercules 265 marine gas well blowout in the Gulf of Mexico. *J. Geophys. Res. Ocean* 121, 706–724. doi: 10.1002/2015JC011037

Romero, I. C., Schwing, P. T., Brooks, G. R., Larson, R. A., Hastings, D. W., Flower, B. P., et al. (2015). Hydrocarbons in deep-sea sediments following the 2010 Deepwater Horizon Blowout in the Northeast Gulf of Mexico. *PLoS One* 10:e0128371. doi: 10.1371/journal.pone.0128371

Romero, I. C., Sutton, T., Carr, B., Quintana-Rizzo, E., Ross, S. W., Hollander, D. J., et al. (2018). A decadal assessment of polycyclic aromatic hydrocarbons in mesopelagic fishes from the Gulf of Mexico reveals exposure to oil-derived sources. *Environ. Sci. Technol.* 52, 10985–10996. doi: 10.1021/acs.est.8b02243

Romero, I. C., Toro-farmer, G., Diercks, A., Schwing, P., Muller-Karger, F., Murawski, S., et al. (2017). Large-scale deposition of weathered oil in the Gulf of Mexico following a deep-water oil spill. *Environ. Pollut.* 228, 179–189. doi: 10.1016/j.envpol.2017.05.019

Ryerson, T. B., Camilli, R., Kessler, J. D., Kujawinski, E. B., Reddy, C. M., Valentine, D. L., et al. (2012). Chemical data quantify Deepwater Horizon hydrocarbon flow rate and environmental distribution. *Proc. Natl. Acad. Sci. U.S.A.* 109, 20246–20253. doi: 10.1073/pnas.1110564109

Schwing, P. T., Chanton, J. P., Romero, I. C., Hollander, D. J., Goddard, E. A., Brooks, G. R., et al. (2018). Tracing the incorporation of carbon into benthic foraminiferal calcite following the Deepwater Horizon event. *Environ. Pollut.* 237, 424–429. doi: 10.1016/j.envpol.2018.02.066

Schwing, P. T., O'Malley, B. J., Romero, I. C., Martínez-Colón, M., Hastings, D. W., Glabach, M. A., et al. (2017). Characterizing the variability of benthic foraminifera in the northeastern Gulf of Mexico following the Deepwater Horizon event (2010-2012). *Environ. Sci. Pollut. Res.* 24, 2754–2769. doi: 10.1007/s11356-016-7996-z

Schwing, P. T., Romero, I. C., Brooks, G. R., Hastings, D. W., Larson, R. A., and Hollander, D. J. (2015). Correction: a decline in benthic foraminifera following the deepwater horizon event in the Northeastern Gulf of Mexico. *PLoS One* 10:e0128505. doi: 10.1371/journal.pone.0128505

Schwing, P. T., Romero, I. C., Larson, R. A., O'malley, B. J., Fridrik, E. E., Goddard, E. A., et al. (2016). Sediment core extrusion method at millimeter resolution using a calibrated, threaded-rod. *J. Vis. Exp.* 2016:e54363. doi: 10.3791/54363

Shigenaka, G., Erd, N., Overton, E., Meyer, B., Gao, H., and Miles, S. (2015). *Comparison of Physical and Chemical Characteristics of in-Situ Burn Residue and Other Environmental Oil Samples Collected During the Deepwater Horizon Spill Response*. New Orleans, LA: Bureau of Safety and Environmental Enforcement (BSEE).

Simoneit, B. R. T., Grimalt, J. O., Wang, T. G., Cox, R. E., Hatcher, P. G., and Nissenbaum, A. (1985). Cyclic terpenoids of contemporary resinous plant detritus and of fossil woods, ambers and coals. *Adv. Org. Geochem.* 10, 877–889.

Simoneit, B. R. T., Oros, D. R., Karwowski, Ł, Szendera, Ł, Smolarek-lach, J., Goryl, M., et al. (2020). Terpenoid biomarkers of ambers from Miocene tropical paleoenvironments in Borneo and of their potential extant plant sources. *Int. J. Coal Geol.* 221:103430. doi: 10.1016/j.coal.2020.103430

Socolofsky, S. A., Adams, E. E., and Sherwood, C. R. (2011). Formation dynamics of subsurface hydrocarbon intrusions following the Deepwater Horizon blowout. *Geophys. Res. Lett.* 38, 1–6. doi: 10.1029/2011GL047174

Sørensen, L., Meier, S., and Mjøs, S. A. (2016). Application of gas chromatography / tandem mass spectrometry to determine a wide range of petrogenic alkylated polycyclic aromatic hydrocarbons in biotic samples. *Rapid Commun. Mass Spectrom.* 30, 2052–2058. doi: 10.1002/rcm.7688

Stout, S. A., and German, C. R. (2018). Characterization and flux of marine oil snow settling toward the sea floor in the northern Gulf of Mexico during the Deepwater Horizon incident: evidence for input from surface oil and impact on shallow shelf sediments. *Mar. Pollut. Bull.* 129, 695–713. doi: 10.1016/j.marpolbul.2017.10.059

Stout, S. A., and Payne, J. R. (2016a). Chemical composition of floating and sunken in-situ burn residues from the Deepwater Horizon oil spill. *Mar. Pollut. Bull.* 108, 186–202. doi: 10.1016/j.marpolbul.2016.04.031

Stout, S. A., and Payne, J. R. (2016b). Macondo oil in deep-sea sediments: part 1 - sub-sea weathering of oil deposited on the seafloor. *Mar. Pollut. Bull.* 111, 365–380. doi: 10.1016/j.marpolbul.2016.07.036

Stout, S. A., Payne, J. R., Ricker, R. W., Baker, G., and Lewis, C. (2016). Macondo oil in deep-sea sediments: part 2 — Distribution and distinction from background and natural oil seeps. *Mar. Pollut. Bull.* 111, 381–401. doi: 10.1016/j.marpolbul.2016.07.041

Sutton, T. T., Frank, T., Judkins, H., and Romero, I. C. (2020). "As gulf oil extraction goes deeper, who is at risk? community structure, distribution, and connectivity of the deep-pelagic fauna," in *Scenarios and Responses to Future Deep Oil Spills*, eds S. Murawski, C. H. Ainsworth, S. Gilbert, D. J. Hollander, C. B. Paris, M. Schluter, et al. (Cham: Springer), 403–418. doi: 10.1007/978-3-030-12963-7_24

Swarzenski, P. W. (2014). "210Pb dating," in *Encyclopedia of Scientific Dating Methods*, eds W. J. Rink and J. Thompson (Cham: Springer), 1–11. doi: 10.1007/978-94-007-6326-5

Valentine, D. L., Kessler, J. D., Redmond, M. C., Mendes, S. D., Heintz, M. B., Farwell, C., et al. (2010). Propane respiration jump-starts microbial response to a deep oil spill. *Science* 330, 208–211. doi: 10.1126/science.1196830

van Eenennaam, J. S., Rahsepar, S., Radović, J. R., Oldenburg, T. B. P., Wonink, J., Langenhoff, A. A. M., et al. (2018). Marine snow increases the adverse effects of oil on benthic invertebrates. *Mar. Pollut. Bull.* 126, 339–348. doi: 10.1016/j.marpolbul.2017.11.028

van Eenennaam, J. S., Wei, J., Bao, P., Foekema, E. M., and Murk, A. J. (2016). Oil spill dispersants induce formation of marine snow by algae-associated bacteria. *Mar. Pollut. Bull.* 104, 294–302. doi: 10.1016/j.marpolbul.2016.01.005

Vonk, S. M., Hollander, D. J., and Murk, A. J. (2015). Was the extreme and wide-spread marine oil-snow sedimentation and flocculent accumulation (MOSSFA) event during the Deepwater Horizon blowout unique? *Mar. Pollut. Bull.* 100, 5–12. doi: 10.1016/j.marpolbul.2015.08.023

Walker, B. D., Druffel, E. R. M., Kolasinski, J., Roberts, B. J., Xu, X., and Rosenheim, B. E. (2017). Stable and radiocarbon isotopic composition of dissolved organic matter in the Gulf of Mexico. *Geophys. Res. Lett.* 44, 8424–8434. doi: 10.1002/2017GL074155

Wang, Z., Fingas, M., and Page, D. S. (1999a). Oil spill identification. *J. Chromatogr. A* 843, 369–411.

Wang, Z., Fingas, M. F., Landriault, M., Sigouin, L., Lambert, P., Turpin, R., et al. (1999b). PAH distribution in the 1994 and 1997 mobile burn products and determination of the diesel PAH destruction efficiencies. *Int. Oil Spill Conf. Proc.* 1999, 1287–1292. doi: 10.7901/2169-3358-1999-1-1287

Wang, Z., and Fingas, M. F. (2003). Development of oil hydrocarbon fingerprinting and identification techniques. *Mar. Pollut. Bull.* 47, 423–452. doi: 10.1016/S0025-326X(03)00215-7

Wang, Z., Yang, C., Brown, C., Hollebone, B., and Landriault, M. (2008). A case study: distinguishing Pyrogenic hydrocarbons froM Petrogenic hydrocarbons. *Intern. Oil Spill Conf.* 2008, 311–320.

Wang, Z., Yang, C., Yang, Z., Brown, C. E., Hollebone, B. P., and Stout, S. A. (2016). "Petroleum biomarker fingerprinting for oil spill characterization and source identification," in *Standard Handbook Oil Spill Environmental Forensics*, eds Z. Stout and S. Wang (Amsterdam: Elsevier Inc), 131–254. doi: 10.1016/B978-0-12-803832-1/00004-0

White, H. K., Marx, C. T., Valentine, D. L., Sharpless, C., Aeppli, C., Gosselin, K. M., et al. (2019). Examining inputs of biogenic and oil-derived hydrocarbons in surface waters following the deepwater horizon oil spill. *ACS Earth Sp. Chem.* 3, 1329–1337. doi: 10.1021/acsearthspacechem.9b00090

White, H. K., Wang, C. H., Williams, P. L., Findley, D. M., Thurston, A. M., Simister, R. L., et al. (2016). Long-term weathering and continued oxidation of oil residues from the Deepwater Horizon spill. *Mar. Pollut. Bull.* 113, 380–386. doi: 10.1016/j.marpolbul.2016.10.029

Xing, L., Zhang, H., Yuan, Z., Sun, Y., and Zhao, M. (2011). Terrestrial and marine biomarker estimates of organic matter sources and distributions in surface sediments from the East China Sea shelf. *Cont. Shelf Res.* 31, 1106–1115. doi: 10.1016/j.csr.2011.04.003

Yan, B., Passow, U., Chanton, J. P., Nöthig, E.-M., Asper, V., Sweet, J., et al. (2016). Sustained deposition of contaminants from the Deepwater Horizon spill. *Proc. Natl. Acad. Sci. U.S.A.* 113, E3332–E3340. doi: 10.1073/pnas.1513156113

Ziervogel, K., McKay, L., Rhodes, B., Osburn, C. L., Dickson-Brown, J., Arnosti, C., et al. (2012). Microbial activities and dissolved organic matter dynamics in oil-contaminated surface seawater from the Deepwater Horizon oil spill site. *PLoS One* 7:e34816. doi: 10.1371/journal.pone.0034816

Zonneveld, K. A. F., Versteegh, G. J. M., Kasten, S., Eglinton, T. I., and Emeis, K. (2009). Selective preservation of organic matter in marine environments - processes and impact on the fossil record. *Biogeosci. Discuss.* 6, 6371–6440.

Conflict of Interest: The authors declare that the research was conducted in the absence of any commercial or financial relationships that could be construed as a potential conflict of interest.

frontiers
in Marine Science

REVIEW
published: 19 July 2021
doi: 10.3389/fmars.2021.642160

Aggregation and Degradation of Dispersants and Oil by Microbial Exopolymers (ADDOMEx): Toward a Synthesis of Processes and Pathways of Marine Oil Snow Formation in Determining the Fate of Hydrocarbons

Antonietta Quigg[1,2]*, Peter H. Santschi[2,3], Chen Xu[3], Kai Ziervogel[4], Manoj Kamalanathan[1], Wei-Chun Chin[5], Adrian B. Burd[6], Andrew Wozniak[7,8] and Patrick G. Hatcher[8]

[1] Department of Marine Biology, Texas A&M University at Galveston, Galveston, TX, United States, [2] Department of Oceanography, Texas A&M University, College Station, TX, United States, [3] Department of Marine Science, Texas A&M University at Galveston, Galveston, TX, United States, [4] Institute for the Study of Earth, Oceans and Space, University of New Hampshire, Durham, NH, United States, [5] Department of Bioengineering, University of California, Merced, Merced, CA, United States, [6] Department of Marine Sciences, University of Georgia, Athens, GA, United States, [7] School of Marine Science and Policy, University of Delaware, Lewes, DE, United States, [8] Department of Chemistry and Biochemistry, Old Dominion University, Norfolk, VA, United States

OPEN ACCESS

Edited by:
Michael R. Stukel,
Florida State University, United States

Reviewed by:
Tian Jian Hsu,
University of Delaware, United States
Johan Robbens,
Institute for Agricultural, Fisheries and Food Research (ILVO), Belgium
Thomas Bryce Kelly,
University of Alaska Fairbanks, United States

****Correspondence:***
Antonietta Quigg
quigga@tamug.edu

Specialty section:
This article was submitted to Marine Pollution, a section of the journal Frontiers in Marine Science

Received: *15 December 2020*
Accepted: *24 June 2021*
Published: *19 July 2021*

Citation:
Quigg A, Santschi PH, Xu C, Ziervogel K, Kamalanathan M, Chin W-C, Burd AB, Wozniak A and Hatcher PG (2021) Aggregation and Degradation of Dispersants and Oil by Microbial Exopolymers (ADDOMEx): Toward a Synthesis of Processes and Pathways of Marine Oil Snow Formation in Determining the Fate of Hydrocarbons. Front. Mar. Sci. 8:642160. doi: 10.3389/fmars.2021.642160

Microbes (bacteria, phytoplankton) in the ocean are responsible for the copious production of exopolymeric substances (EPS) that include transparent exopolymeric particles. These materials act as a matrix to form marine snow. After the Deepwater Horizon oil spill, marine oil snow (MOS) formed in massive quantities and influenced the fate and transport of oil in the ocean. The processes and pathways of MOS formation require further elucidation to be better understood, in particular we need to better understand how dispersants affect aggregation and degradation of oil. Toward that end, recent work has characterized EPS as a function of microbial community and environmental conditions. We present a conceptual model that incorporates recent findings in our understanding of the driving forces of MOS sedimentation and flocculent accumulation (MOSSFA) including factors that influence the scavenging of oil into MOS and the routes that promote decomposition of the oil post MOS formation. In particular, the model incorporates advances in our understanding of processes that control interactions between oil, dispersant, and EPS in producing either MOS that can sink or dispersed gels promoting microbial degradation of oil compounds. A critical element is the role of protein to carbohydrate ratios (P/C ratios) of EPS in the aggregation process of colloid and particle formation. The P/C ratio of EPS provides a chemical basis for the "stickiness" factor that is used in analytical or numerical simulations of the aggregation process. This factor also provides a relative measure for the strength of attachment of EPS to particle surfaces. Results from recent laboratory experiments demonstrate

(i) the rapid formation of microbial assemblages, including their EPS, on oil droplets that is enhanced in the presence of Corexit-dispersed oil, and (ii) the subsequent rapid oil oxidation and microbial degradation in water. These findings, combined with the conceptual model, further improve our understanding of the fate of the sinking MOS (e.g., subsequent sedimentation and preservation/degradation) and expand our ability to predict the behavior and transport of spilled oil in the ocean, and the potential effects of Corexit application, specifically with respect to MOS processes (i.e., formation, fate, and half-lives) and Marine Oil Snow Sedimentation and Flocculent Accumulation.

Keywords: marine oil snow, marine snow, exopolymers, MOSSFA, deepwater horizon, oil

INTRODUCTION

One of the significant new insights from the large research effort launched after the Deepwater Horizon (DwH) oil spill in the Gulf of Mexico in 2010 is the information gained on the fate of oil and dispersants as they were transported to the seafloor (see e.g., reviews of Daly et al., 2016; Passow and Overton, 2021; Quigg et al., 2021a). In particular, it was found that the flocculent material observed in surface waters for several weeks after the incident formed as a result of microbial mucus production (Passow et al., 2012). This material contained significant fossil carbon as determined by the ^{13}C technique (Passow, 2016). The term MOSSFA (Marine Oil Snow Sedimentation and Flocculent Accumulation) was coined to describe the combination of biological, chemical and physical processes that lead to the formation and sinking of this marine oil snow (MOS) material and its accumulation on the seafloor (Daly et al., 2016, 2020; Quigg et al., 2016, 2020; Burd et al., 2020). MOSSFA also includes the fate of oil and the biochemical signature left in exudates and sediments. It has since become clear that similar sedimentation events of oil-laden marine snow have also occurred during other spills, although they went largely undetected at the time (Vonk et al., 2015). Recent estimates suggest that 5–31% of oil reached the seafloor during DwH (Valentine et al., 2014; Chanton et al., 2015; Romero et al., 2015; Xu et al., 2018a,b). Interestingly, a similar proportion of oil (24%) reached the seafloor during the Ixtoc-I oil spill in the Bay of Campeche in 1979–1980 (Boehm and Fiest, 1980; Jernelöv and Lindén, 1981), emphasizing the importance of the MOSSFA process. Indeed, MOSSFA events are now recognized as a potential pathway for oil distribution in the marine environment, and the need to integrate this process into spill response planning has been recognized (Jacketti et al., 2020; Ross et al., 2021). Whereas aggregation between suspended sediments and oil [e.g., oil-sediment aggregations (OSA), also called oil-mineral-aggregates (OMAs), mineral-oil-aggregates (MOA), oil-particle aggregates (OPA) or oil-suspended-particulate-material-aggregates] form predominately via direct coagulation between oil droplets and particulates or sediments (Khelifa and Hill, 2006; Gong et al., 2014; Zhao et al., 2016), exopolymers released by bacteria and phytoplankton are an essential ingredient for the biologically mediated formation of marine snow and MOS (see recent reviews by Quigg et al., 2016; Burd et al., 2020; Santschi et al., 2020; Gregson et al., 2021).

Formation of marine (oil) snow is complex, depending on local conditions (light, UV, temperature, weathering, and minerals) and by a multitude of drivers spanning from molecular to organismal scales (**Figure 1**). This review examines the relationship between the microbial community, their exudates, oil, and dispersants in determining the major processes (dispersion, aggregation, and sinking), which in turn determine the fate of hydrocarbons in the ocean. It is known that most marine microbes, whether auto- or heterotrophic, bacteria or phytoplankton, are capable of producing mucilaginous substances that have varying functional roles and physical properties (Hoagland et al., 1993; Decho and Herndl, 1995; Verdugo, 2012; Decho and Gutierrez, 2017). This frequently leads to the formation of gelatinous mucus-like aggregates (Baelum et al., 2012; Passow et al., 2012; Ziervogel et al., 2012; Gutierrez et al., 2013a,b) such as biofilms and gels that facilitate the development of complex, interacting communities that are hotspots of microbial activity (Verdugo and Santschi, 2010; Doyle et al., 2018, 2020). However, it remains important to understand: (A) what are the general characteristics of EPS? (B) how do microbes respond to oil and dispersants? (C) what are the mechanisms by which EPS aids in the aggregation and/or dispersion of oil or oil plus dispersant, and (D) how does the presence of the resulting ternary system (oil-dispersant-EPS) modify the fate of the oil?

The formation of marine snow and MOS are usually modeled using aggregation theory (Burd and Jackson, 2009; Dissanayake et al., 2018). Some models explicitly focus on the physical processes that bring particles together (e.g., Brownian motion, fluid shear, and differential sedimentation), the probability that particles adhere once a collision has occurred (stickiness), and the sinking of particles through the water column (Kiørboe et al., 1990; Burd and Jackson, 2009). Marine aggregates display fractal properties, and so models use fractal scaling to relate particle diameter to volume. Particle disaggregation is also important and occurs by fluid shear, turbulence, or fragmentation through animal-particle interactions. Although disaggregation models are less well developed, simplified representations of disaggregation are also often included in models which can be sensitive to how disaggregation is parameterized (Burd and Jackson, 2009; Dissanayake et al., 2018). Combining these factors together leads to a system of non-linear, coupled differential equations describing the evolution of the particle size distribution (Burd and Jackson, 2009). Other models, e.g., the "Brownian

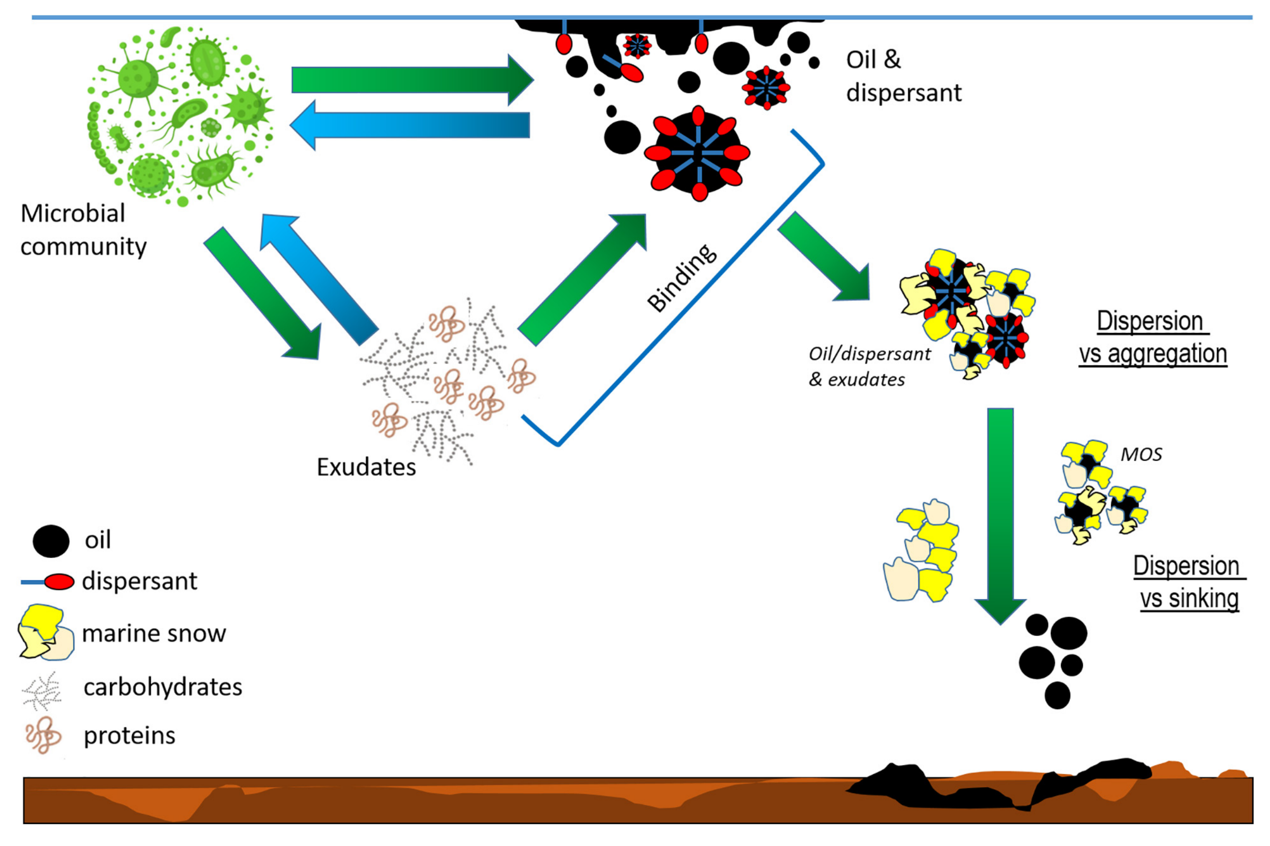

FIGURE 1 | Schematic of potential interactions between the microbial community and the oil or oil plus dispersant. Microbial exudates are released in response to the oil and dispersant, which then triggers a cascade of reactions. The binding between exudates and oil or oil plus dispersant impact the oil's fate (dispersion versus aggregation), which in turn determines its distribution between the water column and sediments (dispersion versus sinking), degradation and grazing rates. The microbial community composition depends on oil and dispersant availability, which in turn determines the characteristics of microbial exudates and dictates the method microbes interact with the oil (direct or via exudates).

Pumping" model of Honeyman and Santschi (1989) express coagulation rates and extent as a non-linear function of particle concentration, to simulate the widely observed particle concentration effect on particle-water partition coefficients and kinetics of radioactive and stable metal sorption coupled to coagulation of colloids to particles. The Brownian Pumping model was also verified in controlled laboratory experiments using hematite particles (Honeyman and Santschi, 1991) and natural particle assemblages (Stordal et al., 1996; Wen et al., 1997).

In all formulations of marine snow formation, purely physicochemical processes are included in models only in the form of an empirical "stickiness" parameter (α) that takes a value between 0 and 1. This is usually regarded as a constant and depends on the amount of EPS particles (Passow, 2002). The aggregation rate ($R\left(d_i, d_j\right)$) between particles of diameter d_i and d_j is then written as:

$$R\left(d_i,\ d_j\right) = \alpha\beta\left(d_i, d_j\right) C_iC_j \tag{1}$$

Where $\beta(d_i, d_j)$ is the coagulation kernel and is the sum of the rates of the physical processes bringing particles together, and C_i is the concentration of particles of diameter d_i.

In this review, we propose that the stickiness parameter (α) should be modified to reflect the composition of EPS. In particular, we have suggested that α should be a function of the protein-to-carbohydrate ratio (ϑ) of the EPS which is in turn a function of microbial biomass and the concentration of oil and dispersant (Quigg et al., 2016; Santschi, 2018; Xu et al., 2019; Chen et al., 2020; Santschi et al., 2020). This modification will explicitly incorporate important biological and chemical contributions into the coagulation models so that the aggregation rate between particles becomes:

$$R_{ij} = \alpha\left(\vartheta\right)\beta_{ij}C_iC_j \tag{2}$$

In this review, we will focus on the above four questions (A–D) as they lead us closer toward an understanding of the processes and pathways of MOS formation in determining the fate of hydrocarbons. Here in, we present a conceptual model that incorporates this information, which is critical to developing better predictions of hydrocarbon fate in the oceans. The reader is referred to the many excellent reviews published to learn more about other processes (e.g., role of zooplankton and food webs) which are equally critical but beyond the scope of the current paper in understanding MOS and MOSSFA (Beyer et al., 2016;

Daly et al., 2016; Burd et al., 2020; Kujawinski et al., 2020; Quigg et al., 2020; 2021a, b; Passow and Overton, 2021; Ross et al., 2021). Nonetheless, additional studies would be invaluable to collecting data which could be used to develop flux measures between compartments and hence, the development of models to examine the fate of hydrocarbons.

What Are the General Characteristics of EPS?

Exopolymeric substances (EPS) represent a vast pool of reversibly self-assembling porous micro-gels released by microbes (bacteria and phytoplankton) that serve as a major source of dissolved organic matter in the oceans. Marine micro- and nano-gels are three-dimensional polymer networks reversibly formed from EPS (Verdugo et al., 2004; Verdugo and Santschi, 2010); they create microenvironments that interact with the surrounding media (Chin et al., 1998) and are thought to be the precursors to the more visible macro-gels. These high molecular weight exopolymers are thought to physically protect microbes (e.g., from heavy metals and pollutants) as well as aid in their attachment to different substrates by forming biofilms and gels (Verdugo and Santschi, 2010; Quigg et al., 2013, 2016; Decho and Gutierrez, 2017; Santschi, 2018; Santschi et al., 2020; and references therein). These exopolymers are composed mainly of polysaccharides and proteins, but also contain nucleic acids and lipids (Azam, 1998; Verdugo et al., 2005; Verdugo, 2007; Decho and Gutierrez, 2017; Santschi et al., 2020). Subclasses of EPS are named depending on the method of characterization (see review of Quigg et al., 2016). If alcian blue staining is used with Xanthan as the standard, the particulate fraction (retained on a filter) is named transparent exopolymer particles (TEP) (Passow, 1995; Bar-Zeev et al., 2011; Xu et al., 2011). If alginic acid is used as a standard, the particulate material is called acid polysaccharides (APS) (Hung et al., 2003). Coomassie Stained Particles (CSP) are proteinaceous particles made visible with Coomassie Blue staining (Nagasaki et al., 2004; Verdugo et al., 2008). It is important to note that often these different measurements are detecting different moieties of the same molecule(s). EPS, are therefore "operationally" defined based upon their characteristics, size(s), and methods of quantification (Bar-Zeev et al., 2015; Quigg et al., 2016). The majority of studies measure one, perhaps two of these operationally defined EPS. However, a recent study compared EPS, TEP, CSP, and microgels in seawater from the Gulf of Mexico (Xu et al., 2019). The study found that biopolymers making up EPS, TEP, and CSP consisted primarily of polysaccharides and proteins, most likely as proteoglycans and glycoproteins, and that overall, concentrations ranked in the order of [gels] > [TEP] > [particulate EPS]. This ranking was the same in the presence of a water accommodated fraction (WAF) of oil prepared with a Macondo surrogate oil. The EPS that was electrostatically held onto particle surfaces (operationally-defined as those extractable by 1% EDTA) accounted for a minor (∼4%) yet relatively constant proportion of TEP.

Polysaccharides, one of the major constituents of EPS, are mostly hydrophilic. Acid polysaccharides such as uronic acids contain carboxyl or sulfate groups and provide bidentate inner-sphere coordination sites for divalent (e.g., Ca^{2+} and Mg^{2+}) or trivalent (e.g., Fe^{3+}) ions, thus causing supra-macromolecular aggregation and Ca^{2+} bridging for structural stability (Verdugo et al., 2004). Proteins, another major EPS component, are amphiphilic and mediate the stability and aggregation of the 3-D networks of biopolymers, through hydrophobic and electrostatic interactions (Ding et al., 2008; Ortega-Retuerta et al., 2009; Song et al., 2015; Sun et al., 2020), as well as light-induced cross-linking (Sun et al., 2017, 2018, 2019, 2020). The hydrophobic domains of EPS (mainly consisting of proteins) were shown previously to absorb organic pollutants, such as petroleum hydrocarbons phenanthrene (Liu et al., 2001) and benzene (Spath et al., 1998). Particulate exudates, like TEP, may promote coagulation of marine particles and provide a matrix for marine snow (component particles > 0.5 mm) (Alldredge et al., 1993; Passow, 2002; Verdugo et al., 2004; Passow et al., 2012). The composition and characteristics of EPS can therefore lead to differences in the interactions with oil and/or dispersants, thus affecting petroleum hydrocarbons' dispersion, degradation, and sedimentation pathways. Recent studies reveal that the hydrophobic interaction between proteins and hydrocarbons results from a selective partitioning with hydrophilic polysaccharides preferentially associating with sinking MOS (Xu et al., 2018a,b, 2019). Marine snow and MOS were found to be extremely sticky; with particles readily attaching in the water column. After losing their buoyancy, marine snow and MOS sink toward the seafloor (Ziervogel et al., 2011; Passow et al., 2012). Recent work by Ye et al. (2020) also shows that when oil droplets are combined with more cohesive bentonite clay, the aggregate density and settling velocity actually increase compared to the clay alone. This is because droplets no longer exist (observed microscopically) and oil is absorbed into the larger aggregate structure. Their observations were carried out at atypically high particle, EPS as Xanthan gum, and/or crude oil concentrations (e.g., 500 mg/L) and should be regarded with caution. However, these observations may be consistent with observations using individual diatom species exposed to a control and to WAF treatment in roller tanks by Passow et al. (2019) who found that measured settling velocities increased in the presence of oil.

How Do Microbes Respond to Oil and Dispersants?

The release of hydrocarbons as a result of a spill triggers a complex cascade of microbial responses (**Figure 1**), whereby not a single species dominates, but complex microbial consortia develop (Head et al., 2006; Baelum et al., 2012; Kleindienst et al., 2015, 2016; Doyle et al., 2018, 2020). The microbial response to oil-contamination and the fate of the oil varies, with some bacteria having genes for hydrocarbon and/or *n*-alkane degradation that can directly utilize components of the oil (Hazen et al., 2010; Valentine et al., 2010; Kessler et al., 2011; Lu et al., 2012; Redmond and Valentine, 2012; Ziervogel et al., 2014; Doyle et al., 2020). Several studies have confirmed that microbes (prokaryotes) indigenous to the Gulf of Mexico comprised largely of Gammaproteobacteria (Hazen et al., 2010; Baelum et al., 2012; Mason et al., 2012; Rivers et al., 2013; Kleindienst et al., 2016) played a significant role in the biodegradation of the oil during and post DwH oil spill (Lu et al., 2012; Mason et al., 2012, 2014). However, other microbial groups were also present (Gutierrez et al., 2013a,b, 2016; Yang et al., 2016; Kamalanathan et al., 2018, 2021) and have been shown to respond to oil spills in other areas (McKew et al., 2007; Prince et al., 2010; McGenity et al., 2012). Members of the genera *Marinobacter*, *Alcanivorax*, *Cycloclasticus*, *Neptuniibacter*, and others dominated the surface water column (Baelum et al., 2012; Kleindienst et al., 2015; Dombrowski et al., 2016; Doyle et al., 2018), while the order Oceanospirillales, and genus *Colwellia* dominated the deep sea plume responses (Redmond and Valentine, 2012; Kimes et al., 2013, 2014; Kleindienst et al., 2015, 2016). A change in microbial community structure was also observed across time, with groups such as *Methylotrophs*, *Alteromonadales*, *Flavobacteria*, *Rhodobacter*, and *Deltaproteobacteria* increasing in abundance following the succession of *Cycloclasticus*, *Oceanospirillales*, *Colwellia*, and *Alcanivorax* (Kimes et al., 2013, 2014). These shifts occur within a few hours of experiment initiation with surface water studies (Doyle et al., 2018, 2020) showing the microbial community response is also much faster in surface waters than those performed at depth (Baelum et al., 2012; Kleindienst et al., 2015). In mesocosms with oil (as a WAF), this manifested as an increase in community diversity due to the outgrowth of several aliphatic- and aromatic-hydrocarbon degrading species, including phytoplankton-associated taxa (Doyle et al., 2020). In contrast, microbial community diversity was reduced in microcosms containing oil (Meng et al., 2016; Kamalanathan et al., 2021) and dispersant (Meng et al., 2016), however, this effect has been shown to be temperature dependent (Techtmann et al., 2017).

Field samples from the site of DwH showed elevated levels of respiration accompanied by higher levels of expression of genes associated with chemotaxis, motility, hydrocarbon degradation pathways such as *n*-alkane and cyclohexane oxidation, and nutrient acquisition, especially denitrification in the prokaryotic microbial community (Edwards et al., 2011; Lu et al., 2012; Mason et al., 2012, 2014). Shifts in extracellular enzyme activities from β-glucosidase (associated with polysaccharide degradation) to lipase (often associated with hydrocarbon degradation) were also observed in mesocosm studies (Kamalanathan et al., 2021). At the sites of the DwH oil spill where both the sediments and their overlying water samples were taken, elevated levels of alkaline phosphatase were measured. This corresponded to a substantial biomass growth in the water column yet a non-significant biomass increase in the sediment (Edwards et al., 2011; Lu et al., 2012). Taken together, these findings indicate oil exposure shifted the metabolism toward hydrocarbon degradation which in-turn drove nitrogen uptake (Mason et al., 2014; Zhao et al., 2020).

Dramatic shifts in heterotrophs, photoautotrophs, and grazers altered the community structure in the water column with diatoms and certain dinoflagellates dominating after exposure to oil and/or oil plus dispersants in a variety of studies (Parsons et al., 2015; Almeda et al., 2018; Bretherton et al., 2019; Finkel et al., 2020; Quigg et al., 2021b). Some dinoflagellates have been shown to directly ingest oil (Almeda et al., 2014), however, the mechanism behind diatom oil tolerance remains unknown. Many physiological studies in the last decade have examined the response of the photosynthetic pathways, respiration, the reactive oxygen system, morphological features and toxin production (Bretherton et al., 2018, 2019, 2020; Kamalanathan et al., 2019) as well as other parameters (see review by Quigg et al., 2021b). Growth and photophysiological responses are often species specific with some showing a tolerance and others a sensitivity to oil or oil plus dispersants (Bretherton et al., 2018, 2020). Reactive oxygen species concentrations have been shown to be one of the major secondary factors leading to growth inhibition in sensitive phytoplankton (Ozhan et al., 2015; Quigg et al., 2021b). The presence of dispersant reduced the growth rate and increased the level of the toxin domoic acid in the diatom *Pseudo-nitzschia* (Bretherton et al., 2019). Nonetheless, a decrease in microbial interactions was also observed in microcosm studies in response to oil exposure, primarily due to a major change in the composition of eukaryotic phototrophs and a decrease in photosynthetic efficiency (Kamalanathan et al., 2021). Surprisingly, the same study found a significant decrease in heterotrophic EPS production with no changes to phototrophic EPS levels, suggesting an indirect impact on phototrophs and heterotroph interactions due to oil exposure.

Amongst the eukaryotes, the community composition shifted more toward fungi in the benthos (Bik et al., 2012) and salt marshes (Lumibao et al., 2018). This is not surprising as fungi have been shown to tolerate and degrade oil either directly (Davies and Westlake, 1979; Al-Nasrawi, 2012) or in conjunction with extracellular enzymes (Verdin et al., 2004; Asemoloye et al., 2018). There is also evidence that marine fungi play a role in oil degradation (Burd et al., 2020; Finkel et al., 2020). Fungi are well-known for their ability to metabolize biochemical compounds including lignin and complex carbohydrates (Hedges et al., 1985), and they have recently been shown to dominate biomass on marine snow in the deep sea (Bochdansky et al., 2017) suggesting their importance to marine organic matter degradation.

After the DwH oil spill, large, EPS-rich, marine snow, and MOS formed with elevated hydrolytic enzyme activities in association with the surface oil layer (Baelum et al., 2012; Passow et al., 2012; Ziervogel et al., 2012; Kleindienst et al., 2015; Kamalanathan et al., 2018). In addition to the above changes in microbial community activity, it was also found that the mucus-like EPS harbored a very distinct community of interacting microbes, with a specific functionality that was different from those persisting in the surrounding seawater (Ziervogel et al., 2012; Arnosti et al., 2015). These eukaryotic microbes and fungi can transform and degrade oil, sometimes in association with bacteria and dispersants including Corexit (Mishamandani et al., 2016; Severin and Erdner, 2019). Thus, marine snow is a hot spot for microbial activity (Azam, 1998; Arnosti et al., 2015; Doyle et al., 2018, 2020) and serves as a transport vehicle for hydrocarbons to the seafloor as well as the associated microbial communities (Kowalewska and Konat, 1997; Kowalewska, 1999; Ziervogel et al., 2012; Ziervogel et al., 2014, 2016; Arnosti et al., 2015). Collectively, these processes directly influence microbial community composition and structure, indirectly influence the quantity and quality of produced exudates, and ultimately influence both remineralization and mobilization of oil-derived carbon, by determining its fate (sinking versus dispersion versus aggregation) and transport (exudates).

Some data also indicates Corexit may serve as a microbial substrate (Baelum et al., 2012; Bacosa et al., 2018) while others show toxicity (Zahed et al., 2010; Hamdan and Fulmer, 2011; Paul et al., 2013). These differences may be due to a dissimilar experimental design, as Baelum et al. (2012) used deep-water samples, while Hamdan and Fulmer (2011) used hydrocarbon degrading isolates. Regardless, it is apparent that the impact of Corexit on microbial community function, in general, and on EPS production and function specifically, is still largely unconstrained. In addition, oceanic regions have distinctly different indigenous microbial communities than coastal regions (Doyle et al., 2020); these populations responded to oil/dispersant intrusion differently as also reflected in the EPS production and composition (Xu et al., 2019). For example, EPS produced by the natural consortia in the coastal seawater was generally more hydrophobic (with a higher P/C ratio, and thus higher α factor, see above) than that produced in the offshore waters. Nutrient status and particle concentrations in these oceanic regions (nearshore versus offshore) could have also been factors that directly affect EPS production and oil-laden aggregate formation (the latter serves as ballast). Such information needs to be taken into consideration when evaluating post-spill MOS formation and sedimentation.

Lastly, most of the research on microbial oil spill toxicology tend to highlight the most enriched microbial species, with less abundant ones grouped together as "others." However, studies have shown that members belonging to order *Burkholderiales*, and *Enterobacteriales*, and phylum *Planctomycetaceae, Hyphomonadaceae, Saprospiraceae*, and *Teridinibacter* decreased in abundance in response to oil and dispersant exposure (Kleindienst et al., 2016; Meng et al., 2016; Kamalanathan et al., 2018). Amongst eukaryotes, *Amoebozoa*, dinoflagellates, diatoms such as *Coscinodiscus, Thalassiosira, Stephanopyxis,* and *Thalassionema* decreased in response to oil and dispersant exposure (Bretherton et al., 2018; Finkel et al., 2020). However, future studies with more emphasis on the oil and dispersant sensitive microbial species would be beneficial, e.g., using them as indicator species of unpolluted areas or areas that recovered post-spill.

What Are the Mechanisms by Which EPS Aids in the Aggregation and/or Dispersion of Oil or Oil Plus Dispersant, Thereby Influencing the Fate of Oil?

Exopolymeric substances acting as biosurfactants can emulsify oil and its breakdown products (Head et al., 2006). For example, EPS produced by *Halomonas* sp. has amphiphilic properties, thereby interacting easily with hydrophobic substrates like hydrocarbons, leading to the solubilization and biodegradation of oil components (Gutierrez et al., 2013a). The exopolymer concentrations with entrained oil droplets grow to form networks that also act as an energy and carbon source to other members of the microbial community (Sinsabaugh et al., 2009; Kamalanathan et al., 2020). In addition, the production of EPS may facilitate attachment of specific microbes (e.g., *Pseudomonas putida)* to polycyclic aromatic hydrocarbons (McGenity et al., 2012). In this way, a complex network of microbes utilizing the different components of oil and the metabolites of the oil degraders will develop (McGenity et al., 2012). Such networks may enhance the formation of aggregates and biofilms (Gärdes et al., 2011).

Most petroleum hydrocarbons are insoluble in seawater so that biodegradation can only take place at the hydrocarbon-water interface. Dispersion or emulsification of oil increases the bioavailability of oil products to biodegradation as these processes introduce fine droplets of oil into the water column by wave action or sea turbulence and keep it dispersed. Given dispersants are designed to form emulsions to prevent oil droplets from coalescing and stabilize them in a suspension, Corexit and other dispersant products are a mixture of nonionic (∼48%) and anionic (∼35%) surfactants with enough solvent or petroleum distillate (∼17%) to make a homogeneous dispersant mixture of the surfactants and aid in their penetration onto and into the oily aggregate (John et al., 2016; Quigg et al., 2021b). As shown in **Figure 2** (Phase 1), surfactants are long amphiphilic molecules that can arrange themselves at an interface such that the hydrophilic head interacts with the water and the hydrophobic tail shuns the water and crosses the interfacial boundary interacting with the air or another hydrophobic substance, such as oil. The presence of these molecules on the surface disrupts the cohesive energy and lowers the surface tension (**Figure 2**, Phase 2).

The purpose of dispersant application is to lower the oil/water interfacial tension to promote entrainment of oil droplets (<100 μm) into the water column (Chen and Yapa, 2007; Testa et al., 2016). The critical micelle concentration (CMC) is the concentration of dispersant at which the surfactant molecules form a uniform monolayer at the oil/water interface (**Figure 2**, Phase 3). The effectiveness of a dispersing agent increases the magnitude of the interfacial tension reduction to CMC (shown as the difference between the surface tension of Phase 1 and that of Phase 2, the greater the difference is, the higher the effectiveness). However, the efficiency is highest when the lowest concentration of dispersing agent is used after the CMC is reached (the surface tension of Phase 3, the lower the value, the higher the efficiency). Recent studies have tested the hypothesis that the exudates of bacteria and phytoplankton may also serve as biosurfactants (Quigg et al., 2016, 2020, Decho and Gutierrez, 2017; Ward et al., 2018). Schwehr et al. (2018) characterized EPS as biosurfactants by determining their effectiveness and efficiency through interfacial tension and CMC rheology measurements. They investigated mechanisms governing the self-assembly and phase separation for protein-polysaccharide-oil-dispersant interactions, thereby adding to our understanding of what is known about the CMC of oil/Corexit mixtures. With hydrophilic and hydrophopic moieties, EPS increases the bioavailability of certain oil components to the microbial community. In this sense, the biosurfactant properties

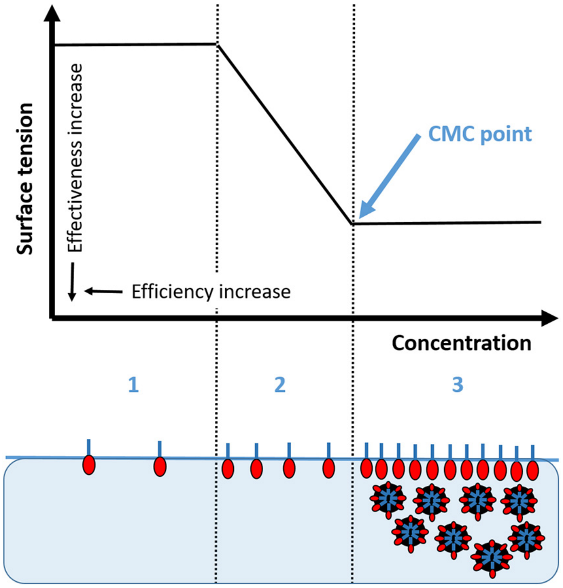

FIGURE 2 | Surface tension as a function of surfactant concentration (logarithmic scale) in three separate phases. (1) low concentration of surfactant, with the round hydrophilic end of the molecule in the water and the long carbon chain or tail interacting with a hydrophobic substance, i.e., air or oil; (2) as the surfactant concentration increases, the interfacial surface tension decreases between the hydrophobic and hydrophilic moieties; and (3) when the concentration of surfactant increases to the critical micelle concentration (CMC) an emulsion is formed where the oil is entrained in the biosurfactant and can be dispersed or form networks or gel.

of EPS are similar to those of dispersants used for oil spill remediation.

Exopolymeric substances with enhanced protein to carbohydrate (P/C) ratios (thus higher sticky factor α, see above) was present in oil and oil plus dispersant treatments, suggesting efficient bioemulsifying effects of proteins in the presence of Corexit (Schwehr et al., 2018; Xu et al., 2018a,b, 2019; Shiu et al., 2020). In addition, bovine serum albumin (used as a model protein) was found to slightly increase surface tension at low concentrations (<few mg/L), but decreased it at higher concentrations of >8 mg/L (Schwehr et al., 2018). These model molecules (including uronic acids such as glucuronic acid with carboxyl moieties and carrageenan with sulfate groups) appeared to be more efficient than Corexit in inducing the self-assembly of micelles in the seawater even when only very low concentrations were present. Schwehr et al. (2018) found Corexit is more effective, i.e., lowers the surface tension more than the EPS constituents, however, the EPS can emulsify oil at far lower concentrations, thus is more efficient (**Figure 2**). In several mesocosm experiments mimicking different environmental settings, the relative petro-carbon concentration (%, petro-carbon to total organic carbon) in the sinking MOS, as determined by ^{14}C method, was found to be positively correlated with both the P/C ratio of colloidal EPS and sinking MOS-EPS (Xu et al., 2019). This result corroborates that EPS plays a similar role to that of Corexit in reducing the surface tension of oil but could have been more efficient than Corexit in forming oil-EPS micelles. This behavior was related to their relative hydrophilicity (i.e., P/C ratio). Passow et al. (2019) suggested that oil droplets may allow for tighter packaging of cells, which decreases porosity and results in faster sinking. Santschi et al. (2020) suggested using the data from Passow et al. (2019) which showed that decreased aggregate diameters and settling velocities were correlated with increased P/C ratios of EDTA extractable EPS to understand how P/C ratios affect stickiness. That is, the presence of oil not only seems to cause a tighter packaging of cells, it also facilitates the production of EPS with higher P/C ratios and incorporation of more hydrophobic biopolymers (shown as higher P/C ratio). Incorporation of these high P/C ratio EPS moieties into the aggregate resulted in a slower sinking velocity of aggregates. P/C ratios of EPS could be different from that of whole EPS (including attached EPS), while P/C ratios of non-attached EPS affect whole oil incorporation, aggregate porosity, buoyancy, and sinking velocity, but the exact relationships in the complex web of processes is not entirely clear.

How Does the Presence of the Resulting Ternary System (Oil-Dispersant-EPS) Modify the Fate of the Oil?

In the last few years, considerable effort has been directed toward understanding how the ternary system (oil-dispersant-EPS) determines the fate and transport of oil (hydrocarbons) in the ocean, particularly considering the role of dispersants. Studies of oil, Corexit and organic matter, including exudates (EPS and TEP) may lead to conflicting observations as to the question of whether Corexit application promotes or hinders MOS formation and/or the subsequent sedimentation unless the findings are carefully dissected (Chiu et al., 2017; Passow et al., 2017, 2019). On one hand, Corexit application leads to significantly more oil droplets, thereby increasing the probability that oil is incorporated into marine snow. On the other hand, Corexit disperses whole oil-laden exudates, thus aggregation and subsequent sedimentation processes decrease (Passow, 2016, Passow et al., 2017). Also, Corexit application to oil appears to result in the formation of fewer but more oil-rich aggregates (Passow et al., 2017). If Corexit fully disperses oil-laden exudates more effectively compared to the scenario in which no Corexit is applied, all MOS formation would be inhibited and no sedimentation would be observed. In contrast to MOS, the formation of oil-sediment aggregates is independent of exudates, and not negatively affected by exudate dispersion (Henry et al., 2020). This finding was reflected in mesocosm studies that showed while the formation of oil-laden aggregates in the colloidal fraction increased, deposition of marine (oil) snow/particles decreased (Xu et al., 2018a,b). This is because each aggregate included higher concentrations of oil droplets thus increasing its buoyancy. In contrast to this, oil-sedimentation rates are less affected (over controls) when no dispersant is applied (Passow et al., 2012; Xu et al., 2018a).

The input of oil/dispersant fueled the microbial community by promoting EPS production and modifying their composition as observed by the positive correlations between EPS production and the reduction of oil/PAH/*n*-alkane when oil/dispersant was present in several mesocosm systems with various environmental settings (Xu et al., 2019). Some interesting patterns were observed: (1) more EPS preferably partitioned into suspended particulate matter (SPM) when dispersant was applied compared to treatments without oil/dispersant or only with oil; (2) riverine particle input in the coastal region enhanced EPS partitioning into the SPM fraction compared to the offshore water which has less terrestrial influence; (3) the coastal microbial communities tend to produce EPS with higher P/C ratio (thus higher α, see above) compared to those in offshore waters, indicating their potentially higher hydrophobicity and thus stronger tendency to form aggregates; (4) a contrasting pattern of consistently higher P/C ratio in sinking aggregate-EPS than in SPM-EPS in all treatments of the offshore region, with an opposite result in all treatments of the coastal water, suggesting EPS was from different sources in these two size fractions (SPM and sinking aggregates) and that different mechanisms regulated MOS formation and sedimentation in these two environmental settings.

Radiocarbon and ^{13}C NMR results have further shown that the presence of dispersants enhances the amount of oil products incorporated into MOS (Hatcher et al., 2018; Xu et al., 2018b). These authors observed that after less than a week of mesocosm conditions replicating an oil spill, most of the chemically-dispersed oil preferentially partitioned into the colloidal and suspended particulate fractions rather than to the sinking MOS. Thus, the oil sedimentation efficiency in treatments with a dispersant was considerably lower than those in the control and oil only treatments, which is almost a universal observation irrespective of environmental settings (nutrients or algae particle addition, oceanic regions, etc.) (Xu et al., 2019). It was determined that 28–93% of sinking organic carbon consisted of petro-carbon in the oil plus dispersant treatment compared to a range of 17–42% for oil-alone treatment, yet the sedimentation efficiency was significantly and consistently lower in the oil plus dispersant treatment (0.1–8% of initial oil carbon) relative to the oil-alone treatment (1.4–27% of initial oil carbon) (Xu et al., 2019). However, in the long term (in a scale of >2-weeks), these above mentioned differences (relative petro-carbon concentration and petro-carbon sedimentation efficiency) of the sinking MOS in oil plus dispersant versus oil-alone treatments diminished indicating that dispersants simply postponed MOS sedimentation. In a parallel effort, estimated oil equivalents used as a proxy for changing oil concentrations in seawater unassociated with MOS, exponentially decreased at rates ranging from –0.013 to –0.027/h (Wade et al., 2017). These were slightly higher than the rate of –0.0066/h reported by Gearing et al. (1979), a MERL mesocosm study in which 12% of added oil was transported to the sediments (Wade and Quinn, 1980).

A clear signal for oil incorporation into MOS comes from a mesocosm study in which oil was observed in aggregate materials (Hatcher et al., 2018). MOS (as bottom particles) was analyzed by a solid-state ^{13}C NMR CPMAS multi-pulse technique (Johnson and Schmidt-Rohr, 2014) modified to allow quantitative characterization of carbon functional groups (Hatcher et al., 2018). The latter study showed oil in chemically enhanced (with Corexit) WAF (CEWAF) treatments to have a very large peak in the aliphatic chemical shift region (**Figure 3B**) relative to controls (no oil added) (**Figure 3A**) indicative of inputs of highly aliphatic oil components. Extraction with dichloromethane (DCM), a solvent frequently used to extract oil, efficiently removed the aliphatic oil component from CEWAF MOS (**Figures 3B,D**); the control spectrum by contrast did not show appreciable changes (**Figures 3A,C**). A molecular mixing model adapted from Baldock et al. (2004) was then used to estimate the contributions of proteins, carbohydrates, lipids, and carbonyl carbon in the samples. After DCM extraction, control particles showed little to no change in the relative contributions of lipids suggesting that the losses in the operationally-defined lipid component for the oil treatment MOS could be attributed to the removal of oil (Δ lipid = oil contribution; Hatcher et al., 2018). Oil contributions were estimated to be 4, 27, and 26% for WAF, CEWAF, and diluted CEWAF (DCEWAF) treatments, respectively, using this technique. The ^{13}C NMR-derived estimates for oil contributions to the sinking MOS matched well with relative oil contributions found in particles collected from the same mesocosm treatments as measured using a Δ^{14}C tracer technique (Xu et al., 2018b). The agreement between these two approaches confirmed the ability to quantitatively extract oil from MOS using DCM for further characterization and assessment of oil degradation.

Oil associated with marine snow appears to be rapidly oxidized (timescales of days rather than years) (Hatcher et al., 2018; Wozniak et al., 2019). DCM extracts of the sunken MOS showed the control treatment to have vastly different molecular characteristics from that in the DCEWAF treatments (**Figure 4**; Wozniak et al., 2019). The sunken MOS DCM extracts show unique formulas at relatively high O/C and low H/C ratios indicating the oxygenation and solubilization of oil components that are not found in either the control sample or the Macondo oil sample (**Figure 4B**) and more likely are produced via degradation processes in the mesocosms. After just 4 days of processing, the oil isolated from the DCEWAF and CEWAF treatments showed a pattern in their CHO-containing molecular formulas that was very different from the Macondo oil which showed most of the spectral signal for CHO formulas to be accounted by CHO_2 formulas (**Figure 4C**). The DCEWAF and CEWAF CHO spectral signal shows reduced contributions from CHO_2 formulas due to contributions from CHO_3 and CHO_4 formulas with increasingly smaller contributions from higher oxygenated formulas. The distribution of CHO formulas in the degraded MOS (CEWAF and DCEWAF) was very similar to oils exposed to weathering processes on Gulf of Mexico beaches for several months (**Figures 4C,D**; Chen et al., 2016; Wozniak et al., 2019). Similar results were found by Hatcher et al. (2018) using GC × GC Mass Spectrometry. Oil degradation has been demonstrated for surface slicks and oiled sands (Aeppli et al., 2012; Ruddy et al., 2014; Chen et al., 2016) but not within complex MOS aggregates. These results suggest that oil degradation in the mesocosm experiments was rapid and facilitated by the microbial community over time scales of hours to days. We also observed significant changes in the fingerprint of the oil in MOS including high relative abundance of oxygenated hydrocarbons (O = 2–4) with likely aliphatic and

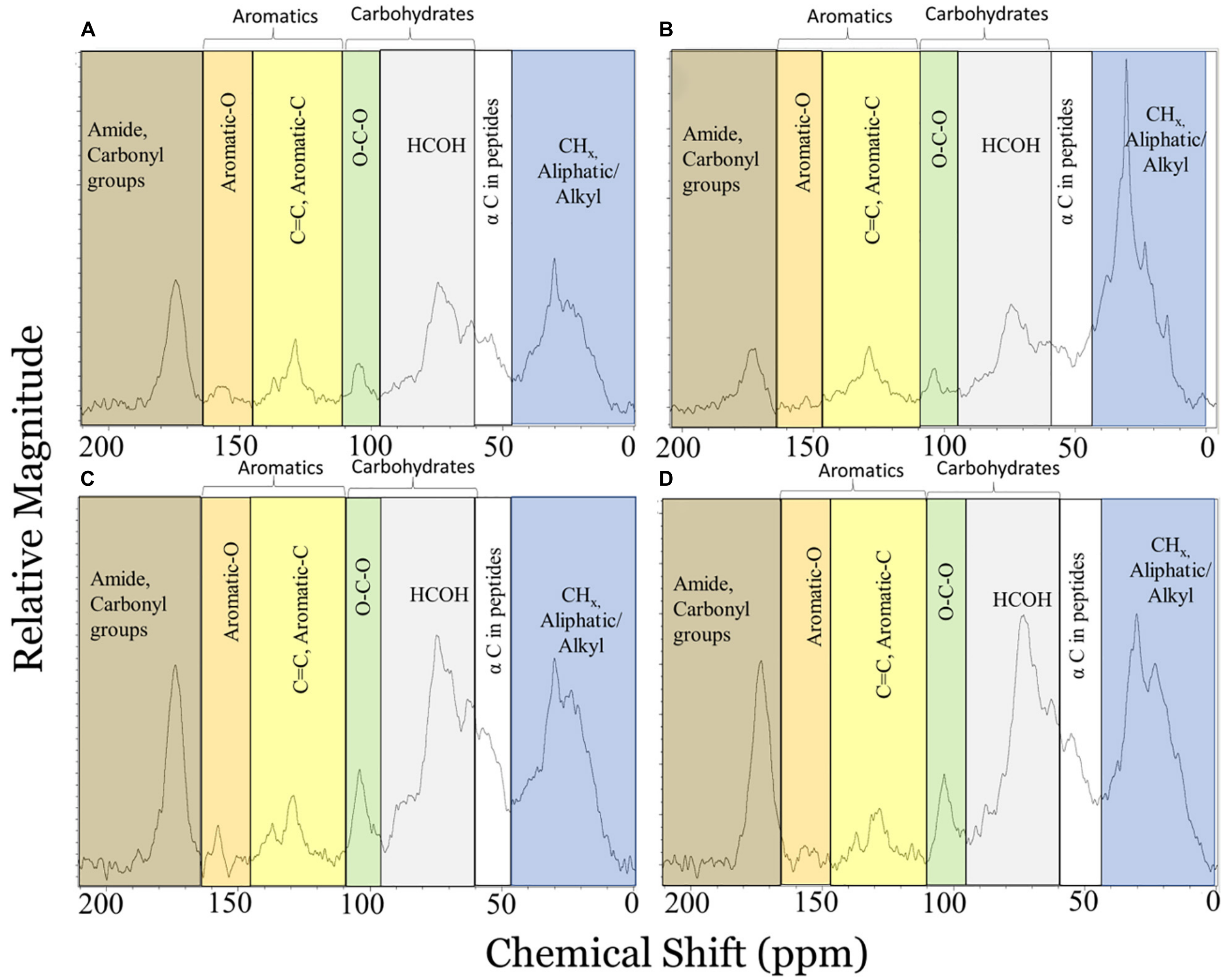

FIGURE 3 | Solid-state ^{13}C NMR spectra using a quantitative multiple cross polarization magic angle spinning pulse sequence for marine oil snow particles collected from the bottom of tanks in mesocosm control **(A,C)** and chemically-enhanced water accommodated fraction **(B,D)** treatments before **(A,B)** and after **(C,D)** extraction with dichloromethane to remove oil components. Shaded portions of the spectra represent chemical shift regions where signal for carbonaceous functional groups typically appear (blue: 0–45 ppm, aliphatic C; white: 46–60 ppm, α C in peptides; gray: 60–95 ppm, carbohydrate HCOH; green: 90–110 ppm, carbohydrate anomeric C; yellow: 110–145 ppm, Aromatic-C; orange: 145–165 ppm, Aromatic-O; brown: 165–215 ppm, Amide, Carbonyl C). Adapted from Hatcher et al. (2018).

aromatic molecular structures (Wozniak et al., 2019). We were, however, *not* able to observe progressive stepwise changes in the oil fingerprint toward aromatic ring oxidation and enrichment in oxygen-containing molecules in polar fractions, changes analogous to those observed during oxidation influenced by air-exposure (Ruddy et al., 2014; Chen et al., 2016). Such information would be invaluable for understanding the rate of oil degradation in the marine environment.

A comparison of PAH composition in MOS from laboratory roller table (Genzer et al., 2020) and mesocosm experiments [Bacosa et al., 2020; and GRIIDC dataset (10.7266/ER1EGZ8E)] with the PAH composition examined in the sediment samples of Gulf of Mexico (Romero et al., 2015), revealed interesting findings (**Figure 5**). Using non-metric multidimensional scaling (NMDS), the data points of both WAF and DCEWAF from roller table and mesocosm experiments clustered together with the sediment samples, suggesting some level of consistency in the PAHs that tend to remain in marine snow. While the DCEWAF samples from a mesocosm experiment clustered relatively closer to the sediment samples, a major fraction of the WAF samples from a mesocosm experiment clustered away, suggesting a slight effect (lower concentration of acenapthene) of the use of dispersant on the PAH composition of the marine snow leading to heterogeneity amongst marine snow composition. One clear pattern that emerged from this analysis, however, is the depletion of naphthalene and fluorene in nearly all the marine snow and the sediment samples relative to the composition of the original Macondo oil and the surrogate oil used in the roller table and mesocosm experiments. This is not surprising, as studies have shown rapid depletion and degradation of water soluble, light,

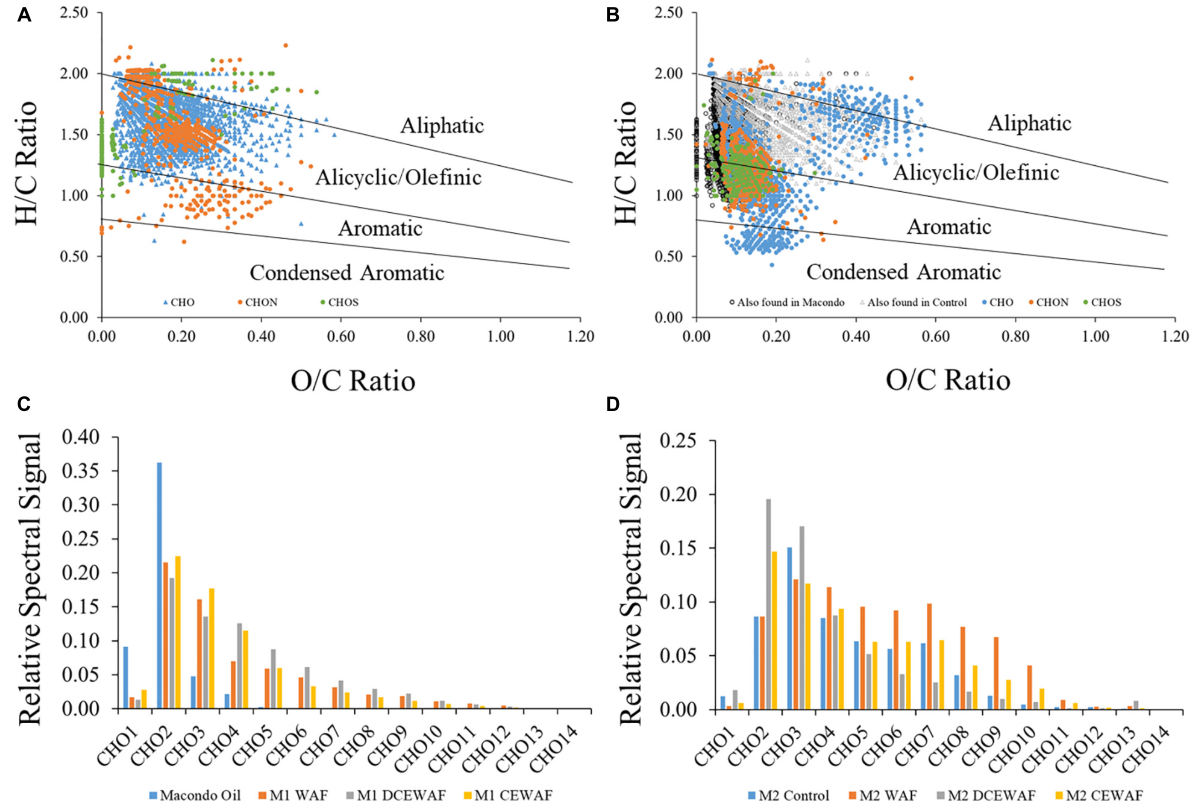

FIGURE 4 | Fourier Transform Ion Cyclotron Resonance Mass Spectrometry (FT-ICR-MS) data for dichloromethane extracts of sinking particles collected from the bottom of tanks in mesocosm treatments displayed as van Krevelen diagrams **(A,B)** for control **(A)** and diluted chemically-enhanced water accommodated fraction (DCEWAF) treatments **(B)**, and as isoabundance plots of oxygen (CHO_{1-14}) **(C,D)** for Macondo oil and Mesocosm 1 water accommodated fraction treatments **(C)** and Mesocosm 2 control and water accommodated treatments **(D)**. DCEWAF formulas also found in Macondo oil and the control treatments are noted as black circles and gray triangles, respectively, in panel **(B)**. Adapted from Wozniak et al. (2019).

volatile, low-molecular weight PAHs such as naphthalene and fluorene (Kappell et al., 2014; Bacosa et al., 2020). Overall, this analysis shows that the marine snow formed in the laboratory experiments such as roller table and mesocosm experiments closely mimicked the material found to be sedimenting in the field, further underscoring the role of MOSSFA phenomena during the DwH oil spill. It also shows that the use of dispersants might not have played a significant role in determining the PAH composition of the MOS.

The changing fingerprints of aliphatic and aromatic hydrocarbons documented preferential loss on *n*-alkanes (Morales-McDevitt et al., 2020) and lower molecular weight PAH (Shi et al., 2020) in mesocosm studies further indicating that biodegradation occurred within the first 24 h. In a recent mesocosm experiment designed to measure the rate of loss of *n*-alkanes over the time period of several days by GC × GC mass spectrometry found that the concentrations of nC_{17} and nC_{18} alkanes in extracts of MOS decreased with half-lives of 0.9 and 1.0 days, respectively. Such a rapid diminution of alkanes is remarkable but indicative of extremely rapid biodegradation of oil that becomes dispersed within the MOS and enhanced by the presence of Corexit that serves to finely disperse the oil within the MOS (Hatcher, pers. comm).

Toward a Synthesis of Processes and Pathways of MOS Formation in Determining the Fate of Hydrocarbons

Predictive numerical models of MOS formation and fate balance processes, such as aggregation, (that produce MOS) and disaggregation (processes that alter and remove MOS, e.g., microbial respiration and sinking) have been attempted. A recent study adapted models of marine snow formation and fate to include oil (Dissanayake et al., 2018). They found that the fraction of oil reaching the seafloor in the model was most sensitive to two factors: the structure of the MOS particles (as measured using the fractal dimension) and the way in which particle stickiness was represented in the model. The values of stickiness of individual components (e.g., oil, phytoplankton, mineral particles, etc.) were held constant, but different ways of combining them to calculate the stickiness of an MOS aggregate were used.

To accurately model these processes requires realistic measures of (i) sinking velocities, (ii) stickiness, (iii) disaggregation kinetics of MOS, and (iv) processes that transform oil. There has been considerable work done over many decades to determine parameterizations of sinking velocities of marine snow (Alldredge and Gotschalk, 1998; Iversen and Lampitt, 2020;

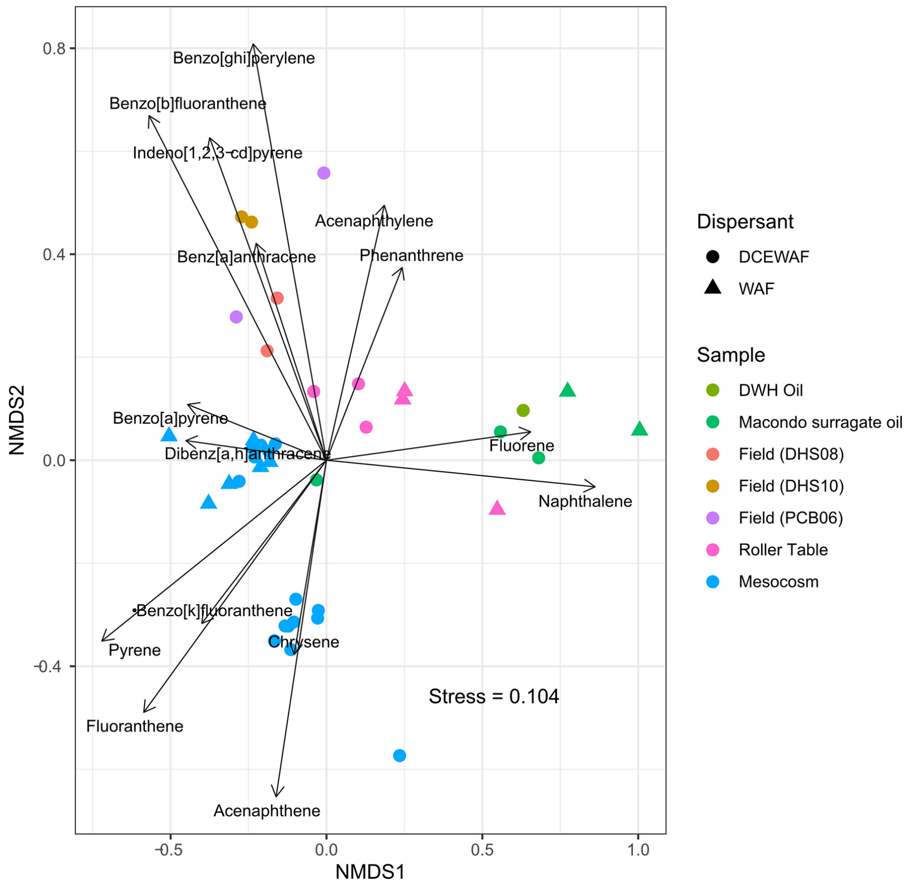

FIGURE 5 | Non-metric multidimensional scaling (NMDS) plot showing clustering of marine snow samples from various mesocosm, roller table studies and field sediment samples from Gulf of Mexico based on PAH composition. Data points clustered to the right are sample from the original Deepwater Horizon (DWH) Macondo oil and the Day 1 sample from surrogate oil used in the laboratory mesocosm and roller table studies, whereas the points clustered largely to the left are marine snow samples from the field and laboratory experiments. Only PAHs such as Naphthalene, Acenaphthylene, Acenaphthene, Fluorene, Phenanthrene, Anthracene, Fluoranthene, Pyrene, Benz[a]anthracene, Chrysene, Benzo[b]fluoranthene, Benzo[k]fluoranthene, Benzo[a]pyrene, Indeno[1,2,3-cd]pyrene, Dibenz[a,h]anthracene, and Benzo[ghi]perylene were used for the analysis, with concentrations of each PAH normalized to percentage of total PAHs in each sample. More details on the PAH extraction, sample collection, field site and design of the roller table and mesocosm studies can be found in Genzer et al. (2020); Bacosa et al. (2020), Romero et al. (2015) and GRIIDC dataset (10.7266/ER1EGZ8E).

Laurenceau-Cornec et al., 2020; and the review by Silver, 2015). In contrast, measurements of stickiness and disaggregation are less ubiquitous (Alldredge et al., 1990; Engel, 2000; De La Rocha and Passow, 2007; Burd and Jackson, 2009).

Accurately modeling the settling velocity of marine snow and MOS is difficult. This is because there appears to be no clear, universal relationship between marine snow characteristics (e.g., size and density, etc.) and settling velocity. For example, recent laboratory experiments have suggested that Stokes' Law modified using the particle fractal dimension provides a good parameterization (Laurenceau-Cornec et al., 2020), but even this parameterization does not account for the considerable scatter in measured settling velocities. Conversely, a recent *in-situ* field study of sinking particles concluded that there is no relationship between marine snow sinking velocity and particle size (Iversen and Lampitt, 2020). Compounding the confusion further, laboratory studies indicate that the incorporation of oil into marine snow can increase settling velocities even though the oil is positively buoyant, and this may be due to a restructuring of the aggregate via capillary bridging (Passow et al., 2019). Current models of MOS formation and fate use modified forms of Stokes' Law to calculate particle settling velocities and take into account the overall density of the aggregate (Dissanayake et al., 2018) producing average settling velocities that are consistent with laboratory observations but do not reproduce the higher velocities seen in those studies.

Marine snow and MOS formation and fragmentation is strongly dependent on particle stickiness (see above). This is defined as the probability that particles adhere once they have collided, varies from 0 to 1, and depends on the chemical and physical nature of the particles. SterlingJr., Bonner et al. (2005) used a particle coagulation model combined with laboratory measurements to determine stickiness between oil and mineral particles, but no corresponding measurements exist for oil and marine snow. Stickiness is thought to be mainly dependent on the composition and concentration of EPS in the water column

(Passow, 2002). This has led to the proposal to use the P/C ratio of EPS as a practical proxy for stickiness (Santschi, 2018; Chen et al., 2020; Santschi et al., 2020). The P/C ratio, and hence stickiness of EPS, varies with the community composition of organisms producing EPS and with the presence of dispersants such as Corexit (Shiu et al., 2020). For example, in mesocosm studies using both Corexit and oil, the P/C ratio of sinking MOS was found to be consistently lower than that of both SPM and colloidal particles. This suggested that Corexit and oil affect the partitioning of different components of EPS (e.g., polysaccharides versus protein) between the water column and sinking material (Xu et al., 2018a,b, 2019; Santschi et al., 2020). Oil-laden aggregates partition more strongly into the colloidal fraction because oil droplets increase the buoyancy of the resulting aggregates, thus temporarily slowing their sinking out of the water. Current models of marine snow and MOS formation use constant stickiness values for different types of particles, but it is not known how the stickiness of a heterogeneous aggregate depends on the stickiness of its components such as oil, mineral particles, and biological detrital material. The recent work by Chen et al. (2020), however, sheds more light and provides a novel magnetic tweezer technique to directly and quantitatively determine the relative stickiness of different EPS fractions to each other or to the solid substrates.

Marine particles can be eroded (small pieces being eroded from the surface of a larger particle), or fragmented (an aggregate breaking up into particles of a range of sizes), potentially affecting their sinking rate and their interactions with organisms in the water column. Adhesive forces between components of a single aggregate contribute to the strength of that aggregate and its ability to resist being broken up. Fragmentation of marine particles can result from turbulent fluid motion (Parker et al., 1972; Alldredge et al., 1990) and mechanical breakage arising from interactions between particles and zooplankton (Dilling and Alldredge, 2000). Indeed, a variety of physical and biological processes (Briggs et al., 2020) can result in particle breakup, including shear stress (Karl et al., 1988; Ruiz, 1997) as well as zooplankton swimming and sloppy feeding (Banse, 1995; Steinberg et al., 1997; Dilling and Alldredge, 2000; Goldtwhait et al., 2004; Giering et al., 2016). However, direct observations of aggregate fragmentation are limited to a few laboratory studies that demonstrate a relation between the particle type/composition and its physical strength under controlled small-scale turbulence (Alldredge et al., 1990; Rau et al., 2018). Conducting a turbulence experiment similar to the one by Alldredge et al. (1990), we found evidence that MOS is physically stronger compared to marine snow (Ziervogel, 2020). The presence of oil in marine snow aggregates will likely affect the particle's cohesiveness (Passow et al., 2019), but this has yet to be quantified.

Existing models of marine snow and MOS fate use ad hoc representations of disaggregation, which can be parameterized for individual scenarios but which lack generality and mechanistic foundations (Burd and Jackson, 2009; Dissanayake et al., 2018). For example, the model used by Dissanayake et al. (2018) allows for particles to fragment when their size is greater than the Kolmogorov length scale and the fragmented particle produces two smaller, equally sized particles. This is an oversimplification because we have very little knowledge of the size distribution of fragmentation products and how the presence of oil and dispersants might affect them. A greater understanding of particle disaggregation and how it is affected by oil is needed in order to constrain the fraction of MOS lost during transit from the point of formation to the point of deposition in sediments, e.g., the fraction that reaches the seafloor, compared to the amount leaving the surface ocean. For example, understanding if the P/C ratio affects the cohesiveness of an aggregate and thereby its resistance to fragmentation would provide a more accurate model representation.

Lastly, as MOS sinks through the water column, it is affected by consumption and remineralization by organisms. Current models use only simple representations of microbial consumption of oil and particles (Dissanayake et al., 2018). To accurately model the fate of MOS will require the use of microbial respiration rates of oil and non-oil components and the corresponding changes in particle density. Models combining the aggregation processes with multiple particle types (e.g., mineral particles, biological particles, and oil) have the potential to synthesize our understanding of the fate of MOS. They also reveal where gaps remain in our understanding. Initial models are able to broadly reproduce evolution of MOS size distributions as material sinks from the surface to the deep ocean, but more work needs to be done to refine these results and be able to follow MOS from when oil is introduced into the system (e.g., from surface spill to deep-sea blow out) to when it settles on the seafloor. Recently developed *in-situ* methods that allow direct observations of the aggregation state of marine particles with respect to the aggregates' physical strength (Ackleson and Rau, 2020) could fill the current data gap on aggregate fragmentation rates in the ocean.

A FEW FINAL WORDS ON AGGREGATE FORMATION

Equation 2 is a mathematical formulation of the conceptual model given in **Figures 1**, **2**. It expresses the idea that it should be possible, based on the current results, to relate the stickiness factor and aggregate formation rate to relevant chemical or biological processes. In this context it needs to be mentioned that EPS concentration, microbial biomass, as well as oil concentration are changing on time scales of hours to days. Thus, an improved formulation of these coupled processes would need to also include the kinetics of each of these processes. In addition, it is not clear which of the possible attachment processes are truly reversible (e.g., disaggregation is only occurring when fluid shear can overcome the binding strength). However, one could safely assume that hydrophobic interactions are less reversible than electrostatic interactions due to their stronger interaction forces (Chen et al., 2020). And, if conditions are favorable, hydrophobic moieties (e.g., in proteins, where they reside in the interior of the macromolecule) can also become exposed (e.g., in case of proteins, upon unfolding) and attach themselves more strongly to other hydrophobic surface moieties, mostly irreversibly, as has been reported recently by Chen et al. (2020). Thus, due to the complexity of the biochemical and biophysical interactions during aggregate formation, the use of a simple predictor of the stickiness or attachment strength of marine snow or MOS, e.g., the P/C ratio, is recommended, with the caveat that aggregate formation can occur in both the colloidal and particulate fractions, depending on their relative buoyancy or excess density.

Overall, this review highlights recent insights into the processes that control interactions between oil, dispersant, microbes, and microbially-produced EPS in producing MOS or dispersed gels that promote microbial degradation of oil compounds. The role of P/C ratios in the aggregation process of colloid and particle formation was also reviewed. We also discuss the factors affecting rapid oil oxidation and microbial degradation, such as indigenous microbes, especially the potential role of microbial succession through time and depth, possible role of nutrient limitation and changes to the physiology and community structure of eukaryotes including phytoplankton and fungi. Other phenomenon such as the processes that result in the sedimentation and preservation/degradation of oil in the sinking MOS are also discussed. This improved understanding has expanded our ability to predict the behavior and transport of released oil, and the potential effects of Corexit application, specifically with respect to MOS (i.e., formation, fate, and half-lives) and MOSSFA processes.

AUTHOR CONTRIBUTIONS

All authors contributed to the ideas and the development of this manuscript, from drafting the outline to the intellectual content. All authors provided approval for the publication of the content.

ACKNOWLEDGMENTS

We thank the editors of this special issue for the invitation to submit a paper. The research presented was made possible by grants from the Gulf of Mexico Research Initiative: Quigg, Santschi, Xu, Ziervogel, Kamalanathan, Chin, Wozniak, and Hatcher: Aggregation and Degradation of Dispersants and Oil by Microbial Exopolymers (ADDOMEx SA15-22 and SA18-13) and Burd: Oil-Marine Snow-Mineral Aggregate Interactions and Sedimentation during the 2010 Deepwater Horizon Oil-Spill. This review was made possible by the dedication of the entire ADDOMEx team (2015–2020), particular co-PI's Terry Wade, Tony Knap, Jason Sylvan, Zoe Finkel, and Andrew Irwin. We also wish to remember our dear friend and colleague, David Hollander, who we lost unexpectedly in 2020. We will always remember his scientific endeavors that aggregated us together over many a conversation, in recent years, around especially the topic of MOSSFA. His insights, humor and good will be missed. We also thank the reviewers whose suggestion's helped improve the final manuscript.

REFERENCES

Ackleson, S. G., and Rau, M. J. (2020). A method to measure marine particle aggregate disruption in situ. *Limnol. Oceanogr. Methods* 18, 644–655.

Aeppli, C., Carmichael, C. A., Nelson, R. K., Lemkau, K. L., Graham, W. M., Remond, M. C., et al. (2012). Oil weathering after the Deepwater Horizon disaster led to the formation of oxygenated residues. *Environ. Sci. Technol.* 46, 8799–8807. doi: 10.1021/es3015138

Alldredge, A. L., and Gotschalk, C. (1998). In situ settling behavior of marine snow. *Limnol. Oceanogr.* 33, 339–351. doi: 10.4319/lo.1988.33.3.0339

Alldredge, A. L., Granata, T. C., Gotschalk, C. C., and Dickey, T. D. (1990). The physical strength of marine snow and its implications for particle aggregation in the ocean. *Liminol. Oceanogr.* 35, 1415–1428. doi: 10.4319/lo.1990.35.7.1415

Alldredge, A. L., Passow, U., and Logan, B. E. (1993). The abundance and significance of a class of large, transparent organic particles in the ocean. *Deep Sea Res.* 40, 1131–1140. doi: 10.1016/0967-0637(93)90129-Q

Almeda, R., Connelly, T. L., and Buskey, E. J. (2014). Novel insight into the role of heterotrophic dinoflagellates in the fate of crude oil in the sea. *Nat. Sci. Rep.* 4:7560. doi: 10.1038/srep07560

Almeda, R., Cosgrove, S., and Buskey, E. J. (2018). Oil spills and dispersants can cause the initiation of potentially harmful dinoflagellate blooms ("Red Tides"). *Environ. Sci. Technol.* 52, 5718–5724. doi: 10.1021/acs.est.8b00335

Al-Nasrawi, H. (2012). Biodegradation of crude oil by fungi isolated from Gulf of Mexico. *J. Bioremed. Biodegrad.* 3, 1–6. doi: 10.4172/2155-6199.1000147

Arnosti, C., Ziervogel, K., Yang, T., and Teske, A. (2015). Oil-derived marine aggregates – hot spots of polysaccharide degradation by specialized bacterial communities. *Deep Sea Res. II* 129, 179–186. doi: 10.1016/j.dsr2.2014.12.008

Asemoloye, M. D., Ahmad, R., and Jonathan, S. G. (2018). Transcriptomic responses of catalase, peroxidase and laccase encoding genes and enzymatic activities of oil spill inhabiting rhizospheric fungal strains. *Environ. Poll.* 235, 55–64. doi: 10.1016/j.envpol.2017.12.042

Azam, F. (1998). Microbial control of oceanic carbon flux: the plot thickens. *Science* 280, 694–696. doi: 10.1126/science.280.5364.694

Bacosa, H. P., Kamalanathan, M., Chiu, M. H., Tsai, S. M., Sun, L., Labonté, J. M., et al. (2018). Extracellular polymeric substances (EPS) producing and oil degrading bacteria isolated from the northern Gulf of Mexico. *PLoS One* 13:e0208406. doi: 10.1371/journal.pone.0208406

Bacosa, H. P., Kamalanathan, M., Cullen, J., Shi, D., Xu, C., Schwehr, K. A., et al. (2020). Marine snow aggregates are enriched in polycyclic aromatic hydrocarbons (PAHs) in oil contaminated waters; insights from a mesocosm study. *J. Mar. Sci. Eng.* 8:781. doi: 10.3390/jmse8100781

Baelum, J., Borglin, S., Chakraborty, R., Fortney, J. L., Lamendella, R., Mason, O. U., et al. (2012). Deep–sea bacteria enriched by oil and dispersant from the Deepwater Horizon spill. *Environ. Microbiol.* 14, 2405–2416. doi: 10.1111/j.1462-2920.2012.02780.x

Baldock, J. A., Masiello, C. A., Gelinas, Y., and Hedges, J. I. (2004). Cycling and composition of organic matter in terrestrial and marine ecosystems. *Mar. Chem.* 92, 39–64. doi: 10.1016/j.marchem.2004.06.016

Banse, K. (1995). Zooplankton—pivotal role in the control of ocean production. *ICES J. Mar. Sci.* 52, 265–277. doi: 10.1016/1054-3139(95)80043-3

Bar-Zeev, E., Berman, T., Rahav, E., Dishon, G., Herut, B., Kress, N., et al. (2011). Transparent exopolymer particle (TEP) dynamics in the eastern Mediterranean Sea. *Mar. Ecol. Progr. Ser.* 431, 107–118. doi: 10.3354/meps09110

Bar-Zeev, E., Passow, U., Romero-Vargas Castrill, S., and Elimelech, M. (2015). Transparent exopolymer particles (TEP): From aquatic environments and engineered systems to membrane biofouling. *Environ. Sci. Technol.* 49, 691–707. doi: 10.1021/es5041738

Beyer, J., Trannum, H. C., Bakke, T., Hodson, P. V., and Collier, T. K. (2016). Environmental effects of the Deepwater Horizon oil spill: a review. *Mar. Poll. Bull.* 110, 28–51.

Bik, H. M., Halanych, K. M., Sharma, J., and Thomas, W. K. (2012). Dramatic shifts in benthic microbial eukaryote communities following the Deepwater Horizon oil spill. *PLoS One* 7:e38550. doi: 10.1371/journal.pone.0038550

Bochdansky, A. B., Clouse, M. A., and Herndl, G. J. (2017). Eukaryotic microbes, principally fungi and labyrinthulomycetes, dominate biomass on bathypelagic marine snow. *ISME J.* 11, 362–373. doi: 10.1038/ismej.2016.113

Boehm, P. D., and Fiest, D. L. (1980). "Aspects of the transport of petroleum hydrocarbons to the offshore benthos during the Ixtoc-I blowout in the Bay of Campeche," in *Proceedings of the Symposium on the Preliminary Results from the September, 1979 Pierce/Research IXTOC-1Cruises*, (Boulder, CO: NOAA).

Bretherton, L., Hillhouse, J., Bacosa, H., Setta, S., Genzer, J., Kamalanathan, M., et al. (2019). Growth dynamics and domoic acid production of Pseudo-nitzschia sp. in response to oil and dispersant exposure. *Harmful Algae* 86, 55–63. doi: 10.1016/j.hal.2019.05.008

Bretherton, L., Hillhouse, J., Kamalanathan, M., Finkel, Z. V., Irwin, A. J., and Quigg, A. (2020). Trait-dependent variability of the response of marine phytoplankton to oil and dispersant exposure. *Mar. Poll. Bull.* 153:110906. doi: 10.1016/j.marpolbul.2020.110906

Bretherton, L., Williams, A., Genzer, J., Hillhouse, J., Kamalanathan, M., Finkel, Z. V., et al. (2018). Physiological response of 10 phytoplankton species exposed to Macondo oil and the dispersant. *Corexit. J. Phycol.* 54, 317–328. doi: 10.1111/jpy.12625

Briggs, N., Dall'Olmo, G., and Claustre, H. (2020). Major role of particle fragmentation in regulating biological sequestration of CO2 by the oceans. *Science* 367, 791–793. doi: 10.1126/science.aay1790

Burd, A., Chanton, J. P., Daly, K. L., Gilbert, S., Passow, U., and Quigg, A. (2020). The science behind marine-oil snow and MOSSFA: past, present, and future. *Prog. Oceanogr.* 187:102398. doi: 10.1016/j.pocean.2020.102398

Burd, A. B., and Jackson, G. A. (2009). Particle aggregation. *Ann. Rev. Mar. Sci.* 1, 65–90. doi: 10.1146/annurev.marine.010908.163904

Chanton, J., Zhao, T., Rosenheim, B. E., Joye, S., Bosman, S., Brunner, C., et al. (2015). Using natural abundance radiocarbon to trace the flux of petrocarbon to the seafloor following the Deepwater Horizon oil spill. *Environ. Sci. Technol.* 49, 847–854. doi: 10.1021/es5046524

Chen, C.-S., Shiu, R.-F., Hsieh, Y.-Y., Xu, C., Vazquez, C. I., Cui, Y., et al. (2020). Stickiness of extracellular polymeric substances on different surfaces via magnetic tweezers. *Sci. Total Environ.* 757:143766. doi: 10.1016/j.scitotenv.2020.143766

Chen, F., and Yapa, P. D. (2007). Estimating the oil droplet size distributions in deep-water oil spills. *J. Hydraulic Eng.* 133, 197–207. doi: 10.1061/(asce)0733-9429(2007)133:2(197)

Chen, H., Hou, A., Corilo, Y. E., Lin, Q., Lu, J., Mendelssohn, I. A., et al. (2016). 4 Years after the Deepwater Horizon spill: Molecular transformation of Macondo well oil in Louisiana salt marsh sediments revealed by FT-ICR mass spectrometry. *Environ. Sci. Technol.* 50, 9061–9069. doi: 10.1021/acs.est.6b01156

Chin, W.-C., Orellana, M. V., and Verdugo, P. (1998). Spontaneous assembly of marine dissolved organic matter into polymer gels. *Nature* 391, 568–572. doi: 10.1038/35345

Chiu, M.-H., Garcia, S. G., Hwang, B., Claiche, D., Sanchez, G., Aldayafleh, R., et al. (2017). Corexit, oil and marine microgels. *Mar. Poll. Bull.* 122, 376–378. doi: 10.1016/j.marpolbul.2017.06.077

Daly, K. L., Passow, U., Chanton, J., and Hollander, D. (2016). Assessing the impacts of oil-associated marine snow formation and sedimentation during and after the Deepwater Horizon oil spill. *Anthropocene* 13, 18–33. doi: 10.1016/j.ancene.2016.01.006

Daly, K. L., Vaz, A. C., and Paris, C. B. (2020). "Physical processes influencing the sedimentation and lateral transport of MOSSFA in the NE Gulf of Mexico," in *Scenarios and Responses to Future Deep Oil Spills*, ed. S. Murawski (Cham: Springer), 300–314. doi: 10.1007/978-3-030-12963-7_18

Davies, J. S., and Westlake, D. W. S. (1979). Crude oil utilization by fungi. *Canadian J. Microbiol.* 25, 146–156. doi: 10.1139/m79-023

De La Rocha, C., and Passow, U. (2007). Factors influencing the sinking of POC and the efficiency of the biological carbon pump. *Deep Sea Res. II* 54, 639–658. doi: 10.1016/j.dsr2.2007.01.004

Decho, A. W., and Gutierrez, T. (2017). Microbial extracellular polymeric substances (EPSs) in ocean systems. *Front. Microbiol.* 8:922. doi: 10.3389/fmicb.2017.00922

Decho, A. W., and Herndl, G. J. (1995). Microbial activities and the transformation of organic matter within mucilaginous material. *Sci. Total Environ.* 165, 33–42. doi: 10.1016/0048-9697(95)04541-8

Dilling, L., and Alldredge, A. L. (2000). Fragmentation of marine snow by swimming macrozoolankton: a new process impacting carbon cycling in the sea. *Deep-Sea Res. I* 47, 1227–1245. doi: 10.1016/s0967-0637(99)00105-3

Ding, Y.-X., Chin, W.-C., Rodriguez, A., Hung, C.-C., Santschi, P. H., and Verdugo, P. (2008). Amphiphilic exopolymers from *Sagittula stellata* induce DOM self-assembly and formation of marine microgels. *Mar. Chem.* 112, 11–19. doi: 10.1016/j.marchem.2008.05.003

Dissanayake, A. L., Burd, A. B., Daly, K. L., Francis, S., and Passow, U. (2018). Numerical modeling of the interactions of oil, marine snow, and riverine sediments in the ocean. *J. Geophys. Res. Oceans* 123:JC013790.

Dombrowski, N., Donaho, J. A., Gutierrez, T., Seitz, K. W., Teske, A. P., and Baker, B. J. (2016). Reconstructing metabolic pathways of hydrocarbon degrading bacteria from the Deepwater Horizon oil spill. *Nat. Microbiol.* 1:16057. doi: 10.1038/nmicrobiol.2016.57

Doyle, S. M., Lin, G., Morales-McDevitt, M., Wade, T. L., Quigg, A., and Sylvan, J. B. (2020). Niche partitioning between coastal and offshore shelf waters results in differential expression of alkane and PAH catabolic pathways. *mSystems* 5, e668–e620. doi: 10.1128/mSystems.00668-20

Doyle, S. M., Whitaker, E. A., De Pascuale, V., Wade, T. L., Knap, A. H., Santschi, P. H., et al. (2018). Rapid formation of microbe-oil aggregates and changes in community composition in coastal surface water following exposure to oil and corexit. *Front. Microbiol.* 9:689. doi: 10.3389/fmicb.2018.00689

Edwards, B. R., Reddy, C. M., Camilli, R., Carmichael, C. A., Longnecker, K., and Van Mooy, B. A. (2011). Rapid microbial respiration of oil from the Deepwater Horizon spill in offshore surface waters of the Gulf of Mexico. *Environ. Res. Lett.* 6:035301. doi: 10.1088/1748-9326/6/3/035301

Engel, A. (2000). The role of transparent exopolymer particles (TEP) in the increase in apparent particle stickiness (a) during the decline of a diatom bloom. *J. Plankton Res.* 22, 485–497. doi: 10.1093/plank/22.3.485

Finkel, Z. V., Liang, Y., Nanjappa, D., Bretherton, L., Brown, C. M., Quigg, A., et al. (2020). A ribosomal sequence-based oil sensitivity index for phytoplankton groups. *Mar. Poll. Bull.* 151:110798. doi: 10.1016/j.marpolbul.2019.110798

Gärdes, A., Iversen, M. H., Grossart, H.-P., and Passow, U. (2011). Diatom associated bacteria are required for aggregation of *Thalassiosira weissflogii*. *ISME J.* 5, 436–445. doi: 10.1038/ismej.2010.145

Gearing, J. N., Gearing, P. J., Wade, T., Quinn, J. G., McCarty, H. B., Farrington, J., et al. (1979). "The rates of transport and fates of petroleum hydrocarbons in a controlled marine ecosystem and a note on analytical variability," in *Proceedings of the 1979 Oil Spill Conference*, (Washington, D.C: American Petroleum Institute), 555–564. doi: 10.7901/2169-3358-1979-1-555

Genzer, J. L., Kamalanathan, M., Bretherton, L., Hillhouse, J., Xu, C., Santschi, P. H., et al. (2020). Diatom aggregation when exposed to crude oil and chemical dispersants: potential impacts of ocean acidification. *PLoS One* 15:e0235473. doi: 10.1371/journal.pone.0235473

Giering, S. L. C., Sanders, R., Martin, A. P., Lindemann, C., Möller, K. O., Daniels, C. J., et al. (2016). High export via small particles before the onset of the North Atlantic spring bloom. *J. Geophys. Res. Oceans* 121, 6929–6945. doi: 10.1002/2016JC012048

Goldtwhait, S. A., Carlson, C. A., Henderson, G. K., and Alldredge, A. K. (2004). Effects of physical fragmentation on remineralization of marine snow. *Mar. Ecol. Prog. Ser.* 305, 59–65. doi: 10.3354/meps305059

Gong, Y., Zhao, X., Cai, Z., O'Reilly, S. E., Hao, X., and Zhao, D. (2014). A review of oil, dispersed oil and sediment interactions in the aquatic environment: Influence on the fate, transport and remediation of oil spills. *Mar. Poll. Bull.* 79, 16–33. doi: 10.1016/j.marpolbul.2013.12.024

Gregson, B. H., McKew, B. A., Holland, R. D., Nedwed, T. J., Princ, E. R. C., and McGenity, T. J. (2021). Marine oil snow, a microbial perspective. *Front. Mar. Sci.* 8:619484. doi: 10.3389/fmars.2021.619484

Gutierrez, T., Berry, D., Teske, A., and Aitken, M. D. (2016). Enrichment of Fusobacteria in sea surface oil slicks from the Deepwater Horizon oil spill. *Microorganisms* 4:24. doi: 10.3390/microorganisms4030024

Gutierrez, T., Berry, D., Yang, T., Mishamandani, S., McKay, L., Teske, A., et al. (2013a). Role of bacterial exopolysaccharides (EPS) in the fate of the oil released during the Deepwater Horizon oil spill. *PLoS One* 8:e67717. doi: 10.1371/journal.pone.0067717

Gutierrez, T., Singleton, D. R., Berry, D., Yang, T., Aitken, M. D., and Teske, A. (2013b). Hydrocarbon-degrading bacteria enriched by the Deepwater Horizon oil spill identified by cultivation and DNA-SIP. *ISME J.* 7, 2091–2104.

Hamdan, L., and Fulmer, P. (2011). Effects of COREXIT® EC9500A on bacteria from a beach oiled by the Deepwater Horizon spill. *Aquat. Microb. Ecol.* 63, 101–109. doi: 10.3354/ame01482

Hatcher, P. G., Obeid, W., Wozniak, A. S., Xu, C., Zhang, S., Santschi, P. H., et al. (2018). Identifying oil/marine snow associations in mesocosm simulations of the Deepwater Horizon Oil Spill event using solid-state 13C NMR spectroscopy and ion cyclotron resonance mass spectrometry. *Mar. Pollut. Bull.* 126, 159–165. doi: 10.1016/j.marpolbul.2017.11.004

Hazen, T. C., Dubinsky, E. A., DeSantis, T. Z., Andersen, G. L., Piceno, Y. M., Singh, N., et al. (2010). Deep-sea oil plume enriches indigenous oil-degrading bacteria. *Science* 330, 204–208. doi: 10.1126/science.1195979

Head, I. M., Jones, D. M., and Röling, W. F. M. (2006). Marine microorganisms make a meal of oil. *Nat. Rev. Microbiol.* 4, 173–182. doi: 10.1038/nrmicro1348

Hedges, J. I., Cowie, G. L., Ertel, J. R., Barbour, R. J., and Hatcher, P. G. (1985). Degradation of carbohydrates and lignins in buried woods. *Geochim. Cosmochim. Acta* 49, 701–711. doi: 10.1016/0016-7037(85)90165-6

Henry, I. A., Netzer, R., Davies, E., and Brakstad, O. G. (2020). The influences of phytoplankton species, mineral particles and concentrations of dispersed oil on the formation and fate of marine oil-related aggregates. *Sci. Total Environ.* 752, 141786. doi: 10.1016/j.scitotenv.2020.141786

Hoagland, K. D., Rosowsky, J. R., Gretz, M. R., and Reomer, S. C. (1993). Diatom extracellular polymeric substances: function, fine structure, chemistry, chemistry and physiology. *J. Phycol.* 29, 537–556. doi: 10.1111/j.0022-3646.1993.00537.x

Honeyman, B. D., and Santschi, P. H. (1989). A Brownian-pumping model for trace metal scavenging: evidence from Th isotopes. *J. Mar. Res.* 47, 950–995.

Honeyman, B. D., and Santschi, P. H. (1991). Coupling of trace metal adsorption and particle aggregation: kinetic and equilibrium studies using 59Fe-labeled hematite. *Environ. Sci. Technol.* 25, 1739–1747. doi: 10.1021/es00022a010

Hung, C.-C., Guo, L., Schultz, G., Pinckney, J. L., and Santschi, P. H. (2003). Production and fluxes of carbohydrate species in the Gulf of Mexico. *Global Biogeochem. Cycles* 17:1055. doi: 10.1029/2002GB001988

Iversen, M. H., and Lampitt, R. S. (2020). Size does not matter after all: No evidence for a size-sinking relationship for marine snow. *Prog. Oceanogr.* 189:102445. doi: 10.1016/j.pocean.2020.102445

Jacketti, M., Beegle-Krause, C. J., and Englehardt, J. D. (2020). A review on the sinking mechanisms for oil and successful response technologies. *Mar. Poll. Bull.* 160:111626. doi: 10.1016/j.marpolbul.2020.111626

Jernelöv, A., and Lindén, O. (1981). Ixtoc I: a case study of the world's largest oil spill. *AMBIO* 10, 299–306.

John, V., Arnosti, C., Field, J., Kujawinski, E., and McCormick, A. (2016). The role of dispersants in oil spill remediation: fundamental concepts, rationale for use, fate, and transport issues. *Oceanography* 29, 108–117. doi: 10.5670/oceanog.2016.75

Johnson, R. L., and Schmidt-Rohr, K. (2014). Quantitative solid-state 13C NMR with signal enhancement by multiple cross polarization. *J. Magnetic Resonance* 239, 44–49. doi: 10.1016/j.jmr.2013.11.009

Kamalanathan, M., Chiu, M.-H., Bacosa, H., Schwehr, K., Tsai, S.-M., Doyle, S., et al. (2019). Role of polysaccharides in diatom *Thalassiosira pseudonana* and its associated bacteria in hydrocarbon presence. *Plant Physiol.* 180, 1898–1911. doi: 10.1104/pp.19.00301.pp.00301.2019

Kamalanathan, M., Doyle, S. M., Xu, C., Achberger, A. M., Wade, T. L., Schwehr, K., et al. (2020). Exoenzymes as a signature of microbial response to marine environmental conditions. *mSystems* 5, e00290–20. doi: 10.1128/mSystems.00290-20

Kamalanathan, M., Schwehr, K., Labonté, J., Taylor, C., Bergen, C., Patterson, N., et al. (2021). "The interplay of phototrophic and heterotrophic microbes under oil exposure-a microcosm study," in *Frontiers in Microbiology-Aquatic Microbiology*, eds M. Kamalanathan, K. Schwehr, J. Labonté, C. Taylor, C. Bergen, N. Patterson, et al.

Kamalanathan, M., Xu, C., Schwehr, K., Bretherton, L., Beaver, M., Doyle, S. M., et al. (2018). Extracellular enzyme activity profile in a chemically enhanced water accommodated fraction of surrogate oil: toward understanding microbial activities after the Deepwater Horizon oil spill. *Front. Microbiol.* 9:798. doi: 10.3389/fmicb.2018.00798

Kappell, A. D., Wei, Y., Newton, R. J., Van Nostrand, J. D., Zhou, J., McLellan, S. L., et al. (2014). The polycyclic aromatic hydrocarbon degradation potential of Gulf of Mexico native coastal microbial communities after the Deepwater Horizon oil spill. *Front. Microbiol.* 5:205.

Karl, D. M., Knauer, G. A., and Martin, J. H. (1988). Downward flux of particulate organic matter in the ocean: a particle decomposition paradox. *Nature* 332, 438–441. doi: 10.1038/332438a0

Kessler, J. D., Valentine, D. L., Redmond, M. C., Du, M., Chan, E. W., Mendes, S. D., et al. (2011). A persistent oxygen anomaly reveals the fate of spilled methane in the deep Gulf of Mexico. *Science* 331, 312–315. doi: 10.1126/science.1199697

Khelifa, A., and Hill, P. S. (2006). Models for effective density and settling velocity of flocs. *J. Hydraulic Res.* 44, 390–401. doi: 10.1080/00221686.2006.9521690

Kimes, N. E., Callaghan, A. V., Aktas, D. F., Smith, W. L., Sunner, J., Golding, B. T., et al. (2013). Genomic analysis and metabolite profiling of deep-sea sediments from the Gulf of Mexico following the Deepwater Horizon oil spill. *Front. Microbiol.* 4:50. doi: 10.3389/fmicb.2013.00050

Kimes, N. E., Callaghan, A. V., Suflita, J. M., and Morris, P. J. (2014). Microbial transformation of the Deepwater Horizon oil spill—past, present, and future perspectives. *Front. Microbiol.* 5:603.

Kiørboe, T., Andersen, K. P., and Dam, H. G. (1990). Coagulation efficiency and aggregate formation in marine phyto–plankton. *Mar. Biol.* 107, 235–245. doi: 10.1007/bf01319822

Kleindienst, S., Grim, S., Sogin, M., Bracco, A., Crespo-Medina, M., and Joye, S. B. (2016). Diverse, rare microbial taxa responded to the Deepwater Horizon deep-sea hydrocarbon plume. *ISME J.* 10, 400–415. doi: 10.1038/ismej.2015.121

Kleindienst, S., Seidel, M., Ziervogel, K., Grim, S., Loftis, K., Harrison, S., et al. (2015). Chemical dispersants can suppress the activity of natural oil-degrading microorganisms. *Proc. Natl. Acad. Sci. U.S.A.* 112, 14900–14905. doi: 10.1073/pnas.1507380112

Kowalewska, G. (1999). Phytoplankton-the main factor responsible for transport of polynuclear aromatic hydrocarbons from water to sediments in the Southern Baltic ecosystem. *ICES J. Mar. Sci.* 56, 219–222. doi: 10.1006/jmsc.1999.0607

Kowalewska, G., and Konat, J. (1997). The role of phytoplankton in the transport and distribution of polynuclear aromatic hydrocarbons (PAHs) in the southern Baltic environment. *Oceanologia* 39:267.

Kujawinski, E. B., Reddy, C. M., Rodgers, R. P., Thrash, J. C., Valentine, D. L., and White, H. K. (2020). The first decade of scientific insights from the Deepwater Horizon oil release. *Nat. Rev. Earth Environ.* 1, 237–250. doi: 10.1038/s43017-020-0046-x

Laurenceau-Cornec, E. C., Le Moigne, F. A. C., Gallinari, M., Moriceau, B., Toullec, J., Iversen, M. H., et al. (2020). New guidelines for the application of Stokes' models to the sinking velocity of marine aggregates. *Limnol. Oceanogr.* 65, 1264–1285. doi: 10.1002/lno.11388

Liu, A., Ahn, I. S., Mansfield, C., Lion, L. W., Shuler, M. L., and Ghiorse, W. C. (2001). Phenanthrene desorption from soil in the presence of bacterial extracellular polymer: Observations and model predictions of dynamic behavior. *Water Res.* 35, 835–843. doi: 10.1016/s0043-1354(00)00324-9

Lu, Z., Deng, Y., Van Nostrand, J. D., He, Z., Voordeckers, J., Zhou, A., et al. (2012). Microbial gene functions enriched in the Deepwater Horizon deep-sea oil plume. *ISME J.* 6, 451–460. doi: 10.1038/ismej.2011.91

Lumibao, C. Y., Formel, S., Elango, V., Pardue, J. H., Blum, M., and Van Bael, S. A. (2018). Persisting responses of salt marsh fungal communities to the Deepwater Horizon oil spill. *Sci. Total Environ.* 642, 904–913. doi: 10.1016/j.scitotenv.2018.06.077

Mason, O. U., Hazen, T. C., Borglin, S., Chain, P. S., Dubinsky, E. A., Fortney, J. L., et al. (2012). Metagenome, meta-transcriptome and single-cell sequencing reveal microbial response to Deepwater Horizon oil spill. *ISME J.* 6, 1715–1727. doi: 10.1038/ismej.2012.59

Mason, O. U., Scott, N. M., Gonzalez, A., Robbins-Pianka, A., Bælum, J., Kimbrel, J., et al. (2014). Metagenomics reveals sediment microbial community response to Deepwater Horizon oil spill. *ISME J.* 8, 1464–1475. doi: 10.1038/ismej.2013.254

McGenity, T., Folwell, B., McKew, B., and Sanni, G. (2012). Marine crude-oil biodegradation: a central role for interspecies interactions. *Aquat Biosyst.* 8:10. doi: 10.1186/2046-9063-8-10

McKew, B. A., Coulon, F., Osborn, A. M., Timmis, K. N., and McGenity, T. J. (2007). Determining the identity and roles of oil-metabolizing marine bacteria from the Thames estuary. *UK. Environ. Microbiol.* 9, 165–176. doi: 10.1111/j.1462-2920.2006.01125.x

Meng, L., Liu, H., Bao, M., and Sun, P. (2016). Microbial community structure shifts are associated with temperature, dispersants and nutrients in crude oil-contaminated seawaters. *Mar. Poll. Bull.* 111, 203–212. doi: 10.1016/j.marpolbul.2016.07.010

Mishamandani, S., Gutierrez, T., Berry, D., and Aitken, M. D. (2016). Response of the bacterial community associated with a cosmopolitan marine diatom to crude oil shows a preference for the biodegradation of aromatic hydrocarbons. *Environ. Micro.* 18, 1817–1833. doi: 10.1111/1462-2920.12988

Morales-McDevitt, M. E., Shi, D., Knap, A. H., Quigg, A., Sweet, S. T., Sericano, J. L., et al. (2020). Mesocosm experiments to better understand hydrocarbon half-lives for oil and oil dispersant mixtures. *PLoS One* 15:e0228554. doi: 10.1371/journal.pone.0228554

Nagasaki, K., Tomaru, Y., Katanozaka, N., Shirai, Y., Nishida, K., Itakura, S., et al. (2004). Isolation and characterization of a novel single-stranded RNA virus infecting the bloom-forming diatom Rhizosolenia. *Appl. Environ. Microbiol.* 70, 704–711. doi: 10.1128/aem.70.2.704-711.2004

Ortega-Retuerta, E., Passow, U., Duarte, C. M., and Reche, I. (2009). Effects of ultraviolet B radiation on (not so) transparent exopolymer particles. *Biogeosciences* 6, 3071–3080. doi: 10.5194/bg-6-3071-2009

Ozhan, K., Zahraeifard, S., Smith, A. P., and Bargu, S. (2015). Induction of reactive oxygen species in marine phytoplankton under crude oil exposure. *Environ. Sci. Pollut. Res.* 22, 18874–18884. doi: 10.1007/s11356-015-5037-y

Parker, D. S., Kaufman, W. J., and Jenkins, D. (1972). Floc breakup in turbulent flocculation processes. *J. Sanit. Eng. Div. Am. Soc. Civ. Eng.* 98, 79–99. doi: 10.1061/jsedai.0001389

Parsons, M. L., Morrison, W., Rabalais, N. N., Turner, R. E., and Tyre, K. N. (2015). Phytoplankton and the Macondo oil spill: a comparison of the 2010 phytoplankton assemblage to baseline conditions on the Louisiana shelf. *Environ. Pollut.* 207, 152–160. doi: 10.1016/j.envpol.2015.09.019

Passow, U. (1995). A dye-binding assay for the spectrophotometric measurement of transparent exopolymer particles (TEP). *Limnol. Oceanogr.* 40, 1326–1335. doi: 10.4319/lo.1995.40.7.1326

Passow, U. (2002). Transparent exopolymer particles (TEP) in aquatic environments. *Progr. Oceanogr.* 55, 287–333. doi: 10.1016/S0079-6611(02)138-136

Passow, U. (2016). Formation of rapidly-sinking, oil-associated marine snow. *Deep Sea Res. II Top. Stud. Oceanogr.* 129, 232–240. doi: 10.1016/j.dsr2.2014.10.001

Passow, U., and Overton, E. B. (2021). The complexity of spills: the fate of the Deepwater Horizon Oil. *Ann. Rev. Mar. Sci.* 13:1. doi: 10.1146/annurev-marine-032320-095153

Passow, U., Sweet, J., Francis, S., Xu, C., Dissanayake, A. L., Lin, Y.-Y., et al. (2019). Incorporation of oil into diatom aggregates. *Mar. Ecol. Prog. Ser.* 612, 65–86. doi: 10.3354/meps12881

Passow, U., Sweet, J., and Quigg, A. (2017). How Corexit Impacts the formation of sinking marine oil snow. *Mar. Pollut. Bull.* 125, 139–145. doi: 10.1016/j.marpolbul.2017.08.015

Passow, U., Ziervogel, K., Asper, V., and Diercks, A. (2012). Marine snow formation in the aftermath of the Deepwater Horizon oil spill in the Gulf of Mexico. *Environ. Res. Lett.* 7, 1–11. doi: 10.1088/1748-9326/7/3/035301

Paul, J. H., Hollander, D., Coble, P., Daly, K. L., Murasko, S., English, D., et al. (2013). Toxicity and Mutagenicity of Gulf of Mexico Waters during and After the Deepwater Horizon Oil Spill. *Environ. Sci. Technol.* 47, 9651–9659. doi: 10.1021/es401761h

Prince, R. C., Gramain, A., and McGenity, T. J. (2010). "Prokaryotic hydrocarbon degraders," in *Handbook of Hydrocarbon and Lipid Microbiology*, ed. K. N. Timmis (Berlin: Springer), 1669–1692. doi: 10.1007/978-3-540-77587-4_118

Quigg, A., Chin, W.-C., Chen, C.-S., Zhang, S., Jiang, Y., Miao, A.-J., et al. (2013). Direct and indirect toxic effects of engineered nanoparticles on algae: role of natural organic matter. *Special Issue Sustain. Nanotechnol. ACS Sustain. Chem. Eng.* 1, 686–702. doi: 10.1021/sc400103x

Quigg, A., Farrington, J. W., Glibert, S., Murawski, S. A., and John, V. (2021a). A decade of GoMRI dispersant science: lessons learned and recommendations for the future. *Accepted Oceanogr.* 34, 98–111. doi: 10.5670/oceanog.2021.119

Quigg, A., Parsons, M., Bargu, S., Ozhan, K., Daly, K., Chakraborty, S., et al. (2021b). Marine phytoplankton responses to oil and dispersant exposures: Knowledge gained since the Deepwater Horizon Oil Spill. *Mar. Poll. Bull.* 164:112074. doi: 10.1016/j.marpolbul.2021.112074

Quigg, A., Passow, U., Chin, W. C., Xu, C., Doyle, S., Bretherton, L., et al. (2016). The role of microbial exopolymers in determining the fate of oil and chemical dispersants in the ocean. *Limnol. Oceanogr. Lett.* 1, 3–26. doi: 10.1002/lol2.10030

Quigg, A., Passow, U., Daly, K. L., Burd, A., Hollander, D. J., Schwing, P. T., et al. (2020). "Chapter 12: Marine Oil Snow Sedimentation and Flocculent Accumulation (MOSSFA) events: learning from the past to predict the future," in *Deep Oil Spills – Facts, Fate and Effects. Springer 608 pp. ISBN 978-3-030-11605-7*, eds S. A. Murawski, C. Ainsworth, S. Gilbert, D. Hollander, C. B. Paris, M. Schlüter, et al. (Berlin: Springer), 199–224. doi: 10.1007/978-3-030-11605-7

Rau, M. J., Ackleson, S. G., and Smith, G. B. (2018). Effects of turbulent aggregation on clay floc breakup and implications for the oceanic environment. *PLoS One* 13:e0207809. doi: 10.1371/journal.pone.0207809

Redmond, M. C., and Valentine, D. L. (2012). Natural gas and temperature structured a microbial community response to the Deepwater Horizon oil spill. *Proc. Natl. Acad. Sci. U.S.A.* 109, 20292–20297. doi: 10.1073/pnas.1108756108

Rivers, A. R., Sharma, S., Tringe, S. G., Martin, J., Joye, S. B., and Moran, M. A. (2013). Transcriptional response of bathypelagic marine bacterioplankton to the Deepwater Horizon oil spill. *ISME J.* 7, 2315–2329. doi: 10.1038/ismej.2013.129

Romero, I. C., Schwing, P. T., Brooks, G. R., Larson, R. A., Hastings, D. W., Ellis, G., et al. (2015). Hydrocarbons in deep-sea sediments following the 2010 Deepwater Horizon blowout in the northeast Gulf of Mexico. *PLoS One* 10:e0128371. doi: 10.1371/journal.pone.0128371

Ross, J., Hollander, D., Burd, A. B., Gilbert, S., Saupe, S., and Quigg, A. (2021). Integrating marine oil snow sedimentation and flocculent accumulation (MOSSFA) events in oil spill response and damage assessment. *Mar. Pollut. Bull.* 165:112025. doi: 10.1016/j.marpolbul.2021.112025

Ruddy, B. M., Huette, M., Kostka, J. E., Lobodin, V. V., Bythell, B. J., McKenna, A. M., et al. (2014). Targeted petroleomics: analytical investigation of Macondo well oil oxidation products from Pensacola Beach. *Energy Fuels* 28, 4043–4050. doi: 10.1021/ef500427n

Ruiz, J. (1997). What generates daily cycles of marine snow? *Deep Sea Res. I* 44, 1105–1126. doi: 10.1016/s0967-0637(97)00012-5

Santschi, P. H. (2018). Marine colloids, agents of the self-cleansing capacity of aquatic systems: historical perspective and new discoveries. *Mar. Chem.* 207, 124–135. doi: 10.1016/j.marchem.2018.11.003

Santschi, P. H., Xu, C., Schwehr, K. A., Lin, P., Sun, L., Chin, W. C., et al. (2020). Can the protein/carbohydrate (P/C) ratio of exopolymeric substances (EPS) be used as a proxy for their 'stickiness' and aggregation propensity? *Mar. Chem.* 218:103734. doi: 10.1016/j.marchem.2019.103734

Schwehr, K. A., Xu, C., Chiu, M.-H., Zhang, S., Sun, L., Lin, P., et al. (2018). Protein/polysaccharide ratio in exopolymeric substances controlling the surface tension of seawater in the presence or absence of surrogate Macondo Oil with and without Corexit. *Mar. Chem.* 206, 84–92. doi: 10.1016/j.marchem.2018.09.003

Severin, T., and Erdner, D. L. (2019). The phytoplankton taxon-dependent oil response and its microbiome: correlation but not causation. *Front. Microbiol.* 10:385. doi: 10.3389/fmicb.2019.00385

Shi, D., Bera, G., Knap, A. H., Quigg, A., Al Atwah, I., Gold-Bouchot, G., et al. (2020). A mesocosm experiment to determine half-lives of individual hydrocarbons in simulated oil spill scenarios with and without dispersant. *Mar. Poll. Bull.* 151:110804. doi: 10.1016/j.marpolbul.2019.110804

Shiu, R.-F., Chiu, M.-H., Vazquez, C. I., Tsai, Y.-Y., Le, A., Kagiri, A., et al. (2020). Protein to carbohydrate (P/C) ratio changes in microbial extracellular polymeric substances induced by oil and Corexit. *Mar Chem.* 223:103789. doi: 10.1016/j.marchem.2020.103789

Silver, M. (2015). Marine snow: a brief historical sketch. *Limnol. Oceanogr. Bull.* 24, 5–10. doi: 10.1002/lob.10005

Sinsabaugh, R. L., Hill, B. H., and Shah, J. J. F. (2009). Ecoenzymatic stoichiometry of microbial organic nutrient acquisition in soil and sediment. *Nature* 462, 795–798. doi: 10.1038/nature08632

Song, W. J., Zhao, C., Mu, S., Pan, X., Zhang, D., Al-Misned, F. A., et al. (2015). Effects of irradiation and pH on fluorescence properties and flocculation of extracellular polymeric substances from the cyanobacterium *Chroococcus minutus*. *Colloids Surf B Biointerfaces* 128, 115–118. doi: 10.1016/j.colsurfb.2015.02.017

Spath, R., Flemming, H. C., and Wuertz, S. (1998). Sorption properties of biofilms. *Water Sci. Technol.* 37, 207–210. doi: 10.2166/wst.1998.0623

Steinberg, D. K., Silver, M. W., and Pilskaln, C. H. (1997). Role of mesopelagic zooplankton in the community metabolism of giant larvacean house detritus in Monterey Bay. *California, USA. Mar. Ecol. Prog. Ser.* 147, 167–179. doi: 10.3354/meps147167

Sterling, M. C. Jr., Bonner, J. S., Ernest, A. N. S., Page, C. A., and Autenrieth, R. L. (2005). Application of fractal flocculation and vertical transport model to aquatic-sol systems. *Wat. Res.* 39, 1818–1830. doi: 10.1016/j.watres.2005.02.007

Stordal, M. C., Santschi, P. H., and Gill, G. A. (1996). Colloidal pumping: Evidence for the coagulation process using natural colloids tagged with 203Hg. *Environ. Sci. Technol.* 30, 3335–3340. doi: 10.1021/es9601806

Sun, L., Chin, W.-C., Chiu, H.-H., Xu, C., Lin, P., Schwehr, K. A., et al. (2020). Sunlight induced aggregation of protein-containing dissolved organic matter (DOM) in the coastal ocean. *Mar. Chem.* 654, 872–877.

Sun, L., Chin, W.-C., Chiu, M.-H., Xu, C., Lin, P., Schwehr, K. A., et al. (2019). Sunlight induced aggregation of protein-containing dissolved organic matter in the ocean. *Sci. Total Environ.* 654, 872–877.

Sun, L., Chiu, M.-H., Xu, C., Lin, P., Schwehr, K. A., Bacosa, H., et al. (2018). The effects of sunlight on the composition of exopolymeric substances affecting the subsequent aggregation process during oil spill and corexit exposure. *Mar. Chem.* 203, 49–54. doi: 10.1016/j.marchem.2018.04.006

Sun, L., Xu, C., Chin, W. C., Zhang, S., Lin, P., Schwehr, K. A., et al. (2017). Light-induced aggregation of microbial exopolymeric substances. *Chemosphere* 181, 675–681. doi: 10.1016/j.chemosphere.2017.04.099

Techtmann, S. M., Zhuang, M., Campo, P., Holder, E., Elk, M., Hazen, T. C., et al. (2017). Corexit 9500 enhances oil biodegradation and changes active bacterial community structure of oil-enriched microcosms. *Appl. Environ. Microbiol.* 83, e03462–16. doi: 10.1128/AEM.03462-16

Testa, J. M., Adams, E. E., North, E. W., and He, R. (2016). Modeling the influence of deep water application of dispersants on the surface expression of oil: a sensitivity study. *J. Geophys. Res. Oceans* 121, 5995–6008. doi: 10.1002/2015jc011571

Valentine, D. L., Fisher, G. B., Bagby, S. C., Nelson, R. K., Reddy, C. M., Sylva, S. P., et al. (2014). Fallout plume of submerged oil from Deepwater Horizon. *Proc. Natl. Acad. Sci. U.S.A.* 111, 15906–15911. doi: 10.1073/pnas.1414873111

Valentine, D. L., Kessler, J. D., Redmond, M. C., Mendes, S. D., Heintz, M. B., Farwell, C., et al. (2010). Propane respiration jump-starts microbial response to a deep oil spill. *Science* 330, 208–211. doi: 10.1126/science.1196830

Verdin, A., Sahraoui, A. L. H., and Durand, R. (2004). Degradation of benzo [a] pyrene by mitosporic fungi and extracellular oxidative enzymes. *Intern. Biodeter. Biodegr.* 53, 65–70. doi: 10.1016/j.ibiod.2003.12.001

Verdugo, P. (2007). Dynamics of marine biopolymer networks. *Polym. Bull.* 58, 139–143. doi: 10.1007/s00289-006-0615-2

Verdugo, P. (2012). Marine microgels. *Annu. Rev. Mar. Sci.* 4, 375–400. doi: 10.1146/annurev-marine-120709-142759

Verdugo, P., Alldredge, A. L., Azam, F., Kirchman, D. L., Passow, U., and Santschi, P. (2004). The oceanic gel phase: a bridge in the DOM-POM continuum. *Mar. Chem.* 92, 67–85. doi: 10.1016/j.marchem.2004.06.017

Verdugo, P., Alldredge, A. L., Azam, F., Kirchman, D. L., Passow, U., and Santschi, P. H. (2005). The oceanic gel phase: a bridge in the DOM-POM continuum. *Mar. Chem.* 92, 65–66.

Verdugo, P., Orellana, M. V., Chin, W. C., Petersen, T. W., van den Eng, G., Benner, R., et al. (2008). Marine biopolymer self-assembly: implications for carbon cycling in the ocean. *Faraday Discuss* 139, 393–398. doi: 10.1039/b800149a

Verdugo, P., and Santschi, P. H. (2010). Polymer dynamics of DOC networks and gel formation in seawater. *Deep Sea Res II* 57, 1486–1493. doi: 10.1016/j.dsr2.2010.03.002

Vonk, S. M., Hollander, D. J., and Murk, A. J. (2015). Was the extreme and widespread marine oil-snow sedimentation and flocculent accumulation (MOSSFA) event during the Deepwater Horizon blow-out unique? *Mar. Pollut. Bull.* 100, 5–12. doi: 10.1016/j.marpolbul.2015.08.023

Wade, T. L., Morales-McDevitt, M., Bera, G., Shi, D., Sweet, S., Wang, B., et al. (2017). A method for the production of large volumes of WAF and CEWAF for dosing mesocosms to understand marine oil snow formation. *Heliyon* 3, e00419. doi: 10.1016/j.heliyon.2017.e00419

Wade, T. L., and Quinn, J. G. (1980). Incorporation, distribution, and fate of saturated petroleum hydrocarbons in sediments from a controlled ecosystem. *Mar. Environ. Res.* 3, 15–33. doi: 10.1016/0141-1136(80)90033-1

Ward, C. P., Armstrong, C. J., Conmy, R. N., French-McCay, D. P., and Reddy, C. M. (2018). Photochemical oxidation of oil reduced the effectiveness of aerial dispersants applied in response to the Deepwater Horizon spill. *Environ. Sci. Technol. Lett.* 5, 226–231. doi: 10.1021/acs.estlett.8b00084

Wen, L. S., Santschi, P. H., and Tang, D. (1997). Interactions between radioactively labeled colloids and natural particles: Evidence for Colloidal Pumping. *Geochim. Cosmochim. Acta* 61, 2867–2878. doi: 10.1016/s0016-7037(97)00139-7

Wozniak, A. S., Prem, P., Obeid, W., Waggoner, D., Quigg, A., Xu, C., et al. (2019). Rapid degradation of oil in mesocosm simulations of marine oil snow events. *Environ. Sci. Technol.* 53, 3441–3450. doi: 10.1021/acs.est.8b06532

Xu, C., Chin, W.-C., Lin, P., Chen, H. M., Lin, P., Chiu, M.-C., et al. (2019). Marine gels, extracellular polymeric substances (EPS) and transparent exopolymeric particles (TEP) in natural seawater and seawater contaminated with a water accommodated fraction of Macondo oil surrogate. *Mar. Chem.* 215:103667. doi: 10.1016/j.marchem.2019.103667

Xu, C., Santschi, P. H., Hung, C. C., Zhang, S. J., Schwehr, K. A., Roberts, K. A., et al. (2011). Controls of (234)Th removal from the oligotrophic ocean by polyuronic acids and modification by microbial activity. *Mar. Chem.* 123, 111–126. doi: 10.1016/j.marchem.2010.10.005

Xu, C., Zhang, S., Beaver, M., Lin, P., Sun, L., Doyle, S., et al. (2018a). The role of microbially-mediated exopolymeric substances (EPS) in regulating Macondo oil transport in a mesocosm experiment. *Mar. Chem.* 206, 52–61. doi: 10.1016/j.marchem.2018.09.005

Xu, C., Zhang, S., Beaver, M., Lin, Y., Wade, T. L., Schwehr, K. A., et al. (2018b). Decreased sedimentation efficiency of petro- and non-petro-carbon caused by a dispersant for Macondo surrogate oil in a mesocosm simulating a coastal microbial community. *Mar. Chem.* 206, 34–43. doi: 10.1016/j.marchem.2018.09.002

Yang, T., Nigro, L. M., Gutierrez, T., D'Ambrosio, L., Joye, S. B., Highsmith, R., et al. (2016). Pulsed blooms and persistent oil-degrading bacterial populations in the water column during and after the Deepwater Horizon blowout. *Deep Sea Res. Part II Top. Stud. Oceanogr.* 129, 282–291. doi: 10.1016/j.dsr2.2014.01.014

Ye, L., Manning, A. J., and Hsu, T. J. (2020). Oil-mineral flocculation and settling velocity in saline water. *Water Res.* 173:115569. doi: 10.1016/j.watres.2020.115569

Zahed, M. A., Aziz, H. A., Isa, M. H., and Mohajeri, L. (2010). Effect of initial oil concentration and dispersant on crude oil biodegradation in contaminated seawater. *Bull. Environ. Contamin. Toxic.* 84, 438–442. doi: 10.1007/s00128-010-9954-7

Zhao, L., Boufadel, M. C., Geng, X., Lee, K., King, T., Robinson, B., et al. (2016). A-DROP: a predictive model for the formation of oil particle aggregates (OPAs). *Mar. Poll. Bull.* 106, 245–259. doi: 10.1016/j.marpolbul.2016.02.057

Zhao, Y., Chen, W., and Wen, D. (2020). The effects of crude oil on microbial nitrogen cycling in coastal sediments. *Environ. Internat.* 139, 105724. doi: 10.1016/j.envint.2020.105724

Ziervogel, K. (2020). *Exopolymeric Substances (EPS) Mechanisms in Aggregation & Dispersion of Oil: Fragmentation of Skeletonema Grethae-775 snow – Disaggregation Dynamics. Distributed by: Gulf of Mexico Research Initiative Information and Data Cooperative (GRIIDC), Harte Research Institute, Texas A&M University–Corpus Christi*. Corpus Christi TX: Texas A&M University–Corpus Christi, doi: 10.7266/n7-qzqh-bq48

Ziervogel, K., D'Souza, N., Sweet, J., Yan, B., and Passow, U. (2014). Natural oil slicks fuel microbial activities in surface waters above cold seeps in the Gulf of Mexico. *Front. Aquat. Microbiol.* 5:188. doi: 10.3389/fmicb.2014.00188

Ziervogel, K., Joye, S. B., and Arnosti, C. (2016). Microbial enzymatic activity and secondary production in sediments affected by the sedimentation pulse following the Deepwater Horizon oil spill. *Deep Sea Res. Part II* 129, 241–248. doi: 10.1016/j.dsr2.2014.04.003

Ziervogel, K., McKay, L., Rhodes, B., Osburn, C. L., Dickson-Brown, J., Arnosti, C., et al. (2012). Microbial activities and dissolved organic matter dynamics in oil contaminated surface seawater from the Deepwater Horizon oil spill site. *PLoS One* 7:e34816. doi: 10.1371/journal.pone.0034816

Ziervogel, K., Steen, A. D., and Arnosti, C. (2011). Changes in the spectrum and rates of extracellular enzyme activities in seawater following aggregate formation. *Biogeosci.* 7, 1007–1015. doi: 10.5194/bg-7-1007-2010

Conflict of Interest: The authors declare that the research was conducted in the absence of any commercial or financial relationships that could be construed as a potential conflict of interest.

frontiers in Marine Science

ORIGINAL RESEARCH
published: 08 October 2021
doi: 10.3389/fmars.2021.617074

Secondary Intrusion Formation of Multiphase Plumes

Dayang Wang* and E. Eric Adams

Department of Civil and Environmental Engineering, Massachusetts Institute of Technology, Cambridge, MA, United States

This work presents a new laboratory study for understanding secondary intrusions in multiphase plumes in quiescent, stratified environments. The study is driven by field observations of secondary intrusions during the Deepwater Horizon (DWH) oil spill. The smaller trap heights observed at DWH for secondary versus primary intrusions could have resulted, in part, from decreasing plume buoyancy (due to gas dissolution) and increasing ambient stratification with elevation above the source. We seek additional mechanisms responsible for the observed smaller secondary trap heights through controlled laboratory experiments where buoyancy and ambient stratification are nominally constant throughout. A novel approach is adopted in the experiments to increase the visibility of secondary intrusions, which are traditionally difficult to visualize, thus investigate. The study reveals that a wider plume source width can also cause the secondary intrusions to trap earlier, providing another plausible explanation for the shallower secondary intrusions observed in the field data.

Keywords: Deepwater Horizon, multiphase flow, oil well blowout, secondary intrusion, plume

Edited by:
Robert Hetland,
Texas A&M University, United States

Reviewed by:
Tamay Ozgokmen,
University of Miami, United States
Chris Lai,
Georgia Institute of Technology,
United States

***Correspondence:**
Dayang Wang
wangd04@gmail.com

Specialty section:
This article was submitted to
Marine Pollution,
a section of the journal
Frontiers in Marine Science

Received: *13 October 2020*
Accepted: *13 September 2021*
Published: *08 October 2021*

Citation:
Wang D and Adams EE (2021)
Secondary Intrusion Formation
of Multiphase Plumes.
Front. Mar. Sci. 8:617074.
doi: 10.3389/fmars.2021.617074

INTRODUCTION

Previously published CTD-CDOM profiles during the Deepwater Horizon (DWH) oil spill showed a prominent intrusion of trapped hydrocarbons near the spill site, typically at elevations about 300–350 m above the seafloor (Valentine et al., 2010; Socolofsky et al., 2011; Camilli, 2014). Some profiles also suggested a second, less prominent intrusion at higher elevations with lower concentrations (Valentine et al., 2010; Camilli, 2014), as indicated in **Figure 1**.

We analyzed 266 CTD-CDOM profiles within a 7 km radius from the wellhead using methods outlined in Socolofsky et al. (2011) and the **Supplementary Information**, and found 19 with a distinct secondary intrusion. To be counted as a secondary intrusion, we required that there must be a distinct vertical interval of background concentration (see **Supplementary Information** for definition) separating the first and second intrusions. Thus the overlapping peaks shown in the bottom portion of the profile in **Figure 1** [and which are frequently observed in the lab (e.g., Socolofsky and Adams, 2005)] are considered part of a single intrusion. In all 19 profiles, the secondary intrusion concentrations were significantly smaller than those in the primary intrusion. Most likely, this stems from the fact that the more soluble hydrocarbons are dissolved near the source and hence enter the first intrusion, resulting in fewer hydrocarbons to enter the secondary (or further) intrusions, even if there are apparent hydrodynamic intrusions.

The first and second intrusion heights were defined by the first spatial moments of the concentration profiles, and are included as **Supplementary Table 1** In all 19 profiles, the heights of secondary intrusions were less than those of the first intrusion, i.e., $h_{T2}/h_{T1} < 1$. Multiple intrusions

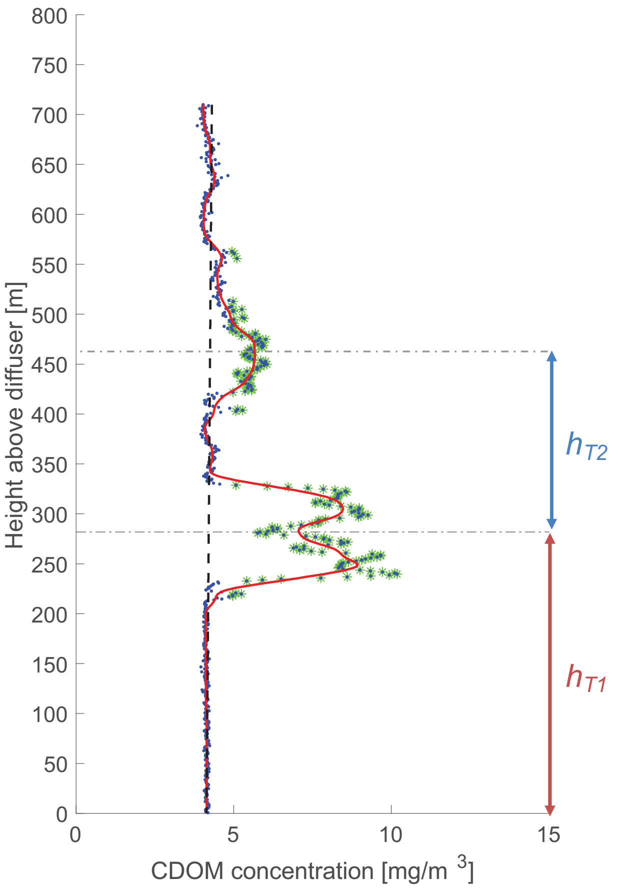

FIGURE 1 | Profile of fluorescence for the field measurement of R/V Walton Smith at station WS048-A on May 31st, 2010. Blue dots are raw measurements. The solid red line is the smoothed curve for the data based on the moving average, and the broken vertical black line is the computed background concentration. A comparison between the background concentration and smoothed curve for data exposes data with excessive fluorescence concentration, highlighted in green. The broken horizontal lines are the observed trap height for the primary and secondary intrusions. h_{T1} and h_{T2} denote primary and secondary intrusion heights, respectively.

have also been observed in laboratory investigations of bubble plumes in a stratified ambient where generally $h_{T2}/h_{T1} < 1$ as well (Asaeda and Imberger, 1993). Data from the field and lab are shown in **Figure 2**, where the combined average is $h_{T2}/h_{T1} = 0.70$.

The primary intrusion height, h_{T1}, scales with both the kinematic buoyancy flux, $B_1 = \frac{Q_g g(\rho_w - \rho_g)}{\rho_w} + \frac{Q_o g(\rho_w - \rho_o)}{\rho_w}$, and the stratification frequency, $N_1 = \left(\frac{g}{\rho}\left|\frac{d\rho}{dz}\right|\right)^{1/2}$, as

$$h_{T1} \sim L_c = \frac{B_1^{1/4}}{N_1^{3/4}} \tag{1}$$

(Morton et al., 1956). Here, Q_g, Q_o are the volumetric flow rates of gas and oil, ρ_g, ρ_o *and* ρ_w are the densities of gas, oil, and water, ρ is the density of seawater as a function of elevation z, and g is gravity.

Depending on the plume type, the plume will restart following the first intrusion, leading to a second intrusion. Asaeda and Imberger (1993); Socolofsky and Adams (2005), and Chan et al. (2014) categorized plume behavior in as many as four types based on a non-dimensional slip velocity $U_N = U_s/(BN)^{\frac{1}{4}}$ where U_s is the particle rising velocity (or settling velocity for sinking particles). Chan et al. (2014) found that secondary intrusions occurred for only two of the four types shown in **Figure 3**.

Assuming h_{T2} scales with the same main parameters,

$$\frac{h_{T2}}{h_{T1}} = \frac{(B_2/B_1)^{1/4}}{(N_2/N_1)^{3/4}} \tag{2}$$

$$or\ \frac{h_{T2}}{h_{T1}} = \frac{(B_2/B_1)^{1/4}}{(\varepsilon_2/\varepsilon_1)^{3/8}} \tag{3}$$

where B_2 *and* N_2 are defined at the elevation at which the plume reforms, and $\varepsilon = \left|\frac{\partial\rho}{\partial z}\right|$.

Spatial variation in either N and B can contribute to the shorter secondary intrusion height. Firstly, Socolofsky et al. (2011) observed that stratification varies nearly quadratically with elevation, in which case

$$\varepsilon = \left|\frac{\partial\rho(z)}{\partial z}\right| = \frac{\partial}{\partial z}\left|\left(\rho_0 + bz^2\right)\right| = 2bz \tag{4}$$

$$\varepsilon_2 \sim h_{T1} + h_{T2} \tag{5}$$

$$\varepsilon_1 \sim h_{T1} \tag{6}$$

Consequently, $\varepsilon_2/\varepsilon_1 > 1$ due to non-linearity in the vertical density profile. Secondly, much of the gas dissolved at or below the first intrusion. The initial plume buoyancy contributed by the gas was up to 81% of the total buoyancy (Socolofsky et al., 2011), and if all of the gas dissolved, then $B_2/B_1 = 0.19$. Combining these two effects,

$$\frac{h_{T2}}{h_{T1}} = \frac{(0.19)^{1/4}}{\left(1 + \frac{h_{T2}}{h_{T1}}\right)^{3/8}} \tag{7}$$

or

$$\frac{h_{T2}}{h_{T1}} = 0.56 \tag{8}$$

Thus it appears that the combination of non-linear stratification and gas dissolution could explain the observed ratios of h_{T2}/h_{T1}.

To explore further, we conducted laboratory experiments that could eliminate the effects of variable B and N on h_{T2}/h_{T1}, by making B_2/B_1 and N_2/N_1 both equal to 1. Our experiments explored the conditions under which secondary intrusions occur in multiphase plumes, and the effects of varying U_N and plume core width on changing the trap depth of secondary intrusions in particle plumes. The trap depth of particle plumes simulated in lab experiments is analogous to trap heights for droplet plumes in the field, and we refer to the two plume types interchangeably. It is noted that additional factors such as ambient current, rotation, and outlet

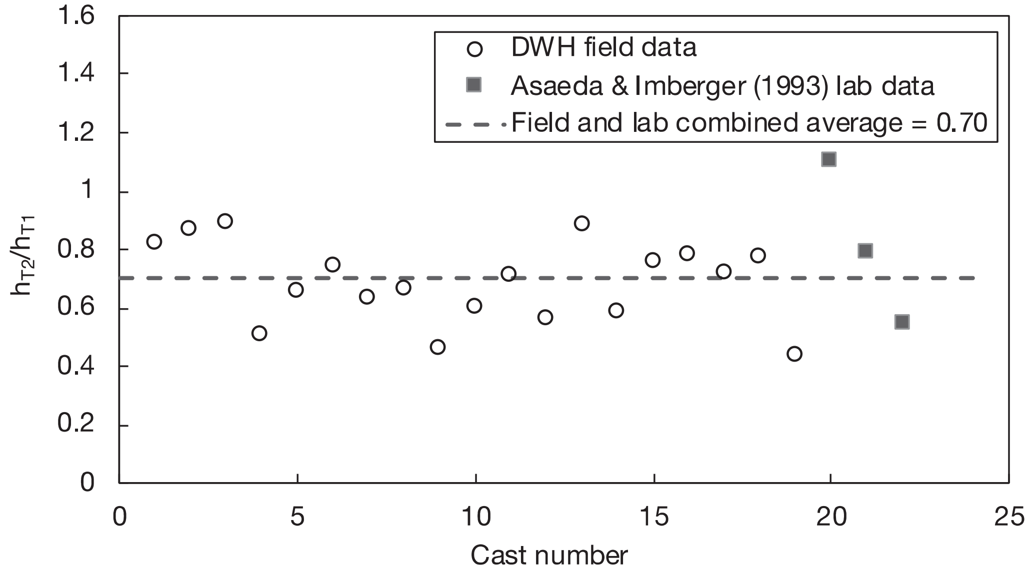

FIGURE 2 | *hT2/hT1* was observed during the Deepwater Horizon (DWH) Oil Spill and in lab experiments by Asaeda and Imberger (1993).

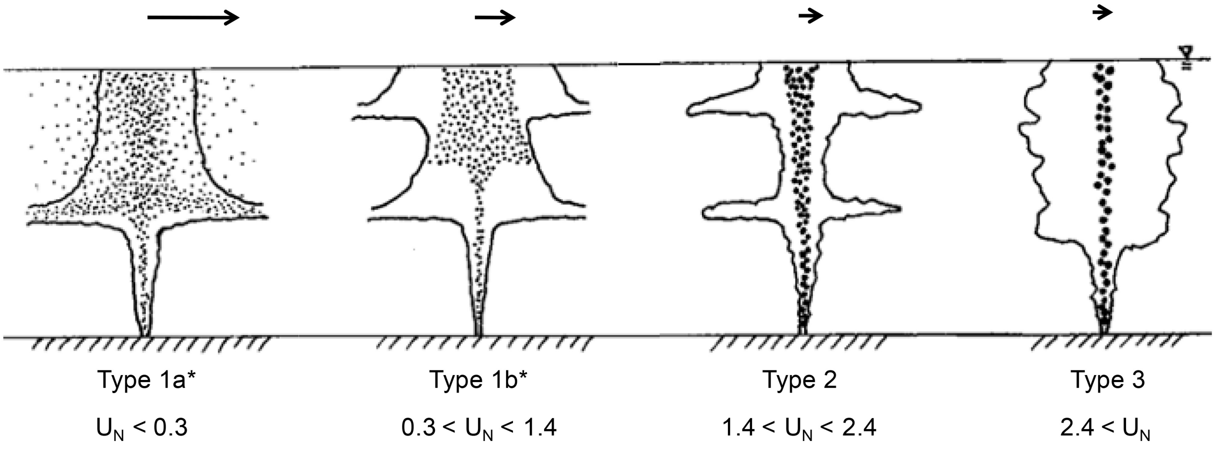

FIGURE 3 | A typology for stagnant multiphase plumes in stratification showing secondary intrusions in Type 1b* and 2 plumes. The arrow length indicates qualitatively the width of the particle distribution. Image adapted from Chan et al. (2014) with permission.

orientation likely affect secondary intrusions, but these factors were not studied.

EXPERIMENTS

Experimental Set-Up

Experiments took place in an acrylic glass tank with dimensions 2.5 m (width) × 1.1 m (length) × 2.2 m (height). A separate cylindrical mixing tank with dimensions 1.57 m (diameter) × 1.5 m (height) was used to create linear stratification using the two-tank method described by Hill (2002). Salt was used as the stratifying agent. To minimize vertical mixing and hence retain stratification, a buoyant splash plate made of marine-grade plywood and overlaid by porous horsehair was attached to the outlet of the flexible filling hose as the tank was filled before each experiment. A conductivity probe was used to determine the conductivity, thus the density of water at various locations in the tank.

Experiments used sinking, negatively buoyant glass beads mixed with brine to simulate rising, positively buoyant oil droplets and gas bubbles in an inverted frame of reference. The discharge mixture was allowed to descend through the tank. During the descent, the plume dynamics were studied via photo imaging and in-situ fluorescence profile measurements at multiple locations after the experiments.

The discharge device consisted of six bottles arranged circularly at equal distances from the center, and each other (**Figure 4**). Each bottle had a flexible tube (3 mm in diameter) extending from the bottom of the bottle. As shown in **Figure 4**, the tubes could be brought close together to form a clustered discharge with a small effective diameter (1 cm between opposing pairs of bottles) or brought farther apart to create a distributed release with a larger effective diameter (8 cm between opposing pairs of bottles). The acrylic bottom plate enabled this by carrying two sets of differentially spaced holes into which the tubes could be plugged.

Experiments were conducted using $N = 1$, 3 or 5 bottles. The flexible tubes connecting each source were identical ensuring equal flow to each "active" bottle. For 3 bottles, every other bottle was filled making the typical distance between filled bottles about 6.9 cm. For 5 bottles, all but one was filled so the typical distance between bottles was 4 cm (We had intended to fill all 6 bottles rather than 5 but found that the secondary intrusion was too close to the tank floor).

Clearly our approach to approximating a distributed source results in non-uniform plume velocity at short distances from the source. However, this distance can be shown to be relatively short. Conservatively assuming that each source is a point source that is advected vertically downward while spreading at a rate of 10% (Fischer et al., 1979), adjacent plumes for $N = 3$ will intersect their neighbors (3.5 cm away) at a depth of about 35 cm which is roughly half of the values of h_{T1} shown in **Table 1** for $N = 3$. For $N = 5$, adjacent sources will begin merging with their neighbors (roughly 2 cm away) at a distance of 20 cm, which is between one-quarter and one-third of the values of h_{T1} shown in **Table 1**. In addition to the assumptions made above, additional conservatism comes from the fact that adjacent jets will experience dynamic pressures on their "inside" that will cause them to be sucked closer together, shortening the merging distance (Lai and Lee, 2012). **Supplementary Figure 1** shows an image of the merging of opposing jets for $N = 5$ (Experiment SG07081865).

Each of the six bottles contained dense spherical glass beads with a specific gravity of 2.45, together with Rhodamine dye and brine, whose density matched the ambient water at the discharge level. The resulting mixture, in the form of a slurry, was kept well-mixed by vibration motors during the release. The mass ratio of glass beads to brine was determined to ensure both phases finished discharging simultaneously. The bead size dictated both the flow rate of the beads and the flow rate of the brine draining through the voids.

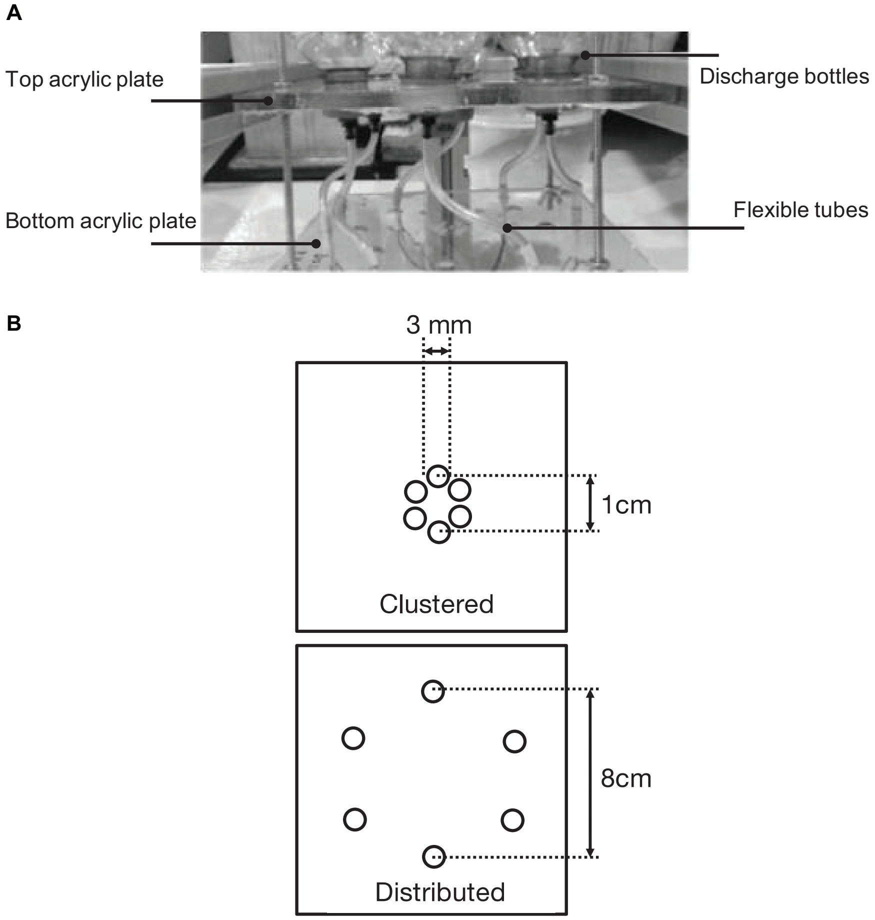

FIGURE 4 | (A) Glass beads dispensing device (Side view). **(B)** Discharge nozzle configurations: clustered and distributed sources. Both configurations consist of six equal-sized holes.

TABLE 1 | Experiment conditions for plume intrusion investigation in stratified, stagnant ambient.

Experiment ID	Particle designation	Particles median diameter (μm)	Discharge nozzle	$U_s \times 10^{-2}$(m/s)	No. of discharge bottles	Q_o (m^3/s)	B (m^4/s^3)	N (/s)	U_N	h_{T1} (m)	h_{T2} (m)
SG021017B1	B	510	Clustered	6.96	1	6.15E-07	8.95E-06	0.18	1.96	0.61	0.61
SG051017AD1	AD	150	Clustered	1.42	1	6.33E-07	9.22E-06	0.16	0.40	0.59	NA
SG131217C3	C	320	Clustered	4.14	3	1.85E-06	2.69E-05	0.15	0.92	0.76	0.70
SG191217B3	B	510	Clustered	6.96	3	1.85E-06	2.69E-05	0.17	1.50	0.79	0.75
SG080118AD3	AD	150	Distributed	1.42	3	1.90E-06	2.77E-05	0.16	0.31	0.68	NA
SG070118AD3	AD	150	Distributed	1.42	3	1.90E-06	2.76E-05	0.15	0.31	0.69	NA
SG151217C3	C	320	Distributed	4.14	3	1.85E-06	2.69E-05	0.15	0.93	0.74	0.67
SG110118B3	B	510	Distributed	6.96	3	1.85E-06	2.69E-05	0.17	1.49	0.63	NA
SG181217B3	B	510	Distributed	6.96	3	1.85E-06	2.69E-05	0.17	1.50	0.63	0.62
SG310718B3	B	510	Clustered	6.96	3	1.85E-06	2.69E-05	0.20	1.45	0.69	0.70
SG010818B3	B	510	Distributed	6.96	3	1.85E-06	2.69E-05	0.19	1.46	0.57	NA
SG020818B3	B	510	Distributed	6.96	3	1.85E-06	2.69E-05	0.19	1.46	0.59	0.59
SG030818B3	B	510	Clustered	6.96	3	1.85E-06	2.69E-05	0.19	1.46	0.73	0.73
SG070818C5	C	320	Distributed	4.14	5	3.08E-06	4.49E-05	0.19	0.76	0.66	0.58
SG080818C5	C	320	Clustered	4.14	5	3.08E-06	4.48E-05	0.21	0.74	0.73	0.64
SG170818AD1	AD	150	Clustered	1.42	1	6.33E-07	9.24E-06	0.19	0.39	0.58	0.47
SG200818AD1	AD	150	Clustered	1.42	1	6.33E-07	9.24E-06	0.20	0.38	0.60	0.42
SG240818AD1	AD	150	Clustered	1.42	1	6.33E-07	9.24E-06	0.16	0.41	0.60	0.39
SG250818AD1	AD	150	Clustered	1.42	1	6.33E-07	9.24E-06	0.19	0.39	0.61	0.46
SG100118B1	B	510	Clustered	6.96	1	6.15E-07	8.95E-06	0.14	2.08	0.72	NA
SG150718B1	B	510	Distributed	6.96	1	6.15E-07	8.95E-06	0.14	2.10	0.58	NA
SG170718B1	B	510	Distributed	6.96	1	6.15E-07	8.95E-06	0.15	2.06	0.53	NA
SG220718B1	B	510	Distributed	6.96	1	6.15E-07	8.95E-06	0.18	1.97	0.48	0.47

Three bead sizes (B, C, and AD) with decreasing settling (slip) velocities U_s were used. The discharge flow rate, thus the buoyancy flux B, could be controlled by using fewer or greater numbers of bottles for the release. The variations in U_s and B were reflected in the change in U_N. **Table 1** describes the properties and discharge conditions of the glass beads. The flow rates were consistent across different discharge bottles and steady in time (**Supplementary Table 2**).

Plume Illumination

For visualization and photo image analysis, a high-power laser was used to illuminate the center cross-section of the axisymmetric plume. We used a Dantec DuoPower 100–100 laser, which could generate pulsed laser light sheets at 2 × 100 mJ at a maximum of 100 Hz, with a wavelength of 532 nm (green light). We chose the dye concentration based on the most desirable brightness and contrasts for imaging the spreading of the dyed, entrained fluid and particles in the plume and the intrusion layer.

In addition to image analysis, vertical fluorescence profiles were taken *in situ* at various locations in the tank after each experiment. In previous experiments, it has proven challenging to visualize and measure secondary intrusions (Socolofsky and Adams, 2005) because the dye was only introduced at the point of discharge with the slurry, and most of it followed the detraining phase(s) into the first intrusion. To better highlight secondary intrusions where they exist, we positioned a rigid, submerged tube aligned with the surface discharge point to deliver dye at the secondary intrusion's anticipated depth. The tube was made of transparent plastic and had an inside diameter of 2 mm. The top of the tube was attached to the bottom of a dye reservoir as in an interveinal injection system to eliminate any air bubbles, and the flow rate of dye could be controlled by adjusting a valve. In order not to disturb the flow, dye was introduced with minimum momentum and with a density close to that of the local ambient. Dye injection began once the plume dynamics were seen to have fully developed. The optimal delivery depth was just above the second intrusion, as suggested in **Figure 5**.

RESULTS

For each experiment, 3–5 profiles were taken. Intrusion depths h_{T1} and h_{T2} (when observed) were computed from the first spatial moments of each profile, and then averaged to provide entries in **Table 1**. Reasonable repeatability in these averages can be seen by comparing runs with similar experimental conditions shown in the table. **Figure 6** plots the experimentally observed ratio of h_{T2}/h_{T1} versus U_N superimposed on plume type as summarized by Chan et al. (2014). The figure suggests no secondary intrusion for Types 3 and 1a*, and declining ratio as one progresses from Type 2 (ratio = 1) to 1b* (ratio approaches 0.7).

It was anticipated that h_{T2}/h_{T1} might be equal to unity as values of B and N do not change over the trajectory of a

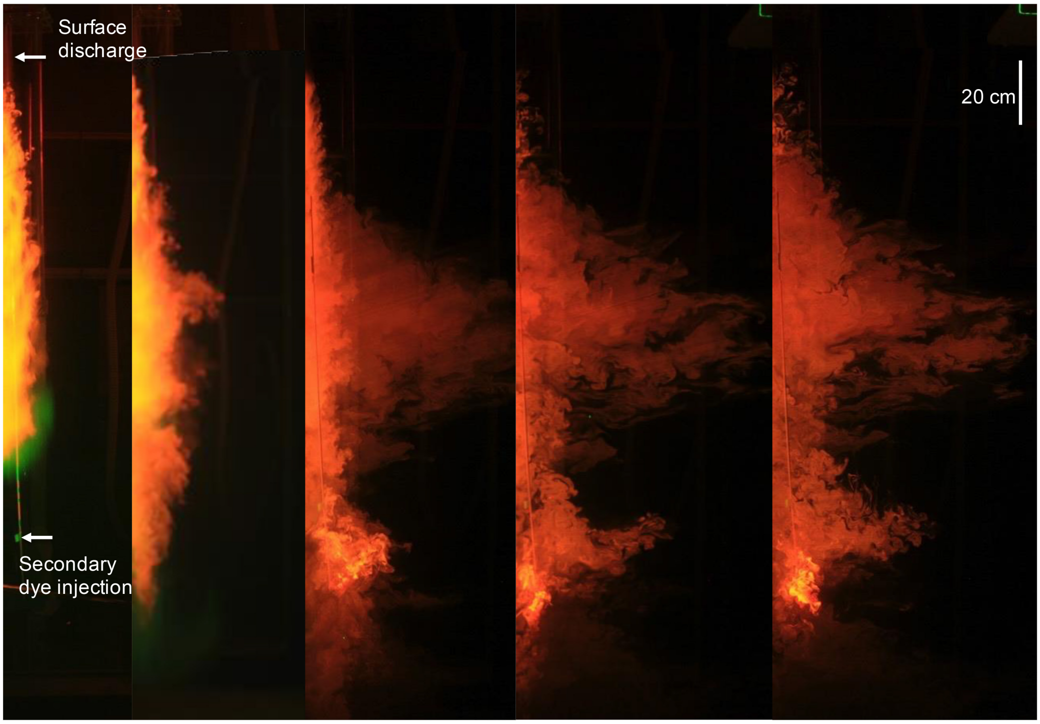

FIGURE 5 | The time revolution of an experimental plume released from the surface ~2.2 m above the tank floor. The development of one side of the plume profile (plume is axisymmetric) with time is shown from left to right.

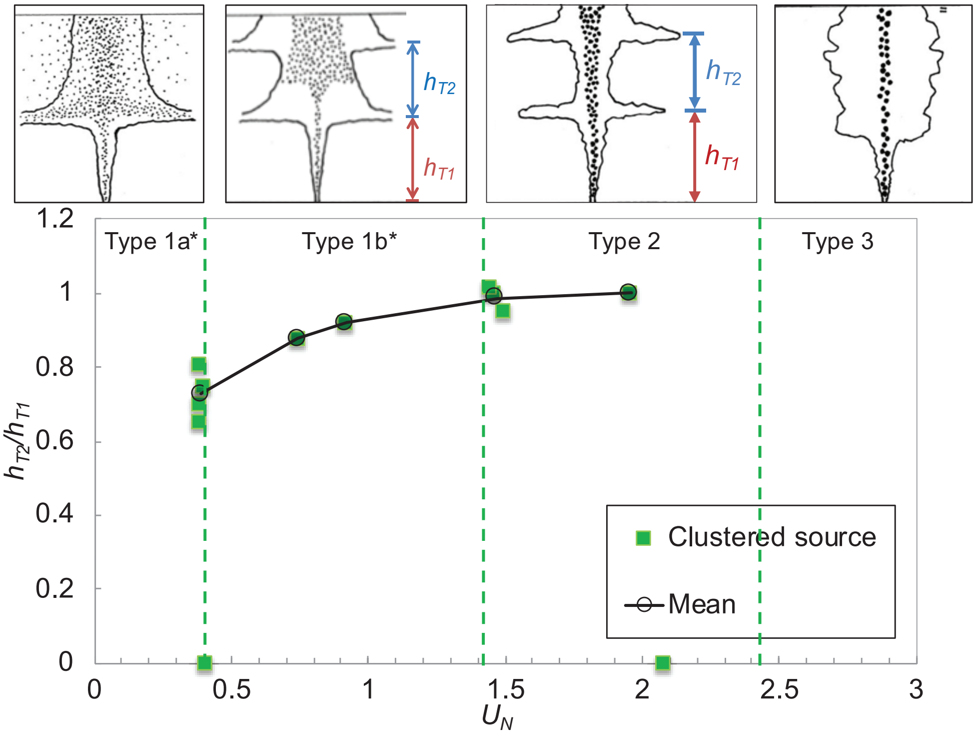

FIGURE 6 | h_{T2}/h_{T1} as a function of U_N, showing increasing h_{T2}/h_{T1} with U_N for clustered source (green squares) configuration. Open circles denote the mean, and the solid line represents the trend. h_{T2}/h_{T1} with a value of zero means no secondary intrusion was observed. Hence secondary intrusion was only observable for a range of U_N. The plume types indicated on top of the figure (top four panels) are consistent with **Figure 3**.

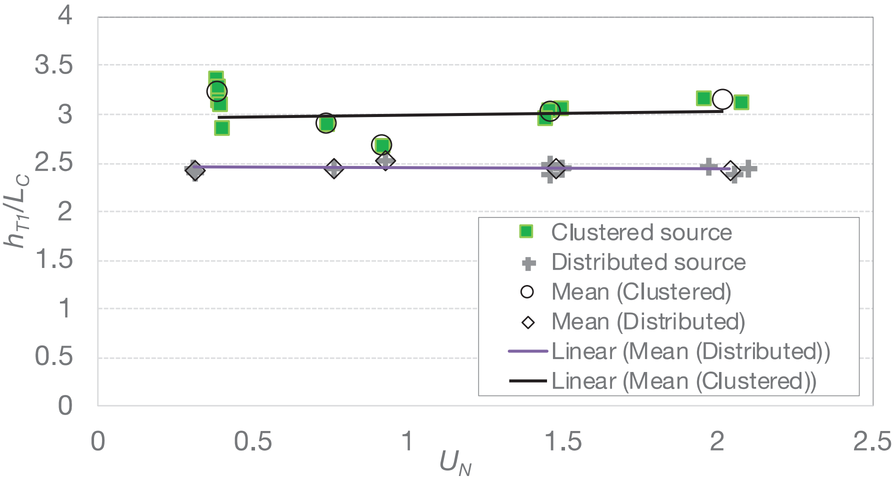

FIGURE 7 | Normalized h_{T1} against U_N for clustered and distributed sources. The solid trendlines are the mean of clustered (black) and distributed (gray) sources.

given experiment. While this was the case for Type 2 plumes ($U_N > 1.5$), h_{T2}/h_{T1} was less than one for Type 1b* ($U_N \sim [0.4, 1.5]$), implying that the secondary intrusion occurs sooner than the primary intrusion. The main difference between the two types, as evident in **Figure 3**, is the width of the plume source as the plume "restarts" after the primary intrusion. As Type 1b* plumes are characterized by droplets that detrain but do not enter the intrusion, they have a wider source for the secondary plume than Type 2 plumes, which do not experience detrainment. The widened plume core in Type 1b* may be responsible for a reduced h_{T2}/h_{T1}.

To further test this hypothesis, we observed the *primary* intrusions created using the two source widths, as illustrated in **Figure 4B**. Other than the effective source width, the two sources were identical, and the buoyancy fluxes, in particular, were identical. By focusing on the primary intrusion, we thus avoided the possibility that the source buoyancy might have been reduced, as discussed above. **Figure 7** shows that for the clustered sources, the mean and std dev of the normalized first intrusion height h_{T1}/L_c were 2.92 (std dev of 0.21), close to the value of 2.8 reported by others (e.g., Mingotti and Woods, 2019). For distributed sources, the corresponding mean and std dev were 2.36 and 0.06.

The mean trapping depth for the distributed sources is, on average, 81% of the trapping depth of the "clustered" source, with no apparent dependence on U_N. The shallower trapping depth of the distributed source makes sense as both single-phase plumes (Hunt and Kaye, 2001) and multiphase plumes (Zhou, 2019) have a negative virtual origin. Zhou (2019) analyzed the trap depths resulting from the numerically simulated bubble plumes generated by large eddy simulations (LES). Zhou found that, compared with bubble plumes emanating from point sources, the trap levels of bubble plumes produced by a source of moderate radius b_o were reduced by a factor of $9b_o / [L_c(4.77-0.34U_N)]$. For wide sources, the fractional reduction was about half of this. Considering our distributed source to be "wide," the percentage reduction in our experiments ranged from 13 to 22%, within the same ballpark as the observed 19% reduction in **Figure 7**.

CONCLUSIONS

Driven by field observations at DWH, we present a laboratory investigation that explores conditions under which secondary intrusions occur in multiphase plumes. The occurrence and the trap elevations of secondary intrusions are correlated with U_N, the non-dimensional particle slip velocity, as well as the plume core width.

We conclude that the smaller trap heights observed at DWH for secondary versus primary intrusions could have resulted, in part, from decreasing plume buoyancy (due to gas dissolution) and increasing ambient stratification with elevation above the source. However, secondary intrusions observed in the lab, where B and N remain nominally constant with depth, also show a smaller ratio of h_{T2}/h_{T1}, with this ratio decreasing with decreasing droplet size (U_N). Additional laboratory experiments focusing on primary intrusions resulting from plumes of different source width, but otherwise similar properties, including B, show that more distributed sources tend to trap at a shallower depth. This observation is consistent with observations of lazy plumes in the literature and could provide at least a partial explanation for the smaller secondary intrusions observed at DWH.

Our paper has explored the height of potential secondary intrusions. These heights are important, environmentally, because they determine the second layer within the water column at which dissolved hydrocarbons, and those remaining in the form of small droplets, are likely to intrude. Of course, hydrocarbon concentrations within the layer are also important, but are more complicated to analyze because they depend not only on the volumetric flow of seawater, but the mass flux of hydrocarbons, entering the intrusion. Such calculations can be addressed with the help of models such as TAMOC (Dissanayake et al., 2018), but are outside the scope of our study.

DATA AVAILABILITY STATEMENT

The original contributions presented in the study are included in the article/ **Supplementary Material**, further inquiries can be directed to the corresponding author.

AUTHOR CONTRIBUTIONS

EA and DW were responsible for conceptualization. DW conducted the lab experiments and wrote the manuscript. EA provided supervision and editing. Both the authors contributed to the article and approved the submitted version.

FUNDING

This research was partially supported by the National Research Foundation Singapore through the Singapore-MIT Alliance for Research and Technology's Center for Environmental Sensing and Modeling Interdisciplinary Research Program, and a grant from the Gulf of Mexico Research Initiative through the Gulf of Mexico Integrated Spill Response Consortium (GOMRI grant number 02-S140209).

ACKNOWLEDGMENTS

The authors thank Maciej Baranski for help in photo imaging and Felice Frankel for improving figure presentation.

SUPPLEMENTARY MATERIAL

The Supplementary Material for this article can be found online at: https://www.frontiersin.org/articles/10.3389/fmars.2021.617074/full#supplementary-material

REFERENCES

Asaeda, T., and Imberger, J. (1993). Structure of bubble plumes in linearly stratified environments. *J. Fluid Mech.* 249, 36–57. doi: 10.1017/S0022112093001065

Camilli, R. (2014). Tracking hydrocarbon plume transport and biodegeneration at deepwater horizon. *Science* 330, 201–204. doi: 10.1126/science.1195223

Chan, G. K. Y., Chow, A. C., and Adams, E. E. (2014). Effects of droplet size on intrusion of sub-surface oil spills. *Environ. Fluid Mech.* 15, 959–973. doi: 10.1007/s10652-014-9389-5

Dissanayake, A. L., Gros, J., and Socolofsky, S. A. (2018). Integral models for bubble, droplet and multiphase plume dynamics in stratification and crossflow. *Environ. Fluid Mech.* 18, 1167–1202. doi: 10.1007/s10652-018-9591-y

Fischer, H., List, J., Koh, C., Imberger, J., and Brooks, N. (1979). *Mixing in Inland and Coastal Waters*. Amsterdam: Elsevier. doi: 10.1016/C2009-0-22051-4

Hill, D. F. (2002). General density gradients in general domains: the "Two-Tank" method revisited. *Exp. Fluids* 32, 434–440. doi: 10.1007/s00348-001-0376-5

Hunt, G. R., and Kaye, N. G. (2001). Virtual origin correction for lazy turbulent plumes. *J. Fluid Mech.* 435, 377–396. doi: 10.1017/S0022112001003871

Lai, A. C. H., and Lee, J. H. W. (2012). Dynamic interaction of multiple buoyant jets. *J. Fluid Mech.* 708, 539–575. doi: 10.1017/jfm.2012.332

Mingotti, N., and Woods, A. W. (2019). Multiphase plumes in a stratified ambient. *J. Fluid Mech.* 869, 292–312. doi: 10.1017/jfm.2019.198

Morton, B. R., Taylor, G., and Turner, J. S. (1956). Turbulent gravitational convection from maintained. *Proc. R. Soc. Math. Phys. Eng. Sci. Instant. Sources* 234, 1–23. doi: 10.1098/rspa.1956.0011

Socolofsky, S. A., and Adams, E. E. (2005). Role of slip velocity in the behavior of stratified multiphase plumes. *J. Hydraul. Eng.* 131, 273–282. doi: 10.1061/(ASCE)0733-94292005131:4(273)

Socolofsky, S. A., Adams, E. E., and Sherwood, C. R. (2011). Formation dynamics of subsurface hydrocarbon intrusions following the Deepwater Horizon blowout. *Geophys. Res. Lett.* 38, 2–7. doi: 10.1029/2011GL047174

Valentine, D. L., Kessler, J. D., Redmond, M. C., Mendes, S. D., Heintz, M. B., Farwell, C., et al. (2010). Propane respiration jump-starts microbial response to a deep oil spill. *Science* 330, 208–211. doi: 10.1126/science.1196830

Zhou, G. (2019). Computational study of the source-area effect for bubble plumes in stratified environments. *J. Hydraul. Eng.* 146:04020039. doi: 10.1061/(ASCE)HY.1943-7900.0001759

Conflict of Interest: DW was employed by the company Exponent.

The remaining author declares that the research was conducted in the absence of any commercial or financial relationships that could be construed as a potential conflict of interest.

frontiers
in Marine Science

ORIGINAL RESEARCH
published: 15 November 2021
doi: 10.3389/fmars.2021.618094

A Fuzzy-Based Framework for Assessing Uncertainty in Drift Prediction Using Observed Currents and Winds

Hauke Blanken [1,2]*, Caterina Valeo [1], Charles Hannah [2], Usman T. Khan [3] and Tamás Juhász [2]

[1] Department of Mechanical Engineering, University of Victoria, Victoria, BC, Canada, [2] Institute of Ocean Sciences, Fisheries and Oceans Canada, Sidney, BC, Canada, [3] Department of Civil Engineering, Lassonde School of Engineering, York University, Toronto, ON, Canada

Edited by:
Robert Hetland,
Texas A&M University, United States

Reviewed by:
Suneel V,
Council of Scientific and Industrial Research (CSIR), India
Daijiro Kobashi,
Texas A&M University, United States

****Correspondence:***
Hauke Blanken
hauke.blanken@dfo-mpo.gc.ca

Specialty section:
This article was submitted to Marine Pollution, a section of the journal Frontiers in Marine Science

Received: *16 October 2020*
Accepted: *20 October 2021*
Published: *15 November 2021*

Citation:
Blanken H, Valeo C, Hannah C, Khan UT and Juhász T (2021) A Fuzzy-Based Framework for Assessing Uncertainty in Drift Prediction Using Observed Currents and Winds. Front. Mar. Sci. 8:618094. doi: 10.3389/fmars.2021.618094

This paper proposes a fuzzy number—based framework for quantifying and propagating uncertainties through a model for the trajectories of objects drifting at the ocean surface. Various sources of uncertainty that should be considered are discussed. This model is used to explore the effect of parameterizing direct wind drag on the drifting object based on its geometry, and using measured winds to parameterize shear and rotational dynamics in the ocean surface currents along with wave-driven circulation and near-surface wind shear. Parameterizations are formulated in a deterministic manner that avoids the commonly required specification of empirical leeway coefficients. Observations of ocean currents and winds at Ocean Station Papa in the northeast Pacific are used to force the trajectory model in order to focus on uncertainties arising from physical processes, rather than uncertainties introduced by the use of atmospheric and hydrodynamic models. Computed trajectories are compared against observed trajectories from five different types of surface drifters, and optimal combinations of forcing parameterizations are identified for each type of drifter. The model performance is assessed using a novel skill metric that combines traditional assessment of trajectory accuracy with penalties for overestimation of uncertainty. Comparison to the more commonly used leeway method shows similar performance, without requiring the specification of empirical coefficients. When using optimal parameterizations, the model is shown to correctly identify the area in which drifters are expected to be found for the duration of a seven day simulation.

Keywords: ocean, surface, drift, uncertainty, fuzzy, shear, observations, station papa

1. INTRODUCTION

The ability to respond to emergencies such as marine contaminant spills and search and rescue efforts is directly linked with the ability to predict the trajectories of objects drifting at the ocean surface (Daniel et al., 2002; Breivik and Allen, 2008; Davidson et al., 2009; Butler, 2015). Better predictions of trajectories also enhance our understanding of marine ecosystem functioning and connectivity (Checkley et al., 1988; Gawarkiewicz et al., 2007; Röhrs et al., 2014; Stark et al., 2018). Drift trajectories of floating objects are governed by currents and winds at the very surface of the ocean. These remain persistently difficult to measure (Soloviev and Lukas, 2014), and the submesoscale variability of these fields can only be measured directly during targeted campaigns of limited duration (Poje et al., 2014; D'Asaro et al., 2018). Therefore, further treatment is generally required to properly characterize uncertainty arising from imprecise measurements of surface currents and winds. In practice, currents and winds used to force drift trajectory simulations are usually obtained from numerical circulation models, which introduces further uncertainty into the problem as these models are by necessity a simplification of reality. For the purposes of this paper, we consider only observational data and the relevant processes giving rise to uncertainty in this data. Model data and associated uncertainties will be considered in future work, since the uncertainties in observations used to verify the model data must first be established in order to accurately estimate the uncertainties in modeled data.

Uncertainty in drift trajectory models is usually treated by applying a series of random kicks to modeled particles (Zelenke et al., 2012; De Dominicis et al., 2013; Cho et al., 2014), ensemble modeling based on the uncertainty in empirically derived forcing parameterizations (Breivik and Allen, 2008; Breivik et al., 2011; Dagestad et al., 2018), or by defining an empirically determined dispersion coefficient (Okubo, 1971). This approach has a long history of relative success. However, the specification of the magnitude of random kicks or dispersion coefficients is generally not obvious, and the assumption that the underlying forcing data is free of systematic uncertainties and biases remains. Usually a large number of perturbed trajectories are computed. Other workers have also computed ensemble predictions from a variety of numerical models (Rixen et al., 2008; Vandenbulcke et al., 2009) or systematic variations of forcing data to capture variability on seasonal time scales (Fine and Masson, 2015).

The present study takes a different approach, by expressing the forcing data for a drift trajectory model as fuzzy numbers. Fuzzy numbers are used to describe imprecise data. They are described by their membership function, which gives the range of possible values of the true data at varying degrees of belief, or membership levels (Zadeh, 1965, 1978). Robust frameworks for propagating the uncertainty described by fuzzy numbers through mathematical models have been developed (Kaufman and Gupta, 1985; Hanss, 2002). The formulation of fuzzy numbers does not require assumptions about the underlying character of the uncertainty, they simplify aggregation of uncertainty from various sources, and they can be constructed from sparse data sets. In environmental sciences and engineering, fuzzy numbers have been applied to a variety of problems involving imprecise knowledge of parameters, such as: description of water masses (Fengqi et al., 1989); tracking of storm systems (Mercer et al., 2002); remote sensing of ocean surface properties (Moore et al., 2009); modeling of water quality in rivers (Khan et al., 2013); and assessing the frequency of landslide occurrence following rain events (Park et al., 2017). Interval analysis, which can be considered a simplification of fuzzy number arithmetic, has been applied to drift trajectory prediction by Ni et al. (2010), who considered a leeway model for drift (Breivik and Allen, 2008) in the absence of waves, and tested this model using idealized uniform current and wind forcing.

The leeway model is commonly used to model drift using current and wind data as forcing. Here the motion of a drifting object is described as the superposition of the current and a fraction of the wind speed (often $\sim$ 3%) directed at an angle to the wind (to the right in the northern hemisphere). Encapsulated in this parameterization are the effects of current shear and rotational dynamics in the upper ocean above the level at which currents are measured, direct wind drag on exposed parts of the drifting object, wave-induced circulation, and wind shear below the level at which winds are measured. The origins of this method date back to Nansen (1902) and Ekman (1905), however it remains an active field of research (Dagestad et al., 2018; Sutherland et al., 2020).

Object geometry has a significant effect on wind response. The work reviewed in Allen and Plourde (1999) showed that empirically fitted leeway parameters (rate and angle) of a variety of drifting search and rescue targets is strongly dependent on the target geometry. Wind response may change quite significantly even for relatively small changes in geometry (Röhrs and Christensen, 2015; Sutherland et al., 2020). Deterministically describing the wind response for a given object geometry remains an active research question, and empirically determined coefficients are more frequently used (Allen and Plourde, 1999; Breivik et al., 2011). A framework for deterministic description of the wind response has been developed based on the force balance on the drifting object (Daniel et al., 2002; Röhrs et al., 2012), and in this paper the wind drag coefficients of five different types of drifting buoys are derived using this framework. These coefficients are used in our trajectory model in conjunction with parameterizations for wave-induced circulation and near-surface wind and current shear, rather than using empirical leeway parameters.

A similar effort is described by Röhrs et al. (2012), who used ship-based wind measurements, near-surface (0.5 m) current measurements from a 1 MHz ADCP, and directional wave spectra in a Norwegian fjord to describe the observations from surface drifters. They found that wave-induced Stokes drift was of first order importance to the trajectory prediction along with winds and currents. Wind effects were parameterized by fitting a drag coefficient to optimize the trajectory description. In a similar vein, Tamtare et al. (2019) considered surface current shear extrapolated from an ocean model of the Gulf of St. Lawrence, coarsely resolved in the vertical direction, to test the effect of adding this shear into a trajectory model. They report noticeably improved predictions.

Here we expand on these efforts by developing a drift trajectory model with uncertainty propagation based on fuzzy numbers, forced with currents and winds measured at Ocean Station Papa (hereafter OSP) in the northeast Pacific. The resulting predictions are verified against observations from five different types of ocean surface drifters launched nearby. Uncertainty in the model is considered as both uncertainty in the forcing data, which is propagated using fuzzy numbers, and uncertainty about the relevant combinations of forcing parameters. To address the latter, we compute an ensemble of drift trajectory predictions using all possible combinations of forcing terms and identify the combination resulting in the optimal predictions for each drifter type. Results from the proposed method are compared to analogous results derived using the leeway method with empirical coefficients corresponding most closely to the object under consideration.

To begin, we describe the trajectory model and the derivation of relevant forcing terms in section 2. Fuzzy numbers are introduced next, and we describe how they are used to propagate uncertainty through this trajectory model in section 3. Next, the observational forcing data used to test and validate the model is described in section 4, followed by the presentation of results on model performance and the optimal combination of forcing terms in section 5, followed by discussion and conclusions.

2. DRIFT TRAJECTORY MODEL

The trajectory of an object drifting at the ocean surface is determined by the balance of forces acting on it. For a drifting object of mass m, this is written as,

$$m\frac{d^2\vec{x}}{dt^2} = \vec{F}_a + \vec{F}_o + \vec{F}_C + \vec{F}_w \tag{1}$$

$\vec{x}$ is the position of the object, $\vec{F}_a$ is wind drag on the airside parts of the drifters, $\vec{F}_o$ is current drag on waterside parts of the drifter, $\vec{F}_C$ is a Coriolis term, and $\vec{F}_w$ is the force due to wave scattering. The force due to wave scattering is negligible since the drifters horizontal dimensions are generally much less than 20% of the wavelength of incident waves (Daniel et al., 2002; Breivik and Allen, 2008; Röhrs et al., 2012). The acceleration of a drifting object to its quasi-steady velocity is generally quick, ∼20 s for a life raft in strong winds (Breivik and Allen, 2008), and therefore we consider $\frac{d^2\vec{x}}{dt^2}$ to be negligible, since it is unlikely to be relevant at the model timestep (300 s for our study).

The contribution of the Coriolis force, which results in a deflection of the drift trajectory to the right of the wind (in the northern hemisphere), is contained in the current and wind forcing and is therefore accounted for in the terms $\vec{F}_o$ and $\vec{F}_a$. The explicit Coriolis term in Equation (1), $\vec{F}_C$, refers to the change in this force caused by the difference between the mass of an ocean surface drifter and a water parcel of equivalent volume. For a small object such as an ocean surface drifter this term is small compared to $\vec{F}_o$ and $\vec{F}_a$ and is therefore considered negligible.

The balance of forces therefore reduces to the balance of airside wind drag and waterside current drag on the drifter. Following Röhrs et al. (2012), with the classical equation for drag force by Morison et al. (1950), this is written as,

$$\begin{aligned}\frac{1}{2}\rho_a A_a C_a\left(\vec{u}_w|_{z=z_{drifter}} - \frac{d\vec{x}}{dt}\right)\left|\vec{u}_w|_{z=z_{drifter}} - \frac{d\vec{x}}{dt}\right| = \\ \frac{1}{2}\rho_w A_w C_w\left(\frac{d\vec{x}}{dt} - (\vec{u}_c|_{z=z_{drifter}} + \vec{u}_{stokes})\right) \\ \left|\frac{d\vec{x}}{dt} - (\vec{u}_c|_{z=z_{drifter}} + \vec{u}_{stokes})\right|\end{aligned} \tag{2}$$

Here $\vec{u}_w|_{z=z_{drifter}}$ is the wind velocity at the ocean surface, $\vec{u}_c|_{z=z_{drifter}}$ is the current velocity at the depth relevant to the drifting object ($z_{drifter}$), and $\frac{d\vec{x}}{dt}$ is the drift speed. The density of air and water are taken as $\rho_a = 1.225\ kg/m^3$ and $\rho_w = 1{,}025\ kg/m^3$, respectively. The airside and waterside cross-sectional areas of the drifter are A_a and A_w, and the corresponding drag coefficients are C_a and C_w, respectively. Their product can be determined from the vertical profiles of effective width, $w(z)$, and approximate drag coefficient, $C(z)$, of the drifting object.

$$A_a C_a = \frac{\int_0^{Z_{max}} w(z)C(z)dz}{\int_0^{Z_{max}} w(z)dz} \tag{3a}$$

$$A_w C_w = \frac{\int_{Z_{min}}^0 w(z)C(z)dz}{\int_{Z_{min}}^0 w(z)dz} \tag{3b}$$

The maximum draft of the object below the water surface and its maximum height above the surface are given by Z_{min} and Z_{max}, respectively.

Assuming that wind speeds are much larger than drift speeds reduces Equation (2) to a well-known linear vector equation for $\frac{d\vec{x}}{dt}$ (Daniel et al., 2002; Röhrs et al., 2012).

$$\frac{d\vec{x}}{dt} = \vec{u}_c|_{z=z_{drifter}} + \vec{u}_{stokes} + \sqrt{\frac{\rho_a A_a C_a}{\rho_w A_w C_w}}\vec{u}_w|_{z=z_{drifter}} \tag{4}$$

For notational simplicity we will write the scaling factor on $\vec{u}_w|_{z=z_{drifter}}$ as

$$\alpha = \sqrt{\frac{\rho_a A_a C_a}{\rho_w A_w C_w}} \tag{5}$$

The assumptions implicit in Equation (4) are that $\vec{u}_c|_{z=z_{drifter}}$ is known at the effective depth of the drifter, and $\vec{u}_w|_{z=z_{drifter}}$ is known at the water surface. This however is generally not the case, as both are measured some distance from the water surface on conventional observation platforms. Therefore some shear in the winds and currents due to boundary layer effects between the measurement level and the effective height (depth) of the drifter is not represented in measurements. Accounting for near-surface current shear has been shown to significantly improve drift predictions based on numerical ocean models (Tamtare et al., 2019). We test whether this holds for drift predictions made using observations of currents at depth z_c and winds at height z_w from OSP, by adding estimates of near-surface current, $\Delta\vec{u}_c|_{z=z_c}^{z=z_{drifter}}$, and wind shear $\Delta\vec{u}_w|_{z=z_{drifter}}^{z=z_w}$ to Equation (4). Therefore, the current at the effective depth of the drifter is $\vec{u}_c|_{z=z_{drifter}} = \vec{u}_c + \Delta\vec{u}_c|_{z=z_c}^{z=z_{drifter}}$, and the wind at the water surface is $\vec{u}_w|_{z=z_{drifter}} = \vec{u}_w + \Delta\vec{u}_w|_{z=z_{drifter}}^{z=z_w}$. $\vec{u}_c$ and $\vec{u}_w$ are the measured currents and winds, respectively. This yields the following model for drift trajectories,

$$\frac{d\vec{x}}{dt} = \vec{u}_c + \Delta\vec{u}_c|_{z=z_c}^{z=z_{drifter}} + \vec{u}_{stokes} + \alpha(\vec{u}_w + \Delta\vec{u}_w|_{z=z_{drifter}}^{z=z_w}) \tag{6}$$

From $\vec{u}_w$ and observed water and air temperatures, we estimate $\vec{u}_{stokes}$, $\Delta\vec{u}_c|_{z=z_c}^{z=z_{drifter}}$, and $\Delta\vec{u}_w|_{z=z_{drifter}}^{z=z_w}$. The processes used to estimate these quantities are discussed in the following sections.

Both Stokes drift, $\vec{u}_{stokes}$, and current shear, $\Delta\vec{u}_c|_{z=z_c}^{z=z_{drifter}}$, exhibit vertical gradients with strong surface intensification. Stokes drift decays rapidly within a few meters of the surface (Clarke and Van Gorder, 2018). Since the shapes of drifters below the water surface are often irregular, we investigate whether the method by which these velocity profiles are integrated has a noticeable effect on trajectory predictions. We compare results derived with Stokes drift and current shear taken either as the value at the geometric centroid of the drifter, or as an area-weighted average of the vertical velocity or drag force profile. For a velocity profile $\vec{u}(z)$, these can be expressed as,

$$\vec{u}_{centroid} = \vec{u}(z)|_{z=z_{centroid}=\frac{\int_{z_{min}}^{0} zw(z)dz}{\int_{z_{min}}^{0} w(z)dz}} \tag{7a}$$

$$\vec{u}_{velocity} = \frac{\int_{z_{min}}^{0} w(z)\vec{u}(z)dz}{\int_{z_{min}}^{0} w(z)dz} \tag{7b}$$

$$\vec{u}_{force} = \sqrt{\frac{\int_{z_{min}}^{0} w(z)C(z)\vec{u}(z)|\vec{u}(z)|dz}{\int_{z_{min}}^{0} w(z)C(z)dz}} \tag{7c}$$

Here all symbols are as previously defined.

In order to address the systemic uncertainty in drift trajectory prediction that arises from the uncertainty around the importance of forcing terms in Equation (6) and methods for applying sheared forcing, we test the sensitivity of the predicted drift trajectory to the inclusion of the forcing terms in Equation (6) and the choice of the three possible methods of applying sheared forcing from Equation (7). This is done by first calculating trajectories for each drifter type using all possible combinations of forcing terms and sheared forcing methods, starting with the simplest case of predicting a trajectory using only a single forcing term, either $\vec{u}_c$, $\vec{u}_w$, or $\vec{u}_{stokes}$. Additional terms are added in subsequent predictions. All predictions are then scored against observations from the type of drifter being modeled at each time step of the prediction, and the combination of terms resulting in the highest skill is reported. A term that is in the solution with the highest skill at the majority of the time steps is considered to be part of the optimal combination of parameters for this drifter.

2.1. Stokes Drift

We estimate Stokes drift (Stokes, 1847) from one-dimensional frequency spectra of sea surface height, which we in turn estimate using the a parametric spectrum for fully developed seas by Pierson and Moskowitz (1964). Stokes drift is assumed to be in the wind direction. Using the classical expression for Stokes drift in non-monochromatic seas given by Kenyon (1969) yields the following expression for the vertical profile of Stokes drift, $U_s(z)$, in the deep-water limit of the dispersion relation (i.e., $\omega^2 = gk$ where ω is angular frequency, k is wavenumber, and g is acceleration due to gravity),

$$U_s(z) = 2\alpha_P g \int_0^\infty \omega^{-2} e^{\left[\frac{2\omega^2 z}{g} - \beta_1 \left(\frac{\omega_p}{\omega}\right)^4\right]} d\omega \tag{8}$$

Here α_P is the Phillips constant, set to 0.0081 following Holthuijsen (2010), and $\beta_1 = 0.74$ is a constant. The peak circular frequency can be approximated as $\omega_p = g/U_{19.5}$, where $U_{19.5}$ is the wind speed at a height of 19.5 m (the same height as the measurements used by Pierson and Moskowitz, 1964). The vertical Stokes drift profile for a given $U_{19.5}$ can be derived by integrating (Equation 8) at discrete depths, z. This profile is the converted to a singular value, $\vec{u}_{stokes}$ for use in Equation (6) using the methods in Equation (7).

We limit the discussion in this paper to parameterized one-dimensional wave spectra of fully developed wind seas. Recent work by Clarke and Van Gorder (2018), including results from OSP, suggests that Stokes drift is well approximated by parameterized one-dimensional spectra and that the contribution of remotely generated swell is small compared to higher frequency wind seas. This is because Stokes drift for a monochromatic wave is proportional to the cube of the waves frequency, implying exponential increases in Stokes drift with increasing wave frequency (note that Equation 8 gives the sum of all frequency bands in the spectrum). Further, the approach adopted here is applicable wherever wind information is available and the deep-water limit of the dispersion relation applies. Fetch-limited locations may be considered using the parametric spectrum proposed by Hasselmann et al. (1973).

It has been well established that the contribution of the Stokes drift to the Coriolis force, i.e., the Coriolis-Stokes force (c.f. Polton et al., 2005), influences near surface currents. However, Coriolis-Stokes forcing is not considered here, since this is an active field of research with evolving understanding of processes and uncertainties, and a detailed contribution to this subject is beyond the scope of the current work. Interested readers may find more information in recent papers and reviews, such as Weber et al. (2015), Clarke and Van Gorder (2018), and van den Bremer and Breivik (2018).

2.2. Current Shear

Wind forcing results in significantly sheared upper ocean currents directed to the right of the wind (in the northern hemisphere), as was first shown by Ekman (1905). Near-surface shear is further enhanced in the shallow wave-affected layer in the few meters immediately below the ocean surface (Craig and Banner, 1994). The resulting difference between the current at the effective depth of the drifter and the depth at which currents are measured is given as $\Delta\vec{u}_c|_{z=z_c}^{z=z_{drifter}}$ in Equation (6).

The wind-driven current shear in the upper ocean can be modeled by numerically solving the unsteady momentum balance between rotation and vertical diffusion of momentum with surface wind forcing using the level 2.5 turbulence closure scheme of Mellor and Yamada (1982), as described in Craig and Banner (1994).

$$\frac{\delta u}{\delta t} - \frac{\delta}{\delta z}\left(A\frac{\delta u}{\delta z}\right) = fv \tag{9a}$$

$$\frac{\delta v}{\delta t} - \frac{\delta}{\delta z}\left(A\frac{\delta v}{\delta z}\right) = -fu \tag{9b}$$

$$\frac{\delta b}{\delta t} - \frac{\delta}{\delta z}\left(lqS_q\frac{\delta b}{\delta z}\right) = lqS_M\left(\left(\frac{\delta u}{\delta z}\right)^2 + \left(\frac{\delta v}{\delta z}\right)^2\right) - \frac{2qb}{Bl} \tag{9c}$$

The first two equations describe the balance of momentum in the u and v directions, and the latter describes the balance of turbulent kinetic energy (TKE). The two relate via the eddy viscosity $A = lqS_M$, which requires the prescription of the turbulent length scale l. $q = \sqrt{b}$ is the turbulent velocity scale, or square root of TKE. S_M is a constant in unstratified water, which use here and assume that the well-mixed condition holds in the upper ocean mixed layer. This is supported by profiles of temperature and salinity observed around the time of the drifter deployments, which show well-mixed water down to 80–90 m depth (**Supplementary Figure 1**).

Apart from two minor adjustments, which are described in the next paragraphs, we retain the formulation of Craig and Banner (1994) and do not reproduce details here. Readers interested in a detailed description are referred to the original paper.

We force the system by converting measured winds to friction velocities, u_*, defined as $\vec{u}_* = \sqrt{C_d \vec{U}_{10}^2 \left(\frac{\rho_a}{\rho_w}\right)}$. C_d is the drag coefficient, interpolated from tables given by Smith (1988) and all other variables are as defined previously. The densities of air/water (ρ_a/ρ_w) are taken as 1.225 kg/m^3 and 1,025 kg/m^3, respectively. For simplicity we take $\vec{u}$ to be in the downwind direction and $\vec{v}$ in the crosswind direction, and rotate the derived velocities back to geographical coordinates once time-stepping is complete.

Using this friction velocity we solve the equations over a depth of 200 m, discretized into 0.5 m bins. This implies the assumption that direct wind-driven currents and TKE are negligible below 100 m.

Once the wind-driven upper ocean current $\vec{u}(z) = [u(z), v(z)]$ has been modeled, we compute the wind-driven current at the effective depth of the drifter, $\vec{u}(z = z_{drifter})$ by the methods in Equation (7) and then derive $\Delta\vec{u}_c|_{z=z_c}^{z=z_{drifter}}$ for use in Equation (6).

$$\Delta\vec{u}_c|_{z=z_c}^{z=z_{drifter}} = \vec{u}(z = z_{drifter}) - \vec{u}_c \tag{10}$$

2.3. Wind Shear

Vertical shear in the wind field between the measurement height (4 m) and the level of the exposed parts of the drifter, taken here as 1 m, can be estimated from atmospheric boundary layer relationships. Smith (1988) gives a review of the necessary theory and tabulates conversion factors for wind speed from 1, 2, 5, and 20 m to the standard 10 m reference height, for varying degrees of atmospheric stability. Atmospheric stability is represented as the difference between virtual sea surface temperature and virtual potential air temperature at the measurement height, which we obtain from measurements of both air and water temperature. We then use the conversion factors, C_{UX_Y}, interpolated from tables in Smith (1988) to convert winds at the measurement height, first to the 10 m reference height, and then to 1 m. Single subscripts denote the vertical level in meters, and double subscripts X_Y denote conversion from level X to level Y. The conversion to derive $\Delta\vec{u}_w|_{z=z_{drifter}}^{z=z_w}$ for use in Equation (6) proceeds as follows,

$$\vec{U}_{10} = \left(\frac{3}{4}C_{U5\_10} + \frac{1}{4}C_{U1\_10}\right)\vec{U}_4 \tag{11a}$$

$$\vec{U}_1 = \frac{\vec{U}_{10}}{C_{U1\_10}} \tag{11b}$$

$$\Delta\vec{u}_w|_{z=z_{drifter}}^{z=z_w} = \vec{U}_1 - \vec{u}_w \tag{11c}$$

In the following section we present a method for propagating uncertainty in currents and winds measured at OSP through the trajectory model described here, including the derivation of the parameterized forcing terms $\vec{u}_{stokes}$, $\Delta\vec{u}_c|_{z=z_c}^{z=z_{drifter}}$, and $\Delta\vec{u}_w|_{z=z_{drifter}}^{z=z_w}$. The method is based on fuzzy numbers, and we begin by giving a brief overview of the relevant theory.

3. UNCERTAINTY PROPAGATION

3.1. Overview of Relevant Fuzzy Number Theory

Fuzzy numbers are used to describe imprecise quantities. At their core, they describe the possible range of values a quantity might take as a function of ones degree of belief in that range of values. This is known as the *membership function*. Membership functions are usually derived through quantitative analysis of the process being considered, coupled with expert knowledge of this process. To illustrate the concept of a membership function, an informal hypothetical example of such a derivation is included in the **Supplementary Information**.

In general, fuzzy numbers are a special case of fuzzy sets (Zadeh, 1965, 1978). The membership function, which describes the fuzzy number, is defined by a unique value that is certainly possible, with a membership of one (the *crisp value*). From that value the function decreases monotonically toward the lowest and highest values thought to be possible, with a decreasing degree of belief as values diverge from the crisp value. This monotonic decrease implies the function is *convex*. The largest range of values thought to be possible is the *support* of the fuzzy number, with a membership of zero.

It is important to note that membership functions, and the fuzzy numbers they represent, are not equivalent to probability distributions. They instead describe the range of values one believes a fuzzy number might take, without making claims about the probability of occurrence of values in this range. Fuzzy numbers are however weakly linked to probability theory through the restriction that the possibility of any value must always be greater than or equal to its probability. This is known as the *consistency principle* (Zadeh, 1965).

Membership functions are generally given as a set of crisp intervals defining a possible range of values at a given degree of possibility, rather than defining a continuous function. We refer to these intervals as membership levels, however they are also known as α-cuts in the literature (Radecki, 1977). Hence a fuzzy number P can be described as a set of membership levels $A^{(j)}$, i.e.,

$$P = \{A^{(0)}, A^{(1)}, ..., A^{(m)}\} \tag{12a}$$

$$A^{(j)} = [a^{(j)}, b^{(j)}] \text{ for } j = 0, 1, ..., m,\ a^{(j)} \leq b^{(j)} \tag{12b}$$

Here $a^{(j)}$ and $b^{(j)}$ are the lower and upper bounds of the membership level j. The membership, or degree of belief, at each level is given by $\frac{j}{m}$.

The simplest, and most common, type of membership function is the triangular function, which is defined by a crisp value and two points defining the support. However, other types of membership functions exist, and some that are more representative of the uncertainty being modeled have been shown to improve results for geophysical applications (Khan et al., 2013; Khan and Valeo, 2016). We do not consider triangular membership functions for the purposes of this paper. Instead we use a probability-possibility transform based on the consistency principle to quantitatively derive membership functions for the current and wind measured at OSP using Gaussian and Laplace distributions. For this we must specify a crisp value, or mean μ_K, and possible variability, or standard deviation σ, as well as the number of membership levels, $j = 0, 1, ..., m$. The functions describing a Gaussian (Laplace) distribution are given by $f(x) = \frac{1}{\sqrt{2\pi\sigma^2}} e^{-\frac{(x-\mu_K)^2}{2\sigma^2}}$ $\left(f(x) = \frac{1}{\sqrt{2}\sigma} e^{-\frac{\sqrt{2}|x-\mu_K|}{\sigma}}\right)$. With this information the symmetric range of possible values around μ_K, denoted as $[\mu_K - a, \mu_K + a]$, can be derived for each membership level by iteratively solving the following integral for a (Dubois et al., 2004; Zhang, 2009).

$$\int_{-\infty}^{\mu_K - a} f(x)dx + \int_{\mu_K + a}^{\infty} f(x)dx = \frac{j}{m} \text{ for } j = 0, 1, ..., m \tag{13}$$

The resulting membership functions are symmetric about μ_K since the Gaussian and Laplace distributions are also symmetric; this is not a general property of fuzzy numbers. The membership levels are also not required to be evenly distributed, though they often are for convenience. Specifying or modifying the shape of a fuzzy number based on expert knowledge is possible, where appropriate, as long as the membership function remains convex. Examples of fuzzy numbers in various forms (triangular, transformed from probability- distributions, and modified by expert knowledge) are shown in **Figure 1**.

Fuzzy numbers can be used to propagate uncertainty through a mathematical model by applying well established rules for performing arithmetic operations on them. Traditionally this has been done by applying interval arithmetic to individual membership levels (Kaufman and Gupta, 1985). However, this method has the drawback that uncertainty is overestimated in systems where a fuzzy-valued term appears more than once in the system's equations. This is because all possible values of the fuzzy term are considered for each instance of the fuzzy term, which results in "double-counting" (Hanss, 2005).

For systems where a fuzzy-valued term appears multiple times, arithmetic should be performed using the transformation method described by Hanss (2002). This method is used here, since parameterizations for wave-induced circulation, near surface current shear, and wind shear all depend on the fuzzy-valued wind velocity. In the transformation method, the fuzzy-valued terms in the system of equations are discretized into arrays describing all possible combinations of all possible values of these terms. The system can then be solved using element-wise operations on these arrays. We give a brief description of the general transformation method here. Interested readers may refer to Hanss (2002) and Hanss (2005) for a thorough summary.

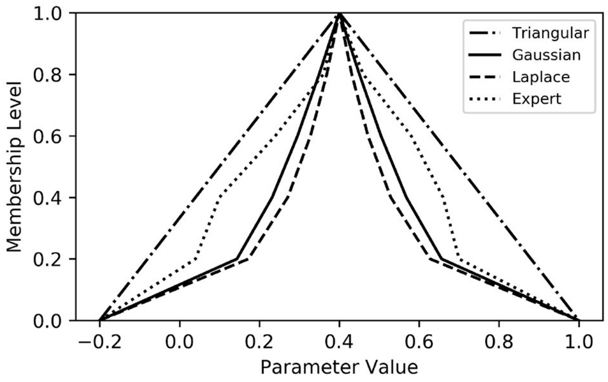

FIGURE 1 | Examples of possible shapes of the membership function for a fuzzy number describing possible values of an arbitrary parameter. Functions for a triangular (dash-dotted), transformed Gaussian (solid), transformed Laplace (dashed), and expert knowledge-informed (dotted) fuzzy number are shown. The transformed membership functions are derived using a crisp value $\mu_K = 0.4$, and standard deviation $\sigma = 0.2$. All functions have a support width of 3σ.

Consider a system of equations with n independent fuzzy variables $P_i, i = 1, ..., n$. Each P_i consists of $m + 1$ membership levels $X_i^{(j)}$. Each membership level $X_i^{(j)}$ is described by the interval $[a_i^{(j)}, b_i^{(j)}]$, which is then discretized into an array $\hat{X}_i^{(j)}$ according to the following equations.

$$P_i = \{X_i^{(0)}, X_i^{(1)}, ..., X_i^{(m)}\} \tag{14a}$$

$$X_i^{(j)} = [a_i^{(j)}, b_i^{(j)}], \quad a_i^{(j)} \leq b_i^{(j)} \tag{14b}$$

$$\hat{X}_i^{(j)} = (\overbrace{\gamma_{1,i}^{(j)}, \gamma_{2,i}^{(j)}, ..., \gamma_{(m+1-j),i}^{(j)}, ..., \gamma_{1,i}^{(j)}, \gamma_{2,i}^{(j)}, ..., \gamma_{(m+1-j),i}^{(j)})}^{(m+1-j)^{i-1} \text{ tuples of length } (m+1-j)} \tag{14c}$$

$$\gamma_{l,i}^{(j)} = \overbrace{(c_{l,i}^{(j)}, ..., c_{l,i}^{(j)})}^{(m+1-j)^{n-i} \text{ elements}} \tag{14d}$$

$$c_{l,i}^{(j)} = \begin{cases} a_i^{(j)} & \text{for } l = 1 \text{ and } j = 0, 1, ..., m \\ \frac{1}{2}\left(c_{l-1,i}^{(j+1)} + c_{l,i}^{(j+1)}\right) & \text{for } l = 2, 3, ..., m - j \text{ and} \\ & j = 0, 1, ..., m - 2 \\ b_i^{(j)} & \text{for } l = m - j + 1 \text{ and } j = 0, 1, ..., m \end{cases} \tag{14e}$$

A graphical example of this discretization, adapted from Hanss (2005), is given in **Figure 2** for a hypothetical fuzzy number described by four membership levels, i.e., $m = 3$. The final result of the transformation of all n fuzzy input variables P_i at one point in time is a set of $m + 1$ arrays $\hat{X}_i^{(j)}$ for each P_i. To illustrate explicitly, consider a system of equations with two fuzzy input variables (i.e., $n = 2$), each similar to the example shown in

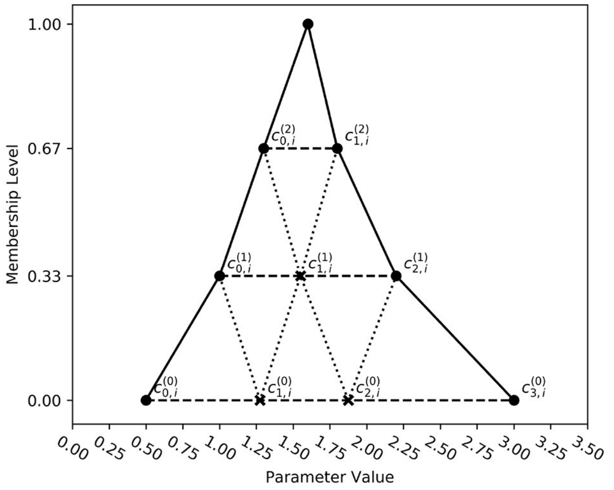

FIGURE 2 | Illustration of the discretization of a fuzzy number into array form using the transformation method. Adapted from Hanss (2005).

Figure 2. The final arrays describing the membership level $j = 1$ are constructed as follows.

$$\hat{X}_1^{(1)} = [c_{0,1}^{(1)}, c_{0,1}^{(1)}, c_{0,1}^{(1)}, c_{1,1}^{(1)}, c_{1,1}^{(1)}, c_{1,1}^{(1)}, c_{2,1}^{(1)}, c_{2,1}^{(1)}, c_{2,1}^{(1)}] \tag{15a}$$

$$\hat{X}_2^{(1)} = [c_{0,2}^{(1)}, c_{1,2}^{(1)}, c_{2,2}^{(1)}, c_{0,2}^{(1)}, c_{1,2}^{(1)}, c_{2,2}^{(1)}, c_{0,2}^{(1)}, c_{1,2}^{(1)}, c_{2,2}^{(1)}] \tag{15b}$$

Using these arrays the system of equations for the membership level can be solved as it would be in a crisp manner, but using element-wise arithmetic on the arrays $\hat{X}_1^{(1)}$ and $\hat{X}_2^{(1)}$.

The result of this element-wise arithmetic for each membership level ($\hat{X}^{(j)}_{result}$) can then be re-transformed into a fuzzy number by taking the minimum and maximum values of each $\hat{X}^{(j)}_{result}$ to be the bounds of the membership level j of the fuzzy result, while ensuring that the fuzzy result remains convex.

$$P_{result} = \{Z^{(0)}, Z^{(1)}, ..., Z^{(m)}\} \tag{16a}$$

$$Z^{(j)} = [a^{(j)}, b^{(j)}], j = 0, 1, ..., m \tag{16b}$$

$$a^{(j)} = min(a^{(j+1)}, min(\hat{X}^{(j)}_{result})) \tag{16c}$$

$$b^{(j)} = max(b^{(j+1)}, max(\hat{X}^{(j)}_{result})) \tag{16d}$$

To apply this method to the prediction of drift trajectories, we begin by applying a probability-possibility transform to convert time series of measured ocean currents and winds at OSP into fuzzy numbers, using (Equation 13) as detailed in the following section. Each value in the resulting fuzzy time series is then transformed into arrays describing each membership level of the currents and winds, $\hat{X}^{(j)}_{\vec{u}_c}(t)$ and $\hat{X}^{(j)}_{\vec{u}_w}(t)$, according to Equation (14). The fuzzy-valued time series of drift speed, $\hat{X}^{(j)}_{\frac{d\vec{x}}{dt}}(t)$ can then be derived by substituting $\hat{X}^{(j)}_{\vec{u}_c}(t)$ and $\hat{X}^{(j)}_{\vec{u}_w}(t)$ into (Equation 6) and re-transforming each value in $\hat{X}^{(j)}_{\frac{d\vec{x}}{dt}}(t)$ into a fuzzy number according to Equation (16).

$$\hat{X}^{(j)}_{\frac{d\vec{x}}{dt}}(t) = \hat{X}^{(j)}_{\vec{u}_c}(t) + \Delta\vec{u}_c|_{z=z_c}^{z=z_{drifter}}\big(\hat{X}^{(j)}_{\vec{u}_w}(t)\big) + \vec{u}_{stokes}\big(\hat{X}^{(j)}_{\vec{u}_w}(t)\big) + \alpha\big(\hat{X}^{(j)}_{\vec{u}_w}(t) + \Delta\vec{u}_w|_{z=z_{drifter}}^{z=z_w}\big(\hat{X}^{(j)}_{\vec{u}_w}(t)\big)\big) \tag{17}$$

As described above, Equation (17) is solved using element-wise array arithmetic. The term $\Delta\vec{u}_c|_{z=z_c}^{z=z_{drifter}}\big(\hat{X}^{(j)}_{\vec{u}_w}(t)\big)$ is derived by applying the procedure described in section 2.2 to all elements of $\hat{X}^{(j)}_{\vec{u}_w}(t)$. Similarly, $\vec{u}_{stokes}\big(\hat{X}^{(j)}_{\vec{u}_w}(t)\big)$ and $\Delta\vec{u}_w|_{z=z_{drifter}}^{z=z_w}\big(\hat{X}^{(j)}_{\vec{u}_w}(t)\big)$ are derived by element-wise solution of the procedures in sections 2.1 and 2.3, respectively. The procedure by which the resulting fuzzy-valued drift velocities are integrated to give the set of all possible displacements is described in section 3.3.

3.2. Fuzzification of Input Data

Fuzzy forms of observed currents and winds can be derived by considering the energy at scales unresolved by the observations, as well as the associated instrument uncertainties. To estimate the energy at time scales that are not resolved in the current and wind measurements, we fit a power law Af^{-B} to the high-frequency tail of the energy spectra of the currents and winds, defined as $P(f) = \frac{1}{2}(P_u(f) + P_v(f))$ where $P_{u/v}(f)$ are the component spectra in the u/v directions. The unresolved energy between the Nyquist frequency, $f_N = \frac{1}{2dt_{obs}}$, and the frequency corresponding to the model timestep, $f_C = \frac{1}{2dt_{model}}$, can be estimated by log-linearly extrapolating the fitted power law to f_C, integrating from f_N to f_C, and finding the associated velocity scale by converting the resulting variance to amplitude, A_v.

$$A_v = \sqrt{2\sigma^2} = \sqrt{2}\bigg(\int_{f_N}^{f_C} Af^{-B} df\bigg)^{\frac{1}{2}} \tag{18}$$

In order to later derive the possible time series of drift velocity, the amplitude of the maximum unresolved accelerations, A_a, can be similarly derived by differentiating the extrapolated velocity energy spectrum. Here,

$$A_a = \sqrt{2}\bigg(\int_{f_N}^{f_C} Af^{-(B-2)} df\bigg)^{\frac{1}{2}} \tag{19}$$

Uncertainty due to spatial variability in the currents fields can only be estimated from numerical model results, or similar products, as observations of currents are only available in a single location. This uncertainty is denoted by σ_s, and the derivation is discussed in section 5.1 as it is case-specific.

To fuzzify the observed currents and winds we then assume that the uncertainty is isotropic, and that the uncertainties in the u and v directions are uncorrelated. The probability-possibility transform (Equation 13) can then be applied to each component separately, using the measured value as the crisp value. The standard deviation of the probability density function to be transformed is taken as the sum of A_v, σ_s, and the instrument uncertainty, σ_i. The approach taken here only requires the assumption of one distribution to describe the total uncertainty (discussed in section 5.1). A support width of $b^{(0)} - a^{(0)} = 6(A_v + \sigma_s + \sigma_i)$, centered on the crisp value was selected, and the bounds of the intermediate membership levels were derived from Equation (13). Once the input variables have been expressed in fuzzy form they are used to solve for the fuzzy drift velocity by Equation (17), which is then integrated to derive the possible displacement of the drifting object.

3.3. Integration of Fuzzy Drift Velocities

The fuzzy set of all possible displacements can be derived by integrating all possible time series of drift velocity within a membership level that adhere to the maximum unresolved acceleration A_a. For each membership level below the crisp solution these time series can be found by first discretizing the membership level at the initial time into a number of starting points, n_S. From each starting point, n_p possible values at the next time step are determined based on the maximum unresolved acceleration and the bounds of the membership level. For each subsequent time step, n_p further possible values are determined from each possible value at the current time step, until the last time step is reached.

Letting the fuzzy drift velocity $P_{\frac{d\vec{x}}{dt}} = Z$ for notational simplicity, a possible value $Z_{k,t}^{(j)}$ (i.e., within membership level j, originating from starting point k, at time t) results in the following possible values at the next time step.

$$Z_{k,t+1}^{(j)}(n) = Z_{k,t}^{(j)} + \Delta Z^{(m)} + \Delta Z^{(j)}(n), \text{ for } n = 1, 2, ..., n_p \tag{20a}$$

$$\Delta Z^{(m)} = Z_{t+1}^{(m)} - Z_{t+0}^{(m)} \tag{20b}$$

$$\Delta Z^{(j)}(n) = 6 A_a F^{(j)}(n) \Delta t \tag{20c}$$

$$F^{(j)}(n) = \frac{\frac{1}{2}(n_p + 1) - n}{\frac{1}{2}(n_p - 1)} \frac{b_{t+1}^{(j)} - a_{t+1}^{(j)}}{b_{t+1}^{(0)} - a_{t+1}^{(0)}} \tag{20d}$$

$$a_{t+1}^{(j)} \leq Z_{k,t+1}^{(j)} \leq b_{t+1}^{(j)} \tag{20e}$$

Here $\Delta t = dt_{model}$ is the model time step, $a_t^{(j)}$ and $b_t^{(j)}$ are the lower and upper bounds of membership level j at time t, and $Z^{(m)}$ is the crisp time series of predicted drift velocities. All other symbols are as previously defined. A schematic of the process detailed in Equation (20) is shown in **Supplementary Figure 2**.

Integrating all unique crisp time series in the resulting set, using the forward Euler method, gives the set of all possible drifter displacements within this membership level $P_{\vec{x}}^{(j)}$ at time $T = N\Delta t$. This is written as follows

$$P_{\vec{x}}^{(j)} = \sum_{t=1}^{N-1} \frac{1}{2}\left(Z_{m,t+1}^{(j)}(n) + Z_{m,t}^{(j)}\right), \text{ for } n = 1, 2, ..., n_p$$

$$\text{, and } m = 1, 2, ... n_S \tag{21}$$

In this case, use of the forward Euler method does not impact the results negatively, due to the assumption that the forcing fields are free of spatial variability. This will change when extending this analysis to include data from numerical ocean and atmospheric models and the associated spatial interpolation.

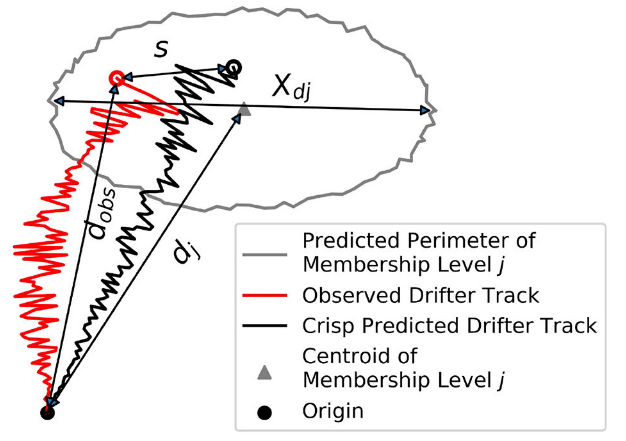

FIGURE 3 | Illustration of instantaneous fuzzy skill score for trajectory evaluation. For clarity only a single membership level is shown.

3.4. Model Evaluation

3.4.1. Skill Score

Drift trajectory models are generally evaluated for their ability to predict a drifting objects position at a snapshot in time (Molcard et al., 2009), as well as their ability to predict the complete path the object took to arrive at this position (Liu and Weisberg, 2011). The latter is a more difficult test, as it requires that the timing, magnitude, and direction of forcing events are captured correctly, whereas the former only requires that the cumulative effect of forcing events up to the time the snapshot is taken is correct. For the purposes of this paper we only evaluate the model performance at snapshots in time.

Our evaluation of model skill is based on the approach outlined in Molcard et al. (2009) and also used in Nudds et al. (2020). We adapt the approach for application to fuzzy results as follows. Model skill is calculated as a weighted sum across the membership levels, $j = 0, 1, ..., m$. Predictions with no skill receive a score of zero, while a perfect prediction receives a score of one.

$$Skill = \frac{\left(1+\beta\right)\left(1 - min\left(1, \frac{s}{d_{obs}}\right)\right) + \sum_{j=0}^{m-1}\left(f_j \frac{j}{m} + \beta\right) min\left(1, \frac{d_j}{X_{dj}}\right)}{\sum_{j=0}^{m}\left(\frac{j}{m} + \beta\right)} \tag{22}$$

The distances relevant to Equation (22) are illustrated in **Figure 3**. The first term in the numerator is the crisp instantaneous skill score, as in Nudds et al. (2020). The distance between the observed and modeled drifter positions, s, is normalized by the distance the observed drifter has traveled, d_{obs}, since a prediction within a fixed s should be considered more skillful as d_{obs} increases (Liu and Weisberg, 2011). This instantaneous skill score becomes zero if $s > d_{obs}$. β is a positive constant (arbitrarily set to 0.1 here) to ensure some skill is assigned to the predictions in the lowest membership level ($j = 0$). The exact value of β is unimportant.

The second term in the numerator is added to assign skill for each membership level $P_{\vec{x}}^{(j)}$ that contains the observed position.

f_j is set equal to $-\beta\frac{m}{j}$ if the observed drifter is not within membership level j, and equal to 1 otherwise. To ensure that overestimation of uncertainty negatively impacts skill scores, scores are reduced proportionally to the ratio of the distance across the membership level, X_{dj}, and the mean displacement of the predicted drifter positions within the membership level d_j. A time series of skill can be derived by solving Equation (22) for each model time step.

3.4.2. Leeway Model Comparison

To contextualize the performance of the proposed drift prediction scheme we compare our results to analogous predictions made using the commonly used leeway method (Breivik and Allen, 2008; Breivik et al., 2011, 2013). In this method, the drift of an object is described as the sum of it's downwind, crosswind, and current-driven motion. The wind-driven component of the motion is object-specific and described using a set of nine coefficients, empirically determined for each object (Allen and Plourde, 1999; Breivik et al., 2011), which describe linear fits of the motion to the downwind, left-crosswind, and right-crosswind components of the motion along with error terms around these fitted values. Uncertainty is considered by perturbing the error terms using a Monte Carlo scheme (Breivik and Allen, 2008). For more details on the leeway method, interested readers are referred to Breivik and Allen (2008) and other works referenced herein.

The trajectories of each drifter type were simulated using the formulation of the leeway model in the OpenDrift trajectory modeling suite (Dagestad et al., 2018), by choosing the leeway object class which most closely corresponds to each drifter type (given in section 4). Simulations were performed using an ensemble of 5,000 particles released in a 100 m radius around the deployment site of the drifters.

For quantitative comparison of the proposed fuzzy number—based method with the leeway method, the results of the leeway method were described as a fuzzy number to enable scoring using the algorithm presented in the previous subsection. To convert the distributions of the 5,000 simulated particles into a fuzzy number, the relative particle density was calculated on a 1 km horizontal grid and this gridded density was then converted to a 2-dimensional fuzzy number by a slight modification of the algorithm presented by Khan and Valeo (2016), which enables the construction of fuzzy numbers from histograms of observed scalar data. Here the binned data comprising the histogram is sorted from largest to smallest bin count, and a membership of 1.0 is assigned to the coordinates of the bin with the largest count. The membership at coordinates corresponding to bins with lower counts is determined as the sum of the relative observation density in all bins lower than that under consideration to satisfy the consistency principle. For a detailed description of this method of constructing fuzzy numbers please refer to Khan and Valeo (2016). To adapt this method to two dimensional data, the coordinates of the bin centers were expressed as a complex number $\vec{x}_{bin} = x_{bin} + iy_{bin}$ and fixed membership levels were determined by delineating the area encompassing all bins with membership greater than or equal to the chosen level. Scoring of the leeway simulations was conducted according to section 3.4.1 once the simulated particle distribution was fuzzified in this manner.

4. FORCING AND VERIFICATION DATA

The observational data used to test the methods presented in sections 2 and 3 was collected near Ocean Station Papa (OSP) in the northeast Pacific during the period Feb 19–Mar 3, 2015. OSP (50.1°N, 144.9°W) has been the site of meteorological and oceanic observations since the early 1940's, and currently hosts a moored observation platform operated by the Ocean Climate Stations Office of NOAA/PMEL (Freeland, 2007). Detailed descriptions of the circulation and water properties at OSP are given in publications such as Pelland et al. (2016) and Cummins and Ross (2020). We make use of measurements of currents and winds recorded at the moored observation platform during a release of 44 ocean surface drifters nearby. The drifter tracks, as well as time series of the winds and currents measured at OSP, are shown in **Figure 4**.

Near-surface currents at OSP are recorded by a single-point 2 MHz Nortek Aquadopp current meter moored in a taut-line configuration at 15 m depth as well as a down-ward looking 300 kHz RDI Sentinel ADCP at 2 m below the water surface. Both instruments sample data over a period of 2 min. The current meter reports data at 10 min intervals, while ADCP profiles are reported at 30 min intervals (National Oceanic and Atmospheric Administration, Pacific Marine Environmental Laboratory, 2020a). The reported current meter accuracy is ±(1% of velocity + 0.5 cms^{-1}), while the accuracy of the ADCP is reported as ± 0.5 cms^{-1}. Both sensors have a resolution of 0.1 cms^{-1}. Winds are recorded 4 m above the water surface by a Gill Windsonic anemometer and averaged to 10 min intervals, with a reported accuracy of ± 2% (3%) of the speed (direction) reading, and a resolution of 0.01 ms^{-1} (1°) (National Oceanic and Atmospheric Administration, Pacific Marine Environmental Laboratory, 2020b).

The current meter record at 15 m depth (**Figures 4C,D**) initially shows northeastward flow in response to northwesterly winds (**Figure 4E**), consistent with descriptions of wind-driven flow in the upper ocean dating back to Ekman (1905). As winds slacken between midday on Feb 21 and the evening of Feb 23, signals consistent with inertial oscillations appear in the current data.

Visual comparison of the current meter record with data from the closest ADCP measurement (centered at 16 m depth) during the first 7 days of the experiment (**Figures 4C,D**) reveals that the current meter indicates higher amplitude of low frequency fluctuations in the flow, and shows less spiking than the ADCP. A more detailed comparison (included in the section 1.2 of the **Supplementary Material**) reveals further differences between the two instruments. The current meter records a northeastward mean flow of ∼ 3–4 cms^{-1}, while the mean flow recorded by the ADCP is much smaller and in the opposite direction. This appears to be a systematic discrepancy between the two instruments. Differences between the two instruments could be due to interference from the point current meter on

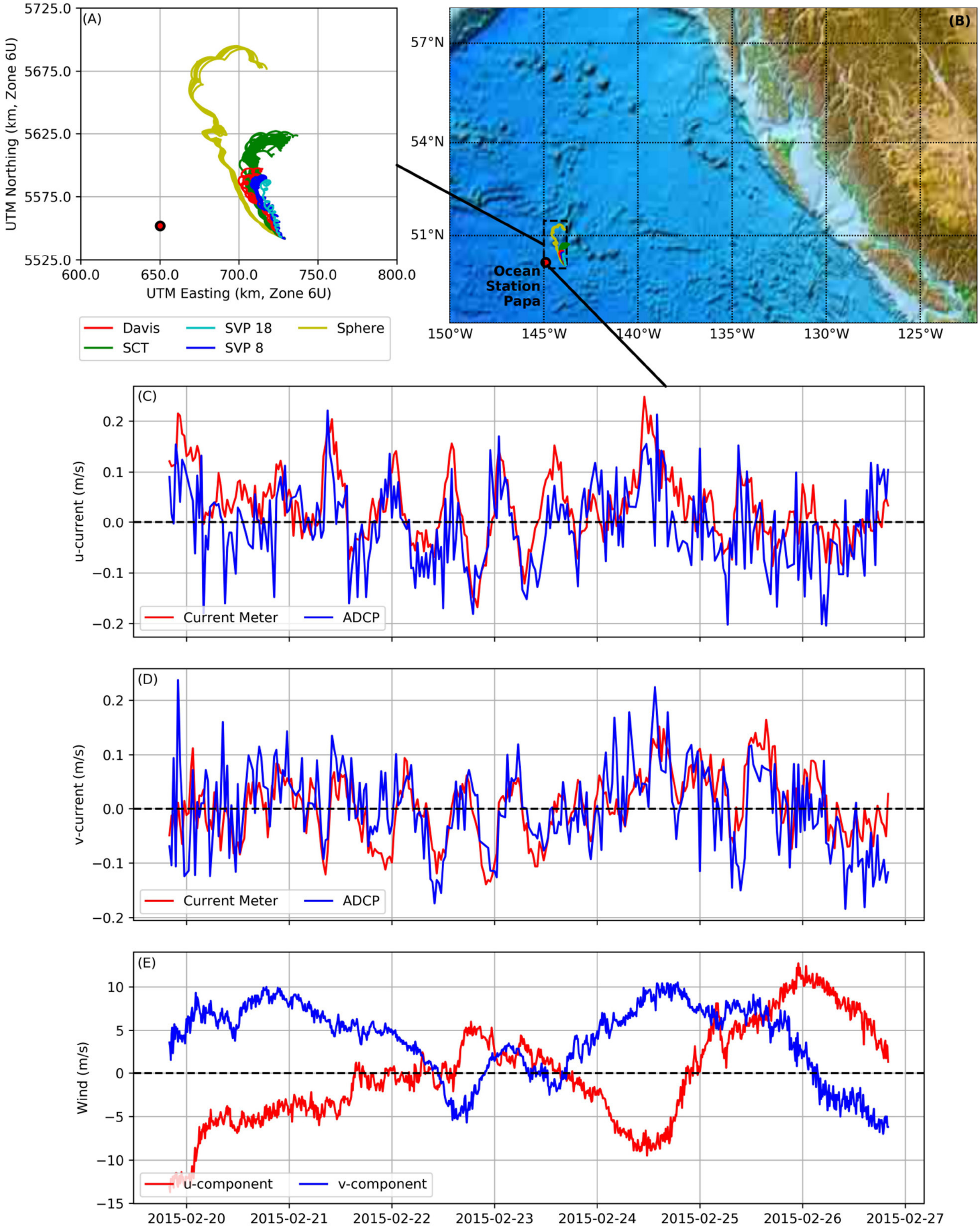

FIGURE 4 | Tracks of drifters for 7 days after deployment near Ocean Station Papa **(A,B)**, and time series of u,v components of currents **(C,D)** and wind **(E)** during the deployment.

the beams of the ADCP (Nathan Anderson, PMEL, personal communication, September 2021) or due to the differences in operating frequency and sampled volume of water (Richard Thomson, DFO, personal communication, September 2021). Drifter trajectories are computed and assessed using the data from both instruments, in order to test which instrument provides more relevant information.

On February 19, 2015 at approximately 20:30H UTC, 44 ocean surface drifters of five different geometries were deployed approximately 75 km east of OSP. These included the following: 8 Sphere drifters which float mostly above the water surface; 28 Surface Circulation Tracker (SCT) (Oceanetic Measurement Ltd., 2016) drifters which float in the upper 37.5 cm of the water column and have been shown to reasonably reproduce oil sheening (Blanken et al., 2020); 3 Davis drifters (Davis, 1985) which float in the upper 1.5 m of the water column and are similar to the SLDMB drifters commonly used for search and rescue applications; and 5 drifters based on the Surface Velocity Program (SVP) design (Poulain and Niiler, 1989; Niiler et al., 1995), 4 with the 4.6 m holey-sock drogue starting at ∼8 m depth (hereafter SVP 8) and one starting at ∼18 m (hereafter SVP 18). SVP drifters are generally used to map near-surface ocean circulation. One of the SCT drifters failed shortly after deployment. Pictures of the drifters and their idealized geometry and drag coefficients are shown in **Figure 5**. Most drifters transmitted data until Mar 3, 2015, however we only consider the first 7 days of the deployment in this study. During this time drifters were within 55–150 km of OSP (**Supplementary Figure 3**). To simulate the trajectories of these drifter types using the leeway method, the following object types were chosen as proxies: Sphere − > bait box (lightly loaded); SCT − > WW2 mine; Davis − > oil drum; SVP (8 and 18 m) − > person-in-water floating vertically. The corresponding leeway coefficients are reproduced in **Supplementary Table 1**.

All drifters followed a mean northeastward trajectory during the first 5 days of their deployment (**Figure 4A**), consistent with the mean wind direction during this time, with a change to westward drift coincident with a change in the wind direction. The lengths of the trajectories are inversely related to drogue depth of the drifter. The Sphere drifter trajectories are approximately twice as long as those of the SCT drifters, which are in turn longer than the Davis, SVP 8, and SVP 18 drifters. The latter three drifter types, which are drogued deeper in the water column, exhibit clockwise looping which is likely due to inertial oscillations like those noted in the current meter record.

5. RESULTS

5.1. Fuzzy Forcing

Converting the current and wind record into fuzzy number equivalents using the procedures described in section 3.2 shows that the uncertainty in these measurements is appreciable once aggregated. To begin, we fit power laws to the tail of the wind and current meter spectra using log-transformed linear regression between frequencies $\frac{1}{2x7200sec}$ and the Nyquist frequency, f_N. The low-frequency threshold is chosen by visual inspection of the energy spectra (**Supplementary Figure 4**). The parameters to the regression Af^B as well as the amplitude of the unresolved velocities and accelerations according to Equations (18) and (19) are given in **Table 1** for a model timestep dt_{model} = 300 s. The amplitude of the unresolved energy A_v is approximately three to five times the instrument uncertainty for the anemometer and the current meter but approximately 17 times larger for the ADCP. This is at least in part due to the longer output interval of the ADCP but also due to the shallower spectral slope that suggests additional noise at high frequencies, as was noted from visual inspection of the time series in section 4.

Uncertainty due to spatial variability is estimated by examining the current fields from the GLORYS12 ocean re-analysis. GLORYS12 is a state-of-the art hindcast numerical simulation of ocean conditions from 1993-present, with data assimilation of satellite altimetry and temperature measurements as well as *in situ* profiles of temperature and salinity (Lellouche et al., 2021). The modeled daily-mean currents at 15 m depth suggest significant spatial structure with maximum fluctuations in current amplitude of ∼0.2 m/s over the duration of the experiment (see **Supplementary Figure 5**). Comparing the modeled currents at OSP to daily averages of the measurements from the current meter and ADCP suggests that at OSP the modeled currents are biased southeasterly by ∼0.045 m/s with respect to the current meter, and easterly by ∼0.05 m/s with respect to the ADCP. RMS errors of the modeled velocity components are ∼0.04–0.06 m/s. A comparison of the modeled currents at the drifter locations with the modeled current at OSP also suggests that currents at OSP are directed more southeasterly than at the drifter locations, with a bias of ∼0.075 m/s and RMS errors of 0.01–0.02 m/s for all drifters except the Sphere drifters which travel further and therefore sample more variability (see **Supplementary Figures 3, 6**). However, there is considerable uncertainty about the accuracy of the mean difference in the modeled currents between the drifter location and OSP given that this difference corresponds well with the identified bias in the currents at OSP. A plausible explanation is that the features shown in **Supplementary Figure 5** may be slightly misaligned in the model. For the purpose of this paper, we approximate uncertainty due to spatial variability by taking $\sigma_s = 0.015$ m/s as the standard deviation of the differences between the modeled currents at OSP and the drifter locations. As the modeled currents leave some doubt about the relevance of the currents at OSP to the drifter locations, trajectories are computed with and without forcing from the measured currents as is later discussed in section 5.2. Further assessment of the modeled surface dynamics in GLORYS12 can be found in Lellouche et al. (2021). As noted previously, the effect of uncertainty in modeled ocean currents on trajectory prediction will be further investigated in future work.

Once uncertainties have been quantified, the current and wind data are converted to a fuzzy number using the probability-possibility conversion in Equation (13). We expect that the uncertainty due to unresolved time scales will follow a distribution that is similar to that obtained by simulating a red noise process with an f^B spectral slope and variance corresponding to the sum of A_v, σ_s, and σ_i (shown for the current meter record in **Supplementary Figure 7**). This

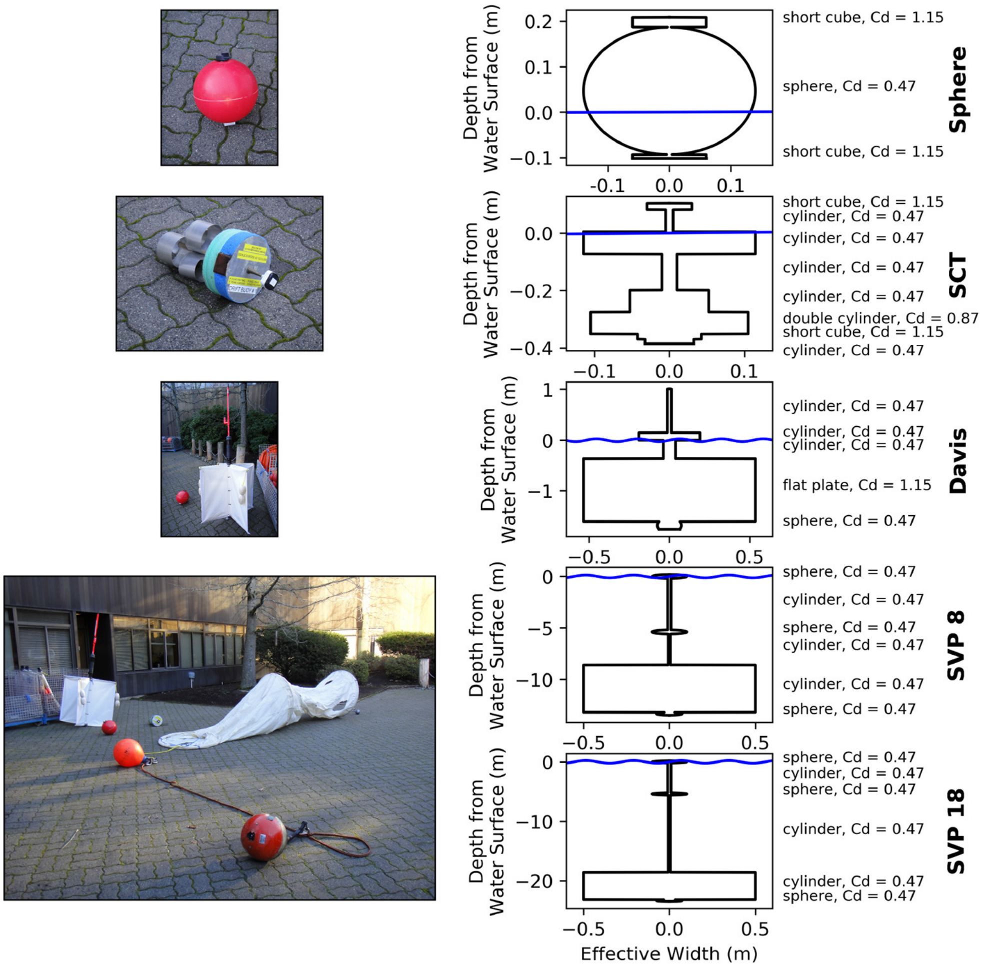

FIGURE 5 | The drifters deployed for this study (left), and their idealized geometry, including approximate drag coefficients (right). The SVP 8 (bottom-left photograph) and SVP 18 drifters (no photograph shown) are identical except for the length of the tether.

TABLE 1 | Amplitude of energy in unresolved timescales and associated power law coefficients.

Data source	A	B	A_v (m/s)	$A_a dt_{model}$ (m/s)
Anemometer	0.19	–0.97	0.46	0.17
Current meter	1.77×10^{-3}	–0.73	0.020	0.0074
ADCP	0.084	–0.49	0.088	0.026

distribution is better represented by a Laplace distribution than by a Gaussian distribution, though both overestimate the tails. The random instrument uncertainty is more likely to follow a Gaussian distribution. Since the unresolved energy in the current data, especially for the ADCP, is significantly larger than the instrument uncertainty we convert it to fuzzy numbers using a Laplace distribution, while a Gaussian distribution is chosen for the wind record. The effect of the choice of distribution should be further investigated, however this is beyond the scope of the current study. Applying Equation (13) with the above distributions, A_v from **Table 1**, σ_s from above, σ_i from section 4, and four equally spaced membership levels on the interval $[0, 1]$, i.e. $m = 3$, yields the fuzzy time series shown in **Figures 6A–D**. The number of membership levels is limited by the computational expense of the current shear calculation. This may be mitigated by employing alternative parameterizations for current shear, however a detailed comparison of possible parameterizations is beyond the scope of the current work.

The fuzzified winds and currents exhibit uncertainties that at times exceed 5 m/s for winds and 0.2 m/s for currents at the lowest membership level, during times when winds and currents are strong. The influence of the relative instrument uncertainty on overall uncertainty is clearly seen in the reduced width of the fuzzy numbers when wind speeds are low, between midday on Feb 22 and midday on Feb 23 (**Figure 6**).

Transforming the fuzzy winds according to Equation (14) allows us to calculate fuzzy values of Stokes drift, current shear, and wind shear according to the procedures outlined in sections 2.1 and 2.2. The time series of these fuzzy vectors are shown in **Figures 6E–J**. Here only values for SCT drifters derived using

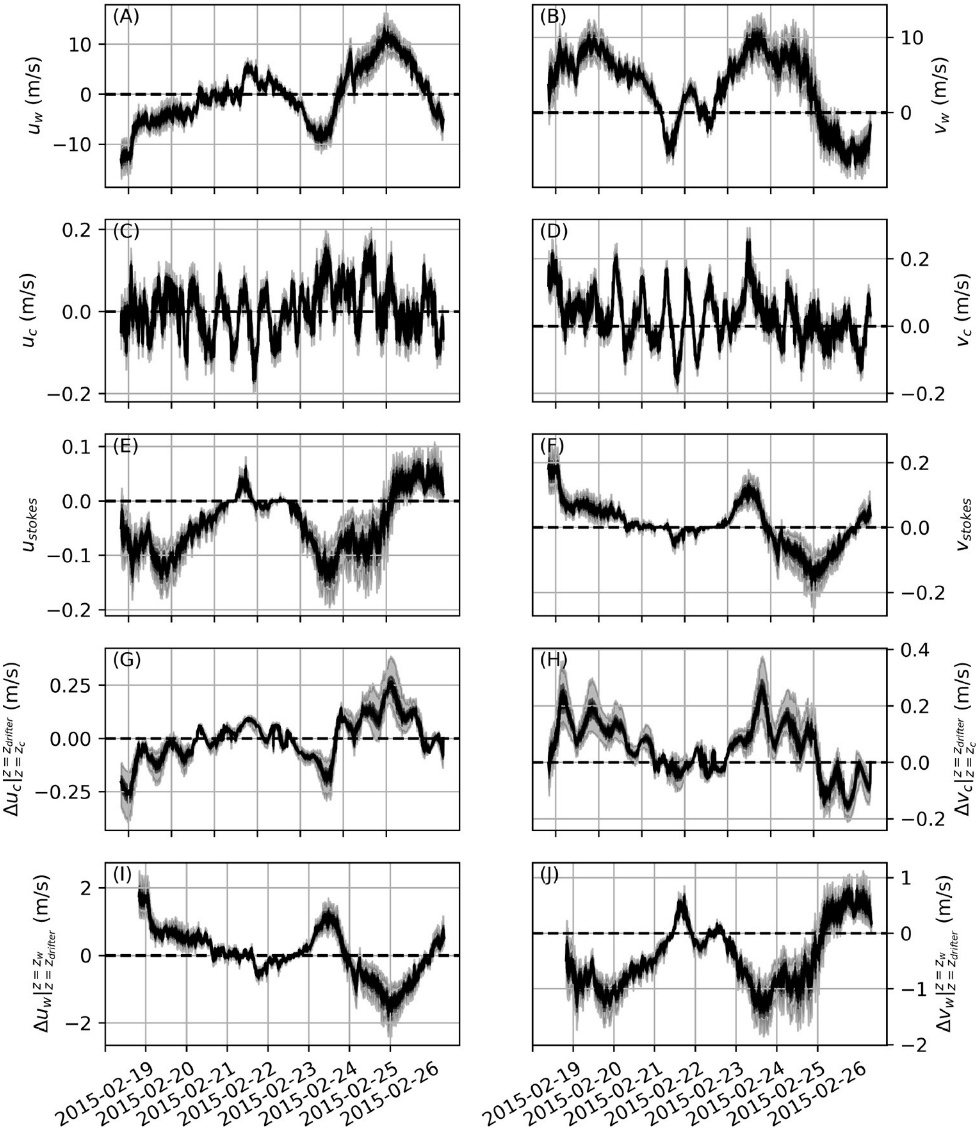

FIGURE 6 | Components of fuzzy wind **(A,B)**, current **(C,D)**, Stokes drift **(E,F)**, current shear **(G,H)**, and wind shear **(I,J)** for the first 7 days of the drifter deployment. The crisp value (measurement) is shown in black and the three fuzzy membership levels are indicated in grayscale. For clarity in **(E–J)** only values for SCT drifters with the velocity profile applied by the "centroid" scheme are shown.

the centroid method (Equation 7a) are shown for clarity. These variables were calculated for each drifter separately by each of the three methods of applying the shear profile given in Equation (7). Stokes drift and current shear on the near-surface SCT drifters are strongly positively correlated with the wind velocity, though both diminish significantly when wind speeds are below ∼5 m/s. During times of strong winds both Stokes drift and current shear are comparable to, or larger than, the measured currents. These terms are therefore expected to have first order impacts on the drift trajectory prediction, consistent with the findings of Röhrs et al. (2012). During strong winds the magnitude of the uncertainty (i.e., the width of the lowest membership level) in the estimated Stokes drift and current shear is comparable to the magnitude of the estimate itself.

Wind shear appears to be a minor factor compared to Stokes drift and current shear. As expected, $\Delta\vec{u}_w|_{z=z_{drifter}}^{z=z_w}$ is inversely correlated with wind velocity, i.e., it reduces the effective wind velocity in Equation (17). The magnitude of wind shear is at most ∼20% of the wind speed, and subject to similar relative uncertainties as Stokes drift and current shear.

5.2. Optimal Forcing Combinations

Drift trajectories were computed for all combinations of forcing terms on the right-hand side of Equation (17), methods of applying sheared forcing as per Equation (7), and sources of current data (current meter or ADCP). Trajectories were then scored at each time step using Equation (22) to determine the optimal combination of parameters by identifying the

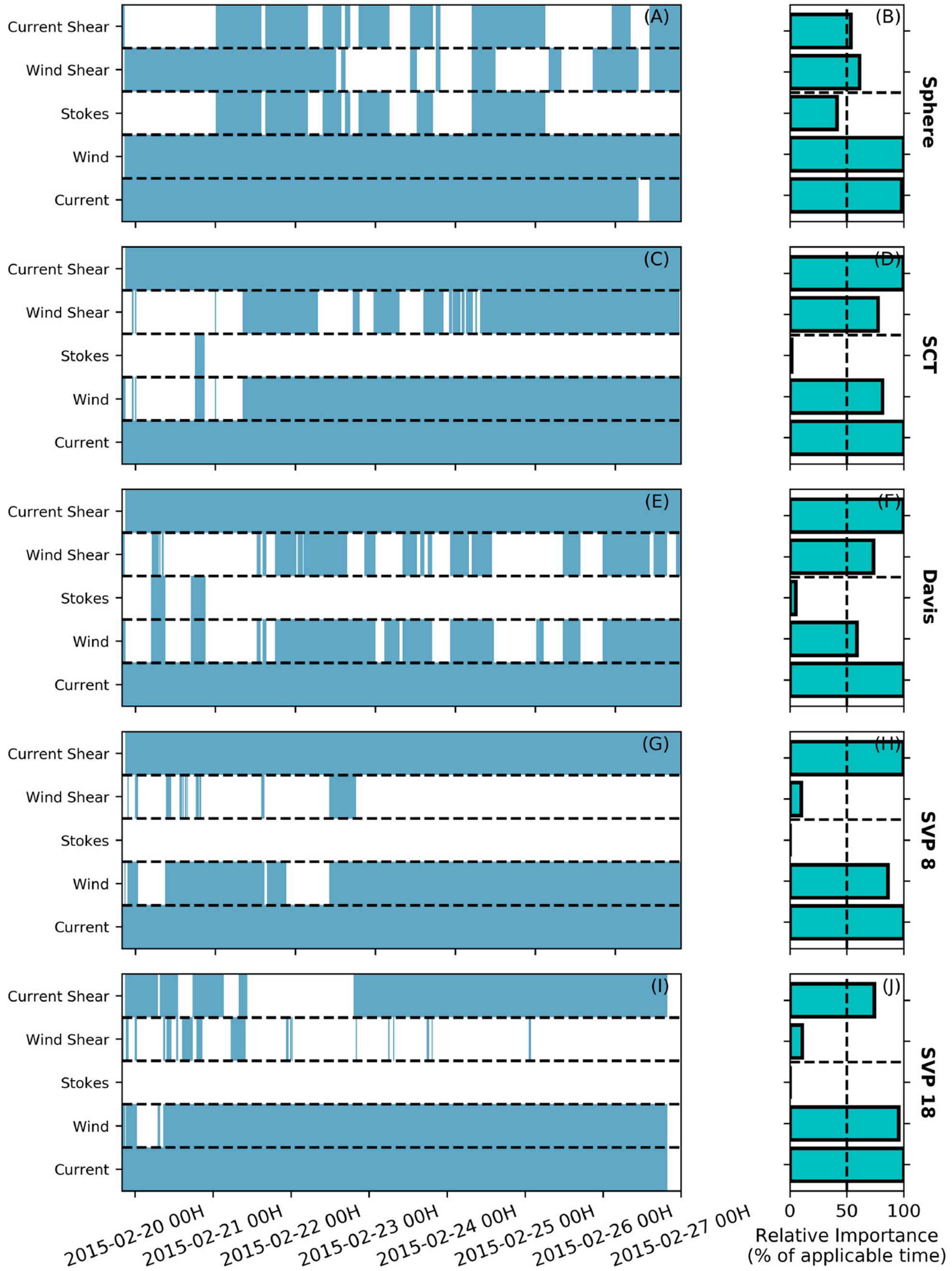

FIGURE 7 | Summary of optimal forcing terms for each drifter as a function of time. In the left-hand **(A,C,E,G,I)**, timesteps where a forcing term contributed to the solution achieving the highest skill score are shaded in blue for each drifter type. In the right hand **(B,D,F,H,J)** the percentage of applicable time each forcing term contributed to the optimal solution is summarized.

combination giving the highest skill score at each time step. We consider a forcing term to be part of the optimal solution if it is present in the solution with the highest skill score, for at least 50% of time steps. Wind shear is only considered during times when wind drag is an important forcing term, however current shear may be considered independently of measured currents. The optimal combination of forcing terms as a function of time is summarized for each drifter in **Figure 7**. The percentage of time each of the three methods of applying profile shear (Equations 7a–c) was most suitable is summarized in **Figure 8**. The optimal parameters for each drifter, and the trajectories predicted using these parameters, are shown in **Figures 9–13**.

Current, wind, and current shear all play an important role in predicting the trajectories of the drifters, and wind shear is

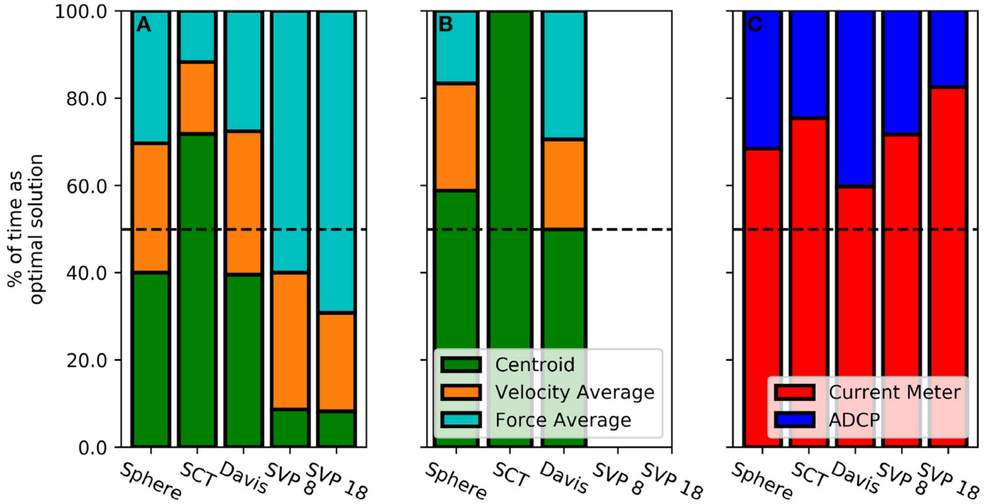

FIGURE 8 | Percentage of time current shear **(A)** and Stokes drift **(B)** profiles applied *via* the centroid and area-weighted average of velocity or force produce the optimal solution for a the trajectories of each of the five drifters. No results are shown for Stokes drift on the SVP drifters, as the analysis indicates that Stokes drift does not contribute to the optimal trajectory prediction at any time. **(C)** Shows the percentage of time the currents measured by the current meter (red) and the ADCP (blue) contribute to the optimal solution.

an important term for the near-surface drifters (Sphere, SCT, and Davis) (**Figure 7**). This suggests that the importance of wind shear increases with the magnitude of the wind drag term. Since forcing from measured currents is consistently part of the optimal solution, we conclude that currents measured at OSP are relevant to the drifter location, despite the separation between these locations. In 60–80% of instances, forcing with the currents measured by the current meter produced a better solution than forcing with currents measured by the ADCP (**Figure 8C**). This is likely due to the higher reporting frequency (every 10 min for current meter compared to every 30 min for ADCP), as well as the possible high frequency noise in the ADCP record discussed earlier. Stokes drift is not part of the optimal solution for any drifter type. It is more frequently of importance for the near-surface drifters however, and not important at any time for the SVP drifters. A possible explanation is that Stokes drift may lag behind wind forcing as the wave field responds to changes in the wind. In general, the potential effects of Stokes drift should be further investigated by a sensitivity analysis to both different methods of calculating Stokes drift as well as time-lagged methods of applying this forcing. The optimal forcing terms are often simultaneously applicable in the latter half of the simulation period, however this is less likely to be the case during the first half of the simulation period. A possible explanation for this is that the lower winds during the first half of the simulation period result in more small scale current variability, such as inertial oscillations, which are not captured in the measurements at OSP.

The deterministically derived wind drag factor, α, from Equation (5) produces appropriate results. Values of α are 5.43, 1.00, 0.53, 0.28, and 0.27% for the Sphere, SCT, Davis, and SVP 8 and 18 drifters, respectively. The values calculated for the SVP drifters agree well with the slippage estimate of 0.2% of the wind speed given by Poulain and Niiler (1989). To assess the sensitivity of the results to the wind drag factor, the changes in mean skill score for trajectory predictions made using values ranging from 0.5α to 1.5α are given in **Table 2**. For the near-surface drifters any increase in the wind drag factor degrades the predictions, while decreases in the wind drag factor can improve the prediction. This improvement is minor (maximum 5.5%) for the SCT and Davis drifters, but can be significant (up to 78% for a 25% reduction of α) for the Sphere drifters. This suggests that perhaps wind shear is underestimated here, which may be expected as winds are calculated at a 1 m reference height while the bulk of the exposed drifter parts are within 0.2 m of the water surface. It is also possible that some dynamics associated with objects that are primarily above the water surface are not captured here, as suggested by the significant differences in the Sphere drifter results. Altering the wind drag factor for the SVP drifter generally resulted in a negligible change to the results. Decreasing α generally resulted in a small (maximum 3.1%) decrease in skill while increasing α resulted in a similarly small (maximum 3.4%) increase in skill.

Optimal methods of applying sheared forcing vary by drifter type. For applying current shear, the centroid method produces the best results for near-surface drifters, while the area-weighted force method produces the best results for the SVP drifters (**Figure 8A**). The grouping of these results is likely in part due to the 1 m vertical discretization used in solving for the current shear, which results in approximately linear velocity profiles over the draft of the near-surface drifters as these are almost entirely in the uppermost vertical level. For the longer SVP drifters, the effect of nonlinearities in the vertical velocity profile becomes both more relevant and better resolved. The centroid method provides the best results for applying Stokes drift for all applicable drifter types (**Figure 8B**).

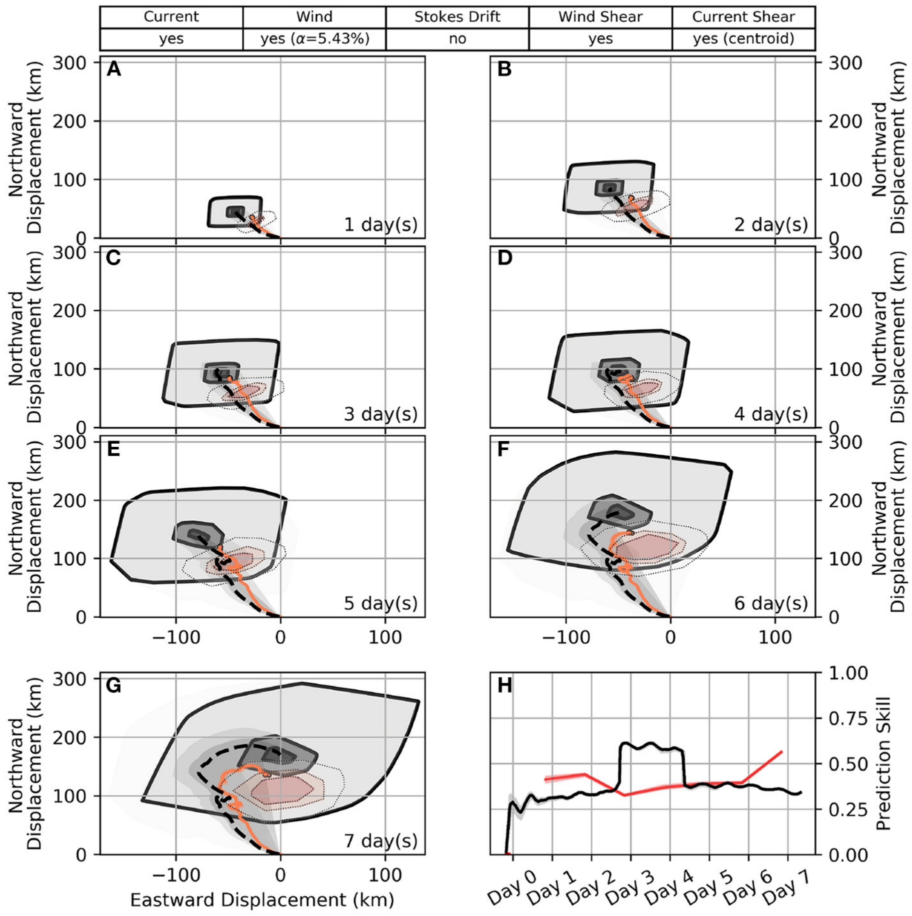

FIGURE 9 | Daily predicted tracks of the sphere drifters for 7 days after deployment using the indicated optimal forcing combination **(A–G)**, and a time series of model skill during this period **(H)**. Membership levels of the possible displacement, $P_{\vec{x}}^{(j)}$ for $j = 0, 1, 2$, are indicated in grayscale shading, increasing in intensity toward the crisp solution ($j = 3$) which is indicated by the dashed black line. Equivalent results obtained using the leeway method are shown in red shading. Observed drifter tracks are superimposed in orange. Model skill is also shown in grayscale for the optimal forcing combination and in red for the leeway method. Shading indicates the maximum and minimum skill for the ensemble of drifters, while the solid line indicates the mean. Red markers on the x-axis of the skill plot indicate times when at least one observed drifter fell outside of the lowest membership level.

5.3. Trajectory Results

The optimal forcing combinations for each drifter lead to predictions that are skillful (i.e., the observed positions remain within the lowest membership level) for at least 7 days. The observed and predicted trajectories of the Sphere, SCT, Davis, SVP 8, and SVP 18 drifters as well as the time series of model skill associated with the prediction are shown in **Figures 9–13**. The analogous results from the leeway method and associated skill scores are also shown.

The trajectories of the near-surface drifters (Sphere, SCT, and Davis) are generally well predicted, especially for the SCT drifters (**Figures 9–11**). In the first 2 days of the simulation, the length of all three trajectories is slightly under-predicted, however the model results converge with observations by the third day. This convergence coincides with a shift in the winds from consistent winds toward the northwest to weaker and more variable winds. The predicted trajectories of the Sphere drifters consistently veer slightly to the west of the observations. On the fifth day of the simulations, the behavior of the three near-surface drifter types diverges. From here, the northward extent of the Sphere drifter trajectories is over-predicted and the predicted trajectories of the Davis drifters begin to shift eastward of the observations, while the predicted tracks of the SCT drifters remain close to the observations. Modeled tracks of both the Sphere and Davis drifters continue to propagate eastward at a higher rate than is observed on days 6–7, while the trajectories of the SCT drifters remain close to the observations. During this time the dispersion of the cluster of SCT drifters becomes comparable to the scale of the 0.67 membership level, which suggests that the size of these membership levels corresponds well with natural dispersion processes associated with unresolved high-frequency fluctuations in the forcing data.

The near-surface drifter locations predicted by the leeway method tend to be slightly to the southeast of the locations predicted by the proposed fuzzy method, with the observed positions in between the two sets of model results. The lowest

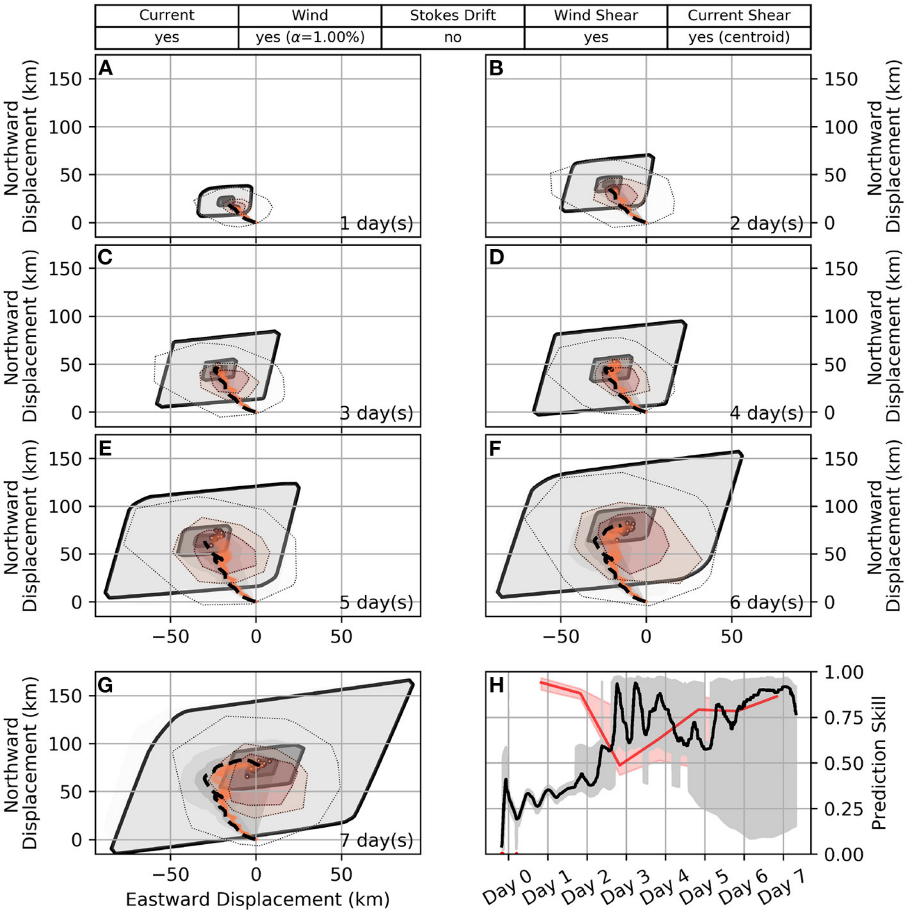

FIGURE 10 | Daily predicted tracks of the SCT drifters for 7 days after deployment using the indicated optimal forcing combination **(A–G)**, and a time series of model skill during this period **(H)**. Same layout as **Figure 9**.

membership level of the predicted positions is larger for the proposed fuzzy method than for the leeway method, while the intermediate membership levels are larger for the leeway method. Skill scores for the two models are quite similar. Whenever a particular model captures one or more of the observed positions in an intermediate membership level (0.33 or 0.67), its skill will rise above the other model temporarily. The skill of the leeway method is higher near the beginning and end of the simulation, however the proposed fuzzy method often has higher skill overall during the intermediate period due to the smaller intermediate membership levels.

For the more deeply drogued SVP drifters, the trajectory length is generally slightly under-predicted and the modeled trajectories also begin to veer eastward of the observations around the fourth day of the simulation. After this point, the modeled trajectories strongly diverge eastward of the observations. The center of the predicted positions is similar between the proposed fuzzy method and the leeway method however, contrary to the near-surface drifters, the membership levels of positions predicted by the leeway method are generally larger than those from the fuzzy method here. Again the skill score of the two methods is similar, with the leeway method scoring higher near the beginning and end of the simulation while the fuzzy method scores higher in the intermediate period.

6. DISCUSSION

The fuzzy number based scheme for describing and propagating uncertainty in trajectory predictions proposed in this paper appears to work well, given that the predicted sets of possible displacements covered the observed position of the drifters. The scheme is advantageous in that it does not require specification of empirical coefficients, and can be applied anywhere concurrent measurements of wind and currents are available. Future work to extend the scheme to include forcing data from numerical models will further expand its utility. The work presented here can also be readily extended to arbitrary or unknown object geometries by describing the direct wind drag coefficient, α, as a fuzzy number.

Regarding the representation of uncertainty, it is worthwhile to consider whether displacements in the lowest membership level should be reported, given that they are representative

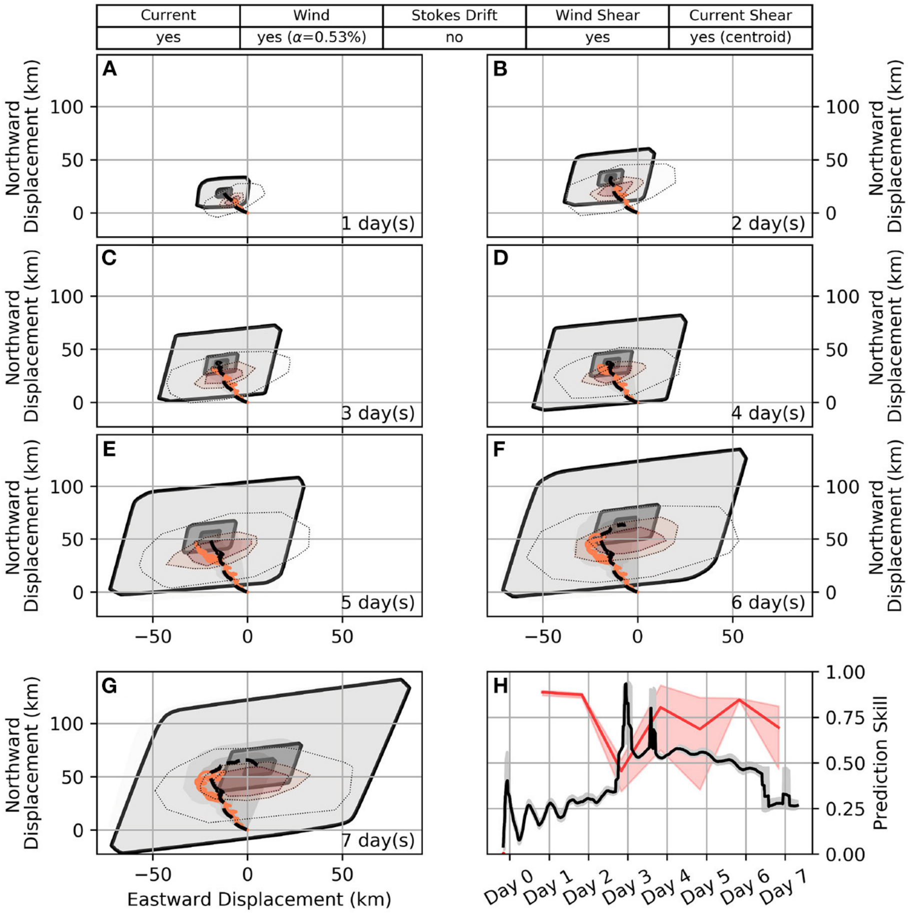

FIGURE 11 | Daily predicted tracks of the Davis drifters for 7 days after deployment using the indicated optimal forcing combination **(A–G)**, and a time series of model skill during this period **(H)**. Same layout as **Figure 9**.

of the largest displacements thought to be possible, without making claims about the probability of such displacements (by definition of a possibility distribution). It is noted that the lowest membership level at times overestimated the uncertainty of predicted positions, which is to be expected as the probability density functions transformed to derive the fuzzy currents and winds were noted to overestimate the extreme values (i.e., the tails) of the represented uncertainty. The form of the input fuzzy numbers clearly affects the results of the trajectory model, similar to previous results from Khan et al. (2013). Increasing the number of membership levels in future work may help resolve this question by better resolving the skill score and the lowest membership level containing observed drifters. However, increasing the number of membership levels comes with significant increases in computational demands, and the 'lowest useful' membership level will always vary as a function of the forcing data quality.

Direct wind drag is a dominant forcing factor on all considered drifter types, and it is shown that a deterministic, geometry-based wind drag coefficient leads to skillful predictions for at least 7 days when the uncertainty in the forcing data is propagated through the prediction (**Figures 9–13**). However, the determined wind drag coefficients at times over-predicted the trajectory length for near-surface drifters and lower values of α would have resulted in higher model skill. Conversely, for the SVP drifters trajectory lengths were slightly under-predicted even without the addition of Stokes drift and wind shear terms, and higher values of α would have resulted in slightly increased model skill (see **Table 2**). Therefore, some uncertainty remains around the processes relevant to the down-wind components of the motion, as direct wind drag, part of the current shear, and Stokes drift act co-linearly and their relative importance is less clear when the uncertainty in the wind forcing is accounted for. Due to this ambiguity in the co-linear forcing terms, a single set of leeway coefficients describing the down-wind motion was noted as beneficial in Breivik et al. (2011). However, within the framework proposed here, further sensitivity analysis of the parameters of the Stokes drift and current shear parameterizations in the proposed method may provide clarification of this ambiguity, though this is beyond the scope of the current paper.

The model proposed here avoids the need to specify empirically determined leeway coefficients while retaining results

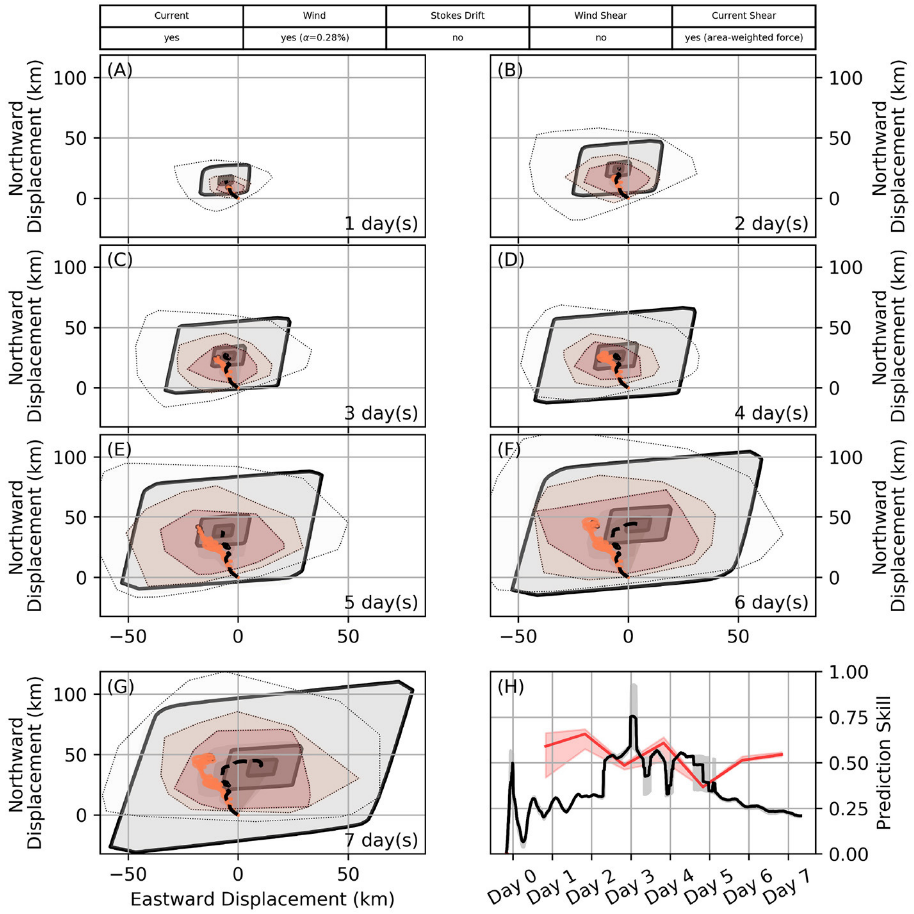

FIGURE 12 | Daily predicted tracks of the SVP 8 drifters for 7 days after deployment using the indicated optimal forcing combination **(A–G)**, and a time series of model skill during this period **(H)**. Same layout as **Figure 9**.

of a similar quality to the commonly used leeway method. This is a clear benefit, as leeway coefficients are not available for every object type and may not be representative of an object for which no coefficients have been determined. This is evident when comparing the correspondence of the leeway and fuzzy results for near-surface and SVP drifters. For near-surface drifters the leeway method results in a smaller range of predicted possible positions at the lowest membership level, though the range of intermediate membership levels is larger. This is to be expected as the lowest membership level represents all possible solutions, which may not be realized during a simulation with 5,000 particles. For the SVP drifters however, the leeway method results in a larger area of possible displacements at all membership levels. For near-surface drifters closely aligned proxy objects are available, with leeway coefficients determined by the direct method (current measured during determination) (Breivik et al., 2011). For the SVP drifters, the closest available proxy object is a vertically oriented person in the water which in reality has a much shallower draft than the SVP drifters. The geometry of a vertical PIW is also quite variable, which is represented in the coefficients and results in a larger uncertainty than is predicted by the fuzzy method.

Closer comparison of the modeled and observed trajectories also suggests that not all physics governing the evolution of a drift trajectory are captured by the trajectory model proposed here. The inclusion of uncertainty compensates for this by capturing the resulting discrepancies in lower membership levels, but the effect of the missing physics remains evident. For four of the five drifter types, a significant eastward displacement is predicted during the last 2 days of the simulation, in response to a change in the winds. This displacement is not seen to the same extent in the observations, which may point to a lagged response to wind forcing or spatial variability in the winds between OSP and the drifter locations. The modeled trajectories also more generally tend slightly to the east (left) of the observed trajectories, which may be due to absence of Stokes drift forcing or due to the chosen values of the constants in the current shear parameterization. A sensitivity analysis of these parameters may yield further insight here, but is beyond the scope of the current study. Alternatively, this eastward tendency may suggest that Coriolis-Stokes forcing plays a role, as its inclusion

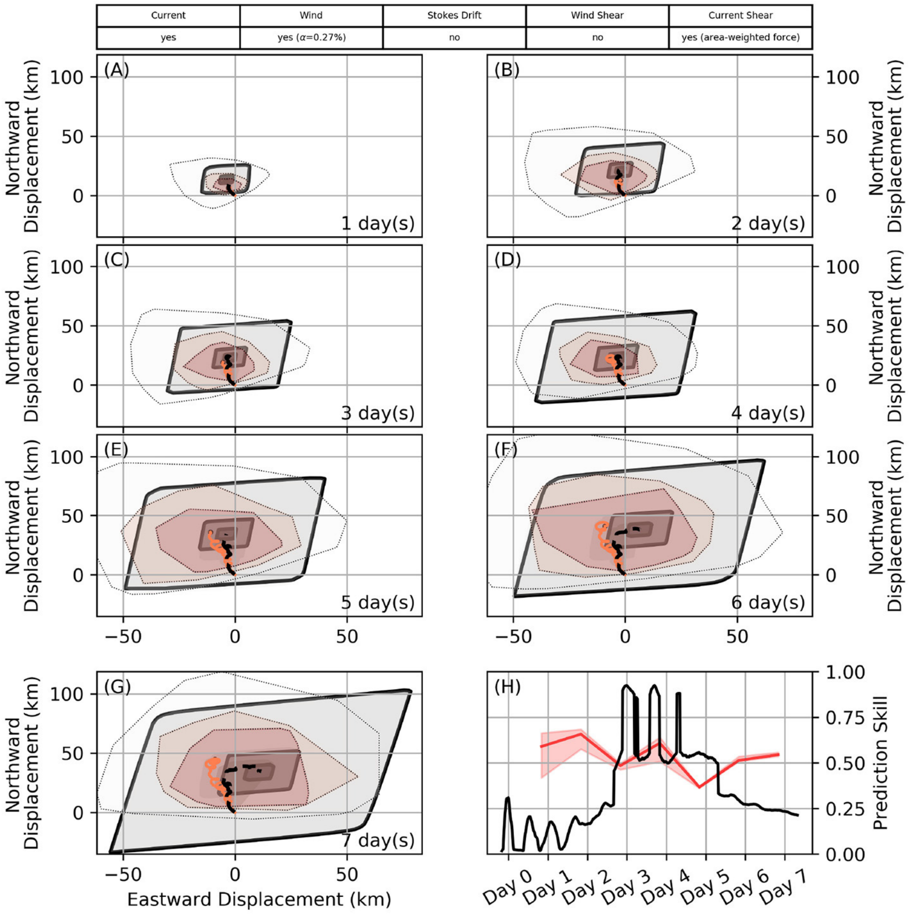

FIGURE 13 | Daily predicted tracks of the SVP 18 drifters for 7 days after deployment using the indicated optimal forcing combination **(A–G)**, and a time series of model skill during this period **(H)**. Same layout as **Figure 9**.

is expected to deflect the surface current further to the right of the wind (Polton et al., 2005; Weber et al., 2015). This may be expected as our estimates of Stokes drift have a similar magnitude to the measured currents, consistent with the results reported by Röhrs et al. (2012). Most common ocean models include parameterizations of Coriolis-Stokes forcing (Röhrs et al., 2012), and therefore extending the method proposed here to numerical modeling results may achieve these improvements and also meet the obvious need for representation of spatial variability in the forcing fields.

TABLE 2 | Percent change in mean trajectory prediction skill for given adjustments to deterministic wind drag factor, α.

	Prediction skill change from deterministic α-value (%)							
Drifter type	**–50%**	**–25%**	**–10%**	**–5%**	**+5%**	**+10%**	**+25%**	**+50%**
Sphere	+17.8	+78.0	+32.5	+12.3	–5.99	–15.8	–35.2	–62.9
SCT	–6.70	+0.97	+2.38	+1.46	–2.55	–5.03	–13.2	–26.1
Davis	+5.48	+3.63	+2.31	+0.87	–1.09	–1.58	–6.17	–17.2
SVP 8	–1.43	–2.15	–1.38	–0.37	+0.53	+0.96	+2.33	+3.37
SVP 18	–3.09	–0.46	+0.27	–0.05	+0.02	+0.11	–0.25	+0.54

7. CONCLUSIONS

Uncertainty in surface drift trajectory predictions is of significant importance when responding to marine contaminant spills and performing search and rescue operations, along with a plethora of other applications. We have presented a method for modeling the trajectories of drifting objects that makes use of fuzzy numbers to characterize the uncertainty inherent in these predictions without relying on specification of empirical dispersion coefficients or random kicks. A comparison of results from this method to observations from five different types of surface drifters suggests that the method works well, and offers similar performance as the frequently used, empirical leeway method. Following a deployment near Ocean Station Papa in the northeast Pacific, 44 observed drifters of five different types remain within the range of modeled possible displacements during the 7 days following their deployment.

Moreover, our results show that the response of drifting objects to direct wind forcing can be reasonably well predicted based on the objects geometry provided that wind-induced Stokes drift and current shear are appropriately parameterized. Even with these parameterizations, we find direct wind drag to be a forcing term of first order importance for all drifters considered here. A novel skill metric for assessing model performance proved to be a useful tool for identifying the optimal combinations of parameterizations. The analysis presented here can be extended to objects of arbitrary geometry, and also unknown or uncertainty geometry when α is expressed as a fuzzy number. Further development and evaluation will expand its utility by incorporating forcing data from numerical models.

DATA AVAILABILITY STATEMENT

Publicly available datasets were analyzed in this study. This data can be found here: www.waterproperties.ca; www.pmel.noaa.gov/ocs/data/disdel/; https://resources.marine.copernicus.eu/?option=com_csw&view=details&product_id=MULTIOBS_GLO_PHY_REP_015_004.

AUTHOR CONTRIBUTIONS

TJ: observation campaign. HB, CH, CV, and UK: conceptual design. HB, CV, and UK: method development. HB and CH: data analysis. HB and TJ: figures and tables. HB: writing. CV, CH, UK, and TJ: editing. All authors contributed to the article and approved the submitted version.

FUNDING

This work was supported through the Oceanography sub-initiative of the Government of Canada's Oceans Protection Plan. Collection of the drifter data was financially supported through the World Class Prevention, Preparedness and Response to Oil Spills from Ships Initiative of the Department of Fisheries and Oceans Canada. Environmental data collected at the Ocean Station Papa mooring was made available through the Ocean Climate Stations (OCS) Office of NOAA/PMEL.

ACKNOWLEDGMENTS

We would like to thank the captain and crew of the *CCGS John P. Tully*, as well as the scientists aboard, for their hard work on the Line P program that made this study possible. We also thank the staff at the Ocean Climate Stations Office of NOAA/PMEL for their work in collecting observations at Ocean Station Papa, and the staff at E.U. Copernicus Marine Service Information for their work in compiling the GLORYS12 numerical model results. We thank both organizations for making these data publicly available. Finally, we would like to thank two reviewers, whose helpful comments and insight improved the quality of this manuscript.

SUPPLEMENTARY MATERIAL

The Supplementary Material for this article can be found online at: https://www.frontiersin.org/articles/10.3389/fmars.2021.618094/full#supplementary-material

REFERENCES

National Oceanic and Atmospheric Administration, Pacific Marine National Oceanic and Atmospheric Administration Pacific Marine Environmental Laboratory (2020b). Seattle, WA: Ocean Station Papa: Sensor Specifications.

Allen, A. A., and Plourde, J. V. (1999). *Review of leeway: Field experiments and implementation*. Final Report CG-D-08-99, United States Department of Transportation and United States Coast Guard, Washington, DC.

Blanken, H., Hannah, C., Klymak Jody, M., and Juhász, T. (2020). Surface drift and dispersion in a multiply connected fjord system. *J. Geophys. Res. Oceans* 125, e2019JC015425. doi: 10.1029/2019JC015425

Breivik, Ø., and Allen, A. A. (2008). An operational search and rescue model for the Norwegian Sea and the North Sea. *J. Mar. Syst*. 69, 99–113. doi: 10.1016/j.jmarsys.2007.02.010

Breivik, O., Allen, A. A., Maisondieu, C., and Olagnon, M. (2013). Advances in search and rescue at sea. *Ocean Dyn*. 63, 83–88. doi: 10.1007/s10236-012-0581-1

Breivik, Ø., Allen, A. A., Maisondieu, C., and Roth, J. C. (2011). Wind-induced drift of objects at sea: the leeway field method. *Appl. Ocean Res*. 33, 100–109. doi: 10.1016/j.apor.2011.01.005

Butler, J. (2015). *Independent review of the M/V Marathassa fuel oil spill environmental response operation*. Technical report, Canadian Coast Guard.

Checkley, D. M., Raman, S., Maillet, G. L., and Mason, K. M. (1988). Winter storm effects on the spawning and larval drift of a pelagic fish. *Nature* 335, 346–348. doi: 10.1038/335346a0

Cho, K.-H., Li, Y., Wang, H., Park, K.-S., Choi, J.-Y., Shin, K.-I., et al. (2014). Development and validation of an operational search and rescue modeling system for the Yellow Sea and the East and South China Seas. *J. Atmos. Oceanic Technol*. 31, 197–215. doi: 10.1175/JTECH-D-13-00097.1

Clarke, A. J., and Van Gorder, S. (2018). The relationship of near-surface flow, Stokes drift and the wind stress. *J. Geophys. Res. Oceans* 123, 4680–4692. doi: 10.1029/2018JC014102

Craig, P. D., and Banner, M. L. (1994). Modeling wave-enhanced turbulence in the ocean surface layer. *J. Phys. Oceanogr*. 24, 2546–2559. doi: 10.1175/1520-0485(1994)024andlt;2546:MWETITandgt;2.0.CO;2

Cummins, P. F., and Ross, T. (2020). Secular trends in water properties at Station P in the northeast Pacific: an updated analysis. *Progr. Oceanogr*. 186:102329. doi: 10.1016/j.pocean.2020.102329

Dagestad, K.-F., Röhrs, J., Breivik, Ø., and Ådlandsvik, B. (2018). Opendrift v1.0: a generic framework for trajectory modelling. *Geosci. Model Dev*. 11, 1405–1420. doi: 10.5194/gmd-11-1405-2018

Daniel, P., Jan, G., Cabioc'h, F., Landau, Y., and Loiseau, E. (2002). Drift modeling of cargo containers. *Spill Sci. Technol. Bull*. 7, 279–288. doi: 10.1016/S1353-2561(02)00075-0

D'Asaro, E. A., Shcherbina, A. Y., Klymak, J. M., Molemaker, J., Novelli, G., Guigand, C. M., et al. (2018). Ocean convergence and the dispersion of flotsam. *Proc. Natl. Acad. Sci. U.S.A*. 115, 1162–1167. doi: 10.1073/pnas.1718453115

Davidson, F., Allen, A., Brassington, G. B., Breivik, Ø., Daniel, P., Kamachi, M., et al. (2009). Applications of GODAE ocean current forecasts to search and rescue and ship routing. *Oceanography* 22, 176–181. doi: 10.5670/oceanog.2009.76

Davis, R. E. (1985). Drifter observations of coastal surface currents during CODE: The method and descriptive view. *J. Geophys. Res*. 90, 4741–4755. doi: 10.1029/JC090iC03p04741

De Dominicis, M., Pinardi, N., Zodiatis, G., and Archetti, R. (2013). MEDSLIK-II, a Lagrangian marine surface oil spill model for short-term forecasting-part 2: Numerical simulations and validations. *Geosci. Model Dev*. 6, 1871–1888. doi: 10.5194/gmd-6-1871-2013

Dubois, D., Foulloy, L., Mauris, G., and Prade, H. (2004). Probability-possibility transformations, triangular fuzzy sets, and probabilistic inequalities. *Reliable Comput*. 10, 273–297. doi: 10.1023/B:REOM.0000032115.22510.b5

Ekman, V. W. (1905). *On the Influence of the Earth's Rotation on Ocean Currents*. Ann Arbor, MI: Arkiv för matematik, astronomi och fysik 2.

Fengqi, L., Yusong, S., Fengqin, W., and Zuxiang, Y. (1989). Discussion of some concepts of the water mass by the theory of fuzzy sets. *J. Ocean Univ. Qingdao* 6, 49–58. doi: 10.1007/BF02846567

Fine, I., and Masson, D. (2015). Oil spill trajectory on the northern British Columbia coast: results from a series of numerical simulations. *Can. Tech. Rep. Hydrogr. Ocean Sci*. 306:27.

Freeland, H. (2007). A short history of Ocean Station Papa and Line P. *Prog. Oceanogr*. 75, 120–125. doi: 10.1016/j.pocean.2007.08.005

Gawarkiewicz, G., Monismith, S., and Largier, J. (2007). Observing larval transport processes affecting population connectivity: progress and challenges. *Oceanography* 20, 40–53. doi: 10.5670/oceanog.2007.28

Hanss, M. (2002). The transformation method for the simulation and analysis of systems with uncertain parameters. *Fuzzy Sets Syst*. 130, 277–289. doi: 10.1016/S0165-0114(02)00045-3

Hanss, M. (2005). *Applied Fuzzy Arithmetic: An Introduction With Engineering Applications*. Berlin; Heidelberg: Springer-Verlag.

Hasselmann, K., Barnett, T., Bouws, E., Carlson, H., Cartwright, D., Enke, K., et al. (1973). Measurements of wind-wave growth and swell decay during the Joint North Sea Wave Project (JONSWAP). *Ergänzungsheft* 8–12.

Holthuijsen, L. (2010). *Waves in Oceanic and Coastal Waters*. Cambridge: Cambridge University Press.

Kaufman, A., and Gupta, M. M. (1985). *Introduction to Fuzzy Arithmetic, Theory and Application*. New York, NY: Van Nostrand Reinhold.

Kenyon, K. E. (1969). Stokes drift for random gravity waves. *J. Geophys. Res*. 74, 6991–6994. doi: 10.1029/JC074i028p06991

Khan, U. T., and Valeo, C. (2016). Dissolved oxygen prediction using a possibility theory based fuzzy neural network. *Hydrol. Earth Syst. Sci*. 20, 2267–2293. doi: 10.5194/hess-20-2267-2016

Khan, U. T., Valeo, C., and He, J. (2013). Non-linear fuzzy-set based uncertainty propagation for improved DO prediction using multiple-linear regression. *Stochastic Environ. Res. Risk Assess*. 27, 599–616. doi: 10.1007/s00477-012-0626-5

Lellouche, J.-M., Greiner, E., Bourdallé-Badie, R., Garric, G., Melet, A., Drévillon, M., et al. (2021). The Copernicus global 1/12 oceanic and sea ice GLORYS12 reanalysis. *Front. Earth Sci*. 9:698876. doi: 10.5194/egusphere-egu21-14961

Liu, Y., and Weisberg, R. H. (2011). Evaluation of trajectory modeling in different dynamic regions using normalized cumulative Lagrangian separation. *J. Geophys. Res. Oceans* 116. doi: 10.1029/2010JC006837

Mellor, G. L., and Yamada, T. (1982). Development of a turbulence closure model for geophysical fluid problems. *Rev. Geophys*. 20, 851–875. doi: 10.1029/RG020i004p00851

Mercer, R., Barron, J., Bruen, A., and Cheng, D. (2002). Fuzzy points: algebra and application. *Pattern Recognit*. 35, 1153–1166. doi: 10.1016/S0031-3203(01)00110-8

Molcard, A., Poulain, P., Forget, P., Griffa, A., Barbin, Y., Gaggelli, J., et al. (2009). Comparison between VHF radar observations and data from drifter clusters in the Gulf of La Spezia (Mediterranean Sea). *J. Mar. Systems* 78, S79–S89. doi: 10.1016/j.jmarsys.2009.01.012

Moore, T. S., Campbell, J. W., and Dowell, M. D. (2009). A class-based approach to characterizing and mapping the uncertainty of the MODIS ocean chlorophyll product. *Remote Sens. Environ*. 113, 2424–2430. doi: 10.1016/j.rse.2009.07.016

Morison, J., Johnson, J., and Schaaf, S. (1950). The force exerted by surface waves on piles. *J. Petroleum Technol*. 2, 149–154. doi: 10.2118/950149-G

Nansen, F. (1902). *The Norwegian North Polar Expedition, 1893-1896; Scientific Results*. Fridtjof Nansen Fund for the Advancement of Science.

National Oceanic and Atmospheric Administration, Pacific MarineNational Oceanic and Atmospheric Administration Pacific Marine Environmental Laboratory (2020a). Seattle, WA: Ocean Station Papa PA008 Mooring Diagram.

Ni, Z., Qiu, Z., and Su, T. (2010). On predicting boat drift for search and rescue. *Ocean Eng*. 37, 1169–1179. doi: 10.1016/j.oceaneng.2010.05.009

Niiler, P. P., Sybrandy, A. S., Bi, K., Poulain, P. M., and Bitterman, D. (1995). Measurements of the water-following capability of holey-sock and TRISTAR drifters. *Deep Sea Res*. 42, 1951–1964. doi: 10.1016/0967-0637(95)00076-3

Nudds, S., Lu, Y., Higginson, S., Haigh, S., Paquin, J.-P., O'Flaherty-Sproul, M., et al. (2020). Evaluation of structured and unstructured models for application in operational ocean forecasting in nearshore waters. *J. Mar. Sci. Eng*. 8:484. doi: 10.3390/jmse8070484

Oceanetic Measurement Ltd. (2016). *SCT (Surface Circulation Tracker) Specification Sheet*. North Saanich, BC.

Okubo, A. (1971). Oceanic diffusion diagrams. *Deep Sea Res*. 18, 789–802. doi: 10.1016/0011-7471(71)90046-5

Park, H.-J., Jang, J.-Y., and Lee, J.-H. (2017). Physically based susceptibility assessment of rainfall-induced shallow landslides using a fuzzy point estimate method. *Remote Sens*. 9:487. doi: 10.3390/rs9050487

Pelland, N. A., Eriksen, C. C., and Cronin, M. F. (2016). Seaglider surveys at ocean station papa: Circulation and water mass properties in a meander of the north pacific current. *Journal of Geophysical Research: Oceans* 121, 6816–6846. doi: 10.1002/2016JC011920

Pierson, W. J. Jr., and Moskowitz, L. (1964). A proposed spectral form for fully developed wind seas based on the similarity theory of S. A. Kitaigorodskii. *J. Geophys. Res*. 69, 5181–5190. doi: 10.1029/JZ069i024p05181

Poje, A. C., Özgökmen, T. M., Lipphardt, B. L. Jr., Haus, B. K., Ryan, E. H., Haza, A. C., et al. (2014). Submesoscale dispersion in the vicinity of the *Deepwater Horizon* spill. *Pro. Natl. Acad. Sci. U.S.A*. 111, 12693–12698. doi: 10.1073/pnas.1402452111

Polton, J. A., Lewis, D. M., and Belcher, S. E. (2005). The role of wave-induced Coriolis-Stokes forcing on the wind-driven mixed layer. *J. Phys. Oceanogr*. 35, 444–457. doi: 10.1175/JPO2701.1

Poulain, P.-M., and Niiler, P. P. (1989). Statistical analysis if the surface circulation in the California Current system using satellite-tracked drifters. *J. Phys. Oceanogr*. 19, 1588–1603. doi: 10.1175/1520-0485(1989)019<1588:SAOTSC>2.0.CO;2

Radecki, T. (1977). Level fuzzy sets. *J. Cybern*. 7, 189–198. doi: 10.1080/01969727708927558

Rixen, M., Ferreira-Coelho, E., and Signell, R. (2008). Surface drift prediction in the Adriatic Sea using hyper-ensemble statistics on atmospheric, ocean and wave models: uncertainties and probability distribution areas. *J. Mar. Syst*. 69, 86–98. doi: 10.1016/j.jmarsys.2007.02.015

Röhrs, J., and Christensen, K. H. (2015). Drift in the uppermost part of the ocean. *Geophys. Res. Lett*. 42, 10349–10356. doi: 10.1002/2015GL066733

Röhrs, J., Christensen, K. H., Hole, L. R., Broström, G., Drivdal, M., and Sundby, S. (2012). Observation-based evaluation of surface wave effects on currents and trajectory forecasts. *Ocean Dyn*. 62, 1519–1533. doi: 10.1007/s10236-012-0576-y

Röhrs, J., Christensen, K. H., Vikebø, F., Sundby, S., Saetra, Ø., and Broström, G. (2014). Wave-induced transport and vertical mixing of pelagic eggs and larvae. *Limnol Oceanogr*. 59, 1213–1227. doi: 10.4319/lo.2014.59.4.1213

Smith, S. D. (1988). Coefficients for sea surface wind stress, heat flux, and wind profiles as a function of wind speed and temperature. *J. Geophys. Res. Oceans* 93, 15467–15472. doi: 10.1029/JC093iC12p15467

Soloviev, A., and Lukas, R. (2014). *The Near-Surface Layer of the Ocean: Structure, Dynamics and Applications, Vol. 48 of Atmospheric and Oceanographic Sciences Library, 2nd Edn*. Heidelberg: Springer Netherlands.

Stark, K. A., Thompson, P. L., Yakimishyn, J., Lee, L., and O'Connor, M. I. (2018). Beyond a single patch: local and regional processes explain diversity patterns in a seagrass epifaunal metacommunity. *bioRxiv*. doi: 10.1101/482406

Stokes, G. G. (1847). On the theory of oscillatory waves. *Trans. Cambridge Philos*. 8, 441–455.

Sutherland, G., Soontiens, N., Davidson, F., Smith, G. C., Bernier, N., Blanken, H., et al. (2020). Evaluating the leeway coefficient of ocean drifters using operational marine environmental prediction systems. *J. Atmos. Oceanic Technol*. 37, 1943–1954. doi: 10.1175/JTECH-D-20-0013.1

Tamtare, T., Dumont, D., and Chavanne, C. (2019). Extrapolating Eulerian ocean currents for improving surface drift forecasts. *J. Operat. Oceanogr*. 14, 71–85. doi: 10.1080/1755876X.2019.1661564 van den Bremer, T. S., and Breivik, Ø. (2018). Stokes drift. *Philos. Trans. R. Soc. A Math. Phys. Eng. Sci*. 376:20170104. doi: 10.1098/rsta.2017.0104

Vandenbulcke, L., Beckers, J.-M., Lenartz, F., Barth, A., Poulain, P.-M., Aidonidis, M., et al. (2009). Super-ensemble techniques: application to surface drift prediction. *Prog. Oceanogr*. 82, 149–167. doi: 10.1016/j.pocean.2009.06.002

Weber, J. E. H., Drivdal, M., Christensen, K. H., and Broström, G. (2015). Some aspects of the Coriolis-Stokes forcing in the oceanic momentum and energy budgets. *J. Geophys. Res. Oceans* 120, 5589–5596. doi: 10.1002/2015JC010717

Zadeh, L. (1965). Fuzzy sets. *Inf. Control* 8, 338–353. doi: 10.1016/S0019-9958(65)90241-X

Zadeh, L. (1978). Fuzzy sets as a basis for a theory of possibility. *Fuzzy Sets Syst*. 1, 3–28. doi: 10.1016/0165-0114(78)90029-5

Zelenke, B., O'Connor, C., Barker, C., Beegle-Krause, C., and Eclipse, L. (2012). *General NOAA Operational Modelling Environment (GNOME) technical documentation*. NOAA Technical Memorandum NOS OR&R 40, U.S. Department of Commerce, Seattle, WA: Emergency Response Division, NOAA.

Zhang, K. (2009). *Modeling Uncertainty and Variability in Health Risk Assessment of Contaminated Sites* (Ph.D. thesis). University of Calgary, Canada.

Conflict of Interest: The authors declare that the research was conducted in the absence of any commercial or financial relationships that could be construed as a potential conflict of interest.

frontiers in Marine Science

ORIGINAL RESEARCH
published: 16 November 2021
doi: 10.3389/fmars.2021.668621

Sediment Resuspension and Associated Extracellular Enzyme Activities Measured *ex situ*: A Mechanism for Benthic-Pelagic Coupling in the Deep Gulf of Mexico

Kai Ziervogel*[1]*, Julia Sweet[2], Andrew R. Juhl[3] and Uta Passow[4]

[1] Institute for the Study of Earth, Oceans, and Space, University of New Hampshire, Durham, NH, United States, [2] Marine Science Institute, University of California, Santa Barbara, Santa Barbara, CA, United States, [3] Lamont-Doherty Earth Observatory, Columbia University, Palisades, NY, United States, [4] Memorial University of Newfoundland, St. John's, NL, Canada

Edited by:
Andrew James Manning,
HR Wallingford, United Kingdom

Reviewed by:
Fay Couceiro,
University of Portsmouth,
United Kingdom
Katrin Linse,
British Antarctic Survey (BAS),
United Kingdom

***Correspondence:**
Kai Ziervogel
kai.ziervogel@unh.edu

Specialty section:
This article was submitted to
Marine Biogeochemistry,
a section of the journal
Frontiers in Marine Science

Received: *16 February 2021*
Accepted: *18 October 2021*
Published: *16 November 2021*

Citation:
Ziervogel K, Sweet J, Juhl AR and Passow U (2021) Sediment Resuspension and Associated Extracellular Enzyme Activities Measured ex situ: A Mechanism for Benthic-Pelagic Coupling in the Deep Gulf of Mexico. Front. Mar. Sci. 8:668621. doi: 10.3389/fmars.2021.668621

Sediment resuspension caused by near-bed currents mediates exchange processes between the seafloor and the overlying water column, known as benthic-pelagic coupling. To investigate the effects of sediment resuspension on microbial enzyme activities in bottom waters (<500 m), we conducted onboard erosion experiments using sediment cores taken with a multi-corer from six deep-sea sites in the northern Gulf of Mexico. We then incubated the core-top water with resuspended sediments in roller tanks to simulate bottom water conditions following sediment resuspension. Bacterial cell abundance, particulate organic matter content, and potential rates of three hydrolytic enzymes (leucine aminopeptidases – PEP; β-glucosidases – GLU, lipases – LIP) were monitored during the experimentally-generated erosion events and subsequently in the roller tanks to examine whether resuspension of deep-sea sediments enhances activities of extracellular enzymes in overlying waters. Surficial sediments were resuspended at critical shear stress velocities between 1.4 and 1.7 cm s^{-1}, which parallel bottom water currents of 28 and 34 cm s^{-1}. Only one of our nine cores resisted experimentally generated bottom shear stresses and remained undisturbed, possibly as a result of oil residues from natural hydrocarbon seeps at the investigated site. The most notable enzymatic responses to sediment resuspension were found for LIP activities that increased in overlying waters of all eight of our resuspended cores and remained at high levels during the roller tank incubations. PEP and GLU showed orders of magnitude lower rates and more variable responses to experimentally resuspended sediments compared with LIP. We also found a disconnect between enzyme activities and bacterial cell numbers, indicating a major role of extracellular enzymes physically disconnected from microbial cells in our experiments. Our results demonstrate that sediment resuspension may promote organic matter breakdown in bottom waters by supplying extracellular enzymes without requiring a bacterial growth response. The marked increase in LIP activity suggests that resuspended enzymes may affect the degradation of petroleum hydrocarbons, including those from the natural seeps that are abundant in the investigation area.

Keywords: sediment resuspension, extracellular enzymes, lipase, benthic-pelagic coupling, deep-sea, northern Gulf of Mexico

INTRODUCTION

Benthic-pelagic coupling in aquatic environments involves the exchange of dissolved and particulate matter from the sediment to the overlying water and vice versa. Resuspension of sedimentary matter by near-bed currents plays a key role in these exchanges, affecting ecosystem functions from nutrient fluxes to energy transfer into food webs (Graf, 1992). Due to their shallow water columns, coastal and estuarine systems are particularly prone to sediment resuspension and such transfers (Griffiths et al., 2017), fueling microbial food webs in overlying waters (Ritzrau and Graf, 1992; Ritzrau, 1996; Ritzrau et al., 1997; Boetius et al., 2000; Ziervogel and Arnosti, 2009; Ziervogel et al., 2016). By comparison, information on benthic-pelagic coupling mediated by sediment resuspension in the deep-sea (>500 m depth) is relatively rare and limited to a few oceanographic regions (Turley, 2000), although resuspension events in the deep ocean are widespread and common (Durrieu de Madron et al., 2017).

The few existing studies on deep ocean biogeochemical cycles affected by sediment resuspension demonstrate the importance of upward fluxes for bathypelagic microbial food webs. For instance, Boetius et al. (2000) found close correlations between total particulate matter and heterotrophic microbial activities in near-bed waters in the deep Arabian Sea (2,000–4,500 m water depths), concluding that heterotrophic metabolism in bottom waters was stimulated by particulate and dissolved organic matter resuspended from the seafloor. Our own previous work in the deep (1,600 m) Gulf of Mexico (GOM) showed elevated microbial metabolic activities in turbid bottom waters containing high levels of lithogenic matter as an indicator for resuspended sediments (Ziervogel et al., 2016). Furthermore, budget calculations revealed that the amount of particulate and dissolved organic matter released through resuspended sediments in the deep ocean could close budget gaps between the carbon supplied to the benthos through sinking organic matter and the prokaryotic carbon demand in the deep-sea (Pfannkuche, 1993; Boetius et al., 2000; Baltar et al., 2010).

The above-mentioned studies on deep ocean microbial responses to sediment resuspension based their interpretations of benthic-pelagic coupling on correlation analysis of microbial metabolic rates and total suspended matter in bottom waters. However, these earlier studies could not distinguish between the effects of locally resuspended versus laterally advected sediment suspensions on near-bed microbial metabolic rates at the investigated sites (Ziervogel et al., 2016). This limitation can be resolved by using erosion chambers or flumes, to simulate local resuspension events of autochthonous sedimentary matter. Moreover, defined hydrodynamic conditions within erosion chambers and flumes allow for the determination of bottom shear stresses at which erosion first begins (i.e., the critical shear stress velocity, u*crit), an important parameter for predicting benthic-pelagic exchange processes in the field.

Past experimental studies with erosion chambers and flumes have focused on the release and vertical transport of organic matter, nutrients, and bulk seabed material during sediment erosion (Wainright, 1987; Thomsen and Gust, 2000; Ziervogel and Bohling, 2003; Kalnejais et al., 2007).

This study focused on the activities of extracellular enzymes in bottom waters following sediment resuspension, which has rarely been investigated in the deep ocean. We conducted onboard erosion chamber experiments on sediment cores followed by roller tank incubations of the core-top water and resuspended material. Experiments were performed at six deep-sea sites in the northern GOM. The sites were located in areas known for their deep-sea coral habitats (AT357, VK826, DC673; White et al., 2012; Fisher et al., 2014); for natural active oil and gas seepage (GC600, MC118; MacDonald et al., 2015; Conti et al., 2016; Martens et al., 2016); and for oil input during the Deepwater Horizon (DWH) oil spill in 2010 (OC26; Atlas and Hazen, 2011; Chanton et al., 2015; Diercks et al., 2021; Romero et al., 2021). Our aim was to examine whether resuspension of deep-sea sediments enhances activities of extracellular enzymes in overlying waters. The focus on enzymatic activities stems from the fact that microbial degradation of complex organic matter is initiated by extracellular enzymes that hydrolyze substrates in the medium outside the cells to sizes sufficiently small for cellular uptake (Arnosti, 2011). We measured potential activities of leucine aminopeptidases, β-glucosidases, and lipases, mediating enzymatic breakdown of peptides, carbohydrates, and lipids, respectively, representing major compound classes within the ocean's organic matter pool. Lipases are also involved in the biodegradation cascade of petroleum hydrocarbons (Margesin et al., 1999; Kamalanathan et al., 2018; Mislan and Gates, 2019), which are an important carbon source for microbial communities in the investigation area (Orcutt et al., 2010; Ziervogel et al., 2014).

MATERIALS AND METHODS

Sampling and Site Description

Nine sediment cores (10 cm in diameter) were collected from six different sites in the northern GOM in June/July 2013 during RV Endeavor cruise 527 (**Figure 1** and **Table 1**) using

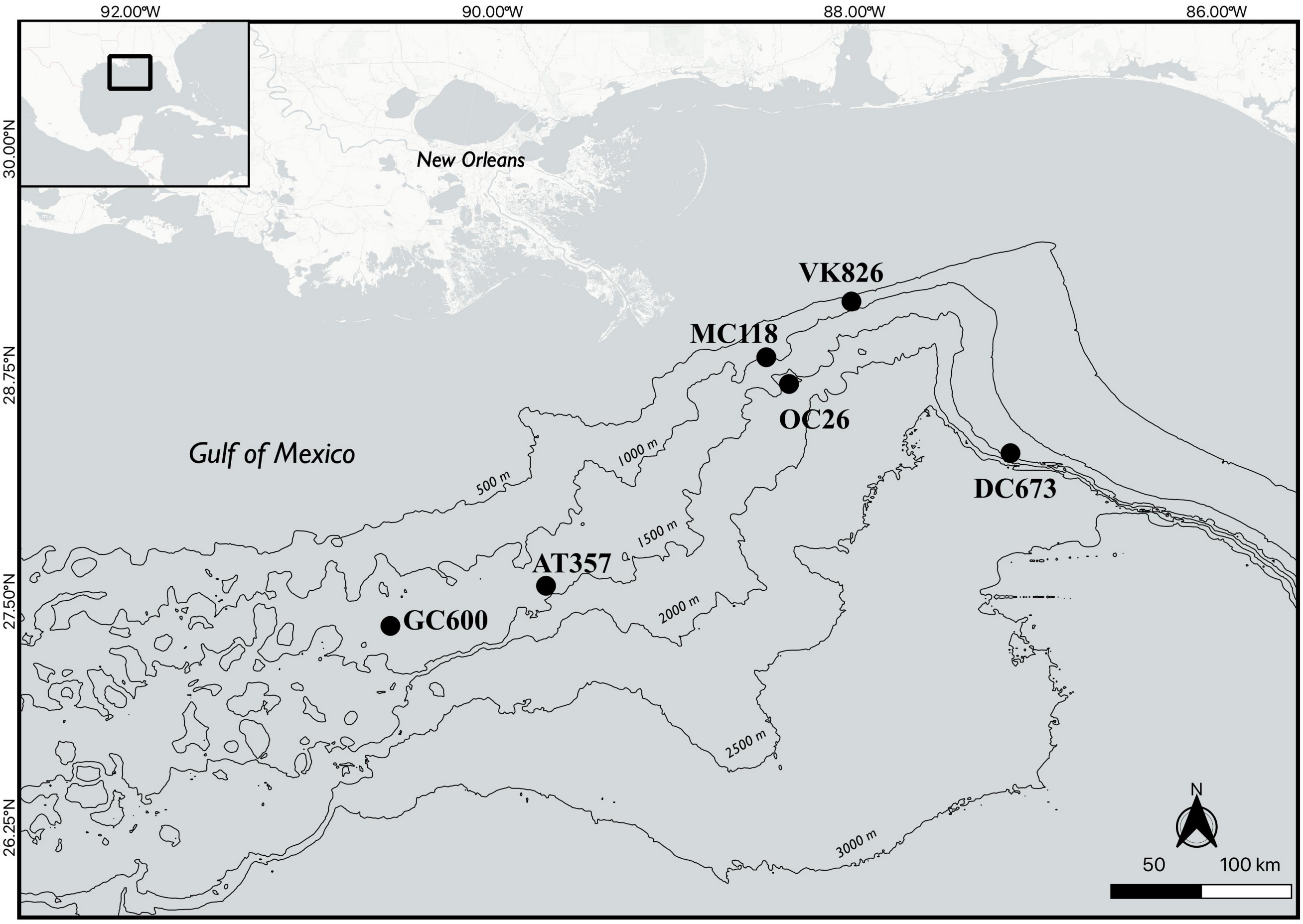

FIGURE 1 | Map of sampling sites.

a multi-corer (MC-800, Ocean Instruments). Immediately after recovery, sediment cores with an undisturbed sediment-water interface indicated by visually undisturbed (clear) water overlying the core, were stored in the dark at 5°C until the onset of the onboard experiments (usually within 12 h of sampling). The experimental procedure for each core consisted of an erosion experiment lasting 40–80 min in total, where an erosion chamber was used to resuspend surface sediment, followed by a 10-h roller tank incubation, that simulated conditions in bottom waters containing resuspended sediments. Note that replicate cores for the present study were only available at two of the six sites (**Table 1**). The remaining sediment cores from each multi-corer cast (8 cores in total) were sectioned and analyzed for different biogeochemical parameters including bulk organic matter (OM) content by loss of ignition, which are reported in **Table 1**. The complete dataset of sediment parameters is publicly available through the Gulf of Mexico Research Initiative Information & Data Cooperative (GRIIDC) (Joye, 2016). Note that grain-size analysis was not conducted on any of the cores from this expedition. We therefore report published results on sediment properties from other sampling campaigns in the investigation area (**Table 1**; Montagna et al., 2013).

Experimental Procedures: Erosion Chamber and Roller Tanks

Sediment cores with overlying water were slowly pushed up into an EROMES laboratory erosion chamber (Kalnejais et al., 2007), yielding a total length of the sediment core in the chamber of 20 cm for each of the experiments. The EROMES consist of a baffled 10 cm inner diameter acrylic core (i.e., same diameter as the sampling cores) with a propeller on top that is connected to a stepper motor. The rotating propeller creates movement of the overlying water, generating defined bottom shear stress velocities (u*) along the sediment-water interface. The chamber was calibrated prior to the expedition, by determining sediment transport of sieved sand as a function of propeller speed. The shear stress required to resuspend sediment grains of known sizes was determined from the Shield's threshold curve for sediment erosion (Soulsby and Whitehouse, 1997). The calibration yielded a linear relationship between rotation speed of the propeller and the respective u^*_{crit} values.

TABLE 1 | Locations of sampling sites and ancillary data.

Station ID and location	Station Lat/Long	Date	Water depth, m	Bottom water temp,°C	%OM*	%Mud (Silt + Clay)#	#cores, #incubations
Vioska Knoll (VK826), coral habitat	29° 09.48′N 088° 01.02′W	06/23/2013	530	7.5	13	95.2	1, 1
Mississippi Canyon (MC118), natural seep	28°51.007′N 088°29.236′W	06/26/2013	900	5.5	11	98.8	1, 1
Atwater Valley (AT357), coral habitat	27°35.22′N 089°42.24′	06/27/2013	1,150	4.7	10	95.3	2, 2
Green Canyon (GC600), natural seep	27°21.922′N 090°33.819′W	06/20/2013	1,200	4.4	16	93.1	1, 1
Desoto Canyon (DC673), coral habitat	28° 19.193′N 087° 8.313′W	07/01/2013	1,350	4.4	9	99	1, 0
Oceanus Site 26 (OC26), DWH	28° 42.14′N 088° 21.70′W	06/24/2013	1,600	4.3	11	97.2	3, 2

**%OM in surface sediments (0–3 cm) by loss of ignition from replicate cores from the same cast; data are from Joye (2016). # %Mud in surface sediments (0–3 cm) taken in September/October 2010 (Montagna et al., 2013).*

The erosion experiments were conducted at room temperature with the chambers kept in an ice bath to maintain close to *in situ* temperature (5°C) at the sediment-water interface. During experiments, the propeller speed was increased in four to eight steps of 10-min each, yielding a range of u* from 0.4 to 2.4 cm s^{-1}, i.e., the maximum u* setting for this instrument. Experiments ended when the water became visibly turbid. The relationship between u* near the sediment interface and the overlying freestream velocity (u) is given by the quadratic stress law (e.g., Dyer, 1986):

$$\tau = \rho u^{*}2 = \rho CDu^{2} \qquad (1)$$

where τ is the bottom shear stress (Pa), ρ is the fluid density (kg m^{-3}), and CD is the dimensionless drag coefficient of 0.0025 (Ross et al., 2009). Thus, the range of u* in our experiments was equivalent to free-stream current velocities above the seafloor (u) of 8 to 48 cm s^{-1}. We defined u^{*}_{crit} as the velocity when total particulate matter (TPM) values in the overlying core water increased above 100 mg (for the total 1700 ml volume). Initial TPM values before erosion were always ≤50 mg.

In all cases, the sediment-water interface remained visually undisturbed following the lowest u* setting ($u^{*}_{INITIAL}$ = 0.4 cm s^{-1}). This low-flow condition represented a more realistic initial condition than stagnant water prior to the onset of the erosion experiment. At the end of the initial and each subsequent 10-min u* step, the overlying water was sampled for the biogeochemical parameters described below (Section "Analytical Methods"). The sample volume removed from the overlying water at each sampling (i.e., 150 mL of 1,700 mL total volume) was replaced with GF/F filtered near-bottom water (i.e., ∼5 m above the seafloor) collected from the same site with a CTD rosette. The dilution, which never exceeded 11% for each erosion step, was accounted for when values of measured parameters were calculated.

To simulate bottom water conditions following sediment resuspension, we collected the water overlying the cores after the final erosion step and transferred the water to roller tanks for an additional 10-h incubation. Cylindrical roller tanks incubated on a roller table are widely used to study suspended particle interactions and associated biogeochemical processes under non-turbulent conditions (Shanks and Edmondson, 1989; Unanue et al., 1998; Ploug et al., 2010). Thus, our two-phased experimental approach enabled us to investigate potential effects of sediment resuspension on bottom water heterotrophic activities in the investigation area.

Acrylic roller tanks (total volume: 1.700 mL) were filled without a headspace with the experimental core water after the final erosion step. The core water was carefully siphoned off the sediment core, leaving behind a small volume of water to prevent further disturbance of the sediment-water interface. The tanks were incubated in the dark at *in situ* temperature (5°C) on a roller table rotating at 2.4 rpm for 10 h, allowing for sufficient time to process the tanks before the start of the next erosion experiment. After the 10-h incubation, the tanks were removed from the roller table and placed upright on a benchtop at room temperature (∼20°C) to allow particles to settle to the bottom of the tanks for 10 min. The upper (visually particle-free) water fraction was carefully siphoned off into a clean beaker. This fraction, hereafter called the surrounding seawater (SSW) fraction, constituted 80% of the tank volume. The second fraction (sediment slurry; SL) contained settled particles in a measured volume of SSW (20% of the tank volume). Both, SSW and SL fractions were separately analyzed for the biogeochemical parameters listed below. As a non-resuspension control, we incubated near-bottom water from a CTD rosette cast at GC600 that did not contain visual particles.

Roller tank incubations were not performed on cores from OC26_1 and DC673. The former core spilled after the conclusion of the erosion experiment, and the latter was taken near the end of the expedition which did not leave enough time for a roller tank experiment. Instead, we decided to extend the erosion experiment with the DC673 core by adding additional shear stress steps (**Figure 2F**).

Analytical Methods

Total particulate matter (TPM) was analyzed in the overlying water from the erosion experiments at the end of each shear stress step and in the two fractions from the subsequent roller tank incubations (SL, SSW). TPM was analyzed by filtering experimental water onto pre-combusted and pre-weighed GF/F filters with a nominal pore size of 0.7 μm (Whatman). Filters were rinsed with milli Q water and stored frozen at −20°C until they were re-weighed in the home lab, following a drying period at 60°C for 24 h.

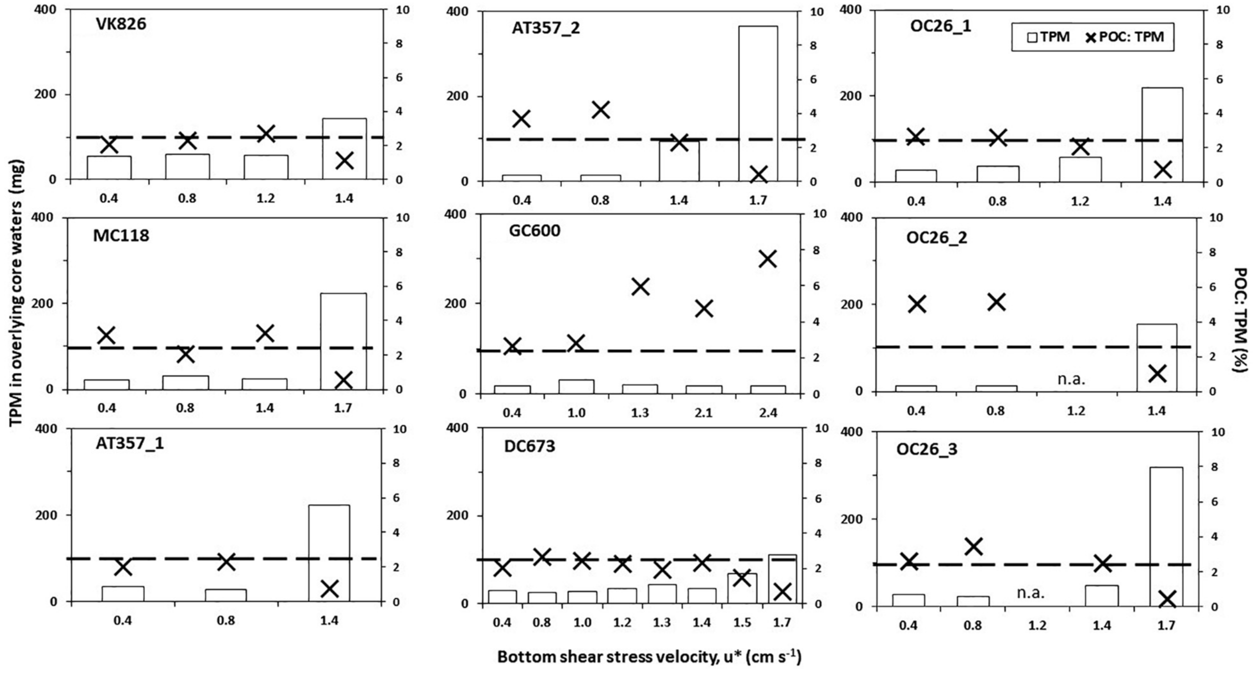

FIGURE 2 | Changes in total particulate matter (TPM; white bars) and organic matter content (POC: TPM; black crosses) in the overlying core waters as a factor of bottom shear stress velocities (u*) during the erosion chamber experiments. TPM were standardized for the total volume of the core water in each case. Dashed line stands for the TPM threshold for type 2 erosion (u^*_{crit}; see text).

Particulate organic carbon (POC) was analyzed in the overlying water from the erosion experiments at the end of each shear stress step and the two roller tank fractions (SL, SSW). Subsamples were filtered onto pre-combusted GF/F filters that were stored frozen at −20°C until analysis. Filters were acidified with 12 M HCl for 12 h to remove inorganic carbon prior to flash combustion on a Carlo-Erba 1500 Elemental Analyzer using acetanilide as a standard (Knap, 2002).

Potential activities of β-glucosidases (GLU), leucine aminopeptidases (PEP), and lipases (LIP) were measured in the water overlying the sediment cores at the first and final u* steps, and in the roller tanks (SL, SSW). Potential enzyme activities were measured using 4-MUF-β-D-glucopyranoside, L-leucine-MCA hydrochloride, and 4-MUF-butyrate as fluorogenic substrate analogs for GLU, PEP, LIP, respectively (Hoppe, 1983). Three mL of experimental water were added to disposable methacrylate cuvettes containing fluorogenic substrate analogs at saturation levels (200 μM for 4-MUF-β-D-glucopyranoside and L-leucine-MCA hydrochloride; 100 μM for 4-MUF-butyrate) as determined at the beginning of the expedition. Duplicate cuvettes per substrate were incubated in the dark, at *in situ* temperature (5°C). Fluorescence was measured immediately after sample addition and at two additional time points over the course of 24 h under buffered conditions (20 nM borate buffer; pH 9.2) using a Turner Biosystems TBS-380 fluorometer (excitation/emission channels set to "UV"; 365 nm excitation, 440–470 nm emission). Fluorescence levels of standard solutions of methylumbelliferone (MUF) and methylcoumarin (MCA) in seawater were used to calculate potential hydrolysis rates from the assays. Minor changes in fluorescence over time were detected in killed controls (i.e., pasteurized seawater) and used to correct enzymatic hydrolysis rates in live water for abiotic substrate hydrolysis. Enzyme activities were not available from the DC673 erosion experiment.

Enzyme activities reported here represent potential hydrolysis rates, since added substrate proxies compete with naturally occurring substrates for enzyme active sites. Potential hydrolysis rates in this study are expressed as volumetric rates rather than normalized to cell abundance. Volumetric rates consider the total hydrolytic potential of the water including cell-free enzyme activities, thus assessing both, enzymes associated with the cells and those free in the surrounding medium. The latter fraction has been found to be particularly important in the deep ocean (Zhao et al., 2020) and in diffusion-limited environments such as sediments (Vetter et al., 1998).

Bacterial cells were enumerated by flow cytometry in subsamples from the overlying water from the erosion experiments (first and final u* steps only) and the two roller tank fractions. One mL subsamples were fixed with 0.1% glutaraldehyde (final concentration) for 10 min at room temperature in the dark and stored frozen at −80°C until analysis (within ∼2 weeks of sampling). Cellular DNA was stained using SYBR Green I (Gasol and Del Giorgio, 2000) and bacterial cells were counted on a BD Accuri C6 Flow Cytometer.

All analytical parameters measured here (TPM, bacterial cell numbers, enzyme activities) are expressed as absolute values standardized for the total volume of the respective experimental device (i.e., 1,700 mL in both cases). This allows for the direct comparison between the parameters measured in the erosion chamber and the roller tanks with the SL and SSW fractions.

Statistical Analysis

Pearson's correlation coefficients (r) between enzymatic activities and TPM measured at the initial and the final erosion step from the eight eroded cores were calculated in Excel® using the data analysis tool pack. For this analysis we used the differences between the two erosion steps rather than the absolute values to account for variation in baseline enzyme activities among experiments.

RESULTS

Visual examination of the nine cores revealed that none of the cores showed indications of recently sedimented material in the form of fluffy layers. Most notably, the core taken at GC600 had visible oil residues in the uppermost layer. Sediment cores from GC600 had higher organic matter content (OM) in the upper three centimeters (16% OM) than cores from the other sites where OM ranged between 9% (DC673) and 13% (VK826) (**Table 1**).

Erosion Thresholds

Eight of the nine cores reached TPM levels in the overlying water exceeding the 100 mg threshold, indicating u^*_{crit} values between 1.4 cm s^{-1} (OC26_1, OC26_2, VK826, AT357_1) and 1.7 cm s^{-1} (OC26_3, MC118, AT357_2, and DC673). TPM levels in the GC600 core did not reach this threshold even at u* of 2.4 cm s^{-1} (i.e., maximum u* setting), ranging between 17.1 and 31.6 mg (**Figure 2**). The other cores showed TPM levels in the overlying water at u^*_{crit} between 112 mg (DC673) to 366 mg (AT357_2). POC: TPM ratios as a measure of the organic matter content of the resuspended material varied between 0.4% (AT357_2) and 2.5% (OC26_3), and in most cores decreased with increasing shear stress reflecting the initial resuspension of lighter POC relative to mostly inorganic matter within the TPM pool at higher shear stresses.

Enzyme Activities in Response to Sediment Resuspension

Potential activities of the three enzymes assayed in our experiments showed similar levels among the cores and tanks, decreasing in the following order: lipase (LIP) > > peptidase (PEP) > glucosidase (GLU) (**Table 2**). LIP activities increased between the initial and final shear stress step in all of the resuspended cores by factors 1.5 (OC26_2, OC26_3, MC118), 2 (OC26_1, AT357_1, AT357_2) and 9 (VK826), following the increase in TPM ($r = 0.7$, $p = 0.1$, $n = 7$). The GC600 core that lacked sediment erosion showed a decrease in LIP activities by three orders of magnitude during the erosion chamber experiment. LIP activities remained at high levels at the end of the 10-hour roller tank incubations except for the VK826 tank that showed substantially lower LIP activities compared to the core water at u^*_{crit}. Total LIP activities at the end of the VK826 tank experiment were almost 100% associated with the sediment

TABLE 2 | Enzyme activities (nmol h^{-1}) in the overlying core waters at the initial ($u^*_{INITIAL}$) and final (u^*_{END}) shear stress step during the erosion experiments, and at the end of the roller tank incubations with the partitioning between sediment slurry (SL) and surrounding seawater (SSW).

Site _core#	Sediment core						Roller tank					
	$u^*_{INITIAL}$			u^*_{END}			SSW			SL		
	LIP	PEP	GLU	LIP	PEP	GLU	LIP	PEP	GLU	LIP	PEP	GLU
VK826	30.1 ± 16.7	12.9 ± 0.6	3.3 ± 1.1	277.4 ± 27.4	16.5 ± 0.1	2.0 ± 0.1	5.9 ± 0.0	13.0 ± 0.6	0.5 ± 0.3	96.1 ± 5.9	12.3 ± 0.4	1.5 ± 0.1
MC118	904.5 ± 5.5	148.3 ± 2.5	9.1 ± 6.4	1122 ± 32.0	43.0 ± 2.4	4.0 ± 0.2	716.5 ± 2.7	33.2 ± 3.8	1.9 ± 2.0	299.0 ± 0.0	18.3 ± 0.1	2.1 ± 0.5
AT357_1	114.0 ± 6.9	56.4 ± 34.7	n.d.	22.9 ± 23.3	16.0 ± 1.6	n.d.	95.7 ± 1.8	12.6 ± 0.2	n.d.	123.4 ± 1.8	12.6 ± 0.4	0.9 ± 0.01
AT357_2	143.8 ± 1.3	3.3 ± 0.5	n.d.	301.8 ± 6.1	30.1 ± 1.2	n.d.	122.5 ± 7.9	14.7 ± 1.9	n.d.	140.0 ± 1.6	18.1 ± 0.3	1.2 ± 0.01
GC600	255.2 ± 16.9	63.0 ± 2.1	5.0 ± 1.7	1.2 ± 0.0	72.9 ± 4.2	9.6 ± 0.3	72.5 ± 1.3	27.7 ± 1.4	1.6 ± 0.03	18.8 ± 1.5	5.9 ± 0.5	0.4 ± 0.1
OC26_1	142.3 ± 5.8	7.9 ± 2.0	1.4 ± 0.2	347.8 ± 43.1	24.8 ± 2.3	3.8 ± 0	n.a.	n.a.	n.a.	n.a.	n.a.	n.a.
OC26_2	778.7 ± 32.9	54.2 ± 3.7	8.7 ± 0.1	1017 ± 35.6	72.9 ± 0.4	19.1 ± 13.9	585.3 ± 15.3	45.6 ± 4.3	2.0 ± 0.0	155.5 ± 3.3	19.5 ± 1.7	3.7 ± 0.2
OC26_3	190.6 ± 2.1	44.3 ± 3.6	5.8 ± 0.1	268.2 ± 3.6	23.8 ± 12.7	12.8 ± 0.1	194.6 ± 3.4	32.5 ± 2.8	7.7 ± 0.5	151.3 ± 4.9	19.6 ± 3.6	3.9 ± 0.2
Control water	–	–	–	–	–	–	n.d.	0.71 ± 0.0	n.d.	–	–	–

Activities are normalized to the total volume of either the core water or the tank water. LIP, lipases; PEP, peptidases; GLU, glucosidases. Enzyme activities are expressed as absolute values standardized for the total volume of the respective sample. Enzyme activities are averages of n = 2 (±range). n.d., means not detectable, n.a., means not available.

TABLE 3 | Absolute values of total particulate matter (TPM, mg) and POC: TPM ratios at the end of roller tank incubations with the partitioning between sediment slurry (SL) and surrounding seawater (SSW).

Tank ID	TPM		POC: TPM (%)	
	SSW	SL	SSW	SL
VK826	13.8	65.0	3.0	3.3
MC118	9.1	63.0	3.6	2.4
AT357_1	13.1	67.5	2.2	2.4
AT357_2	37.1	363	0.6	0.3
GC600	8	6.5	4.2	6.1
OC26_2	17.4	90	2.5	1.0
OC26_3	8.8	49.4	2.8	2.5
Control water	3.4	–	6.8	–

Control water was taken with the CTD near the bottom at GC600.

slurry (SL), which had the highest POC: TPM ratio among the eroded cores (**Table 3**). LIP activities in the other six tanks were more evenly distributed between SSW and SL (**Figure 3**).

Responses of PEP and GLU to sediment resuspension were more variable compared with LIP. PEP activities increased in four of the seven resuspended cores by factors 1.3 (OC26_2, VK826, GC600), 3 (OC26_1), and 9 (AT357_2) and decreased in the other three cores by factors 2 (OC26_3) and 3 (MC118, AT357_1) (**Table 2**). PEP activities at the end of the roller tank incubations were at the same level compared to u^*_{crit} (OC26_2, GC600) or increased by up to a factor 2 (OC26_3, MC118, AT357_1, AT357_2) with 30–50% of activity associated with SL (**Figure 3**). GLU activities almost doubled between the initial and final shear stress step in the three OC26 cores and the GC600 core that lacked resuspension. At the same time, GLU decreased by a factor 2 in VK826 and MC118 while remaining undetectable throughout the erosion experiments with the two AT357 cores (**Table 2**). The non-resuspension control tank with bottom water taken with the CTD at GC600 showed only PEP activities among the three enzymes assayed at levels about one order of magnitude lower than those in the experimental water (**Table 2**).

Bacterial Cell Numbers in Response to Sediment Resuspension

Total bacterial cell numbers in overlying core waters at the beginning of the erosion experiments (after exposure of $u^* = 0.4$ cm s^{-1}) ranged between $1.8*10^7$ (OC26_3) and $13.3*10^7$ (MC118) (**Figure 4**). Bacterial cell numbers remained at the same level (± 20%; GC600, OC26_2, VK826, AT357_1, AT357_2) or decreased by a factor 2 (OC26_3, MC118) between the initial shear stress step and u^*_{crit}. Bacterial cell numbers in the roller tank (SL + SSW) increased during four of the six roller tank incubations (OC26_3, VK826. MC118, GC600) or remained at the same levels compared to those at u^*_{crit} (AT357_1, AT357_2). In contrast, cell numbers at the end of the OC26_2 roller tank incubations were a factor 6 lower compared to those at u^*_{crit}. The non-resuspension control tank with bottom water taken with the CTD at GC600 had $1.3*10^7$ bacterial cells at the end of the incubation (**Figure 4**), which was similar to the OC26_3 tank.

DISCUSSION

Sediment resuspension and subsequent fluxes of sedimentary organic matter into the overlying water play an important role in bottom water elemental cycling. Our two-phased experimental approach was designed to investigate the erosion thresholds and microbial enzymatic responses to experimentally resuspended sediments in deep GOM waters. In addition to providing new insights into benthic-pelagic coupling processes at the investigated sites, our results provide important data for predicting sediment transport in the deep GOM.

The u^*_{crit} values reported here of 1.4 to 1.7 cm s^{-1} correspond to near-bottom flow velocities of 28 to 34 cm s^{-1}, which are in the range of bottom currents reported in the investigation area. Martens et al. (2016) reported peak near-bed currents at MC118 of 20 cm s^{-1}, while near-bed currents at VK826 were found to reach approximately 30 cm s^{-1} (Davies et al., 2010). Shallower nearby sites with water depths around 300 m regularly experience near-bed current velocities of up to 50 cm s^{-1} (Ross et al., 2009). We therefore conclude that bottom water flow velocities in our investigation area regularly exceed critical values for sediment resuspension.

Our u^*_{crit} values for deep GOM sediments are in the same range as those reported for type 2 erosion from other deep-sea environments, characterized by mass or bulk erosion of the seabed (Amos et al., 1992). Using a laboratory flume, Thomsen and van Weering (1998) reported a u^*_{crit} value of 1.60 cm s^{-1} for sediment cores from the deep NE Atlantic Ocean (Goban Spur). Similarly, erosion chamber experiments with deep slope sediments, also from Gobun Spur, revealed u^*_{crit} values up to 2 cm s^{-1} (Thomsen and Gust, 2000). Earlier studies on sediment resuspension in the area of OC26 reported lower u^*_{crit} values than those reported here (0.25–0.8 cm s^{-1}; Diercks et al., 2021, 2018). This lower u^*_{crit} is comparable to values measured for type 1 erosion, which describes resuspension of unconsolidated surficial layers often of biogenic origin (known as fluffy layers) without an appreciable increase in TPM in the water above the sediment (Amos et al., 1992). Resuspension of fluffy layers have been reported at other deep-sea (Beaulieu and Baldwin, 1998; de Jesus Mendes et al., 2007) and coastal water sites (Ziervogel and Bohling, 2003) but not in any of the cores examined in the present study.

The erodibility of marine sediments depends on a combination of sedimentological (e.g., grain size, mineralogy) and biological properties of the benthos (Amos et al., 1992). Surficial sediments from our investigated sites have previously been classified as terrigenous clay (Balsam and Beeson, 2003) with a mud content ranging between 93% (GC600) and 99% (MC118) (Montagna et al., 2013; **Table 1**). Thus, minor variations in sediment grain sizes and mud contents cannot explain the observed differences in erosion behavior between GC600 and our other investigated sites. The GC600 sediment core had visible oil residues in the uppermost layer, presumably from natural seeps in the area. Oil residues stemming from natural seeps episodically reach the seafloor by a variety of pathways at this station (Giering et al., 2018). Moreover, oil and gas seepage in this area have been shown to fuel

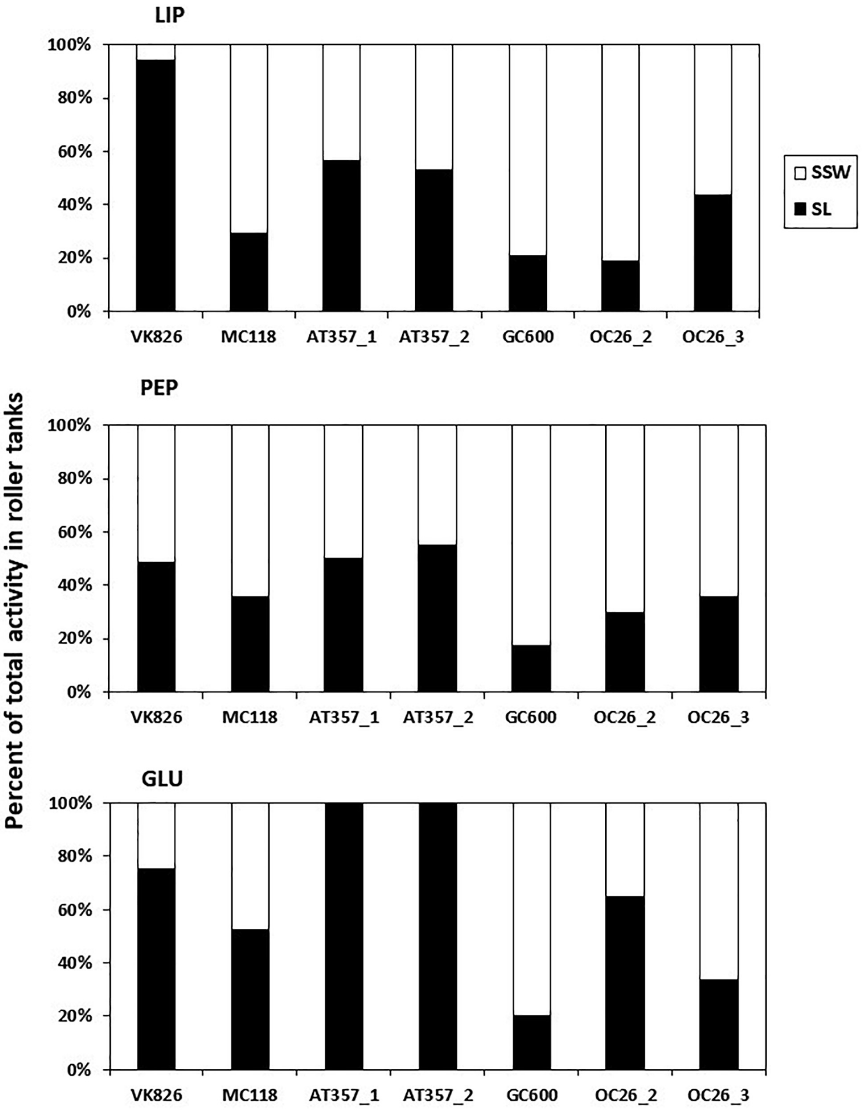

FIGURE 3 | Percent distribution of absolute enzyme activities at the end of roller tank incubations with the partitioning between sediment slurry (SL) and surrounding seawater (SSW). LIP, lipases; PEP, peptidases; GLU, glucosidases.

elevated benthic microbial metabolism (Orcutt et al., 2010). At the time of our sampling, microbial methane oxidation and sulfate reduction rates in surficial sediments at GC600 were orders of magnitude higher compared to sediments from the other investigated sites (Joye, 2016). Enhanced microbial metabolic activities are often coupled with the release of exopolymeric substances (EPS) and the formation of biofilms. EPS interact with sediment particles acting as glue and thus increasing the cohesiveness and stability of the sediment (Tolhurst et al., 2002). In addition, crude oil residues in the GC600 sediment core possibly added to the stability of the sediment, enhancing its physical strength and resistance to erosion.

Additional biological properties that affect sediment stability include macrofaunal burrows and structures such as polychaete tubes that act as biological roughness elements on the near-bed flow (Friedrichs et al., 2000). Polychaete tubes were present in our sediment cores at varying abundance and distribution based on visual observation. Heterogeneity of macrofaunal abundance and their structures, which has been observed in soft sediments at scales of centimeters to meters (Morrisey et al., 1992), may result in small scale variations of erosion thresholds. The latter may in part explain the range of u^*_{crit} among replicate cores observed at OC26 and AT357 (**Figure 2**).

Sediment resuspension in our experimental chamber affected extracellular enzyme activities in overlying waters. Most notable enzymatic responses were found for lipase activities (LIP) that followed increasing TPM in the overlying water in all of the experimentally resuspended cores. The other two enzyme

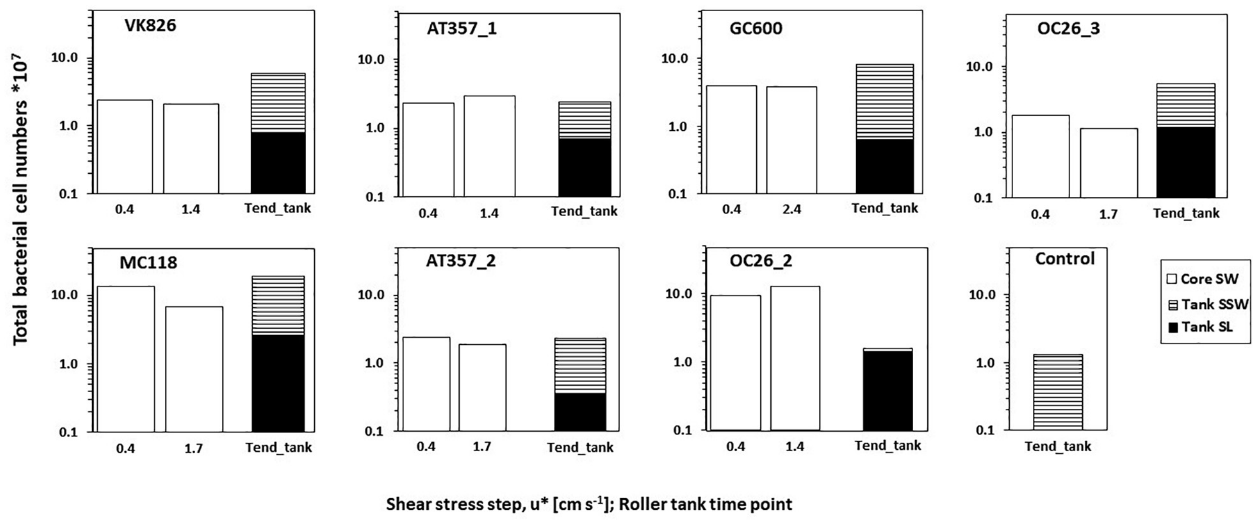

FIGURE 4 | Bacterial cell numbers in the overlying core waters at the initial and final (= u*crit) shear stress step during the erosion experiments (Core SW), and at the end of roller tank incubations (Tend_tank) with the partitioning between sediment slurry (Tank SL) and surrounding seawater (Tank SSW). Cell numbers are standardized for the total volume of either the core water or the tank water.

TABLE 4 | Maximum enhancement as the fold increase of potential enzyme activities in bottom waters affected by resuspension.

Sampling site; water depth; experimental device	LIP	PEP	GLU	References
Northern GOM; 530–1,600 m water depth; erosion chamber	9	9	2.6	This study
Northern GOM – OC26; 1,600 m water depth; bottom water before and after resuspension event	n.a.	4	5	Ziervogel et al., 2016
Coastal Baltic Sea; 4 m water depths; *in situ* enclosures	n.a.	3.5	4	Chrost and Riemann, 1994
Coastal North Atlantic Ocean; intertidal; laboratory flume	n.a.	7	8	Mallet et al., 2014
Coastal Adriatic Sea; 12 m water depth; laboratory mesocosm	n.a.	1.75	1.3	Pusceddu et al., 2005

LIP, lipase; PEP, peptidase; GLU, β -glucosidase. n.a., not available.

activities assayed here (i.e., peptidases [PEP] and glucosidases [GLU]) showed orders of magnitude lower rates and more variable responses to experimentally resuspended sediments compared with LIP.

The order of enzyme activities observed here, with maximum LIP activities, differs from the order of PEP > GLU > LIP frequently observed in surface seawaters (Hoppe and Arnosti, 2002). Somewhat higher LIP activities at rates similar to PEP have been reported for deep ocean sediments (Poremba and Hoppe, 1995). Enhanced LIP activities were also found in the benthic-boundary layer of the deep Arabian Sea (Boetius et al., 2000), supporting the notion that deep-sea sediments may be an important source of lipid hydrolyzing enzymes in near-bed waters.

Refractory organic matter from surface water productivity, which is usually enriched in lipid complexes following sedimentation (Rullkötter, 2006) may stimulate LIP activities in marine sediments. Petroleum hydrocarbons from natural seeps and the DWH fallout that accumulated in surficial sediments in our investigation area following the spill (Romero et al., 2021) represent additional substrates for LIP in the investigated sediments (Kamalanathan et al., 2018). A connection between petroleum hydrocarbons and LIP activities were also found in one of our earlier studies at OC26 where rapid LIP activities reflected degradation of sedimented oily particulate matter (known as marine oil snow) following the DWH oil spill (Ziervogel et al., 2016).

Our results show that sediment resuspension in the northern GOM has the potential to enhance bottom water enzymatic activities by up to one order of magnitude relative to calm conditions. The extent of enzyme activity enhancement observed here is comparable to those reported from earlier field observations at OC26 and other experimental studies conducted in shallow coastal waters (**Table 4**). Increasing enzyme activities following sediment resuspension as in the case of LIP, were not always accompanied by increasing bacterial cell numbers between the beginning and the end of the erosion experiments. This pattern was observed in four of the experimentally resuspended cores for which cell counts were available (**Figure 4**). The disconnect between LIP and bacterial cell numbers in our experiments point to the importance of extracellular enzyme activities dissociated from the cells that produced the enzymes. Cell-free enzymes play an important role in marine elemental cycles (Baltar, 2018), particularly in diffusion-limited environments such as sediments (Vetter et al., 1998). Cell-free enzymes in sediments attach to particles forming sediment-enzyme complexes, which protect the enzymes from degradation and thus enhance their hydrolytic lifetimes relative to dissolved enzymes (Ziervogel et al., 2007). Higher sorption capacities of LIP relative to PEP and GLU with mineral surfaces could preserve the former in sediments, representing an alternative explanation for the elevated LIP activities reported here.

CONCLUSION

Our results from onboard erosion experiments coupled with roller tank incubations reveal the following scenario for benthic-pelagic coupling in our investigation area: Following a resuspension event, hydrolytic enzymes produced by benthic microbes and sorbed to sediment particles get entrained into the overlying water where they remain active over extended periods of time as demonstrated by the high levels of enzyme activities at the end of the roller tank incubations. The magnitude of enzyme activities in roller tanks associated with resuspended sediments, which in most cases was between 40% and 100% of total tank water activities (**Figure 4**), are particularly important considering the fate of sediment-associated hydrolytic activities in near-bed waters. However, resuspended sediments often coagulate and aggregate, resulting in rapid particle redeposition on the seafloor (Thomsen and McCave, 2000). Resuspended particles that remain dispersed in the water, as observed in our 10-hour roller tank experiments, likely experience extended residence times in bottom waters. Field observations from other deep-sea environments reported residence times of bottom water turbidity layers of weeks to months (Puig et al., 2013; Durrieu de Madron et al., 2017; Jia et al., 2019). Lingering 'clouds' of resuspended sediments may stimulate enzymatic breakdown and microbial activity in deep ocean waters that generally exhibit lower microbial metabolic rates compared with those in the upper ocean (Aristegui et al., 2009). Enhanced enzymatic breakdown of resuspended organic matter (e.g., LIP) potentially increases degradation of more refractory sedimentary material, including petroleum hydrocarbons that are abundant in the northern GOM.

DATA AVAILABILITY STATEMENT

The data presented in this study are publicly available through the Gulf of Mexico Research Initiative Information & Data Cooperative (GRIIDC) at https://data.gulfresearchinitiative.org/data/R4.x268.000:0101.

AUTHOR CONTRIBUTIONS

KZ, JS, and UP planned the research. KZ and JS carried out the shipboard experiments with AJ who conducted the flowcytometry measurements. KZ wrote the manuscript with input from all co-authors. All authors contributed to the article and approved the submitted version.

FUNDING

Funding was provided by a grant from BP/the Gulf of Mexico Research Initiative to support the ECOGIG research consortium administered by the University of Georgia. This is ECOGIG contribution # 572.

ACKNOWLEDGMENTS

We thank the captain and crew of the RV Endeavor cruise 527 as well as chief scientist Joe Montoya (Georgia Tech) for assistance during sampling. We also thank Carol Arnosti (UNC) who gave invaluable advice during planning of the experiments, Tracy Villareal (UTex) who let us use his flow cytometer at sea, and Linda Kalnejais (UNH) who provided the EROMES chamber.

REFERENCES

Amos, C. L., Daborn, G. R., Christian, H. A., Atkinson, A., and Robertson, A. (1992). In situ erosion measurements on fine-grained sediments from the Bay of Fundy. *Mar. Geol.* 108, 175–196. doi: 10.1016/0025-3227(92)90171-D

Aristegui, J., Gasol, J. M., Duarte, C. M., and Herndl, G. J. (2009). Microbial oceanography of the dark ocean's pelagic realm. *Limnol. Oceanogr.* 54, 1501–1529. doi: 10.4319/lo.2009.54.5.1501

Arnosti, C. (2011). Microbial extracellular enzymes and the marine carbon cycle. *Annu. Rev. Mar. Sci.* 3, 401–425. doi: 10.1146/annurev-marine-120709-142731

Atlas, R. M., and Hazen, T. C. (2011). Oil biodegradation and bioremediation: a tale of the two worst spills in US history. *Environ. Sci. Technol.* 45, 6709–6715. doi: 10.1021/es2013227

Balsam, W. L., and Beeson, J. P. (2003). Sea-floor sediment distribution in the Gulf of Mexico. *Deep Sea Res. Part Oceanogr. Res. Pap.* 50, 1421–1444. doi: 10.1016/j.dsr.2003.06.001

Baltar, F. (2018). Watch out for the "living dead": cell-free enzymes and their fate. *Front. Microbiol.* 8:2438. doi: 10.3389/fmicb.2017.02438

Baltar, F., Arístegui, J., Sintes, E., Gasol, J. M., Reinthaler, T., and Herndl, G. J. (2010). Significance of non-sinking particulate organic carbon and dark CO2 fixation to heterotrophic carbon demand in the mesopelagic northeast Atlantic. *Geophys. Res. Lett.* 37, 1–6. doi: 10.1029/2010GL043105

Beaulieu, S., and Baldwin, R. (1998). Temporal variability in currents and the benthic boundary layer at an abyssal station off central California. *Deep Sea Res. Part II Top. Stud. Oceanogr.* 45, 587–615. doi: 10.1016/S0967-0645(97)00095-7

Boetius, A., Springer, B., and Petry, C. (2000). Microbial activity and particulate matter in the benthic nepheloid layer (BNL) of the deep Arabian Sea. *Deep-Sea Res. Part Ii-Top. Stud. Oceanogr.* 47, 2687–2706. doi: 10.1016/S0967-0645(00)00045-X

Chanton, J., Zhao, T., Rosenheim, B. E., Joye, S., Bosman, S., Brunner, C., et al. (2015). Using natural abundance radiocarbon to trace the flux of petrocarbon to the seafloor following the deepwater horizon oil spill. *Environ. Sci. Technol.* 49, 847–854. doi: 10.1021/es5046524

Chrost, R. J., and Riemann, B. (1994). Storm-stimulated enzymatic decomposition of organicmatter in benthic/pelagic coastal mesocosms. *Mar. Ecol.-Prog. Ser.* 108, 185–192. doi: 10.3354/meps108185

Conti, A., D'Emidio, M., Macelloni, L., Lutken, C., Asper, V., Woolsey, M., et al. (2016). Morpho-acoustic characterization of natural seepage features near the Macondo Wellhead (ECOGIG site OC26, Gulf of Mexico). *Deep Sea Res. Part II Top. Stud. Oceanogr.* 129, 53–65. doi: 10.1016/j.dsr2.2015.11.011

Davies, A. J., Duineveld, G. C. A., van Weering, T. C. E., Mienis, F., Quattrini, A. M., Seim, H. E., et al. (2010). Short-term environmental variability in cold-water coral habitat at Viosca Knoll, Gulf of Mexico. *Deep Sea Res. Part Oceanogr. Res. Pap.* 57, 199–212. doi: 10.1016/j.dsr.2009.10.012

de Jesus Mendes, P. A., Thomsen, L., Holscher, B., de Stigter, H. C., and Gust, G. (2007). Pressure effects on the biological degradation of organo-mineral aggregates in submarine canyons. *Mar. Geol.* 246, 165–175. doi: 10.1016/j.margeo.2007.05.012

Diercks, A.-R., Dike, C., Asper, V. L., DiMarco, S. F., Chanton, J. P., and Passow, U. (2018). Scales of seafloor sediment resuspension in the northern Gulf of Mexico. *Elem. Sci. Anthr.* 6:32. doi: 10.1525/elementa.285

Diercks, A. R., Romero, I. C., Larson, R. A., Schwing, P., Harris, A., Bosman, S., et al. (2021). Resuspension, redistribution, and deposition of oil-residues to offshore depocenters after the deepwater horizon oil spill. *Front. Mar. Sci.* 8:630183. doi: 10.3389/fmars.2021.630183

Durrieu, de Madron, X., Ramondenc, S., Berline, L., Houpert, L., Bosse, A., et al. (2017). Deep sediment resuspension and thick nepheloid layer generation by open-ocean convection. *J. Geophys. Res. Oceans* 122, 2291–2318. doi: 10.1002/2016JC012062

Dyer, K. R. (1986). *Coastal and Estuarine Sediment Dynamics.* New York, NY: Wiley Interscience Publication.

Fisher, C. R., Hsing, P.-Y., Kaiser, C. L., Yoerger, D. R., Roberts, H. H., Shedd, W. W., et al. (2014). Footprint of Deepwater Horizon blowout impact to deep-water coral communities. *Proc. Natl. Acad. Sci. U S A.* 111, 11744–11749. doi: 10.1073/pnas.1403492111

Friedrichs, M., Graf, G., and Springer, B. (2000). Skimming flow induced over a simulated polychaete tube lawn at low population densities. *Mar. Ecol. Prog. Ser.* 192, 219–228. doi: 10.3354/meps192219

Gasol, J. M., and Del Giorgio, P. A. (2000). Using flow cytometry for counting natural planktonic bacteria and understanding the structure of planktonic bacterial communities. *Sci. Mar.* 64, 197–224. doi: 10.3989/scimar.2000.64n2197

Giering, S. L. C., Yan, B., Sweet, J., Asper, V., Diercks, A., Chanton, J. P., et al. (2018). The ecosystem baseline for particle flux in the Northern Gulf of Mexico. *Elem. Sci. Anthr.* 6:6. doi: 10.1525/elementa.264

Graf, G. (1992). Benthic-pelagic coupling - a benthic view. *Oceanogr. Mar. Biol.* 30, 149–190. doi: 10.1007/s11356-015-4997-2

Griffiths, J. R., Kadin, M., Nascimento, F. J. A., Tamelander, T., Törnroos, A., Bonaglia, S., et al. (2017). The importance of benthic–pelagic coupling for marine ecosystem functioning in a changing world. *Glob. Change Biol.* 23, 2179–2196. doi: 10.1111/gcb.13642

Hoppe, H.-G. (1983). Significance of exoenzymatic activities in the ecology of brackish water: measurements by means of methylumbelliferyl-substrates. *Mar. Ecol. Prog. Ser.* 11, 299–308. doi: 10.3354/meps011299

Hoppe, H.-G., and Arnosti, C. (2002). "Ecological significance of bacterial enzymes in the marine environment," in *Enzymes in the Environment,* eds R. G. Burns, and R. P. Dick (New York, NY: Marcel Dekker), 73–97.

Jia, Y., Tian, Z., Shi, X., Liu, J. P., Chen, J., Liu, X., et al. (2019). Deep-sea sediment resuspension by internal solitary waves in the Northern South China sea. *Sci. Rep.* 9:12137. doi: 10.1038/s41598-019-47886-y

Joye, S. (2016). *R/V Endeavor: EN527 Water and Sediment Chemistry, Gulf of Mexico, June 20 – July 2, 2013.* Gulf of Mexico Research Initiative Information and Data Cooperative (GRIIDC). Available online at: https://data.gulfresearchinitiative.org/data/R1.x132.134:0026

Kalnejais, L. H., Martin, W. R., Signell, R. P., and Bothner, M. H. (2007). Role of sediment resuspension in the remobilization of particulate-phase metals from coastal sediments. *Environ. Sci. Technol.* 41, 2282–2288. doi: 10.1021/es061770z

Kamalanathan, M., Xu, C., Schwehr, K., Bretherton, L., Beaver, M., Doyle, S. M., et al. (2018). Extracellular enzyme activity profile in a chemically enhanced water accommodated fraction of surrogate oil: toward understanding microbial activities after the deepwater horizon oil spill. *Front. Microbiol.* 9:798. doi: 10.3389/fmicb.2018.00798

Knap, A. H. (2002). *Manual of Methods used in JGOFS.* Los Angeles, CA: Pangaea.

MacDonald, I. R., Garcia-Pineda, O., Beet, A., Asl, S. D., Feng, L., Graettinger, G., et al. (2015). Natural and unnatural oil slicks in the Gulf of Mexico. *J. Geophys. Res. Oceans* 120, 8364–8380. doi: 10.1002/2015JC011062

Mallet, C., Agogué, H., Bonnemoy, F., Guizien, K., Orvain, F., and Dupuy, C. (2014). Structures of benthic prokaryotic communities and their hydrolytic enzyme activities resuspended from samples of intertidal mudflats: an experimental approach. *Trophic Significance Microb. Biofilm Tidal Flats* 92, 158–169. doi: 10.1016/j.seares.2014.01.005

Margesin, R., Zimmerbauer, A., and Schinner, F. (1999). Soil lipase activity – a useful indicator of oil biodegradation. *Biotechnol. Tech.* 13, 859–863. doi: 10.1023/A:1008928308695

Martens, C. S., Mendlovitz, H. P., Seim, H., Lapham, L., and D'Emidio, M. (2016). Sustained in situ measurements of dissolved oxygen, methane and water transport processes in the benthic boundary layer at MC118, northern Gulf of Mexico. *Gulf Mex. Ecosyst. - Macondo Blowout* 129, 41–52. doi: 10.1016/j.dsr2.2015.11.012

Mislan, M., and Gates, I. D. (2019). Release of sugars and fatty acids from heavy oil biodegradation by common hydrolytic enzymes. *Sci. Rep.* 9:15584. doi: 10.1038/s41598-019-51796-4

Montagna, P. A., Baguley, J. G., Cooksey, C., and Hyland, J. L. (2013). *Deepwater Horizon Oil Spill: Assessment of Potential Impacts on the Deep Soft-Bottom Benthos. Interim Data Summary Report. NOAA Technical Memorandum NOS NCCOS 166.* Charleston, SC: NOAA, National Centers for Coastal Ocean Science.

Morrisey, D. J., Howitt, L., Underwood, A. J., and Stark, J. S. (1992). Spatial variation in soft-sediment benthos. *Mar. Ecol. Prog. Ser.* 81, 197–204. doi: 10.3354/meps081197

Orcutt, B. N., Joye, S. B., Kleindienst, S., Knittel, K., Ramette, A., Reitz, A., et al. (2010). Impact of natural oil and higher hydrocarbons on microbial diversity, distribution, and activity in Gulf of Mexico cold-seep sediments. *Gulf Mex. Cold Seeps* 57, 2008–2021. doi: 10.1016/j.dsr2.2010.05.014

Pfannkuche, O. (1993). Benthic response to the sedimentation of particulate organic matter at the BIOTRANS station, 47°N, 20°W. *Deep Sea Res. Part II Top. Stud. Oceanogr.* 40, 135–149. doi: 10.1016/0967-0645(93)90010-K

Ploug, H., Terbrüggen, A., Kaufmann, A., Wolf-Gladrow, D., and Passow, U. (2010). A novel method to measure particle sinking velocity in vitro, and its comparison to three other in vitro methods. *Limnol. Oceanogr. Methods* 8, 386–393. doi: 10.4319/lom.2010.8.386

Poremba, K., and Hoppe, H.-G. (1995). Spatial variation of benthic microbial production and hydrolytic enzymatic activity down the continental slope of the Celtic Sea. *Mar. Ecol. Prog. Ser.* 118, 237–245. doi: 10.3354/meps118237

Puig, P., de Madron, X. D., Salat, J., Schroeder, K., Martin, J., Karageorgis, A. P., et al. (2013). Thick bottom nepheloid layers in the western Mediterranean generated by deep dense shelf water cascading. *Prog. Oceanogr.* 111, 1–23. doi: 10.1016/j.pocean.2012.10.003

Pusceddu, A., Fiordelmondo, C., and Danovaro, R. (2005). Sediment resuspension effects on the benthic microbial loop in experimental microcosms. *Microb. Ecol.* 50, 602–613. doi: 10.1007/s00248-005-5051-6

Ritzrau, W. (1996). Microbial activity in the benthic boundary layer: small-scale distribution and its relationship to the hydrodynamic regime. *J. Sea Res.* 36, 171–180.

Ritzrau, W., and Graf, G. (1992). Increase of microbial biomass in the benthic turbidity zone of kiel bight after resuspension by a storm event. *Limnol. Oceanogr.* 37, 1081–1086. doi: 10.4319/lo.1992.37.5.1081

Ritzrau, W., Thomsen, L., Lara, R. J., and Graf, G. (1997). Enhanced microbial utilisation of dissolved amino acids indicates rapid modification of organic matter in the benthic boundary layer. *Mar. Ecol. Prog. Ser.* 156, 43–50. doi: 10.3354/meps156043

Romero, I. C., Chanton, J. P., Brooks, G. R., Bosman, S., Larson, R. A., Harris, A., et al. (2021). Molecular markers of biogenic and oil-derived hydrocarbons in deep-sea sediments following the deepwater horizon spill. *Front. Mar. Sci.* 8:637970. doi: 10.3389/fmars.2021.637970

Ross, C. B., Gardner, W. D., Richardson, M. J., and Asper, V. L. (2009). Currents and sediment transport in the mississippi canyon and effects of hurricane georges. *Cont. Shelf Res.* 29, 1384–1396. doi: 10.1016/j.csr.2009.03.002

Rullkötter, J. (2006). "Organic matter: the driving force of early diagenesis," in *Marine Geochemistry,* 2 Edn. eds H. D. Schulz, and M. Zabel (Berlin: Springer-Verlag), 125–186.

Shanks, A. L., and Edmondson, E. W. (1989). Laboratory-made artificial marine snow: a biological model of the real thing. *Mar. Biol.* 101, 463–470. doi: 10.1007/bf00541648

Soulsby, R. L., and Whitehouse, R. (1997). "Threshold of sediment motion in coastal environments," in *Proceedings of the Pacific Coasts and Ports '97 Conference,* Vol. 1, (Christchurch: University of Canterbury), 149–154.

Thomsen, L., and Gust, G. (2000). Sediment erosion thresholds and characteristics of resuspended aggregates on the western European continental margin. *Deep*

Sea Res. Part Oceanogr. Res. Pap. 47, 1881–1897. doi: 10.1016/S0967-0637(00)00003-0

Thomsen, L., and van Weering, T. (1998). Spatial and temporal variability of particulate matter in the benthic boundary layer at the N.W. European Continental Margin (Goban Spur). *Prog. Oceanogr.* 42, 61–76. doi: 10.1016/S0079-6611(98)00028-7

Thomsen, L. A., and McCave, I. N. (2000). Aggregation processes in the benthic boundary layer at the Celtic Sea continental margin. *Deep-Sea Res. Part - Oceanogr. Res. Pap.* 47, 1389–1404. doi: 10.1016/S0967-0637(99)00110-7

Tolhurst, T., Gust, G., and Paterson, D. M. (2002). "The influence of an extracellular polymeric substance (EPS) on cohesive sediment stability," in *Fine Sediment Dynamics in the Marine Environment, Proceedings in Marine Science Series*, eds J. Winterwerp and C. Kranenburg (Pergamon: Elsevier inc), 409–425. doi: 10.1016/s1568-2692(02)80030-4

Turley, C. (2000). Bacteria in the cold deep-sea benthic boundary layer and sediment-water interface of the NE Atlantic. *FEMS Microbiol. Ecol.* 33, 89–99. doi: 10.1016/S0168-6496(00)00058-1

Unanue, M. A., Azua, I., Arrieta, J. M., Herndl, G. J., and Iriberri, J. (1998). Laboratory-made particles as a useful approach to analyse microbial processes in marine macroaggregates. *FEMS Microbiol. Ecol.* 26, 325–334. doi: 10.1111/j.1574-6941.1998.tb00517.x

Vetter, Y. A., Deming, J. W., Jumars, P. A., and Kreiger-Brockett, B. B. (1998). A predictive model of bacterial foraging by means of freely released extracellular enzymes. *Microb. Ecol.* 36, 75–92. doi: 10.1007/s002489900095

Wainright, S. C. (1987). Stimulation of heterotrophic microplankton production by resuspended marine sediments. *Science* 238, 1710–1712. doi: 10.1126/science.238.4834.1710

White, H. K., Hsing, P.-Y., Cho, W., Shank, T. M., Cordes, E. E., Quattrini, A. M., et al. (2012). Impact of the deepwater horizon oil spill on a deep-water coral community in the Gulf of Mexico. *Proc. Natl. Acad. Sci. U S A.* 109:20303. doi: 10.1073/pnas.1118029109

Zhao, Z., Baltar, F., and Herndl, G. J. (2020). Linking extracellular enzymes to phylogeny indicates a predominantly particle-associated lifestyle of deep-sea prokaryotes. *Sci. Adv.* 6:eaaz4354. doi: 10.1126/sciadv.aaz4354

Ziervogel, K., and Arnosti, C. (2009). Enzyme activities in the Delaware Estuary affected by elevated suspended sediment load. *Estuar. Coast. Shelf Sci.* 84, 253–258. doi: 10.1016/j.ecss.2009.06.022

Ziervogel, K., and Bohling, B. (2003). Sedimentological parameters and erosion behaviour of submarine coastal sediments in the south-western Baltic Sea. *Geo-Mar. Lett.* 23, 43–52. doi: 10.1007/s00367-003-0123-4

Ziervogel, K., Dike, C., Asper, V., Montoya, J., Battles, J., D×Souza, N., et al. (2016). Enhanced particle fluxes and heterotrophic bacterial activities in Gulf of Mexico bottom waters following storm-induced sediment resuspension. *Deep Sea Res. Part II Top. Stud. Oceanogr* 129, 77–88. doi: 10.1016/j.dsr2.2015.06.017

Ziervogel, K., D'souza, N., Sweet, J., Yan, B., and Passow, U. (2014). Natural oil slicks fuel surface water microbial activities in the northern Gulf of Mexico. *Front. Microbiol.* 5:188. doi: 10.3389/fmicb.2014.00188

Ziervogel, K., Karlsson, E., and Arnosti, C. (2007). Surface associations of enzymes and of organic matter: consequences for hydrolytic activity and organic matter remineralization in marine systems. *Mar. Chem.* 104, 241–252. doi: 10.1016/j.marchem.2006.12.001

Conflict of Interest: The authors declare that the research was conducted in the absence of any commercial or financial relationships that could be construed as a potential conflict of interest.

Advantages of publishing in Frontiers

OPEN ACCESS
Articles are free to read
for greatest visibility
and readership

FAST PUBLICATION
Around 90 days
from submission
to decision

HIGH QUALITY PEER-REVIEW
Rigorous, collaborative,
and constructive
peer-review

TRANSPARENT PEER-REVIEW
Editors and reviewers
acknowledged by name
on published articles

Frontiers
Avenue du Tribunal-Fédéral 34
1005 Lausanne | Switzerland

Visit us: www.frontiersin.org
Contact us: frontiersin.org/about/contact

REPRODUCIBILITY OF RESEARCH
Support open data
and methods to enhance
research reproducibility

DIGITAL PUBLISHING
Articles designed
for optimal readership
across devices

FOLLOW US
@frontiersin

IMPACT METRICS
Advanced article metrics
track visibility across
digital media

EXTENSIVE PROMOTION
Marketing
and promotion
of impactful research

LOOP RESEARCH NETWORK
Our network
increases your
article's readership